Lecture Notes in Electrical Engineering 296

Jinsong Wang
Editor

Proceedings of the First Symposium on Aviation Maintenance and Management-Volume I

Springer

Lecture Notes in Electrical Engineering

Volume 296

For further volumes:
http://www.springer.com/series/7818

About this Series

"Lecture Notes in Electrical Engineering (LNEE)" is a book series which reports the latest research and developments in Electrical Engineering, namely:

- Communication, Networks, and Information Theory
- Computer Engineering
- Signal, Image, Speech and Information Processing
- Circuits and Systems
- Bioengineering

LNEE publishes authored monographs and contributed volumes which present cutting edge research information as well as new perspectives on classical fields, while maintaining Springer's high standards of academic excellence. Also considered for publication are lecture materials, proceedings, and other related materials of exceptionally high quality and interest. The subject matter should be original and timely, reporting the latest research and developments in all areas of electrical engineering.

The audience for the books in LNEE consists of advanced level students, researchers, and industry professionals working at the forefront of their fields. Much like Springer's other Lecture Notes series, LNEE will be distributed through Springer's print and electronic publishing channels.

Jinsong Wang
Editor

Proceedings of the First Symposium on Aviation Maintenance and Management-Volume I

Springer

Editor
Jinsong Wang
Northwestern Polytechnical University
Xi'an
People's Republic of China

ISSN 1876-1100 ISSN 1876-1119 (electronic)
ISBN 978-3-642-54235-0 ISBN 978-3-642-54236-7 (eBook)
DOI 10.1007/978-3-642-54236-7
Springer Heidelberg New York Dordrecht London

Library of Congress Control Number: 2014931982

Printed on acid-free paper

Springer is part of Springer Science+Business Media (www.springer.com)

Preface

Proceedings of the First Symposium on Aviation Maintenance and Management collects selected papers from the First Symposium on Aviation Maintenance and Management in China held in Xi'an on November 25–28, 2013. The book features state-of-the-art studies on aviation maintenance, test, fault diagnosis, and prognosis of aircraft electronic and electrical systems. The selected works can help promote development of maintenance and test technology towards the important and complex systems of aircraft. Researchers and engineers in the field of electrical engineering and aerospace engineering can benefit from the book.

We received 265 complete submissions, the largest number of submissions in the domain of aircraft maintenance. Thirty excellent papers were selected for oral presentation and 117 papers for poster presentation, resulting in acceptance rates of 11.3 % for oral, 44.2 % for poster, and 55.5 % in total.

The following is a brief description of the review process. After the submission deadline, each paper was assigned to one member of the Program Committee with the help of keyword searching system. Each member then made reviewer suggestions (an average of five per paper), which were load-balanced and conflict-resolved, giving two reviewers for each paper and a maximum of ten papers per previewer. For the decision process, members of the Program Committee met in Northwestern Polytechnical University. They read the reviews and consolidation reports, jointly discussed all the submitted papers, and made acceptance\acceptance with revision\rejection decisions. They also recommended a small number of top-ranked papers for oral presentation, and made final oral and poster decisions.

We wish to thank everyone involved for their valuable time and dedication to making this conference possible, including authors who produced high-quality research, reviewers who gave professional comments, and committee members who made important decisions. The success of the conference entirely relied on their time and effort.

December 2013 Jinsong Wang

Committee

Editors

Jinsong Wang, Professor, Northwestern Polytechnical University, China
Jianping Yuan, Professor, Northwestern Polytechnical University, China

Program Committee Member

Weixin Wu, Professor, Beijing Aviation Technical Research Center, China
Feng Liu, Professor, Beijing Aviation Technical Research Center, China
Bifeng Song, Professor, Northwestern Polytechnical University, China
Guoqing Wang, Professor, Chinese Aeronautical Radio Electronics Research Institute, China
Mingyuan Jiang, Professor, Air Force Command College, China
Yujun Fu, Professor, Army Air Force College, China
Xueren Li, Professor, Air Force Engineering University, China
Changchun Deng, Professor, Aviation University of Air Force, China
Jianhua Zhang, Professor, First Aviation Academy of Chinese Air Force, China
Benwei Li, Professor, Naval Aviation Engineering Institute, China
Jun Diao, Professor, Naval Aviation Engineering Institute, China
Suguang Dong, Professor, China Southern Airlines, China
Yuliang Hu, Professor, Aircraft Maintenance and Engineering Corporation, China
Jie Bai, Professor, Civil Aviation University of China, China
Zuo Yang, Professor, Beijing Institute of Technology, China
Xicheng Chen, Professor, Shenyang Aircraft Design and Research Institute, China
Haifeng Wang, Professor, Chengdu Aircraft Design and Research Institute, China
Zhenguang Mou, Professor, AVIC Shenyang Aircraft Corporation, China
Wensheng Jiang, Professor, AVIC Chengdu Aircraft Corporation, China
Zheng Li, Professor, AVIC Chengdu Aero-Engine Corporation, China
Ge Gao, Professor, AVIC Liming Aero-Engine Corporation, China
Xiping Zhang, Professor, China Flight Test Establishment, China
Qiang Fu, Senior Engineer, AVIC Information Technology Co. Ltd, China

Ansheng Hou, Senior Engineer, AVIC Information Technology Co. Ltd, China
Cunbao Ma, Professor, Northwestern Polytechnical University, China
Haitao Wang, Associate Professor, Northwestern Polytechnical University, China
Zhenbao Liu, Associate Professor, Northwestern Polytechnical University, China
Hongkai Jiang, Associate Professor, Northwestern Polytechnical University, China
Shuhui Bu, Associate Professor, Northwestern Polytechnical University, China
Yong Zhou, Associate Professor, Northwestern Polytechnical University, China

Invited Keynote Speakers

Michael Pecht, Professor, University of Maryland, USA
Brian G. Falzon, Professor, Queen's University Belfast, UK
Guoqing Wang, Director, China Aeronautical Radio Electronics Research Institute, China
Andrei Zagrai, Associate Professor, New Mexico Institute of Mining and Technology, USA
Chuanjun Liu, Professor, Commercial Aircraft Corporation of China, China

Contents

Chapter 1
Study of Airplane Engine Temperature Measurement System Through Lasers and Pyroelectric Detector

Yuan-Fei Xia, Xue-Yuan Li and Qiang Ren

Abstract Thermoelectric couple was employed in traditional airplane engine nozzle temperature measurement system with the disadvantages of large size, heavy weight, big error, and slow response. This paper presents a new kind of real-time temperature measurement system using laser diode InGaAs/I as light source, and using pyroelectric detector LiTa03 as an optical receiving unit and using a microprocessor as signal processing center. This instrument consists of three parts: optical emitting and receiving system, signal amplifying and controlling system, and display system. The principle, structure, and anti-interference measurement of the system are introduced. Experimental results of airplane engine real-time temperature measurement show that temperature measurement accuracy and response time conform to our requirement in the range of 300–800 °C and agree with prediction of theory. All these prove that the design is correct.

Keywords Thermoelectric detector · Temperature measurement · Laser diode · Real-time measurement · Temperature measurement by radiation

1.1 Introduction

As the heart of airplane, engine is in a very important position. Its performance seriously affects flight safety and operational tasks. Airplane engine failure is characterized by temperature deviation from the specified value, so the airplane engine operating temperature real-time online monitoring is very important.

Y.-F. Xia (✉) · X.-Y. Li · Q. Ren
The First Aeronautic Institute of Air Force, No.23 HangKong Rd, Xinyang, Henan, China
e-mail: xiayuanfei1965@sina.com

X.-Y. Li
e-mail: lixueyuan1966@163.com

Q. Ren
e-mail: ren001@sina.com

J. Wang (ed.), *Proceedings of the First Symposium on Aviation Maintenance and Management-Volume I*, Lecture Notes in Electrical Engineering 296,
DOI: 10.1007/978-3-642-54236-7_1,

Airplane engine operating temperature can be measured in two ways: contact and noncontact temperature measurement. For noncontact radiation thermometry is concerned, can be achieved by two means: passive and active radiation thermometry. Airplane engine herein real-time measurement system, is a typical active radiation measurement system. Because it uses the diode laser InGaAs/I (wavelength 2 μm) as a measurement light source, it can real time, accurately measure the true temperature of target engine's exhaust gas, and has a high accuracy. Furthermore, it uses lithium tantalate pyroelectric detector as light receiving device, which overcomes the drawbacks of low sensitivity when measuring temperature below 600 °C when using PIN photodiode as light receiving device in conventional laser thermometer, and has good application prospects.

High-power laser diode in the military, industrial, and medical applications is critical, so a lot of work has been put into the high-power laser diode structure design and performance optimization studies, so that the device can try to meet the high beam quality, high efficiency, low loss, high reliability and small size, and other conditions. Study found that in the real-time temperature measurement system taking lithium tantalate pyroelectric detector as photoelectric conversion devices, and InGaAs/I diode laser as the light source, which designed by the author, the system's temperature measurement uncertainty is affected by the laser wavelength (operating wavelength of the thermometer) and the emission energy, bandwidth of the thermometer operating wavelength, bandwidth of frequency-selective amplification circuit, the detector sensitive element area, the relative aperture of the optical system, and system parameters such as anti-jamming capability, etc. Therefore, these parameters must be optimally designed. Documents [1–3] studied the best working wavelength of the instruments, bandwidth, the best light source, and other technical parameters (including the choice of detector, the bandwidth of frequency-selective amplifying circuit and the optical system relative aperture, etc.). In order to improve anti-jamming capability of measurement system, this paper analyzes the sources of interference, and constructs passive and negative interference mathematical model based on different electromagnet interference, and presented its corresponding suppression measures to optimize the design of the new filter. The experimental result verified that the temperature stability of the system meets the design requirements [1–3].

1.2 Basic Principle

The basic principle of the system is shown in Fig. 1.1.

Under the working state, the diode laser and the detector probe were placed symmetrically on both sides of the surface normal. When no laser beam entered the detection probe, the detector receives only the radiation energy P_1 from target.

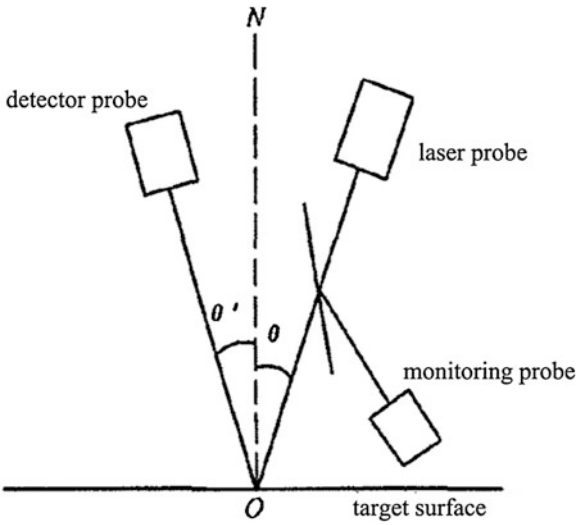

Fig. 1.1 Position of laser and detector

$$P_1 = \frac{\pi}{4}\left(\frac{D}{f'}\right)\tau_0 A\eta \int_{\lambda_1}^{\lambda_2} \varepsilon_\lambda \tau_\lambda L_\lambda \mathrm{d}\lambda \tag{1.1}$$

where: D is aperture; f' is the focal length of the optical system; τ_0 is the atmospheric transmission coefficient; A is sensitive element of the detector area; η is the modulation factor of the modulation disk; ε_λ is the emission rate on wavelength λ of the target with temperature T; L_λ is the monochromatic radiation energy on wavelength λ of a blackbody with temperature T; τ_λ is the total transmittance rate of the optical system for the light λ.

When the laser beam enters the detection probe, the energy P_2 received by the detection probe consists of two parts: laser energy reflected by the target and infrared energy radiated by the target:

$$P_2 = \frac{\pi}{4}\left(\frac{D}{f'}\right)^2 \tau_0 A\eta \int_{\lambda_1}^{\lambda_2} \varepsilon_\lambda \tau_\lambda L_\lambda \mathrm{d}\lambda + \frac{\pi}{4}\left(\frac{D}{f'}\right)^2 \tau_0 A\eta \int_{\lambda_1}^{\lambda_2} \lambda\beta\tau_\lambda E_\lambda \mathrm{d}\lambda \tag{1.2}$$

where: λ is the reflect rate of the target surface; β is the optical correction coefficient of the specular reflection properties of the test target surface; E_λ is the monochromatic laser energy of the incident target surface.

By the Kirchhoff's law, there is

$$\gamma = 1 - \varepsilon_\lambda. \tag{1.3}$$

Within a very narrow band ($\triangle\lambda = 10$ nm), ε_λ and τ_λ can be considered independent of wavelength. For the same surface, the optical correction coefficient β of the mirror reflection characteristics is a constant. Accordingly, the formulae (1.1) and (1.2) can be simplified as:

$$P_1 = \frac{\pi}{4}\left(\frac{D}{f'}\right)\tau_0 A\eta\varepsilon_\lambda\tau_\lambda\int_{\lambda_1}^{\lambda_2} L_\lambda \mathrm{d}\lambda \tag{1.4}$$

$$P_2 = \frac{\pi}{4}\left(\frac{D}{f'}\right)^2\tau_0 A\eta\varepsilon_\lambda\tau_\lambda\int_{\lambda_1}^{\lambda_2} L_\lambda \mathrm{d}\lambda + \frac{\pi}{4}\left(\frac{D}{f'}\right)^2\tau_0 A\eta\lambda\beta\tau_\lambda\int_{\lambda_1}^{\lambda_2} E_\lambda \mathrm{d}\lambda \tag{1.5}$$

The formula (1.4) and formula (1.5) can derive:

$$\varepsilon_\lambda = 1 - \frac{4f'^2(P_2 - P_1)}{\pi D^2\tau_0 A\eta\tau_\lambda\beta P_3} \tag{1.6}$$

The formula:

$$P_3 = \int_{\lambda_1}^{\lambda_2} E_\lambda \mathrm{d}\lambda \tag{1.7}$$

The incident target surface laser energy monitored by the monitoring probe is combined with the blackbody radiation formula:

$$L_\lambda = 2\pi hc^2\lambda^{-5}\left[\exp\left(\frac{hc}{\lambda kT}\right) - 1\right]^{-1} \tag{1.8}$$

The target temperature can be measured. In formula (1.8), h is the Planck constant; k is the Boltzmann constant; c is the speed of light.

Combined formula (1.4) can be derived:

$$P_1 = \frac{\pi^2}{2}\left(\frac{D}{f'}\right)^2\tau_0 A\eta\varepsilon_\lambda\tau_\lambda hc^2\int_{\lambda_1}^{\lambda_2}\lambda^{-5}\left[\exp\left(\frac{hc}{\lambda kT}\right) - 1\right]^{-1} d\lambda \tag{1.9}$$

Formula (1.9) can be solved by a variety of methods. Therefore, as long as ε_λ is obtained from the formula (1.6), the temperature T_0 [4, 5] can be obtained by using formula (1.9).

1.3 System Implementation

System structure diagram is shown in Fig. 1.2.

When the temperature measurement system is running, the continuous laser beam produced by the diode laser first collimated by collimating lens, expanded by the beam expander, modulated to pulse laser beam by modulate disk, then launched after split by the beam splitter. On the one hand, after modulation and filtering by modulation plate, optical signal received by the detection receiver lens was converted to electrical signal by the photoelectric conversion system composed of lithium tantalate pyroelectric detector (detection probe). This signal is

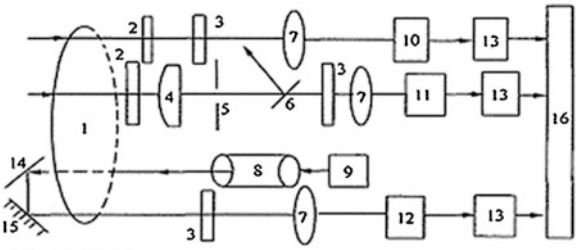

Fig. 1.2 The system structure diagram

1.Modulate Plate;
2.Protection window;
3.Narrow band interfere filter;
4.Objective;
5.Aperture diaphragm;
6.Field diaphragm;
7.Focusing lens;
8.Collimation and beam expander lens group;
9.Diode laser;
10.Sync Detector;
11.Detector probe;
12.Monitoring probe;
13.Signal amplifier and processing circuit;
14.Beam Splitter;
15.Holophote;
16.SCM system

preamplified, frequency-selective amplification, pulse compression, and A/D converted into the SCM system; On the other hand, part of the laser beam split by the beam splitter, is also converted to electrical signal by photoelectric conversion system composed of the lithium tantalate detector (monitoring detector) after filtered by the narrow band interference filter. After being amplified and A/D converted, this signal is also entered into the SCM system to standardize the emitting energy of the laser source [6, 7].

All triggering and synchronization of the various signals in the circuit are generated by the synchronous optical system. The optical signal passing through the synchronization filter mounted on the modulate plate is converted to electric signal directly via the photoelectric conversion system composed of lithium tantalate pyroelectric detector, and then transmitted into the SCM after amplification by shaping amplifier system. At last, after an appropriate delay by the software, this signal triggers and synchronizes all necessary devices [8].

1.4 Interference and Suppression

1.4.1 Light Interference and Suppression

Disturbance light into the probe is mainly infrared radiation from the nonmeasurement area of the target surface, reflection of the background target to target infrared radiation, background target infrared radiation and infrared reflection of

the target surface to background target; followed by natural light and other kind of background light. For these light interferences, this system's main suppression measures taken are:

(a) Paste a narrow band interference filter with center wavelength of 2 μm, bandwidth of 10 nm in the modulation plate window, so that filter out laser or laser and infrared radiation for detecting the response of the photoelectric conversion system while modulating the incident light.
(b) Using water cooling masking plate to reduce the temperature of the module plate, and to maintain the temperature of the module plate are relatively stable. Combining with method *f*, this approach is the most effective way to restrict background radiation (reflect radiation) and other stray light from entering into the detector system and improves the measurement accuracy.
(c) Place an optical filter with center wavelength of 2 μm, Bandwidth $\triangle\lambda = 150$ nm to filter out the noise radiation from the modulation disk, etc., and also allows the laser and infrared radiation to pass through.
(d) Use Aperture diaphragm as a helper methods to prevent the stray light from entering the detector system.
(e) Use a narrow band interference filter with the central wavelength of 2 μm, the bandwidth of 10 nm to filter the stray radiation that mixed into the monitoring signal.
(f) Use of electrical compensation method to eliminate the thermal radiation from the modulate plate, the probe shell itself, the windows and the lenses, etc., that affects the accuracy of temperature measurement [9].

1.4.2 Electrical Interference and Suppression

1.4.2.1 Interference Mathematical Model

Electrical interference signals include active and passive interference, that is:

$$J_{\mathrm{RF}}^{k}(t) = J_{\mathrm{IRF}}^{k}(t) + J_{\mathrm{ARF}}^{k}(t) \tag{1.10}$$

where, $J_{\mathrm{IRF}}^{k}(t)$ stands for the passive interference signal, $J_{\mathrm{ARF}}^{k}(t)$ for the active interference signals.

(1) Passive interference signal model

This gives only a general mathematical model of passive interference. The interference signal expression is:

$$J_{\mathrm{IRF}}^{k}(t) = K_{\mathrm{RF}} \cdot \sqrt{\frac{P_t \cdot L_s}{(4\pi)^3}} \cdot \frac{g_{\mathrm{vt}}(\theta_{\mathrm{Jc}}) \cdot g_{\mathrm{vr}}(\theta_{\mathrm{Jc}})}{R_{\mathrm{Jc}}^2(t)} \cdot \lambda \cdot \sqrt{\sigma_{\mathrm{kJc}}(t)} \cdot \exp\left[j\omega_c(t - \frac{2R_{\mathrm{Jc0}}}{c} - kT_r)\right] \cdot \exp\left[j\pi b(t - \frac{2R_{\mathrm{Jc}}(t)}{c} - kT_r)^2\right] \cdot \exp\left[j\omega_k(t - \frac{2R_{\mathrm{Jc1}}(t)}{c} - kT_r)\right] \mathrm{ect}\left[\frac{t - \frac{2R_{\mathrm{Jc}}(t)}{c} - kT_r}{T_r}\right] \tag{1.11}$$

In Eq. (1.11), K_{RF} is the attenuation coefficient; P_t is the power; L_s is the path loss; g_{vt} is the interference gain; g_{vr} is the receive gain; R_{JC} is the interference distance; λ is the wavelength; σ_{KJC} is the receiving area; T_r is the temperature; J_C is the interference noise; κ is the Boltzmann constant.

(2) Active interference signal model

Let the interference signal J_t is a noise signal, P_J is the emission power ω_J is the center frequency, BW_J is the bandwidth. The active interference module of bandwidth BW_J can be expressed as:

$$J_r(t) = \left[\frac{\lambda^2 P_J L_J L_r \mathrm{BW}_r}{(4\pi)^2 R_j^2(t) \mathrm{BW}_J}\right]^{1/2} \cdot g_v(\theta_J) \cdot g_J \cdot A_{J(t)} \cdot \exp\{j[\omega_1 t + \varphi_J(t)]\} \cdot k_{\mathrm{RF}} \cdot G_{\mathrm{IF}}\mathrm{IF} \tag{1.12}$$

In Eq. (1.12), λ is the wavelength; L_J is the path loss; L_r is the receive loss; R_J is the interference distance; g_v is the interference gain; g_J is the receiver's gain; A_J is the receive area; Φ_J is the phase angle; K_{RF} is the attenuation coefficient; G_{IF} is the IF gain; L_{IF} is the IF losses.

The main sources of interference are two: First, the noise from the power supply and the environment, the other is through the coupling between the various devices. For electrical interference from the coupling between the various devices, the main method is to take electrostatic shielding; for interference from the power supply, the main method is to take software and hardware filter to eliminate or inhibit [10].

1.4.2.2 Filtering

In hardware solution, the detection signal amplification circuit takes frequency-selective amplification technology to filter 50 Hz frequency, 100 Hz frequency multiplication and interference that may be brought before the interference level, the center frequency of the frequency-selective amplifier circuit is located at $f_0 = \frac{1{,}200}{30} \times 2 = 80$ Hz, the bandwidth is 10 Hz. Here, in order to stabilize the output signal of the sampling circuit to 80 Hz, a tuning fork precision clock oscillator is taken and divided 2,000.

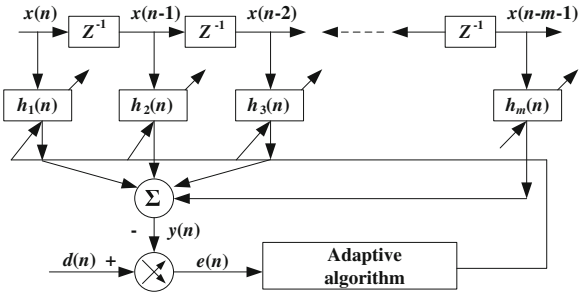

Fig. 1.3 Adaptive filter structure

In software solution, a signal averaging and minimum mean square error (LMS) adaptive filtering algorithm is taken to process the signals in fixed-point DSP TMS320F2812 platform. The adaptive filtering algorithm has the ability to tracking signals and noise, and to make the dynamic characteristics of the filter changing with the signal and the noise to achieve optimal filtering effect. The basic principle is to take filter parameters get from the filter, automatic adjust and update filter parameters present time to adapt the signal and the noise statistics of the unknown or time varying statistical properties. Adaptive filters are commonly made of adjustable parameters of the filter structure and the adaptive algorithm, the structure shown in Fig. 1.3.

In Fig. 1.3, $x(n)$ is the signal input, Z^{-1} is the delay unit which can determine the order according to the real time and the accuracy requirements, $y(n)$ is the output filter, the output signal is compared with the standard signal $d(n)$, to obtain the error signal $e(n)$, and to adjust parameters of the filter by an adaptive algorithm such that statistical error signal $e(n)$ reaches a certain minimum, repeat this process, the filter will gradually learning input signal and noise regularities. The key of this filter is that it can automatically adjust weight to achieve the purpose of adaptive filter by finding $E[e^2(n)]$ weight reaches the minimum value using adaptive algorism based on $e(n)$ and $x(n)$. We take the most commonly used algorithm in adaptive filter, LMS (least mean square error) algorithm. Its outstanding advantages are calculation amount is small, easy to implement, robust performance. By adjusting coefficient, it can output error sequence to minimize the mean square value, especially for online signal processing.

From the adaptive filter structure we obtain:

$$y(n) = \sum_{i=1}^{m} h_i(n)x(n-i-1) = h^T(n)x(n) \tag{1.13}$$

$$e(n) = d(n) - x(n) \tag{1.14}$$

Select the performance function:

$$\xi(n) = \left[e^2(n)\right] = \left(d(n) - h^T(n)x(n)\right)^2 \tag{(1.15)}$$

Table 1.1 Comparison result of temperature measurement results and calculation results under different temperature level

Temperature (K)	600	700	800	900
Experimental results	601.1	701.7	802.3	902.4
Calculation results	601.7	702.2	802.5	901.9

Seen from the above equation, the performance function is a quadratic function of the filter coefficients $h(n)$ to form a bowl-shaped ultra-parabolic (performance surface). Initial value of the adaptive filter coefficients locates in a certain point of the performance surface, after the adaptive adjust, the changing point of filter coefficient moves to the minimum point of the bowl bottom and eventually achieve optimal Wiener filter. Takes the negative direction increased of the performance $\xi(n)$ as the weight update direction:

$$\frac{dh(n)}{dn} = -\frac{d\xi(n)}{dh(n)} = 2e(n)x(n) \tag{1.16}$$

In the filter implementation, the weight coefficient update algorithm is as follows:

$$h(n+1) = h(n) + 2\mu e(n)x(n) \tag{1.17}$$

Formula (1.17) is the adaptive filter weight update recurrence formula. μ is an update step. From the above algorithm step, LMS algorithm for each new input and output sampling only need about $2(m+1)$times multiply–add operations, and its realization process is relatively simple and easy to implement. The algorithm is actually a recursive algorithm, and therefore the signal does not require a priori knowledge of the statistical characteristics, only use his transient estimate value. Here, the value obtained by calculation is only an estimate of the filter coefficients, with the change of time, the filter coefficients will be adjusted gradually, and this estimate value will also gradually improve to achieve convergence. Seen from the formula, the weight update need ideal reference signal $d(n)$ must be known, but for the actual sampling signals, the reference inputs are unknown, so we can take the present sampling value of input signal as reference signal $d(n)$ to constituting the line enhancer of the adaptive filter device [11].

1.5 Conclusion

Taking airplane engine (working temperature 300–800 °C, $\varepsilon\lambda = 0.52 \sim 0.56$) as a field measurement target, using a wavelength of 2 μm of InGaAs/I diode laser as the laser source and the structure shown in Fig. 1.2, the experimental results obtained are shown in Table 1.1. From Table 1.1, the experimental results and the calculated results agree that the measurement error is small. This result confirms that the hardware structure of the system and test analysis is correct.

References

1. Hu R, Luan S, Sun NK (1998) Infrared Technol 02(2)20:21–22 (in Chinese)
2. Zhang J, Liu L (2013) Modulating lateral modes of diode laser by photonic crystal structures. Infrared Laser Eng 42(1):69–72 (in Chinese)
3. Khan MA, Allemand C, Eagar TW (1991) Noncontact temperature measurement I: interpolation based techniques. Rev Sci Instrum 62(2):392–402
4. Hahn JW, Rhee C (1987) Reference wavelength method for a two—color pyrometer. Appl Opt 26(24):5276–5279
5. Guo G, Ye M (2008) Analysis of the application of laser technology in missile weapons and its effects. Infrared Laser Eng 20(3):123–126 (in Chinese)
6. Lu G, Huang Y, Lei Z (2012) Lifetime evaluation on high power Cm-bars. Infrared Laser Eng 41(9):2328–2332 (in Chinese)
7. Han F, Zeng C, Liang J, Chen Z (2011) Method for measuring relative gain curve of pulse laser range finder. Infrared Laser Eng 40(12):2413–2417 (in Chinese)
8. Chang S, Mao J, Yang J (2012) Beam pattern transformation of fresnel diffraction of gaussian beam throughout micro-circular apertures. Laser Technol 36(4):568–571 (in Chinese)
9. Wang T, Gu G, Li Y (2006) Applications of laser in the technology of mechanical manufacture. Laser J 27(3):75–76 (in Chinese)
10. Zhou J, Chang M, Zhang X, Zhang Q (2012) Measurement technique research of multi-diopter lensers' power. Laser J 33(1):20–21 (in Chinese)
11. Wang J, Huang Z, Yang X (2012) Simultaneous measurement of the temperature and refraction index based on multimode interference and long-period fiber grating. Chin J Lasers 39(9):83–87 (in Chinese)

Author Biographies

Yuan-Fei Xia: (1956-) male, from Dalina, Liao Ning Province, China, Doctor's Degree, Professor, got a bachelor's degree from Huazhong University of Science and Technology in 2006, mainly engages teaching and research works of aviation maintenance engineering, E-mail: xiayuanfei1965@sina.com

Xue-Yuan Li: (1966-) male, from Wu Han, Hu Bei Province, Master's degree, associate professor, got Master's degree from China PLA Air Force Command College in 2001, mainly engages teaching and research works of aviation maintenance engineering E-mail: lixueyuan1966@163.com

Qiang Ren: (1976-) male, from Nan Yang, He Nan Province, Master's degree, E-mail: ren001@sina.com

Chapter 2
Design of Multichannel Waveform Recorder of Aircraft Ground Electric Power Sources

Zhen Wang, Jianfei Si and Yuanfeng Zhang

Abstract A multichannel waveform recorder is raised to solve the puzzling problem of failures of aircraft ground power sources. The hardware system is established with embedded single-board computer PC/104 and multichannel parallel data acquisition card, etc. Windows XP Embedded and LabVIEW are used in software architecture. Strategies for automatic segmentation of massive data block are proposed. System testing is done on the medium frequency electric power source. Testing results show that this multichannel waveform recorder is easy to operate, accurate in measurement, and has good stability and portability. It can be used to monitor power supply of aircraft ground electric power source for a longtime, and thus is of high practical value and economic significance.

Keywords Aircraft ground power sources · PC/104 · LabVIEW · Automatic segmentation

2.1 Introduction

Aircraft ground electric power source is necessary for aircraft maintenance and ground engine starting [1]. In recent years, quality reduction of ground electric power source has led to many accidents such as starting failure, crash, reboot, and

Z. Wang (✉)
College of Automation Engineering, Qingdao University, Qingdao 266071, China
e-mail: wangzhen_623@163.com

J. Si · Y. Zhang
Naval Aeronautical Engineering Institute Qingdao Branch, Qingdao 266041, China
e-mail: 32435906@163.com

Y. Zhang
e-mail: yfzhang09@163.com

J. Wang (ed.), *Proceedings of the First Symposium on Aviation Maintenance and Management-Volume I*, Lecture Notes in Electrical Engineering 296,
DOI: 10.1007/978-3-642-54236-7_2,

even over-burning. It is difficult to locate and analyze faults, because these failures seldom reoccur. Power source parameter recorders have been assembled on some new power units. However, it is said that only steady state parameters can be recorded, which play a feeble role in analyzing faults once the power fails. An effective means of locating and analyzing faults accurately is to record the power waveform by a data recorder [2]. But high price and complicated operation limit its promotion. A multichannel waveform recorder of aircraft ground electric power source at a lower cost is designed in this document. It can provide effective detection means of estimating electric power quality and locating and analyzing faults.

2.2 Technical Requirements Analysis

Various types and technological disparity of military aircraft bring high requirement for the ground electric power source. There are two kinds of them: vehicle electric power source and static power. They can provide low voltage DC power and medium frequency AC power. Some special ones can supply 28.5 V/57 V (boost) and 0–70 V DC power for different aircraft engines starting. Therefore, multichannel signals including AC voltage, AC current, DC voltage, and DC current should be recorded simultaneously. Detail specifications are as follows:

a. 10-channel electrical parameters record: three-phase AC voltage (0–300 V), three-phase AC current (0–200 A), 2-channel DC voltage (0–100 V), 2-channel DC current (0–600 A, 0–3000 A).
b. Sampling mode: Single channel 200 kS/s, parallel acquisition.
c. Record duration: More than 1 h.
d. Others: Well portability, wide temperature range, and anti-seismic, etc.

2.3 System Design

The hardware platform is mainly made up of embedded single board computer (SBC) PC/104 [3] and multichannel parallel data acquisition (DAQ) card PL-2346B [4]. Windows XP-Embedded and LabVIEW are used in software architecture.

PC/104 platform has many advantages such as small size, reliable electrical connection. Above all, it has high data handing capacity though under lower power dissipation. Windows XP Embedded is the successor to Windows NT Embedded 4.0. Based on the same binary files as Windows XP Professional, it enables us to rapidly develop reliable and full-featured devices.

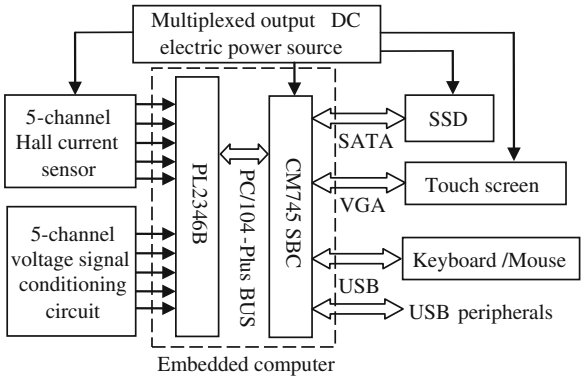

Fig. 2.1 Block diagram of hardware System

2.3.1 Hardware Implementation

The hardware system is consisting of Hall current sensor, signal conditioning circuit, embedded computer system, DC electric power source, industry touch screen and solid state disk (SSD). Block diagram of hardware system is shown in Fig. 2.1.

Hall current sensor: Hall current sensor detects AC/DC electrical current and generates an analog voltage output in ±10 V proportional to it. It runs in tracking mode to record waveform. There are 5-channel current sensors. Three of them are used for three-phase AC current measurement ranging from 0 to 200 A. One of the rests is used for low voltage DC current measurement ranging from 0 to 600 A. Actual current can be up to 2800 A when the electric power unit directly starts. So the last one is used for 0–3000 A, and it is mainly used to support direct starting of electric power unit.

Voltage signal conditioning circuit [5]: In the conditioning circuit voltage signal can be reduced to suitable value for DAQ. It also delivers over-voltage protection and filtering function. Schematic diagram of single channel voltage signal conditioning circuit is shown in Fig. 2.2, in which RC filter, precision resistance, and fast recovery voltage-regulator diodes are included.

Embedded computer system: It is composed of AD-Link's CM745 SBC and ZTIC's multi-function DAQ PL2346. CM745 is an exceptionally high integration, high performance, compatible with PC/104 standard. Its features are as follows: Intel Atom^{TM} Processor D525, up to 4 GB single channel DDR3 SDRAM, Intel 82574 Gigabit Ethernet, 4 GB SSD onboard, single Channel 18-bit LVDS and analog VGA. PL2346B is a 12-channel, multi-function DAQ module for PC/104-Plus form factor. The A/D on it features a sampling rate of up to 450 kS/s. So CM745 and PL2346B are particularly well suited to either embedded or portable applications and meet the size, power consumption, temperature range, quality, and reliability demands of embedded system applications.

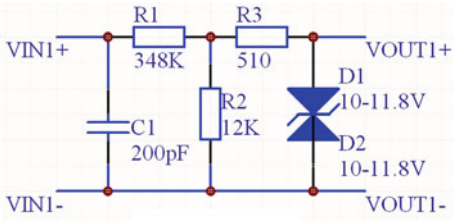

Fig. 2.2 Schematic diagram of single channel voltage signal conditioning circuit

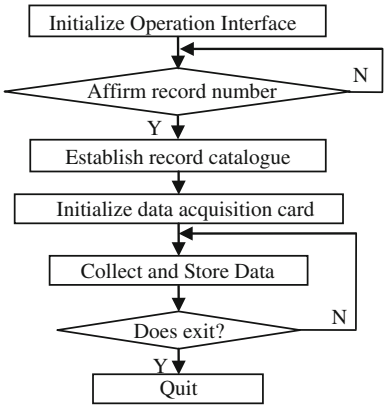

Fig. 2.3 Overall software flowchart

Multichannel DC electric power source: It supplies ±12, 5 V for sensors, computer, disk, and screen. Total power is less than 100 W, and then the system's size can be controlled in a low range.

2.3.2 Software Design

Windows XP Embedded is used as the embedded operating system delivering the power of the Windows operating system in componentized form to rapidly build reliable and advanced embedded devices. Data integrity can be achieved. The software platform and development environment is LabVIEW. Overall software flowchart is shown in Fig. 2.3.

Waveform data format and size: Acquired data is 64-bit double precision floating point type [6], which are 8 bytes (1 byte = 8 bits). At the sampling rate of 200 k, 10-channel data size in a second is: 200 k × 10 × 8 byte / 10242 ≈ 15.26 MB.

Relationship between sampling rate, sampling time, and data size is shown in Table 2.1.

Table 2.1 Relationship between sampling rate, sampling time, and data size

Sampling rate	Sampling time	Data size	Notes
200 k	1 s	16 MB	Reduce corresponding times when sampling rate is reduced
	1 min	916 MB	
	30 min	26.8 GB	
	60 min	53.6 GB	
	120 min	107.2 GB	

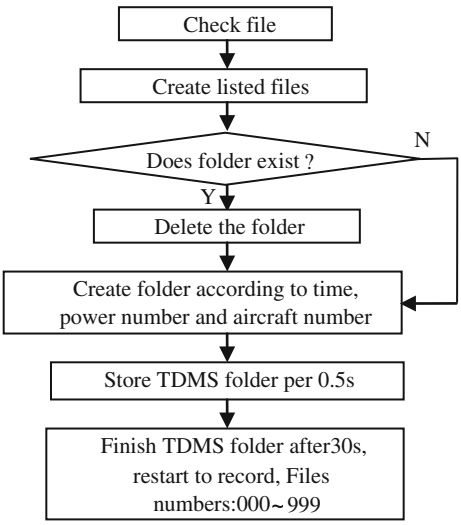

Fig. 2.4 Flowchart of storing data segmentation

Workflow of data acquisition: To ensure data integrity, data acquisition must be synchronized with data storage. DAQ works in continuous mode and storage is done once buffer data is detected.

Automatic segmentation of data block: As mentioned, data size of 1 min is nearly 1 GB at 200 kS/s. When time goes by, data size increasingly increases, which results in huge occupancy of system resources. So strategies for automatic segmentation are adopted in the system. Flowchart of storing data segmentation is shown as in Fig. 2.4. Program schematic diagram is shown as in Fig. 2.5.

2.4 System Testing

The system testing is finished on AC power source DS053AT which can supply three-phase AC voltage (0–346 V) from 300 to 500 Hz.

Here, only medium frequency three-phase AC voltage is recorded as an example. Measurement of other types of single is similar to them. So, output of the

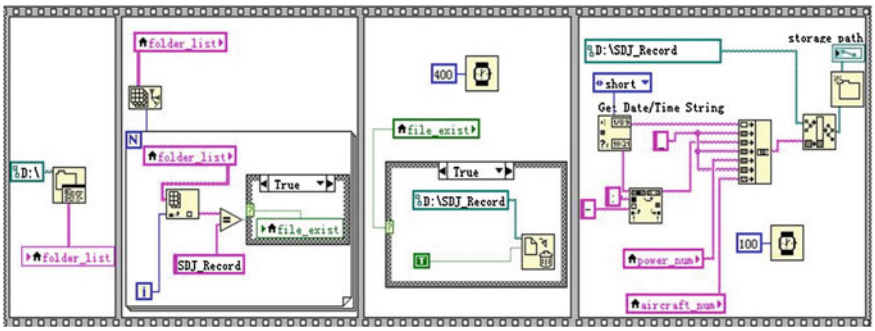

Fig. 2.5 Program schematic diagram

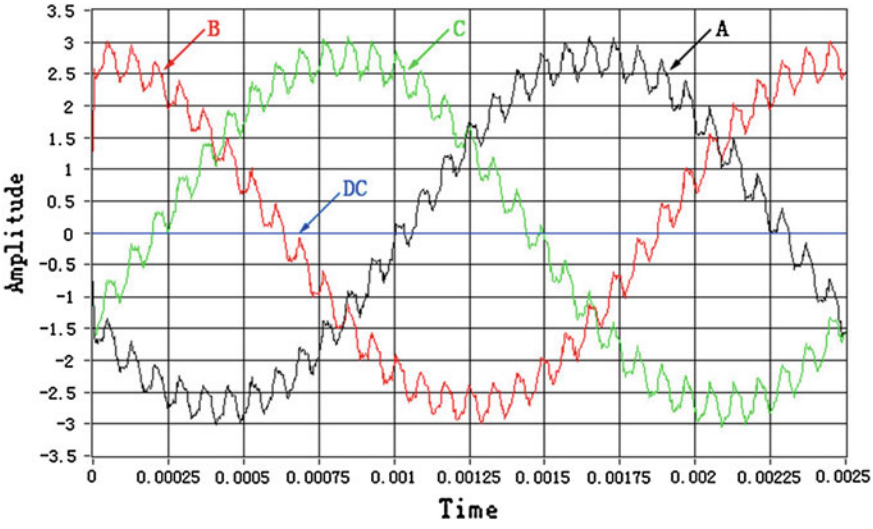

Fig. 2.6 Testing waveform

AC power source is set to 400 Hz, 115 V which is the input of the multichannel waveform recorder.

When recording, every execution time is less than 500 ms, which meets the requirement of that every data acquisition time is no more than 0.5 s. Waveform files are numbered correctly and every size is less than 500 MB. They can be easily transcribed. TDMS waveform data is opened by LabVIEW. Testing waveform is shown as in Fig. 2.6, in which A, B, C indicates every phase. We can get integrated waveform without DC element and serious distortion. Meanwhile, software testing verifies the system's working stability during long hours.

2.5 Conclusion

A multichannel waveform recorder of aircraft ground electric power sources is proposed based on embedded computer PC/104 and DAQ PL2346B. The system can be used to monitor power supply of aircraft ground electric power source for longtime. The hardware selection and architecture, parts of software workflows are presented. To avoid huge occupancy of system resources by high speed recording, strategies for automatic data segmentation are adopted in the system, so that a single data size is limited and system efficiency and reliability increases correspondingly. After practical testing, the system can work reliably and steadily. Design requirements are completed. Nevertheless, response speed of software system could be improved and files' storage format should be optimized further.

References

1. Zhou J (2010) Aircraft electrical system. Science Press, Beijing (In Chinese)
2. Hu X (2012) Design and realization of multi-channel real-time data acquisition and storage system. North University of China, Taiyuan (In Chinese)
3. Bin J, Zhong Z (2005) General test system of airplane power supply product based on PC/104 bus. Aviat Metrol Meas Technol 3:51–53 (In Chinese)
4. Xianhong S (2003) Development of embedded data acquisitions and control system based on VxWorks. Northwestern Polytechnical University, Xi'an (In Chinese)
5. Zhang X, Zhang P, Dong Y (2009) Design of test system of Autocar power management system. Machin Electron 6:49–52 (In Chinese)
6. Liu S, Liu X (2011) LabVIEW bible. Publishing House of Electronics Industry, Beijing (In Chinese)

Chapter 3
Study and Analysis to the Failure Cable Plug Resulting in X-Type Airplane Engine Stopping in the Air

Xinkun Wang, Binshi Xu, Shicheng Wei and Libo Chen

Abstract In this paper, the reasons that induce one of the engines to stop working in the air have been studied. By means of macro analysis, component analysis, and contrast tests, the reason that the pin breaks away from the plug is due to the swelling of the rubber in the plug by the lubrication oil. This makes the silicon rubber in the plug lose spring and the jacks in the plug lose the fastening ability to the pin. Effective measures have been suggested that will prevent similar accidents happening.

Keywords Failure · Study and analysis · Cable plug · Airplane engine

3.1 Introduction

As the engine is the heart of an airplane, its reliability will greatly influence the flight security of airplanes. Whether avion or civil airplane, failures of engine have been an intangible killer which always threatens the flight of airplane. They not only decrease the capability of engine but also result in serious flight accidents, which will make the nation and the passengers lose a huge quantity of property and even life. So, the security of airplane engines is one of the most important facts, and the engine maintenance is especially emphasized during the lifetime.

X. Wang (✉)
School of Materials Science and Engineering, Beihang University, Beijing 100191, China
e-mail: wangxinkun1010@163.com

X. Wang · L. Chen
Beijing Aeronautical Technology Research Center, Beijing 100076, China

B. Xu · S. Wei
Faculty of Remanufacturing Engineering, Academy of Armored Force Engineering, Beijing 100072, China

J. Wang (ed.), *Proceedings of the First Symposium on Aviation Maintenance and Management-Volume I*, Lecture Notes in Electrical Engineering 296,
DOI: 10.1007/978-3-642-54236-7_3,

With the development of science and technology, the ratio of flight accidents every 100,000 flight hours has dramatically decreased. During the past 100 years, this ratio of avion serious accidents has decreased more than 350 times, and that of civil airplane has also notably decreased, reaching two times every 100,000 flight hours. There are many factors that can affect the security of airplane flights. The scientific failure analysis and study of failure will not only find the main reasons, but will also prevent serious accidents from happening.

Measures that are effective and practical may be put forward, which will prevent or cut down similar failures from happening. But in practice, when accidents happen, in order to escape responsibility the relevant companies or organizations usually hold back the fact. This makes analysis more difficult and complex.

The following is a typical failure analysis and study process of an airplane engine stopping in the air. Reasons have been finally found without any interrelated material, by means of macro analysis, component analysis, and contrasting tests. The suggested measures are not only effective but also prevent similar accidents happening.

3.2 Process of Accident and Effect

The case study is a big cargo aircraft belonging to a certain freight aviation company. One day, one of the two engines stopped working during flight without any warning. The ground inspection found that one of the cable plugs on the accessory gearbox had been damaged, and the plug had come off from the jack. So the current was cut and the engine stopped working. The place of plug installation on the engine is shown in Fig. 3.1. As there are no relevant data and information available about the material of the plug and the medium under which the plug works, the studies mostly include component analysis and capability test. By contrasting the FT-IR of the rubber and the oil in the failure plug, they have been identified by testing and analyzing the rubber in the oil under different temperatures. The fundamental reasons are that there is lubricating oil in the failure plug and resistance to the oil of the rubber is poor.

3.3 Macro Analysis of Plug Failure

Disassembling of failure plug and macro-appearance of the rubber inside the plug and the new one is shown in Figs. 3.2 and 3.3, respectively. From the figures, we can see the rubber in plug failure has been seriously damaged, most of the jack along the outside rubber has seriously cracked, and the sizes of jacks have become bigger than those of the new one; the spring of the rubber is bad. The body of rubber has expanded obviously. Furthermore, there is some type of oil in the body of rubber and

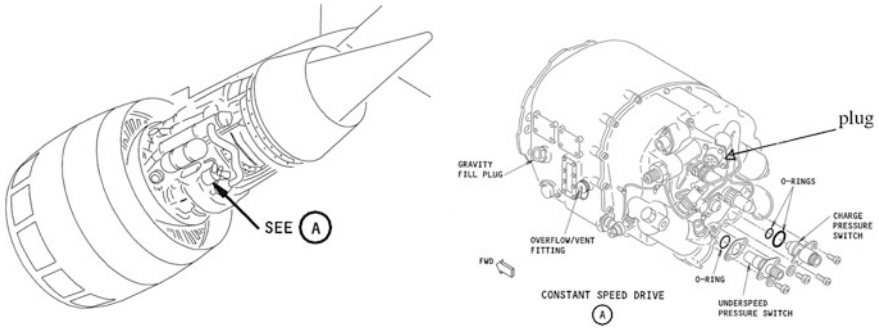

Fig. 3.1 Installation place of the failure plug in the engine

Fig. 3.2 Macro-appearance of the rubber inside the plug failure

Fig. 3.3 Macro-appearance of the new plug

in the shell of the failure plug. According to the rules of the plug, the rubber inside the plug should be kept away from the oil, therefore the this accident of engines stopping working in the air may have arisen from the effect of oil in the plug.

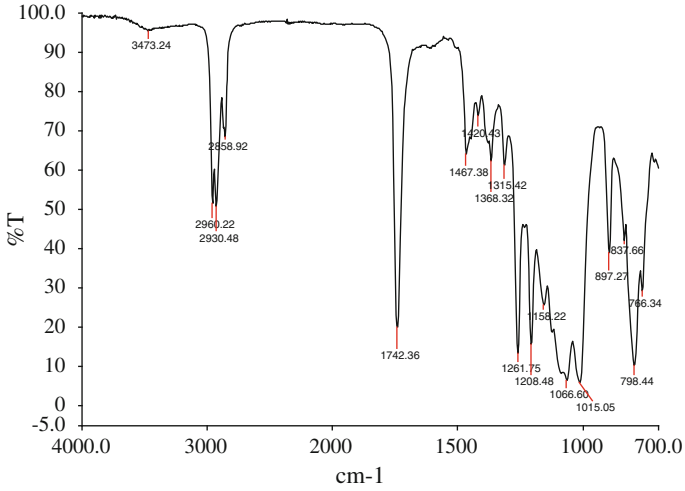

Fig. 3.4 FT-IR chart of oil in the shell

3.4 Study and Analysis of the Type Oil

Obviously, the existence of oil in the plug disobeys the use rules. But how to find the main mechanism which has resulted in this serious accident; why there is oil in the plug, and what type it is must be detected first.

The installation blueprint manifests that the distance between the plug and the box of lubricant oil is very close and there are not strict seal measures in the plug. When the engine is running, there is violent vibration, and a certain quantity of lubricant oil leaked from the lubricant box infiltrates into the plug with help of the vibration from the gap of the plug. The rubber inside the plug is actually soaked in the lubricant oil, with the use time prolonging, the property of the rubber inside the plug becomes worse and worse.

In order to identify whether the oil in the failure plug comes from the lubricant oil box or not, the type of oil inside the plug failure and that of lubricant system have been contrasted. The Figs. 3.4, 3.5, 3.6, and 3.7 are the FT-IR chart of the oil inside the failure plug shell, failure sample, the lubrication system, and the compound chart separately.

From Figs. 3.4 and 3.5, we can see there are strong absorption at the 1740 and 1155 cm^{-1}, these are typical absorptions of ester-radical compound, these typical absorptions are consistent with those of Fig. 3.6, which are the typical absorption of the oil in the lubrication system, and the Fig. 3.7 also make sure that the oil in the failure plug and that in the lubrication system are the same kind substance, so the oil in the plug failure comes from the nearby lubrication system. The differences of FT-IR charts between the oil in the failure plug and that in the lubrication system are that there are obvious absorption at 1261, 1028, 1066, 897, and

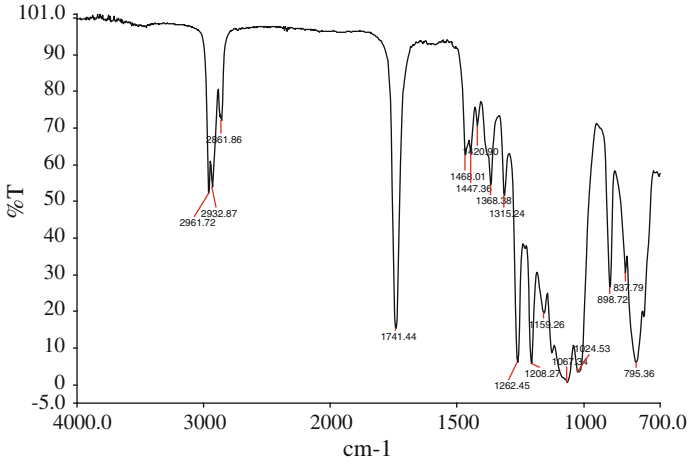

Fig. 3.5 FT-IR chart of oil in the rubber

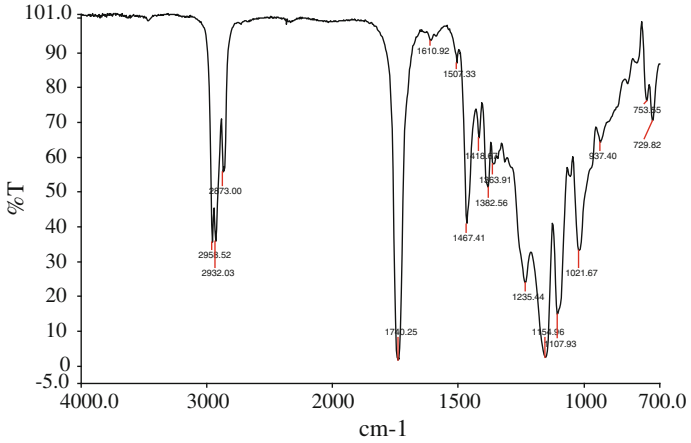

Fig. 3.6 FT-IR chart of oil in the lubrication system

798 cm^{-1}, these are the typical absorption of containing silicon compound. These information may have come from the rubber in the failure plug.

3.5 Study and Analysis of the Rubber in Failure Plug

From the appearance, the substance in the failure plug is likely to be rubber. But different rubber has different property. In order to identify the type of rubber, select the rubber in the failure plug and the new one as study objects. By extraction to the

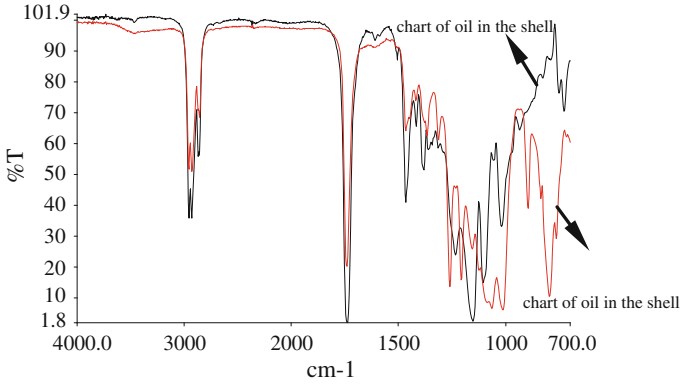

Fig. 3.7 Compound chart of oil in the shell and in the lubrication system

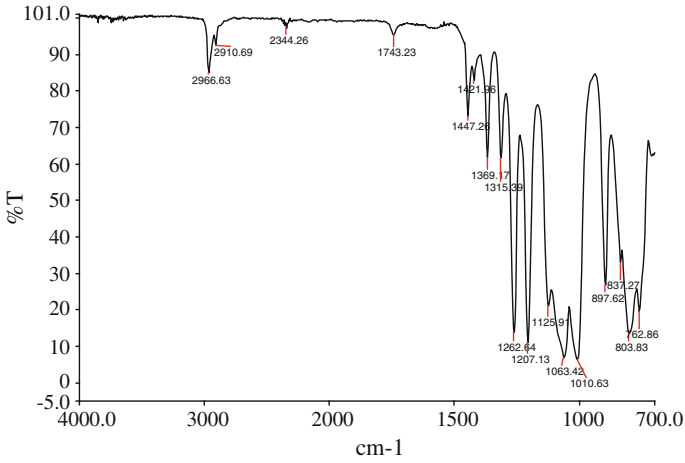

Fig. 3.8 FT-IR chart of rubber

rubber using ether, test the infrared characteristic using PE system-2,000 infrared spectrum. The results are shown in Figs. 3.8, 3.9, and 3.10. Figures 3.8 and 3.9 are FT-IR chart of the rubber in the plug failure and that in the new one, Fig. 3.10 is the compound chart of the two.

The information in Figs. 3.7 and 3.8 shows that there are obvious absorption at 1262, 1207, 1063, 1010, 897, and 803 cm^{-1} both the failure rubber and the new, these are the typical absorption of containing silicon compound, so the rubber in the failure plug is silicon rubber. This assert is testified by Fig. 3.9. This result make sure that the silicon typical absorption of oil in the failure plug.

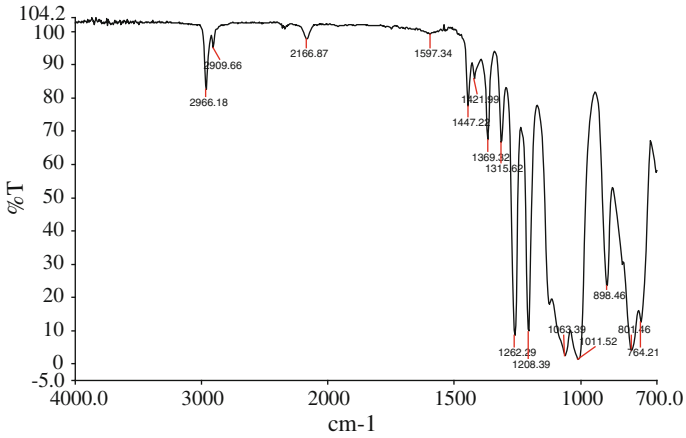

Fig. 3.9 FT-IR chart of rubber in the new plug

3.6 Property Test and Analysis of Rubber

The existence of lubrication oil in the plug obviously disobeys the rules of the plug use. How does the oil affect the rubber in the plug? What extent is it? What are the effective and practical measures which will prevent or cut down the similar faults happening?

3.6.1 Test Principle

In this study, the procedure evaluation to the oil resistivity of rubber is as follows:

(1) According to dependent criterion, prepare the test samples and sign them, weigh the quality of the different samples, measure the volume of the samples using draining method, record the corresponding data;
(2) Under the temperature of 24 and 150 °C separately, soak the samples;
(3) Clean them using aero-washing gasoline for 30 s, wipe off the liquid on the surface using filter paper, keep 30 min under room temperature, according to the method related in (3.1), weigh the sample and measure the volume, record the corresponding data;
(4) According to the formula (3.1) and (3.2), evaluate the oil resistivity of rubber.

$$\Delta V(\%) = \frac{(m_3 - m_4 + m_5) - (m_1 - m_2 + m_5)}{m_1 - m_2 + m_5} \times 100 \tag{3.1}$$

$$\Delta m(\%) = \frac{m_3 - m_1}{m_1} \times 100 \tag{3.2}$$

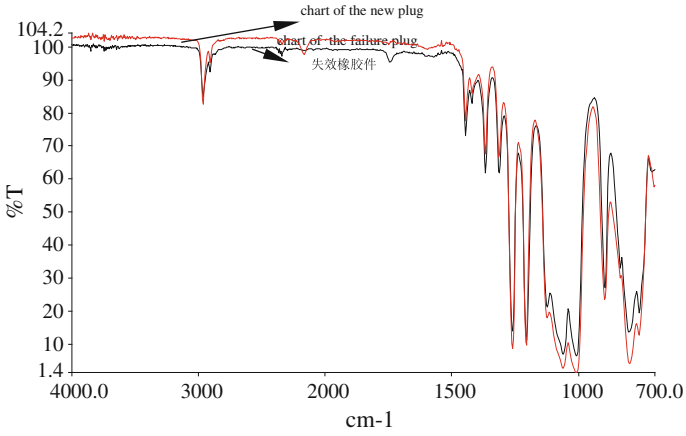

Fig. 3.10 Compound chart of rubber in the failure plug and that in the new one

In the formula, m_1, m_2, m_3, m_4 are separately the quality of the sample in the air before soaked in the oil, in the distilled water before soaked in oil, in the air after soaked in the oil and in the distilled water after soaked in oil; m_4 is the quality of plummet in the distilled water; ΔV and Δm are separately the change percent of the sample volume and that of the sample quality.

3.6.2 Analysis of Oil Resistivity of the Rubber Under Room Temperature

Tables 3.1, 3.2, and 3.3 are separately the results of the oil resistivity of the rubber in the plug which are tested under the 24 °C after soaked 24, 48, and 72 h accordingly. The results show that the degree of the sample swelling become more and more notable along with the soaking time prolonging, and the quantity of absorbed into the sample increase. Under the condition of (24 °C, 72 h), the average value of ΔV and Δm are 21.06 and 15.92 % separately. Although there are not notable change among the three values when the samples have been soaked 24, 48, and 72 h, the trends that the change percent of the samples volume and the quality become bigger and bigger with the test time prolonging.

By diffusing and infiltrating, some molecules of lubrication oil enter the gaps among the molecule chain, at the same time, as there are similar polarity, the molecules of the sample and the oil can act each other, some chemical bonds between the molecules of the sample may be weakened or destroyed, the type of the molecules tight array has been changed to some extent. With the soaking time prolonging, some large molecule chains become smaller and smaller.

Table 3.1 Results of oil resistivity under 24 °C, 24 h

Result	1#	3#	4#
m_1 (g)	1.650	1.715	1.560
m_2 (g)	0.265	0.280	0.256
m_3 (g)	1.842	1.914	1.757
m_4 (g)	0.243	0.257	0.221
ΔV (%)	15.45	15.47	17.79
Δm (%)	11.64	11.60	12.63
Average of ΔV (%)	16.24	Average of Δm (%)	11.96

Table 3.2 Results of oil resistivity under 24 °C, 48 h

Result	1#	3#	4#
m_1 (g)	1.650	1.715	1.560
m_2 (g)	0.265	0.280	0.256
m_3 (g)	1.893	1.971	1.792
m_4 (g)	0.238	0.247	0.228
ΔV (%)	19.49	21.14	19.94
Δm (%)	14.73	14.93	14.87
Average of ΔV (%)	19.86	Average of Δm (%)	14.84

Table 3.3 Results of oil resistivity under 24 °C, 72 h

Result	1#	3#	4#
m_1 (g)	1.650	1.715	1.560
m_2 (g)	0.265	0.280	0.256
m_3 (g)	1.911	1.986	1.812
m_4 (g)	0.242	0.250	0.225
ΔV (%)	20.50	20.98	20.70
Δm (%)	15.82	15.80	16.15
Average of ΔV (%)	21.06	Average of Δm (%)	15.92

3.6.3 Analysis of Oil Resistivity of Rubber Under High Temperature

When engine works, temperature around the plug keep will about 150 °C, so select 150 °C as test temperature, and the test results will truly show the oil resistivity of the rubber.

Tables 3.4, 3.5, and 3.6 are separately the results of the oil resistivity of the rubber under 150 °C after soaked for 24, 48, and 72 h. Similar to 5.2, the trends of the change percent of the samples volume and the mass become bigger and bigger. At the condition of 150 °C, the maximum of the average change percent of the sample volume and the mass are 53.91 and 42.72 %. Comparing the value of the test results under the different temperature when the soaked time is same, we find

Table 3.4 Results of oil resistivity under 150 °C, 24 h

Result	2#	5#	6#
m_1 (g)	1.520	1.526	1.540
m_2 (g)	0.254	0.254	0.255
m_3 (g)	2.104	2.112	2.127
m_4 (g)	0.203	0.218	0.217
ΔV (%)	50.16	48.90	48.64
Δm (%)	38.42	38.40	38.12
Average of ΔV (%)	49.23	Average of Δm (%)	38.31

Table 3.5 Results of oil resistivity under 150 °C, 48 h

Result	2#	5#	6#
m_1 (g)	1.520	1.526	1.540
m_2 (g)	0.254	0.254	0.255
m_3 (g)	2.123	2.132	2.151
m_4 (g)	0.216	0.222	1.222
ΔV (%)	50.63	50.16	50.12
Δm (%)	39.67	39.71	39.68
Average of ΔV (%)	50.30	Average of Δm (%)	39.68

Table 3.6 Results of oil resistivity under 150 °C, 72 h

Result	2#	5#	6#
m_1 (g)	1.520	1.526	1.540
m_2 (g)	0.254	0.254	0.255
m_3 (g)	2.167	2.179	2.199
m_4 (g)	0.207	0.243	0.211
ΔV (%)	54.82	50.20	54.71
Δm (%)	42.57	42.79	42.79
Average of ΔV (%)	53.91	Average of Δm (%)	42.72

that the average percent of the volume change and the quality change at the condition of 150 °C are two and a half times more than those of at the condition of 24 °C, and the change of the value at the same temperature is not notable following the soaked time prolonging. So the temperature is the main factors that affect oil resistivity of the rubber.

3.7 Analysis and Discussion

The component analysis's by infrared spectrum manifest that the rubber in the failure plug belongs to silicon rubber. The ability of oil resistivity of this type rubber is bad. Furthermore, the study in Sects. 3.6.2 and 3.6.3 shows that the

temperature will greatly affect oil resistivity of rubber. So the failure of cable plug derives from the swelling action of lubrication oil, and the high temperature promotes the process of this action.

The component analysis is by infrared spectrum manifest that the oil in the shell of the failure plug and the oil in the lubrication system of the engine are the same type. As the failure plug is near to the lubrication box of engine, when the engine works, there is violent vibration, some lubrication oil leaks from the lubrication system. At the same time, there is no strict seal measures, a certain quantity of oil infiltrates into the plug with the help of the vibration from the gap of plug, and the oil weak or destroy some chemical bonds between the molecules of the rubber in the plug, the type of the molecules tight array has been changed to some extent, the spring of the rubber becomes worse and worse, the fastening ability of jacks in the rubber body to the pins becomes weaker and weaker. With the help of vibration, the eventually takes away from the jacks along with the using time prolonging, cut down the current to the engine and cause it stopping in the air.

3.8 Conclusion

(1) The reason that the pin breaks away from the plug is due to the swelling of the lubrication oil in the plug. This makes the silicon rubber in the plug lose spring and the jacks in the plug lose the fastening ability to the pin, causing the engine to stop in the air.
(2) The oil comes from the lubrication system nearby the failure plug, and the vibration of the engine promotes the oil infiltration into the plug from the gap, and the surrounding higher temperature promotes the oil swelling action to rubber in the plug, accelerating the failure plug.

3.9 Suggestion

(1) Strengthen the check to the plug on the engine, replace them if there are relaxation between the jacks and the pin;
(2) Strengthen the maintenance to the plug, clean the shell, pin, and jack in the plug periodically, remove the oil on the surface of the shell, pin, and jack;
(3) Improve the plug seal effect by design department, prevent oil infiltrating into plug.

Chapter 4
Incipient Fault Detection for a Hypersonic Scramjet Vehicle

Le-yao Li, Xin-min Wang and Ling-xia Mu

Abstract Incipient fault detection is an important technical issue for hypersonic scramjet vehicle safety. To extract faulty residual from signals that affected by system uncertainty, disturbance, and noise at the same time, a hybrid fault detection scheme is proposed, in which model transformation, wavelet de-noising, as well as online KPCA methods are adopted. The model transformation method is used to select appropriate residual signal; and the latter two methods are used to detect incipient faults. A simulate example is presented to illustrate this scheme.

Keywords Incipient fault detection · Wavelet transform · Principal component analysis

4.1 Introduction

Hypersonic Scramjet Vehicle (HSV) is one of today's leading-edge technology products. More and more countries and international agencies involve into this field, pursuing its potential military and commercial benefits. However, research on HSV does not get on well all the time, most HSV-related projects and their demonstrators have suffered from air crush, such as X-43A, HTV-2, X-51A, etc.

In order to improve the reliability and safety of HSV, reduce costs, and shorten design cycles, NASA and U.S. Air Force sponsored several research projects [1]

L. Li (✉) · X. Wang · L. Mu
Automation School, Northwestern Polytechnical University, Xi'an 710129, China
e-mail: Leyaoli@gmail.com

X. Wang
e-mail: wxmin@nwpu.edu.cn

L. Mu
e-mail: lingxiamu2013@gmail.com

J. Wang (ed.), *Proceedings of the First Symposium on Aviation Maintenance and Management-Volume I*, Lecture Notes in Electrical Engineering 296,
DOI: 10.1007/978-3-642-54236-7_4,

on Fault Tolerant Autonomous Systems, Integrated Vehicle Health Management Systems, and Online Trajectory Reshaping Algorithms, trying to save HSV from accidents.

Sensor fault is one of the main causes for fatal HSV accidents. As earlier detection provides more response time, detecting incipient fault, instead of abrupt fault, seems more important to HSV due to its highly integrated airframe-engine structure, complex aerothermoelastic effects, and wide flight-envelop.

However, few documents are available on this problem. On similar issues, Zhongsheng Wang et al. present a robust incipient fault identification methods for aircraft engine prognostics, in which they use wavelet-based method for weak signature enhancement and correlation dimension for fault diagnosis [2]; L. Ren et al. use process noise and structure noise to analysis single-sensor incipient faults, but their methods cannot analyze online process [3]; R. Nikoukhah et al. design an auxiliary signal for robust incipient fault detection based on a multi-model (MM) formulation of normal and faulty systems [4]; J. Zhang et al. propose a new scheme for detection and isolation of incipient sensor faults for a class of uncertain nonlinear systems by combining sliding mode observers (SMOs) with a Luenberger observer [5]. These methods can, in general, be classified into two classes: signal processing-based methods and model-based methods.

In this paper, a hybrid incipient fault detection scheme for HSV is proposed. With respect to HSV's tough working environment, a model-based method is used to deal with model uncertainty, while signal processing-based methods are used to address process disturbance and measurement noise. Simulation results are given to illustrate the proposed scheme.

4.2 Preliminary

The HSV, which is suffering from incipient sensor faults and various extreme situations can be modeled as:

$$\begin{cases} \dot{x} = Ax + Bu + E\psi \\ y = Cx + D\eta \end{cases} \tag{4.1}$$

where $x \in \mathbb{R}^n$ is the state variables, $u \in \mathbb{R}^m$ the plant inputs, $y \in \mathbb{R}^p$ the plant outputs; ψ models the structure system uncertainties μ and process disturbance d; $\eta \in \mathbb{R}^q$ models the incipient faults f_s and measurement noise ζ; while all system matrices are of appropriate dimensions.

To capture the incipient faults without annoy false alarm rate or under reporting, one must extract fault characteristics from clutter system signals, which are also affected by model uncertainty and disturbance ψ, as well as sensor noise ζ. As incipient faults f_s usually present relatively small altitude, slow development, and sometimes be masked by other signals, observer-based methods might cope

with this challenge very costly, while signal processing-based methods can hardly handle uncertainty. Therefore, we turn to a hybrid scheme.

Assumption 1: The HSV model described by (4.1) satisfies that:

$$\text{rank}(B) = m,\ \text{rank}(E) = r,\ \text{rank}(C[B \quad E]) = m + r.$$

4.3 Main Results

In this section, a hybrid fault detection scheme is proposed to deal with incipient sensor fault of a generic HSV described by (4.1). At first, the residual signals are selected via a model transformation method to avoid model uncertainties; then, adaptive wavelet de-noising method is used to filter measurement noise; At last, fault detection is achieved by online kernel principle component analysis (KPCA).

4.3.1 Residual Signals Selection

Lemma 1: Under assumption 1, there exist state and output transformations:

$$z = \begin{bmatrix} z_1 \\ z_2 \end{bmatrix} = T \begin{bmatrix} x_1 \\ x_2 \end{bmatrix},\ w = \begin{bmatrix} w_1 \\ w_2 \end{bmatrix} = S \begin{bmatrix} y_1 \\ y_2 \end{bmatrix} \tag{4.2}$$

Such that in the new coordinate, the system matrices become:

$$TAT^{-1} = \begin{bmatrix} A_1 & A_2 \\ A_3 & A_4 \end{bmatrix},\ TB = \begin{bmatrix} B_1 \\ B_2 \end{bmatrix},\ TE = \begin{bmatrix} E_1 \\ 0 \end{bmatrix}$$

$$SCT^{-1} = \begin{bmatrix} C_1 & 0 \\ 0 & C_4 \end{bmatrix},\ SD = \begin{bmatrix} 0 \\ D_2 \end{bmatrix}$$

where $T \in \mathbb{R}^{n\times n}$, $S \in \mathbb{R}^{p\times p}$, $z_1 \in \mathbb{R}^r$, $w_1 \in \mathbb{R}^r$, $A_1 \in \mathbb{R}^{r\times r}$, $A_4 \in \mathbb{R}^{(n-r)\times(n-r)}$, $B_1 \in \mathbb{R}^{r\times m}$, $C_1 \in \mathbb{R}^{r\times r}$, $C_4 \in \mathbb{R}^{(p-r)\times(n-r)}$ and $D_2 \in \mathbb{R}^{(p-r)\times q}$. B_1 and C_1 are invertible and D_2 has the structure $D_2 = \begin{bmatrix} 0 \\ \overline{D}_2 \end{bmatrix}$, $\overline{D}_2 \in \mathbb{R}^{q\times q}$.

Using lemma 1, system in (4.1) can be converted into two subsystems:

$$\text{subsystem-1}: \begin{cases} \dot{z}_1 = A_1 z_1 + A_2 z_2 + B_1 u + E_1 \psi \\ w_1 = C_1 z_1 \end{cases} \tag{4.3}$$

$$\text{subsystem-2}: \begin{cases} \dot{z}_2 = A_3 z_1 + A_4 z_2 + B_2 u \\ w_2 = C_4 z_2 + D_2 \eta \end{cases} \tag{4.4}$$

with uncertainty entry only appears in subsystem-1 and faulty entry only appears in subsystem-2. In addition, as the state z_1 can be obtained from the measured output via:

$$z_1 = C_1^{-1} S_1 y,\ S = \begin{bmatrix} S_1^T & S_2^T \end{bmatrix}^T \tag{4.5}$$

Subsystem-2 is free from system uncertainties. Hence, signal w_2 is one good candidate for residual signal selection.

This fascinating feature has been exploited in several papers such as [5] and [6], where they further assumed that (4.1) satisfies minimum phase condition in order to apply observer-based fault detection methods. Unfortunately, our HSV model violates this assumption. In the rest of this paper, two signal processing-based fault detection methods: wavelet transform and online kernel principle component analysis (KPCA) are adopted.

4.3.2 Adaptive Wavelet De-noising

Before proceeding with signal w_2 obtained from $w_2 = S_2 y$, measurement noise ζ needs to be filtered. In this paper, ζ is modeled as white noise produced by the environment with lower power according to [3]. Since the variances and amplitudes of the details of white noise at various levels decrease regularly as the level increases, the multi-resolution wavelet decomposition method proposed by [7] is capable of removing measurement noise from output signals.

Herein, following adaptive threshold function is introduced to improve wavelet de-noising effect:

$$\hat{W}_{l,k} = \begin{cases} \operatorname{sign}\left(W_{l,k}\right) \cdot \left(W_{l,k} - \alpha\beta_l\right), & \left|W_{l,k}\right| \geq \beta_l \\ 0, & \left|W_{l,k}\right| \leq \beta_l \end{cases} \tag{4.6}$$

where $W_{l,k}$ is the wavelet coefficients; $0 \leq \alpha \leq 1$ is the adaptive coefficient according to noise density; and β_l is the de-noising threshold at level l that calculated by:

$$\beta_l = \frac{\sigma_l \sqrt{2\ln(N_l)}}{\ln(l+1)} \tag{4.7}$$

where σ_l is the Gaussian white noise standard deviation at level l, N_l is the wavelet coefficients length at level l [2].

4.3.3 Online KPCA-Based Fault Detection

Denote the filtered w_2 signal as $\hat{w}_2$, then an online KPCA [8–10] is imposed on $\hat{w}_2$. The fault detection procedure is as follows:

1. Acquire normal data set from nominal model or experience data; extract nonlinear principal components and calculate the residual threshold from Q-statistics [11]. The selected kernel function is:

$$k(x,\ y) = \exp\left(-\frac{\|x-y\|^2}{c}\right). \tag{4.8}$$

2. Map $\hat{w}_2$ into a feature space and extract its nonlinear principal components in the feature space;

3. Check if the Q-statistics of $\hat{w}_2$ and its principal components exceed the residual threshold. If the threshold is exceeded, gives out a fault alarm.

Note this procedure is of compute-efficiency as it involves only eigenvalue problem but no optimization problem.

4.4 Simulation

The longitudinal LTI model of a generic HSV at a trimming point is given in (4.1). System matrices only contain rigid-body states; while the first three elastic modes are treated as model uncertainty. Four System outputs are velocity, altitude, pitch angle, and pitch rate. The first three outputs are directly measured from sensors.

All channels of w_2 will be monitored during flight. Hence, we can define the dimension of normal data set $\{x\}$ as 3×120.

Suppose the velocity sensor will suffer from following incipient fault signal during HSV cruise phase:

$$f_s = \begin{cases} 0, & t < 13\,\text{s} \\ 0.05\exp(0.01u), & 13\,\text{s} \le t < 26\,\text{s} \\ 0.07\exp(0.03u), & t \ge 26\,\text{s} \end{cases} \tag{4.9}$$

And the sampling rate is 30 Hz. As f_s starts from 13 s, normal $\{x\}$ and its statistics are simply sampled and calculated in any two 4 s before $t < 13$ s.

The w_2 signals are shown in Fig. 4.1. Though f_s directly imposed on channel 1, it is almost masked by various extensive interferences.

Set $\sigma_l = 10$, the $\hat{w}_2$ signal obtained via a 5-levels wavelet de-noising is depicted in Fig. 4.2. There still remain a few noise components.

Figure 4.3 presents the first three principle components of both normal and faulty data sets in feature space. The Cumulative percent variance is 92.7 %. When Normal data and faulty data have a clear boundary in feature space, and data of

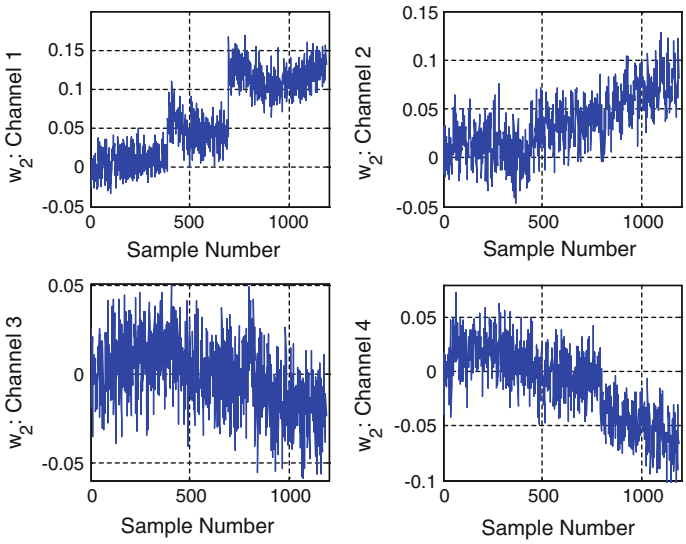

Fig. 4.1 Original w_2 signal

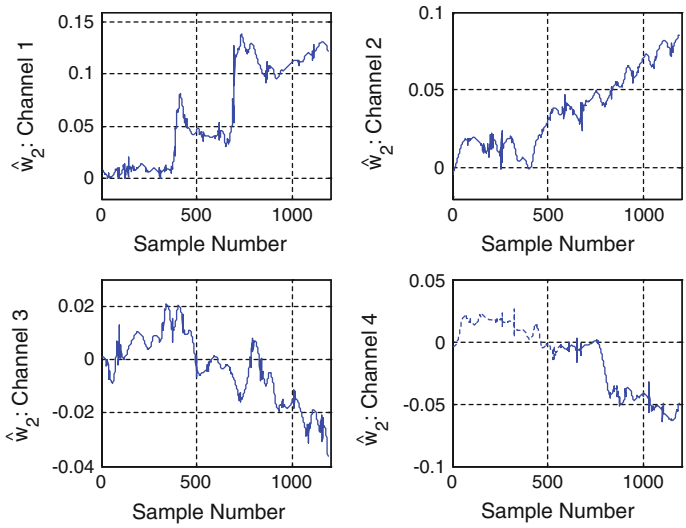

Fig. 4.2 Filtered $\hat{w}_2$ signal

different fault phase converge to different direction. Note, the faulty data is added onto feature space one by one. And design parameter $c = 50$ in (4.8).

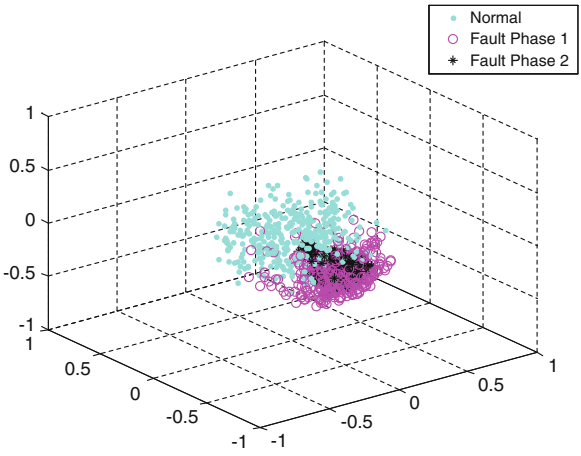

Fig. 4.3 Principle components distribution

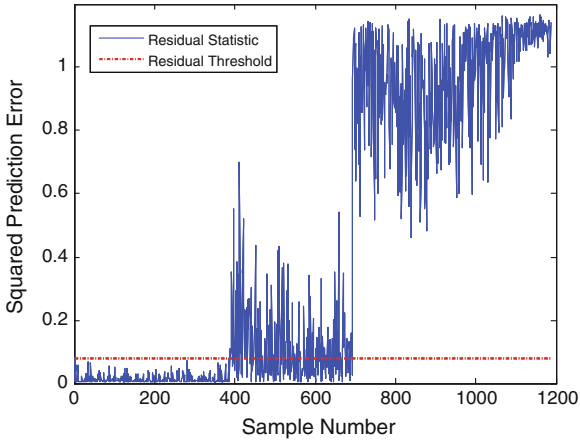

Fig. 4.4 Residual signal and its threshold

At last, Fig. 4.4 gives the final residual signal squared prediction error and its threshold. The threshold is 0.083 with confidence level at 99 %. The incipient fault is captured at $t = 13.067$ s.

4.5 Conclusion

Simulation result shows that though the presence of system uncertainties, process disturbance, and measurement noise, the proposed hybrid scheme can extract sensor incipient fault signals efficiently during HSV cruise phase.

To avoid further performance degeneration, fault isolation and fault tolerant control need to be considered after fault detection. However, this problem is left out in this paper and will be completed in our future work.

References

1. David BD, Michael WO, Michael AB (2006) Progress in guidance and control research for space access and hypersonic vehicles. In: Proceedings of the 45th IEEE conference on decision and control, San Diego, pp 6837–6851
2. Zhongsheng W, Hongkai J (2010) Robust incipient fault identification of aircraft Engine rotor based on wavelet and fraction. Aerosp Sci Technol 14:221–224
3. Ren L, Xu ZY, Yan XQ (2011) Single-sensor incipient fault detection. IEEE Sens J 11:2102–2107
4. Nikoukhah R, Campbell SL, Drake K (2010) An active approach for detection of incipient faults. Int J Syst Sci 41:241–257
5. Zhang J, Swain AK, Nguang SK (2012) Detection and isolation of incipient sensor faults for a class of uncertain non-linear systems. IET Control Theory Appl 6:1870–1880
6. Raoufi R, Marquez HJ (2010) Simultaneous sensor and actuator fault reconstruction and diagnosis using generalized sliding mode observers. In: Proceedings of American control conference, Baltimore, pp 7016–7021
7. Mallat SA (1989) Theory for multi resolution signal decomposition: the wavelet representation. IEEE Pattern Anal Mach Intell 11:674–693
8. Jong-Min L, Cang-Kyoo Y, Sang WC (2004) Nonlinear process monitoring using Kernel principal component analysis. Chem Eng Sci 59:223–234
9. Ji-Hoon C, Jong-Min L, Sang WC et al (2004) Sensor fault identification based on Kernel principal component analysis. In: Proceedings of the 2004 IEEE international conference on control application. Taipei, pp 1223–1228
10. Viet HN, Jean-Claude G (2010) Fault detection based on Kernel principal component analysis. Eng Struct 32:3683–3691
11. Nomikos P, MacGregor JF (1995) Multivariate SPC charts for monitoring batch processes. Technometrics 37:41–59

Chapter 5
Laser Shearography Testing for Aircraft Composite and Honeycomb Components

Gongjin Qi, Hong Lei, Peng Jing, Gangqiang Fu, Haisheng He and Qi Guo

Abstract With the rapid development of aircraft industry, high performance composite and honeycomb components are widely used. Various defects, such as delamination or debonding in composites, will lead to structural failure even flight accidents. Effective nondestructive testing methods, therefore, must be used to inspect the composite and honeycomb components. The objective of this paper was to introduce the test theory and characteristics of laser shearography method, exhibit the structure and performance of typical shearography testing instrument, and show testing examples for aircraft composite and honeycomb components. The developing trend for laser shearography testing technology was directed at the end.

Keywords Laser shearography · Aircraft · Composite · Nondestructive testing

5.1 Introduction

Aircraft structures are susceptible to fatigue cracks and impact defects during service in harsh environmental and working conditions, leading to a tendency to catastrophic failures of critical structural components if not detected and repaired. The problem of guaranteeing reliable and efficient checks has received great attention for early detection of aircraft structure defects to prolong the service life by necessary maintenance operations. A lot of advanced materials including high performance composite and honeycomb components have been used in aircraft industry [1], thus resulting in new problems for the structural integrity inspections. The defects, such as delamination or debonding, will lead to structural failure.

G. Qi (✉) · H. Lei · P. Jing · G. Fu · H. He · Q. Guo
Beijing Aeronautical Technology Research Center, Beijing 100076, China
e-mail: qgjin@sina.com

J. Wang (ed.), *Proceedings of the First Symposium on Aviation Maintenance and Management-Volume I*, Lecture Notes in Electrical Engineering 296,
DOI: 10.1007/978-3-642-54236-7_5, © Springer-Verlag Berlin Heidelberg 2014

Effective nondestructive testing (NDT) methods, therefore, must be used to inspect the composite and honeycomb components.

Various NDT techniques have been developed to date in addition to the conventional ultrasonic and eddy current testing technologies. Optical NDT is an area that is likely to experience increasing interest for the inspection of composite materials. The objective of this paper is to introduce the test theory and characteristics of laser shearography method, exhibit the structure and performance of typical shearography testing instrument, and show some testing examples for aircraft composite and honeycomb components.

5.2 Test Theory and Characteristics

Coherent optical inspection was first devised in 1965 by Powell and Stetson. Industrial exploitation was hampered, however, by the impracticalities of unreliable pulsed lasers and photographic processing of the exposed holograms. Optical inspection moved a step closer to industrialization in 1971 with the advent of a video-based version of holographic interferometry, i.e., electronic speckle pattern interferometry (ESPI). Unfortunately, ESPI is of limited value for production NDT because its extreme sensitivity to the environment can lead to speckled correlation between the two exposures. A further breakthrough came in 1979 when Hung developed laser shearography. He demonstrated that optical inspection is feasible in industrial environments if the separate reference beam used in ESPI to encode the phase information of the speckles is replaced by a sheared component of the object beam. The use of sheared wave fronts provides the additional advantage that the fringes depict changes in surface slope, rather than out-of-plane displacement [2].

Shearography is a laser-based interferometry in conjunction with the digital imaging processing technique for full-field measurement of surface deformation. It reveals defects in an object by looking for defect-induced deformation anomalies. It does not require special vibration isolation, and with the development of a small and mobile measuring device (portable inspection system), it can be employed easily in field/factory environments. One of the important thing for successful application is the combination of the shearography inspection method with choosing the adequate loading method for a given structure to be tested. There are three general types of loading which are mostly selected: (a) vacuum; (b) thermal load using infrared radiators, flash or heat gun, etc.; (c) mechanical load caused, e.g., by pressure changes in the test environment, or vibration load caused by a shaker. Figure 5.1 exhibits the basic testing theory for thermal shearography testing [2].

The potential advantages of shearography inspection are: (a) rapid large area inspection; (b) noncontact testing without immersion of the component, or the use of water jets; (c) ability to inspect regions that attenuate or scatter ultrasound; (d) ability to indicate structural strength in addition to providing passive defect detection [3].

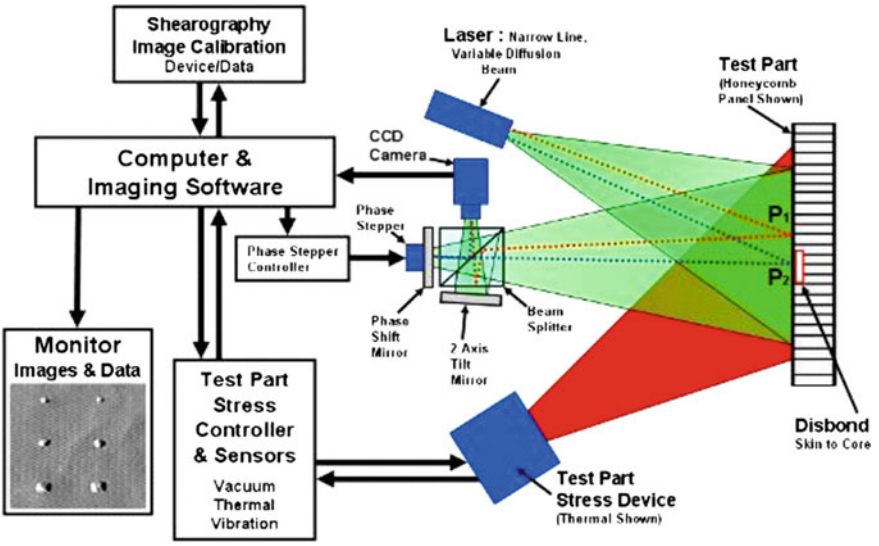

Fig. 5.1 Basic testing theory for thermal shearography

5.3 Shearography Testing System

With the development of sensor technology, it becomes possible to achieve an economic integration in inspection systems, including automatic shearography inspection systems and portable inspection systems [4, 5]. Laser Technology Inc. led the development of the shearography camera as a tool for nondestructive testing, delivering the world's first production shearography NDT system to Northrop Grumman in 1987 for the manufacturing of the USAF B2 Stealth Bomber.

Among the commercial products, some portable instruments are useful for field testing. For example, LTI-6200S portable thermal shearography system was produced by the Laser Technology, Inc. The system is a self-contained laser interferometer and thermal stressing system designed for the inspection of composite using thermal stressing. The LTI-6200S has been designed as a portable system to facilitate the inspection of structures where the use of a traditional stand alone shearography camera and thermal stressing source is impractical. The standard LTI-6200S shearography system is composed of three parts; the shearography camera/inspection hood, the travel case which incorporates the systems support electronics, and the shearography image processor (see Fig. 5.2).

Fig. 5.2 LTI-6200S portable thermal shearography system

Fig. 5.3 Shearography test on aluminum honeycomb panel

5.4 Testing Examples

The shearography testing system has been successfully used in the inspection of various type composite structures (i.e., Graphite, fiberglass, or metallic skins with honeycomb or foam cores). Figure 5.3 presents the application in aluminum honeycomb panel testing. The camera/inspection hood can easily be placed in any position to the surface by vacuum attaching. Figure 5.4 exhibits the shearography

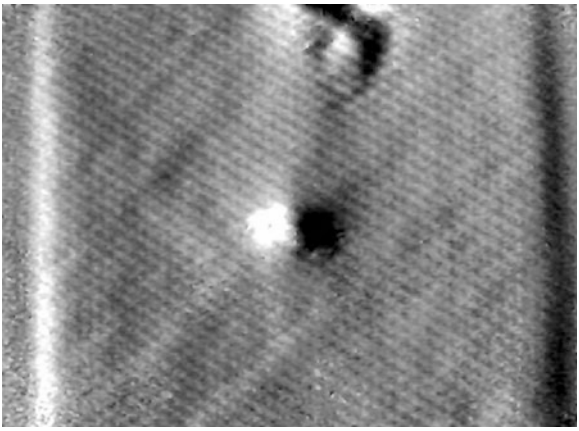

Fig. 5.4 Shearography results with two disbonding areas in graphite-skinned nomex honeycomb panel

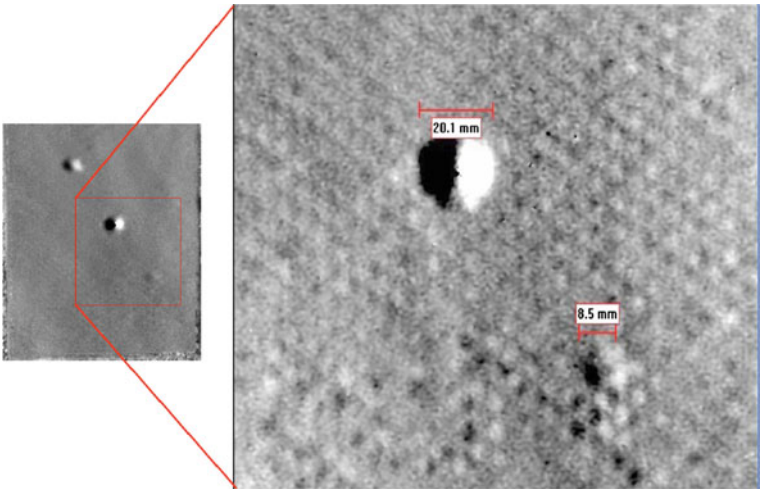

Fig. 5.5 Aluminum honeycomb panel with several defects tested by shearography

test results of two areas of disbonding on a raised honeycomb section of graphite skinned, nomex honeycomb test panel. Advanced image processor can give the size of the defects in aluminum honeycomb structures shown in Fig. 5.5.

5.5 Summary

In comparison to conventional NDT techniques, laser shearography offers the advantages of noncontact, full-field inspection, and rapid inspection ability.

Shearography has become a mature and cost-effective NDT technology for aircraft applications in the testing of composite materials and honeycomb structures, not only for process control but also for field inspection. In the future, the development of shearography should focus on improving the service life of the instrument, increasing the testing adaptability in harsh environmental conditions, and decreasing the whole cost of the system.

References

1. Burg T, Crosky A (2001) Aeronautical materials—teacher reference. School of Material Science and Engineering, University of New South Wales
2. Zhang J, Geng, R (2008) Studies on digital shearography for testing of aircraft composite structures and honeycomb-based specimen. In: Paper presented at 17th world conference on nondestructive testing, Shanghai, China
3. Kalms M, Osten W (2002) Advanced shearographic system for non-destructive testing of industrial and artwork components. Proc of SPIE 4915:34–43
4. Moser E (2008) Detection capabilities of state-of-the-art shearography systems. In: Paper presented at 17th world conference on nondestructive Testing, Shanghai, China
5. Newman JW (2008) Aerospace NDT with advanced laser shearography. In: Paper presented at 17th world conference on nondestructive testing, Shanghai, China

Chapter 6
Research of Aircraft Fuel System Feeding Failure Based on Flowmaster Simulation

Zehai Gao and Dong Song

Abstract Fuel system as an important part of the aircraft has a major impact on the safety of the aircraft. In order to study the failure status of aircraft fuel system, the simulation model of aircraft fuel system is built. The feeding process and failure of key component boost pump are simulated using fluid software of Flowmaster. The normal simulation data and failure simulation data of fuel system are got. The several failure conditions of aircraft fuel system are studied and analysis. The result provides a foundation for aircraft model-based failure diagnosis and failure prediction.

Keywords Aircraft fuel system · Model-based · Boost pump · Failure simulation

6.1 Introduction

Fuel system is an important component of the aircraft in all kinds of flight conditions and working conditions. Fuel system should provide an uninterrupted feeding of fuel pressure and fuel flow to the engine according to a certain order. The quantity of fuel and the boost pump pressure outlet signal are important indications of aircraft fuel system [1]. These indications will be primary standards of aircraft fuel system performance.

Model-based fault study approach is a new type of intelligent reasoning technology. It can overcome the shortcomings of the traditional fault technique [2]. In this paper, a precise fuel system model is built, and aircraft fuel feeding system has been simulated by one-dimensional fluid simulation software Flowmaster. In the end, fuel system model is verified by the simulation of aircraft fuel feeding system and research of the simulation results of normal operation and fault conditions.

Z. Gao (✉) · D. Song
School of Aeronautics, Northwestern Polytechnical University, Xi'an 710072, China
e-mail: 710341300@qq.com

J. Wang (ed.), *Proceedings of the First Symposium on Aviation Maintenance and Management-Volume I*, Lecture Notes in Electrical Engineering 296,
DOI: 10.1007/978-3-642-54236-7_6,

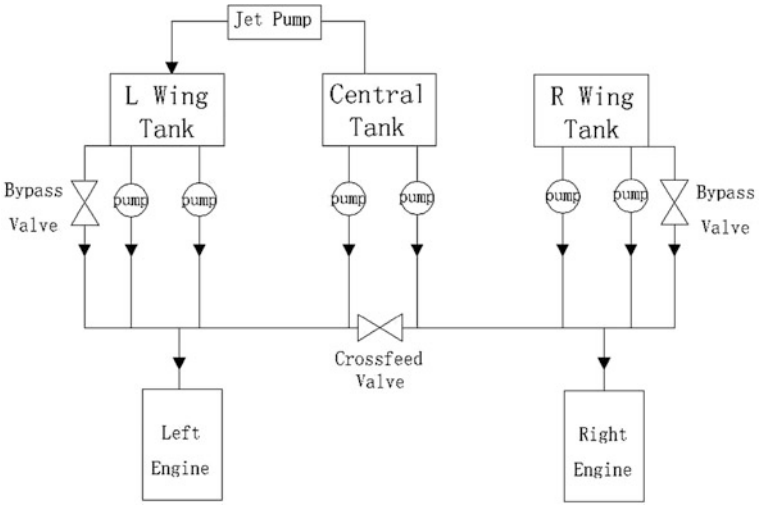

Fig. 6.1 Aircraft fuel feeding system structure diagram

6.2 System Modeling

6.2.1 Aircraft Fuel Feeding System Structure

In this paper, aiming at Boeing737 aircraft, feeding system is studied and analyzed. Boeing737 is aTwin-engine aircraft, has central tank, left wing tank, and right wing tank. To ensure feeding security, each of the tanks has two boost pumps. So, both engines can be fed by one side wing tank when the supply line of the other side is failure [3]. The ordering of provide fuel: first by the center tank feeding fuel, and then by the wing tank feeding fuel. In order to guarantee feeding order, it is controlled by the different pressure of central and wing tank boost pump outlet valve [4]. When the left wing tank fuel weight drops to 448T pounds (1,990 kg), the float valve which connect Left wing tank with the central tank opens. The bottom fuel of central tank will be pumped to the left wing tank by jet pump. When both sides of the wing tank boost pumps are failure, bypass valve opens, gravity feeding starts. Its basic structure is just like in Fig. 6.1.

6.2.2 Flowmaster System Modeling

The fundamental task of the aircraft fuel system is feeding fuel to the engine as a certain pressure and flow. In order to detect whether or not this system is working properly, typically, fuel system analyzes the data of fuel quantity and pump outlet pressure signal.

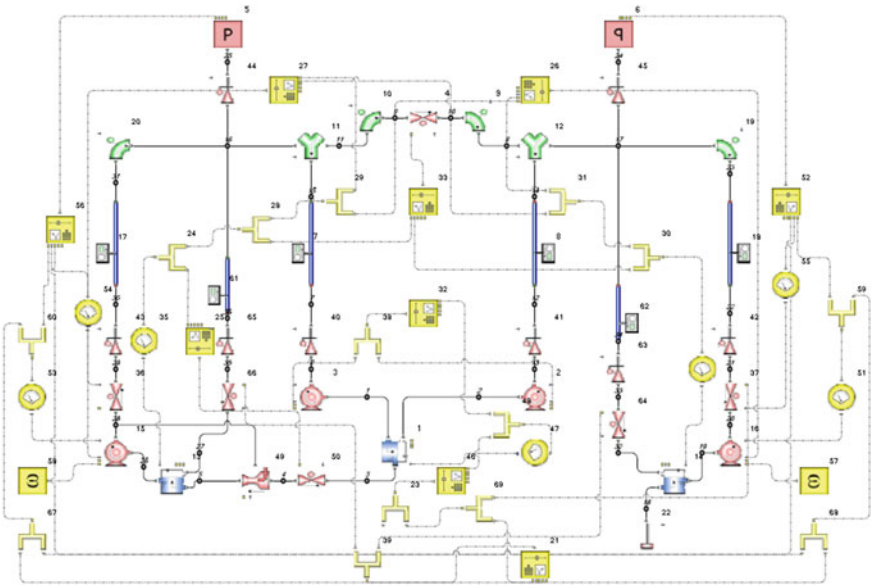

Fig. 6.2 Aircraft fuel system simulation model

In this simulation, pressure sources stand for two engines [5]. In Fig. 6.2, they are components 5, 6. Three 3-Armed Tanks, components 1, 13, 14, represent three fuel tanks. The left and right wing tanks have two boost pumps. In order to simulate fewer iterations and fast convergence, two boost pumps are fitted to one. Components 15, 16 are fitted wing tank boost pumps, Components 2, 3 are central tank boost pumps. Components 40, 41 stand for central tank boost pump outlet Check Valves. Combination of components 36 with 43, 37 with 42 to simulate wing tank boost pump outlet check valves. Combination of components 63 with 64, 65 with 66 to simulate two sides bypass valves. Component 4 represents cross-feed valve. Component 49 is jet pump. Its function is pumped fuel from the central tank to the left wing tank. Component 50 is the float valve which connect central tank with left wing tank. Components 44, 45 are spar valves.

Yellow components are Signal separation, measure, and control components, Components 34, 35, 47 measure the liquid level in three tanks. Components 51, 53, 54, 55 measure the speed of boost pumps and the state of outlet valves of each wing tank, respectively. Components 57, 58 control the speed of boost pump in wing tanks,components 26, 27, 32 control the state of each boost pump. Component 33 control the state of cross-feed valve, components 25, 46 control the state of float valve and feeding line valve. Component 21 controls the bypass valve opening and closing.

The other components are bends, pipes, junctions, Signal separation, and Zero Flow Blank End, black points are the nodes between components [6, 7].

6.3 Aircraft Fuel System Feeding Fault Simulation

All the simulation time is 4800 s. Step is 1 s. The simulation altitude is 10,607 m at cruise stage. Fuel type is JET 8 (JP-8) aviation kerosene.

Initial simulation center tank liquid level is 0.3 m. Center tank begin to feed fuel to engine in normal working condition. When the central fuel tank level is lower than 0.05 m, the center tank boost pumps stop working. Wing tanks start to feed fuel. Wing tanks are set full of fuel. Liquid level is 0.65 m.

Fuel system wing tank boost pump performance degradation is simulated. The left and right wing tanks use the same boost pumps, but the boost pump of left wing tank is working at rated speed 11,500 rpm. Right wing tank is working at 10,000 rpm. The speed is deviation from the best operating point. At this moment, the weight which left wing tank fuel supply is greater than the right wing tank. The weights of left and right wing fuel tanks become unbalance gradually. When the difference of two wing tanks fuel weight is more than 453.60 kg, left wing tank boost pump stops. The cross-feed valve opens, Left wing tank feed two engines. At this moment, the difference decreases gradually. When the weight difference of fuel is less than 90 kg, left wing tank boost pump works. The cross-feed valve closes.

Fuel system boost pump of wing tank failure is simulated. At first, in the simulation, central tank feed fuel, and then wing tank feed. However, when the system detects corresponding signal, in order to ensure flight the bypass valve opens and gravity feeding starts in the condition of both sides wing tanks boost pumps failure.

With the continuous fuel supply,the left wing tank is less than 448T pounds (1,990 kg), float valve opens. The jet pump pumps the bottom fuel of central tank to the left wing tank.

6.4 Feeding System Simulation Analysis

6.4.1 Normal Condition Feeding System Simulation Analysis

When the aircraft fuel system is working in normal condition, entire flight, the aircraft's fuel tank is supplied according to the order. At this condition, the aircraft fuel system could measure the fuel quantity. Figure 6.3 shows the results. Line 1 is the center tank fuel level changing curve. Line 2 and line 3 are the right and left wing tank fuel level changing curve. Line 4 is the time when float valve opens.

Before 1401 s engines is fed by the central tank, and then the engines is fed by the wing tank. Until 4351 s, float valve opens. Bottom fuel of central tank is pumped to the left wing tank. Fuel liquid level of left wing tank becomes higher than the right wing tank gradually.

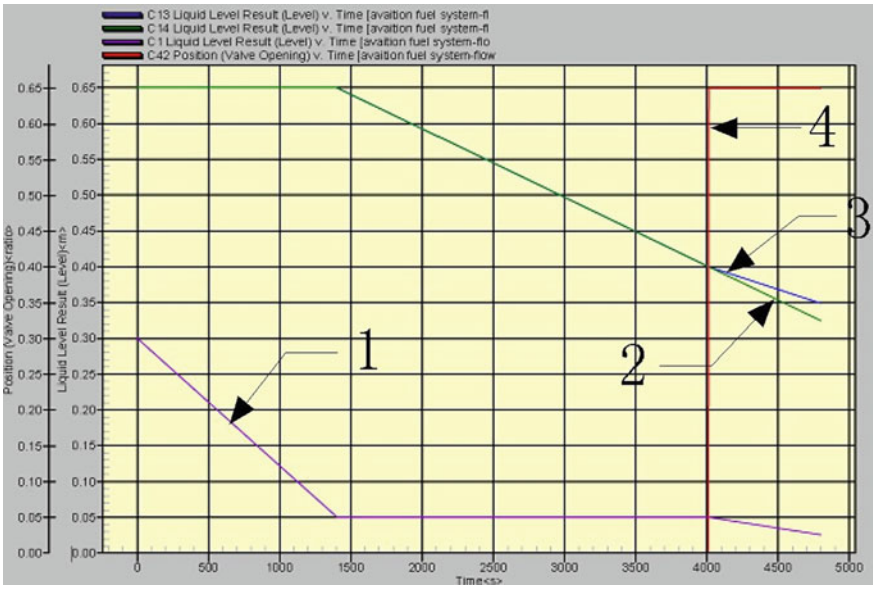

Fig. 6.3 Fuel level changing curve in normal working condition

6.4.2 Wing Tank Boost Pump Performance Degradation Simulation Analysis

The central tank boost pumps are working in normal condition. Left wing tank boost pump is set performance degradation. In this process, the engine inlet pressure should vary as the start and stop of the boost pump. Therefore, a curve of boost pump outlet pressure versus boost pump speed has been fitted. In Fig. 6.4, line 1 is that the speed of boost pump decreased from rate speed to zero. Line 2 is the boost pump outlet pressure which changing accordingly.

This curve has been loaded into DATA CURVE of controller template component. This component belongs to Flowmaster software. Script is written in Csharp. So, outlet pressure is read according to boost pump working speed. This pressure minus pipeline pressure drop is the final pressure. The final pressure is given to pressure source, which standing for engine inlet pressure. The different speed will lead to different pressure. If one side boost pump damaged, two sides engine inlet pressures is offered by the other side boost pump. As the lengths of boost pump to two engines are different. The lengths of pipeline are different. The two engine inlet pressures are different.

Simulation result shown as in Fig. 6.5. Line 1 is the center tank fuel level changing curve. Line 2 is the left wing tank fuel level changing curve. Line 3 is the right wing tank fuel level changing curve. Line 4 shows the time when the cross-feed valve opens and closes. Line 5 shows the time when the float valve opens.

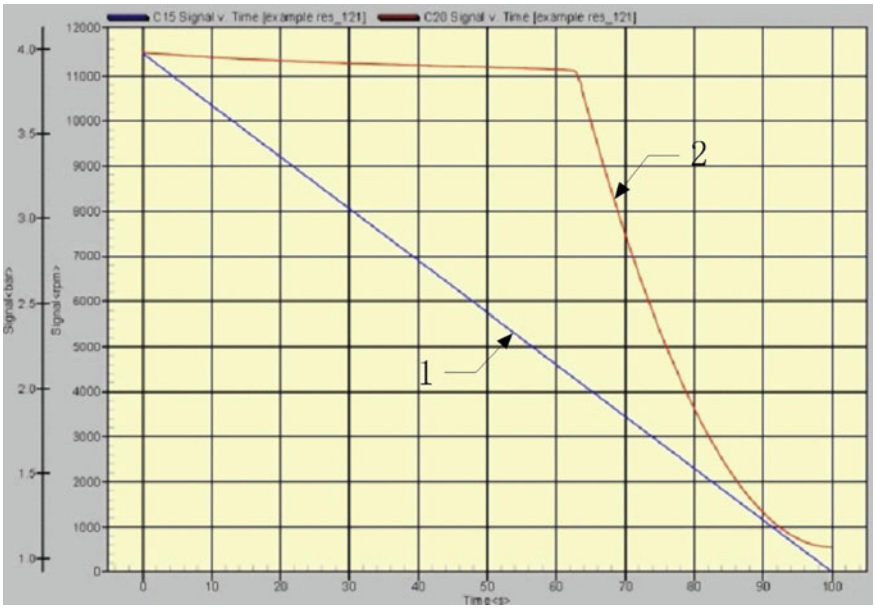

Fig. 6.4 Boost pump speed versus Boost pump outlet pressure

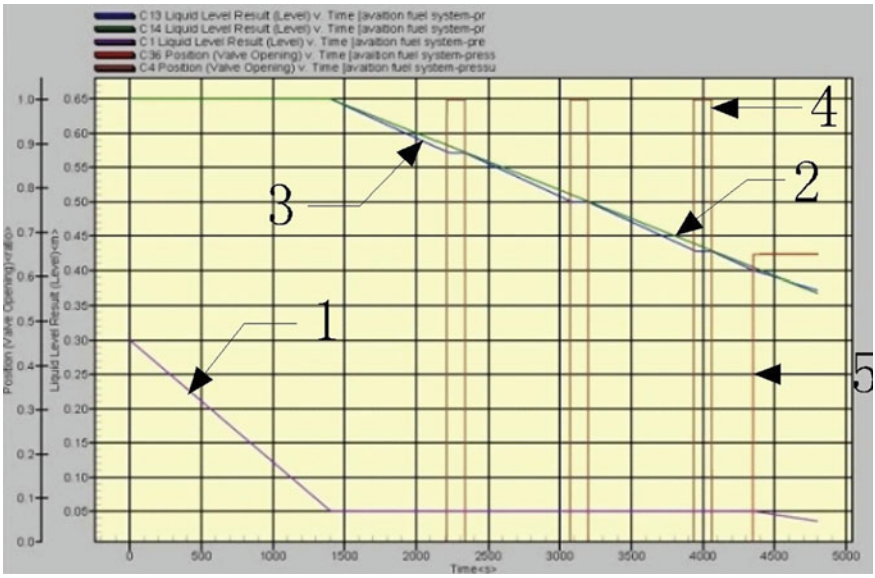

Fig. 6.5 Fuel level changing curve in the condition of boost pump performance degradation

As we know after central tank stop feeding fuel, it is time to supply engines by wing tanks. But the left and right wing tank boost pumps work in different speed. Two tank fuel level drops at different rates. When the fuel level difference overrun, cross-feed valve opens. And then, gradually, the fuel level difference become narrow and cross-feed valve closes. However, the left and right wing boost pumps always work in a different speed. The fuel level and the state of the cross-feed valve will present cycle image. Until float valve opens, Left wing tank fuel level relative consumption rate decreases.

Compare the results of boost pump performance degradation and normal condition. As we know the same boost pump have the same ability. If the Center Instrument Panel shows two wing tanks fuel level difference increases, cross-feed valve is opened periodically. So the boost pump performance probably degenerate.

6.4.3 Wing Tank Boost Pump Damage Simulation Analysis

If one wing tank boost pump is damaged and cross-feed valve could not open, or two sides wing tank boost pump is damaged, to ensure the aircraft flight, gravity feeding starts. At the same time, no matter which boost pump is damaged,there is a corresponding warning signal display in fuel control panel.

If both sides wing tank boost pumps damage, namely the pumps speed are 0, the bottom level of each tanks are higher than engine inlet level. In this simulation pressure source is the engine inlet pressure. Initially, this pressure is provided by the central tank boost pumps, and then the pressure is related to flight altitude, engine boost pump suction, and pipes pressure drop. Finally, the pressure is obtained.

Figure 6.6 shows the simulation result of each tanks fuel level changing curve in the condition of both wing tanks pump damage. Line 1 is central tank fuel level changing curve. Line 2 is right wing tank fuel level changing curve. Line 3 is left wing tank fuel level changing curve. First stage central tank feed fuel, and then turn to wing tanks.

Compared with the curve in normal condition,we know the feeding rate in the condition of gravity feeding is significantly slower than boost pump feeding rate. After float valve opens, the fuel level of center tank is not declined. Instead, the center tank fuel level rises. In the end, the left wing tank fuel level is lower than the right wing tank. Because there is no power source for jet pump after the boost pump failure. Left wing tank fuel level is higher than central tank and float valve opens, fuel flows from left wing tank to central tank. This is one kind of failures. If there are boost pumps outlet pressure warning signals, the boost pumps and float valve damage will be known.

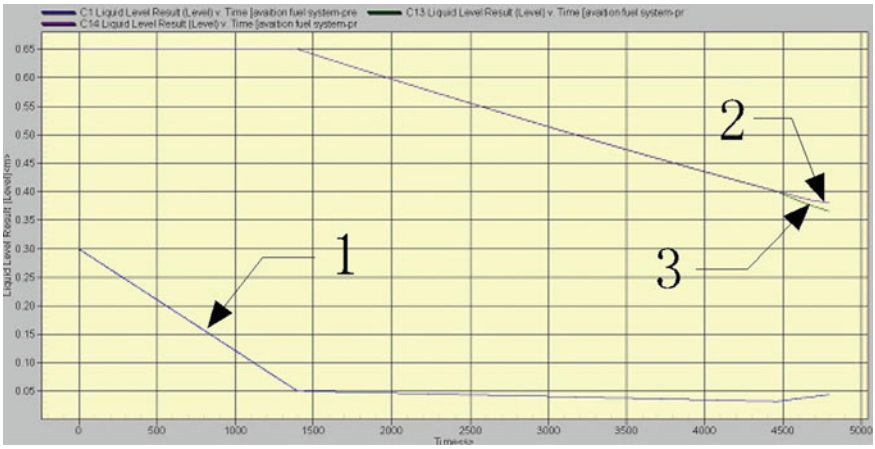

Fig. 6.6 Fuel level changing curve in the condition of boost pump damage

6.5 Conclusion

In this paper, we use fluid simulation software Flowmaster building the fuel system model, aiming at fuel feeding system for a series of simulation and analysis. The data of fuel system working in normal condition is obtained. The results in the condition of that one side wing tank boost pump performance degradation and both sides wing tanks boost pump damage has been studied. The simulation results would lay a foundation for Aircraft Prognostic Health Management.

References

1. Zhaohong Song (1993) Typical failure analysis for aircraft engine (in Chinese), 1st edn. Beihang University Press, Beijing
2. Song ZH (1993) Typical failure analysis for aircraft engine (in Chinese), 1st edn. Beihang University Press, Beijing
3. Przytula KW (2006) Reasoning framework for diagnosis and prognosis. In: Paper presented at 2006 IEEE aerospace conference, Big Sky, Montana, 7–14 March
4. Xiong H, Liu X, Zhen B (1990) Aircraft flight dynamics. Aviation Industry Press, Beijing
5. Yong-shou L, Zhen-zhou F, Kua-hai Y etal (2007) Influence of fuel pump failure on the stability of an aircraft fuel system. In: Paper presented at 7th AIAA aviation technology, integration and operations conference, Belfast, England, AIAA2007–7826
6. Shen T, Wan FY, Cui WM, Song BF (2010) Application of prognostic and health management technology on aircraft fuel system, In: Proceedings of 2010 prognostics and system health management conference
7. Gao F, Liu Y, Vue Z (2008) A study of the fuel feeding stability of an aircraft fuel transport system. Mech Sci Technol Aerosp Eng 27: 1541–1544

Chapter 7
Numerical Simulation Study on Thermal Shearography Testing

Rili Hou, Aiguo Wu and Yan Li

Abstract As the principle of shearography testing is complicated, it is not easy to select testing parameters and interpret the testing signals exactly. Taking LY12 aluminum alloy and T300 carbon fiber reinforced composite as model materials, the relations between testing signal and loading temperature, heating time, and cooling time have been studied by finite element numerical simulation. The results show that composite such as T300 will produce distinct deformation in damaged region when it is heated, and increasing loading temperature can amplify testing signals obviously; prolonging the heating time can only amplify the testing signals at the initial stage; during cooling time, the relative deformation between damaged and undamaged area will change from positive to negative, which will make the two-bladed interference pattern from "left-white, right-black" to "left-black, right-white." Metal such as LY12 cannot deform obviously in damaged region when it is heated, no matter how you adjust the testing parameters, so it is unsuitable to test metal structure by using thermal shearography.

Keywords Laser · Shearography · Thermal loading · Metal · Composite

7.1 Introduction

Shearography testing, as a new NDT technique, is developed along with the development of computer technique, CCD, and digital image processing techniques from 1980s [1, 2]. It has been applied in aerospace and automobile manufacture [3–5] for its high sensitivity, high efficiency, and noncontact. But on the other hand, as the shearography is based on testing derivative of the out-of-plane displacement of

R. Hou (✉) · A. Wu · Y. Li
The First Aeronautic Institute of Air Force, Xinyang 464000 Henan, China
e-mail: hrl6319@sina.com

J. Wang (ed.), *Proceedings of the First Symposium on Aviation Maintenance and Management-Volume I*, Lecture Notes in Electrical Engineering 296,
DOI: 10.1007/978-3-642-54236-7_7,

workpiece surface, the relation between testing parameters and testing signals is indirect, and the two-bladed interference pattern which represents the flaw signal is not intuitionistic, so it is not easy for NDT personnel to select testing parameters and interpret the testing signals exactly. Taking LY12 aluminum alloy and T300 carbon fiber reinforced composite, the two major aircraft structure materials as model materials, the relation between testing parameters and testing signals has been studied by finite element numerical simulation in this paper.

7.2 Finite Element Models

7.2.1 Fundamental of Thermal Shearography Testing

Because all the surface of workpiece cannot be ideally smooth, when it is irradiated by laser, the rays will be reflected from different concavo-convex points. As we know, according to Huygens' principle, every reflection point can be regarded as an independent light source, the reflected rays from different light source will interfere and form interference pattern that is called laser speckle.

The laser speckle testing technique is divided into single-beam and double-beams interference techniques. The single-beam interference technique is that all the interference rays are directly reflected from different fractions of the workpiece surface. This technique is also called speckle photography. The double interference means that the interference speckles are formed by two beams: usually, one beam is the rays reflected from the workpiece, the other is a reference beam. The double-beams interference technique is also divided into two methods: One which is usually applied to measure displacement and deformation is called speckle interference; the other which is applied to measure strain and derivative of out-of-plane displacement is called shearography.

The principle of shearography can be described as Fig. 7.1.

The laser beam from the laser generator is reflected from reflector 1 to the workpiece, and then it will be reflected to the spectroscope from which the beam is separated into two beams: one beam travels to reflector 2, and is reflected to CCD camera; the other will travel to dephasing reflector. Because the dephasing reflector is a little oblique, and the beam reflected from it will deviate the beam reflected from reflector 2 in the CCD camera, this dislocation is also called shearing displacement. The two beams will interfere in the camera and form interference pattern.

During testing, the workpiece will be loaded, and two interferograms will be taken before and after loading. Making subtraction between the two pictures can get displacement information of the workpiece surface. Here, we just take the out-of plane displacement into account. If there is a flaw (taking a circular flaw for example) in the workpiece, the surface near the flaw will deform like Fig. 7.2a, and differentiating the out-of-plane displacement curve can get the derivative curve

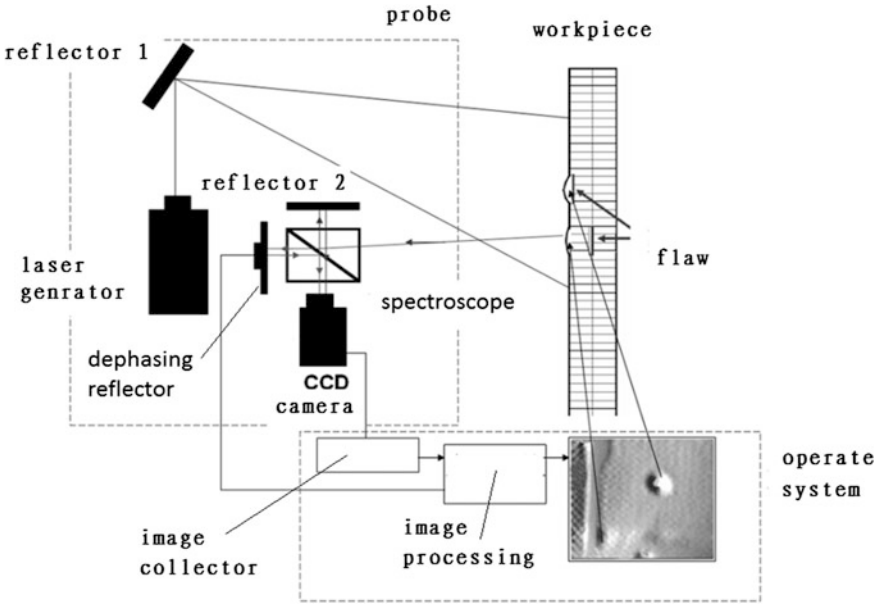

Fig. 7.1 The principle of shearography testing

which is shown in Fig. 7.2b. This function can be realized by special circuit design and image processing. In shearography testing system, the derivatives of the out-of-plane displacement are displayed by shade of gray. The bigger the derivative value, the brighter the speckle picture. So it is not difficult to understand that the circular flaw will give a special blank-white two-bladed pattern shown in Fig. 7.2c.

There are a lot of loading methods for shearography testing, such as thermal loading, pressure loading, and vacuum loading, etc. In this paper, we just discuss the thermal loading. Because the thermal conductivity of flaw is usually much smaller than the workpiece material's, when the workpiece is heated, the thermal energy will be accumulated near the flaw, which will make the temperature of the damaged region a little high than the undamaged area. For the same reason, the out-of-plane displacement in the damaged area is also a little bigger than the surrounding undamaged material's. From above all, we can draw a conclusion that if the thermal conductivity of the flaw is close to the workpiece material, the flaw cannot be tested by thermal shearography.

7.2.2 Modeling for Finite Element Analyzing

To simulate the thermal shearography testing process, the most important thing is analyzing the temperature, out-of-plane displacement, and its derivative of the

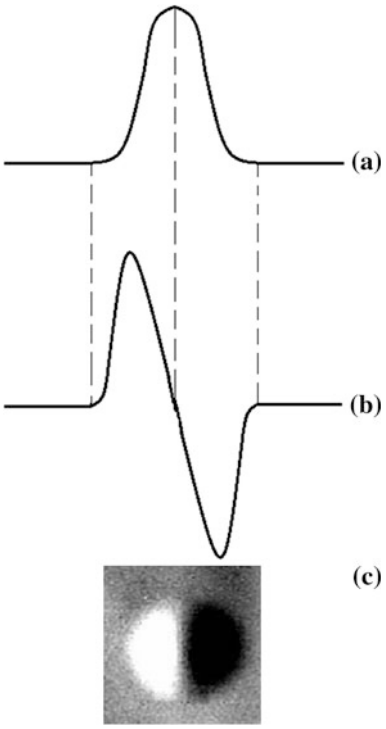

Fig. 7.2 The principle of shearography signal processing. **a** Out of plane displacement. **b** Out of plane displacement derivative. **c** Shearography pattern

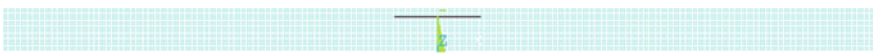

Fig. 7.3 Finite element model

workpiece surface when it is heated, that is a question of transient thermal-structure coupling analyzing.

As the thickness of the workpiece of aircraft structure is usually much smaller than its width and length, even it is much smaller than the probe size of the thermography testing system, we can only take the cross-section of the workpiece into account, and simplify the analyses as a matter of plane strain, so the ANSYS software and its coupled field plane13 element are selected.

In this paper, we take the sample sizes as 100 mm × 100 mm × 5 mm, and supposing there is a 10 mm wide defeat in it, which is at the center of the sample and just 1 mm below the upper surface. The finite element model is shown in Fig. 7.3.

The loading method for the analyzing mode is determined by the heating equipment of the testing system. As we know, the thermal shearography testing systems usually use halogen lamp as heating source, and there are fans in the probes

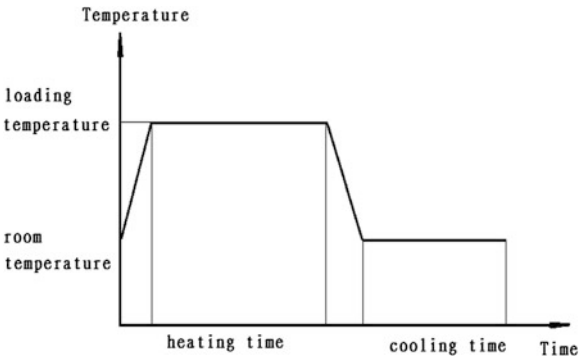

Fig. 7.4 Loading curve

to make air-forced convection. So, we suppose that the workpiece is heated by hot air and cooled by room-temperature air. The loading curve is shown in Fig. 7.4.

7.3 Simulation Results and Analyzing

LY12 aluminum alloy and T300 fiber reinforced composite, the two major aircraft structure materials are taken as model materials, the testing parameters such as loading temperature, heating time, and cooling time are taken into account.

7.3.1 Simulation for LY12 Aluminum Alloy

The parameters of LY12 aluminum alloy are shown in Table 7.1.

There are three work conditions: (1) Loading temperature is 50 °C, heating time is 3 s, cooling time is 45 s, the temperature, out-of-plane displacement, and its derivative at different time are analyzed. (2) Loading temperature is 100 °C, heating time is 3 s, cooling time is 45 s, the effect of temperature on testing signal is studied. (3) Loading temperature is 50 °C, the effect of heating time on testing signal is simulated. Some of the results are presented as follows.

Figure 7.5 shows that when the sample is loaded, the heat energy will be accumulated in the damaged region because of the low conductivity of the flaw, and the temperature of the damaged zone is higher than the undamaged area, so is the out-of-plane displacement, which is shown in Fig. 7.6. Figure 7.7 shows that though the center of flaw has the biggest displacement, the edge of the flaw is still unclear. The main reasons are that the conductivity of the LY12 aluminum alloy is very big, and the material is isotropic, so the accumulated heating energy can be spread to the surrounding area quickly, and every direction has the same degree of thermal expansion. Here, we can conclude that the flaws cannot be tested by only measuring the displacement for LY12.

Table 7.1 Parameters of LY12 aluminum alloy [6]

Conductivity/ (W.m. °C)	Specific heat/ (J/kg. °C)	Thermal expansion	Density/ (kg/m^3)	Elastic model/(Pa)	Poisson's ratio
121	921	22.7×10^{-6}	2800	68×10^9	0.33

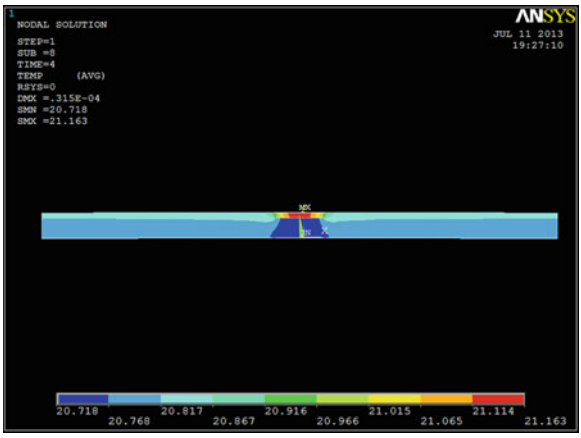

Fig. 7.5 Temperature of the LY12 sample at 4 s

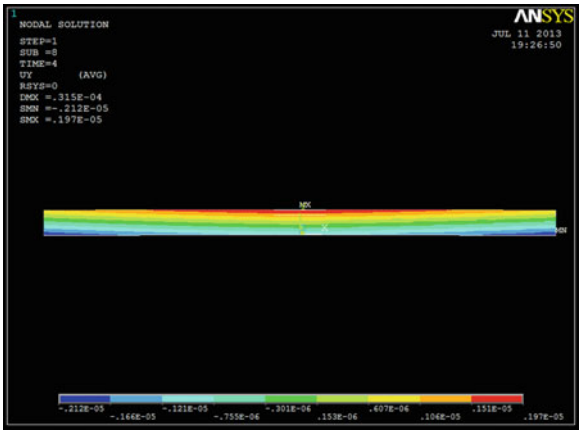

Fig. 7.6 Out-of-plane displacement of the LY12 sample at 4 s

Figure 7.8 shows that the out-of-plane displacement derivative will change abruptly at the edge of damage region. According to the principle of shearography testing, the periodic changed derivative will make a special blank-white two-bladed pattern which indicates a flaw. But Fig. 7.8 also shows that the degree of derivative is very low, and the testing signal must be very weak.

Figures 7.9 and 7.10 represent the change tendency of temperature and out-of-plane displacement of different points when the sample is cooled, respectively. Here, the curve 1 is the center point of the flaw, the curve 2 is the edge point of the

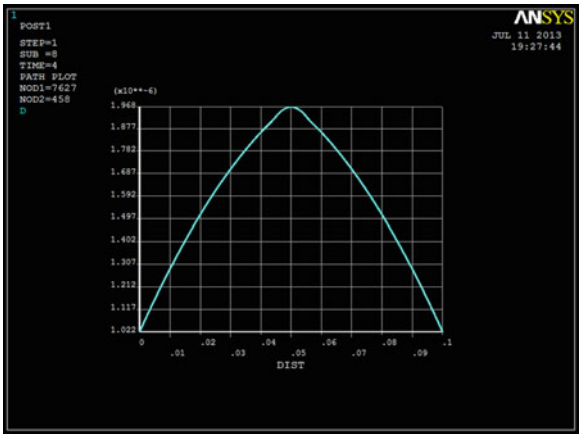

Fig. 7.7 Out-of-plane displacement of the LY12 surface at 4 s

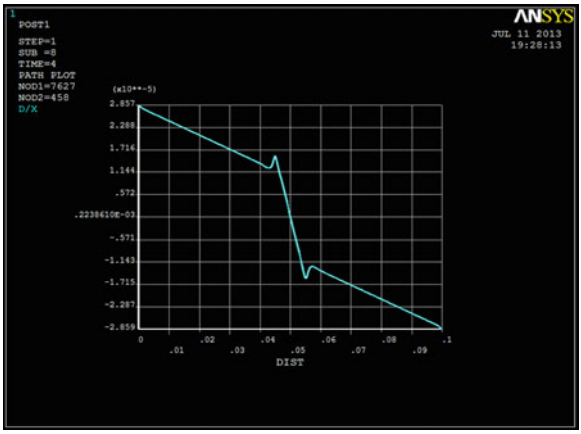

Fig. 7.8 Out-of-plane displacement derivative of the LY12 surface at 4 s

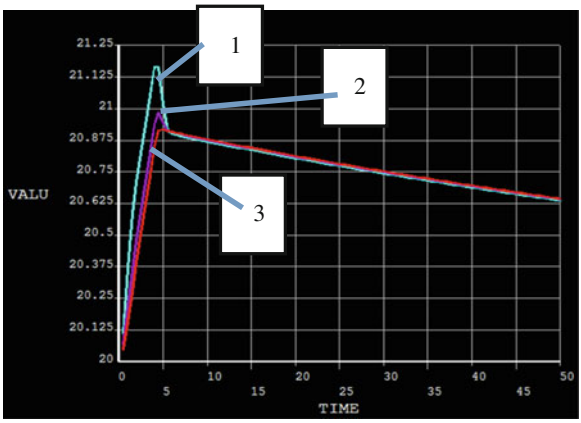

Fig. 7.9 Effect of cooling time on the temperature of the LY12 sample

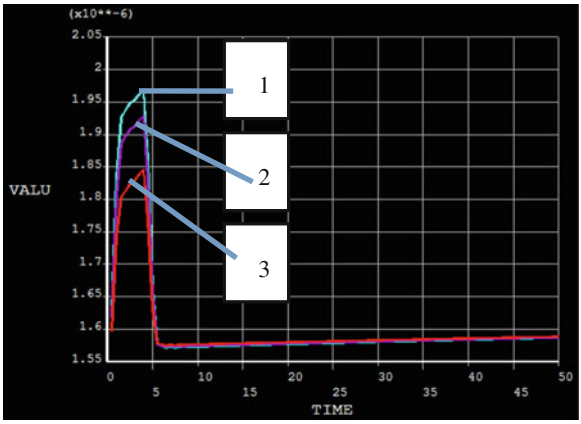

Fig. 7.10 Effect of cooling time on the out-of-plane displacement of LY12

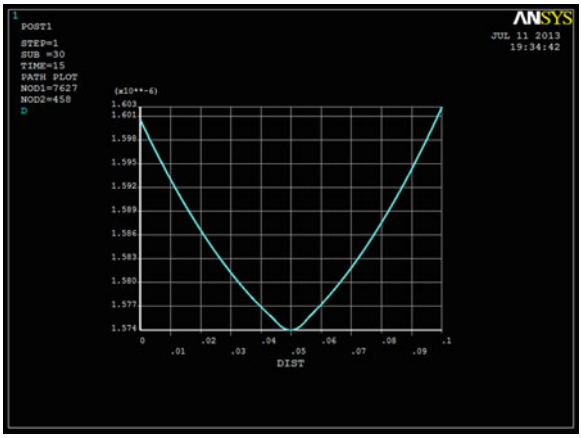

Fig. 7.11 Out-of-plane displacement of the LY12 sample surface at 15 s

flaw, the curve 3 is the point from undamaged area (the curves in Figs. 7.13, 7.14, and Figs. 7.17, 7.18, 7.19 and 7.20 have the same definitions). These figures show that the temperature of the damaged area decrease faster than the undamaged zone when the sample is cooled, so does the thermal deformation. The out-of-plane displacement of the damaged region is even smaller than the undamaged area if the cooling time is long enough, which can be seen in Fig. 7.11, and then, the change trend of derivative will upset. That is to say, the trend will change from "up-down-up" to "down-up-down." Accordingly, the interference pattern is changed from "left-white, right-black" to "right-white, left-black" Fig. 7.12.

The effect of the heating time on testing signal is shown in Fig. 7.13. With the increasing of heating time, the displacements of all the points will also increase. But their relative displacements are almost unchanged. This result can be explained by the big conductivity and isotropic property of aluminum. That is to say, increasing heating time cannot improve the testing signal for aluminum Fig. 7.14.

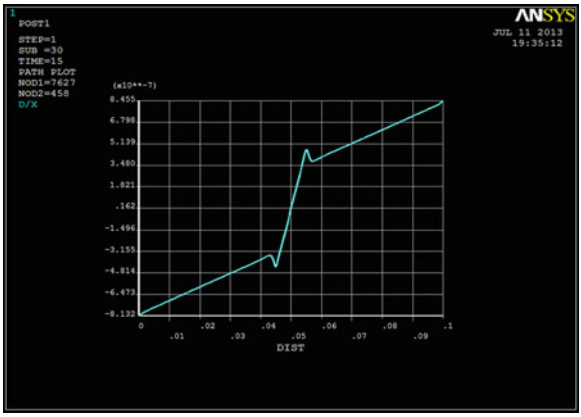

Fig. 7.12 Out-of-plane displacement derivative of the LY12 sample surface at 15 s

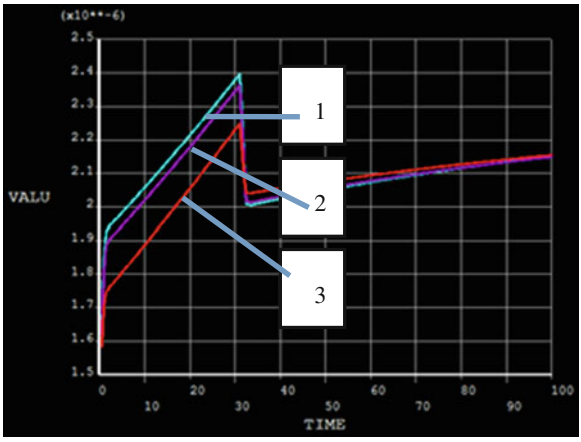

Fig. 7.13 Effect of heating time on the out-of-plane displacement of LY12

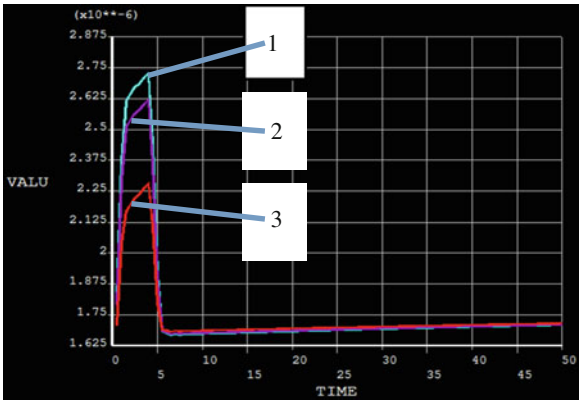

Fig. 7.14 Effect of heating temperature on the out-of-plane displacement of LY12

Table 7.2 The parameters of T300 carbon fiber reinforced composite [7]

Density/ (kg/m^3)	Specific heat (J/kg. °C)	Elastic model (X)/Pa	Elastic model (Y)/(Pa)	Poisson's ratio
1600	1060	1.35×10^{11}	9.4×10^{7}	0.28

Thermal expansion (X)	Thermal expansion (Y)	Conductivity (X)/ (W.m. °C)	Conductivity (Y)/ (W.m. °C)
0.01×10^{-6}	25×10^{-6}	5.23	0.75

7.3.2 *Simulation for T300 Carbon Fiber Reinforced Composite*

The parameters of T300 carbon fiber reinforced composite are shown in Table 7.2. The work conditions are totally the same as Sect. 7.3.1.

As the composites of aircraft structures are made from different lamina which has different orientation, and what we are interested in shearography testing is the displacement of thickness direction, so it can be regarded as macroscopically isotropic in the other two directions.

Simulation results show that the T300 has a lot of similar characteristics as LY12. First, because the conductivity of the flaw is much smaller than the structure material's, and the heat energy will be piled in the damaged area when the material is heated. For the same reason, the temperature of the damaged region is higher than the undamaged area. Second, when the structure is heated, the whole material will deform due to heat expansion, and the deformation of damaged area is bigger than the other area. Third, when the material is cooling down, the temperature of damaged area decreases faster than the undamaged area, the tendency of derivative will also change from "up-down-up" to "down-up-down," and the interference pattern will change from "left-white, right-black" to "right-white, left-black."

As the conductivity of T300 carbon fiber reinforced composite is much smaller than metal's, and the material is anisotropic, especially, the expansivity of thickness direction is much bigger than the other direction's, this material has some special characteristics. First, the temperature in damaged area is obviously higher than the undamaged area, so is the displacement, from the out-of-plane displacement curve (Fig. 7.15), the damage boundary can be seen clearly. Second, the degree of displacement derivative is much bigger than LY12 (Fig. 7.16), that is to say, the testing signal is stronger than the LY12's. Third, the cooling curves of T300 (see Fig. 7.17) are not as sharp as LY12, there is a period of time in which the out-of-plane displaces of damaged area are obviously bigger than the undamaged area, see Fig. 7.18, we can select this period to test. Fourth, Figs. 7.19 and 7.20 show that the heating time and loading temperature affect the testing signal evidently, so we can adjust these parameters to amplify testing signals, and it had best select high-power halogen lamp for the shearography testing system.

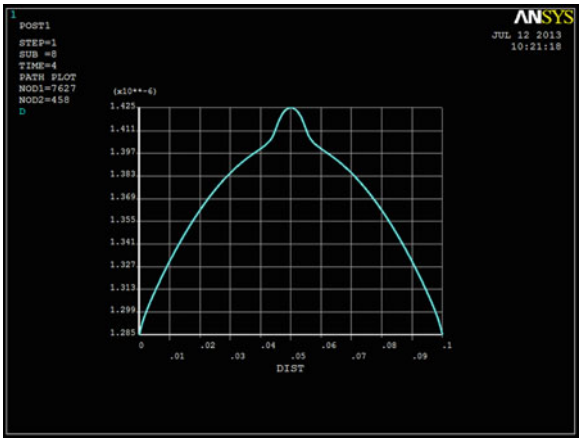

Fig. 7.15 Out-of-plane displacement of T300 at 4 s

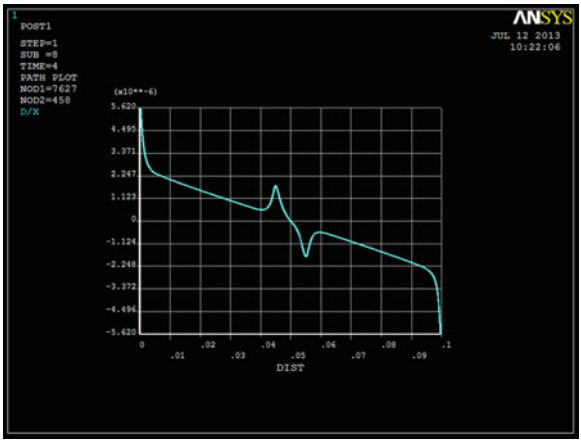

Fig. 7.16 Out-of-plane displacement derivative of the LY12 surface at 4 s

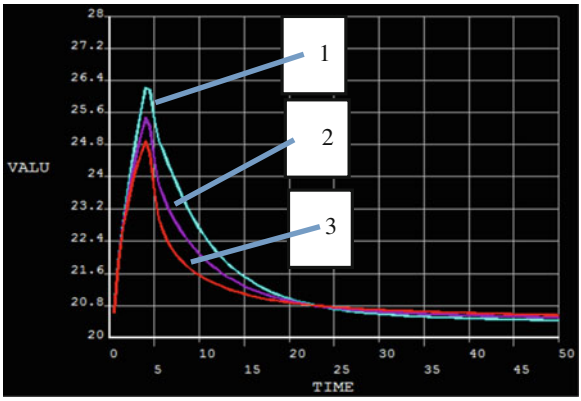

Fig. 7.17 Effect of cooling time on the surface temperature of T300

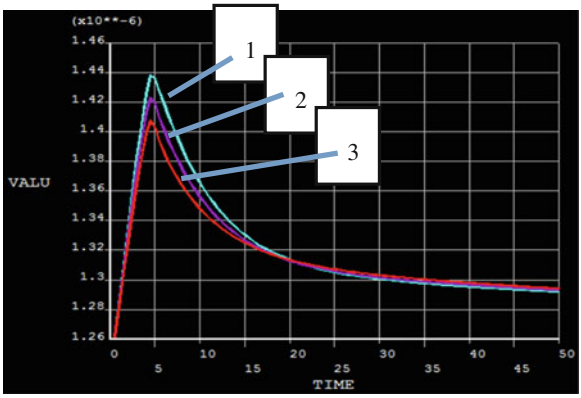

Fig. 7.18 Effect of cooling time on the out-of-plane displacement of T300

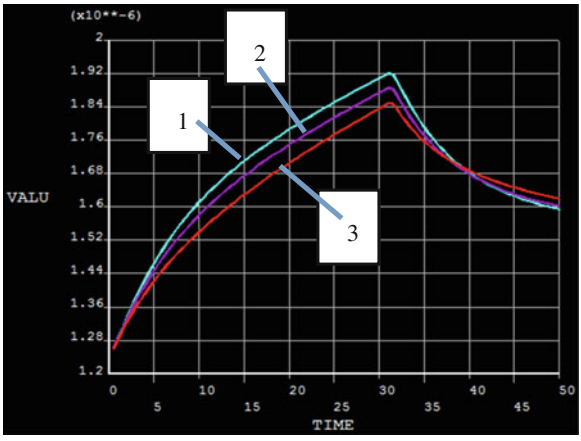

Fig. 7.19 Effect of heating time on the out-of-plane displacement of T300

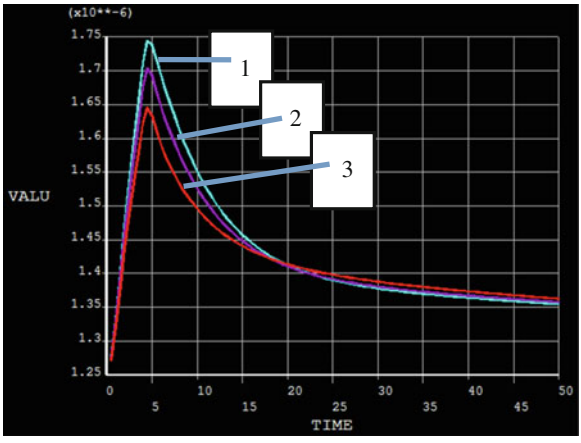

Fig. 7.20 Effect of loading temperature on the out-of-plane displacement of T300

7.4 Summary

For metals as LY12 aluminum alloy, as they usually have big conductivity, the local temperature and out-of-plane displacement caused by heat energy piled in damaged area are only a little higher than the undamaged material's, the value of derivatives are usually very low, so the testing signals are usually very weak. That is to say, it is unsuitable to select thermal loading method to test metal structure.

For composites such as T300 carbon fiber reinforced material, as they usually have small conductivity and are anisotropic, especially, the expansivity in thickness direction is much bigger than the other direction's, the local temperature and out-of-plane displacement caused by heat energy piled in damaged area are obviously bigger than the undamaged material's, and the degree of derivatives are also higher than metal's. So they are suitable to be tested by thermal shearography. Simulating results show that the higher the loading temperature, the bigger the displacement, and the stronger the testing signal; the heating time can only affect the testing signal at the initial stage of loading; the effect of cooling time on testing signal is somewhat complicated: at the initial stage, the relative displacement between damaged and undamaged area will increase with the cooling time, and then it will decrease along with the cooling time. There is a transition from which the relative displacement will change from positive to negative, and the interference double-bladed pattern will change from "left-white right-blank" to "left-blank right-white," so the testing time cannot be selected near the transition.

References

1. Hung YY (1999) Applications of digital shearography for testing of composite structures. J Compos: Part B 30:765–773
2. Hung YY, Ho HP (2005) Shearography: An optical measurement technique and applications. J Mater Sci Eng 49:61–87
3. Liu CH, Tang JF (2010) Nondestructive testing technique of aerospace composite materials based on DSSPI. J Comput Meas Control 18(5): 103–1041
4. Chen W, Zhang J (2012) The application of laser shearogphy speckle testing aircraft composite structure(in Chinese). J Qingdao Univ (E&T) 27(4): 80–83
5. Wang M (2011) Study on detection of structural defects based on DSSPI (in Chinese). Nanjing University of Aeronautics and Astronautics, D. Nanjing
6. Editorial committee of handbook of engineering material (2002) Handbook of engineering material (in Chinese), vol 3. Chinese Standard Press, Beijing
7. Editorial committee of handbook of engineering material (2002) Handbook of engineering material (in Chinese), vol 6. Chinese Standard Press, Beijing

Chapter 8
Study on the Method of the Fatigue Test for a Certain Aircraft Movable Wings

Zhao Junjie, Yang Huiyu, Wang Zhi, Song Haiping and Xue Jun

Abstract In order to simulate the real flight load of aircraft structure, the fatigue test of the movable wings (including leading-edge flap, flaperon, stabilator) of a certain aircraft gives a new requirement. That is, the movable wing is rotating while the fatigue load is applying on it. This is a new challenge to the method of aircraft structure fatigue test. Aiming at this problem, this paper proposes a movable wing fatigue test method that can simulate the loading state of the movable wing in its rotating process, and solves the problem of coordinated loading between wing rotation angle and fatigue loading. The method successfully completed fatigue tests of aircraft leading-edge flaps, flaperon, and stabilator of a certain type aircraft. The test results show that, fatigue damages of key parts on movable wings in fatigue tests are basically the same fatigue damages during service.

Keywords Aircraft · Fatigue test · Aircraft movable wing

8.1 Introduction

The movable wings of a certain aircraft are leading-edge flap, flaperon, and stabilator. The pilot operates movable wings to change the flight attitude, so the stress feature of these wings is that, the wing is rotating while the fatigue load is applying on it.

The design of movable wings is according to the general stiffness, and their fatigue strength is not examined in the previous aircraft structural fatigue test. They are just as a part of wings, and the joints of them are examined in full-scale fatigue test, or their control system fatigue strength is only examined. This approach is clearly inconsistent with the actual flight.

Z. Junjie (✉) · Y. Huiyu · W. Zhi · S. Haiping · X. Jun
Beijing Aeronautical Technology Research Center, 9203, Beijing 100076, China
e-mail: zhaojunj@163bj.com

J. Wang (ed.), *Proceedings of the First Symposium on Aviation Maintenance and Management-Volume I*, Lecture Notes in Electrical Engineering 296,
DOI: 10.1007/978-3-642-54236-7_8,

A new generation aircraft's fatigue test gives a new requirement, the movable wing is rotating while the fatigue load is applying on it, in the fatigue test. It is a new challenge to the method of aircraft structure fatigue test. The paper proposes a new method for the movable wing fatigue test. The method meets the requirement of "rotating and loading." Using this method, fatigue tests of movable wings of a certain type aircraft have been completed.

8.2 Fatigue Tests of Movable Wings

8.2.1 Test Article, Mounting, and Loading Mode

The test articles are full-scale movable wings (leading-edge flap, flaperon, stabilator) on a full-scale aircraft, and the necessary components which support them for rotating are, for example, hydraulic system, mechanical system, and fly-by-wire control system. The aircraft is a test article for the full-scale fatigue test, and suspension-mounted soft constraints support mode. After the full-scale aircraft fatigue test finished, movable wings fatigue tests were carried out. The loading mode was suspended loading.

8.2.2 The Fatigue Test Load Spectrum

Leading edge flap fatigue test load spectrum graphics are Fig. 8.1. Flaperon fatigue test load spectrum graphics are Fig. 8.2. Stabilator fatigue test load spectrum graphics are Fig. 8.3.

According to the spectrums, the fatigue loading is applying on the movable wings, meanwhile they are rotating. The key point of fatigue test is coordinated control between wing rotation angle and fatigue loading.

8.2.3 Fatigue Test Controller and Loading Equipment

The fatigue test controller is a multi-channel electro-hydraulic servo closed-loop control system, automatically controlled by a computer. It realizes the multi-channel coordinated loading.

Loading equipment is comprised of a load sensor, a hydraulic actuator, and a servo valve. The equipment is controlled by the fatigue test controller.

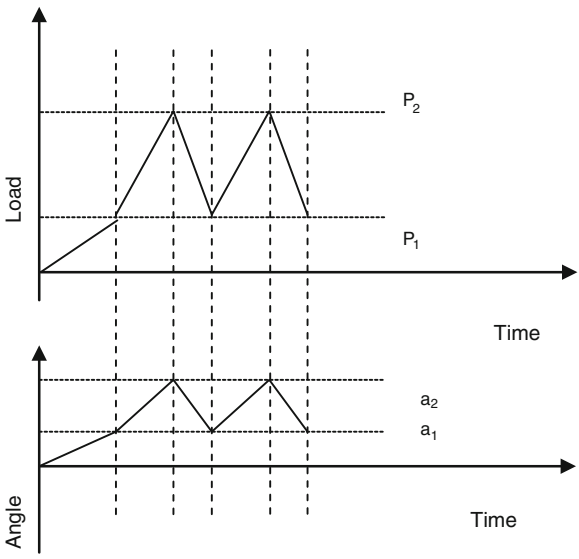

Fig. 8.1 Load spectrum graphics of leading-edge flap fatigue test

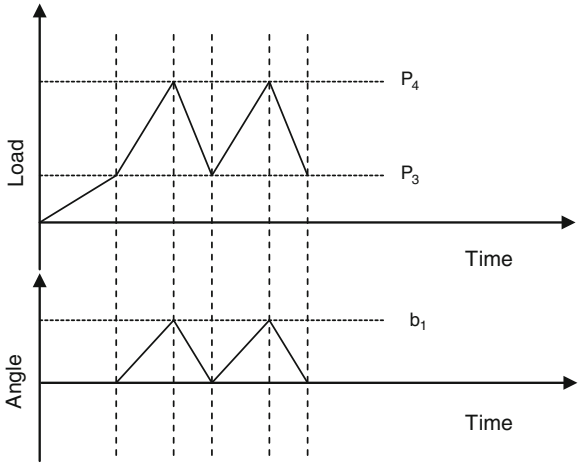

Fig. 8.2 Load spectrum graphics of flaperon fatigue test

8.2.4 Control Method of Movable Wings Fatigue Tests

8.2.4.1 The Control Principle of the Rotation of The Movable Wings

In order to make the movable wings rotating, the hydraulic system and the control system are installed in the test article; a special ground console is set up to simulate the aircraft control system to control rotation of the movable wings.

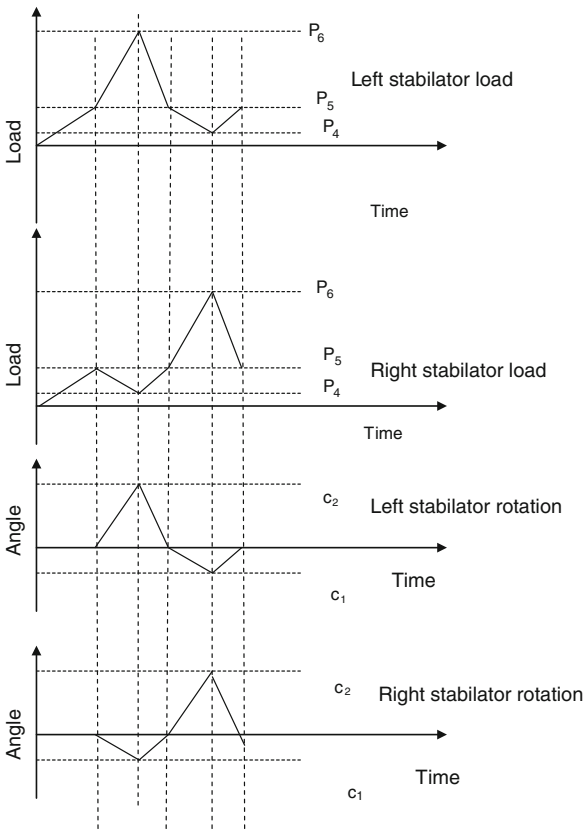

Fig. 8.3 Load spectrum graphics of stabilators fatigue test

The aircraft hydraulic system is supported by a ground hydraulic system; the pressure and flow are same as the actual flight. The ground console connects to the aircraft control system with a signal cable. An external DC voltage signal is an input for the console to control leading-edge flaps, flaperons, and stabilators rotating.

8.2.4.2 The Control Signal Calibration for the Rotation of the Movable Wings

Before the test start, the control signal needs to calibrate to accurately control the rotation angle of the movable wings. The calibration method is as follows:

1. Install a protractor on the movable wing;
2. Input a DC voltage signal to the console;
3. Record rotation angle and DC voltage;
4. Calculate curves of angle VS voltage.

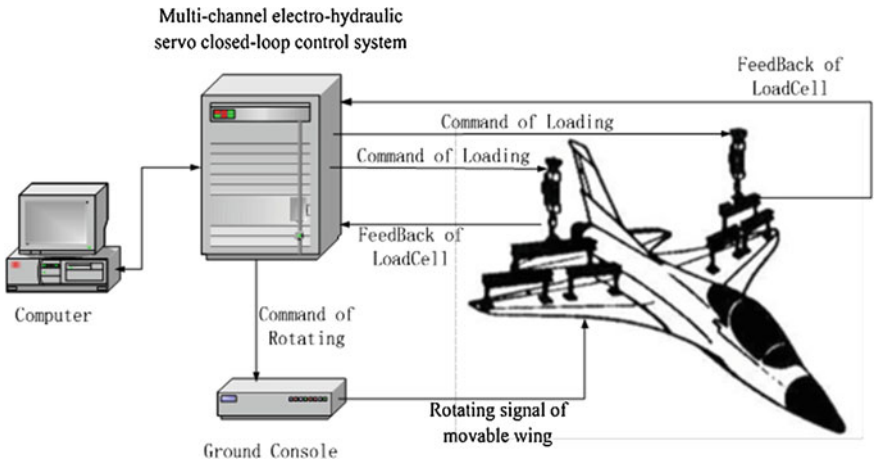

Fig. 8.4 Movable wings fatigue test control logic diagram

8.2.4.3 The Coordinated Control Between Wing Rotation Angle and Fatigue Loading

In order to coordinate control between wing rotation angle and fatigue loading, a control channel in the test channel configuration for control wing rotation is added. The control channel command is the calibrated DC voltage in the Sect. 8.2.4.2. The channel command signal DC voltage output is connected to the console through a cable, as the input signal of the console, to control rotation angle of wing.

So in the fatigue test process, the loading signal and rotating signal is generated synchronously by the test controller, thus ensuring the coordinated control of fatigue load and movable wing angle of rotation.

Figure 8.4 is the fatigue test control logic diagram.

8.3 The Results of the Movable Wing Fatigue Tests

During the movable wing fatigue tests of a certain type aircraft, there are two kinds of fatigue damage:

1. Fatigue cracks on the rib of stabilators, hinge for flaperon join to outer wing, and root of joint;
2. Control system function failure and wear of stabilators actuator disk.

Damages above are basically the same as damages that are found in the overhaul and found in service. This shows that the method proposed in this paper

can make a real simulation of aircraft flight. The test results provide reliable test data for the determining fatigue life of aircraft structure, and provide technical support for the development of aircraft overhaul technical measures.

Acknowledgments Dr. Chen Qunzhi gave strong support and help during paper writing, we express our heartfelt gratitude.

Chapter 9
Research on Integration Modular Avionics System Health Management

Miao Wang, Lihua Zhang, Qingfan Gu and Guoqing Wang

Abstract Integrated Modular Avionics (IMA) synthesizes the information, resource, ability, and process of avionics system to form unified information collection, united resource allocation, unified capacity organization, unified process synergy, unified function integration, and unified system management through sharing, integration, synergy, and fusion so as to achieve the goal of low cost, high efficiency, high efficacy, high performance, and high reliability. However, realization of avionics system integration will be confronted with many problems. In this paper, we first analyze the problems of IMA system and the relations among each problem in detail and describe organizational process of system heath capability; second, aiming at the above problems, we propose the solution to system health management, analyze, and summarize the solution in detail.

Keywords IMA · Health management · Failure · Capability

9.1 Introduction

Integration is currently the most important development direction of avionics system. Both Airbus A380 and Boeing 787 regard system integration as the core technology and capacity for development of avionics system. However, realization of avionics

M. Wang (✉) · L. Zhang · G. Wang
Science and Technology on Avionics Integration Laboratory, Guiping Road 432, Shanghai 200233, China
e-mail: wang_miao@careri.com

L. Zhang · G. Wang
School of Computer Science and Engineering, Northwestern Polytechnical University, YouYiXiLu 127, Xi'An 710072, China

M. Wang · Q. Gu · G. Wang
China National Aeronautical Radio Electronics Research Institute, Guiping Road 432, Shanghai 200233, China

J. Wang (ed.), *Proceedings of the First Symposium on Aviation Maintenance and Management-Volume I*, Lecture Notes in Electrical Engineering 296,
DOI: 10.1007/978-3-642-54236-7_9,

system integration will be confronted with the following problems: (1) resource integration gives rise to failure spread; (2) function information fusion causes failure implication and chaos; (3) mission synthesis leads to the difficulty in diagnosing the failure and expansion of failure damages. To solve the above problems, the new generation of avionics system will develop Prognostics and Health Management (PHM) [1–4] which can carry out health diagnosis, prediction and failure slowdown, and make sure the airplane fly healthily so as to improve the safety of the system. Meanwhile, with PHM technology, the use and guarantee cost will reduce, and Condition-based maintenance, and autonomous guarantee can be achieved.

PHM is the basis of new generation of avionics system resource organization and system reconfiguration, and also the guarantee to complete the mission by the system [5–8]. Currently, PHM technology based on IMA system (hereinafter, PHM system is PHM based on IMA system) has been applied in 787 airplane type of Boeing Company. At present, the researches about IMA technology in China are still in the initial stage. Besides, in the failure prognostic and diagnosis field, this is still no project material on health assessment and emulation proof for IMA system. Therefore, it is badly necessary to establish health guarantee, measurement and evaluation system for IMA system so as to lay the foundation for driving application of IMA systems engineering. So, focusing on system failure spread, system operation safety guarantee, fault information fusion and diagnosis faced by avionics system of large airplanes, it is necessary to explore health analysis, measurement, and evaluation techniques of avionics system of large airplanes to satisfy the engineering application demand for IMA system safety and validity of large airplanes and provide scientific instruction and technical support for developing and improving comprehensive abilities of avionics system of next generation of large airplanes.

Health describes the validity of internal body state of the system and reflects the ability of the current state of system to adapt current environment and mission of the system. Prognostics describe anomalous change features of internal state of the system and reflect the relevance of anomalous features of current system state and scheduled abnormal conditions of the system according to the differences of current system operating state and system health state. PHM forms current system health conditions in line with analysis of current operating state; forms system variation and development prognostics in line with evaluation of system health conditions; implements resource, function, and mission reorganization management in line with the analysis of the relevance between the states of various abnormal results and system prognostics as well as the operation requirement of system mission.

Therefore, the missions of PHM mainly include five aspects: (1) PHM provides system health state of current system resource, function, and mission state validity according to analysis of current system operating state; (2) PHM provides the type (fault, error, failure, and invalidation) of current system failure and validity (resource, function, mission, and mode) influence according to current system health state; (3) PHM provides the methods for fault tolerance, reconfiguration, and isolation management for the system according to prognostics of system health state; (4) PHM provides system mission, function, resource reorganization, and

management according to the operation requirements of current system mission; (5) PHM provides system safety and degradation management according to current system health and prognostic.

In accordance with mission demands of PHM system, PHM system should contain the functions in the following three aspects: (1) to improve the current capability of the system to complete the mission; (2) to enhance the capability of prognostic support and heath maintenance of the system; (3) to boost system maintenance guarantee capability. So, its functional objectives are: (1) to detect system faults in real time; (2) to accurately grasp system failures; (3) to master system-wide valid capabilities; (4) to predict system environment changes and mission support capability (service life); (5) to carry out system error tolerance and failure management; (6) to support resource reorganization and mission reconfiguration; (7) to support system maintenance and logistical guarantee.

In order to satisfy functional objectives of PHM system, PHM system puts forward new requirements for present avionics system, mainly including eight aspects: (1) information acquisition: collect and fuse environmental information, enhance system test, and provide system health state report; (2) system diagnosis: enhance system diagnosis, implement fault analysis, position and isolate faults, and confirm fault influence scope; (3) failure management: detect failure state; establish failure model, implement model reasoning, and supply failure information; (4) system capability: set up mission and environment model, carry out system analysis, evaluate system state, and master system capability; (5) mission capability: establish system reliability model; implement prognostic analysis, and support prognostics of surplus life of system resources and components; (6) system safety: strengthen system safety and provide system safety, confidentiality and integrity detection as well as protection capability; (7) system validity: support system reconfiguration and gentle degradation, and improve mission continuity capability; (8) maintenance guarantee: support autonomous logistics maintenance guarantee, improve maintenance capability, and reduce maintenance time.

Based on the above analysis, this paper first analyzes the problems of IMA system and the relations among each problem in detail and describes organizational process of system heath capability; second, aiming at the above problems, this paper proposes the solution to system health management, analyzes, and summarizes the solution in detail; finally, in allusion to the solution to system health management, this paper sets up top-down and bottom-up PHM system health management modes and analyzes their respective characteristics. The detailed content of above mentioned will be introduced in the following part.

9.2 System Fails Description

System fails, which is mainly composed of four parts: resource fault, functional error, mission failure, and system invalidation. Fault refers to the insufficiency of system features; error means system operation result deviates from expected

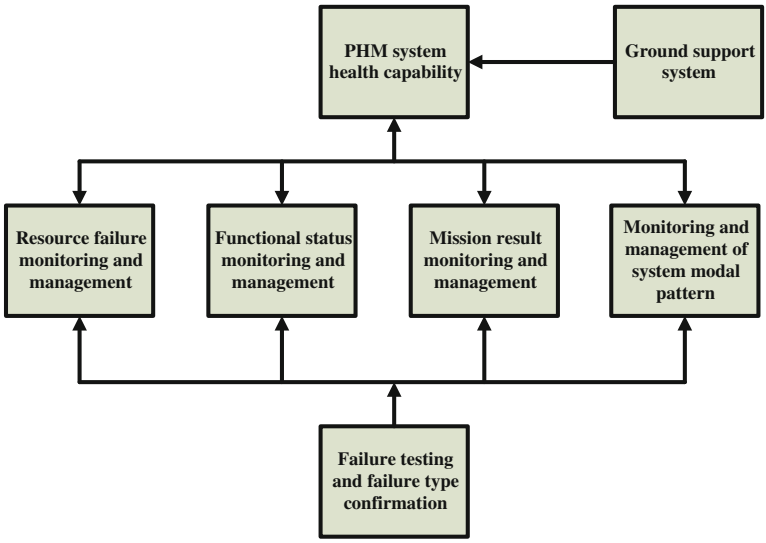

Fig. 9.1 Organizational chart of system health ability

intention; failure reflects unsuccessful system mission; invalidation means the system enters the state of paralysis. Fault discovery and treatment directly influence the occurrence of errors, while error discovery and treatment influence the emergence of failures. Failure accumulation scale has the direct bearing on the possibility of system invalidation. So, organization and management of PHM system health capability should involve the following six aspects: (1) failure testing and failure type confirmation; (2) resource failure monitoring and management; (3) functional status monitoring and management; (4) mission result monitoring and management; (5) monitoring and management of system modal pattern; (6) ground support system. The relationship of these six parts is as shown in Fig. 9.1.

9.2.1 Failure Testing and Failure Type Confirmation

Failure testing and failure type confirmation is the configuration of system health state, as shown in Fig. 9.2. It is necessary to confirm the type of health problems in accordance with system resource failure mode so as to lay the foundation for system reconfiguration, including data processing problem detection, data storage problem detection, data transmission problem detection, control time limit problem detection, and control flow problem detection. Failure testing and failure type confirmation is the foundation of monitoring and management of resource fault failure, functional error state, mission failure result, and system invalidation modal

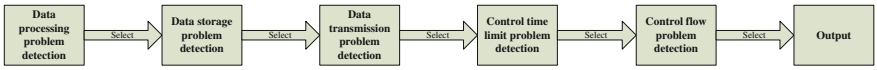

Fig. 9.2 Flow graph of system failure testing and diagnosis

pattern. Through this unit, reconfigurable resource fault, functional error, and mission failure can be confirmed under system state so as to carry out PHM for system problems.

9.2.2 Resource Failure Monitoring and Management

Since the mission of PHM is to monitor the system in real time in allusion to the above problems, it is necessary to predict problems and provide health management decision for the system. Resource fault is the imperfection of resource operation set for resource features. Besides, PHM system cannot carry out PHM for all faults. According to the detection degree of resource fault, resource fault can be classified into five types: all resource faults, faults tested, faults tracked, faults positioned and isolated, and reconfigurable faults. The faults tested refer to those which can be identified by PHM system; faults tracked means the faults of the resource can be tracked, i.e., resource faults which will give rise to functional error, mission failure or system invalidation; faults positioned and isolated means among the resource faults tested, some are caused by other resources and are not the faults of the resource itself. If "evoked" resource faults are eliminated, the faults of this resource will disappear so that the resource faults which can be positioned and isolated can be gained. Reconfigurable faults refer to those which can be positioned and isolated among the resource faults which will lead to functional error, mission failure, or system invalidation. Therefore, PHM system should include monitoring and prognostic mechanism for the above resource faults. Such monitoring and prognostic mechanism are able to produce different health management strategies aiming at different resource faults so as to ensure system health to the largest extent at the resource layer. The constitution relationship of resource faults described above is shown in Fig. 9.3a.

Resource failure monitoring and management is the organization of system health resource capacity validity, as shown in Fig. 9.4. System resource health maintenance is accomplished through resource failure phenomena, problem positioning, resource relevance, resource isolation, and resource reorganization. Resource failure monitoring and management mainly consider the following elements: resource fault prognostic, resource fault classification, resource fault relevance, resource fault isolation, resource fault reorganization. Thus unit forecasts resource faults. For the resource faults which cannot be positioned at the resource layer, function state monitoring and management unit is connected with result function error to position them. After the resource fault is positioned, it is required

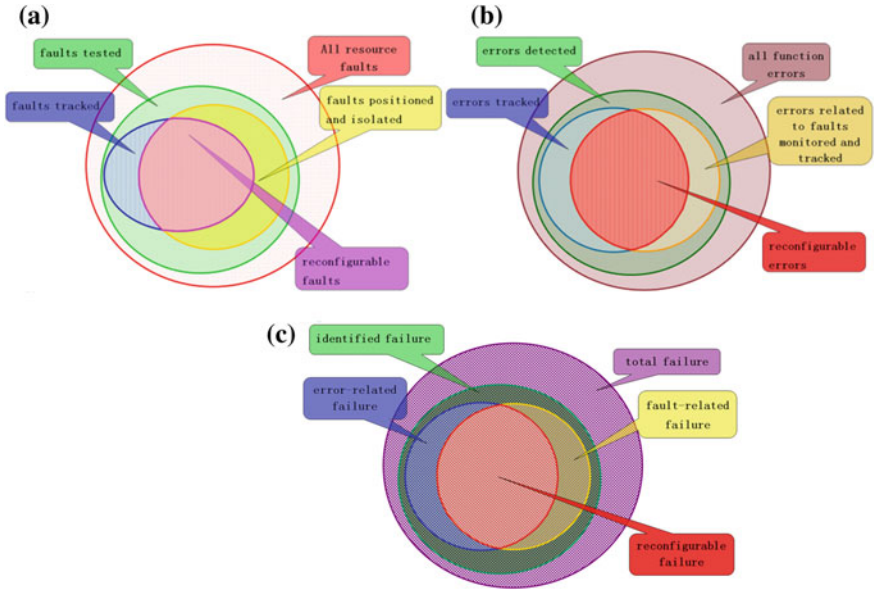

Fig. 9.3 **a** Fault constitution and relationship; **b** error constitution and relationship; **c** failure constitution and relationship

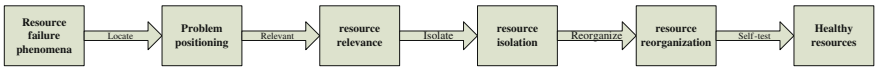

Fig. 9.4 Flow chart of resource failure monitoring and management

to analyze the expression form and type of the resource problem as well as resource fault relevance so as to confirm the resource fault which can be isolated. Then, reconfiguration is carried out at the resource layer to produce a new group of resources to guarantee healthy system operation.

9.2.3 Functional Status Monitoring and Management

Functional status monitoring and management is the organization of system health function capability validity, as shown in Fig. 9.5. System function health maintenance is finished through system function error monitoring, function relevance, function isolation, function reorganization, and function self-test. Functional status monitoring and management mainly consider the following elements: function error prognostic, function error relevance, function error isolation, function error reorganization, and function error self-test. This unit predicts function errors, analyzes function error relevance according to functional framework relation, organization

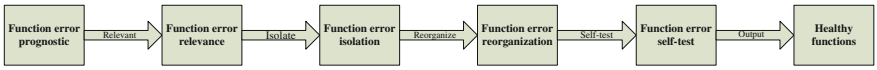

Fig. 9.5 Flow chart of functional status monitoring and management

relation and synchrony relations, and confirms the function errors isolated; then, the reconfigurable function errors can be confirmed according to functional framework relation, organization relation, and process relation; then, reconfiguration is implemented through functional framework relation, organization relation, synchrony relations, and process relation; besides, function self-test is carried out according to functional organization relation and process relation; function errors for which self-test is unavailable are positioned at the resource layer.

Function error is the deviation of relative functional standard of operation process and result. Similar to resource fault constitution, function errors can also be classified into five types: all function errors, errors detected, errors tracked, errors related to faults monitored and tracked, and reconfigurable errors. The constitution relationship is shown in Fig. 9.3b. Since function error is caused by resource fault, the essence of reconfiguration of function error is to reconfigure resource fault of this function. Thus, reconfigurable error must be the error related to the fault monitored and tracked, and this error must be the one that the system can track. Therefore, PHM system should contain monitoring and prognostic mechanism for the above function errors. Such monitoring and prognostic mechanism are able to produce different health management strategies aiming at different errors so as to ensure system health to the largest extent at the function layer.

9.2.4 Mission Result Monitoring and Management

Mission result monitoring and management is the organization of system health mission management capability validity, as shown in Fig. 9.6. System mission health maintenance is completed through clearly knowing mission problem, relevance between mission and function, mission instantaneity, mission result validity, and system reconfiguration. Mission result monitoring and management mainly consider the following elements: mission failure prognostic, mission failure influence, mission instantaneity, system output influence, and system output reconfiguration ability. Thus unit predicts mission failure and analyzes the relevance between failure mission and function so as to confirm the influence range of mission failure. It is necessary to confirm system output validity according to the requirement of mission instantaneity, and confirm mission reconfiguration based on system output capability according to system output demand.

Mission failure means the service objective which should be supplied by system mission cannot be achieved. Mission failure is also classified into five types: total failure, identified failure, error-related failure, fault-related failure, and

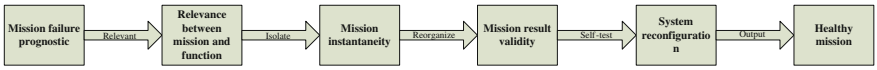

Fig. 9.6 Flow chart of mission result monitoring and management

reconfigurable failure. The constitution relationship of mission failure is shown in Fig. 9.3c. Because the mission layer is above the function layer and resource layer, the causes of the failure are from function error and resource fault. Though function error also comes from resource fault, not all function errors are related to faults detected and tracked. However, these function errors cannot be eliminated through resource fault reconfiguration. So, reconfigurable failure must be error-related failure or fault-related failure. Therefore, PHM system should contain monitoring and prognostic mechanism for the above mission failures. Such monitoring and prognostic mechanism is able to produce different health management strategies aiming at different failures so as to ensure system health to the largest extent at the mission layer.

9.2.5 Monitoring and Management of System Modal Pattern

Monitoring and management of system modal pattern is the organization of system health modal management capability validity, as shown in Fig. 9.7. System invalidation means the system loses all mission capabilities and is broken down. When the key mission in the system goes wrong, the system will enter invalidation state. System safety and health maintenance is finished through clearly knowing system invalidation problem, mission relevance, function relevance, resource relevance, and modal reconfiguration. Monitoring and management of system modal pattern mainly consider the following elements: system invalidation prognostic, mission relevance and isolation, function relevance and isolation, resource relevance and isolation, and system modal organization. Thus unit confirms mission failure related to system invalidation through analyzing occurrence time of mission failure, failure size, mission importance, and the influence on system safety. As well, this unit confirms the relevant function error which can be isolated through analyzing mission type and the degree of association. Then, thus unit confirms reconfigurable resource fault set through analyzing the function error and the relevance with resource fault and eliminates system problems through resource reconfiguration. In the end, self-test is implemented for the resource reconfigured. New system safety grade and organizational structure are confirmed according to the results.

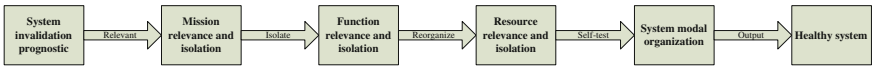

Fig. 9.7 Flow chart of monitoring and management of system modal pattern

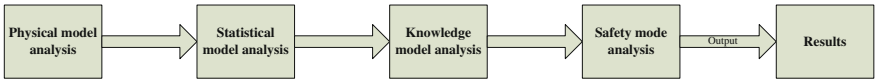

Fig. 9.8 Flow chart of ground support system

9.2.6 Ground Support System

Ground support system is the organization of system health validity maintenance reference, as shown in Fig. 9.8. Aiming at prognostic conditions, failure mode analysis is completed through delivering health conditions to ground support system according to failure type. Then, the health conditions are delivered to online information system to provide system health maintenance reference. Ground support system mainly considers the following elements: physical model analysis, statistical model analysis, knowledge model analysis, and safety mode analysis. Physical model is developed by component and system experts. The failure diagnosis system is formed through large quantities of data verification. Statistical model usually contains statistics of the resulting data formed by normal and known failure conditions. Knowledge model is rule-based expert system and fuzzy logic system formed according to experience and knowledge; safety model is system safety work pattern according to the data and state defined by system standards.

After the type of system problems is analyzed, it is necessary to monitor and manage different system problems. When the system goes wrong, PHM system is able to timely discover or predict system problem and ensure system health through health management way. Based on the above analysis, integrated avionics PHM system is composed the following four parts: (1) resource fault PHM system; fault monitoring and detection method is validity test oriented to system hardware resource, provides system management with current resource health state and PHM of system ill health caused by hardware resource fault; (2) function error PHM system; error monitoring and detection method is validity test oriented to system function and provides system management with current function health state and PHM of system ill health caused by function error; (3) mission failure PHM system; failure monitoring and detection method is validity test oriented to system mission and provides system management with current mission health state and PHM of mission failure system ill health; (4) system invalidation PHM system; invalidation monitoring and detection method is validity test oriented to system operation and provides system management with current operation safety health state and PHM of system safety ill health caused by system invalidation. In next section, we will present health management strategies adopted by each system problem.

9.3 System Health Management Strategies

The mission of PHM system is to send out early warning for the system before the system goes wrong and supplies decision information for system health management. Therefore, during system operation period, it is necessary to conduct health monitoring for the system. When system problem is monitored or predicted, it is necessary to carry out health management of the system. Aiming at different system problems, PHM system monitoring and health management is divided into three levels: resource fault monitoring and health management, function error monitoring and health management, and mission failure monitoring and health management. On the basis of the above three-level health management, PHM system sets up system invalidation monitoring and management. This section will introduce health management strategies in PHM system. Diverse system problems will have different system health management strategies.

At the resource layer, diverse resources own different capacities. Different capacity demands will give rise to different resource combinations. Different resource organizations have different capacity integration ways, while capacity integration ways may lead to resource failure spread or dissemination. Thus, it is necessary to conduct testing and failure diagnosis for the resource according to resource capacity and organization process so as to obtain state constitution when the resource goes wrong and form prognostic information. At the function layer and mission layer, state health or validity testing is also required to form prognostic information. The process is similar to that of the resource layer. When problem prognostic information at the above three layers is formed, each layer sends state information and prognostic information collected to the ground station through data chain. It is required to reason health prognostic information of the three layers through analytical model in ground support system and conjecture system invalidation mode triggered by resource, function and mission prognostic information so as to provide decision support for selection of system reconfiguration strategy.

When the system enters invalidation state, if the system detects the resource fault (reconfigurable resource fault) which can be tracked, positioned and isolated simultaneously, but cannot detect the traceable function error (reconfigurable function error) which is related to the fault detected and tracked and cannot identify the mission failure (reconfigurable mission failure) related to function error and resource fault, the system can enter the safety state meeting the minimum operation demand through fault resource reconfiguration, i.e., safety mode based on resource reconfiguration. If the system detects reconfigurable resource fault and reconfigurable function error, but cannot identify reconfigurable mission failure, the system can enter the safety state meeting the minimum operation demand through error function reconfiguration, i.e., safety mode based on function reconfiguration. If the system detects reconfigurable resource fault, reconfigurable function error and reconfigurable mission failure simultaneously, the system can

enter the safety state meeting the minimum operation demand through failure mission reconfiguration, i.e., safety mode based on mission reconfiguration.

It can be seen from the above analysis that when the system becomes invalid, the system can transform to safety mode for operation to ensure system health through selecting different reconfiguration ways according to the level of resource fault reconfiguration, function error reconfiguration, and mission failure reconfiguration. The precondition of the above reconfiguration is that the system must be able to detect the resource fault tracked, positioned, and isolated simultaneously, i.e., reconfigurable resource fault. This is because reconfigurable function error can exist only when there is reconfigurable resource fault; only when reconfigurable resource fault and reconfigurable function error exist simultaneously can reconfigurable function failure exist. When the system becomes invalid, different reconfiguration strategies can be taken according to reconfigurable level detected.

If the system does not become invalid, but has identified reconfigurable mission failure and cannot detect and test reconfigurable function error and reconfigurable resource fault, system degradation can be taken to reduce mission execution force and range as well as the system requirement by the mission so as to ensure healthy execution of the mission. If the system does not become invalid, has identified reconfigurable mission failure and can detect reconfigurable function error, but cannot detect reconfigurable resource fault, system degradation can be taken to reduce mission and function execution force and range as well as the system requirement by the mission and function so as to ensure healthy execution of the mission and function. If the system does not become invalid and can neither identify reconfigurable mission failure nor detect reconfigurable resource fault, but can detect reconfigurable function error, system degradation can be taken to reduce function execution force and range as well as the system requirement by the function so as to ensure healthy execution of the function.

It can be seen from the above analysis that when the system becomes invalid, if the system fails to detect reconfigurable resource fault, whether the system detects or identifies reconfigurable error and reconfigurable mission failure, the system cannot be reconfigured. This is because regardless of function error reconfiguration and mission failure reconfiguration, they will finally be subject to resource fault reconfiguration. In other words, function error and mission failure reconfiguration can be ensured only when resource fault is reconfigured (Table 9.1).

If the system does not become invalid and can detect reconfigurable resource fault, but cannot detect reconfigurable function error and reconfigurable mission failure, resource reconfiguration can be adopted to conduct health management for the system so as to improve system health attribute. If the system does not become invalid and can detect reconfigurable resource fault and reconfigurable function error at the same time, but cannot identify reconfigurable mission failure, function reconfiguration can be adopted to conduct health management for the system so as to improve system health attribute. If the system does not become invalid and can detect reconfigurable resource fault, reconfigurable function error and reconfigurable mission failure at the same time, mission reconfiguration can be adopted to conduct health management for the system so as to improve system health

Table 9.1 Health management based on system prognostics

	Reconfigurable resource fault	Reconfigurable function error	Reconfigurable mission failure	System state	Health management mode
1	Untested	Undetected	Unidentified	Valid	Monitor
2	Untested	Undetected	Identified	Valid	System degradation
3	Untested	Detected	Unidentified	Valid	System degradation
4	Untested	Detected	Identified	Valid	System degradation
5	Tested	Undetected	Unidentified	Valid	Resource reconfiguration
6	Tested	Detected	Unidentified	Valid	Function reconfiguration
7	Tested	Detected	Identified	Valid	Mission reconfiguration
8	Tested	Undetected	Unidentified	Invalid	Safety mode based on resource reconfiguration
9	Tested	Detected	Unidentified	Invalid	Safety mode based on function reconfiguration
10	Tested	Detected	Identified	invalid	safety mode based on mission reconfiguration

attribute. If the system does not become invalid and cannot detect reconfigurable resource fault, reconfigurable function error and reconfigurable mission failure at the same time, mission reconfiguration can be adopted to conduct health management for the system so as to improve system health attribute. It can be seen form the above analysis that when the system does not become invalid and can detect reconfigurable resource fault, the system can adopt resource reconfiguration, function reconfiguration, and mission reconfiguration to improve system health degree in line with whether it can detect reconfigurable function error and identify reconfigurable mission failure.

9.4 Conclusion

In this paper, we first analyze the problems of IMA system and the relations among each problem in detail and describes organizational process of system heath capability; second, aiming at the above problems, this paper proposes the solution to system health management, analyzes and summarizes the solution in detail; finally, in allusion to the solution to system health management.

Acknowledgments This paper is supported by Avionics Science Foundation (No. 20125552053), National Key Basic Research Program of China (No. 2014CB744900), and Graduate starting seed fund of Northwestern Polytechnical University (No. Z2013130).

References

1. Pecht M et al (2010) A prognostics and health management roadmap for information and electronics-rich systems. Microelectron Reliab 50:317–323
2. Zhang S, Kang R et al (2008) China's efforts in prognostics and health management. IEEE Trans Compon Packag Technol 31(2):509–518
3. Garvey DR et al (2007) Dynamic prognoser architecture via the path classification and estimation (PACE) model. Artificial intelligence for prognostics. In: AAAI fall symposium, pp 44–49
4. Brotherton T, Luppold R et al (2005) Generic integrated PHM/controller system. In: IEEE Aerospace Conference, pp 3422–3437
5. Eli D (2009) Introduction to the special section on prognostic and health management. IEEE Trans Reliab 58(2):262–263
6. Microelectronics Reliability (2007) Life cycle cost impact of using prognostic health management(phm) for helicopter avionics. Microelectron Reliab 47(12):1857–1864
7. Groza V, Mansour HA et al (2007) A self-reconfigurable Platform for built-in self-test applications. IEEE Trans Instrum Meas 56(4):1307–1315
8. Gizopoulos D, Hatzimihail M et al (2008) Systematic software-based self-test for pipelined processors. IEEE Trans Very Large Scale Integr Syst 16(11):1441–1453

Chapter 10
Research on Reducing Built-in Test Subsystem's False Alarm in Aero-Engine Control System

Shan Shi and Shuoxun Chen

Abstract Aero-engine control system is a key system in aircraft. Its testing and maintenance rely more and more on effective work of built-in test (BIT) subsystem. However, BIT subsystem suffers false alarm all the time. BIT subsystem and its influence on the reliability of aero-engine control system are introduced first in this paper. Then the cause of false alarm in BIT subsystem is analyzed and measures of reducing false alarm are proposed. Finally, it takes MBIT of power converter in starter/generator, for example, to verify the proposed measures. The theoretical result has significance in promoting wide application of BIT technology.

Keywords Aero-engine control system · Built-in test · False alarm

10.1 Introduction

Built-in test (BIT) is defined as a technology that systems or equipments complete fault diagnosis and isolation by circuit and program of their own. It is an important way to improve systems or equipments' testability and maintainability. Airborne equipments get more and more complex along with new advanced technology's development. According to Ref. [1], the time spent on searching and isolating fault accounts for about 60 % of maintenance time when adopting manual way to maintain the grassroots-level equipments. However, the time will be half when adopting BIT technology. Research on BIT technology was launched in the 1970s mainly by foreign airline company and large-scale military enterprises. Nowadays, the most advanced BIT theories, techniques, and methods have been successfully

S. Shi (✉) · S. Chen
Aviation and Aerospace Engineering College of Airforce Engineering University, Xi'an 710038, China
e-mail: snshi@sohu.com

J. Wang (ed.), *Proceedings of the First Symposium on Aviation Maintenance and Management-Volume I*, Lecture Notes in Electrical Engineering 296,
DOI: 10.1007/978-3-642-54236-7_10,

applied to a variety of military and civilian aircraft, such as F-16, F/A-18, F-22 and Boeing 777. They make extensive use of BIT technology.

In order to adapt to new applications, new aero-engine control systems develop with digital electronic controller almost entirely. The testing and maintenance of aero-engine control system are completed by the BIT subsystem. However, the use of BIT has exposed high rate of false alarm, and then results in difficulties in aircraft use and maintenance, such as affecting flight safety and mission completion, replacing its well line replaceable unit (LRU) mistakenly, resulting in ineffective maintenance, and so on. How to reduce BIT subsystem's false alarm has become a restriction for the BIT technology application.

10.2 BIT Subsystem

According to Ref. [2], the basic frame of aero-engine control system's BIT subsystem is shown in Fig. 10.1. It is divided into two levels. The first level is a test to the central computer. The second level is another test to fuel adjustment device, sensors, starter/generator device, and so on.

BIT subsystem has different operating modes in different stages, such as PBIT, MBIT, and IFBIT. Their characteristics are described as follows:

(a) Ground crew takes PBIT to check the states of aero-engine control system before flight. It motivates the components which have BIT function in them to test whether related components can work or not.
(b) Ground crew sets up MBIT to do ground maintenance and repair, including the entire process of aero-engine control system's testing and treatment. MBIT is used to assist ground crew to perform detailed test in order to locate fault and do reporting quickly.
(c) IFBIT works continuously in flight to make components of aero-engine control system get real-time online monitoring. It can confirm corresponding fault, then aircrew take measures to reduce the impact of fault.

PBIT and MBIT work when aeroplane is on the ground which is different from IFBIT. They will affect normal operation of aero-engine control system, so they are forbidden when flying.

Aero-engine control system's subsystem is constituted of central computer embed BIT component which consists of certain hardware and software. BIT subsystem inherent possibility of fault or false alarm will cause lower reliability to aero-engine control system. On the other hand, BIT subsystem completes required test function, monitors states of aero-engine control system, participates in system redundancy management and reconstruction, reduces nonmission boot time and prevents human error, so it improves the system reliability. As long as BIT subsystem's fault rate and false alarm rate are at a specified range, it will favor the

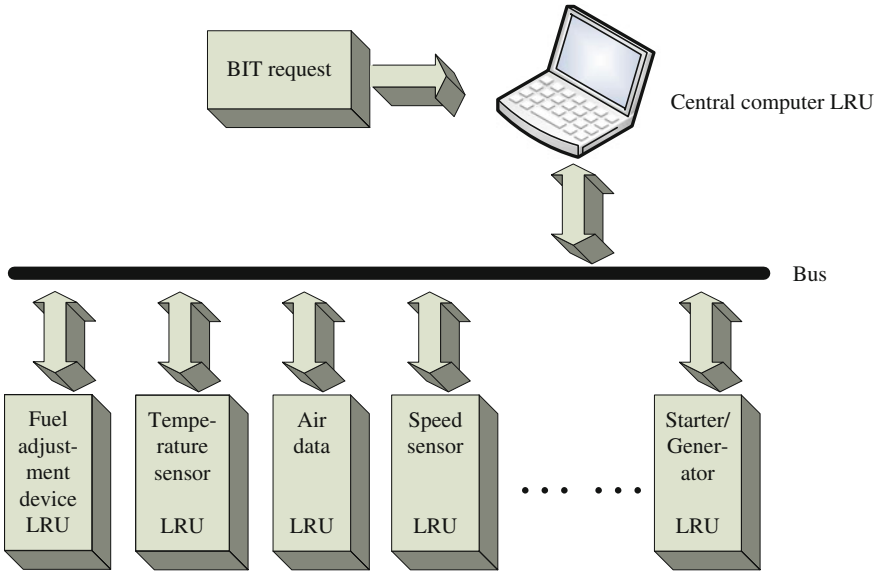

Fig. 10.1 Basic frame of aero-engine control system's BIT subsystem

Fig. 10.2 Relation of BIT subsystem and aero-engine control system's reliability

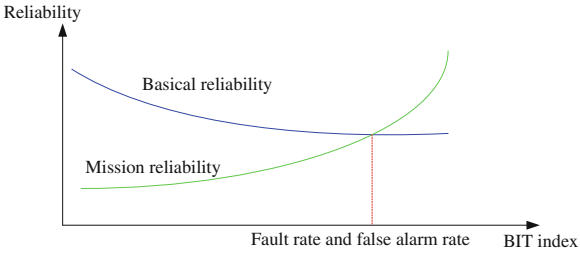

reliability of aero-engine control system. The relation of BIT subsystem and aero-engine control system's reliability is shown in Fig. 10.2.

10.3 Analysis on BIT Subsystem's False Alarm

False alarm existed since BIT technology was proposed. It causes inconvenience for use and maintenance. There are differences in definition for false alarm in Ref. [3]. U.S. military standard MIL-STD-2165 defined false alarm as: BIT or other detection components indicate the unit under test is fault, however a fault condition is not present in this unit in fact. According to GJB2547-95 of Equipment Testability Outline, false alarm is defined as: BIT or other monitoring circuits indicate a fault but it does not exist in reality.

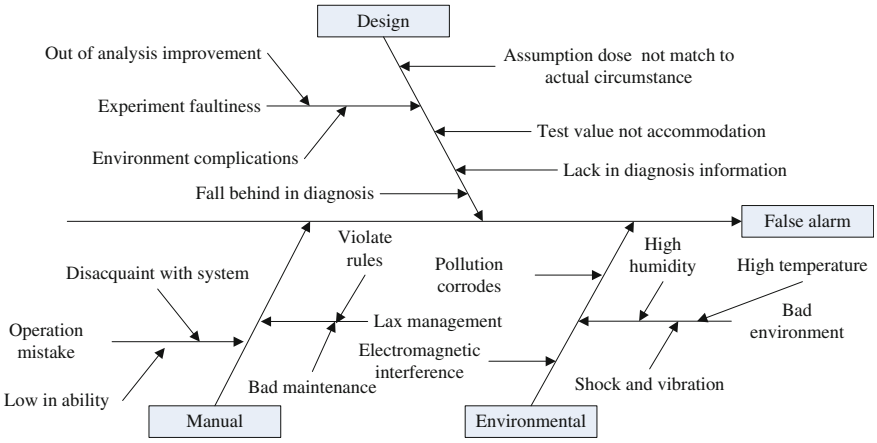

Fig. 10.3 Cause of BIT subsystem's false alarm

10.3.1 Reasons of False Alarm

According to experiments and statistical maintenance data from outfield, BIT subsystem's false alarm is caused by design, human, and environmental factors, as shown in Fig. 10.3.

In regard to environmental factors, various environmental stresses are one of the main reasons that cause BIT subsystem's false alarm. Its physical, chemical, and electrical properties change when BIT subsystem suffers various environmental stresses all the time. High temperature not only makes the material resistance to increase, the sensor parameter drift occurs, but also affects the electronic components cooling, accelerates aging, and even heat insulator breakdown, which then results in product failure. Shock and vibration cause parts of structure to loosen or worn out, poor contact of electrical connectors, and so on. High humidity accelerates corrosion of circuit board, lowers insulation performance, changes dielectric properties, and then results in electrical short. The contact components are accessible to poor contact along with high temperature. Electromagnetic interference is equivalent to impose undue incentive. It affects normal operation of system, and leads to transient faults and then false alarm occurs. Pollution corrodes electronic circuits to short or open, and electrical connectors and switches are not reliable.

10.3.2 Influence of False Alarm

When aero-engine control system's BIT subsystem has false alarm, it will cause serious consequences in flight mission, maintenance, use, logistical support, and other aspects, induced as follows:

(a) Affecting flight safety and mission execution. False alarm not only makes some of the equipments unusable, but also makes the pilot misjudge the situation which then leads to misuse, thereby affecting flight safety and mission success rate.
(b) Resulting in ineffective maintenance. Ground crew disassembly and repair LRU which is well in maintenance when false alarm occurs. It increases maintenance costs and time, reduces aircraft's integrity and attendance, results in manpower, time, and cost wastage.
(c) Affecting the supply of spare parts for maintenance. Due to False alarm, logistical person cannot grasp the repairing aircraft materials accurately. It may cause for a certain type of spare parts beyond the actual needs, wasting a lot of procurement, transportation, and storage costs.
(d) Resulting in maintenance staff's distrust. High false alarm rate will lead to pilots and ground crew to suspect the accuracy of BIT subsystems. If it is not analyzed and disposed properly, ignoring some of the correct information in flight or maintenance, there will be a hidden fault.

10.4 Methods of Reducing BIT Subsystem's False Alarm

There are appropriate measures in three aspects to reduce BIT subsystem's false alarm of aero-engine control system based on analysis of reasons of false alarm.

10.4.1 Analysis Improvement of Design

Methods on hardware to reduce false alarm are:

(a) Adopting components with higher reliability, optimizing BIT subsystems design and improving reliability of their own.
(b) Adding hardware filter to eliminate interference impact on diagnostic decision of BIT subsystem, such as voltage fluctuations and electromagnetic radiation.
(c) According to failure mode effects and criticality analysis, selecting redundancy detection and voting faults to determine whether aero-engine control system is fault or BIT subsystem's fault leads to false alarm.
(d) Taking fiber optic data bus to improve quality of data transmission.
(e) Taking distributed test programs to improve accuracy of fault isolation.
(f) Increasing sensor and test points to expand sources of diagnostic data of BIT subsystem.

Methods on software to reduce false alarm are:

(a) Taking intelligent theories and its related technique into BIT subsystem, such as neural network, experts system, and so on to improve diagnostic capabilities, identify true fault, and filter out false alarm caused by transient faults and intermittent faults according to Ref. [4].
(b) Monitoring and saving information continuously to take advantage of historical data and experience to capture intermittent faults.
(c) Doing more judgment or postpone to report fault will eliminate transient faults caused by short-term improper incentives.
(d) Adopting digital filter, Kalman filtering techniques and other measures eliminate all kinds of interference effectively.
(e) Taking adaptive threshold method to adapt to various working conditions.
(f) Perfecting error protection program with corresponding interlock mechanism to prevent false alarms caused by human errors.

10.4.2 Environmental Measures

Considering each environmental factor, we should take different measures to reduce environmental stress and its impact on BIT subsystem. Besides, installing environmental stress measurement device to put environmental stress data into BIT diagnostic algorithms and creating relationship between false alarm and environmental stress will get more accurate identification of false alarms and reduce false alarm rate. For electromagnetic interference, taking electromagnetic shielding measures seems to weaken electromagnetic radiation interference effectively.

10.4.3 Manual Measures

In order to reduce false alarms caused by human factors, we should be in accordance with maintenance procedures and technical specifications of aero-engine control system operation and maintenance strictly to prevent misuse and false alarms caused by operator error. For example, it is not allowed to run MBIT in flight, disassembly maintenance is forbidden when electrified on the ground, cable must be connected correctly, test plug need to be covered, and so on to prevent human damage to aero-engine control system. Stored spare can be installed after MBIT shows that they are well, and operational processes cannot be simplified privately. In addition, we'd better minimize unnecessary self-test operation, because frequent switching of contacts during testing will affect their life and may develop into error operation and results in false alarm eventually. Besides, starting from the management level, learning more business skills improves regulation and supervision so that maintenance could be ensured.

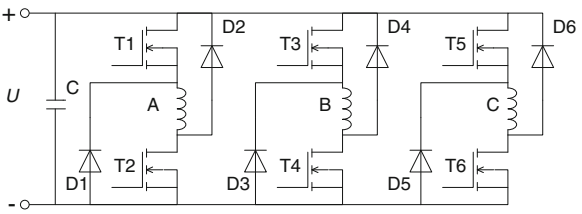

Fig. 10.4 Main circuit of common power converter

Table 10.1 Fault diagnosis table of power converter

sgn	E_n	Conduction command		Fault type	Faulty switch
		T1	T2		
1	1	On	Off	Short-circuit	T2
1	1	Off	On	Short-circuit	T1
1	1	Off	Off	Short-circuit	T1(T2)
−1	1	On	On	Open-circuit	T1(T2)
−1	1	On	Off	Open-circuit	T1
−1	1	Off	On	Open-circuit	T2

10.5 Instance Validation

At present, the advanced aero-engine is built in integrated starter/generator device. As constituted part of starter/generator device's control system, power converter is also a part of aero-engine control system. In Ref. [5], it is often at fault due to overcurrent, overvoltage, overheating of components, and so on. Open- and short-circuit fault in the converter power switches are most common. Main circuit of common power converter is shown in Fig. 10.4.

The conventional MBIT alarms once slightly abnormal current is detected. In fact, it is a false alarm most of the time. Take phase A for example, by improving MBIT software, setting adaptive threshold k, looking up Table 10.1, it will not only determine the fault mode, but also locate the fault.

The parameters are the measured dc bus current i, the estimated dc bus current i_e, the reference phase current I_{ref}, the phase current i_n, and the diagnostic variables h_n and E_n. The formulas are shown as follows:

$$\text{sgn} = \begin{cases} -1 & \text{if } i - i_e < -k \\ 0 & \text{if } -k < i - i_e < k \\ 1 & \text{if } i - i_e > k \end{cases} \tag{10.1}$$

$$k = 1.5 + 0.05 I_{\text{ref}} \tag{10.2}$$

$$h_n = |i - i_e| - i_n \tag{10.3}$$

$$E_n = \begin{cases} 0 & \text{if } |h_n| \geq k \\ 1 & \text{if } |h_n| \leq k \end{cases} \tag{10.4}$$

I_{ref} changes as long as working condition changes, so does k. It avoids false alarm which was caused by the changing of working condition and ensures the validity of MBIT.

10.6 Conclusion

Aero-engine control system's maintenance and testing depend on the BIT subsystem. BIT subsystem monitors the whole system and insulates the fault. In a word, it is indispensable in aero-engine control system. Taking measures to reduce BIT subsystem's false alarm will make airplanes get more reliability and safety.

References

1. Kerry W (2000) F/A-18D(RC) Built-in test false alarms. Naval Air Warfare Center Aircraft Division, Patuxent River, pp 2961–2970
2. Shi S (2010) Electromechanical built-in test technology in aeroplane (in Chinese). National Defence Industry Press, Beijing
3. Wen X, Xu Y, Yi X, et al (2002) Theory and application of intelligent built-in test (in Chinese). National Defence Industry Press, Beijing
4. Benvenga C, Murray D (2007) Embedding model-based diagnostics into a complex instrument to improve reliability through self diagnosis. In: Agilent Technical Conference
5. Gameiro NS, Cardoso AJM (2012) A new method for power converter fault diagnosis in SRM drives. IEEE Trans Ind Appl 48(2):653–662

Chapter 11
Exploration on Repair Technology of Shipborne Aircraft on Aircraft Carrier

Huakai Wei, Peizhong Zhao and Bolin Ji

Abstract In this paper, the possible repair technology problems about ship borne aircraft were analyzed. According to the present research progress, the surface damage repair, lever measurement, general repair technology, and preventive maintenance were reviewed and studied.

Keywords Shipborne aircraft · Damage · Repair · Preventive maintenance

11.1 introduction

The service conditions of the shipborne aircraft are more abominable than those of the land-based one. At the same time, the structure of the shipborne aircraft is more complicated, too. As a result, the damage probability becomes high [1–3]. More seriously, the technology support is limited on the aircraft carrier. The general preventive or periodic maintenance is difficult to be carried out. In addition, many special materials and structures are applied in the shipborne aircraft [4]. The repair crews will be different from the general. Their division of the work may not be definite and fine. Considering above all factors, the repair technology of the shipborne aircraft will face more complicated and difficult problems on the aircraft carrier. Therefore, it is necessary and urgent to study the related repair technology in order to supply reliable support.

H. Wei (✉) · P. Zhao · B. Ji
Qingdao Branch department of mechanics, Naval Academy of Aeronautical Engineering, Qingdao 266041, China
e-mail: weihuakai@163.com

J. Wang (ed.), *Proceedings of the First Symposium on Aviation Maintenance and Management-Volume I*, Lecture Notes in Electrical Engineering 296,
DOI: 10.1007/978-3-642-54236-7_11,

11.2 Research Progress

The tonnage of American aircraft carrier is big, therefore, working space and repair force can be enough to perform relatively extensive maintenance and repair working [5, 6]. For the bigger aircraft carrier, there is aero engine test equipment. The advanced repair technology, such as semi-cured composite patch, is also applied to repair quickly damaged structure of aircraft.

For PLA, it is the first time to have aircraft carrier equipment. Consequently, there is no ripe and successful experience. However, in the recent years, studies on the new technology, new processing, and new material about structure repair have been developed greatly. Based on these developments, it is possible to support reliable repair technology after necessary and systemic test. For example, the laser process and manufacture technology has progressed greatly. The condition to equip laser device for the repair factory has become ripened. In our lab, laser welding, laser cladding, and laser modification repair have been studied extensively for more then 10 years.

In our aircraft carrier, there is some repair working space. Also, some repair equipments are equipped. However, the working space is small and dispersed. This does not benefit repair. Therefore, it is necessary and significant to optimize the space and utilize the present and limited resources as much as possible. Regulation or lay out again supporting the resources is one of the key factors to improve the present repair ability and technology lever.

Because of the limitation of the service condition, the repair equipments for the land-based aircraft are not applicable to the shipborne aircraft. As a result, it is important to design new repair tools and devices. At the same time, it is also necessary to corporate with the stationed airport and integrated support base to form new and applicable shipborne aircraft repair mechanism.

11.3 Common Repair Technology

11.3.1 Surface Damage Repair Technology of Metallic and Nonmetallic Structure

According to the experience of the escort missions in the Gulf of Aden, the corrosion of the metallic and nonmetallic structure of the aircraft was very serious, which exceeded the most serious degree of the land-base or seashore airport. The main induction of the corrosion is the partial invalidation of the surface protection. So, studies on the surface repair are very important. The surface repair technologies mainly include sanding and rinsing procedure, surface passivation or sealing procedure, and fast curing processing and devices of the coating. Theses technologies will supply the enough repair support.

11.3.1.1 Study on the Main Invalidation Modes of the Shipborne Aircraft Surface

Compared with other airports, the corrosion will be the main damage mode of the shipborne aircraft. Under the oceangoing conditions, complex action of the high temperature and salt fog, the mechanism of the corrosion may be complicated. Therefore, it is important to study the typical damage modes. These are the foundation to develop the applicable surface repair technology.

11.3.1.2 Surface Pretreatment of the Shipborne Aircraft Structure

Considering the complex of the servicing conditions of the shipborne aircraft, it maybe necessary to perform the pretreatment to eliminate the oil or rust contamination. After pretreatment, the surface state should satisfy the further treatment. The pretreatment process needs to be studied and formulate in time.

11.3.1.3 Surface Treatment of the Shipborne Aircraft Structure

The surface treatment procedure is the key factor and important procedure to restore the surface protection. Based on the invalidation mode study mentioned above, the surface treatment process and daily maintenance rules can be established.

11.3.1.4 Posttreatment and Inspection of the Shipborne Aircraft Structure Surface

For some special materials, the posttreatment is needed in order to passivate and seal the treated surface. After the posttreatment, the protection function can be improved further.

After the surface treatment, the necessary inspection must be performed to ensure the eligible treatment quality. The methods of inspection mainly include the microscopic and macroscopic analysis. The microscopic analysis aims to inspect the morphology, thickness, and microstructure of the treated surface. The macroscopic method aims to test the mechanic property, anticorrosion property, and adhesive strength of the treated surface.

11.3.2 Lever Measurement and General Repair Technology on Aircraft Carrier

On land, the lever measurement can give the data to ascertain the whole state of the aircraft. However, on the aircraft carrier, the dynamic condition make the lever measurement become difficult, or even disabled. According to this condition, the following two methods may be feasible. The first, based on the geometry parameters of the aircraft garage, the lever data can be obtained by fixing the location and support. The second, by use of the roll sensor made by Switzerland, the lever data can be measured by appointing the deck as the zero point. These two methods have the different features. At present, contrastive studies are necessary to select a reliable and convenient method, which can be used on the aircraft carrier.

The existing repair tools and devices are designed according to the maintenance of the land-based aircraft. However, in view of the differences of the shipborne aircraft, proper improvement or redesign is required. The usage of the tools under the dynamic condition may face some problems, which are nonexistent on land. Therefore, relative studies should be carried out to find the usage character of the repair tools or devices on the deck.

11.3.3 Preventive Maintenance of Shipborne Aircraft

The maintenance and repair areas are planned on the aircraft carrier. However, these areas are dispersed and small. Moreover, the devices are simple now. Optimization of the present repair and maintenance areas is required in order to utilize the space and resources adequately. Addition or backout of the repair devices may be a feasible method to improve the repair ability. At the same time, the working contents and depth of the periodic inspection should be given reasonably and scientifically. In addition, the cooperation with the stationed airport can produce positive effect on the repair ability.

The following two points should be paid more attention to increase the preventive maintenance and repair ability.

(1) Daily maintenance, monitoring, and periodic inspection regulations contents;
(2) Based on the present condition, optimization of the cabins and devices.

These two points supplements each other. The former decides the requirement of the working space and devices. The latter can provide the condition for the repair working and give some limits. The maintenance and repair working contents on the aircraft carrier should be studied. According to the necessity of the working contents and existing condition, some working contents for the land-based aircraft may be simplified or deleted. As a result, the study should include what are absent or not enough to satisfy the repair requirement according to the present condition. It is also necessary and important to predict what a lever of the possible condition may be after optimization.

11.4 Conclusions

Repair work has been become urgent after the aircraft carrier was equipped for the army, especially when the shipborne aircrafts are on the aircraft carrier. According to the present condition, it is important to perform repair technology studies energetically based on our ability and referring to the abroad advanced experience. New technology and devices suitable for the repair on aircraft carrier, such as structure and surface damage repair, need to be studied extensively and profoundly. At the same time, working contents of the periodic inspection and daily maintenance should be established referring to the relative studies of the land-based aircraft. In general, the conditions and resources are limited now. Consequently, more effort must be made to satisfy the repair need on the aircraft carrier.

References

1. Tirpak JA (2009) The sixth generation fighter. Air Force 9:38–42
2. Weaver JT (1997) Generation of magnetic signal by waves and swell, in transient and induced variations in aeromagnetic. Rec Aust Geol Surv Organ 27:15–16
3. Robert M, Stammer A (1992) Database approach to aircraft carrier airplan production. Naval Postgraduate School, Monterey
4. Applying design of experiments(DOE) methodology to sortie generation rate(SGR) evaluation[C/OL]//10th annual NDIA systems engineering conference. http://www.dtic.mil/ndia/2007systems/Tuesday/PM/Track2/5489.pdf
5. Incorporation of the virtual carrier(VCVN) into operational test[R/OL]. http://www.Avwtech.com/press/VCVN_MS_Brief_(Final)_15_Jan_10.pptx
6. Defense Management Opportunities to Reduce Corrosion Costs and Increase Readiness (2003) United States General Accounting Office

Chapter 12
Synthesis Based on Genetic Algorithm Parameters in Air Engine Fault Monitoring

Jiao Zhun and Zhang Rong

Abstract In engine fault monitoring and early warning process, how to deal with different types of sensor data and information is a key problem. This paper presents a comprehensive parameter method and the genetic algorithm to determine the weight of integrated parameters problem. Through experimental analysis, genetic algorithm to determine the composite index is more accurate and sensitive to reflect the deterioration of engine performance.

Keywords Genetic algorithm · Comprehensive parameter method · Fault monitoring

12.1 Introduction

Aircraft engine monitoring and diagnostics of complex systems of this type often require different types of sensors to obtain the state parameters to monitor. How to blend and deal with the data and information from different sensors is a very important research projects.

12.2 A Comprehensive Parametric

Composite parameter is a method proposed by a Russian Kaskalouv in his "The reliability of radio electronic equipment and technical status of forecasting" published in Soviet Radio. The main idea of this method is to use one-dimensional

J. Zhun (✉) · Z. Rong
The First Aviation College of Air Force, Xin Yang, China
e-mail: Jiaozhun204@aliyun.com

J. Wang (ed.), *Proceedings of the First Symposium on Aviation Maintenance and Management-Volume I*, Lecture Notes in Electrical Engineering 296,
DOI: 10.1007/978-3-642-54236-7_12,

components to be monitored to describe the function of monitoring system for multi-dimensional process [1].

By monitoring the flight and engine parameters related to the changes and to analyze trends, the method is effective to achieve early warning of air engine fault. Engine parameters recorded by Su-27 aircraft flight data recording system are: inlet total temperature, low-pressure rotor speed, low-pressure compressor inlet guide vane angle, high-pressure compressor variable stator blade angle, exhaust gas temperature after turbine, last nozzle position indicator values, and vibration, oil pressure, throttle angle, inlet location. How to achieve these parameters of the engine fault diagnosis with an integrated approach? The following are the specific application steps, using a comprehensive method for data fusion of engine performance in the aviation monitoring and fault diagnosis.

12.2.1 To Determine the Relative Value of Engine State Parameters: The Standard Value (Effect Function)

Whether an integrated monitoring engine performance parameter method results good or bad largely depends on the determination of the optimal value and the boundary value. To determine the boundary values should take into account the actual work of the engine [2]. When the engine is in perfect condition, it takes comprehensive parameter value $Q(t) = 1$; when the deviation between the engine state and the given state arrives at maximum allowable value, taking $Q(t) = 0$. When the engine works normally, the comprehensive parameter should be between 0 and 1, namely:

$$0 < Q(t) \leq 1$$

As the condition of the engine is represented by parameters in different dimensions, it therefore needs to be normalized into a standard value for comparison in integration. First, extract the parameters which can best indicate the engine condition and the on-board recording devices to record the parameters as the characteristic parameters of the state of the engine. Unify these parameters into a standard value for comparison. In engine operating parameters and performance parameters, some hope to moderate, such as the engine rotor speed, exhaust temperature, position adjustable blade angle, slip, or to say these parameters have the optimum values; some parameters hope to be as large as possible, such as thrust, the efficiency of various parts, stop after the inertia time; some hope to be as small as possible, such as the vibration value, fuel consumption, or that only the left and right boundary values exist in these parameters [3]. Transform work parameters and performance parameters into the standard value (power function) with the formula:

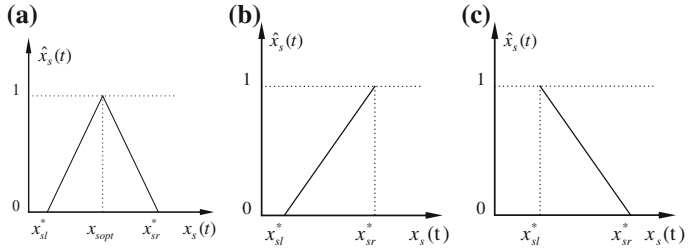

Fig. 12.1 The computing model of standard value (power function)

If there is the best parameter,

$$\hat{x}_s(t) = \frac{x_s(t) - x_{\mathrm{sl}}^*}{x_{\mathrm{sopt}} - x_{\mathrm{sl}}^*} \quad x_{\mathrm{sopt}} > x_s(t) \tag{12.1}$$

$$\hat{x}_s(t) = \frac{x_{\mathrm{sr}}^* - x_s(t)}{x_{\mathrm{sr}}^* - x_{\mathrm{sopt}}} \quad x_{\mathrm{sopt}} < x_s(t) \tag{12.2}$$

When there is only the left and right boundary and the parameters hope to be as large as possible,

$$\hat{x}_s(t) = \frac{x_s(t) - x_{sl}^*}{x_{\mathrm{sr}}^* - x_{\mathrm{sl}}^*} \tag{12.3}$$

When there is only the left and right boundary and the parameters hope to be as small as possible,

$$\hat{x}_s(t) = \frac{x_{\mathrm{sr}}^* - x_s(t)}{x_{\mathrm{sr}}^* - x_{\mathrm{sl}}^*}. \tag{12.4}$$

The three calculation methods in Fig. 12.1a show the condition with the best value, (b), (c) with the left and right boundary.

In the figure, $\hat{x}_s(t)$ is the standard value for the measured parameters, $x_s(t)$ stands for the measured parameters measured parameters, x_{sl}^*, x_{sr}^* for the left and right limits of the boundary value, x_{sopt} for the corresponding parameter value when the engine is at its best. Seen from the formula of the standard value, after the measured parameters transform into the standard value, the value is between 0 and 1. According to the degree how the value is close to 0 or 1, we can see performance status of the engine it represents. When the engine is at optimal working state, $\hat{x}_s(t) = 1$; when the engine is in fault state, $\hat{x}_s(t) = 0$. $\hat{x}_s(t)$ is called the power function in Ref. [4]. The following describes the specific method of calculating the effectiveness function.

When the parameters of the effectiveness function to calculate fit Figure (a), they are the best parameters, such as the engine rotor speed, and the boundary value as well as the best value should be first determined. Suppose we know the best value

x_{sopt} is 98 %, the left boundary value is 95.5 %, and the right boundary value is 99 %, while the actual measured parameter $x_s(t)$ is 97 %, then according to Eq. (12.1), we can get the standard value of the measured parameters $\hat{x}_s(t)$ as 0.6.

When the parameters of the effectiveness function to calculate fit Figure (b), or we hope parameters are as large as possible, such as engine thrust, we can use Eq. (12.3) to calculate. If the left boundary value x_{sl}^* is decided as 10,000 kg, the right boundary value as 12,500 kg, while the actual engine thrust as 11,750 kg, then the standard value of the engine thrust $\hat{x}_s(t)$ is 0.7.

When the parameters of the effectiveness function to calculate fit Figure (c), or we hope parameters are as small as possible, such as engine vibration value, we can use Eq. (12.3) to calculate. If the left boundary value x_{sl}^* is decided as 0 mm/S, the right boundary value x_{sr}^* as 50 mm/S, while the actual value of the engine vibration $x_s(t)$ as 25 mm/S, then the standard value of the engine vibration value $\hat{x}_s(t)$ is 0.5.

12.2.2 Deciding and Processing Comprehensive Parameters

In the fusion process, it is very important to identify a comprehensive parameters $Q(t)$ which can show the engine performance. Its size directly reflects the engine performance.

Comprehensive parameter calculation methods are of many kinds, such as fixed weighted method, principal component weighting method, distance synthesis method, discriminant function, factor weighting, index synthesis, associated with sequencing, quasi-RSR.

Weighting method is used in this section to calculate the comprehensive parameters, that is, to give a certain weight to standard value of each parameter, then summing them up. Calculated as follows:

$$Q(t) = \frac{\sum_{s=1}^{k} w_s \cdot \hat{x}_s(t)}{\sum_{s=1}^{k} w_s} \quad k = 1, 2, \ldots m \tag{12.5}$$

Of which:

m is the number of engine parameters to be monitored; w_s is the weight of the parameter x_s, reflecting the importance of the parameter while being monitored.

Based on previous formula and definition of the standard value, integrated range of parameter changes within:

$$0 < Q(t) \leq 1$$

Only when all the monitored parameters exceed a given range, $Q(t) = 0$; when the engine is in optimal working condition, $Q(t) = 1$. Therefore, by integration methods to integrate parameter, $Q(t)$ values can be got and used to monitor the engine condition.

Treatment: After treatment being integrated, if the comprehensive parameter fluctuation changes a lot, assuming it exceeds a set threshold, the performance of the engine shows an obvious deterioration, suggesting that the engine broke down.

The question now is, there are more aircraft engine parameters to be monitored, and we cannot know exactly the importance represented by various engine performance parameters. Therefore, it is difficult to determine a reasonable weight of each parameter. According to the importance of engine parameters to be monitored under the overall performance, Ref. [5] gives separately the weight by using a Delphi method (i.e., expert investigation) and lending experts' experience in engine. Thus it is unavoidably subjective.

However, the paper will explore the principles of genetic algorithms to determine the w_s value in (12.5), that is, the weight of the fusion parameters.

12.3 Synthesis Based on Genetic Algorithm Parameters

The core of synthesis based on genetic algorithm parameters is to use the genetic algorithm to determine the weights w_s of engine integration parameters. The basic idea is: when the engine performs well, its genetic algorithm parameters must be as large as possible, and the composite index values between the discrete degree should not be much; in engine performance deterioration or failure, the composite index value must be as small as possible, and the failure of the composite index values between the discrete degree should not be much. The resulting composite index can clearly recognize whether the engine performs well or the decreasing speed when it works normally.

Fusion method using integrated parameters tracks and monitors a certain type of aircraft engine. Integration of information—performance parameters got from the Flight Data Recorder. Aircraft engine indicators selected according to the principles and criteria select high-pressure rotor conversion speed n_{hcor}, low-pressure rotor conversion speed n_{lcor}, high-pressure rotor vane angle $alpha_{\mathrm{h}}$, low-pressure guide vane angle $alpha_{\mathrm{l}}$, turbine exhaust temperature after T4, the end of the value of le jet direction le, and vibration B, oil pressure pl, the slip S as integration information of genetic algorithm parameters. d_1–d_9 can be acquired through the method above, respectively, corresponding their effects function values. The nine weight of the parameters: w_1–w_9 need to be determined.

Composite index based on genetic algorithm to determine the value of the expression is [5]:

$$Q(t) = \frac{\sum_{i=1}^{9} w_i \times d_i}{\sum_{i=1}^{9} w_i}. \tag{12.6}$$

Based on the ideas of the analysis above, select the optimization criteria:

$$f = \frac{|u_n - u_f|}{\sigma_n + \sigma_f}. \tag{12.7}$$

In it:

u_n, σ_n are the average index value and variance of the genetic algorithm parameter $Q(t)$ when the engine is in normal state;

u_f, σ_f are the average index value and variance of the genetic algorithm parameter $Q(t)$ when the engine is at its failure or erratic performance.

Seen from Type (12.7), as f grows greater, the composite index values got from weight coefficient can reflect the performance of the engine more accurately, and the power factor is also more reasonable. So, we select f as optimization criteria to evaluate the merits of income weights.

Fitness function defined as:

$$F(i) = f^2(i) \quad i = 1 \sim n. \tag{12.8}$$

In it, the square form of $f(i)$ is to enhance the differences between individual fitness values.

Of a turbofan engine [4], take power function values of nine parameters when it works normally 30 times and 30 failures (abnormal). This data works as the optimization criteria of the engine work and fault status data. First, determine the scope of 9 weights is between [0, 1]. Use binary encoding length of 10 to reflect 9 variations, respectively. Link the nine 10-bit long string of binary code to form a 90-bit long string of binary code. It represents an individual's genotype, with every 10 bit for a variable value. Use mode selection operation as proportional selection. Reference [5] introduces and uses actual test data. It selects the population size 400, the outstanding individuals 40, the probability of reproduction 0.2, probability of hybrid 0.95, and mutation probability 0.6. After 20 cycles, accelerate the optimal value. According to the best individuals, decode and get the weights of 9 decimal numbers.

Integrated parameter index value can be calculated from Eq. (12.6).

12.4 Experimental Analysis

Test analysis is divided into two steps:

1. When to calculate the comprehensive parameter effectively in the simulation test, based on experience and expertise, the nine sources of information weight in the monitoring and early warning indicator system are: high-, low-pressure rotor speed, and slip are converted 1/8.7, exhaust temperature and vibration values are 2/8.7, high- and low-pressure guide vane angles were 0.05/8.7, tail vents direct value of 1.5/8.7, and oil pressure 0.1/8.7.

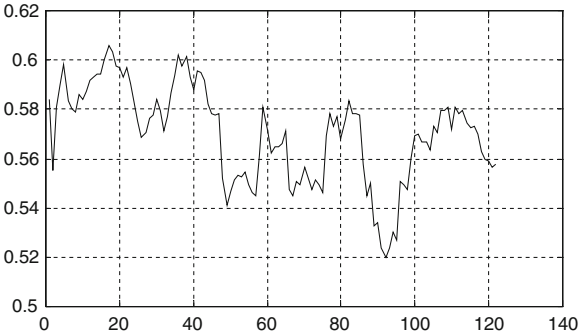

Fig. 12.2 Left-fat synthesis parameters of the situation over time

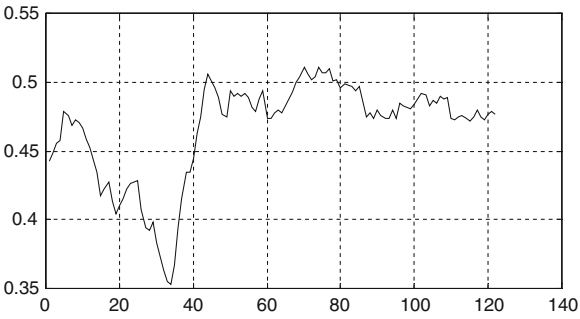

Fig. 12.3 Right-fat synthesis parameters of the situation over time

Using fusion method to get integrated parameters, we can calculate comprehensive parameter changes of 41# plane left and right engine, as shown in Figs. 12.2 and 12.3.

Comparing the two graphs, a more substantial decline occurred in the use of the left-fat synthesis parameter values, fluctuating between 0.12 and 0.15, indicating a marked deterioration in the performance of the engine. The fact is that the engines in the installed capacity of 37.45 h of work, electronic-integrated regulator failure, the replacement of electronic-integrated regulator. In Fig. 12.2, the reason of a sharp drop in index was: before failure in the regulator, the working parameters drift and the work has been in the abnormal state, resulting in the parameters of the engine deviate from normal value. As the regulator parameters continue to drift, when working for 37.45 h, regulator fails and the composite index value reaches its lowest point. Although the comprehensive parameter of the right fat does not appear a similar great change in the course, the most significant fluctuation is 0.06 which is far less than the left fat, it declines overall, indicating that this engine has a recession after long use.

2. Improvements of integration by verifying the genetic algorithms.

Using improved genetic algorithm, we can obtain the nine sources of information weight in monitoring and early warning indicator system:

High-pressure rotor conversion speed 0.402637/5.515927,

Fig. 12.4 Fixed weights based on genetic algorithm and the integrated parameters change over time

Low-pressure rotor speed 0.457798/5.515927,
Slip rate 0.956398/5.515927,
Exhaust temperature 0.008698/5.515927,
Vibration values are 0.965507/5.515927,
Pressure guide vane angle 0.875358/5.515927,
Low angle 0.425128/5.515927,
Last vents direct value 0.625424/5.515927,
Oil pressure 0.798979/5.515927.

Using fusion method to get integrated parameters, we can calculate comprehensive parameter changes of 41# plane left engine. And compare it to Fig. 12.4.

Seen from Fig. 12.4, a genetic algorithm significantly improved engine performance when the index value is normal (from 0.483 to 0.635), reducing the Composite Index value (from 0.356 to 0.311 reduced) in the engine failure (erratic performance), and the variance of the genetic algorithm parameter has also been reduced (from 0.0033 to 0.0024 reduced) when at a normal state. So, it is more accurate and sensitive to reflect the deterioration of engine performance by using the genetic algorithm. If monitoring and controlling the engine in the maintenance, the performance index value was found significantly reduced; taking troubleshooting checks can provide an early warning of potential failure.

12.5 Conclusion

Using genetic algorithms to optimize and generate the weights of the parameters of sensor information, the composite index value of the object can be achieved. In the past, the weight of each information parameter relies on experts and experience. So genetic algorithm is more objective, and then parameter values integrated through weighted composite can also better reflect the actual situation. By a turbofan engine monitoring, the method is proved effective. Moreover, it is easy to

promote the use of the method to other types of engines. As long as we can collect working data (normal and fault) of the engine and adjust certain control parameters of genetic algorithm, the effective engine performance index can be achieved. Then, monitoring the changes of performance, if it is a great one, check can be ranked, so that early detection of faults and remove achieve.

References

1. Wang YJ (2001) Design of monitoring system of A 几-31ϕ engine (in Chinese). The master's degree paper of AFEU
2. Zhou ZC, Xie SS, Ling YH, Xie HT (1996) Paper of adjusting A 几-31ϕ engine performance and eliminating faults, 04–28
3. Xie SS (1998) Research on SU-27 engine fault diagnosis and performance monitoring (in Chinese). The doctor's degree paper of NPU
4. Jin JL, Yang XH, Ding J (1994) The improved project of standard GA—accelerated GA (in Chinese). Theory Pract Syst Eng 5:96–100
5. Goldberg DE (2000) Genetic algorithms in search, optimization and machine learning. Technical report, CUED/F-INFENG/TR380, Engineering Department

Chapter 13
The Practicability Study of the Input-Parallel and Output-Series Converters with Equal Pulse Width of Driving Signals

Linbing Wang, Yujing Chen, Yangzhou Wang, Yue She, Haifei Chen and Jiajia Liu

Abstract The practicability of the IPOS (input-parallel and output-series) DC-DC converters with equal pulse width of driving signals for all the switching devices is studied in this paper. Push–pull forward converters, double-transistor forward converters, and phase-shifted full-bridge converters are chosen as the modular cells in the IPOS system. The influence of the circuit component parameters for the output voltage of each module is analyzed. The research conclusions show that the IPOS dc-dc converters can be controlled with equal pulse width of driving signals in some low cost area.

Keywords DC-DC converters · Push–pull forward converters · Double-transistor forward converters · Phase-shifted full-bridge converters

13.1 Introduction

Due to convenient maintenance, modular power converter has become a development trend of aviation electrical. But the present complex control methods of the modular power converter increase failure rate of the whole system; so finding a simple control strategy for it is a valuable work.

Parallel-series converters have been an effective solution for the problems of serious electromagnetic interference and bad reliability met by single DC-DC converters in the large power and high voltage application area. Although topologies and control strategies of IPOS (input-parallel and output-series) DC-DC converters have been a spot [1–5], negative topic of components' parameter difference existing in the different module is seldom discussed formally. Wang and Yang [6] studied on

L. Wang (✉) · Y. Chen · Y. Wang · Y. She · H. Chen · J. Liu
School of Aeronautics, Northwestern Polytechnical University, Xian, China
e-mail: wlb109@163.com

J. Wang (ed.), *Proceedings of the First Symposium on Aviation Maintenance and Management-Volume I*, Lecture Notes in Electrical Engineering 296,
DOI: 10.1007/978-3-642-54236-7_13,

simple control strategies in the input-parallel and output-series full-bridge converters. This paper studied the practicability of IPOS modular DC-DC converters consisted of push–pull forward converters [7, 8], double-transistor forward converters, and phase-shifted full-bridge converters with equal pulse width of driving signals and consideration of module parameter difference.

13.2 Operation Principle of IPOS Converters with Equal Pulse Width of Driving Signals

An input-parallel output-series modular DC-DC converter is shown in Fig. 13.1. If output voltages of the each module of IPOS converters are equal, the output powers will be equal because that the input voltage and output current of the each converter cell are equal due to the circuit structure of input-parallel and output-series connection. Driving strategies of the IPOS converter in Fig. 13.1 is that all other modules track the driving signal of one main module, so all the modules have equal pulse width of driving signals. Sharing the output voltage of different modules is a key factor for the good practicability of this IPOS converter.

If all the component parameters of every separate converter are same, each module shares the load well. But, it is unpractical to produce a same converter module in reality. So the bad influence of parameter variance in different modules on the whole system cannot be negligible without deep research. Push–pull forward converters, double-transistor forward converters, and full-bridge converters are chosen to research as modules of the IPOS converter. The sharing performance of output voltage alone needs to be researched in this system. Drain-source on-state resistance of switching devices in the input port, transformer leakage inductors, output filter inductors, and switching frequency of different modules are researched as main circuit parameters. Parameter values of the anterior three items have an error range up to 30 %, while the fourth changes only a little since the reference clocks of all the modules have a high precision in the real system. A hypothesis is made ahead at the beginning of analysis: only one parameter of the four varies during each analysis process. In other words, the influence of every parameter on the whole system is studied separately.

Figures 13.2, 13.3 and 13.4 is all an IPOS connection converter consisted of different two modules. Each module has the equal switching frequency and equal pulse width of driver signals.

The output voltage Vo of the IPOS connection converter is:

$$V_o = V_{o1} + V_{o2} + \ldots + V_{\mathrm{on}} \tag{13.1}$$

$$V_{o1} = 2n_1 \cdot D_{e1} \cdot V_{\mathrm{in1}} \tag{13.2}$$

$$V_{\mathrm{oj}} = 2n_j \cdot D_{\mathrm{ej}} \cdot V_{\mathrm{inj}} \quad j = 1, \ldots, n \tag{13.3}$$

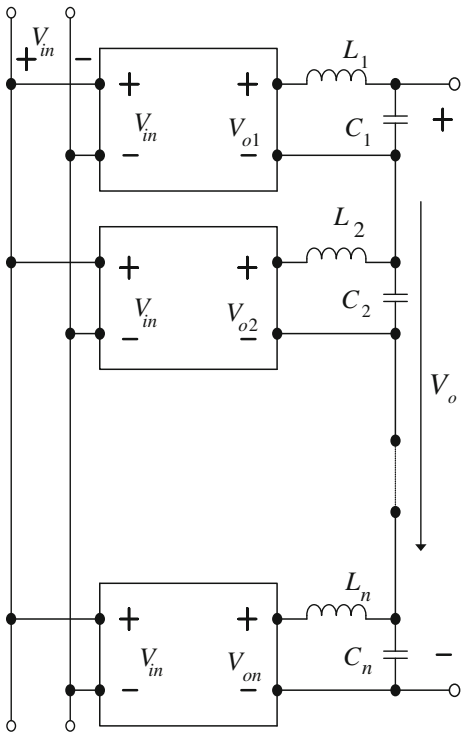

Fig. 13.1 An IPOS modular DC-DC converter

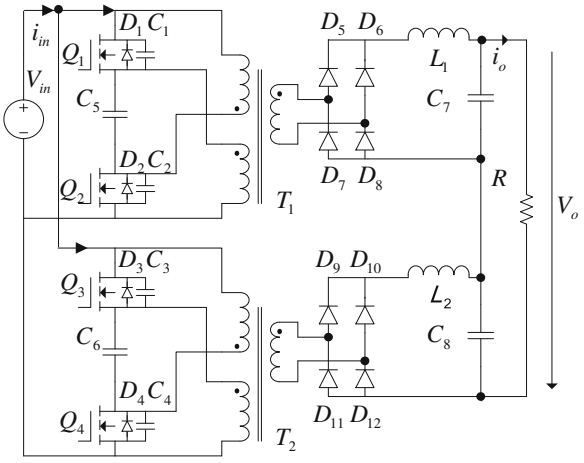

Fig. 13.2 An IPOS converter consisted of two push–pull forward converters

$V_{\text{in}1}$, V_{inj}, V_{o1}, V_{oj}, n_1, n_j, D_{e1} are input voltage, output voltage, turns of transformer, and effective duty cycle. For each module, the effective duty cycle is:

$$D_e = D - D_{\text{loss}} \tag{13.4}$$

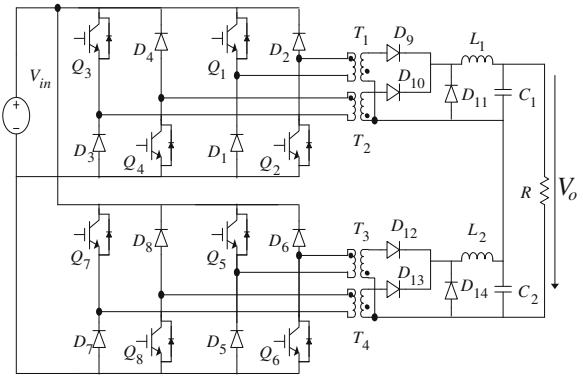

Fig. 13.3 An IPOS converter consisted of two double-transistors forward converters

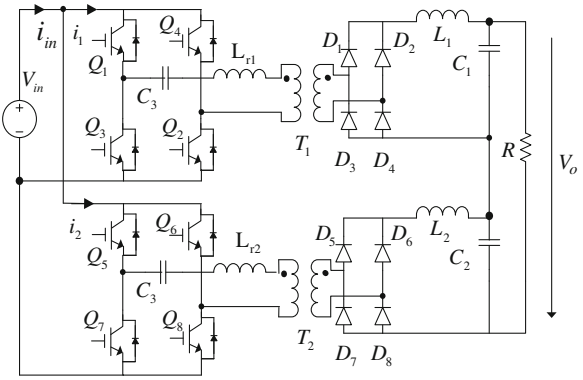

Fig. 13.4 An IPOS converter consisted of two full-bridge converters

The output voltage error ratio of one module is:

$$deltv = \frac{\frac{V_o}{n} - V_{\mathrm{oj}}}{\frac{V_o}{n}} \quad j = 1, \ldots, n \tag{13.5}$$

The relation between the output voltage error and the component parameters of different modules can be derived by the above mathematical expressions. The relation between system performance and component parameters can be revealed for different module cells when putting their duty cycle losses in the above expressions. So, the mathematical expressions of duty cycle losses for different modules need to be developed.

13.3 The Relation Between Output Voltage Error of Each Module and Its Component Parameters

The following items listed the circuit specification of an IPOS converter with two modules:

Input voltage: 24 V
The operating duty cycle: 0.42
Output filter inductor: 500 μH
Transformer leakage inductor o: 0.2 μH
Transformer turns ratio: 11
Switching frequency: 60 kHz
Output current: 2 A

The relation between output voltage of each module and its component parameters can be disclosed distinctly through statistical analysis based on the circuit parameters of specification and the mathematical equation of output voltage error.

An IPOS converter consisted of two push–pull forward modules is shown in Fig. 13.2. The duty cycle loss of push–pull forward converter is:

$$D_{\text{Loss}} = \frac{n \cdot L_k}{2V_{\text{in}} \cdot T_s}\left(I_L - \frac{1}{2} \cdot \frac{V_o}{L}(1-2D) \cdot \frac{T_s}{2}\right) \tag{13.6}$$

So the output voltage of each module is:

$$V_{o1} = \frac{2n \cdot V_{\text{in1}} \cdot D - n^2 \cdot I_L \cdot f_{s1} \cdot L_{k1}}{1 - n^2(1-2D)\frac{L_{k1}}{4L_1}} \tag{13.7}$$

$$V_{o2} = \frac{2n \cdot V_{\text{in2}} \cdot D - n^2 \cdot I_L \cdot f_{s2} \cdot L_{k2}}{1 - n^2(1-2D)\frac{L_{k2}}{4L_2}} \tag{13.8}$$

So, it is easy to know the relation between the parameter variance and the output voltage error in the IPOS converter consisted of push–pull forward modules from the mathematical expression of (13.7), (13.8), and (13.5).

13.3.1 The Relation of Drain-Source On-State Resistance of Switching Devices to the Output Voltage Error

A reasonable hypothesis is made to simulate parameter change in the real application situation before the analysis. The on-state resistances of switching devices have a variable value from 7 to 13 mΩ in the first module, while they are 10 mΩ in the second module; all the other components have the same parameter value

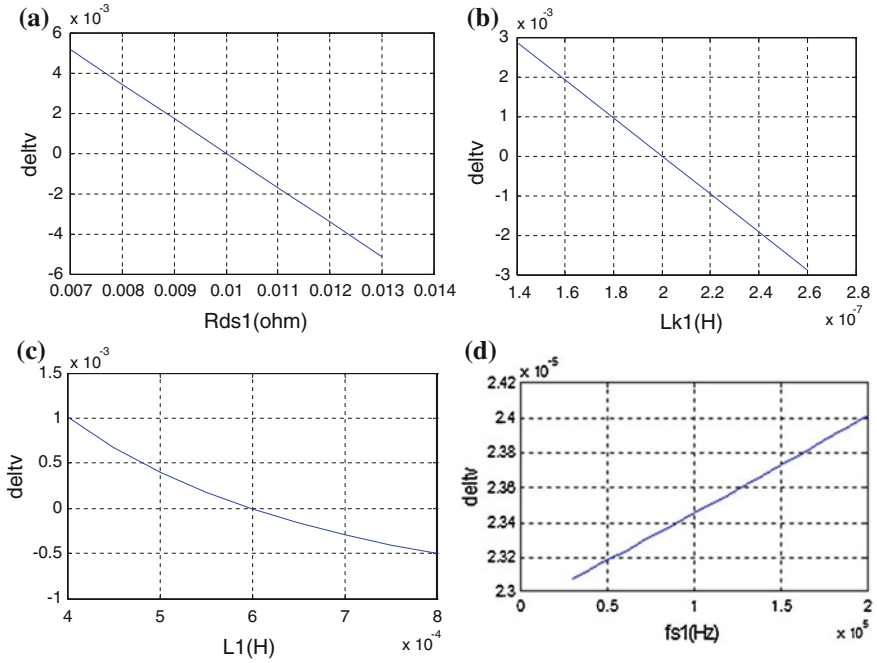

Fig. 13.5 The curve graph of component parameter and output voltage error of push–pull forward modules. **a** The curve graph of on-state resistance and output voltage error. **b** The curve graph of leakage inductor and output voltage error. **c** The curve graph of output filter inductor and output voltage error. **d** The curve graph of switching frequency and output voltage error

except on-state resistance. The curve graph of the output voltage error and the drain-source on-state resistance of the switching devices are shown in Fig. 13.5a. From the graph the following conclusion can be drawn: output voltage error and on-state resistance of switching devices has a linear relation of constant ratio for the different modules in the system, and the larger the on-state resistance is, the larger the output voltage error is. The voltage error reaches the maximum peak value of 0.5 % when the on-state resistance has a 30 % error value.

13.3.2 The Relation of the Leakage Inductor to the Output Voltage Error

The hypothesis similar to that in the previous paragraph is made for analyzing the relation of the leakage inductor, output filter inductor, and switching frequency to the output voltage error. The leakage inductor of the transformer in the first module has a variable value from 0.14 to 0.26 μH, while it is 0.20 μH in the second module; all the other components have the same parameter value except

leakage inductor. The curve graph of the output voltage error and the leakage inductor of the transformer are shown in Fig. 13.5b. From the graph the following conclusion can be drawn: output voltage error and leakage inductor have a linear relation of constant ratio for the modules of the system, and the larger the leakage inductor is, the larger the output voltage error is. The voltage error reaches the maximum peak value of 0.3 % when the leakage inductor has a 30 % error value.

13.3.3 The Relation of the Output Filter Inductor to the Output Voltage Error

The output filter inductor of the first converter has a variable value from 350 to 650 μH, while it is 500 μH in the second module; all the other components have the same parameter value except output filter inductor. The curve graph of the output voltage error and the output filter inductor of the converter are shown in Fig. 13.5c. From the graph the following conclusions can be drawn: output voltage error and output filter inductor have a linear relation of constant ratio for the modules of the system, and the larger the output filter inductor is, the larger the output voltage error is. Output voltage error reaches the maximum peak value of 0.1 % when the output filter inductor has a 30 % error value.

13.3.4 The Relation of the Switching Frequency to the Output Voltage Error

The switching frequency of the first module has a variable value from 30 to 200 kHz, while it has a 1 kHz frequency error in the second module; all the other components have the same parameter value except switching frequency. The curve graph of the output voltage error and the switching frequency of the converter are shown in Fig. 13.5d. From the graph the following conclusions can be drawn: the output voltage error and the switching frequency have a linear relation of constant ratio for the modules of the system, and the higher the switching frequency is, the larger the output voltage error is. Output voltage error reaches the maximum peak value of 0.0024 % when the switching frequency reaches 200 kHz. The switching frequency difference of different modules is very small because the reference clocks of all the modules have a high precision in reality.

Analysis of IPOS converter consisted of push–pull forward modules shows small parameter difference of different modules has negligible influence on the output voltage error when each parameter functions separately.

Then IPOS converters consisted of other modules will be studied too. An IPOS converter consisted of two double-transistor forward modules is shown in Fig. 13.3. The duty cycle loss of double-transistor forward converter is:

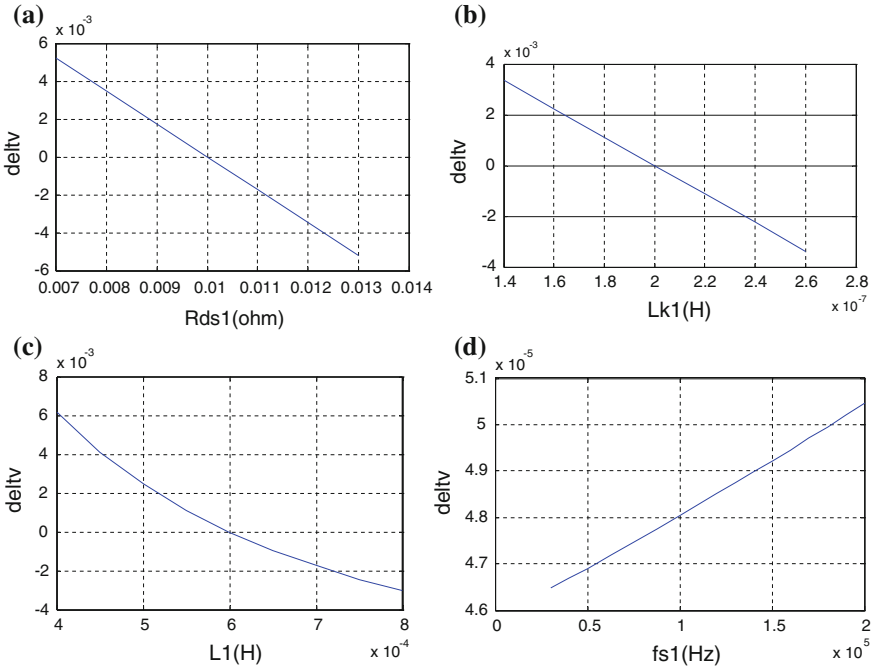

Fig. 13.6 The curve graph of component parameter and output voltage error of double-transistor forward modules. **a** The curve graph of on-state resistance and output voltage error. **b** The curve graph of leakage inductor and output voltage error. **c** The curve graph of output filter inductor and output voltage error. **d** The curve graph of switching frequency and output voltage error

$$D_{\text{Loss}} = \frac{n \cdot L_k}{V_{\text{in}} \cdot T_s}\left(I_L - \frac{1}{2} \cdot \frac{V_o}{L}(1-2D) \cdot \frac{T_s}{2}\right) \tag{13.9}$$

So the output voltage can be derived:

$$V_{o1} = \frac{2n \cdot V_{\text{in}1} \cdot D - 2n^2 \cdot I_L \cdot f_{s1} \cdot L_{k1}}{1 - n^2(1-2D)\frac{L_{k1}}{2L_1}} \tag{13.10}$$

$$V_{o2} = \frac{2n \cdot V_{in2} \cdot D - 2n^2 \cdot I_L \cdot f_{s2} \cdot L_{k2}}{1 - n^2(1-2D)\frac{L_{k2}}{2L_2}} \tag{13.11}$$

So, from (13.10), (13.11), and (13.5) it is easy to know the relation between the parameter difference and the output voltage error in the IPOS converter consisted of two double-transistors forward modules. Analysis method adopted in double-

transistors forward modules is similar to that used in the push–pull forward modules. And Fig. 13.6 is the curve graph of component parameters and output voltage error of double-transistor forward modules. The output voltage error reaches its maximum peak value of 0.5, 0.3, and 0.6 %, respectively when drain-source on-state resistance, leakage inductor, and output filter inductor have 30 % error value.

And for the phase-shifted full-bridge modules in the IPOS converters, the following mathematical expressions and conclusions can be draw:

The duty cycle loss of phase-shifted full bridge in Fig. 13.4 is:

$$D_{\text{Loss}} = \frac{n}{\frac{V_{\text{in}}}{L_k} \cdot T_s} \left(2I_L - \frac{V_o}{L}(1 - 2D) \cdot \frac{T_s}{2} \right) \tag{13.12}$$

So the output voltages of the two modules are:

$$V_{o1} = \frac{2n \cdot V_{\text{in1}} \cdot D - 4n^2 \cdot I_L \cdot f_{s1} \cdot L_{k1}}{1 - n^2(1 - 2D)\frac{L_{k1}}{L_1}} \tag{13.13}$$

$$V_{o2} = \frac{2n \cdot V_{\text{in2}} \cdot D - 4n^2 \cdot I_L \cdot f_{s2} \cdot L_{k2}}{1 - n^2(1 - 2D)\frac{L_{k2}}{L_2}} \tag{13.14}$$

The output voltage error reaches its maximum peak value of 0.5, 1.2, and 0.4 % respectively when drain-source on-state resistance, leakage inductor, and output filter inductor have 30 % error value.

In a word, sharing the output voltage is easy to achieve in the IPOS converters with equal pulse width of driving signal.

13.4 Experimental Results

An experimental prototype of IPOS converter consisted of the full-bridge modules is set up to test the previous analysis. Circuit specifications of the prototype listed below:

Input voltage: 24 V
Output voltage: 380 V
Output power: 400 W
Switching frequency: 60 kHz
Dc isolation capacitors: 9.4 μF
Transformer turns ratio: 11
Transformer leakage inductor Lr1: 0.205 μH
Output capacitor: 470 μF

Two groups of experiment were done. One is used to verify the relation between output filter inductor and output voltage error in which the leakage inductor Lr2 is 0.196 μH. Another is used to verify relation between leakage inductor and output

Table 13.1 Experimental datasheet with different output filter inductors

L1 (mH)	L2 (mH)	I(Lr1) (A)	I(Lr2) (A)	deltv (%)
0.502	0.311	8.20	8.35	0.7
0.502	0.823	8.21	8.15	0.9
0.502	0.499	8.23	8.14	0.6

Table 13.2 Experimental datasheet with different leakage inductors

Lr1 (μH)	Lr2 (μH)	I(Lr1) (A)	I(Lr2) (A)	deltv (%)
0.205	0.132	8.22	8.37	0.8
0.205	0.266	8.20	8.14	0.9
0.205	0.196	8.22	8.16	0.6

voltage error in which the output filter inductors are 502 μH and 499 μH. The switching devices are chosen randomly; the drain-source on-state resistance is random distribution. Tables 13.1 and 13.2 list the experimental data. Seen from experimental data, control strategy with equal pulse width of driving signal for IPOS converters is feasible.

13.5 Conclusions

The relation between component parameter and output voltage error is studied for the IPOS modular DC-DC converters consisted of push–pull forward converters, double-transistor forward converters, and phase-shifted full-bridge converters with equal pulse width control strategy. 30 % error value of drain-source on-state resistance, transformer leakage inductor, and output filter inductor will not result in the imbalance of output voltage. The IPOS DC-DC converters with equal pulse width of driving signal have good practicability. The IPOS DC-DC converters can be controlled with equal pulse width of driving signals in some low cost area.

Acknowledgments This work was funded by Education Department of Shaanxi Provincial Government of China (NO. 2010JK879).

References

1. Zhang MT, Jovanovic MM, Lee FCY (1998) Analysis and evaluation of interleaving techniques in forward converters. IEEE Trans Power Electron 13(4):690–698
2. Wang L, He X (2007) Input- series and output- parallel connection modular DC-DC converters with interleaved constant duty cycle control strategy. In: IEEE industrial electronics society (IECON'07), pp 1901–1906

3. Bhinge A, Mohan N, Giri R, Ayyanar R (2002) Series parallel connection of DC-DC converter modules with active sharing of input voltage and load current. APEC 2:648–653
4. Giri R, Ayyanar R, Ledezma E (2004) Input-series and output-series connected modular DC-DC converters with active input voltage and output voltage sharing. In: IEEE applied power electronics conferenc (APEC'04), vol 3, pp 1751–1756
5. Wang L (2007) Input- parallel and output- series connection modular DC–DC converters with one common filter inductor. In: IEEE EUROCON conference (EUROCON 2007), pp 1398–1402
6. Wang L, Yang B (2006) A combined ZVS converter with naturally sharing input-current and high voltage gain. In: IEEE International Power Electronics and Motion Control Conference (IPEMC 06), vol 1, pp 1–5
7. Xu P, Ye M, Lee FC (2002) Single magnetic push-pull forward converter featuring built-in input filter and coupled-inductor current doubler for 48 V VRM. APEC 2:843–849
8. Wang L, Zhang T (2011) System performance analysis of the input-parallel and output-series full-bridge converters concerning parameter difference. In: International conference on electronics computer technology (ICECT 2011), vol 3, pp 177–181

Chapter 14
Reliability Evaluation for Mechatronic Equipment Truncation Life Data Based on the Weibull Distribution Model

Ruixiang Zhou, Jin Zhang and Bolin Shang

Abstract Based on a small commercial aircraft mechatronic equipment field data which were collected, we made use of three-parameter Weibull distribution model to analyze the fault data, and theoretically studied the random censoring data preprocessing method, correlation coefficient optimization method, and the least square method combined with parameter estimation method in detail, and circularly solved the example in MATLAB by programming. We used the K-S test method and Monte Carlo simulation to test the result of reliability evaluation. The results show that this paper has put forward the model that properly fits the mechatronic equipment field data, and the calculation process is rigorous with strong operability. This model can be used to accurately obtain the mechatronic equipment reliability distribution, failure rate distribution, and to provide a scientific basis for improvement of equipment and its repair method.

Keywords Mechatronic equipment · Random truncation · Correlation coefficient · Monte Carlo simulation · Reliability evaluation

14.1 Introduction

A small civil aircraft, because of ultra sensitiveness, low fuel consumption and long voyage, is in favor with airline companies around the world from its service. This aircraft has almost accumulated 1,00,000 flying hours and a mass of field fault data. But it still has some defects, especially the low reliability of mechatronic equipment, which has a great influence on the satisfaction from airlines.

R. Zhou (✉) · J. Zhang · B. Shang
Air Force Engineering University, Xi'an 710038, China
e-mail: Zhouruixiang01@163.com

J. Wang (ed.), *Proceedings of the First Symposium on Aviation Maintenance and Management-Volume I*, Lecture Notes in Electrical Engineering 296,
DOI: 10.1007/978-3-642-54236-7_14,

In this paper, based on a critical component-low pressure relay from the aircraft, we organized the fault data by using statistical method and made use of three-parameter Weibull distribution model to estimate the reliability of this equipment. Then we can improve and complement the existing maintenance mode from the estimation, and lay a foundation for the mechatronic equipment of these aircrafts in security and economy work.

14.2 Pretreatment of Field Data

The fault data, from front line of airfield maintenance, is more typical than the data of simulation from lab. And it can virtually reflect the situation in the working environment and maintenance conditions. But because of the different inceptions of service-time, some equipments were still working. So when collecting the field fault data, these data contained a characteristic of random censored data.

When calculating the distribution function of cumulative failure, we always adopt residual ratio method or mean rank order method. Residual ratio method applies to the condition of a large sample, because we obtain it from probability multiplication formula. However, the mean rank order method not only applies to a large sample but also applies to a small sample, because it adopts an approximate middle rank formula. So in this paper, we have used mean rank order method to calculate the distribution function of cumulative failure of equipment [1].

We cannot use the methods, mean rank order method or approximate middle rank formula to calculate, because forecasting the certain time for a group of samples with censored data is impossible, where some of the sample were suspended and did not breakdown. However, according to the fault sample and censored sample, we can estimate out all of the possible rank orders, and then get the mean rank order. By substituting the mean rank order into approximate middle rank formula, we can work out its distribution function of cumulativeness. And because calculating the mean rank order method by using permutation and combination method is complex, so we summed up the increments formula of mean rank order method from statistics [2, 3]:

$$\Delta A_k = \frac{n+1-A_{k-1}}{n-i+2}. \tag{14.1}$$

$$A_k = A_{k-1} + \Delta A_k = A_{k-1} + \frac{n+1-A_{k-1}}{n-i+2}. \tag{14.2}$$

where n is the sum of the equipment. A_k is the mean rank order of fault equipment, and $A_0 = 0$. ΔA_k is the increment of mean rank order of fault equipment. k is the serial number of fault equipment and r is the amount of fault equipment, $k \leq r$. i is the total serial number of the whole equipment, which is ranked by the magnitude of fault time and censored time.

From the mean rank order, we can calculate the distribution function of cumulative failure of the sample by substituting the approximate middle rank formula:

$$F(t_{(k)}) = \frac{A_k - 0.3}{n + 0.4}. \tag{14.3}$$

14.3 Determination of Three-Parameter Weibull Distribution Model

Three-parameter Weibull distribution model is one of the most proper models to study on aircraft mechatronic equipment. The standard three-parameter Weibull distribution model can fit different kinds of lifetime data and calculate the index of equipment reliability.

The parameter estimation of three-parameter Weibull distribution model is complex, so we always adopt the maximum likelihood estimation method or the correlation coefficient method to estimate. We can conclude a high accuracy result by using the maximum likelihood estimation method, but this method is also complex for the process to solve three transcendental equations. Considering this problem, we adopt the correlation coefficient optimization method to figure out the location parameter, and then the least square method to figure out the shape parameter and scale parameter. So we can obtain the model of three-parameter Weibull distribution and then improve the accuracy of reliability analysis and evaluation of mechatronic equipment [4, 5].

The cumulative failure distribution function of three-parameter Weibull distribution is:

$$F(t) = 1 - \exp[-(t-\gamma)^{\beta} \Big/ \eta^{\beta}]. \tag{14.4}$$

where β is the shape parameter, $\beta > 0$, η is the scale parameter, $\eta > 0$, γ is the location parameter.

The density function and the failure rate function of Weibull distribution are respectively as follow:

$$f(t) = \frac{\beta}{\eta}(t-\gamma)^{\beta-1} \exp[-(t-\gamma)^{\beta} \Big/ \eta^{\beta}]. \tag{14.5}$$

$$\lambda(t) = \frac{\beta}{\eta^{\beta}}(t-\gamma)^{\beta-1}. \tag{14.6}$$

According to the equations above, when $\beta = 1$, we conclude the failure rate is *DFR* (*Decreasing Failure Rate*) by Eq. (14.6), fit the modeling of initial failure. When $\beta = 1$, the failure rate is a constant, fit the modeling of random failure.

When $\beta > 1$, the failure rate is *IFR* (*Increasing Failure Rate*), fit the modeling of abrasion or aging failure. We can control the trend of increasing failure rate by adopting periodical replacement and maintenance.

Equation (14.4) can also be written as:

$$\begin{aligned} &y = \ln[-\ln(1 - F(t))],\ x = \ln(t - \gamma). \\ &B = -\ln \eta^{\beta}. \end{aligned} \tag{14.7}$$

And can be linearized as:

$$y = \beta x + B. \tag{14.8}$$

We obtained the parameter evaluation by using least square method:

$$\begin{cases} \hat{\beta} = \dfrac{\sum\limits_{i=1}^{r} x_i y_i - r\bar{x} \cdot \bar{y}}{\sum\limits_{i=1}^{r} x_i^2 - r\bar{x}^2} \\ \hat{\eta} = \exp\left(-\dfrac{\bar{y} - \hat{\beta}\bar{x}}{\hat{\beta}}\right) \end{cases}. \tag{14.9}$$

From the sample data ($t(i)$, $F(t(i))$), we can obtain (x_i, y_i) to calculate the correlation coefficient R(x, y) between x and y.

$$R(x, y) = \frac{\left(\sum\limits_{i=1}^{r} x_i y_i - r\bar{x} \cdot \bar{y}\right)}{\sqrt{\left(\sum\limits_{i=1}^{r} x_i^2 - r\bar{x}^2\right)\left(\sum\limits_{i=1}^{r} y_i^2 - r\bar{y}^2\right)}}. \tag{14.10}$$

where $R(x, y)$ is the function of location parameter γ. So we can use γ as a variable, $|R(x, y)|$ as objective function to figure out its maximum, and the γ, associated with the maximum, is the evaluation of location parameter $\hat{Y}$.

To optimize the evaluation model for calculating $\hat{Y}$, make:

$$\begin{aligned} \max|R(\hat{\gamma})| = &\left| \frac{\left(\sum\limits_{i=1}^{r} x_i y_i - r\bar{x} \cdot \bar{y}\right)}{\sqrt{\left(\sum\limits_{i=1}^{r} x_i^2 - r\bar{x}^2\right)\left(\sum\limits_{i=1}^{r} y_i^2 - r\bar{y}^2\right)}} \right|. \\ &0 \le \hat{\gamma} \le t_1 \end{aligned} \tag{14.11}$$

where t_1 is the minimum in the data point, and we finished the solution procedure by using golden section method to one-dimensional searches [6].

14.4 Instance Analysis

In this paper, we undertook the disposal of the data from a low pressure relay of a small civil aircraft, and then obtained 53 failure data at the deadline of July 3rd 2011. After deleting some daily maintenance and nonassociated failure data, we retained 28 of them. This equipment in some aircrafts had not been in failure at the deadline, which we define as censored data. Shown in Table 14.1, data with "+" is censored data. Because this equipment is used in various kinds of airlines' aircrafts, in different flight and maintenance conditions, the data can virtually be a response to the level of reliability of low pressure relay.

Statistical analysis on the failure data in Table 14.1 and drawn a histogram. We obtained the frequency histogram and empirical cumulative distribution function by failure data in EXCEL, as shown in Fig. 14.1. Then from Fig. 14.1, we can preliminarily conclude that the distribution follows Weibull model, because the failure data is almost coincided with it.

According to the method above, we obtained the disposal flow of the data from a low pressure relay, as shown in Fig. 14.2 [7–9].

The particular calculating process is complex, and always need dozens of iterative calculation to finish. So we programmed functions for the algorithm, based on MATLAB, by defining the number of iteration as 200. We obtained that the location parameter is 16.5324 and the maximum of correlation coefficient is 0.9797.

Substituting the location parameter into Eq. (14.9), we obtained the shape parameter and scale parameter respectively: 0.8666 and 1792.6.

In Table 14.2, we tested the fitting degree of probability distribution of cumulative failure by using *K-S* (*Kolmogorov-Smirnow*) method and correlation coefficient method. We also obtained Weibull probability paper of the model, as shown in Fig. 14.3.

In order to improve the accuracy and range of applications of the test method, we used Monte Carlo simulation method to widely test the parameter evaluation method in this paper. In the test, we assumed the initial distribution parameters that fit Weibull distribution, firstly, and then used Monte Carlo method to do stochastic simulation, where we obtained a series of pseudo data fitting this distribution due to the requirement of set sample. Finally, we compared the fitting line of failure data points of random generation with the figure of distribution function of parameter generation.

From the different kinds of value of test method and Fig. 14.3, the distribution model of Weibull we obtained in this paper can properly fit the actual data, and the model can be applied in engineering. There is only one variable in the paper (*location parameter*), so we programmed the cycle solution, which implies simplicity and saving time.

According to the parameters from three-parameter Weibull distribution model, we obtained the sketch map of its probability density, the map of its reliability curve, and the map of its failure rate curve respectively, shown in Fig. 14.4–14.6.

Table 14.1 Low pressure relay completely with censored data table

Flight hours			
36.46	40.14	66.18	90.05
119.40	145.72	167.40	269.85
302.24+	314.34	324.02+	355.22
358.22	451.54+	466.55	485.88
548.99	554.18	575.79	666.44
685.88	759.08	810.94	835.28
850.14+	864.97	934.45+	1013.47
1023.89+	1031.13+	1052.85	1212.79+
1271.58	1323.02+	1401.09	1574.63
1691.74+	1830.42	1869.21	1917.82+
2086.50	2423.91+	2587.22	2675.01+
2872.78	2898.67+	2924.13	2985.13+
3065.22	3211.86	3266.62	3794.92

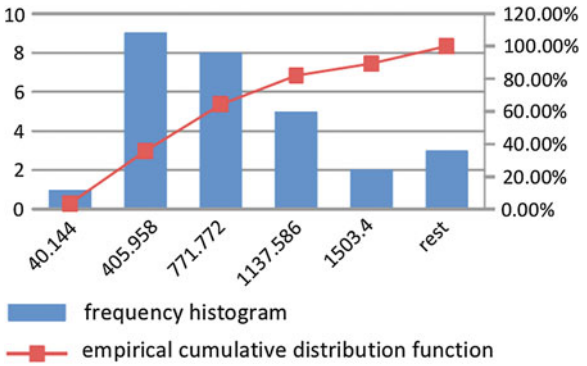

Fig. 14.1 Low pressure relay fault frequency histogram and cumulative distribution function diagram

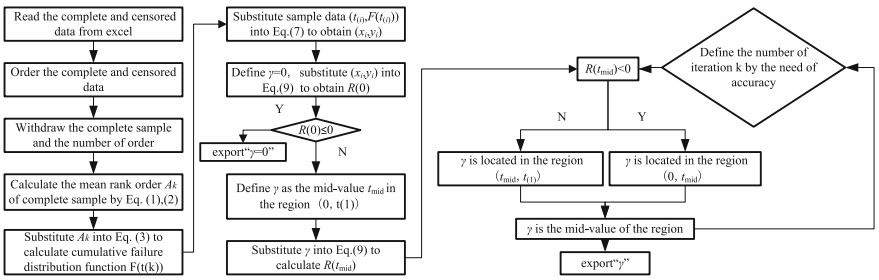

Fig. 14.2 Data processing flow diagram

Table 14.2 Results of parameter estimation and test results

Item	Γ	B	H	*K-S test*	Correlative coefficient
Calculated value	16.5324	0.8666	1792.6	0.1822	0.9797

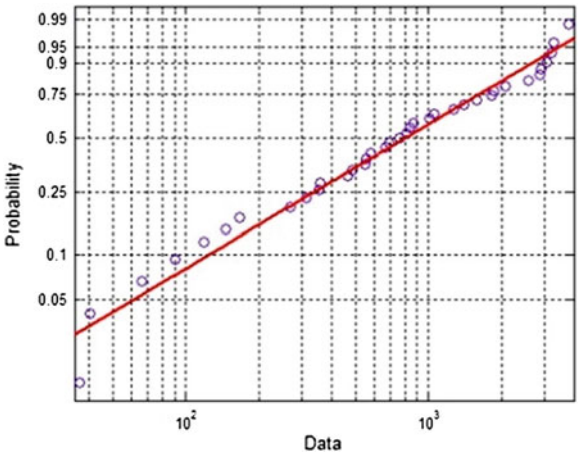

Fig. 14.3 Low pressure relay Weibull probability paper map

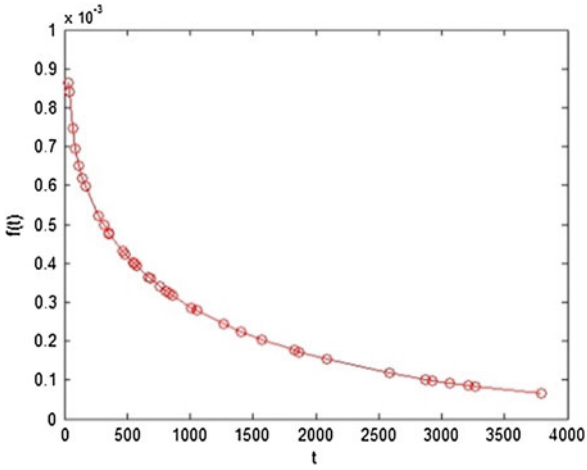

Fig. 14.4 The three-parameter Weibull distribution

Due to the conclusion above and the requirement of safety in practical application, we can obtain the proper overhaul period of mechatronic equipment.

1. We can see in Fig. 14.5 that the failure rate decreases as the time goes on, which means that low pressure relay was in early phase of overhaul period. So we always maintain adopting failure detection maintenance or periodical replacement method.
2. Early failure happens at the beginning of the working time of products. At that time, products happen to be not only with a high failure rate, but also with a low

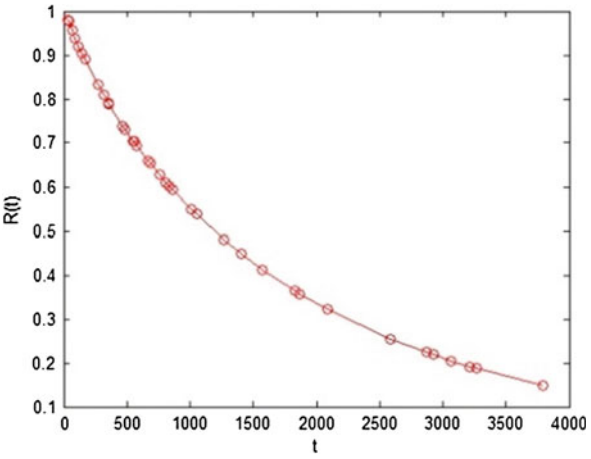

Fig. 14.5 The three-parameter Weibull probability density function curve distribution reliability curve

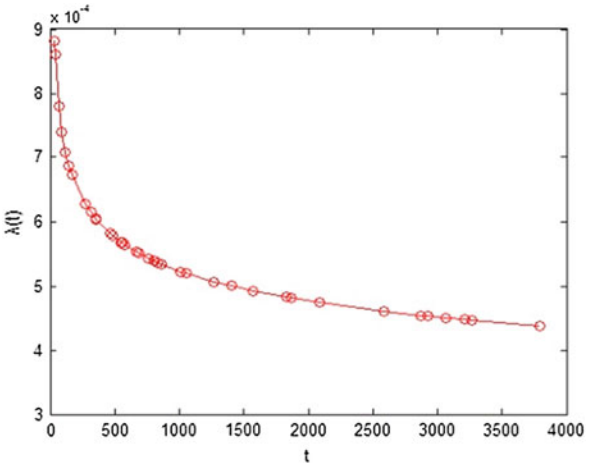

Fig. 14.6 The three-parameter Weibull distribution failure rate curve

reliability. However, the failure rate is going down with the time increasing. The main reason of early failure of a low pressure relay is due to either defects of the design and manufacture process or defects of the structure of parts and material. So before delivering, we should do some correlative experiments if we want to shorten the failure period, and do our best to reduce the failure frequency in early failure as well as enacting the fault remedy time according to its location parameter.

3. Because the low pressure relay belongs to a part, they have a great influence on the safety. So it must be with high reliability. The definite reliability is decided by the decision maker. According to the formula of reliability, we can obtain the run time of a low pressure relay without failure.

14.5 Conclusion

In this paper, we undertook the disposal of the data from a low pressure relay of a small civil aircraft, made use of three-parameter Weibull distribution model to do modeling analysis. Used mean rank order method, least square method, and correlation coefficient optimization method to study the calculating process of the model in detail. We programmed functions for the algorithm which is based on MATLAB. Then we tested our analysis by calculating the field data of an important part-low pressure relay.We can conclude that the method is feasible and convenient in engineering.

References

1. Zhao Y, Yang J (2009) Reliability data analysis (in Chinese). Beijing University of Aeronautics and Astronautics Press, Beijing
2. He GF (1997) Field reliability data of interval estimation (in Chinese). Electron Prod Reliab Environ Test (1):19–24
3. Gao HX (1995) Statistical calculation (in Chinese). Peking University Press, Beijing
4. He GF, Xu GB (1995) Collection and analysis of reliable data (in Chinese). National Defence Industry Press, Beijing
5. Shi J, Yang X, Chen X (2009) Comparative study on parameter estimation methods for 3-parameter Weibull distribution (in Chinese). J Henan Agric Univ (4):405–410
6. Yu XH, Zhang LB, Wang ZH, Duan LX (2007) Reliability life analysis of the equipment based on new Weibull distribution parameter estimation method (in Chinese). J Mech Strength 29(6):932–936
7. Wang L, Xu Y, Zhang J (2008) Research on reliability analysis model for key components and parts of railway equipment and its application (in Chinese). J China Railway Soc (8):93–98
8. Bailey RT (2006) Estimation from zero-failure data. Risk Anal 17(3):375–380(2006)
9. Singpurwalla ND, Song MS (1988) Reliability analysis using Weibull lifetime data and expert opinion. IEEE Trans Reliab 37(3):340–347

Chapter 15
The Technical Research of PHM in Aeronautical Mechanical and Electronical System Based on IETM

Fei Meng, Jien Yang, Hang Xu and Xiaolei Li

Abstract The key parameters of aero-engine reflect the varieties of the system at a certain extent. The varieties will represent affirmatively when the system will or has appeared failure. Through the methods of modeling the key data which reflect aero-engine capability, vibration, and abrasion, the failure prognostics curves can be fit based on the working data in practice. By using the PHM curves to prognose the intending values, it has extraordinary meaning for predicting the aero-engine states in advance and making the maintenance steps available in order to avoid momentousness accidents.

Keywords IETM · PHM · Aviation mechatronics system

15.1 Introduction

Interactive Electronic Technical Manual (IETM) and Prognostics and Health Management (PHM) are new theories and technologies which are used in aviation maintenance recently. The use of IETM can reduce the overhead expenses of equipment technical information and the maintenance expenses of equipment ensurence. PHM is a promising technology which can improve the quinary qualities [1] (reliability, maintenance, testing, indemnificatory, and security) and reduce life cycle expenses of a complex system in army and civilian. Both technologies can exert great effection in modern aviation maintenance and produce great influence reply to the theory, mode, and effect of aviation maintenance.

F. Meng (✉) · J. Yang · H. Xu · X. Li
The First Aeronautic Institute of Air Force, Xinyang, Henan, China
e-mail: mengfei1979@yeah.net

J. Wang (ed.), *Proceedings of the First Symposium on Aviation Maintenance and Management-Volume I*, Lecture Notes in Electrical Engineering 296,
DOI: 10.1007/978-3-642-54236-7_15,

15.2 The Application Research of IETM in Aviation Maintenance

15.2.1 The Function Structure of IETM

At present, to combine with the factual characteristic of work, an all-around IETM should have the following functions based on the concept and function of IETM. ① The interactive search of information which can offer real-time digital maintenance datum to engineer who is on working; ② The interactive booking in of information which includes all kinds of technical bulletin, filling in the task card of plane, noting failures, and so on. ③ The management of aviation material which can offer aviation material information on line to engineer. ④ PHM which can manage aviation equipments with expert system of fault diagnosis or long-distance failure diagnosis by wireless network. ⑤ Technical training which uses IETM to achieve highly effective training.

The IETM equipped for engineers in aerodrome should have the following functions. ① The maintenance procedure, security regulation, and checking measures of the plane. ② The technical datum, theoretical teaching material, and book of circuit diagram. ③ All kinds of labor cards such as failure information, swap or change equipments, and application for aviation material which can be contacted with the quality or aviation material managements. ④ EMS (engine monitoring system). ⑤ Expert system which can offer information in case of failure.

15.2.2 The Use and Management Mode of IETM

IETM has brought immense revolution in aviation in datum management and use because of storage medium and instrument of IETM.

a. Use and management mode of stand-alone IETM

All the technical data and fixing program designed by an IETM manufacturer are packed into a CD-ROM. When the user installs the program in PMA after receiving the CD-ROM and the operating system, the scheme database and display system will automatically get fixed. Then the engineer authorized can use IETM in work. If there are any changes, the IETM manufacturer or superior department releases the correlated mend program to users. The “data mend” is an executable program which can automatically run involved with data need to be refreshed.

b. Use and management mode of network IETM

An IETM manufacturer designs and executes the setting program, original data, and technical mends of the equipment first and disposes them firsthand to the Common Source Data Base (CSDB) of the central data server. With the conjunction of Web server, the engineer accredited can use the IETM by use of the Portable Maintenance Aid (PMA), PDA, or other terminal client conjoint by server

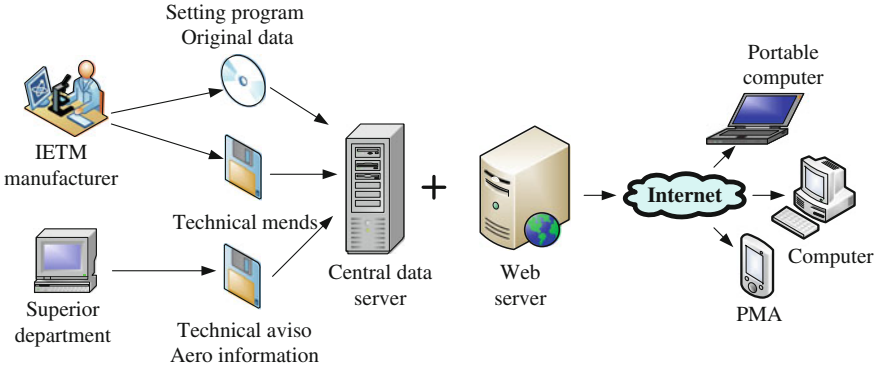

Fig. 15.1 The use and management mode of network IETM

anywhere and anytime. The engineer can browse and search the technical data of the equipment in Internet by IETM based on B/S structure. The use and management mode of the network IETM is shown in Fig. 15.1.

15.3 The Technical Research of PHM in Aeronautically Mechanical and Electronical System

In course of equipment working, we should monitor their working state. When the equipment will or has gone wrong, we must estimate the pattern, place, and aftereffect of the failure immediately. Then what we should do next are isolating, equalizing, restraining, or weakening the failure in order to let the equipment work a period of time to achieve the task. In the end, we can bring forward the maintenance policy by use of IETM, in order to reduce the expense of maintenance and to improve the utilizing rate of the equipment.

15.3.1 The Basic Thinking Flow of PHM

EMS is the most important system composing of aeronautical mechanical and electronical system. The informations collected by it reflect the state of engine accurately. So these informations are the basements of engine PHM. The reliability of mechanical and electronical systems is the precondition of engine PHM. If any failures individually occur in any accessories or sensors, it will lead to disnicety reacted to engine state even false alarms. So it is important to analyze the reliability of mechanical and electronical equipments and monitoring the state of them. Health Management is the other important conjunction of PHM. The

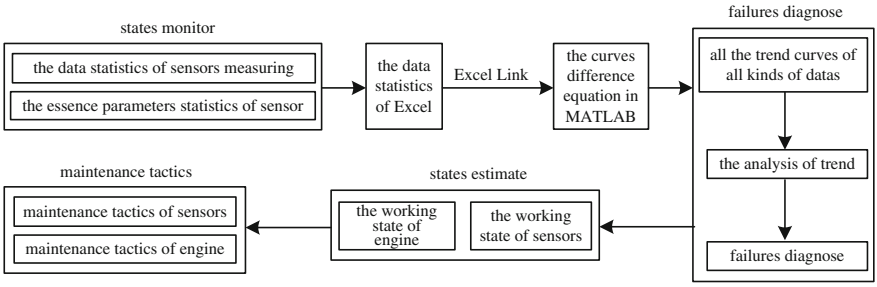

Fig. 15.2 The basic idea flow of PHM in EMS

veracious prognostics can offer reliable life remain in order to judge whether the equipment can achieve the task or not. Also, adopting the correct maintenance policy is the precondition on which the equipment working relies on.

In conclusion, the basic idea flow of PHM in EMS is shown in Fig. 15.2.

15.3.2 The Basic Means of PHM

The basic means of PHM in aero-mechanical and electronical system is composed of libration sensor, pressure sensor of lubricating oil, temperature sensor of lubricating oil, and spectral analysis of lubricating oil which are correlative with the state of engine. The means of PHM to libration sensor is prognostics of real-time remain life which based on invalidation physics model. The means of PHM to pressure and temperature sensor of lubricating oil are monitor method which is based on essence parameter. The means of PHM to spectral analysis of lubricating oil is mathematics statistic method of time series. All of three means above can estimate "rotate speed fall" synthetically. As a whole every means of PHM is not isolated. In practice we need to examine, monitor, analyze, and prognose continuously, then the PHM of aero-mechanical and electronical system will be exact and effective. The idea flow of PHM is shown in Fig. 15.3.

15.3.3 The PHM Based on Essence Parameter

In aero-maintenance, an engineer measures a large number of data of voltage or resistance. The PHM based on essence parameter can be used to all the sensors of the engine which reflect its state in order to PHM engine [2]. These sensors examine the correlative state of engine at any moment by means of voltage or resistance to estimate the capability guideline of engine. Sometimes the sensors will lead to false alarm when they are disabled or the state of work is changing. In

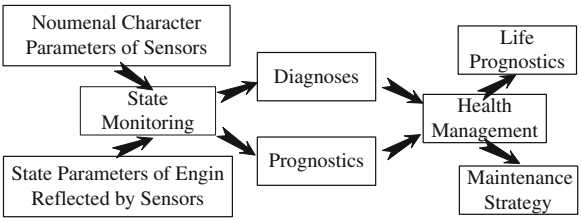

Fig. 15.3 The idea flow of PHM

maintenance, we can note these data, classify and find the mathematics model of difference equation, then analyze the curve of trend educed, and command the history of working state in order to guide the next work of maintenance.

15.4 The Antetype System of PHM Based on IETM

15.4.1 The PHM of State Parameters of Engine Reflected by Sensors Based on IETM

The state parameters of engine reflected by the sensors indicate the state of engine real time. For example [3], libration sensor of some planes reflect the libration of all the states of the engine and changes them from displacement to voltage, which the flight data processing system and alarm system will note and alarm. The pressure or temperature sensor of the lubricating oil notes the pressure or temperature and change them to electronical signals to performance institution in order to estimate the "rotate speed fall." Spectral analysis of lubricating oil can ascertain the state of engine in another way. These postural parameters reflect engine working state can be noted and analyzed daily in order to PHM the engine.

The flight data processing system memorizes the libration of engine working [4], then the engineer can transfer them to observe the changing of libration of engine. There are two intentions for this, one is observing the libration changing with rotation speed; if there are any diversifications or exceeding standards in them; the other is accumulating the historical time sequence to analyze the state of engine in order to PHM. It has proved that the means has obvious action to prevent the "rotate speed fall." Figure 15.4 shows the libration changing of some engines in "most" state before flying off in 2 months. From the curve, we can adopt the maintenance policy in order to prevent accident in the next day and prognosticate the libration will be 32 mm/s.

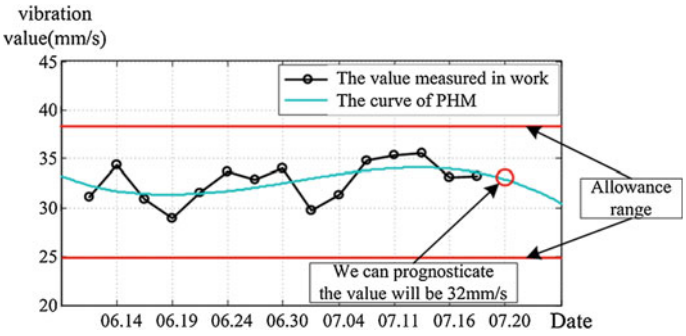

Fig. 15.4 The libration changing and PHM curve

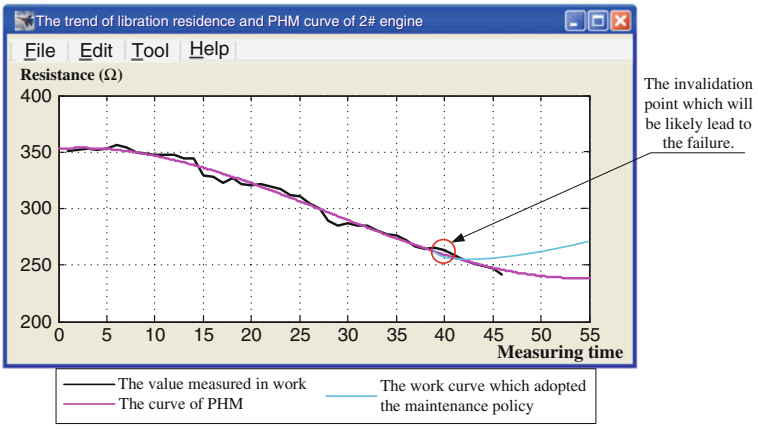

Fig. 15.5 Analyze chart of resistance and PHM trend of libration sensor

15.4.2 The PHM of Noumenal Character Parameters of Sensors Based on IETM

The state parameters of engine reflected by sensors reflect the working state of engine real time, but it is very important for sensors to working normally. If the sensors will or have failed, then the state parameters will not be exact and can lead to false alarm. Mass of signals measured by sensors are voltage or residence. We can record these data in Excel and fit curve by means of the interlinkage of Excel and Matlab. Figure 15.5 shows the trend of libration residence and PHM curve. From the figure, we can analyze the work state of this sensor next way, judge the state of sensor which it will or has failed in order to adopt any maintenance policy to low the fault fate and improve the security of plane. From the figure, we can prognosticate the invalidation point which will be likely lead to the failure and the residence should be 248 Ω.

This means that PHM based on the essence parameter is the most economical and fast method for diagnosing and eliminating failures in a plane's EMS, especially the failure of "rotate speed fall." It can be used along with the libration sensor, pressure sensor , and temperature sensors of lubricating oil, and spectral analysis of lubricating oil. According to our statistics, the "rotate speed fall" failure fate falls down to 11 %. It has brought favorable action to reducing the labor intension of the engineer and preventing the fatal failure.

15.5 Summary

With the broad application of electron technique and the expediting of plane, it is obligatory to strengthen the research of aero-maintenance and detecting measures in order to improve the precision of failure detecting and insulating. This means of PHM that is based on the essence parameter has acquired better affection in some plane EMS. In addition, it should strengthen the research and analysis and gather of failure causing in proclitic research. The comprehensive treatment will lead to better PHM.

References

1. Bill B, She J (2007) No fault found. J Aviat Maintenance Eng 3:15–17
2. Chen G (2007) Technic introduction of aerostat examine and diagnosis, China Civil Aviation Publications, Beijing
3. Zhang S-Y, Yang W-J (2011) Analysis of aeronautical maintenance errors and preventative measure. J Xi'an Aerotech Coll 1:35–38
4. Jorgensen EL (1999) Proposed DoD guidelines for implementation of a web-based joint IETMs architecture (JIA) to assure the interoperability of DoD IETMS. Submitted to carderock division, Naval Surface

Chapter 16
Research of the Performance Assessment Interval of the B737NG ACM, Based on Weibull Distribution

Renhe Fu and Quansheng Zheng

Abstract The primary task of the preventive maintenance is to setup the reliability model, which is based on the unschedule removal data of its own fleet, and then determine a suitable replacement interval or performance assessment interval. In this paper, based on the unschedule removal data of the ACM, B737NG fleet, in one airlines, set up the Weibull distribution, and used the Kolmogorov criterion to test the distribution, then determine a performance assessment interval. Maintenace experience shows that the performance assessment interval has good consistency.

Keywords Weibull distribution · Kolmogorov criterion · ACM · Performance assessment interval

16.1 Introduction

The B737NG Maintenance Plan, based on the MSG-3, is the foundation of the airlines to arrange its maintenance task, but the difference between the condition of the plane design, experimental, and the environment of actual operation, maintenance ability, often caused the unschedule removal. So in order to increase the reliability of the fleet, the airlines should set up its own reliability model, based on the characteristics data of its own fleet, and determine a performance assessment interval, which must meet the requirement of Maintenance Plan.

R. Fu (✉) · Q. Zheng
Henan Branch of China Southern Airlines, Zhengzhou, China
e-mail: furenhe@csair.com

Q. Zheng
e-mail: zhengqs@csair.com

J. Wang (ed.), *Proceedings of the First Symposium on Aviation Maintenance and Management-Volume I*, Lecture Notes in Electrical Engineering 296,
DOI: 10.1007/978-3-642-54236-7_16,

How to collect accurate data and determine reliability function of the components is the key to determine the interval. Nowadays, the widely studied distribution is Weibull distribution, exponential distribution, normal distribution, and lognormal distribution, and the Weibull distribution is more widely used in the field of aviation maintenance. This paper is based on the least square method to estimate the parameters of Weibull distribution, and uses Kolmogorov test to verify the validity of the distribution model. Then based on the unschedule removal data of the ACM of one airlines, according to the above methods, set up the reliability function, and determine a performance assessment interval. Then according to the working principle of A/C system, the ACM assessment method is also proposed under this assessment interval.

16.2 Weibull Distribution

As the widely studied distribution, the Weibull distribution can effectively describe the life of the operational system, components, and parts, under the condition that the related parameters are reasonably estimated [1].

The life distribution function of Weibull distribution is:

$$F(t) = 1 - \mathrm{EXP}\left[-\left(\frac{t}{\alpha}\right)^{\beta}\right] \tag{16.1}$$

Reliability function is

$$R(t) = \mathrm{EXP}\left[-\left(\frac{t}{\alpha}\right)^{\beta}\right] \tag{16.2}$$

Failure rate function is

$$\lambda(t) = \frac{\beta t^{\beta-1}}{\alpha^{\beta}} \tag{16.3}$$

16.3 The Estimate of the Weibull Distribution Parameters

16.3.1 Parameter Estimated Based on the Least Square Method

In order to estimate the parameter with the method of least square method, the first step is to linearize the weibull distribution.

Take logarithm twice on both side of Formula (16.1):

$$\ln \ln \left[\frac{1}{1-F(t)}\right] = \beta(\ln t - \ln \alpha) \tag{16.4}$$

$$\text{Set } x = \ln t;\ y = \ln \ln \left[\frac{1}{1-F(t)}\right];\ A = \beta;\ B = \beta \ln \alpha; \tag{16.5}$$

So Formula (16.4) changed to Formula (16.6):

$$Y = AX + B \tag{16.6}$$

For Linear regression Formula (16.6), the least squares estimate of the A and B is:

$$\dot{A} = \frac{\sum X_i Y_i - \frac{\sum X_i \sum Y_i}{n}}{\sum X_i^2 - \frac{\left(\sum X_i\right)^2}{n}} \tag{16.7}$$

$$\dot{B} = \frac{\sum Y_i}{n} - \dot{A}\frac{\sum X_I}{n} \tag{16.8}$$

Then according to Formula (16.5), and the estimate of the A & B, so:

$$\beta = A \quad \alpha = \text{EXP}\left(\frac{B}{\beta}\right) \tag{16.9}$$

16.3.2 Empirical Distribution Function

The middle-rank-method is a good way to calculate the empirical distribution function, so:

$$F_n(t_i) = \frac{i - 0.3}{n + 0.4} \tag{16.10}$$

Among them, i is the fault serial number of the component, n is the number of sample. Based on the unschedule removal data and Empirical distribution function, according to the median rank formula, and with the least square method, the parameters of the Weibull distribution can be calculated. Then the Specific distribution model is available, then combined with the specific failure data, in accordance with the principle of goodness of fit test, to determine whether a distribution model conforms to the real failure data.

16.4 Kolmogorov Criterion

Kolmogorov criterion [2] is:

Set the distribution function to $\underline{F}(t)$, consider the hypothesis test is :

$$H_0 : F(t) = F_0(t)$$

Drawn n samples from the capacity, then the order statistics is:

$$T_{(1)} \ll T_{(2)} \ll \ldots \ll T_{(n)}$$

So:

$$\delta_i = \max\left\{\left|F_0\left(x_{(i)}\right) - \frac{i-1}{n}\right|, \left|F_0\left(x_{(i)}\right) - \frac{i}{n}\right|\right\}, (i = 1, \ldots., n) \tag{16.11}$$

Choose the largest one from the δ_i, δ_2,…,δ_n, and set it to Dn, so:

$$D_n = \max\{\delta_i\}$$

For a given level of significance and a sample size n, according to the Kolmogorov test result table, get the critical value dn, a, If $D_n \leq d_{n,a}$, then accept H0, Otherwise refuse the H0.

If H0 is accepted, it means this failure time data conforms to the established Weibull distribution.

16.5 Example-Reliability analysis of ACM of one airlines

As the key components of the A/C system, the reliability of the ACM largely determines the reliability of the air conditioning system. In the process of the ACM unschedule removal data collection, in order to eliminate the deformity data of the different component repair factory, all the data comes from the new ACM unschedule removal data, between the date 2010.1.1 and 2012.12.31. Then get 29 points (29 times unschedule removal), such as the Table 16.1.

16.5.1 The Estimate of the Weibull Distribution Parameters

Based on the Formula (16.10) and (16.5), calculate empirical distribution function. As shown in Table 16.2.

Based on the x,y in Table 16.2, and according to Formula (16.7) and (16.8), so:

$A = 3.3471$; $B = -33.66$

Then, according to Formula (16.9), so:

$\alpha = 3.3471$; $\beta = 23330.65$

Table 16.1 Unschedule removal of the new ACM data (the date between 2010.1.1 and 2012.12.31)

Serial number	TSN (time since new)	Serial number	TSN (time since new)
1	7484.7	16	21963.9
2	9406.183	17	22050.38
3	11520.72	18	22112.17
4	13010.16	19	23389.15
5	13994.21	20	23953.57
6	14575.55	21	24484.68
7	16809.85	22	27060.3
8	17103.11	23	27085.88
9	17564.68	24	28184.43
10	17592.02	25	28219.74
11	18665.82	26	29053.32
12	19000.88	27	29515.95
13	19082.16	28	29599.59
14	21289.35	29	30325.13
15	21475.69		

So the life distribution function is:

$$F(t) = 1 - \mathrm{EXP}\left[-\left(\frac{t}{23330.65}\right)^{3.3471}\right] \tag{16.12}$$

16.5.2 Kolmogorov Criterion

Test Formula (16.12) with Kolmogorov criterion, so:

H_0: the life distribution function of the ACM is:

$$F(t) = 1 - \mathrm{EXP}\left[-\left(\frac{t}{23330.65}\right)^{3.3471}\right] \tag{16.12}$$

Then as shown in Table 16.3:

According to Table 16.3, the Dn is 0.09024, and the level of significance, $\delta = 0.2$, so:

$$d_{29,0.2} = 0.19348$$

$D_n = 0.09024 < d_{29,0.2} = 0.19348$,so accept the H_0, and ACM fault time conforms to the Weibull distribution (the parameters of $\alpha = 3.3471$, $\beta = 23330.65$), so the ACM fault time distribution function is:

$$F(t) = 1 - \mathrm{EXP}\left[-\left(\frac{t}{23330.65}\right)^{3.3471}\right] \tag{16.12}$$

Table 16.2 The empirical distribution function of the ACM

i	Middle-rank Parameters		x = lnt	$y = \ln \ln\left[\frac{1}{1-F(t)}\right]$
	T	$F_n(t_i)$		
1	7484.7	0.02381	8.920616	−3.72565
2	9406.183	0.057823	9.149123	−2.82073
3	11520.72	0.091837	9.351902	−2.33996
4	13010.16	0.12585	9.473486	−2.00616
5	13994.21	0.159864	9.546399	−1.7476
6	14575.55	0.193878	9.587101	−1.5347
7	16809.85	0.227891	9.72972	−1.35236
8	17103.11	0.261905	9.747016	−1.19177
9	17564.68	0.295918	9.773646	−1.04737
10	17592.02	0.329932	9.775201	−0.91535
11	18665.82	0.363946	9.834449	−0.79303
12	19000.88	0.397959	9.852241	−0.6784
13	19082.16	0.431973	9.856509	−0.56989
14	21289.35	0.465986	9.965962	−0.46628
15	21475.69	0.5	9.974677	−0.36651
16	21963.9	0.534014	9.997156	−0.26971
17	22050.38	0.568027	10.00109	−0.17508
18	22112.17	0.602041	10.00388	−0.08185
19	23389.15	0.636054	10.06003	0.010694
20	23953.57	0.670068	10.08387	0.10334
21	24484.68	0.704082	10.1058	0.196941
22	27060.3	0.738095	10.20582	0.292501
23	27085.88	0.772109	10.20677	0.39129
24	28184.43	0.806122	10.24652	0.495018
25	28219.74	0.840136	10.24778	0.60619
26	29053.32	0.87415	10.27689	0.728834
27	29515.95	0.908163	10.29269	0.870349
28	29599.59	0.942177	10.29552	1.047448
29	30325.13	0.97619	10.31973	1.318462

16.5.3 The Estimate Interval of Performance Assessment

In general, there are two preventive maintenance methods, namely, the first one is the aircraft parts, which is unable to quantify its performance status, and can be determined a reliable life according to the reliability distribution function; when the reliable life comes, remove the parts; and for the other parts, which is able to quantify its performance status, can be determined a reasonable performance assessment interval. When the specified interval comes, sample and evaluate the parts working data, so as to decide whether to remove it on the condition of the working data.

Table 16.3 The calculations of the Kolmogorov criterion

i	T	$F_0(t)$	(i-1)/n	i/n	$\left\|F_0(x_{(i)}) - \frac{i-1}{n}\right\|$	$\left\|F_0(x_{(i)}) - \frac{i}{n}\right\|$
1	7484.7	0.022005	0	0.034483	0.022005	0.012478
2	9406.183	0.046684	0.034483	0.068966	0.012201	0.022281
3	11520.72	0.089944	0.068966	0.103448	0.020979	0.013504
4	13010.16	0.132019	0.103448	0.137931	0.028571	0.005912
5	13994.21	0.165332	0.137931	0.172414	0.027401	0.007082
6	14575.55	0.187059	0.172414	0.206897	0.014645	0.019837
7	16809.85	0.283806	0.206897	0.241379	0.076909	0.042427
8	17103.11	0.297913	0.241379	0.275862	0.056534	0.022051
9	17564.68	0.320686	0.275862	0.310345	0.044824	0.010342
10	17592.02	0.322056	0.310345	0.344828	0.011711	0.022772
11	18665.82	0.37746	0.344828	0.37931	0.032633	0.00185
12	19000.88	0.395303	0.37931	0.413793	0.015993	0.01849
13	19082.16	0.399665	0.413793	0.448276	0.014128	0.048611
14	21289.35	0.520995	0.448276	0.482759	0.072719	0.038236
15	21475.69	0.531317	0.482759	0.517241	0.048558	0.014076
16	21963.9	0.558266	0.517241	0.551724	0.041025	0.006542
17	22050.38	0.563019	0.551724	0.586207	0.011294	0.023188
18	22112.17	0.566409	0.586207	0.62069	0.019797	0.05428
19	23389.15	0.635204	0.62069	0.655172	0.014514	0.019968
20	23953.57	0.664523	0.655172	0.689655	0.009351	0.025132
21	24484.68	0.691301	0.689655	0.724138	0.001646	0.032837
22	27060.3	0.806555	0.724138	0.758621	0.082417	0.047935
23	27085.88	0.807559	0.758621	0.793103	0.048939	0.014456
24	28184.43	0.847795	0.793103	0.827586	0.054692	0.020209
25	28219.74	0.848993	0.827586	0.862069	0.021407	0.013075
26	29053.32	0.875557	0.862069	0.896552	0.013488	0.020995
27	29515.95	0.888871	0.896552	0.931034	0.00768	0.042163
28	29599.59	0.891171	0.931034	0.965517	0.039864	0.074347
29	30325.13	0.909756	0.965517	1	0.055761	0.090244

Therefore, for the ACM, whose performance can be evaluated, consider the second method of preventive maintenance.

(1) *Interval of performance assessment*
According to Formula (16.12), the reliability function of the ACM is:

$$R(t) = 1 - F(t) = \mathrm{EXP}\left[-\left(\frac{t}{23330.65}\right)^{3.3471}\right] \tag{16.13}$$

Based on the experience of the Boeing company [3], the importance of ACM in air conditioning system and the reliability function of the ACM, the interval of ACM performance assessment is:

$$T_R = \beta[-\ln(0.9)]^{\frac{1}{z}}$$

Table 16.4 The unschedule removal **data** of ACM in 2013 (From January to June)

Serial number	TSN (Time since new)
1	11181.55
2	11266
3	11512.12
4	11710.47
5	12275.02
6	12391.4
7	30259.35
8	30755.85

So,the interval is:

$$T_R = 23330.65(-\ln 0.9)^{\frac{1}{3.3471}}$$

Namely: $T_R = 11910.67$

Considering the life of ACM is greatly affected by the environment of aircraft operations and the practice of Aircraft maintenance, so the interval can be reduced to 11,500 flight hours.

(2) *Performance assessment*

There are three main parts of the B737NG ACM, namely fan, compressor, and turbine. For the cooling parts of A/C system, its cooling performance mainly depends on heat taken away by the ram air (The law of conservation of energy). There are mainly three factors deciding the heat taken away by the ram air: the parameters of the ram air (relating to the fan performance, especially on the ground), the capability of the conversion from the gas energy to ACM rotational energy (the expansion capability of turbine), the temperature difference between the outlet of the primary exchanger, and the inlet of the secondary exchanger (compression capacity of compressor). And considering the operability of the aircraft maintenance, the ACM performance can be assessed by measuring the temperature of the gas circuit parameters involving the ACM.

So, combined with the reliability distribution function of the ACM, it is suggested that for 11,500 h, the temperature of the gas circuit parameters involving the ACM should be measured to assess the performance of the ACM.

(3) *The contrast by the fleet unschedule removal data*

Compared with the unschedule removal data in 2013 (From January to June) which is shown in Table 16.4, the times of the new ACM unschedule removal (whose TSN is more than 11,500 flight hours) is 7 times (the total removal times is 9), the times of the unschedule removal (whose TSN is more than 12,000 flight hours) is 6 times (the total removal times is 9). So interval of performance assessment set to 11,500 can catch the attenuation performance of ACM.

16.6 Summary

As an important part of B737NG A/C system, how to set a suitable interval of performance assessment, based on the unschedule removal data, is very important to the preventive maintenance. In the paper, based on Weibull distribution, the determined interval is set and compared with the unschedule removal data. It is found that this method has high consistency, and can be used as a good method of ACM performance assessment.

References

1. Jialin G, Jianyin G (2003) Estimation of the Weibull distribution parameters based on the censored data. J Harbin Univ Sci Technol 10(2):61–63
2. Yu Z, Jun Y, Xaobin M (2011) Data analysis of reliability. National Defence Industry Press, Washington, D.C
3. Hao W (2011) A Study on determining the maintenance task interval of civil aircraft system. Aircr Des 31(6):58–60

Chapter 17
Based on the Theory of a Certain Type of Black-Box Testing Electronic Equipment Within the Field of Research and Development Detector

Ying Zhu, Ping Zou, Jun-lie Wang and Jia-wei Chen

Abstract For a certain type of electronic equipment fault code is unknown, but the detection signal types and large quantities, transform complex relationships and other problems, the use of black-box testing methods proposed step test data format, content, and send and receive signals, analyzing stimulus and response characteristics of the signal, the timing method; using interrupt is triggered automatically in response to receiving and transmitting method to solve the fault code for bipolar continuous code difficult to decipher the puzzle.

Keywords Black-box testing electronic equipment

17.1 Introduction

An aircraft airborne electronic equipment through field testing to obtain electronic equipment failure information, real-time alarm, fault codes, and other data will be analyzed and stored up information processing to prepare the infield for system integrity of points off. But does not provide fault code development side, while the five detection signal cables are 55 lines, divided into the excitation signal and the response signal 16,419 signals (32 consecutive bipolar serial code), test, analyze workload high degree of difficulty. Based on black-box theory, cause and effect diagrams, orthogonal test method, test boundary method, touch your fault codes, developed within the field of the detector [1].

Y. Zhu (✉) · P. Zou · J. Wang · J. Chen
Beijing Aeronautical Technology Research Center, Beijing, China
e-mail: 790108430@qq.com; zhuying713272@126.com

J. Wang (ed.), *Proceedings of the First Symposium on Aviation Maintenance and Management-Volume I*, Lecture Notes in Electrical Engineering 296,
DOI: 10.1007/978-3-642-54236-7_17,

17.2 Black-Box Theory

Black-box testing, also known as functional testing, the purpose is to find software requirements or design specifications for errors. Program under test as a black box will not open the box, testers cannot see the code, only to see the functional description of the software or module. Black-box testing can be used to verify whether the software or module functions to be realized [2].

Visible, black box commonly used in software testing, but can also be the function or the hardware portion of the internal structure of the unknown as a black box is to handle, so that you can use a number of methods for hardware black-box testing.

17.2.1 Causal Diagram Method

Consider a variety of conditions suitable to describe the combination of multiple actions in the form of consequential to consider the design of test cases, which requires the use of cause and effect diagram (logic model). Cause and effect diagram method the resulting decision table which is suitable for checking various combinations of input conditions.

Determine the composition table

Conditions pile (Condition Stub): lists all conditions usually considered the conditions listed in the order does not matter. Action piles (Action Stub): lists the rules may take. These operations the order is not binding. Conditions of entry (Condition Entry): lists the values for the conditions in all possible cases of true and false values. Action Item (Action Entry): lists the various values of the conditional term situations should take action.

Rule: Any combination of specific values of a condition and the corresponding action to be performed in the determination table in the action item through the condition item and a row is a rule. Obviously, it is determined how many sets of conditions listed in the table value, also with how many rules and conditions of entry and action items both how many columns.

Establishing step determination table determines the number of rules, and if there are n conditions they have two values for each condition (0, 1), so it is 2n types of rules.

① All of the conditions listed in piles and piles action.
② Fill condition items.
③ Filled action items. Wait until the initial decision table.
④ Simplified merger similar rules (same action).

Bezier points out the use of decision tables designed to fit the conditions of the test case:

① Specification given in tabular form in order to determine, or easily converted into a determination table.
② Condition does not affect the order in which actions.
③ Whenever a rule has been met and to determine the action to perform after having tested other rules.
④ If a rule is met to perform multiple operations that the execution order is irrelevant.

17.2.2 Test Boundary Value Analysis

Not only attach importance to the input boundary conditions, but must also consider the output field boundaries.

(1) If the input conditions that the range of values is to be taken just reached the boundary values of this range and just beyond the boundary values of this range as the test input data.
(2) If the input condition specifies the number of values, then use the maximum number, the minimum number of less than the minimum number one, number one more than the maximum number as the test data.
(3) According to the conditions of each output specification, using the principle of a front.
(4) According to the conditions of each output specification, the application of the principles of the previous two.
(5) If the input field is given specification or output field is an ordered set, should select the set of the first element and the last element as a test case.
(6) If an internal data structure, then the internal data structure should be selected on the boundary value as the test cases.

17.2.3 Orthogonal Design Method

That has made good use of the orthogonal table to arrange the test data analysis and a method of a test object with the least the highest test coverage.

First, according to test requirements regarding functional requirements specification and performance indicators, define the appropriate test requirements report, which developed the highest standards of black-box testing, after all the testing work will be carried out around the test requirements, which meet the test requirements is qualified, on the contrary that is unqualified; while also appropriately selected test content and test resources.

The test plan formulation phase testing requirements decomposition, refinement into a number of executable test process, and for each of the testing process to select the appropriate test cases (test case selection is good or bad will directly affect the validity of test results).

17.3 Based on Black-Box Theory Test Fault Code

A certain type of electronic device via the external field test to provide fault code, infield tester reads out the code to be able to complete the whole performance testing, fault isolation; extension unit performance testing, functional testing, and fault isolation positioning. However, the code format is unknown. The infield tester signal types and large quantities, five signal cables are 55 lines, divided into the excitation signal and the response signal 16,419 signal (32 consecutive bipolar serial code), testing, analysis of work large, high degree of difficulty. 8 rounds/8,419 signals received large volumes of data, data formats, content and transform relations between the sending and receiving signals, etc., are all within the field of basic and critical examination; stimulus and response characteristics of the signal, the timing is within the field of inspection, etc., the foundation and key. To this end, the use of black-box testing methods to the user's perspective, from 8 rounds/8 closed 419 signal input data and output data, the excitation signal in response to correspondence between the starting signals for testing.

Established using the causal diagram method determination table, the condition of the electronic equipment are listed pile 45 all the excitation signal component, action may be taken pile list a predetermined switching operation, the control signals and instructions 16, the conditions for the normal breakdown and the value of a fault condition, the action items listed in the conditions of a variety of items ranging situations should take action.

Orthogonal test method, in accordance with the test requirements for fault location is based on the division of hardware units, for all test items in a certain order by the former (input) backward (Opposite the side) or from back to front carried out one after detection. If all are normal, normal instruction is issued when a project is not normal, the interrupt routine performance testing into the fault localization and diagnosis results are displayed. Therefore, the test data format, content, and send and receive signals, the excitation signal and the response signal of the characteristics, the timing; step interrupt trigger, automatic response is detected using an oscilloscope receive and transmit signal characteristics.

Boundary using the test method, select exactly equal to, greater than, or just less than just the value of the boundary (such as the response signal, the display signal) as the test data, rather than the typical equivalence class selected value or any value as the test data. So, point by point thrust reversers to solve the two categories (OM failures and HY fault) 45 fault code issues; identify 8 rounds eight received 419 signals, including one pair transceiver to complete and Electronic Equipment Directive receipt yards receiving and forming; another seven expansion in checking component, receives its bipolar continuous code evacuation OM component, the data processing and conversion, and then sent back to the HY components.

Testing performed by the unit testing, combinatorial testing, integration testing, system testing, and regression FBI steps, test the spirit of scientific personnel responsible attitude, step by step test to solve the fault code for bipolar continuous code difficult to decipher problem.

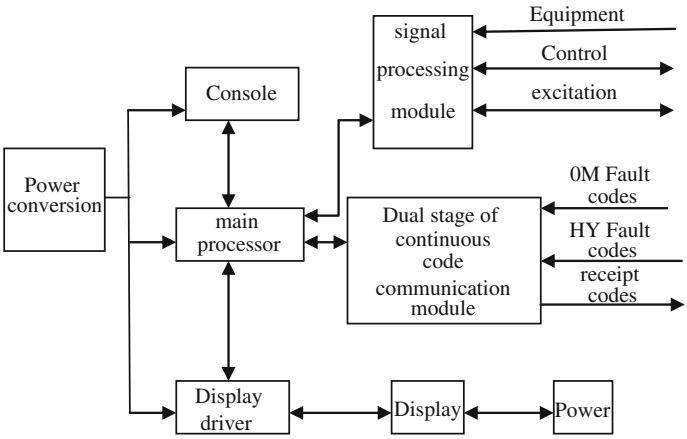

Fig. 17.1 Block diagram of field tester

17.4 Infield Inspection Instrument Design

Within the field inspection apparatus mainly by the power conversion circuit, the console, the main processor, the signal processing module, a bipolar continuous code communication module, a display driving circuit, a display and other components, shown in Fig. 17.1. Infield tester for fault identification is to rely on the signal processing module and communication module bipolar conducted continuous code. Especially in light of the state of bipolar continuous code can determine what failure. Seen from Fig. 17.1, through the "normal equipment" and "OM fault code," "HY fault code," etc., will be judged for the machine malfunctions and failures extension faults.

Infield tester and electronic equipment is connected via signal interface, signal interface testing resources of all input/output interface sockets, cables, etc., and the corresponding interface of the system under test linking the infield tester arranged on the console above various interfaces, mainly by the chassis, switches, lights, sockets, cables, and other components.

Infield tester receives directives issued electronic devices, according to the script of the input signal conversion and processing, and the formation of the excitation signal. In order to confirm the received command, the tester within the field code to the electronic device is formed receipt. A script is bipolar continuous 32 yards, with the address part (1–8), the information part (16–31 bits), parity bit (32), the free-bit (9–15 bits).

PC/104 super main processor module, complete the "bipolar continuous code communication module," "signal processing module," the control and data processing and display control.

Bipolar continuous code communication module using field-programmable FPGA chip as the core, with the corresponding peripheral circuit transmit and receive circuits.

Signal processing module mainly by: microcontroller, A/D, D/A and other components. Implement external interfaces, resulting in a variety of inspection equipment required for the excitation signal, and measuring the response signal from the device to the host computer reports the results.

Power conversion circuit mainly by: SMP-1151SB, SMP-1251SB, CW117, CW137, etc., to achieve the desired infield tester +5, +15,−15, +10, +5.6, +9, +3.4, −4.6,−5 V.

17.5 Conclusion

With the increasing complexity of aviation equipment, systems, test equipment systems affect aviation has become an important factor in good condition, and only fully tested in order to obtain highly reliable avionics systems [3]. To ensure the integrity of electronic countermeasures and attendance rates, developed within the field of electronic warfare detector operating voltage of the device can be determined, the azimuth channel's ability to work, and check the "audio" signal formation can check components within the system under test work to meet the related models of electronic warfare machine testing and routine testing missions.

References

1. Cai H-X, Wang C (2011) Fields, Field testing electronic equipment technical methods research. Measur control technol 30:100–106 (in Chinese)
2. Xiang R (2009) Explore the black-box testing methods. Softw Tribune 8:33–34 (in Chinese)
3. Shu T-X (2001) Automatic test technology development discussion. Astronaut Metrol Measur Technol 21:46–50 (in Chinese)

Chapter 18
Life Consumption Comparison Between Endurance Test Case and Field Service Case for a Type of Aeroengine

Yongqi Wang, Haibing Zhang, Shenhui Zhang, Tao Qin and Zhide Yu

Abstract The second HP turbine rotor blade and disk are the key components of a type of aeroengine, for comparing the value of life consumption of the type of aeroengine in endurance test case with field service case, used finite element method to analyze the simulative steady temperature field and stress field of the second HP turbine rotor blade and disk. Based on the fatigue analysis theory of EGD-3 and damage cumulative theory, evaluated the fatigue damage of access points after analyzing the flight parameters and data in endurance test. The endurance damage of blade and disk were achieved by the method of interpolation and Larson-Miller formula. Based on the principle of equivalent damage, compared the damage degree in endurance test case with field service case, the life consumption value in endurance test amount to 1.642 as much as in field service in the same time.

Keywords Aeroengine · Life consumption · Comparison · Endurance test · Turbine blade · Turbine disk

Y. Wang (✉)
Postgraduate Managing Brigade of Naval Aeronautical Engineering Institute, Qingdao 266041 Shandong, China
e-mail: wangchengguo2011@126.com

H. Zhang
Qingdao Campus of Naval Aeronautical Engineering Institute, Qingdao 266041 Shandong, China

S. Zhang
NO. 92514 Troops, Yantai 264002 Shandong, China

T. Qin
NO. 91379 Troops, Laiyang 265200 Shandong, China

Z. Yu
Shandong Vocational College of Science and Technology, Weifang 261053 Shandong, China

J. Wang (ed.), *Proceedings of the First Symposium on Aviation Maintenance and Management-Volume I*, Lecture Notes in Electrical Engineering 296,
DOI: 10.1007/978-3-642-54236-7_18,

18.1 Introduction

After completing the endurance test, both the whole aeroengine and its major components have residual life for a certain type of aeroengine. To continue the use of the aeroengine, we need to determine the life consumption of the whole aeroengine and its major components, provide the life consumption basis for the continued use, and life management after delivered to the units. Because the load case of the endurance test is quite different from the field service case, we need to compare the life consumption value in the two cases. The life consumption should be calculated based on the aeroengine load spectrum of endurance test, and should be converted to the field service condition to achieve the life control and management after the engine was delivered of use units.

The second HP turbine rotor blades and disks are the key and important parts of the engine, this article studied the equivalent conversion of life consumption from endurance test to the field service based on engineering need.

18.2 The Analysis of Flight Load Spectrum and Lasting Test Load Spectrum

18.2.1 The Analysis of Flight Load Spectrum

Flight data records 473 sets of engine data. Each set of data records the usage of two engines which belong to the same aircraft, the two engines have the same flight altitude and mach number. In the life assessment process, only the heat load and the centrifugal force were considered, other loads were not considered. The permanent damage of the turbine rotor blades and disk was considered, which was related to gas temperature, speed, time, etc. So the relevant time matrix of turbine speed and turbine gas temperature was added up. The rain flow counting method was used to add up these parameters, the arrays of the duty cycle and parameter assignment were shown in Tables 18.1 and 18.2.

18.2.2 The Statistical Analysis of Endurance Test Spectrum

Only the matrix of considering adjustment test was listed for space reason, as shown in Tables 18.3 and 18.4.

Table 18.1 Array of rotate speed cycle based on flight parameter statistic (%)

Speed valley	Speed apex					
	95 above	90–95	80–90	70–80	60–70	60 below
90 above	74	0	0	0	0	0
80–90	1255	2505	1358	0	0	0
70–80	269	307	1075	10	0	0
60–70	47	52	146	112	17	0
50–60	924	26	202	1292	360	81
40–50	34	4	11	4	0	0
below 40	969	5	9	1	0	12

Table 18.2 Time correlative array of rotate speed (%)/exhaust temperature (°C) based on flight parameter statistic

Rotate speed	Exhaust temperature					
	750 above	700–750	650–700	600–650	550–600	500–550
95 above	192	28005	55900	18099	1740	1131
90–95	17	2060	25025	114875	137078	78457
85–90	–	354	3028	41012	522323	2186775
80–85	–	69	1902	3073	7284	187812
70–80	–	11	2380	3264	1698	21073
60–70	–	5	724	4174	2332	7346
50–60	–	20	177	5268	23392	120113
40–50	–	–	–	4	122	892
30–40	–	–	–	–	13	187
below 30	–	–	41	8	537	640

Table 18.3 Array of rotate speed cycle based on 150 h test data (%)

Speed valley	Speed apex					
	95 above	90–95	80–90	70–80	60–70	60 below
90 above	0	0	0	0	0	0
80–90	4	2	0	0	0	0
70–80	0	1	3	0	0	0
60–70	0	0	0	0	1	0
50–60	4	3	2	3	1	0
40–50	0	0	0	1	0	1
below 40	15	1	4	5	1	68

Table 18.4 Time correlative array of rotate speed (%)/exhaust temperature (°C) of endurance test

Rotate speed	Exhaust temperature							
	700–750	650–700	600–650	550–600	500–550	450–500	400–450	400
95 above	1	5245	542	1	–	–	–	–
90–95	–	193	856	1634	14	–	–	–
85–90	–	–	28	1064	770	286	–	–
80–85	–	–	–	69	684	1004	–	–
70–80	–	2	21	116	2486	2250	1	–
60–70	–	2	35	97	357	562	8	–
50–60	–	–	48	1960	12958	2400	17	–
40–50	2	3	150	436	195	34	58	5
30–40	–	–	8	42	102	167	210	564
below 30	–	–	–	–	–	11	72	4327

18.3 The Analysis of Flight Load Spectrum and Endurance Test Load Spectrum

According to above calculations, using the Patran/Nastran software to construct the finite element model of blade and disk and analyze the temperature field and stress field confirmed the damage analysis points of blade and disk based on the calculation results.

18.3.1 The Temperature Field Analysis of Turbine Rotor Blades and Disk

The blade temperature distribution law is similar in typical exhaust temperatures [1–3]. Only the calculation result in the design state is listed below for the space reason, as shown in Fig. 18.1. The left is the view of blade basin direction, and the right is the view of blade back direction. Figure 18.2 is the temperature field of the second high-pressure turbine disk in design state.

18.3.2 The Stress Field Analysis of Turbine Rotor Blade and Disk

See from Refs. [2–4], to simplify the analysis, the strength analysis of the second high-pressure turbine rotor blade only considering the centrifugal loads; the strength calculation of disk considering the centrifugal load and temperature load.

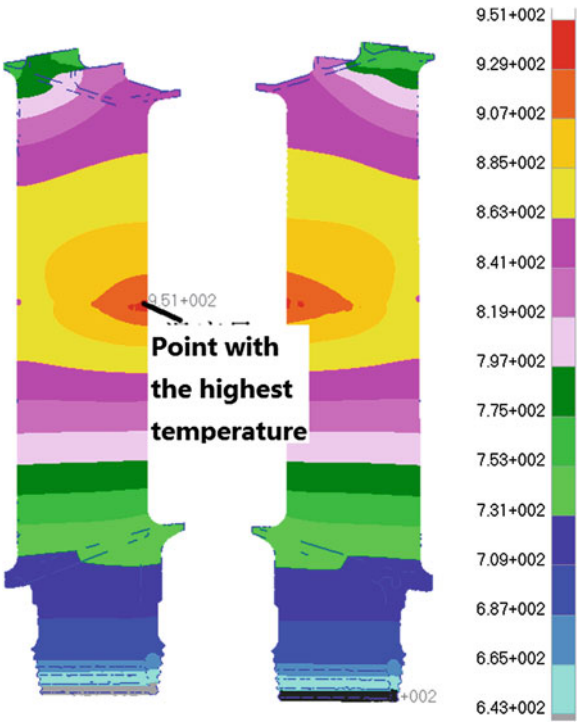

Fig. 18.1 Temperature field of second HP turbine blade

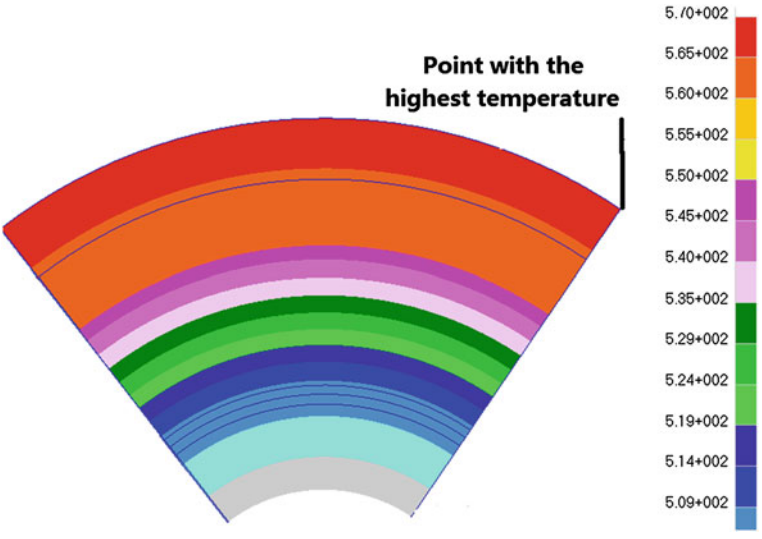

Fig. 18.2 Temperature field of second HP turbine disk

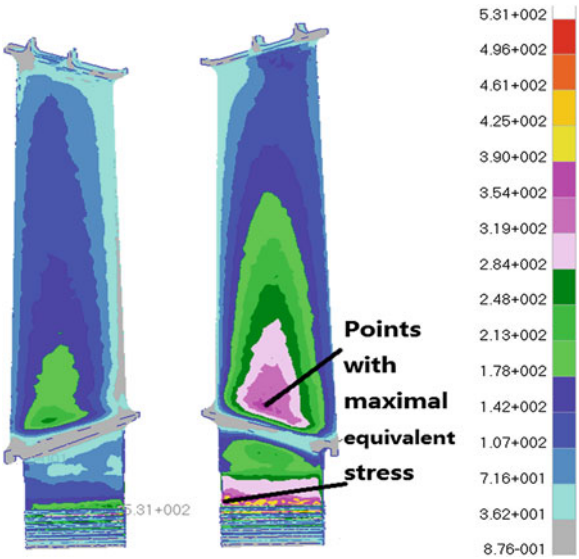

Fig. 18.3 Von Mises stress field of second HP turbine blade in the design state

After determining the displacement boundary conditions, the Von Mises equivalent stress fields of each typical rotate speed was calculated, only contours of 90 % rotate speed was listed for space reason, as shown in Fig. 18.3. The left is the view of blade basin direction, and the right is the view of blade back direction.

The thermoelastic stress of the second high-pressure turbine disk in each typical rotate speed and corresponding exhaust temperature was calculated. Only the calculation result in design state was listed for space reason, as shown in Fig. 18.4.

From the calculation results, we can conclude that the maximal thermoelastic radial stress and maximal equivalent stress of the second high-pressure turbine disk in each state all appeared in the 1/4 webs.

18.3.3 The Selection of Damage Analysis Assessment Point of Blade and Disk

According to EGD-3 stress criteria [6] and the above analysis of temperature field and stress field, select the following three points as the blade damage assessment points: point 1, whose temperature is the highest in blade, is located in the central section of blade body at the intake side; point 2, whose equivalent stress is the highest, is located in the extension root back approaching the tenon at the intake side; point 3, where exists a certain degree of stress concentration and the temperature is higher, is located in the fillet where extension root connect the inframarginal.

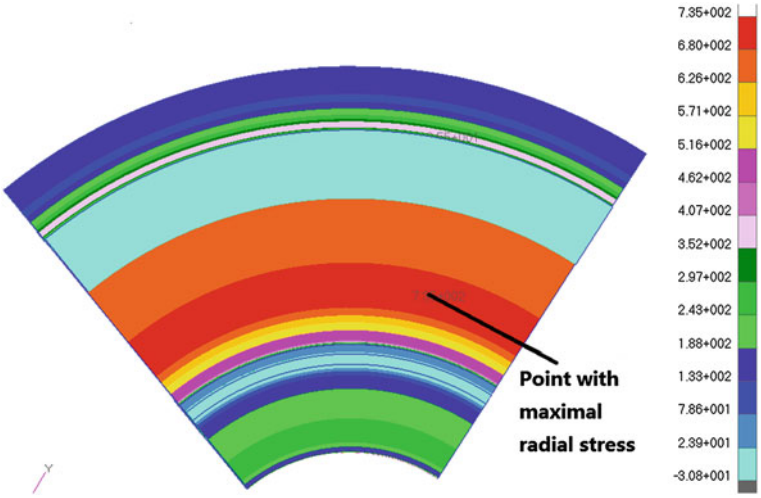

Fig. 18.4 Thermoelastic stress distribution of second HP turbine disk in the design state

Table 18.5 The basic information of blade damage access points

	Point 1 (MPa)	Point 2 (MPa)	Point 3 (MPa)
Stress value at the speed of 100 % Nh	176.36	656.47	481.13

Table 18.6 The basic information of turbine disk damage access points

	Point 1 (MPa)	Point 2 (MPa)	Point 3 (MPa)
Stress value at the speed of 100 % Nh	644	670	724

The basic information of the three access points are shown in Table 18.5.

According to finite element results, the second high-pressure turbine disk is still in elastic zone in each working state. Select the point in the 1/4 webs of the second high-pressure turbine disk as one of the damage assessment points, where the thermoelastic radial stress is the highest. Select the point along the radial direction at the first rabbet whose equivalent stress is maximal and the point at the second rabbet whose tensile stress is maximal. So that the second high-pressure turbine disk has three damage assessment points, as shown in Table 18.6.

18.4 Damage Analysis of Turbine Rotor Blades and Disk

18.4.1 Convert S-N Curve of Material into the S-N Curve of Structure

The S-N curve of the material is generally obtained by fatigue test, but in case of lacking experimental data, the EGD-3 method was used as simplified method to obtain a fatigue life curve of symmetrical cycle (S-N curve). The EGD-3 method use Goodman map to consider the effect of mean stress. We can take a safety factor (fatigue safety factor) [5, 6] for getting safety fatigue life (fatigue strength). This paper selects 1.15 as fatigue reserve factor [7].

18.4.2 Calculate the Damage of Each Cycle

By the finite element analysis results, all the stress values of damage assessment point were in the elastic range, the stress value is proportional to the rotate speed, as long as the calculated damage analysis evaluation point in the stress at 100 % Nh obtained in a single speed cycle corresponds to the stress cycle, and then gets the mean stress and stress amplitude of the cycle, then uses the Goodman curve anti-interpolation to get the corresponding number of cycles. Linear cumulative damage theory, Miner theory, each cycle fatigue damage is converted into the standard cycle of damage and calculate the linear cumulative damage value.

18.4.3 Calculate Endurance Damage

For the disk, the material data provided Larsen—Miller (L-M) for calculating persistent life:

$$\lg t = b_0 + b_1/T + b_2 x/T + b_3 x^2/T + b_4 x^3/T \tag{18.1}$$

Take the stress and temperature value of assessment points into the above formula, we can get the persistent life Tci in the stress level.

By fitting data can get the endurance strength—life formula for blade:

$$\lg s = a + b\lg T \tag{18.2}$$

In the formula, S is endurance strength (Mpa), T is life (h), a and b are constant which related to temperature.

18.4.4 The Calculation of Fatigue/Endurance Damage of Blade and Disk

According to the Miner theory [8], adding fatigue damage of time-independent D_f and endurance damage of time-related D_c can get the blade damage D:

$$D = D_f + D_c \tag{18.3}$$

If there is no fatigue/endurance interaction, the life depleted when D value closed to 1; when deviated from 1, it indicates the existence of fatigue/lasting interaction.

18.5 The Life Consumption Comparison Between Endurance Test Field Service

According to the above calculations, based on the principle of damage equivalence, established the conversion of life consumption from endurance test to outward field for turbine components which is shown in Table 18.7.

18.5.1 Equivalent Conversion of Life Consumption for Blade

The maximal damage value of blade is 0.154 in endurance test; the maximal damage value is 1.5455 in the flight load spectrum. The damage of endurance test is equivalent to 9.97 % of actual damage of the field service, the equivalent use time is 144.19 h.

18.5.2 Equivalent Conversion of Life Consumption for Disk

Using the same method with blade, we can get the equivalent use time T4 is 246.37 h.

According to the above calculation, the conversion of life consumption from endurance test to field service should be based on the second HP turbine disk for safe reason, the conversion ratio is 1.642.

Table 18.7 Comparison of damage under two load spectrums

	Access point	Fatigue damage	Endurance damage	Total damage	The ratio of fatigue damage (%)	The ratio of endurance damage (%)
Flying load spectrum						
Blade	1	0.0026	0.21	0.2126	1.21	98.79
	2	1.5111	0.0344	1.5455	97.77	2.33
	3	0.1661	0.0778	0.2439	68.11	31.89
Turbine disk	1	0.2957	0.0019	0.2976	99.37	0.63
	2	0.6037	0.0858	0.6895	87.558	12.442
	3	0.3645	0.0308	0.3953	92.2	7.8
Endurance test spectrum						
Blade	1	2.61e-4	0.1539	0.1541	0.17	99.83
	2	0.1138	0.0313	0.1451	78.44	31.56
	3	0.0067	0.0751	0.0818	8.25	91.75
Turbine disk	1	0.0338	0.0011	0.0348	96.96	3.04
	2	0.0639	0.0536	0.1175	54.42	45.58
	3	0.0403	0.0206	0.0609	66.176	33.824

18.6 Conclusions and Recommendations

(1) Based on the temperature field, stress field, and contact stress analysis results, determine the life assessment points of blade and the disk, use Miner cumulative damage theory to analyze fatigue and persistent damage. The calculations show that the low-cycle fatigue damage is the major factor in the flight load spectrum for the second high-pressure blade and disk, the endurance damage has lower percentage; the percentage of endurance damage in endurance test increased significantly, the fatigue damage and endurance damage are almost same.

(2) Compared with the life consumption value between endurance test case and field service case in accordance with the principle of equivalent damage. When translate the engine life consumption of endurance test to actual service life consumption we should consider adjusting test, where the conversion rate is 1.642.

Acknowledgments The research work was supported by Innovation Foundation Project of Naval Aeronautical Engineering Institute for Doctoral Student under Grant No. 2013111014.

References

1. Su Q-Y (2004) Manual of determining life for main parts of aero turbojet and turbofan engine (in Chinese). Aviation Industry Press, Beijing, pp 225–226

2. Melis ME, Zaretsky EV (1999) Probabilistic analysis of aircraft gas turbine disk life and reliability. J Propul Power 15:658–666
3. Zhao X (2005) Strength analysis and life prediction of a turboprop gas turbine rotor (in Chinese). Nanjing University of Aeronautics and Astronautics Press, Nanjing, pp 41–45
4. Fu N (2006) Turbine disc and blade's strength analysis (in Chinese). Northwestern Polytechnical University Press, Xi'an, pp 36–39
5. Song Z-H (1987) Research on engine life (in Chinese). Aviation Industry Press, Beijing, pp 81–85
6. Rolls-Royce LTD (1979) Stresses standard of spey MK-202 (in Chinese). International Aviation Editorial Department, pp 146–150
7. Xu K-J, Ye X-N (2006) Study on assessment method of comprehensive flight conversion ration for aeroengine (in Chinese). J Propul Technol 27:25–27
8. Song Z-H (1988) Strength design of aero gas turbine engine (in Chinese). Aviation Institute Press, Beijing, pp 5–30

Chapter 19
Blades Grinding Technology in the Installed State for Aeroengine

Yong Sun, Pingya Cao and Naigang Liu

Abstract Compressor rotor blade is one of the key components of aeroengine. Fan blades and compressor blades rotate at high speed when engine works. They used to be damaged by foreign objects. This paper studies how to grind blades with the use of video endoscopy and grinding devices in the installed state. The study aims to reduce maintenance costs and improve maintenance efficiency, thus improving the maintainability of the aeroengine.

Keywords Blade · FOD · Grind · Installed state · Aeroengine maintainability · Video endoscopy technique · Foreign object damage tolerance design

19.1 Introduction

During aircraft takeoff, landing, or low-altitude flight, objects such as sand, stones, flying birds, metal debris, and ice cubes are easily ingested into the airflow course, thus damaging engine fans or compressor blades. This kind of damage is called Foreign Object Damage (FOD).

Since jet engines were put into service, Frequent FOD problems have brought about huge damage. The severe FOD incidents may have resulted in the immediate breakup of a blade or fracture failure of a blade in a very short time due to the serious declining of carrying capacity caused by FOD. Worse still, the fallen blade debris may possibly impact the other blades or the engine casing, thus causing a succession of damage or even uncontained blade accident which is rated as serious flight accident.

Y. Sun (✉) · P. Cao · N. Liu
AVIC Shenyang Liming Aero-engine (Group) Corporation Limited, Shenyang 110043, China
e-mail: sunyong701219@163.com

J. Wang (ed.), *Proceedings of the First Symposium on Aviation Maintenance and Management-Volume I*, Lecture Notes in Electrical Engineering 296,
DOI: 10.1007/978-3-642-54236-7_19,

Fig. 19.1 Blades damage

As the millimeter-deep notch as shown in Fig. 19.1, most FODs are not very severe. It does not matter much to ignore the notch initially. But after some time, the crack initiation and development and the subsequent fracture failure under the action of loadings may possibly lead to aircraft accidents if nothing is done to the FOD or the FOD has not been found out even after checking.

Therefore, it is of great significance to timely discover and repair the blades badly damaged by FODs. Usually, the damaged blades have to be replaced at a high cost and the maintenance is time-consuming. One way to bring down the high cost generated by the shortened engine life cycle and to cut down the maintenance time is to apply grinding technology to the FODs within the tolerant range in the installed state.

19.2 Blade Damage Tolerance Technology

In the early 1990s, Requirements were made for FOD tolerance design in the American MIL-E-5007D (1973), i.e., FOD tolerance design is equivalent to withstand to a notch with a stress concentration factor (K_t) not exceeding 3.0 at the most critical locations of flow path components. Similar requirements were put forward in DEF STAN 00-970 PART 11 ENGINES by the British Ministry of Defense in January, 2006.

According to aircraft engine design specifications and standards, the development of FOD tolerance design criteria is divided into three phases: initially FOD-related failures were mainly regarded as prevention and maintenance problems; later FOD tolerance design was equivalent to withstand to a notch with a stress concentration factor (K_t) not exceeding 3.0 at the most critical locations of flow path components; and at present the more scientific probabilistic design criteria prevails.

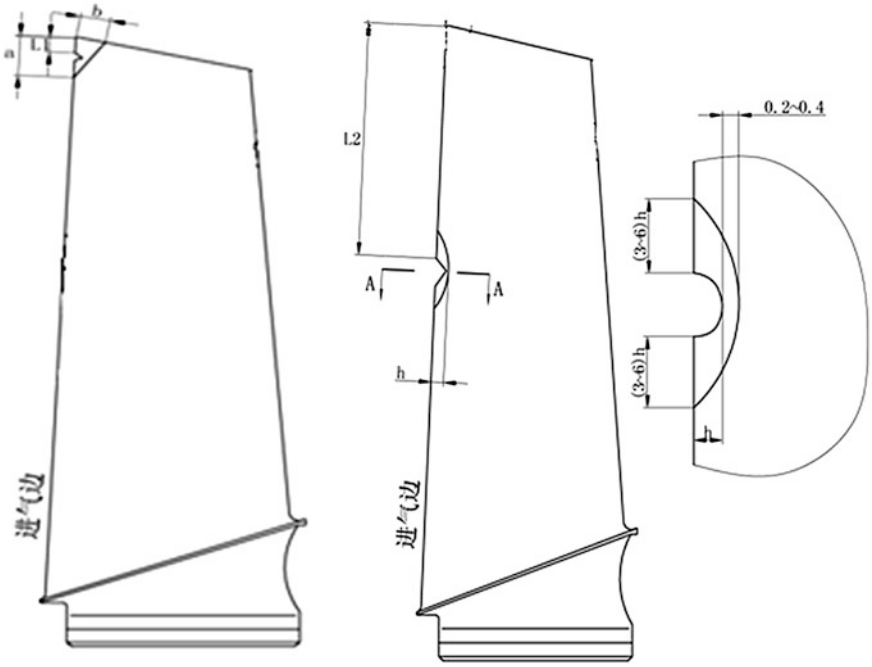

Fig. 19.2 Diagram of a compressor blade damage

The FOD probabilistic design criteria are, on one hand, based on the fact that the impact of a FOD on the blade strength and the ultimate crack growth corresponds with the randomness of FOD occurrences. On the other hand, the criteria are built on substantial experimental and analytical data about the impact of real FOD on the blade strength and the ultimate crack growth, thus making the formulation of more scientific scrapping standard and maintenance criteria possible.

The aircraft engine design specifications and standards in China are GJB241A-2010 and GJB242-87, which adopt the criteria of the American MIL-E-5007D in terms of FOD tolerance design. At Present, it is evident that FOD tolerance design in China is stepping further with multiple models of engines developed and fielded. Figure 19.2 and Table 19.1 indicate the damage tolerance standard of a certain Piece of blade of a certain aeroengine.

19.3 The In situ Testing Technology Applied to Blades FOD

The so-called "in situ" refers to an engine that has not been moved or decomposed from its original place of deposition. Similar to applying gastroscopy to patients, field technicians make on-equipment testing to the damaged blades with the

Table 19.1 The FOD tolerance blade of a certain aeroengine

Blade edge	The range and size of damage tolerance allowing no finishing		The range and size of damage tolerance allowing finishing	
	The distance to the blade tip L (mm)	Damage severity no more than h (mm)	The distance to the blade tip L (mm)	Damage severity no more than h (mm)
Air inflow side	0–15	0.3	0–40	4.0
	15–110	0.1	40–250	2.0
	110–265	0.2		
	The distance to the blade root 10	0.1		
	0–25	0.5	0–25	4.0
	25–85	0.1	25–210	2.0
	85–215	0.2		
	The distance to the blade root 10	0.1		

Fig. 19.3 Industrial video endoscopic equipment

industrial video endoscopic equipment. The flexible fiber released by the video endoscopic equipment (Fig. 19.3) is passed over the observing window of an engine case. Quick and gentle manipulation under vision guides the fiber into the flow path and is gradually advanced down the designated position for testing and measurement.

Presently, quite a number of manufacturers home and abroad are able to provide video endoscopic equipments which make it possible to check on the interior of the engine with ease. For instance, through the observing window of the engine

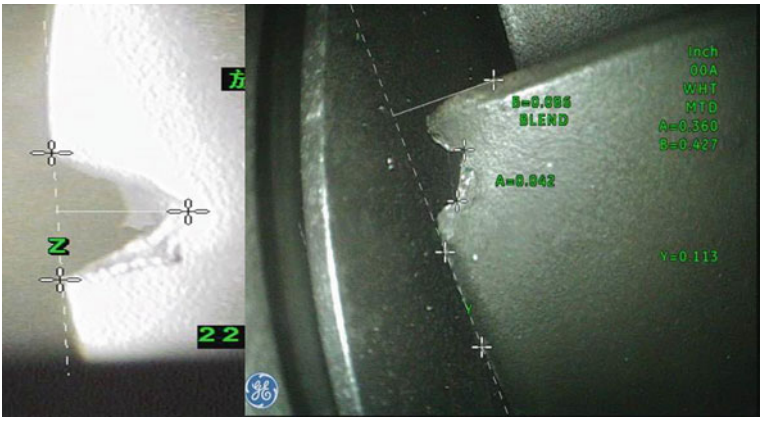

Fig. 19.4 Measurement of engine damage

stator case, the side view lens can be used to examine and measure one rotor blade at a time, and by spinning the engine, all blades of a certain grade can be finally detected. Accurate measurement can be made in the following ways:

19.3.1 Laser Measurement

The advantages of laser measurement lie in its simplified operation since there is no need to replace the lens of the video endoscopic equipment, and no need to use split screen or complicated aiming device. At Present, German WOLF Company is the only supplier of this technology reaching precision sensitivity over 0.1 mm, which meets the accuracy requirement of blade damage measurement specified by aeroengine technology specifications.

19.3.2 Shadow Measurement

Based on the theories of shadow projection and triangular geometry, shadow measurement technique (Everest VIT) is made possible by means of probes casting shadows. The measuring accuracy is closely related to the amplification factor. The accuracy level can reach as much as 0.1 mm when endoscopic lens is amplified by 5 times or more. The only defect is that lens replacement is needed for accurate measurement (Fig. 19.4).

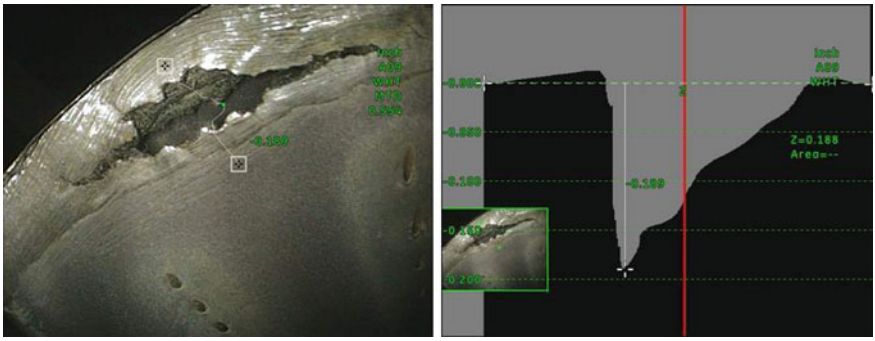

Fig. 19.5 Three-dimensional phase scanning measurement

19.3.3 Double Objective Lens Measurement

Double objective lens measurement excels in making the observation of the interior parts of an engine easier because the video endoscopic equipment can extend the range of visibility and change the direction of sight line. To gain a wider range of visibility within the limited aperture, the use of wide angle objective lens with large visual field is made necessary, thus causing optical distortion (barrel distortion) in the endoscopic image. Evidently, the operators of video endoscopic equipment must be expert in aeroengine professional knowledge and be well-informed of the blade shape they are going to observe. The accuracy level can reach as much as 0.1 mm, but frequent lens replacement is needed for accurate measurement.

19.3.4 Three-Dimensional Phase Scanning Measurement

By means of the three-dimensional phase scanning measurement (Everest VIT), phase Scanning is done to the detected area on the basis of phase shift; as a result, the three-dimensional model of the detected object is established. Three-dimensional phase scanning measurement is recognized as a milestone of visual testing. Though there is a hard time aiming well while employing this technique, the accuracy level can reach as much as 0.1 mm, and there is no need to replace lens when testing (Fig. 19.5).

Without exception, the techniques above can reach an accuracy level of 0.1 mm or more. The measuring error can be limited within 5 %. Therefore, it is evident that all the measurement techniques above-mentioned can be employed to meet the measuring requirement of engine blades damage, thus laying foundation for performing maintenance according to the specific damage tolerance.

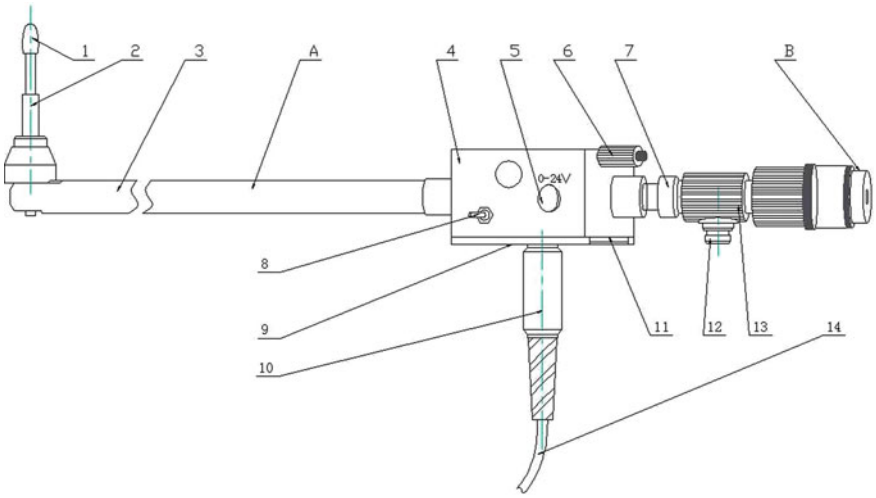

Fig. 19.6 Basic structure of the endoscopic in situ remediation device. *1* Grinding head, *2* Special adapter, *3* Shell, *4* Casing, *5* Variable speed knob, *6* Angle adjustment knob, *7* Lock necklet, *8* Switch, *9* Set screw, *10* Handle (built-in motor), *11* Set sliding rail, *12* Light guide connector, *13* Eyepiece focusing knob, *14* Power line, *A* Feeler lever, *B* Eyepiece

19.4 In situ Remediation of Compressor Blade Under the Damage Tolerance

19.4.1 Device Selection

In terms of the rotor blade of the fan-type grade within reach, manual repair or repair by power-driven files is strongly recommended. In terms of the blades of the other grades which are out of reach manually, adequate devices have to be selected. For instance, a wise choice is the endoscopic equipment manufactured by German WOLF Company. Like minimally invasive surgery, the grinding head of the endoscopic equipment is passed over the observing window into the flow path; thereby repair is made on the damaged compressor blade with the engine in the installed state.

As shown in Fig. 19.6, the structure of the endoscopic repair device is similar to the conventional optical endoscope. An axle is fixed within the path of the endoscope; the angle of the grinding head can be adjusted (0–90°); the motor-driven grinding head can rotate at a speed of several thousand revolutions per minute (0–5000 RPM); grinding heads of diversified shapes and accuracies are provided; surface roughness after repair lives up to the blade roughness specifications.

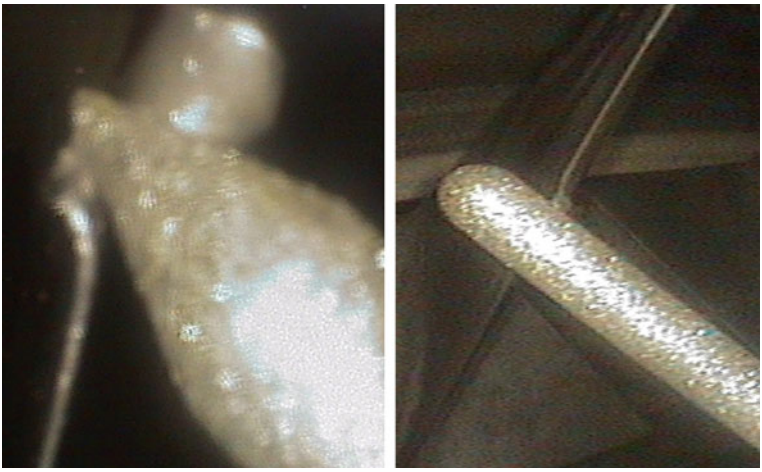

Fig. 19.7 The engine blade repair course in the installed state

19.4.2 Engine Blade Repair Course

The size of the damaged blade is identified by means of the industrial video endoscopic equipment; and the remediation size is determined according to the technical requirement of damage tolerance.

The endoscopic in situ remediation devices are put in place and the grinding head of adequate size and shape is selected according to the location of the blade damage.

With the angles of the grinding head and feeler lever adjusted to about zero, the grinding head of the endoscopic equipment is passed over the observing window into the engine flow path.

Having reached the location needing repair, the grinding head is kept perpendicular to feeler lever and aiming at the damaged area (Fig. 19.6). Dynamic tool setting and grinding are performed initially as a trial to the damaged area at a lower rotational speed. Make sure the position of the grinding head is appropriate in no touch with the other parts of the blade. With everything in place, grinding can be adjusted to the normal rotational speed (Fig. 19.7).

In accordance with the repair size requirement, the damaged blade is repaired to the right size. The next step is to polish surface with appropriate polishing head. Finally, the repaired size should be confirmed by the video endoscopic equipment to meet the technical requirements.

The whole course of grinding and polishing can be observed and monitored by means of the WOLF high-definition optical system or the endoscopic video equipment.

Fig. 19.8 Grinding head

19.4.3 Points for Attention

As the Endoscopic blade Remediation Device is a rigid design, the operator can apply force directly to the damaged blade and has a first-hand experience about the polishing process. Therefore, the operator should watch closely the fastening of grinding head and see that nothing is left over in the engine.
Grinding heads of various lengths should be selected such as the grinding head of pyramid shape, domed shape, and other special shape. The polishing head of cone shape and ball shape, and other special shape are also provided (Fig. 19.8).
Because of the small grinding size and the limit of the feed rate, the grinding must be accompanied with measuring from time to time. Exceeding tolerated remediation limitation is strictly prohibited.
Because of the narrow gap between the aeroengine blade and the casing, cone-shaped grinding head should be applied to the blade tip which is close to the air inflow side or outflow side (Fig. 19.6), thus avoiding the damage on the engine case while dome-shaped grinding head is applicable to the other parts of the blade.
The wide-chord blade cannot be reached even by long grinding head; so the lengthened grinding head should be used and rotational speed should be well-controlled. Feeler lever 8 mm long or more should be used to reduce the vibration caused by the lengthened grinding head.

19.5 Conclusion

The industrial video endoscopic equipment serves as an advanced assistance in fulfilling the task of testing and measuring blade damage in the installed state. Based on the damage tolerance, the equipment ascertains a remediation method

and the repairing process is formulated according to the specific situation of the blade damage. Then with the adequate type of endoscopic remediation device selected, the in situ remediation of the compressor blade is finally completed. Characterized by high efficiency, the application of the in situ remediation technique guarantees high serviceability rate and improved engine maintainability. In addition, maintenance efficiency is improved and maintenance cost is reduced.

Chapter 20
Design and Realization of General Purpose In Situ Radio Set Testing System

Qi-Dong Xu and Tao Jia

Abstract Against the problems, such as function fewness, poor versatility, stable testing frequency, and so on, of existing communications testing equipment, this article addresses the design thought and realization method of a general-purpose in situ radio set testing system. The system can implement in situ performances testing of various radio sets to solve the rapid maintenance issue in outside field.

Keywords Radio set · In situ testing · Rapid maintenance

20.1 Introduction

An airborne radio set is a main equipment to communicate in voice or data of an aviation vehicle. Its performance to complete tasks is very important. Nowadays, in outside field, the usual resolution to assess its function is performing a communication between a ground station and an airborne set [1]. That may not test the performance of the radio set, also may cause channel occupying and information leading. Furthermore, earlier test equipments have less testing functions, stable testing frequencies and poor versatility, and it only can monitor discrete signals not radio frequency (RF) signals. The general purpose in situ testing system can rapidly and accurately test main performances of radios without occupying other channels and leaking radio spectrum information. By this way, the problem of how to maintain airborne radio in an overall, rapid, and secure way in outside field is solved.

Q.-D. Xu (✉) · T. Jia
The Aeronautic Electronic Engineering Department, The First Aeronautic Institute of the Air Force, Xinyang, Henan, China
e-mail: sherilljames@163.com

T. Jia
e-mail: viewpoint08@163.com

J. Wang (ed.), *Proceedings of the First Symposium on Aviation Maintenance and Management-Volume I*, Lecture Notes in Electrical Engineering 296,
DOI: 10.1007/978-3-642-54236-7_20,

Based on the original intension, in an outside field, the testing system can examine the performances of various radios in situ. The system may examine the performance of the whole system by testing the emitting power of the antenna quantitatively at fixed frequency points, and give a conclusion about operation status of radio acquired by its main performance rapidly self testing, and provide frequency hopping (FH) signal source to satisfy the requirements of HF anti-jamming radio test, and have menu operating interface to perform indicate operating process and results dynamically, and store, printed and access testing data automatically. It also provides a RS232 interface to edit the parameters.

20.1.1 Airborne Communication System Whole Performance Test

A quantitative examination method is applied to test whole performance by the in situ radio set testing system [2]. First, fix the testing system in a specific position opposite to an antenna of a communication system. Then, at a fixed frequency point, the testing system receives power emitted from the communication system, and responds to the communication system automatically until the power is reached a critical value. At the same time, a voice that "communication system is normal" may be heard by the earphone of this communication system, which means the system is normal.

20.1.2 Radio Set Performance Automatic Test

The testing system may include signal excitation, response signal analysis, and measurement and status control. So, the system can examine a radio's performance connecting by a testing cable. An operator can select the type of the radio and start examination through menu, and the system can perform it and indicate results automatically.

20.1.3 Design Thoughts

Considering the requirements, software radio thought is applied to the in situ testing system. Applying digital signal processing (DSP), field programmable gate array (FPGA) and synthesis indication technologies, contribute a universal, flexible, and popular used aviation radio synthesis testing system to realize in situ examination and contract maintenance consuming time. The block diagram of this system is shown on Fig. 20.1.

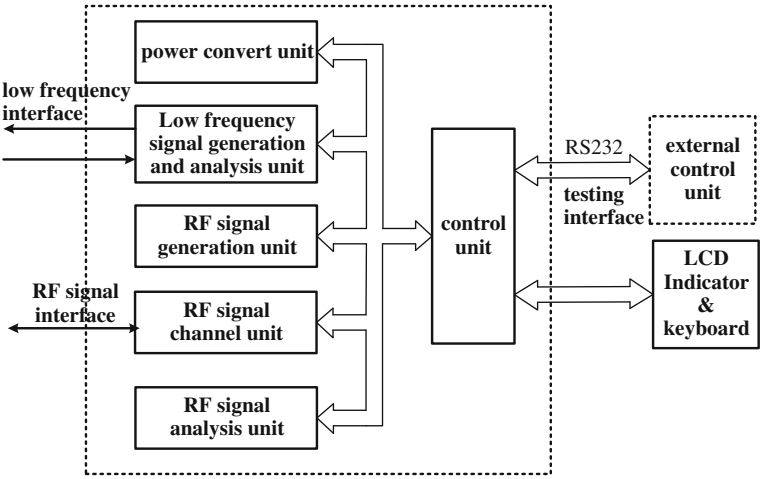

Fig. 20.1 Aviation communication test system block diagram

The aviation communication system is composed of six units. They are power management unit, low frequency signal generation and analysis unit, RF signal generation unit, RF channel unit, and RF signal analysis unit. There are four interfaces designed for test. The low frequency and RF signal interfaces can provide low frequency signal and RF signal. The testing interface is connected to an external control unit by RS232 bus. The LCD indicator can show a menu. By this menu and keyboard an operator can select functions, and commands are acquired and disposed by the control unit. When a test procedure is finished, test results are shown on this indicator.

20.2 Hardware Design

20.2.1 Power Conversion Unit

The power management unit is to convert input power into different powers to other units. There are two input power sources, external power adaptor and internal lithium battery. In normal condition, the external source is to provide 12 V and internal one outputs 7.2 V. The internal source might be used only if there is no external source applied. And, the internal source can be charged by external power and measured by voltammeter to record its left quantity of electricity (Fig. 20.2).

When the power-on button on the keyboard is pressed, a power-on signal is generated and the elementary regulator is on. Then, the power source, either internal or external, is converted into 8.4 V. After the secondary regulator, positive and negative 5, 3.3 V, and analog 5 V are generated and outputted to other units.

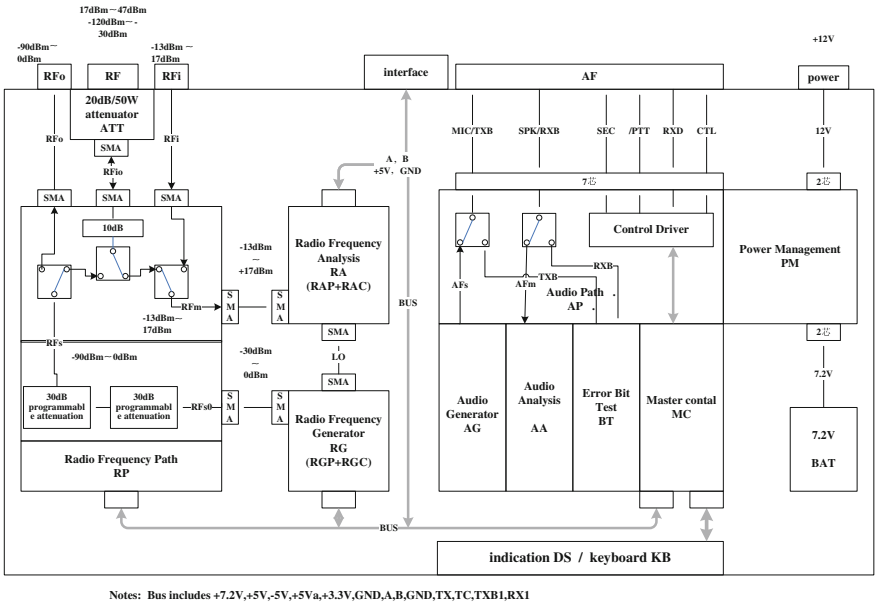

Fig. 20.2 Block diagram of platform

20.2.2 Low Frequency Signal Generation and Analysis Unit

This unit is to implement two functions. The first one is to generate signal sources for radios in the range from 10 Hz to 10 kHz with various formats [3]. For aircrafts, radios can implement many functions, except for voice communication, such as data communication, spread spectrum (SS) communication, FH communication, and so on. The second function is to analyze received low frequency signals in the same range test and acquire detail indexes, such level, distortion, and so on.

This generator is a classic direct digital synthesizer (DDS). It is composed of reference signal source, DDS chips, amplifiers, adders, filter, and driver. The DDS is a technology can provide more rapid more flexible change of frequency than traditional synthesizer. The amplitude and frequency are settled by control signals from control unit according to different test requirements. Because the frequency changing speed is very fast, if DDS is controlled by a pseudo random code, this generator can provide a FH signal.

The DSP is the central component of this analysis unit. When an audio signal is received from low frequency interface, after matching its impedance and filtering, it is changed to differential path and enters into AD chip. Then, this digital signal is disposed in DSP according to testing requirements and algorithm, and returns results to the control unit.

20.2.3 RF Signal Generation Unit

The RF signal generator is to generate a RF signal in the range from 1 to 500 MHz based on the requirement of tests. The crystal oscillator is to provide stable 20 MHz signal as a signal source for VCO1, VCO2, FPGA, and DDS. The control signals generated by control unit are transferred to FPGA, VCO1, VCO2 after disposing MCU to produce signals in different frequency ranges. After twice mixing processes, a RF signal in the range from 1 to 500 MHz is outputted through a switch in two paths controlled by Rx/Tx signal. One path is outputted to RF analysis unit, the other path is outputted to RF channel unit after an attenuator, whose factor is controlled by MCU.

Meanwhile, a digital signal is received by FPGA from RF analysis unit, and a CVSD modulation is performed by DDS, which is also controlled by FPGA.

20.2.4 RF Channel Unit

The RF channel unit is to provide different paths according to different conditions. It is composed of programmable attenuators, fixed attenuators, and electronic switches. The programmable attenuators are to decide whether RF signals are needed to attenuated or not controlled by RF generation unit. And then, after switches, an output path is selected for RF signal. If the RF in/out path is selected, it means the RF signal is to attenuated 30 dB. For input path, there are also two paths can be selected, and then, RF signals is to be analyzed in RF analysis unit.

20.2.5 RF Analysis Unit

The RF analysis units have similar functions as low frequency signal one. The difference is the frequency range and indexes. There are two input RF signals, one is from RF generation unit, the other is from RF channel unit. After preprocessing, they are divided into three paths. The first path is to demodulate this RF signal. When the two RF signals are mixed, an intermediate frequency (IF) signal is generated, and after demodulator, the IF signal is converted into audio signal. The second path is to shape this signal to suitable for following frequency counting process. The last path is to detect its power. Three signals are entered to FPGA and MCU. After disposing, frequency data, power data, amplitude modulation factor and frequency deviation data are generated by this unit and outputted to control unit to show on LCD.

20.2.6 Control Unit

The control unit is the central of this test set. It is constituted of master controller MCU, LCD, keyboard, status control circuit, and interface control circuit. The control unit has two operating status. This first one is called as "master mode." It means control signals are produced by master controller according to the operating on keyboard and LCD and outputted to other units inside testing set through internal RS232/RS485 bus. The next mode is "slave mode". It shows an external controller, such as PMA or MCU, is connected to test set by RS232 bus and takes the place of master controller.

20.3 Software Design

This test set is required a friend interface with operators and maintainers, and it also required plenty of functions. So, the software is designed in Lab/Windows platform by using CVI software.

20.3.1 Total Structure

The structure of this test and measure system is an open system and transplantable. The redundant design is utilized for key components, such as data acquisition, malfunction identification, to guarantee their functions [4]. The system includes six modules. Every module is to perform an independent function, and there are interfaces to interact with two modules (Fig. 20.3).

20.3.2 Program Design

The system self-test program is to perform malfunction identification and isolation by embedding circuits in every module. According to the results on the indicator, the customs can supervise this test set conveniently and eliminate potential malfunctions. By this program, it can increase the reliability and maintainability (Fig. 20.4).

The item test module is to implement the test for communications system and radio devices automatically. The indexes that can be tested for radio are peak envelope power, frequency error, sensitivity, audio signal output, modulation factor of tactical short-wave radio; carrier power, frequency error, sensitivity, audio signal output, and error rate of tactical ultra short-wave radio.

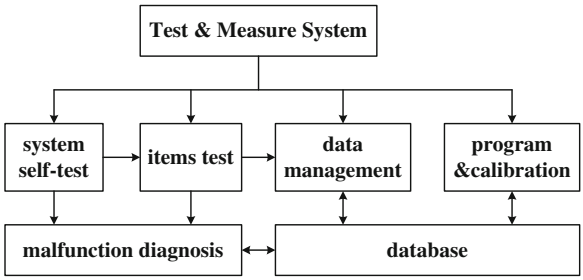

Fig. 20.3 Block diagram of test and measure system

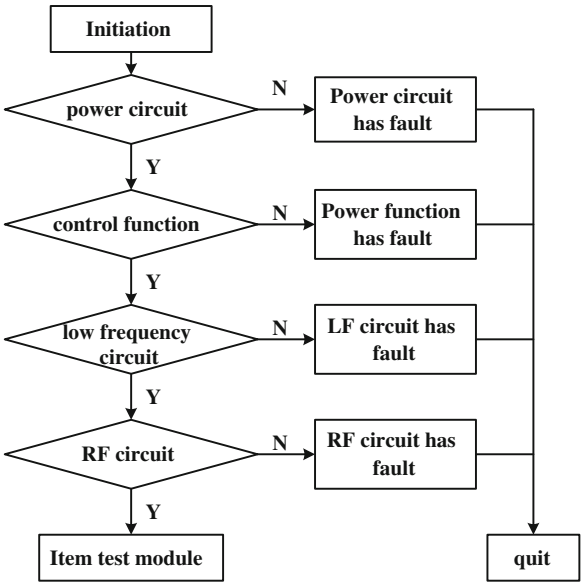

Fig. 20.4 Program flow diagram of self-test program

The data management module can perform filing, inquiring, and printing documents.

The malfunction module is to test and diagnose faults of test set. Based on the embedded in self-test circuit, test, analyze, and judge the position of fault. The database includes item-test database, malfunction database, and system database. The malfunction database is to provide data to self-test. The system database can perform introduce, verify, and manage system.

The program and calibration module is to load program by RS232 interface from computer. This test set is a general purpose set and it can perform test for various equipments. Because different equipments require different performances, the program flow may differ. So, the designer can program on an external computer, and then download it by this interface.

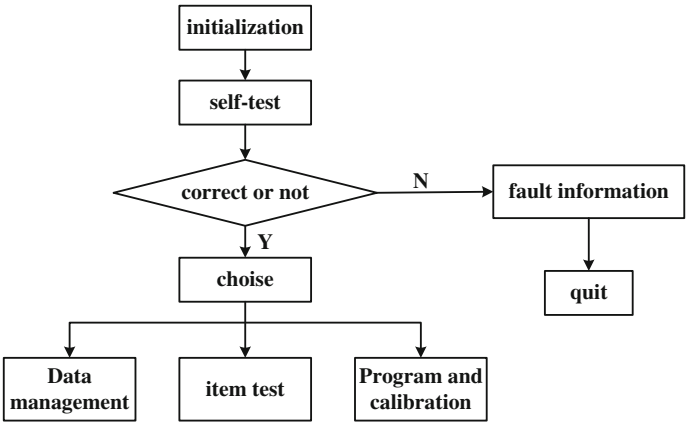

Fig. 20.5 Program flow diagram of whole program

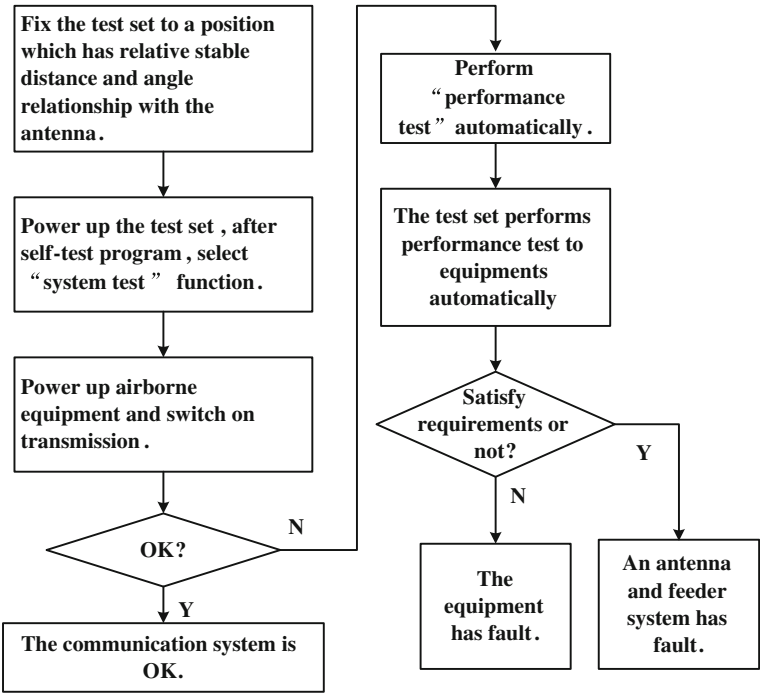

Fig. 20.6 Item test procedure

20.3.3 Program Flow

The whole program flow of the test set is shown on Fig. 20.5.

After initialization, the test set begins to test itself. If there is nothing wrong in this system, the set may choose different functions according to the selections on menu on LCD. Otherwise, the fault information may show on the indicator and program is quit. If the item test is chosen, the set may perform system functional test and equipment performance test.

The system functional test is to test the function of this system. When set the test set to a position, which has relatively distance and angle relationship with antenna, select "system function" on menu. Then, put on the airborne equipment and switch on transmission status. After several seconds, the test set may show the power value received by this system. If the value is higher than a rated power, the indicator shows the system is correct, and the test is finished. Otherwise, the program enters into "performance test" automatically. In this program, there are several fixed indexes. And, if every index reaches its requirements, it means the equipment is normal and the antenna feeder system has fault. Otherwise, the equipment has fault (Fig. 20.6).

20.4 Conclusion

Compared with former test sets, this test set takes FPGA and MCU as central and applies advanced technologies, such as high-speed data processing, multi-bus fusion, DDS, and so on. Therefore, this test set is a portable device, small in size, and light in weight. It is easy to generate various signals and perform system and equipment tests. At present, this system has been utilized in some units and its operating result is satisfied with users.

References

1. Chendehuang (2005) A design of a control and test platform of a synthesis communications system. Comput Eng 31:225–227
2. Wushudong, Nietao (2006) Design of aviation communication equipment automated test instrument. Missile guidance report, vol 26, pp 307–310
3. Wanglei, Fangjian (2012) The analog and digital signal source design based on FPGA. Sci Technol Consult Her 25:30–31
4. Xufuxin, Shenwenwu (2012) Design of opening experimental test system based on wireless communication. Comput Eng 8:84–89

Chapter 21
Design and Analysis of High-Reliability Universal Airborne RVDTs

Yong Zhou, Yufeng Zhang, Chao Zhang and Qixun Zhou

Abstract This paper analyzed the basic structure and working principle of rotary variable differential transformers (RVDTs), and comprehensively analyzed the characteristics of different types of RVDTs, and finally selected reluctance RVDT as the sensor detecting angular displacement of airborne servos. To ensure the versatility, the author adopted the design plan of one pair of pole reluctance RVDTs, completed the main design parameters, built a Maxwell 2D model and conducted the meshing. Through electromagnetic finite element software analysis, the author also verified the correctness of the output signals of the RVDTs.

Keywords Airborne servo system · Angular detecting · RVDT · Electromagnetic analysis

21.1 Introduction

With the continuous development of defense technology, aviation, aerospace, marine, and other control systems such as radar directional navigation system, wing servo system, gun control system have increasingly high requirements for accuracy, speed, reliability, and consistency. One of the key requirements for a high-performance nongear-reduction-type rotary airborne servo system is to accurately measure the angular displacement of the servo output shaft, and the commonly used angle measurement sensors include absolute grating encoders, Hall sensors, and rotary transformers [1, 2]. Absolute grating encoders can directly convert the shaft angles into digital signals, so their application is easy and convenient, but due to the environmental adaptability, price and other factors, they are

Y. Zhou (✉) · Y. Zhang · C. Zhang · Q. Zhou
School of Aeronautics, Northwestern Polytechnical University, Xi'an, China
e-mail: yongstar@nwpu.edu.cn

J. Wang (ed.), *Proceedings of the First Symposium on Aviation Maintenance and Management-Volume I*, Lecture Notes in Electrical Engineering 296,
DOI: 10.1007/978-3-642-54236-7_21,

difficult to be applied in the high-temperature and harsh airborne environment; each Hall sensor has a simple structure, but it is difficult to meet the high-precision angle measurement requirements, so its application is limited; with reliable structure, high timeliness, strong environmental adaptability, and other advantages, rotary variable differential transformers (RVDT) are widely used in high-precision airborne servo systems [3, 4]. This paper analyzed the basic structure and working principle of RVDTs, and comprehensively analyzed the characteristics of different types of RVDTs, and finally selected reluctance RVDT as the sensor detecting angular displacement of airborne servos. To ensure the versatility, the author adopted the design plan of one pair of pole reluctance RVDTs, completed the main design parameters, built a Maxwell 2D model and conducted the meshing. Through electromagnetic finite element software analysis, the author also verified the correctness of the output signals of the RVDTs.

21.2 RVDT Mathematical Model

RVDT basic structure is shown in Fig. 21.1 Both D1D2 and D3D4 are stator windings with effective turns ND, in the running of the stator windings, an AC voltage with fixed amplitude and frequency is put on D1D2 to generate a working magnetic flux, so the windings are also known as excitation windings; both Z1Z2 and Z3Z4 are rotor windings with effective turns NZ, outputting voltage signals, they are also called output windings [5, 6].

Assuming that the output windings Z3Z4 and Z1Z2 are open, the excitation magneto-motive force formed when an AC excitation current passes the excitation winding D1D2 is bound to generate a radial pulsating magnetic flux Φ_d in the same direction as the axial direction of D1D2 winding. When RVDT rotor is at the coincident position of the axes of the two windings Z1Z2 and D1D2, the radial pulsating magnetic flux Φ_d will completely go through the winding Z1Z2, and generate the electromotive forces $\dot{E}_D$ and $\dot{E}_Z$ in D1D2 and Z1Z2, respectively, and the valid values are:

$$\begin{cases} E_D = 4.44 f N_D \Phi_{dm} \\ E_Z = 4.44 f N_Z \Phi_{dm} \end{cases} \tag{21.1}$$

where Φ_{dm} is the virtual value of pulsation magnetic flux Φ_d.

$$\frac{E_D}{E_Z} = \frac{N_D}{N_Z} = k \tag{21.2}$$

And the k is called RVDT turns ratio. If ignoring the resistance and leakage reactance of the excitation winding, $U_D = E_D$, and the effective value of the voltage across the winding Z1Z2 is $U_{z12} = E_z$, so $U_{z12} = kU_D$. Since the direction of Φ_d is perpendicular to the axis of winding Z3Z4, and does not generate induced

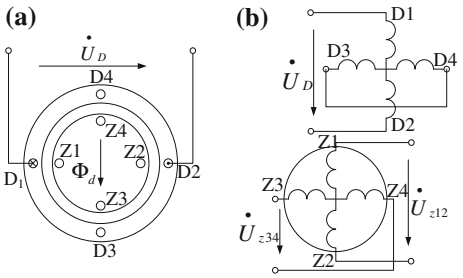

Fig. 21.1 RVDT structure schematic diagram. **a** Overall structure schematic diagram. **b** Winding schematic diagram

electromotive force in the winding, and thus the voltage across the winding Z3Z4 $U_{z34} = 0$.

The position where the axis of winding Z1Z2 coincides with the axis of winding D1D2 is defined as the electrical zero position of the RVDT, and the angle of rotor deviating from the electrical zero position is called rotor angle. When the rotor angle is not zero, for example, when the rotor clockwise deflects from the electrical zero position for angle θ, the magnetic flux of the radial pulsation magnetic flux Φ_d passing through the two rotor windings are:

$$\begin{cases} \Phi_{d12} = \Phi_d \cos\theta \\ \Phi_{d34} = \Phi_d \cos(90^\circ - \theta) = \Phi_d \sin\theta \end{cases} \tag{21.3}$$

Thus, the induced electromotive force generated in the rotor winding was respectively:

$$\begin{cases} E_{z12} = E_z \cos\theta = kE_D \cos\theta \\ E_{z34} = E_z \sin\theta = kE_D \sin\theta \end{cases} \tag{21.4}$$

The output voltages are:

$$\begin{cases} U_{z12} = kU_D \cos\theta \\ U_{z34} = kU_D \sin\theta \end{cases} \tag{21.5}$$

Obviously, as long as the amplitude of the excitation voltage U_D keeps constant, the output winding voltage and the rotor deflection angle θ will maintain an accurate cosine function relationship.

21.3 Reluctance RVDTs

According to the different structures, RVDTs can be divided into contact type and noncontact type. Because of brushes and slip rings, the conversion accuracy, running speed, working life, and maintenance performance of contact-type RVDTs

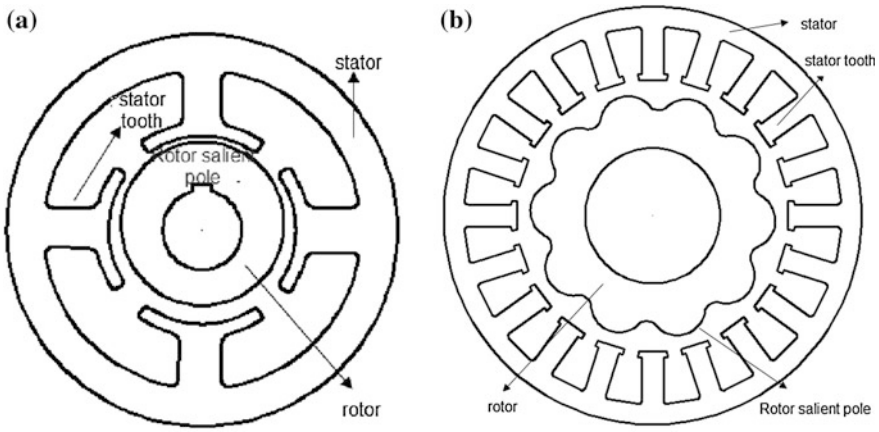

Fig. 21.2 Schematic diagrams of reluctance RVDT structures. **a** Concentrated winding structure. **b** Distributed winding structure

are affected. Noncontact-type RVDTs can be divided into brushless wound-rotor RVDT and magnetic-reluctance RVDT.

Brushless wound-rotor RVDTs use coupling transformers to replace brushes and slip rings, and the rotor cores are generally made of 0.2 $\sim$ 0.4 mm cold-rolled silicon steel sheets through lamination, and the punching plate outer edges are processed into fine tooth spaces to embed the reentrant windings. The requirement for fine structure increases the difficulty of processing, while restricting the miniaturization of the RVDT external dimensions. Furthermore, the width of the air gap between the RVDT rotor and the stator is generally 0.1 $\sim$ 0.3 mm, after the RVDT rotor is mounted coaxially with the PMSM rotor, if the PMSM rotor bearing radially rocks, the rocking will cause that the outer edge winding of the rotor RVDT (average diameter is generally 0.2 mm, or even smaller) scratches the stator, causing the closed rotor winding opening, and thus the RVDT will lose the function of angle measurement [7, 8]. Therefore, the structural defects of brushless wound-rotor RVDT limit its applications in the fields of aeronautics and astronautics having high requirements for size and reliability.

According to the different winding methods of output windings, reluctance RVDTs are divided into concentrated winding structure and distributed winding structure shown in Fig. 21.2. The stators of both two structures have semi-closed slots, and the excitation winding and the output winding are wound with the same teeth. The output windings of concentrated winding structure adopt concentrated and same-turn winding method, and the output windings of distributed winding structure are generally distributed within the stator tooth space in accordance with certain rules. The rotors of both two structures are made of laminated silicon steel sheets with specific shape, so the constant component and fundamental component account for the dominant part of the air gap magnetic flux, generating the sine signals varying with the rotor position in the output winding.

Table 21.1 Optimization results and proposed values of some parameters

Parameter names	Optimal of recommended values	Proposed values
Stator outside diameter	Consider based on the installation space	23 mm
Stator tooth length	Consider based on the installation space	7 mm
Stator tooth profile	Arc/straight line	Arc
Pole arc coefficient	0.4 ~ 0.6	0.428
Stator inside diameter	Consider based on the installation space	12 mm
Minimum width of air gap	0.3 ~ 0.6 mm	0.5 mm
Rotor outside diameter	Consider based on the installation space	9.1 mm
Rotor inside diameter	Consider based on the installation space	5.5 mm
Sine coefficient	1.5 ~ 2.0	1.85

21.4 Design of Reluctance RVDT

21.4.1 Determination of Main Parameters

When a RVDT is used to detect the angular displacement of the servo output shaft, it is coaxially installed with the output shaft, and therefore, the diameter and the installation space of the measured output shaft basically determine the RVDT's dimensions. The main parameters of a RVDT are determined generally based on the design experience in motor design manual as well as the requirements of specific application situation for the dimensions, and due to the limited space, taking the detection of the rotor position of a permanent magnet synchronous motors as an example [4], this paper gave its main design results as shown in Table 21.1.

21.4.2 Model Construction and Meshing

After determining the RVDT main parameters, the RVDT should undergo a system modeling and meshing, the model and meshing results of an antipode concentrated winding RVDT are shown in Figs. 21.3 and 21.4.

21.4.3 Winding Adding

The windings in stator socket can be divided into three groups, namely excitation winding, sine winding, and cosine winding, and the winding design results are shown in Fig. 21.5: the excitation winding is evenly distributed in four sockets, and each tooth contains 80 turns, the winding directions of the adjacent sockets are opposite; sine winding is evenly distributed in the sockets 1 and 3, and each tooth

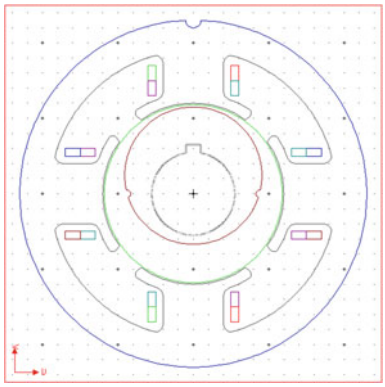

Fig. 21.3 Structure of a concentrated winding RVDT

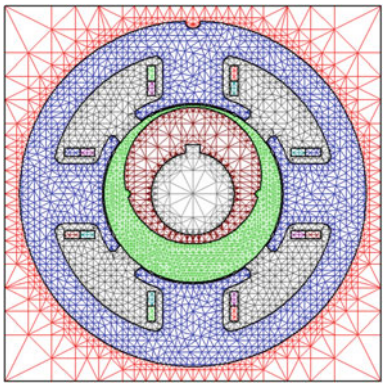

Fig. 21.4 Meshing diagram of a concentrated winding RVDT

contains 495 turns, the winding directions of the adjacent sockets are opposite; the cosine winding is evenly distributed in sockets 2 and 4, and each tooth contains 495 turns, the winding directions of the adjacent sockets are opposite.

21.5 Analysis of RVDT Output Signal

The author added a sine wave voltage signal with the effective value of 10 V and the frequency of 5 kHz into the excitation winding, and set the RVDT rotor speed as 100 r/min. Running analysis in Maxwell 2D, the magnetic fluxes of sine winding and cosine winding present a curve varying with time which is shown in Figs. 21.6 and 21.7, it can be seen from the figures that the flux curve varies by sine law with the change of rotor position.

The author opened the sine winding and the cosine winding output circuit, and measured the induced electromotive force at the output terminals, the output curve is shown in Fig. 21.8, the obtained signals on the RVDT output winding are sine

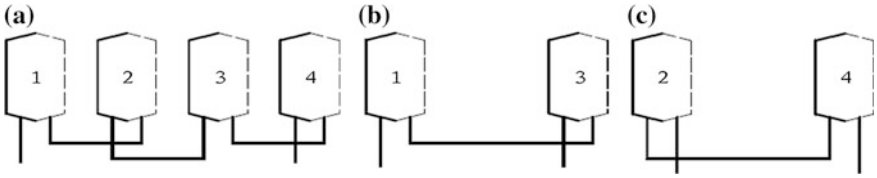

Fig. 21.5 Winding distribution diagram of concentrated winding RVDT. **a** Excitation winding distribution. **b** Sine winding distribution. **c** Cosine winding distribution

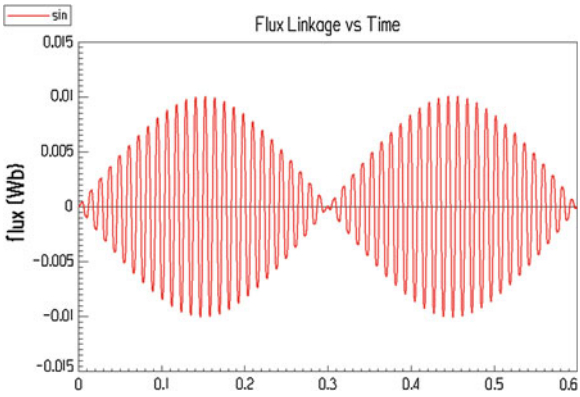

Fig. 21.6 Sine winding flux curve

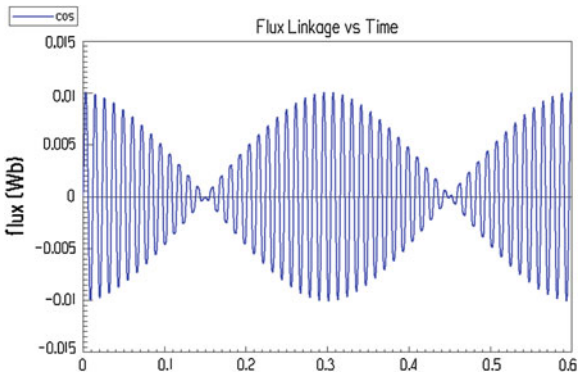

Fig. 21.7 Cosine winding flux curve

envelope and cosine envelope, respectively, the carrier wave and the excitation signal have the same frequency. The Lissajou's figures of the sine and cosine envelopes are shown in Fig. 21.9, the rotor rotates one cycle, and the output curve forms a complete circle, so the rotor position information can be obtained by detecting the two groups of output signals.

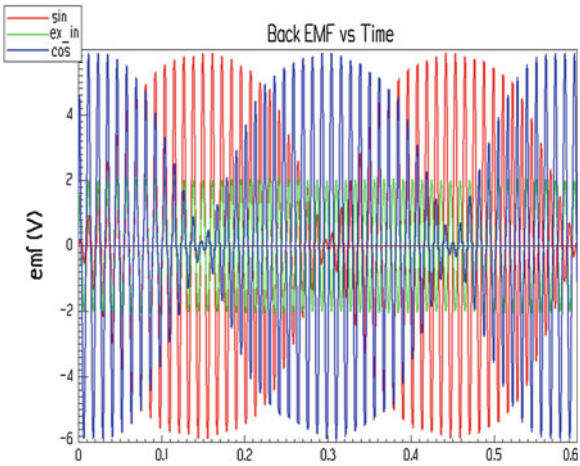

Fig. 21.8 Induced EMF waveforms of sine and cosine windings

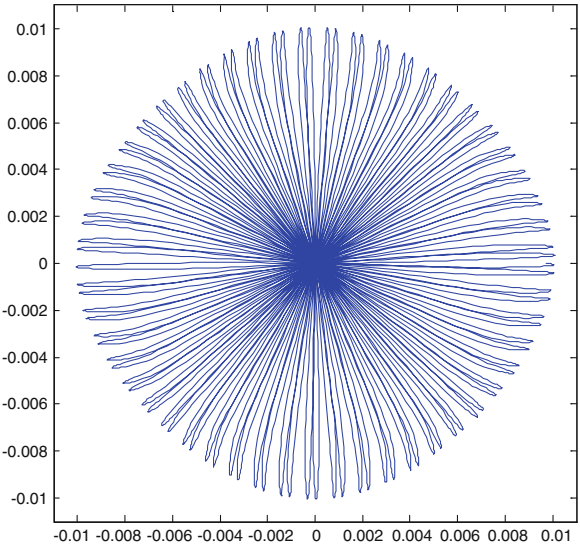

Fig. 21.9 Lissajou's figures of sine and cosine winding induced EMFs

21.6 Conclusion

The paper mainly discussed how to improve the reliability of airborne servo angular displacement detection, and made a comprehensive comparison of the advantages and disadvantages of grating encoders, Hall sensors and RVDTs, finding that RVDTs have a more reliable structure, a better timeliness, a stronger environmental adaptability, and other advantages, being more suitable for the airborne equipment requiring high reliability. This paper completed the structural design, electromagnetic design, and finite element analysis of 1 antipode

reluctance RVDT, and the results showed that the output signals of 1 antipode reluctance RVDT showed a one-to-one corresponding relationship within 360° angle position range, so RVDTs can be used as universal angular displacement sensors of airborne servos in the field of aerospace.

Acknowledgments This work was supported by the National Natural Science Foundation of China (Nos. 51207129, 61104030 and 51307137). The authors would also like to thank the anonymous reviewers for their valuable comments and suggestions to improve the quality and readability of the paper.

References

1. Andreas B, Stephan B (2004) High-performance speed measurement by suppression of systematic resolver and encoder errors. IEEE Trans Industr Electron 51(1):49–53
2. Lidozzi A, Solero L, Crescimbini F (2007) SVM PMSM drive with low resolution Hall-effect sensors. IEEE Trans Power Electron 22(1):282–290
3. Beccue PB, Pekarek SD, Deken BJ (2007) Compensation for asymmetries and misalignment in a Hall-effect position observer used in PMSM torque-ripple control. IEEE Trans Ind Appl 43(2):560–570
4. Li SJ, Zhou QX, Lu G (2007) Digital calibration and compensation for angle measure system based on resolver-RDC. Small Spec Electr Mach 35(6):26–28 (in Chinese)
5. Mohieddine B, Lazhar BB, Mohd AA (2004) A novel resolver-to-360° linearized converter. IEEE Sens J 4(1):96–101
6. Zhao H, Zou JW, Li TC (2002) A novel angle measuring method in resolver mode. Chin J Sci Instrum 23(3):68–69 (in Chinese)
7. Nirei M, Yananoto Y, Kitazawa K (2002) Angular error analysis of an 8X-VR resolver with an eccentric rotor. J Magn Magn Mater 24(2):1202–1205
8. Nowlin N, McEndree S, Butcher D (2004) A radiation-hardened high-precision resolver-to-digital converter (RDC). In: 2004 IEEE radiation effects data workshop—workshop record. pp 96–103

Chapter 22
Error Analysis and Compensation Method Research of Airborne Reluctance RVDTs

Qixun Zhou, Yufeng Zhang, Yong Zhou and Dengxiu Yu

Abstract As the key sensor, the airborne reluctance Rotary Variable Differential Transformers (RVDTs) played an important role in the aircraft servo system. The measurement accuracy of an angle measurement system mainly depends on the measurement accuracy of the rotary transformer and the conversion accuracy of Resolver-to-Digital Converter (RDC). The main factors affecting the measurement accuracies of sine and cosine RVDTs are the sine and cosine function error and cross-axis error, and due to the limit of processing, as well as the impacts of magnetic material, nonlinear, linear characteristics, and assembly accuracy. These two errors are difficult to get a large improvement to a certain extent. To ensure the accuracy of servo system positioning, this paper presents an error analysis and compensation method.

Keywords Rotary variable differential transformers · Resolver-to-digital converter · Error analysis · Compensation method

22.1 Introduction

One of the core functions of airborne permanent magnet brushless DC servo system is the angular position measurement of servo motor output shaft. According to the different methods of measuring angular position, the measurement equipment can be divided into non-position sensor and position sensor. Non-position sensors have simple structures and small sizes, but are difficult to apply in the systems with high requirements of motor starting performance and low-speed running performance [1–3]. The commonly used rotor position sensors include

Q. Zhou (✉) · Y. Zhang · Y. Zhou · D. Yu
Department of Electrical and Control Engineering, Xi'an University of Science and Technology, Xi'an, China
e-mail: zhouqixun029@163.com

J. Wang (ed.), *Proceedings of the First Symposium on Aviation Maintenance and Management-Volume I*, Lecture Notes in Electrical Engineering 296,
DOI: 10.1007/978-3-642-54236-7_22,

grating encoders, Hall sensors, and rotary transformers. Incremental grating encoders cannot determine the absolute position of the motor rotors, so they are difficult to be applied in servo systems; absolute grating encoders can directly transform rotor angles into digital pulse signals, so the application is simple and convenient, but they are very expensive and so difficult to be used widely; Hall sensors have a simple structure, but their angle measurement accuracies are limited; with high reliability, fastness, strong antijamming ability and other advantages, rotary transformers are widely used in high-precision servo systems [4, 5]. The measurement accuracy of an angle measurement system mainly depends on the measurement accuracy of the rotary transformer and the conversion accuracy of RDC. The main factors affecting the measurement accuracies of sine and cosine RVDTs are the sine and cosine function error and cross-axis error, and due to the limit of processing, as well as the impacts of magnetic material, nonlinear, linear characteristics, and assembly accuracy, these two errors are difficult to get a large improvement to a certain extent [1]. To ensure the accuracy of servo system positioning, the rational design of angle measurement system as well as the elimination and compensation of angle measurement error has become very critical.

22.2 Basic Structure of a Reluctance RVDT

According to the different winding methods of output windings, reluctance RVDTs are divided into concentrated winding structure and distributed winding structure. The stators of the two structures have semi-closed slots, their excitation windings and output windings are wound within the same teeth. The output windings of concentrated winding structure adopt concentrated and same-turn winding method, and the output windings of distributed winding structure are generally distributed within the stator tooth space in accordance with certain rules. The rotors of both the structures are made of laminated silicon-steel sheets with specific shape, so the constant component and fundamental component account for the dominant part of the air gap magnetic flux, generating the sine signals [6, 7] varying with the rotor position in the output winding.

The basic principle of the two structures is to use the salient effect of rotor magnetic poles, the mutual inductance between the excitation winding and output winding varies with the rotor position changes, and this paper takes the 1 pole-pair concentrated winding reluctance RVDT as an example, to outline how it works: the number of RVDT rotor salient-pole pairs $p = 1$, phase number of output winding $m = 2$, number of stator teeth $Z_S = 2mp = 4$, the excitation winding is wound in series by reverse tooth by tooth, the output winding is wound in positive and negative order and in series every $m - 1$ teeth, and every two phases of the output winding is separated by $Z_S/m - 1$ teeth, the excitation winding and output winding turns, winding direction and connection method on each tooth are shown in Table 22.1.

Table 22.1 Winding connection method

Stator teeth size	Excitation winding parameters		Output winding parameters			
	Winding direction	Turns	Winding direction	Turns	Output type	θi
1	+	Nm	+	Nc	Cosine	θ
2	−	Nm	+	Ns	Sine	$\theta + 90°$
3	+	Nm	−	Nc	Cosine	$\theta + 180°$
4	−	Nm	−	Ns	Sine	$\theta + 270°$

Since windings are wound concentrically on the stator teeth, the induced electromotive force of each winding is related to the change of the magnetic permeance under the corresponding tooth. The air gap permeance under each tooth is a periodic function of the rotor position angle, and the following formula can be obtained through expansion with Fourier poles:

$$\Lambda_i = \Lambda_0 + \sum_{\mu=1}^{\infty} \Lambda_\mu \cos\left[\mu p\theta + (i-1)\frac{2\mu p\pi}{Z_S}\right] \tag{22.1}$$

where: Λ_0 is the amplitude value of magnetic permeance DC component, Λ_μ is the μ harmonious wave amplitude value of the magnetic permeance.

$$\sum_{i=1}^{Z_s} \Lambda_i = Z_s\Lambda_0 + \sum_{\mu=1}^{\infty}\sum_{i=1}^{Z_s} \Lambda_\mu \cos\left[\mu p\theta + (i-1)\frac{2\mu p\pi}{Z_S}\right] \tag{22.2}$$

The excitation windings on each tooth are connected in series in opposite direction, the air gap synthetic permeance is a constant value, so the excitation current does not change with the changes, and the total magneto-motive force and the synthetic magnetic flux is constant, so the excitation magnetic flux under each tooth is:

$$\phi_i = \phi_0 + \sum_{\mu=1}^{\infty} \phi_\mu \cos\left[\mu p\theta + (i-1)\frac{2\mu p\pi}{Z_S}\right] \tag{22.3}$$

where: ϕ_0 is the amplitude value of magnetic flux DC component, ϕ_μ is the μ harmonious wave amplitude value of the magnetic flux.

The specific shape design of the rotor makes the air gap permeance be expressed as:

$$\Lambda = \Lambda_0 + \Lambda_1 \cos p\theta \tag{22.4}$$

Combining the formulas (22.2), (22.3) and (22.4), the following formula can be obtained:

$$\phi_i = \phi_0 + \phi_1 \cos\left[p\theta + (i-1)\frac{2p\pi}{Z_S}\right] \tag{22.5}$$

According to the connection method of the output windings, the flux linkage of sine winding and cosine winding can be expressed as:

$$\begin{cases} \psi_s = \sum_{i=1,3} N_s(-1)^{\left(\frac{i-1}{2}\right)}\phi_i \\ \psi_c = \sum_{i=2,4} N_c(-1)^{\left(\frac{i-1}{2}\right)}\phi_i \end{cases} \tag{22.6}$$

Substitute Eq. 22.5 into 22.6 and simplify it, we can get:

$$\begin{cases} \psi_s = Z_S N_S \phi_1 \sin\theta \\ \psi_c = Z_C N_C \phi_1 \cos\theta \end{cases} \tag{22.7}$$

Through the relationship between induced electromotive force and the flux linkage—$e = -\frac{d\psi}{dt}$, the output signal amplitude of sine and cosine output windings can be obtained:

$$\begin{cases} E_s = E_m \sin\theta \\ E_c = E_m \cos\theta \end{cases} \tag{22.8}$$

It can be seen from formula (22.8), that the output signal of reluctance RVDT and position angle θ of the rotor form a sine and cosine function relationship.

22.3 Analysis of RVDT Accuracy Impact

Due to structural reasons, the detection accuracies of low-pole-pair-number concentrated winding reluctance RVDTs are subject to the coil winding process. Currently, most of the widely used concentrated winding reluctance RVDTs adopt multi-pole-pair structure of (e.g., four pole pairs, eight pole pairs, etc.), and multi-pole-pair RVDTs have a poor commonality. In this section, an analysis of the factors affecting the accuracy of RVDTs were made, to provide references for the improvement of the accuracy of low-pole-pair reluctance RVDTs.

The stator windings adopting centralized winding method does not exist the round-off error caused by turns rounding, and the coil winding process is the main factor affecting the accuracy of concentrated winding or reluctance RVDTs. Currently, there are two commonly used winding processes: manual winding and special winding machine. Because of the small number of processed reluctance RVDTs in China, subject to the limit on the production costs, manual winding is generally adopted, resulting in the difficulty of achieving a consistent tightness of the coils in each socket, and the coil positions are difficult to keep symmetric.

Asymmetric coil positions have two kinds of impacts on the accuracy of RVDTs, namely asymmetry of excitation winding coil positions and asymmetry of output winding coil positions. To, respectively, establish the position of asymmetry

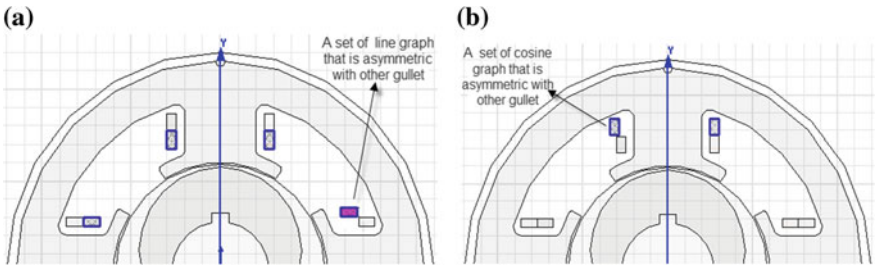

Fig. 22.1 Asymmetric geometric model of winding coil. **a** Position asymmetry of excitation winding coil. **b** Position asymmetry of cosine winding coil

Table 22.2 Calculation results obtained when concentrated winding excitation coil is asymmetric

Actual rotor position (degrees)	Sine winding inductive EMF (V)	Cosine winding inductive EMF (V)	Calculate rotor position (degrees)	Position calculation error (degrees)
0	0.395	4.551	4.960	−4.960
90	4.781	0.220	87.365	2.635
180	−0.140	−4.780	181.678	−1.678
270	−4.785	−0.218	267.391	2.609

geometric models of excitation winding coil and output winding coil (with cosine winding coil as an example) in the finite element software, the relative quantity of asymmetric positions is 5 %, as shown in Fig. 22.1.

22.3.1 Impact of Excitation Winding Coil Position Asymmetry

RVDT rotor rotated at a uniform speed of 100r/min, and a finite element calculation of the excitation winding coil position asymmetry model in Fig. 22.1a was conducted, and the output winding signals were obtained, and some of the data undergoing software processing were listed in Table 22.2. As can be seen from the table, because the excitation winding coil wound in socket one (rotor position of 0°) was looser than the coils in other sockets, when the rotor position was 0°, the calculated value of the sine winding output was 0.395 V higher than the theoretical value 0 V, and the calculated value of the cosine winding output was 0.449 V lower than the theoretical value 5 V, and the error between the rotor position calculated value and the theoretical value reached 4.960°. There were also similar errors in other sockets, but the error values were smaller than the error at rotor position 0°. Obviously, the farther the asymmetric winding position is, the smaller

Table 22.3 Calculation results obtained when concentrated winding cosine coil is asymmetric

Actual rotor position (degrees)	Sine winding inductive EMF (V)	Cosine winding inductive EMF (V)	Calculate rotor position (degrees)	Position calculation error (degrees)
0	0.039	4.476	0.499	−0.499
90	4.981	0.315	86.381	3.619
180	−0.019	−4.683	180.232	−0.232
270	−4.979	−0.297	266.586	3.414

the impact is. After the excitation winding underwent a relative position movement of 5 %, the calculation error of rotor position was up to 5°, showing that the detection accuracy of 1-pole-pair concentrated winding reluctance RVDT was very sensitive to the winding process of excitation windings.

22.3.2 Impact of Output Winding Coil Position Asymmetry

RVDT rotor rotated at a uniform speed of 100 r/min, the finite element calculation of the output winding coil position asymmetry model in Fig. 22.1b was conducted, and the output winding signals were obtained, and some of the data undergoing software processing were listed in Table 22.3. As can be seen from the table, because the cosine winding coil wound in socket two was looser than the coils in other sockets, within the scope 360° around the rotor position, there was a large error between the calculated value and theoretical value of cosine winding EMF output. The impact of the cosine winding position asymmetry on the sine winding EMF output was very small, and the calculated value was close to the theoretical value. After the cosine winding underwent a relative position movement of 5 %, the calculation error of rotor position was approximate 4°; due to the symmetry of signals, if the sine winding positions were asymmetric, the results would be similar. Therefore, the detection accuracy of 1-pole-pair concentrated winding reluctance RVDT was very sensitive to the winding process of sine and cosine output windings.

22.4 Reluctance RVDT Error Compensation Method

In order to improve the detection accuracy of the RVDT, the author modified concentrated winding RVDT structure into the distributed winding structure to reduce the impact of coil winding process on RVDT accuracy. The structure of concentrated winding reluctance RVDT is simple, and the windings are easy to insert, but the impact of winding process on detection accuracy is very great. The concentrated winding structure was modified into a distributed winding structure,

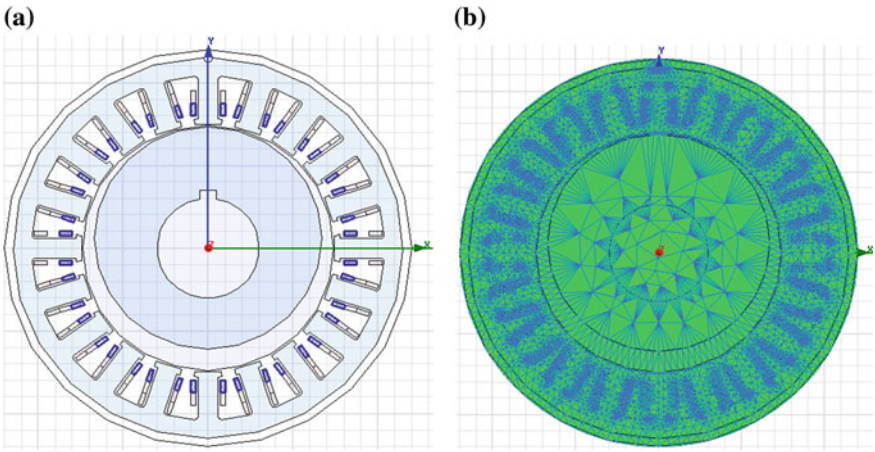

Fig. 22.2 Structure and meshing diagrams of 1-pole-pair distributed winding reluctance RVDT. **a** Structure diagram. **b** Meshing diagram

and the stator socket number is expanded from 4 to 20, and the structure and meshing are shown in Fig. 22.2.

Like concentrated winding structure, the windings in the stator socket of distributed winding structure can also be divided into three groups, namely excitation winding, sine winding, and cosine winding. The excitation winding was evenly distributed in 20 stator sockets, each tooth contains 80 turns, and the socket winding directions of two adjacent stators are opposite. The sine and cosine windings were distributed in each stator sockets according to the sine and cosine laws, the calculation formula is as follows:

$$\begin{cases} W_{\mathrm{SK}} = W_0 \sin[2\pi(K-1)\dfrac{Z_r}{Z} + \theta] \\ W_{\mathrm{CK}} = W_0 \cos[2\pi(K-1)\dfrac{Z_r}{Z} + \theta] \end{cases} \tag{22.9}$$

where:

W_{SK} and W_{CK}	represent the sine and cosine winding turns in the K-th socket of the stator, respectively;
Z_r	Rotor teeth, also the number of RVDT pole pairs, in this paper, the $Z_r = 1$;
Z	Total of stator sockets, in this paper, the $Z = 20$;
K	No. of stator sockets;
W_0	Maximum number of turns, in the paper, the $W_0 = 120$;
θ	To enable the two phases to output modulation with symmetrical windings, in the paper, the $\theta = 0$

Table 22.4 Calculation results obtained when distributed winding excitation coils are asymmetric

Actual rotor position (degrees)	0	90	180	270
Sine winding induced EMF (V)	0.096	4.930	−0.024	−4.934
Cosine winding induced EMF (V)	4.915	0.051	−4.957	−0.055
Calculate rotor position (degrees)	1.119	89.407	180.277	269.361
Position calculation error (degrees)	−1.119	0.593	−0.277	0.639

Table 22.5 Calculation results obtained when distributed winding cosine coils are asymmetric

Actual rotor position (degrees)	0	90	180	270
Sine winding induced EMF (V)	0.013	4.989	–0.011	–4.991
Cosine winding induced EMF (V)	4.926	0.093	–4.897	–0.102
Calculate rotor position (degrees)	0.151	88.932	180.129	268.829
Position calculation error (degrees)	–0.151	1.068	–0.129	1.171

To test the impact of coil winding process on the detection accuracy of distributed winding reluctance RVDTs, an asymmetry relative amount of 5 % was set for the winding coil in a certain socket, the test method was similar to the method shown in the Sect. 22.2, and the test results of excitation winding coil asymmetry and cosine winding coil asymmetry are shown in Tables 22.4 and 22.5.

It can be seen from Tables 22.4 and 22.5—when the excitation or output winding coils were asymmetric, although there also emerged the errors of position calculation, yet the calculation errors of distributed winding structure were significantly less than that of concentrated winding structures. Due to the increase in stator sockets, the proportion of winding coils showing asymmetry accounting for the whole set of winding coils were significantly reduced, so the errors were also reduced. However, after the distributed winding structure was adopted, the sine and cosine distribution laws of output windings would bring some rounding errors.

22.5 Conclusion

This paper mainly discussed the measurement of error analysis and compensation of low-pole-pair-number reluctance RVDT, analyzed the 1-pole-pair RVDT excitation winding and the output winding structure, and established the RVDT electromagnetic relation model. It also analyzed in detail the impact of excitation winding coil or output winding coil asymmetry on the measurement accuracy of concentrated winding structure RVDTs. The author improved the concentrated winding structure into the distributed winding structure, and reduced the measurement errors by 4° through the rational selection of parameters, so as to meet the detection requirements of airborne servo motor rotor positions.

Acknowledgments The author would like to state his great appreciation to the Teaching Reform and Research Projects of Xi'an University of Science and Technology, which the foundation number is JG10069. This work was also supported by the National Natural Science Foundation of China (Nos. 51307137 and 51207129). The authors would also like to thank the anonymous reviewers for their valuable comments and suggestions to improve the quality and readability of the paper.

References

1. Li SJ, Zhou QX, Lu G (2007) Digital calibration and compensation for angle measure system based on resolver-RDC. Small Spec Electr Mach 35(6):26–28 (in Chinese)
2. Zhao J, Liu YJ, Wan SY (2004) Research on PMSM drive technology based on resolver. Power Electron 38(1):10–12 (in Chinese)
3. Bose K (1992) Rotor position estimation scheme of a permanent magnet synchronous machine for high performance variable speed drive. IEEE IAS 1:48–53
4. Nirei YK et al (2002) Angular error analysis of an 8X-VR resolver with an eccentric rotor. J Magn Magn Mater 24(2–5):1202–1205
5. Tommaso AO, Miceli R (2003) A new high accuracy software based resolver-to-digital converter. In: The 29th annual conference of the IEEE industrial electronics society, vol 3. pp 2435–2440
6. Alhamadi MA, Benammar M, Ben-brahim L (2004) Precise method for linearizing sine and cosine signals in resolvers and quadrature encoders applications. In: IECON 2004—30th annual conference of IEEE industrial electronics society. pp 1935–1940
7. Zhao H, Zou JW, Li TC (2002) A novel angle measuring method in resolver mode. Chin J Sci Instrum 23(3):68–69 (in Chinese)

Chapter 23
Design of Control System of Airborne Redundant Generators Based on CAN-Bus

Qixun Zhou, Yufeng Zhang, Yong Zhou and Dengxiu Yu

Abstract In order to enhance the reliability of airborne generating units, this paper designed a control system of quad-redundant generators based on CAN-bus communication network. A control strategy for the multi-DSC control network of four Brushless DC Motors is presented. The hardware platform of this structure is composed of host-computer, master-controller, and slave-controllers. On this platform every generator could be driven independently via the CAN-bus communication network. Using this system, the control structure of generators could be simplified and the speed of communication could be improved. After analyzing the process of redundant control strategy, the flowchart program of this system is given. At the end of this paper, the experiment results verify that the control system of 30 kW generators is reliable, the control strategy is rational, and the system has better dynamic response.

Keywords Airborne generators · Redundant · BLDCM · CAN-bus communication

23.1 Introduction

The safety and reliability of airborne generators are very important in the field of aerospace. The control system of airborne generator is a complex system; it consists of aerodynamics, kinematic of machinery, fuel system, air-fuel mixture system, and so on [1]. Because of the complexity of the generator system, it is difficult to ensure the reliability of system in traditional control structure [2–6]. To enhance the reliability of system and to ensure the safety of load, this paper

Q. Zhou (✉) · Y. Zhang · Y. Zhou · D. Yu
Department of Electrical and Control Engineering, Xi'an University of Science and Technology, Xi'an, China
e-mail: zhouqixun029@163.com

J. Wang (ed.), *Proceedings of the First Symposium on Aviation Maintenance and Management-Volume I*, Lecture Notes in Electrical Engineering 296,
DOI: 10.1007/978-3-642-54236-7_23,

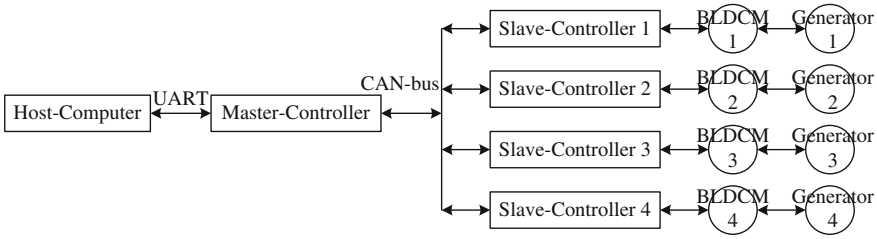

Fig. 23.1 Control structure of quad-redundant system

designed a quad-redundant system for controlling the airborne generators. This system depends on the CAN-bus to realize the function of communication network. Using this system, the control structure of generators could be simplified and the speed of communication could be improved.

23.2 Design of Redundant System

The entire system consists of one host-computer, one master-controller, four slave-controllers, four Brushless DC Motors (BLDCM), and four generators. We use the PC as the host-computer; it monitors and administers every controller. The master-controller connects the host-computer to the CAN-bus and realizes the function of communication.

The DSC in the slave-controller receives and sends the relative data, meanwhile controls the speed and rotor position of the corresponding motor. BLDCM controls the electromagnetic valve, and makes the generator to change its power generation automatically according to the request of load. The control structure is shown in Fig. 23.1.

23.2.1 Communication Network of Master-Controller

As the link between host-computer and slave-controllers, the master-controller has two functions mainly. First, it receives the command from the host-computer, and sends them to different slave-controllers respectively. Second, the master-controller receives the real-time data of motor from the slave-controllers, such as motor speed and rotor position, and sends them to the host-computer as the feedback. In this quad-redundant generator control system, the DSC in master-controller is dsPIC30F4011. This DSC consists of CAN module, high-speed Analog-to-Digital Converter (ADC) module with 10-bit, Universal Asynchronous Receiver Transmitter (UART) module, and so on. To avoid the external

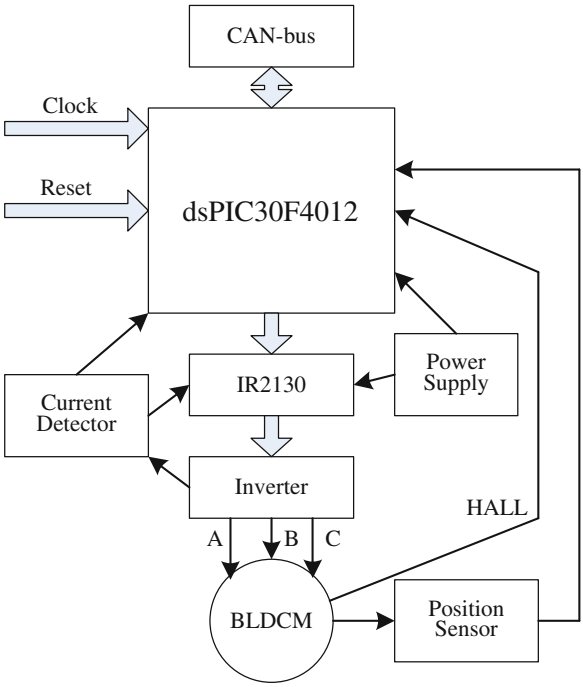

Fig. 23.2 Schematic diagram of slave-controller

disturbance, this system uses the UART as the communication method between host-computer and master-controller.

In this paper, the communication data between master-controller and slave-controller includes motor speed and rotor position. The requirements of this part are as follows. First, the system needs multipoint communication; second, the communication distance is not more than 1 m; third, the system needs good real-time performance. Because of the CAN-bus contains advanced technique and unique design, it has many advantages, such as high reliability, excellent real-time performance, and flexibility. So, the CAN-bus is used in this control system.

23.2.2 Design of Slave-Controller

The DSC in slave-controller is dsPIC30F4012, it has the modified Harvard architecture and DSP engine features. Because of its high performance in computation, the dsPIC30F4012 became one of the best solutions for the motor control systems. The schematic diagram of the slave-controller designed in this paper is shown in Fig. 23.2. The controller includes clock circuit, reset circuit, voltage regulator circuit, and drive circuit mainly.

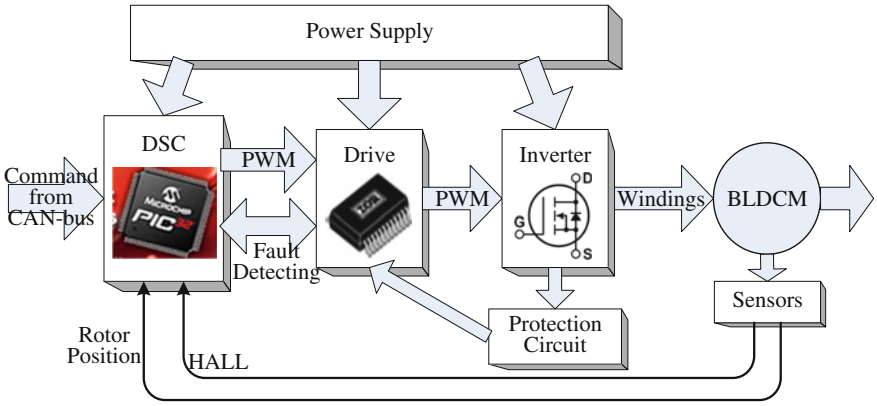

Fig. 23.3 Control structure of slave-controller

The dsPIC30F4012 receives command via the CAN-bus and receives the feedback data of BLDCM via sensors. Then, the dsPIC30F4012 converts analog feedback into digital signal via its internal 10-bit ADC. Compared the command with the digital signal of feedback, the dsPIC30F4012 computes the difference, and then enables the internal PWM module. The PWM signal can be amplified via the drive unit IR2130. The amplified PWM signal controls the voltage of motor windings via the inverter, and then the motor speed and rotor position could be regulated precisely. To enhance the reliability of inverter, the protection circuit of over current is designed. If the over current occurred, the IR2130 will send a signal named "FAULT" to dsPIC30F4012 to terminate the output of PWM. The control structure is shown in Fig. 23.3.

23.3 Design of CAN-MESSAGE

The CAN-bus is a serial communication protocol which efficiently supports distributed real-time control with a very high level of security. Information on the bus is sent in fixed format messages of different but limited length. When the bus is free any connected unit may start to transmit a new message. Message transfer is manifested and controlled by four different frame types, they are as follows [7].

23.3.1 Data Frame

A data frame is composed of seven different bit fields: start of frame, arbitration field, control field, data field, CRC field, ACK field, and end of frame. The data field can be of length zero. There are two different formats which differ in the

length of the identifier field: frames with the number of 11 bit identifier are denoted as Standard Frames; in contrast, frames containing 29 bit identifier are denoted as Extended Frames.

23.3.2 Remote Frame

A station acting as a receiver for certain data can initiate the transmission of the respective data by its source node by sending a remote frame. A remote frame exists in both standard format and extended format. In both cases it is composed of six different bit fields: start of frame, arbitration field, control field, CRC field, ACK field, end of frame.

23.3.3 Error Frame

The error frame consists of two different fields. The first field is given by the superposition of error flags contributed from different stations. The following second field is the error delimiter. There are two forms of an error flag: an active error flag and a passive error flag. The active error flag consists of six consecutive "dominant" bits. The passive error flag consists of six consecutive "recessive" bits unless it is overwritten by "dominant" bits from other nodes.

23.3.4 Overload Frame

The overload frame contains the two bit fields: overload flag and overload delimiter. Overload flag consists of six "dominant" bits. The overall form corresponds to that of the active error flag. The overload flag's form destroys the fixed form of the intermission field. As a consequence, all other stations also detect an overload condition and on their part start transmission of an overload flag. In case that there is a "dominant" bit detected during the third bit of intermission then it will interpret this bit as start of frame. Overload delimiter consists of eight "recessive" bits. The overload delimiter is of the same form as the error delimiter.

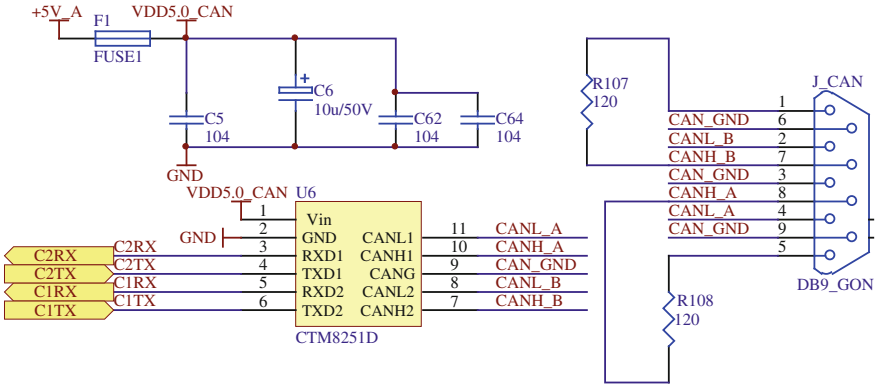

Fig. 23.4 Circuit diagram of CAN-bus

23.4 Design of CAN-Bus Network

23.4.1 Design of Hardware

The hardware unit of CAN-bus communication network designed in this paper is composed of three components: the MCU, the independent CAN-bus controller MCP2515, and the CAN transceiver PCA82C250. The schematic diagram of CAN-bus connection is shown in Fig. 23.8. To enhance the immunity of CAN-bus node to interference and to realize the electric isolation between every CAN-bus node, the pins TXCAN and RXCAN of MCP2515 connect to PCA82C250 via the high-speed optical coupler 6N137 instead of direct connection.

To enhance the reliability of communication, some other protections are taken. (1) To avoid the shock of over current, the pins CANH and CANL of PCA82C250 are connected to CAN-bus via a resistance. (2) To filter the high frequency interference on the bus and to enhance the electromagnetic compatibility, the pins CANH and CANL are connected with two capacitances paralleled. (3) To avoid the instantaneous high voltage, the lightning proof is connected to the CAN-bus. The circuit diagram is shown in Fig. 23.4.

23.4.2 Design of Control Strategy

The CAN-bus connects the master-controller and all four slave-controllers. The interrupt mode is applied in the receiving process of the CAN unit in master-controller. This CAN unit receives data of motor speed and position which come from every slave-controller. The dsPIC30F4011 saves all these data to a particular array which named RX. And then, according to the different identifier and

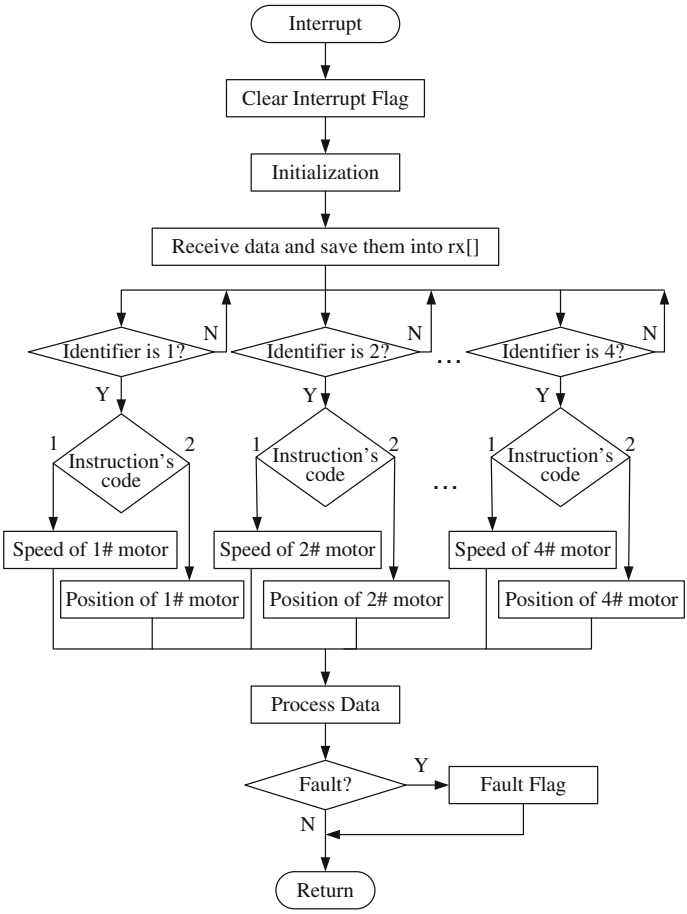

Fig. 23.5 Control strategy in master-controller

instruction's code, this DSC will compute and process these data respectively. And the system confirms that the send buffer is not full at first, and writes the identifier and outgoing message into this buffer. According to the different requirements, every slave-controller receives its own message. The flow chart of control strategy of master-controller is shown in Fig. 23.5.

In the slave-controller, the subprogram of CAN-bus is also set in an interrupted function call. Every slave-controller has its own unique node identifier. The controller only receives the specific data pack which the identifier corresponds with the controller's identifier. And then the controller processes these data according to their instructions' codes. The flow chart of control strategy of slave-controller is shown in Fig. 23.6.

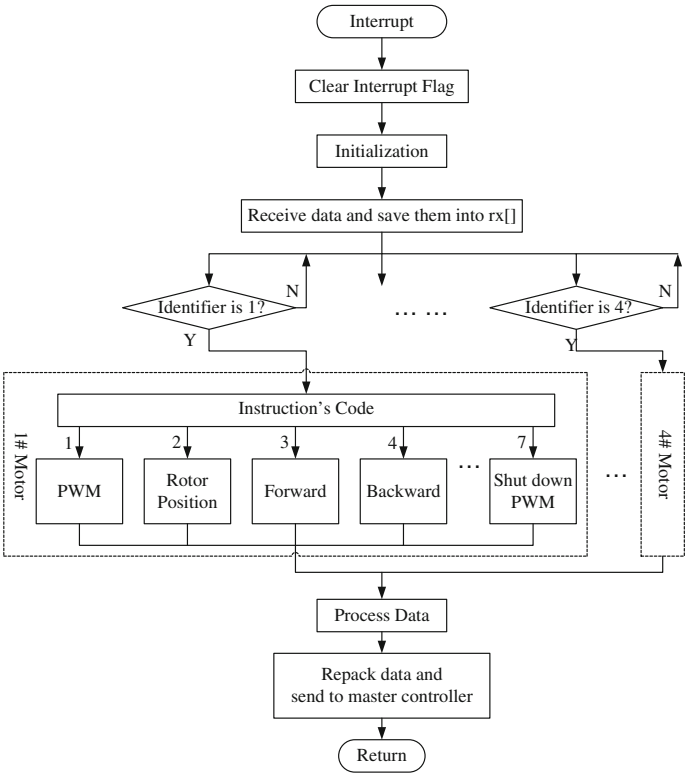

Fig. 23.6 Control strategy in slave-controller

23.5 Experiments

The composing of actual control system is shown in Fig. 23.7. The actual system consists of one master-controller and four slave-controllers.

To verify the real-time performance and synchronization of the quad-redundant system designed in this paper, the following experiments are taken. First, under the control of this quad-redundant system, we make generators operate steadily without load. At this state, the speed command of BLDCMs is 1750 rpm. Then, we add the full load of which the power is 30 kW on the generators instantaneously. To meet the requirement of generators, the speed command of BLDCMs jumps to 2500 rpm. After around 3 s, the system is resumed to the state of no-load manually.

The response characteristic of this quad-redundant system is shown in Table 23.1 and Fig. 23.8.

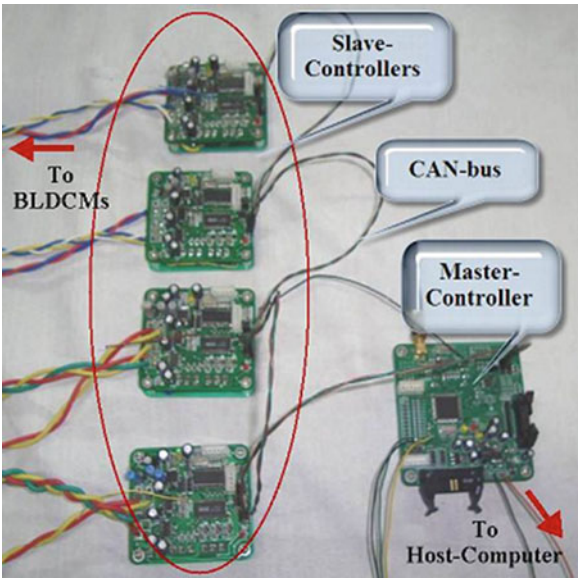

Fig. 23.7 Composing of actual control system

Table 23.1 Experiments of on-loading and off-loading

Motors	Time from no-load to full load (s)	Time from full load to no-load (s)
NO.1	0.623	0.325
NO.2	0.583	0.350
NO.3	0.626	0.306
NO.4	0.603	0.386

The experiments results verified:

1 With this quad-redundant control system, the generators have favorable response performance, whether at the steady state or at the dynamic state.
2 When the load changed, some small amplitude variation comes out at the output voltage of generators. But with the regulation of control strategy, the output could resume the steady state rapidly.
3 The quad-redundant generators implement the structure of parallel connection, so the system has good fault-tolerant capability. Furthermore, the system implements the function of uninterrupted power supply, so the reliability could be enhanced markedly.

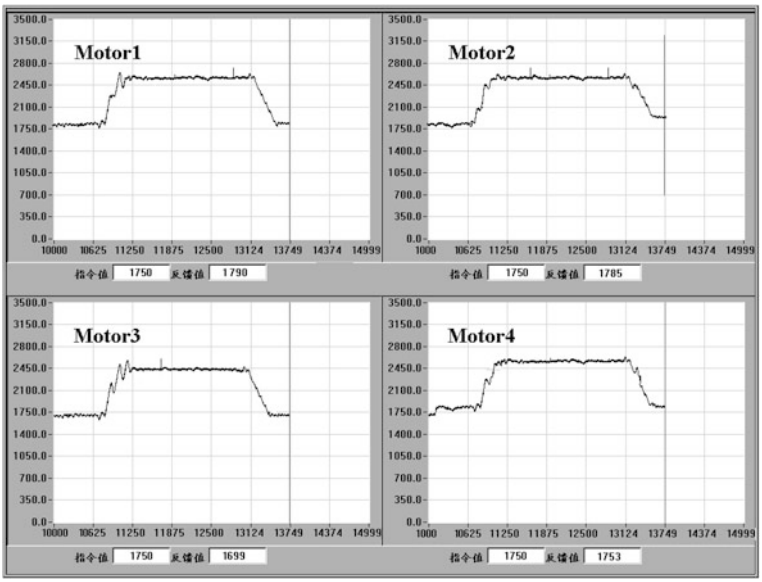

Fig. 23.8 Response curves of four motors

23.6 Conclusion

To enhance the reliability of generators system, and to make sure the data transmits fast and steadily, a quad-redundant control system which is based on CAN-bus communication network is developed in this paper. The hardware platform of this control system is composed of a master-controller and four slave-controllers, on this platform every branch generator could be controlled independently via the relative BLDCM.

Compared with traditional redundant control system, this system has some outstanding advantages, such as high real-time performance, high reliability, and predominant expandability. The experiment results verified that this quad-redundant system is reliable, the control strategy is rational, and the generators applied this control system has better dynamic response and higher reliability.

Acknowledgments The author would like to state his great appreciation to the Teaching Reform and Research Projects of Xi'an University of Science and Technology, of which the foundation number is JG10069. This work was also supported by the National Natural Science Foundation of China (Nos. 51307137 and 51207129). The authors would also like to thank the anonymous reviewers for their valuable comments and suggestions to improve the quality and readability of the paper.

References

1. Sun ZH, Zhang B, Cheng L, Zhang WJ (2011) Application of the redundant servomotor approach to design of path generator with dynamic performance improvement. Mech Mach Theory 46:1784–1795 (in Chinese)
2. Liu MM, Zhou YJ (2008) The reliability prediction of an electro-mechanical actuator of aircraft with the hybrid redundant structure. In: IEEE vehicle power and propulsion conference, pp 1–5
3. Bertacchini A, Pavan P, Tamagnini L, Mistrorigo M, Morandi M (2006) Hardware-in-the-loop approach for redundant brushless motor control system. In: 32nd annual conference on IEEE industrial electronics, pp 4054–4059
4. Jaison H, Anas SR, Gopinath A, Subathra MSP (2011) A dual redundancy technique for electromechanical actuation system applied to launch vehicles. In: International conference on emerging trends in electrical and computer technology, pp 352–357
5. Wang N, Zhou YJ (2009) Research on reliability of a hybrid three-redundant electro-mechanical actuator. In: International conference on mechatronics and automation, pp 1066–1070
6. Zhou QX, Li SJ, Lu G, Zhou Y (2009) Crossed-feedback control of dual-redundancy permanent magnetic brushless dc servo system used in electro-hydrostatic actuator. In: International conference on electrical machines and systems, pp 1237–1241
7. Robert BG (1991) CAN specification version 2.0. Berlin, pp 85–112

Chapter 24
Improvement of the Cooling System in the Aero-Oxygen Plant

Lijun Xie, Dexin Wang, Hongqiang Zhao and Feng Yan

Abstract The flowing resistance of the cooling system is increased using ground cooling water in the aero-oxygen plant. It gets running failure about the signal device of rate-water flow that is in the ZL2.8/194 model regenerative refrigerator. The reason of running failure is analyzed in this paper. The improvement method and the observation noticed are given.

Keywords Aero-oxygen plant · Cooling system · Improvement

24.1 Introduction

The aero-oxygen plant can run normally using the closed cooling water cycle system in any fieldwork. That is set on truck providing much mobility. The cooling effect of the closed cycle system is not fine. It brings the power consumption to

Xie Lijun, associate professor, engaged in teaching and research about the technical support and equipments for aviation depot. Wang Dexin, associate professor, engaged in teaching management and research about the aviation technical support and equipments. Zhao Hongqiang, Yan Feng, instructor, engaged in teaching management and research about the aviation technical support and equipments.

L. Xie (✉) · D. Wang · H. Zhao · F. Yan
Qingdao Branch, Naval Academy of Aeronautical Engineering, Qingdao 266041, China
e-mail: lijunxieqd@sina.com; XieLijun@Springer.com

D. Wang
e-mail: WangDexin@Springer.com

H. Zhao
e-mail: ZhaoHongqiang@Springer.com

F. Yan
e-mail: YanFeng@Springer.com

J. Wang (ed.), *Proceedings of the First Symposium on Aviation Maintenance and Management-Volume I*, Lecture Notes in Electrical Engineering 296,
DOI: 10.1007/978-3-642-54236-7_24,

increase, and gets the output of air separation to fall. The ground cistern is built to normally run the oxygen plant in the workroom, when the weather is torridity summertime or at high temperatures. Because the cooling water pipeline coming into or out is disposed without reason, the flowing resistance of cooling system is increased to result in running failure of the signal device of rate-water flow that is in the ZL2.8/194 model regenerative refrigerator. The reason of running failure is analyzed, and the improvement method is given.

24.2 Analyzing the Reason About Running Failure of the Signal Device of Rate-Water Flow

The closed cooling water cycle system of the aero-oxygen plant is shown in Fig. 24.1 [1]. For convenience analyzing, the object researched is taken, that is, the section *A–A* of out-water pipe (input-water pipe of heat radiator) of the heat exchanger, and the section *B–B* of input-water pipe (out-water pipe of heat radiator) of the water pump. The out-water pressure of the signal device of rate-water flow is affected by the hydraulic pressure in the section *A–A*. The head water tank is located in the water pipe import of the outer water pump. The hydraulic pressure in the section *B–B* equals to approximately the water pressure head in the head water tank at high location. The pipe diameter is almost equal for the section *A–A* and the section *B–B*, and their height is also approximately the same. Based on the Law of Conservation of Energy, the hydraulic pressure $P_{A\text{-}A}$ can be got in the section *A–A* of the cooling system closed cycle.

When the cooling system closed cycle is connected with the ground cistern, the cooling system is changed to opening cycle. The cooling water is imported from the heat radiator to the ground cistern. The hydraulic pressure P^*_{A-A} can also be got in the section *A–A* of cooling system opened cycle. By all appearances, $P^*_{A-A} > P_{A-A}$. The flowing resistance of cooling system opened cycle is shown to be increasing.

The signal device of rate-water flow (shown Fig. 24.2) is fixed on the drainpipe of the cooler of regenerative refrigerator [1]. The limit switch is connected in series to the operation electro-circuit of regenerative refrigerator. It is used to detect cooling water flow for the running safety of regenerative refrigerator. It works based on Bernoulli's Theorem.

Let Z_1, P_1 and u_1 be the height, the pressure and the velocity of the station before cooling water is coming out of the nozzle. Z_2, P_2 and u_2 be the height, the pressure and the velocity of the station when cooling water is coming out of the nozzle. Z_3, P_3 and u_3 be the height, the pressure and the velocity of the station when cooling water is coming out of the divergent diffuser. After the loss h_{fD} is considered, when cooling water is getting across the nozzle inducer, and the frictional loss of the other place is ignored, based on Bernoulli Equation, [2] we have

$$z_1 + \frac{p_1}{\gamma} + \frac{u_1^2}{2g} = z_2 + \frac{p_2}{\gamma} + \frac{u_2^2}{2g} + h_{\mathrm{fD}} = z_3 + \frac{p_3}{\gamma} + \frac{u_3^2}{2g} + h_{\mathrm{fD}} \tag{24.1}$$

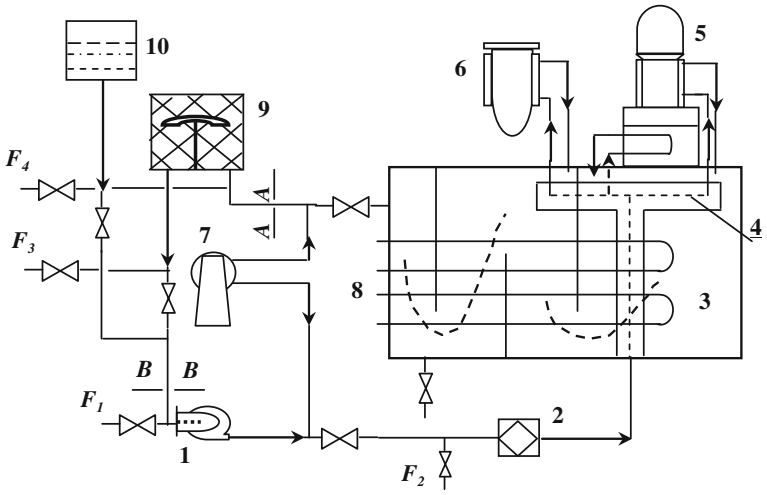

Fig. 24.1 The cooling water cycle system of the aero-oxygen plant. *1* water pump, *2* water filter, *3* water tank, *4* water distribution pipe, *5* regenerative refrigerator, *6* dryer, *7* air compressor, *8* air compressed colder, *9* heat radiator, *10* water tank at high location; F_1 giving water valve of water pump in oxygen plant, F_2 giving water valve of water pump on ground, F_3 wet-pit valve giving water to ground cistern before improvement, F_4 wet-pit valve giving water to ground cistern after improvement

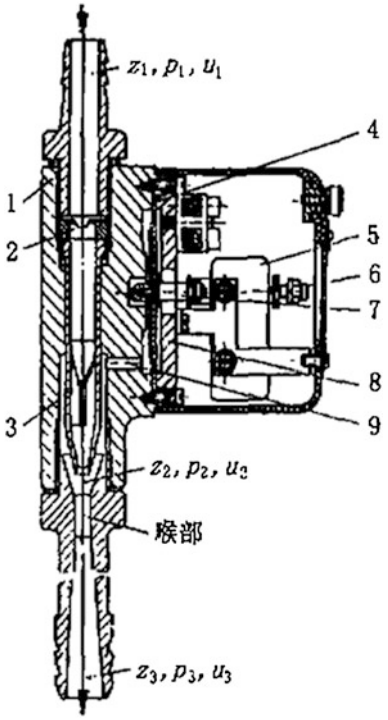

Fig. 24.2 The signal device of rate-water flow. *1* pump body, *2* nozzle, *3* inducer, *4* rubber film, *5* limit switch, *6* adjusting screw, *7* coupling screw, *8* hold-down plate, *9* channel of negative pressure cavity, *10* throat

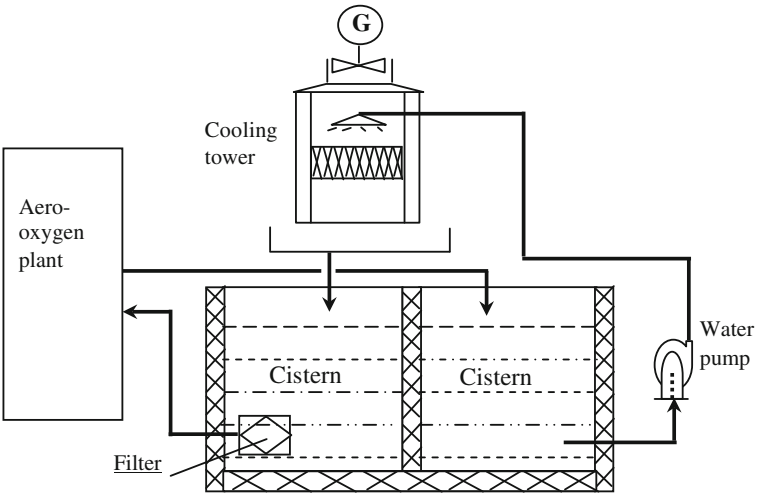

Fig. 24.3 The pipeline disposal of the cooling system using the cooling tower

Because the height difference can be ignored among Z_1, Z_2 and Z_3 in the signal device of rate-water flow, Eq. (24.1) can be predigested as follows.

$$\frac{p_1}{\gamma}+\frac{u_1^2}{2g}=\frac{p_2}{\gamma}+\frac{u_2^2}{2g}+h_{\mathrm{fD}}=\frac{p_3}{\gamma}+\frac{u_3^2}{2g}+h_{\mathrm{fD}} \tag{24.2}$$

It is descried from Eq. (24.2) that u_2 up and P_2 down go with the reducing section when cooling water passes through the signal device of rate-water flow.

When P_2 gets below the environmental atmospheric pressure, the cavity around the nozzle is formed district of negative pressure, and the elastic force of spring is conquered by the rubber sheet for moving the lever inside. If flow of the cooling water comes down to less than 0.8 m^3/h, namely, u_2 up and P_2 down, enough of district negative pressure can not be formed resulting in opening of the limit switch, and the regenerative refrigerator cannot start-up or automatic stop run. If the flowing resistance of the cooling system is increased, namely, P_3 up, P_3–P_2 is increased to bring vortex on the water seal of the divergent diffuser laryngeal to P_2 up [2]. P_2 can not come down even if the cooling water flow is increased. The limit switch can not be closed, and the regenerative refrigerator could not start-up. This is the reason why the signal device of rate-water flow runs failure when using ground cooling water.

If the signal device of rate-water flow is adjusted getting out of line to put the regenerative refrigerator start-up, the safety control function would be lost about the signal device of rate-water flow, some times, the regenerative refrigerator would be burnt out.

24.3 Improvement the Cooling System Using the Ground Cooling Water

The cooling system opened cycle has two methods, namely using the ground cistern and the cooling tower.

The flowing resistance of the heat radiator in oxygen plant is greater. The heat radiator in the aero-oxygen plant is not used to falling flowing resistance. This method is that *ZG*1½ three-way valve is fixed and formerly three-way valve is removed before the pipe of heat radiator under the aero-oxygen plant chassis. The cutoff valve is used to control at the exit of the new three-way valve. The cooling water in the cooling system is gone into the ground cistern by the new valve (shown Fig. 24.1). If the cooling system closed cycle need to be used, the cutoff valve would be closed up. The 2″ galvanized steel pipe should be used to coming into or out the cooling water that is from the aero-oxygen plant to the ground cistern. Its length should be brief and bends should be lessended. The pipe mouth can not be higher than the water level. The water level of the ground cistern must be higher than the water inlet of the ground water pump. If the water pump of the aero-oxygen plant is used, the water level of the ground cistern must be higher than 1.6 m than the height of the aero-oxygen plant over ground.

The cooling method using the ground cistern is spontaneous elimination of heat to the atmospheric environment with the cooling water in the ground cistern. Its power consumption is fewer and impoundment in the ground cistern is more. Based on the count and experience, the water-surface acreage must be bigger than 30 m^2 in order to spontaneously eliminate heat to the atmospheric environment.

The cooling method using the cooling tower is forced-cooling by cooling water, meeting the heat-transfer medium fully. Its cooling efficiency is on a higher level and impoundment in the ground cistern is less. The cooling system using the cooling tower is composed of the heat cistern and the cold cistern. Its pipeline disposal is shown in Fig. 24.3.

The infra-cement wall of two cisterns are connected with ϕ 50 mm pipe for the water level equality. The two cycles are built using two water pumps to give water. The water pump flow giving water to the cooling tower must not be fewer than the water pump flow giving water to the cooling system, in order to avoid water in the heat cistern going directly into the cold cistern. After the evaporation and the leakage losses are considered, the primary impoundment in the ground cistern is well about 4–5 ton.

When the cooling system opened cycle is used, the following should be noticed: (1) Keep the cooling water clean and of quality. The cooling water is sometimes softened, cleaned and sterilized. (2) The pipe inlet of water pump is more than 30 cm over the cistern bottom. The water filter must be fixed for avoiding some dirt in the cistern to be breathed into the cooling system. (3) Before the aero-oxygen plant operated, the water filter in the oxygen plant must be cleaned to keep water pipeline unobstructed.

References

1. (2006) Hangzhou oxygen plant manufactory: KL-15 model aero-oxygen plant installation. Hangzhou Oxygen Plant Factory, pp 1–3, 7–12
2. Douglas J.F., Gasiorek, JM (2001) Fluid mechanics. Pearson Education Limited, pp 22–55, 167–180

Chapter 25
Study on the Condition Monitoring System of Certain Type of Turboshaft Engine Based on Flight Data

Haibin Yu, Huguo Sun, Ling Yan and Kai Zhang

Abstract The study of the condition monitoring system was the basis of the condition based maintenance which is the mode adopted by the advanced aero-engine. Referring to the work and maintenance features of a certain type of turboshaft engine, the engine condition monitoring system based on flight data has put forward the function, structure, and monitoring methods. It has been shown that the system is very effective and reliable to analyze the state of the engine health and locate the faults.

Keywords Turboshaft · Flight data · Condition monitoring

25.1 Introduction

At present, the in-service military aero-engine in our country mainly adopts scheduled maintenance mode, which is simple and needs to disassemble, inspect, overhaul, or replace the engine and its accessories regularly. But the maintenance is work-consuming, uneconomical and less pertinent and cannot monitor all the time when the engine will break down [1]. One of the efficient ways to solve the problem is to maintain the engine and predict the faults according to the engine's status information to realize the on-condition maintenance. The on-condition maintenance requires making continuous or periodical monitoring to the parameters of the engine technical status to judge its health state and to decide whether to dissemble, inspect, overhaul, or replace the engine and its accessories. The mode can reflect the engine's status to make the maintenance more pertinent, economical, and reliable. The monitoring of the engine's condition is the key to the

H. Yu (✉) · H. Sun · L. Yan · K. Zhang
Department of Aviation Machinery, Qingdao Branch of Naval Aviation Engineering Institute, Qingdao, China
e-mail: yuhaibin1001@hotmail.com

J. Wang (ed.), *Proceedings of the First Symposium on Aviation Maintenance and Management-Volume I*, Lecture Notes in Electrical Engineering 296,
DOI: 10.1007/978-3-642-54236-7_25,

on-condition maintenance and an effective way to improve the maintenance efficiency and to lower the cost [2].

Airborne flight parameter system provides an important objective basis for aircraft maintenance, flight training quality evaluation, and accident investigation analysis, and enhances greatly informationized level of the aviation equipment. The flight parameters system of some type of helicopter recorded 36 kinds of information altogether (16 analog variables and 20 switching variables), half of which are related with engine. The working data of the engine provide the basis to evaluate the engine's status objectively and to monitor the engine. Based on flight parameters, aero-engine condition monitoring technology provides various engine information, hidden in a great deal of flight data, get effective utilization and provide scientific basis and method for the study on the faults and life [3].

In this paper, two power turbine engines of some type of helicopter are taken as the research object. A condition monitoring system of some type of turboshaft engine based on flight data has been developed, on the basis of Window XP SP3 as a platform, and used Access as database and VC++ 6.0 as development tool.

25.2 Major Functions and Structure

25.2.1 System Functions

The condition monitoring system of some type of turboshaft engine analyzes the technical state of the whole engine, its parts, and working system by using engine parameters from flight data (e.g., temperature, pressure, rotor speed, and the parameters of related working systems), and isolates the faults into the whole engine, parts, or related working systems. On one hand, the system can monitor the working status of the engine and give warning to the maintenance personnel; on the other hand, it can assess the engine's health state, diagnose the fault type and locate its position to provide basis to use and maintain the engine. On the basis of analyzing deeply the working system and flight data system of some free power turbine engine, and according to the needs of the outfield maintenance reform, the condition monitoring system of some turboshaft engine based on flight data expands the following functions except the monitoring function (over-limit monitoring mostly) the original flight data system has:

(1) Define the engine's operation state

The system should have the ability to define the engine's "operation state" parameters in any case, including checking the performance parameters of the whole engine and its working system. Only when the parameters of the whole engine and its working system are confirmed to be normal, can the engine be used to ensure the safety and reliability of the engine. If some parameters of the engine and its working system are abnormal, the system can quickly find them, thus providing guidance for the maintenance personnel to analyze and solve the faults quickly.

(2) Predict the performance trend
According to the known historical parameter data, the future performance trend can be predicted and assessed, and the performance trend diagram can be depicted. According to trend diagram, the maintenance personnel can analyze the engine's health state and locate the possible faults to judge the engine's utilization status and to know the performance degeneration degree by comparing the performance in different times and by making order of the engine performance. The engines with poor performances are monitored with attention to prevent the engine performance from deteriorating quickly by taking pertinent maintenance measures.

(3) Monitor life
Because the proportion of the different working status to total life is different in the life control of some type of engine, the system can define the working time of the engine in different working status, according to the flight data and the algorithm provided by the manufacturer in order to control the engine life. For example, the proportion of the time of the rated status to the whole life should be less than 22.5 %, the time of the take-off status (continuous working time is less than 6 min) to the whole life should be less than 5 %, and the time of the take-off status (continuous working time is 6–15 min) to the whole life should be less than 1.25 %.

25.2.2 System Structure

The engine condition monitoring system, with the functions of data collection, treatment, and analysis combined together, is the comprehensive system to monitor the health state of every part of the engine and their working system and to isolate the faults. The system adopts the structuralized and modularized development method, as is shown in Fig. 25.1. The whole system can be divided into the following functional modules: flight parameter input module, data treatment module, criterion editor and expert rule bank module, data recording module, result output module, and data configuration management module.

The flight data input module inputs the flight data into the system and then decodes the data, and filters out the data information which the engine condition monitoring needs. After filtering, all the parameter information is listed in Table 25.1, among which there are 18 kinds of analog variables and 20 kinds of switching variables. In addition, the use and maintenance information needs to be collected to build up the basic and maintenance information bank. These two kinds of information data are the basis of the engine condition monitoring and data treatment module.

The extracted flight data of the engine are treated by the engine condition monitor algorithm in the data treatment module. The criterion editor module can edit new criterion according to new expert rules to enrich and perfect the auto-reading capability of the system. So the status assessment, performance trend

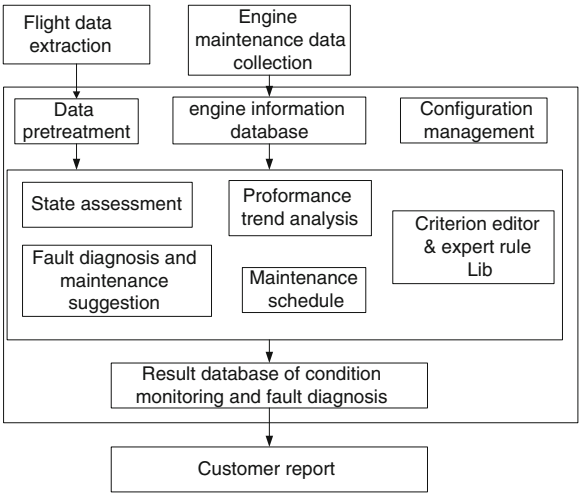

Fig. 25.1 The condition monitoring system structure of a turboshaft engine based on flight data

analysis, fault diagnosis, and maintenance suggestion and schedule can be obtained and all the treatment results are saved in Access database.

According to the recorded information in engine information database and the monitoring result database, the result output module can display the monitoring results in time, and can provide the engine monitoring report and maintenance suggestion in the form of report, even including the complete set of technical file since the use of the engine.

25.3 Condition Monitoring Algorithm

25.3.1 Monitoring Parameter Selection

The working status of the engine is shown by the parameters which can characterize the engine state. The number of the measured parameters reflect the degree to know the working status of the engine. Whether the monitoring parameter selection is reasonable or not greatly influences the accuracy of the system diagnosis and the complication of the system. Usually the more there are monitoring parameters, the more powerful the monitoring and diagnosis function and the ability to characterize the faults are, the more accurate the diagnosis is, so it is very important to select the measured parameters and the performance parameters to characterize the faults. The monitored parameters are limited because of restriction of the number of the sensors and measurement technology. One of the selection principles is that the parameters are sensitive to the change of the engine state, and the other is that the parameters are less correlative as possible. The major

Table 25.1 Some flight data of a turboshaft engine

No.	Analog variable	Measurement range	Sampling frequency	No.	Switching variable	Sampling frequency
1	Altitude (pressure ALT and radio ALT)	0–300	2	1	Clogging of the left engine fuel filter	4
2	Airspeed	50–300	2	2	Left engine stop switch at "off" position	4
3	Barametric temperature	−50 to +50	2	3	Left engine fire switch at "off"position	4
4	Outlet compressor pressure of the left engine	0–10	3	4	Left engine power turbine overspeed	4
5	Gas temperature at power turbine inlet of the left engine	0–1100	2	5	Left engine emergency	4
6	Gas generator speed of the left engine	0–110	1	6	left engine lower oil pressure	4
7	Rotor speed	0–110	1	7	Metal crumbles in left engine oil	4
8	Left fuel in main tank	125–2662	2	8	reducer lower oil pressure	4
9	Vibration of the left engine	0–100	4	9	reducer oil limited temperature	4
10	Collective pitch position	0–35°40′	4	10	Metal crumbles in reducer oil	4
11	Left engine power lever position	0–120	2	11	icing	4
12	Outlet oil temperature of left engine	−50 to +150	1	12	Fire at left engine	4
	…				…	

monitored parameters and its number system extracts and filters from flight data are listed in Table 25.1. These parameters can satisfy basically the needs to monitor this type of engine.

25.3.2 Data Pretreatment

The flight parameters are saved in time sequence. It reflects the working status of engines and information on various flight statuses and is the major basis for the engine condition monitoring, fault diagnosis, prediction, and other series of analysis treatment. Because the original flight parameters have problems of data distortion and different sampling rate of every parameter caused by noise interference, analysis cannot be made directly in the original flight parameter sequence.

The data pretreatment can improve data quality and analysis result and exclude the interference in the data. The steps of pretreatment are data sort-out, data integration, and data conversion [4].

(1) Data sort-out method of the flight parameters. Mark the data effectiveness according to data frame sign, delete isolated points according to the performance parameters of the flight manual and save and treat smoothly the noise data in data segment according to flight daily report table.
(2) Data integration method of the flight parameters.
The parameters with the same features are barometric height and radio height, indication airspeed and true airspeed, etc.; the computed parameter are Mach number and true airspeed, etc.
(3) Data conversion method. Make linear conversion to the original data by the mini-max standardized method and map them into the specific zone in proportion, usually [0.0, 1.0].

25.3.3 Condition Monitoring Method

Aero-engine condition monitoring system is the modern scientific and technological synthesis, which depends on sensitive technology, testing technology, computer technology, engine structure, and thermodynamic performance analysis and a great deal of maintenance tests to develop. The essence of the engine condition monitor is to identify the working status of the engine and to classify its status. Its basic task is to identify engine state, check the performance, capability, and accuracy of the engine and judge the faults according to the running information. There are a lot of research methods for engine condition monitor, for example, the methods based on mathematic model, based on artificial intelligence, based on information integration, etc. At present, most of the systems developed by these methods still stay in the phase of lab research or theoretical research, which have a long way to go to application. Some type of turboshaft engine is introduced from abroad, which lacks the basis of mathematic model. The system monitors this type of engine through setting up assessment criterion on the turboshaft engine performance parameters, adopting parameter comparison, and referring to performance trend analysis of civil aviation. The specific methods are listed as follows:

(1) Establishment of the assessment criterion on the turboshaft engine performance parameters.

In order to compare the performances of the engine in different surroundings, the assessment criteria are established on some turboshaft engine performance parameters. Namely, the conversion equations based on the analogue rule are used to compare the performance parameters by conversing them into the same sea level and standard atmospheric conditions, thus providing basis for the performance parameter assessment [5].

Monitoring on flight data

L eng SN: R eng SN:

Aircraft family: Aircraft SN:

Flight date: Flight No: 1 Airport Pres: 101325 Airport Temp: 27

		IDILE		CURISE II		CRUISE I		RATING		TAKEOFF		EMERGENCY	
NTK Core Speed	L	76.51		91.67		94.15		95.67		97.40		_	
	R	77.51		92.53		95.21		96.29		97.56		_	
Nem Rotor speed	Single	40~55	45.73	88~92	91.39	88~92	85.09	88~92	85.45	87~89	85.58	87~89	_
	Double	55~70	60.18										
Tr Gas Temp	L	<=780	640.00	<=870	747.00	<=910	802.00	<=955	838.00	<=990	873.00	<=990	_
	R	<=780	628.00	<=870	750.00	<=910	816.00	<=955	837.00	<=990	852.00	<=990	_
Tm Oil Temp	L	-40~140	52.07	30~140	96.45	30~140	102.37	30~140	102.37	30~140	103.35	30~140	_
	R	-40~140	42.76	30~140	52.68	30~140	103.27	30~140	100.30	30~140	100.30	30~140	_
Pm Oil Pres	L	>=2	0	3~4	0	3~4	0	3~4	0	3~4	0	3~4	_
	R	>=2	0	3~4	0	3~4	0	3~4	0	3~4	0	3~4	_
Tmpcq Reducer oil Temp		-4~30	0	30~80	0	30~80	0	30~80	0	30~80	0	30~80	_
Pmpcq Reducer oil Pres		>0.5	0	3~4	0	3~4	0	3~4	0	3~4	0	3~4	_

Calculate natural parameter: 1: L 2: R

Oil Temp MAX	107.30	107.24	Time Startup	37	32	Time Accel	4	3	MAX Vib	10.86	18.82
Gas Temp MAX	909.00	883.00	Time cool	86	86	Time Inertia	69	69	Double B-speed		8.81

Fig. 25.2 Parameter comparison table in different working status of a turboshaft engine

(2) Parameter comparison method

The performance parameters of the working status (idle, cruise II, cruise I, rated status, take-off, or emergency) of the turboshaft engine on ground and in flight are computed by certain algorithm to get the conversed values of four key performance parameters in standard atmospheric conditions (gas generator speed NTK, power turbine speed NCT, gas temperature T3, and specific fuel consumption SFC), as is shown in Fig. 25.2.

The conversed values of these performance parameters are compared with the reference values (uninstalled standard specifications). The parameter comparison is used to quickly find the abnormality of the engine. At the same time, the fault can be located according to the expert system because different working status of the engine is controlled by different controllers; at the same time, the same parameters and change trend of two helicopter-borne engines of this type recorded at the same time can be compared. The "operation state" inspection can be realized by these methods and the error caused by flight condition and surroundings can be avoided.

(3) Performance trend analysis

The performance parameters of the engine are the important reference basis to predict engine state and its development trend. The trend analysis is: at first, collect monitored parameter data and record corresponding engine working status and exterior surroundings at the same time; then calculate the conversed values of the monitored parameters, subtract the reference values in this working status from the conversed values to get the deviation of the monitored parameters, and then treat all the differences smoothly; then subtract its original values from the differences of the smooth monitored parameters to get the final deviation

corresponding to the monitored parameters of the engine; at last, draw performance monitor trend diagram according to final differences. The maintenance personnel analyze different change trend of every deviation on the trend diagram and locate the possible fault by referring to the example of the component fault-parameter deviation, which can be obtained according to a great deal of maintenance experiences.

The above engine performance monitoring can only make trend analysis to the known historical data. In order to predict more accurately the change trend of the performance parameters of the engine, the prediction mathematic model of the aero-engine should be established based on the historical data.

25.4 Application Examples and Conclusions

The system has verified more than 50 faults and found 20 faults of this type of engine for maintenance personnel in the past one year. For example, when XX aircraft was flying, the power turbine speed is higher than 102.5 % (102 % normally), the conversed speed of the left gas generator is normal, that of the right gas generator is lower than the normal value by 0.5 %, and the exhaust temperature at the engine combustor outlet and other parameters are normal. The system found all working statuses are normal except rated status. According to the fact that this status is controlled by power turbine speed control system, the expert system specified that the maintenance personnel need readjust bolt #4 of fuel regulator of the right engine. The fault was solved after the maintenance personnel adjusted the screw by two circles counterclockwise. The application of the system shows that the system has the ability to judge accurately the engine abnormality.

Engine monitoring is a systematic, comprehensive and complicated task. The engine monitoring technology can analyze effectively, judge the engine health state, and locate the faults, thus providing reliable and credible reference basis for engine use and maintenance. The effect would be better if it can integrate oil spectral analysis, oil consumption rate monitor, and borescope inspection.

References

1. Jaw LC (2005) Recent advancements in aircraft engine health management (EHM) technologies and recommendations for the next step [R]. In: ASME GT2005-68625
2. Jiang C, Sun Z, Wang X (2009) Critical technologies for aero-engine prognostics and health management systems development (in Chinese). J Aerosp Power 24(11):2589–2593
3. Jiang Z, Liu J, Wen Y, Hu W (2010) Research and design on control system of aero-engine in flight course (in Chinese). Aircr Des 30(4):41–44
4. Liang J, Sun X, Du J (2005) The Research of flight data disposing technique based on data mining (in Chinese). J Proj Rocket Missiles Guidance 25(1):76–79
5. Huang K, Huang J, Ren D (2010) Performance parameter equivalent correction of turboshaft engine (in Chinese). J Aerosp Power 25(9):2036–2039

Chapter 26
Probabilistic Neural Network Application in Fault Diagnosis of Airborne Fire Control System

Caikun Zhang, Qi Feng and Zhaohui Bai

Abstract Aiming at resolving the problem that fault diagnosis model of complex airborne fire control system is difficult to establish, an approach to fault diagnosis is proposed based on Probabilistic Neural Network (PNN). The mechanism of fault diagnosis of the airborne fire control system was analyzed first, and the fault diagnosis model based on PNN was established. Simulation results showed that this model has strong fault identification ability, good generalization ability, and powerful anti-noise ability. Meanwhile, the simulation results demonstrated that the model can meet the needs of practical engineering, and provides a useful reference method for fault diagnosis of airborne fire control system.

Keywords Probabilistic neural network · Fire control system · Fault diagnosis

26.1 Introduction

The traditional fault diagnosis method is expert system [1–3], which is based on the special large knowledge and use this knowledge to solve some practical problems. Although the theory and application of the expert systems has made significant progress, its inherent defect in information processing mechanisms causes many problems, such as the knowledge acquisition, knowledge of vulnerability, poor self-learning ability, low reasoning efficiency, and monotonicity of reasoning, etc. With a strong learning ability, artificial neural network can learn from examples data, and in the form of weights, and threshold values stored in the network.

C. Zhang · Q. Feng (✉)
Department of Electronic Information, Northwestern Polytechnical University, Xi'an 710129 Shanxi, China
e-mail: qifeng@nwpu.edu.cn

Z. Bai
Shenyang Aircraft Design and Research Institute, Shenyang 110035 Liaoning, China

J. Wang (ed.), *Proceedings of the First Symposium on Aviation Maintenance and Management-Volume I*, Lecture Notes in Electrical Engineering 296,
DOI: 10.1007/978-3-642-54236-7_26,

Neural network has wonderful parallel computing, robustness, and so on. The network repeatedly adjusts the weights through learning algorithm in response to the changes of environment. This paper analysis the mechanism of fault diagnosis of the airborne fire control system [4], and uses probabilistic neural network (PNN) [5, 6] to establish fault diagnosis model of airborne fire control system. Simulation results show that the method is reasonable and feasible.

26.2 Fault Diagnosis Mechanism of Airborne Fire Control System

Fault diagnosis is to find source and cause according to the failure symptom information and determine the failure mode. The failure symptom information of airborne fire control system comes from various sensors. These sensors are mainly monitoring parameters of the various components in the system, including voltage, current, pressure, magnetic field, and other parameters, and then system features are extracted from these parameters. By means of fault identification on the basis of diagnosis mechanism, reasonable maintenance decisions scheme are made. The general process of airborne fire control system fault diagnosis is shown in Fig. 26.1.

26.3 Fault Diagnosis Model Based on PNN

The operation essence of PNN is parallel algorithm based on Bayesian minimum risk criterion. When applied in solving classification problems, it is able to use linear learning algorithm to solve the nonlinear problem, while keeping the nonlinear features such as high accuracy characteristics. Therefore, this method is suitable to solve the problem of fault classification and fault diagnosis. Compared with back propagation neural network, its main advantages include:

(1) Fast training speed;
(2) As long as the training sample data number is enough, no matter how complex problems, can guarantee to obtain the optimal solution under the Bayesian criterion;
(3) Only considering the probability characteristics of the sample space, allows increasing the training samples without spend a long time for re-training.

26.3.1 PNN Structure

Generally, PNN is composed of three layers forward network. The first layer is input layer, formed by the source node; the second layer is hidden layer, the number of units by the described problem; the third layer is output layer. The PNN structure is shown in Fig. 26.2.

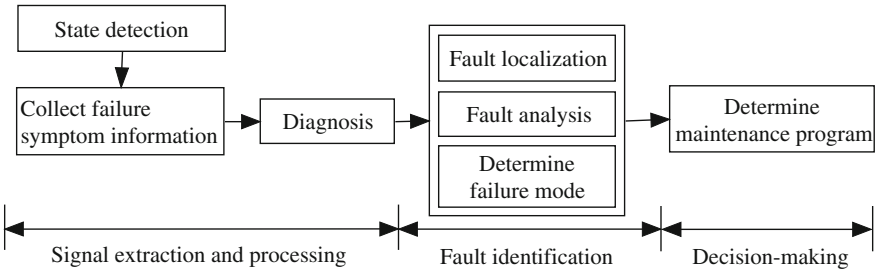

Fig. 26.1 The flow diagram of airborne fire control system fault diagnosis

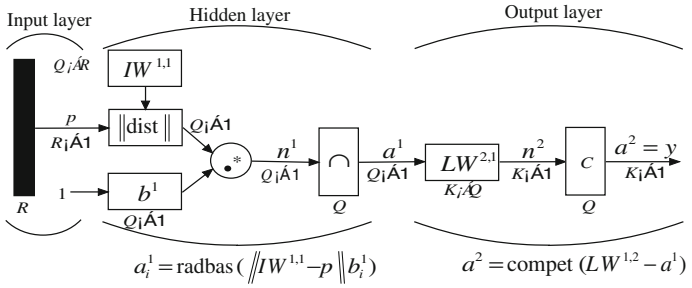

Fig. 26.2 The structure of PNN

In Fig. 26.2, a_i^1 is the ith element of vector a^1; ${}_iIW^{1,1}$ is the ith row vector of the weight matrix $IW^{1,1}$; R is the number of input vector elements; Q is the number of input target samples, i.e., the number of the first layer neurons; K is the number of input vector type, namely, the number of the second layer neurons.

26.3.2 PNN Classification Principle

The input weight matrix $IW^{1,1}$ of the first layer is transposed matrix $\boldsymbol{P}'$ of input samples matrix $\boldsymbol{P}$, and by the ||dist|| calculation, the output vector of the first layer represent the proximity of the input vector and the training sample vector, multiplied by the threshold vector through the transfer function. Input vector with which the input sample is the most close, the neuron output a^1 corresponding element is 1. The second layer weight matrix $LW^{1,2}$ as expected value matrix $\boldsymbol{T}$, only one of 1 element in each row vector, the 1 element represents the corresponding category of the problem, and the remaining elements are 0. Then, calculate the product Ta^1. Finally, select by competitive transfer function, a maximum probability of class value is 1 and the other is 0.

26.3.3 Data Normalization

Fault diagnosis is a process of finding fault based on the data information of each component of the measurement system, such as voltage, current, pressure, and magnetic field, etc. Because magnitude of these data and dimension of property values are different, so the sample data must be normalized. By means of normalization, different dimension, and different magnitude data are changed into the same dimension and the same number to reduce the impact of differences between each attribute on the diagnosis results, so that all type of data to each other arithmetic. The sample data is normalized to the [0,1] range by the formula (26.1).

$$\overline{x_i} = \frac{x_i - x_{i\min}}{x_{i\max} - x_{i\min}} \tag{26.1}$$

where $\overline{x_i}$ is normalized value; x_i is actual value; $x_{i\min}$ is maximum value of the ith fault test point; $x_{i\max}$ is minimum value of the ith fault test point.

26.4 Simulation Analysis

26.4.1 PNN Fault Identification Analysis

During the simulation, a certain type of airborne fire control system seized 15 key points for testing, and these points can reflect 11 components failure and normal situation. Wherein the measured data as shown in Table 26.1, and output expected matrix as formula (26.2).

In Table 26.1, y_1–y_{12} respectively for trouble-free, antenna fault, high-frequency receiver fault, low-frequency receiver fault, frequency oscillator fault, transmitter fault, synchronizer fault, control component fault, transform component fault, adjustment component fault, computer fault, power fault.

$$K = \begin{array}{c} \\ y_1 \\ y_2 \\ \vdots \\ y_{12} \end{array} \begin{array}{c} \begin{array}{cccc} k_1 & k_2 & \cdots & k_{12} \end{array} \\ \begin{bmatrix} 1 & 0 & \cdots & 0 \\ 0 & 1 & \cdots & 0 \\ \vdots & \vdots & \ddots & \vdots \\ 0 & 0 & \cdots & 1 \end{bmatrix} \end{array} \tag{26.2}$$

where k_1–k_{12} represents the output desired vector under the different failure mode.

According to the formula (26.1), for processing the measured data, and obtain normalized sample matrix $\boldsymbol{P}$.

Table 26.1 The measured data table

Data	y_1	y_2	y_3	y_4	y_5	y_6	y_7	y_8	y_9	y_{10}	y_{11}	y_{12}
x_1	4.80	0.23	4.80	4.78	1.33	4.80	4.79	4.80	2.11	4.80	0.03	4.80
x_2	23.5	23.48	23.49	23.50	23.50	23.50	23.49	23.49	23.10	23.50	0.10	1.01
x_3	0.06	0.06	0.06	0.05	0.06	0.06	0.06	0.01	0.02	0.06	0.01	0.06
x_4	3.50	3.50	1.23	3.49	3.50	3.50	0.13	3.46	0.10	3.50	0.80	3.50
x_5	4.90	4.90	2.13	4.90	4.92	0.42	4.90	4.88	1.24	0.06	4.90	4.90
x_6	5.00	3.23	5.00	1.98	5.00	0.53	2.13	4.99	4.78	0.03	1.99	5.00
x_7	0.01	0.01	0.01	0.01	0.02	0.01	0.02	0.01	0.00	0.01	0.01	0.01
x_8	3.60	3.60	3.60	1.12	3.57	3.59	0.30	0.32	3.58	1.10	3.60	3.60
x_9	4.80	4.80	2.10	4.80	4.76	4.80	4.79	0.41	4.77	1.05	4.77	0.03
x_{10}	4.00	3.90	4.00	0.36	4.00	1.26	4.00	0.22	4.05	4.00	3.90	0.41
x_{11}	3.90	1.20	3.89	3.90	3.90	3.89	3.88	3.89	0.16	4.00	3.90	0.20
x_{12}	1.60	1.57	1.61	1.60	0.12	1.59	1.60	0.08	0.10	1.60	1.60	1.60
x_{13}	18.00	17.90	17.90	18.00	17.99	18.00	17.98	18.00	17.95	18.00	17.99	0.98
x_{14}	6.00	6.00	5.98	0.23	6.00	5.99	6.00	5.58	0.05	6.00	0.22	6.00
x_{15}	2.80	2.80	2.80	2.76	2.78	2.81	0.52	1.02	0.03	2.80	2.79	0.08

$$P = \begin{bmatrix}
1 & 0.042 & 1 & 0.996 & 0.273 & 1 & 0.998 & 1 & 0.436 & 1 & 0 & 1 \\
1 & 0.999 & 0.999 & 1 & 1 & 1 & 0.999 & 0.999 & 0.983 & 1 & 0 & 0.039 \\
1 & 1 & 1 & 0.800 & 1 & 1 & 1 & 0 & 0.200 & 1 & 0 & 1 \\
1 & 1 & 0.332 & 0.997 & 1 & 1 & 0.009 & 0.988 & 0 & 1 & 0.206 & 1 \\
0.996 & 0.996 & 0.426 & 0.996 & 1 & 0.074 & 0.996 & 0.992 & 0.243 & 0 & 0.996 & 0.996 \\
1 & 0.644 & 1 & 0.392 & 1 & 0.101 & 0.423 & 0.998 & 0.956 & 0 & 0.394 & 1 \\
0.500 & 0.500 & 0.500 & 0.500 & 1 & 0.500 & 1 & 0.500 & 0 & 0.500 & 0.500 & 0.500 \\
1 & 1 & 1 & 0.248 & 0.991 & 0.997 & 0 & 0.006 & 0.994 & 0.242 & 1 & 1 \\
1 & 1 & 0.434 & 1 & 0.992 & 1 & 0.998 & 0.800 & 0.994 & 0.214 & 0.994 & 0 \\
0.987 & 0.961 & 0.987 & 0.037 & 0.987 & 0.272 & 0.987 & 0 & 1 & 0.987 & 0.961 & 0.500 \\
0.974 & 0.271 & 0.971 & 0.974 & 0.974 & 0.971 & 0.969 & 0.971 & 0 & 1 & 0.974 & 0.010 \\
0.993 & 0.974 & 1 & 0.993 & 0.026 & 0.987 & 0.993 & 0 & 0.013 & 0.993 & 0.993 & 0.993 \\
1 & 0.994 & 0.994 & 1 & 0.999 & 1 & 0.999 & 1 & 0.997 & 1 & 0.999 & 0 \\
1 & 1 & 0.997 & 0.030 & 1 & 0.998 & 1 & 0.929 & 0 & 1 & 0.029 & 1 \\
0.996 & 0.996 & 0.996 & 0.982 & 0.989 & 1 & 0.176 & 0.356 & 0 & 0.996 & 0.993 & 0.018
\end{bmatrix}$$

The matrix $\boldsymbol{P}$ input to the PNN fault diagnosis model for the results of fault diagnosis, as shown in Table 26.2. The results show that the model has strong fault identification ability.

26.4.2 PNN Generalization Analysis

In order to test the generalization ability of the fault diagnosis based on PNN model, take any two sets of measured data, as shown in Table 26.3. The data of

Table 26.2 The results of the fault diagnosis based on PNN model

	PNN output failure mode											
Output vector	k_1	k_2	k_3	k_4	k_5	k_6	k_7	k_8	k_9	k_{10}	k_{11}	k_{12}

Table 26.3 was normalized according to the formula (26.1), and observe the accuracy of the fault identification, the diagnosis results as shown in Table 26.4.

By the Table 26.3, the first set of data is the data of the low-frequency receiver fault; the second is the data of the adjustment component fault. Table 26.4 shows that the fault diagnosis based on PNN model can fully identify the faults of the measured data.

26.4.3 PNN Anti-noise Analysis

The simulations show that the model has the strong fault identification ability and good generalization ability. But the model must be tested on the anti-noise ability if the model was applied in practice.

For data in Table 26.1, according to the following formula (26.3) superimposed noise.

$$x_i = x_i + A\sigma_f \times randn(1, 5) \tag{26.3}$$

where A is amplitude of the noise, The greater the A value, the greater the noise; σ_f is standard deviation of each test point parameters; the function of randn() is to generate pseudo-random number, these data follow a normal distribution that the mean value is 0 and the standard deviation is 1.

According to the formula (26.3) deal with the original data of Table 26.1, and normalization in the line with the formula (26.1) and input to the fault diagnosis model. By superimposing different noise and observing the accuracy of the fault identification, the diagnosis results are as shown in Table 26.5.

Table 26.5 shows that the fault diagnosis method based on the PNN model have powerful anti-noise ability; it also demonstrates that the model could meet the practical requirements.

26.5 Conclusions

The mechanism of fault diagnosis of the airborne fire control system was analyzed in this paper, and the fault diagnosis based on PNN model was established. The fault identification ability, generalization ability, and anti-noise ability have been analyzed through a series of simulations. Simulation results show that the fault

Table 26.3 Two sets of measured data

Fault component	y_4	y_{10}
x_1	4.66	4.82
x_2	23	23.5
x_3	0.05	0.06
x_4	3.39	3.53
x_5	4.78	0.04
x_6	4.91	0.03
x_7	0.01	0.02
x_8	1.12	0.18
x_9	4.8	1.25
x_{10}	0.36	4
x_{11}	4.9	3.78
x_{12}	1.60	1.34
x_{13}	18	18
x_{14}	0.23	6.00
x_{15}	2.67	2.82

Table 26.4 The fault diagnosis results of the two sets of measured data

	PNN output failure mode	
Output vector	k_4	k_{10}

Table 26.5 Fault diagnosis results of superimposed noise

A value	0.05	0.1	0.15	0.2	0.25	0.3	0.35	0.4	0.45	0.5
Fault identification accuracy	1.00	1.00	1.00	1.00	1.00	0.97	0.97	0.95	0.80	0.83

diagnosis of airborne fire control system based on PNN model is not only has strong fault identification ability, but also has good generalization ability, and has powerful anti-noise ability.

Acknowledgments This research was co-supported by the Aeronautical Science Foundation of China (No. 20115553021) and the Fundamental Research Foundation of Northwestern Polytechnical University (No. JC20110222).

References

1. Shao Y, Zhai W (2011) Development of fire control system onboard the next generation fighters (in Chinese). Electron Opt Control 18:60–63
2. Zeng S, Pecht MG, Wu J (2005) Status and perspectives of prognostics and health management technologies (in Chinese). Acta Aeronautica et Astronautica Sinica 26:626–632

3. Kamel MN, McCaffrey MJ, Metzler PG (1996) Analysis, design, implementation, and deployment of a prototype maintenance advisor expert system for the MK92 fire control system. Expert Syst Appl 10:193–207
4. Jin Y, Yongtian L, Fengyun C (2009) Studies on fault diagnosis mechanism of aerial fire control system (in Chinese). Comput Meas Control 17:1574–1575
5. Specht DF (1990) Probabilistics neural networks. Neural Netw 3:109–118
6. Wu H, Li Q, Xia Y, Liu W (2012) Fault identification for wide area backup protection based on probabilistic neural network (in Chinese). Power Syst Prot Control 40:4–49

Chapter 27
Avionics System Failure Prediction Based on Bacteria Evolution and Gray Neural Network

Chaoqi Gu, Deyun Zhou and Xiaoyang Li

Abstract Aiming at the problem of the gray neural network easy to fall into local optimization, a failure prediction algorithm with bacterial evolutionary and gray neural network is proposed. First, a gray neural network fault detection model is established. Then, the bacterial evolutionary algorithm is selected to optimize the initial weights and thresholds of the network to solve the defect of network easy to fall into local optimization. Finally, several kinds of fault prediction effect of the algorithm are compared through the simulation experiment. The simulation results show that the algorithm combining bacterial evolutionary and gray neural network can achieve optimal prediction effect quickly.

Keywords Fault prediction · Fault diagnosis · Neural network · Bacteria evolution

27.1 Introduction

According to the definition of Engel, a fault prediction is to provide early detection of a part of the fault symptom or the initial state (that is, the very small failure), and has the technology and method to deal with and forecast ability damage to a part of the fault state development [1]. Existing fault prediction technology has a variety of classification method, classification of parametric model method and nonparametric model method are proposed in the [2]. Parametric model methods include polynomial curve fitting, subjective probability forecast, regression forecast model, kalman filter, stochastic time series, and the gray model, etc. These kinds of method of prediction performance are related to the selection of model,

C. Gu (✉) · D. Zhou · X. Li
Northwestern Polytechnical University, Xi'an, China
e-mail: guchaoqi2011@126.com

J. Wang (ed.), *Proceedings of the First Symposium on Aviation Maintenance and Management-Volume I*, Lecture Notes in Electrical Engineering 296,
DOI: 10.1007/978-3-642-54236-7_27,

if the model assumption does not accord with the actual, the forecast performance is poor. Nonparametric model prediction method does not need precise mathematical model and the method has wider application range than the parameter model. Nonparametric model prediction methods include neural network, rough set theory, wavelet neural network, and combination forecast method, etc.

Gray neural network [3], which fully combines the advantages of gray system and neural network can effectively use small sample, change and nonlinear data of weak changing trend fault forecast. But the gray neural network easy to fall into local optimization, so the algorithm with bacterial evolutionary and gray neural network is proposed and established the gray neural network model for fault detection and selected the bacterial evolutionary algorithm to optimize network's initial weights and threshold [4–6]. In the end, several kinds of fault prediction effect of the algorithm are compared through the simulation experiment.

27.2 Gray Neural Network Models

Gray neural network is the method of gray system modeling combined with neural network method. This model can solute the problems of the complex uncertainty model.

Given the characteristic value of the original data sequence as formula (27.1):

$$X^{(0)} : \{x^{(0)}(t)\}, t = 0, 1, 2, \cdots, N-1 \tag{27.1}$$

After an accumulation, the sequence is as formula (27.2):

$$X^{(1)} : \{x^{(1)}(t)\}, t = 0, 1, 2, \cdots, N-1 \tag{27.2}$$

The GM (1, 1) model of the first-order gray differential equation is as formula (27.3):

$$\alpha^{(1)} X^{(1)} + aZ^{(1)} = b \tag{27.3}$$

Where $Z^{(1)}$ is the next domain mean of $X^{(1)}$ of the generated sequence.

In order to make the later formula convenient, the original data sequence $X^{(0)}$ expressed as $x(t)$, after an accumulation of data sequence $X^{(1)}$ is expressed as $y(t)$, predicted results is expressed as $Z(t)$. To the gray neural network forecasting model which has n input parameters, the differential equation is as formula (27.4):

$$\frac{dy_1}{dt} + ay_1 = b_1 y_2 + b_2 y_3 + \cdots b_{n-1} y_n \tag{27.4}$$

Where $y_2,\ldots,y_n$ is the system input parameters; y_1 is the system output parameters; a, $b_1,\ldots,b_n$ is coefficient of differential equation.

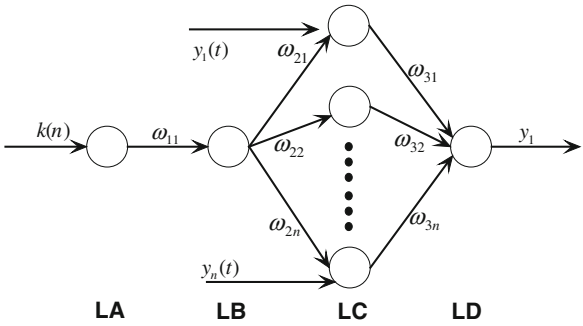

Fig. 27.1 *Gray* network topology

The time responses of formula (27.4) are as formula (27.5):

$$\begin{aligned} z(t) = (y_1(0) - \frac{b_1}{a} y_2(t) - \frac{b_2}{a} y_3(t) - \cdots - \frac{b_{n-1}}{a} y_n(t))e^{at} \\ + \frac{b_1}{a} y_2(t) + \frac{b_2}{a}(t) + \cdots + \frac{b_{n-1}}{a} y_n(t) \end{aligned} \tag{27.5}$$

Let, Formula (27.4) can be converted into formula (27.6):

$$\begin{aligned} z(t) &= ((y_1(0) - d) \bullet \frac{e^{at}}{1 + e^{at}} + d \bullet \frac{1}{1 + e^{at}}) \bullet (1 + e^{at}) \\ &= ((y_1(0) - d) \bullet (1 - \frac{1}{1 + e^{at}}) + d \bullet \frac{1}{1 + e^{at}}) \bullet (1 + e^{at}) \\ &= ((y_1(0) - d) - y_1(0) \bullet \frac{1}{1 + e^{at}}) + 2d \bullet \frac{1}{1 + e^{at}}) \bullet (1 + e^{at}) \end{aligned} \tag{27.6}$$

Then make formula (27.6) mapped to an extension of the BP neural network which has n input parameter and one output parameter of gray neural network. The gray network topology 3 is shown in Fig. 27.1.

Where $k(n)$ is the input sample sequence, $y_1(t),\ldots,y_n(t)$ is the network input parameters, is the network weights, is the projection of the network, LA, LB, LC, LD is the four layers of gray neural network, respectively.

Let, the network's initial weights and threshold is as follows: LA layer to LB weight of, LB to LC layer has a weight of, LC layer to LD weight of, LD output node threshold for layer. Network LB layer neurons of incentive function is sigmoid function as formula (27.7):

$$\varphi(x) = \frac{1}{1 + \exp(-x)} \tag{27.7}$$

Other layer neuron incentive function is set as a linear function.

27.3 Network Weights and Threshold Optimization Based on Bacteria Evolution

27.3.1 Bacterial Evolution Algorithm

In consideration of the defect of gray neural network easy to fall into local optimum, this paper chooses bacterial evolutionary algorithm to optimize the initial weights and thresholds of the network. In the optimization process, each individual bacterium represents a set of neural network weights and threshold. In order to get the best individual and the optimal initial weights and thresholds, the fitness of each evolution bacterial is calculated. Bacterial evolutionary algorithm mainly includes three parts: generating initial population, bacterial mutation, and gene transfer.

(1) Initial population generation: The generation of initial population is generating group of bacteria individuals, each individual contains a set of weights and thresholds. This paper employ the method of binary encoding and assuming that bacteria population is Nind, each bacteria represents a group of gray neural network parameters, each initial individuals generated in the {0, 1} randomly.
(2) Bacterial mutation: Bacterial mutation operators acting on each individual bacterium. First, reproduce a bacteria several times, in order to produce many clones. Then randomly selected a part of a clone and change its parameters. Finally, estimate all of the clones which have variant, calculate the fitness, and find the best individual, then copy the variant part of the optimal individual to all clones. The cycle is terminated until all the fragments are variant, the original individual and clone will be into the same code at last, the best bacteria is reserved and the clone is removed. Bacterial mutation schematic diagram is shown in Fig. 27.2.
(3) Gene transfer: Gene transfer operation is acting on the entire population. First, for the entire population, by means of the evaluation of the fitness of each individual, the population is divided into superior and inferior species. Then randomly select an individual in superior populations and inferior populations, respectively. Finally, select a part in superior individual and copy the part to an inferior individual. Gene transfer diagram is shown in Fig. 27.3.

27.3.2 The Implementation Steps of Network Weights and Threshold Optimization Based on Bacteria Evolution

The algorithm implementation process as shown in Fig. 27.4.

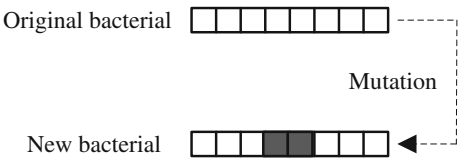

Fig. 27.2 Bacterial mutation schematic diagram

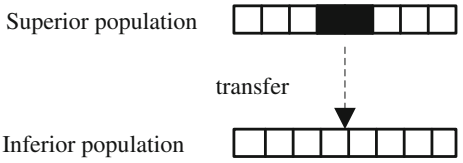

Fig. 27.3 Gene transfer diagram

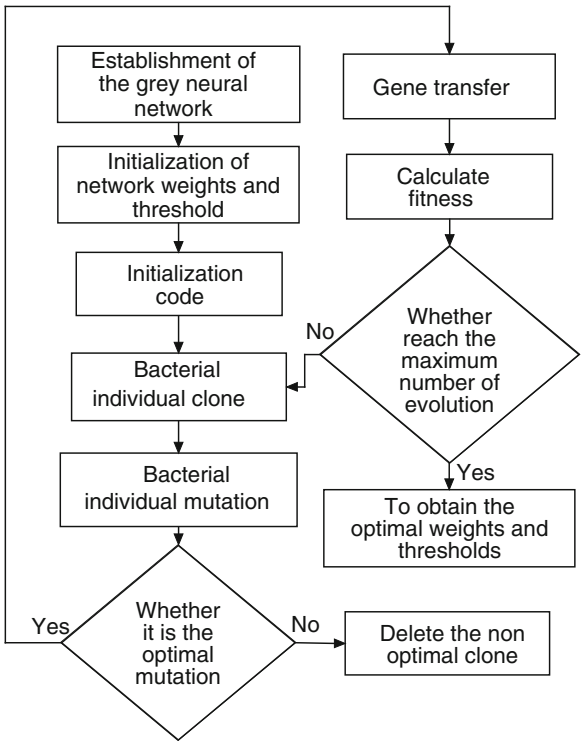

Fig. 27.4 Network weights and threshold optimization based on bacteria evolution algorithm implementation process

27.4 Simulation Results

The radar transmitter high voltage power supply ripple voltage value is chosen in this paper as an original training data in [2], At the same time, 40 groups of ripple voltage value is chosen as an accumulation of data, and then input these data as gray neural network training data into the network.

Table 27.1 Predicted accuracy comparison of different prediction algorithms

The measured values (v)	PSO optimization gray predictive value	The relative prediction error	The predictive value of BP network	The relative prediction error	The predictive value of BP gray network	The relative prediction error	The predictive value of gray neural network based on bacteria optimization	The relative prediction error
66.00	64.848	0.0174	69.320	0.0503	64.020	0.0300	66.9500	0.0144
70.25	70.157	0.0013	71.2360	0.0140	69.7800	0.0067	70.2350	0.0002
76.00	75.221	0.0102	76.3600	0.0047	76.8900	0.0117	75.8920	0.0014
82.80	81.352	0.0175	80.6500	0.0260	82.6520	0.0018	82.9000	0.0012
89.87	89.755	0.0013	92.9260	0.0340	89.8050	0.0007	89.9700	0.0011
The average relative error	0.0297		0.0762		0.01018		0.00366	

In the optimization process of initial weights and threshold, the selection of initial population Nind = 20, clone number Nclone = 50, gene transfer number Ninf = 50, maximum number of evolution Ngen = 50. According to the earlier stated algorithm of gray neural network, the input layer node number is designed in 5, hidden layer nodes is 10, the output node is 1, and the function of hidden layer is S excitation function, other layers is linear incentive function. Use these parameters to establish the gray neural network, and then uses bacteria optimization method to optimize parameters. After obtaining the optimal parameter, use this parameter as the initial weights and threshold of gray neural network, then training the network. Because there is no known impact factor, so the four gray neural network model is simplified to three layers gray neural network model.

In order to contrast the optimization effect of error, last 5 predicted is taken in this paper, groups of algorithm's error is compared, respectively such as the gray prediction algorithm, BP prediction algorithm, gray neural network prediction algorithm, and gray neural network based on bacteria optimization. Table 27.1 lists the initial value, all kinds of prediction, prediction relative error of prediction algorithm, and the average relative error value.

In the contrast test, the average relative prediction error of gray neural network based on bacteria optimization prediction algorithm is better than others; because of the initial weights and threshold is random, the BP network and nonoptimization gray neural network is easy to fall into local optimum, but the bacteria evolved to optimize the initial weights and thresholds can effectively avoid this; in this paper, PSO optimization gray predictive value has reached one-level of accuracy, and the optimization of the proposed method also reached the level of prediction accuracy requirements and is better than others; Due to bacteria evolutionary optimization weights and thresholds, the training time of bacterial optimization of gray neural network is longer than the BP neural network, but since most of the gray neural network is to deal with less sample data, and the hardware operation condition is very good now, we can completely ignore the time cost.

27.5 Conclusions

Gray neural network based on bacterial evolutionary algorithm for fault prediction of avionics system is proposed in this paper, aiming at defects of gray neural network easy to fall into local optimization, bacterial evolutionary algorithm is selected to optimize network's initial weights and threshold, in order to prevent the network into a local optimum. The simulation experimental results show that the average relative prediction error of gray neural network based on bacteria optimization is better than other prediction algorithms.

Acknowledgments This research was co-supported by the Aeronautical Science Foundation of China (No. 20115553021) and the Fundamental Research Foundation of Northwestern Polytechnical University (No. JC20110222).

References

1. Spitzer CR (2010) Digital avionics technology (in Chinese). Aviation Industry Press, Beijing
2. Xu LJ (2009) Study on fault prognostic and health management for electronic system (in Chinese). University of Electronic Science and technology, Chengdu
3. Huang Y, Hu CH (2006) Construction of GNNM (3, 1) and its application in missile fault prediction(in Chinese). Electro Opt Control 13(5):39–41
4. Nawa NE, Furuhashi T (1999) Fuzzy system parameters discovery by bacterial evolutionary algorithm. IEEE Trans Fuzzy Syst 7(5): 608–616
5. Cabrita C, Botzheim J, Ruano AE, Kóczy LT (2004) In: Design of B-spline neural networks using a bacterial programming approach in international joint conference on neural networks, Budapest, Hungary, pp 2313–2318
6. Hocaoglu C, Sanderson AC (2001) Planning multiple paths with evolutionary speciation. IEEE Trans Evol Comput 5:169–192

Chapter 28
Time Series Weighted Prediction Method Using Multikernel LS-SVR

Guo-Chang Zhou, Yang-Ming Guo and Jie-Zhong Ma

Abstract Fault or health condition prediction of complex systems has attracted more and more attention in recent years. Due to complex dynamic behavior and uncertainty in running, complex systems are always difficult to establish precise physical model. Therefore, the time series of complex equipments are often used to perform the prediction in practice. In order to satisfy the requirements of application, which are good prediction accuracy and less calculation time, we utilize multiple relevant time series and propose a new prediction method based on multikernel LS-SVR. In this method, we proposed a simple computational method to obtain combining weights of multikernel, and the new prediction model considers the different effect of historical data into the prediction process. Prediction experiment is made by two relevant time series of one complex avionics equipment. The results indicate preliminarily that the proposed method is a practical and effective prediction method for its good prediction precision within less time cost.

Keywords Time series · Weighted prediction · Least squares support vector regression (LS-SVR) · Multiple kernel learning (MKL)

G.-C. Zhou
Academy of Space Technology, Xi'an, China
e-mail: zhouguochang2000@163.com

Y.-M. Guo (✉) · J.-Z. Ma
School of Computer Science and Technology, Northwestern Polytechnical University, Xi'an, China
e-mail: yangming_g@nwpu.edu.cn

J.-Z. Ma
e-mail: majz@nwpu.edu.cn

J. Wang (ed.), *Proceedings of the First Symposium on Aviation Maintenance and Management-Volume I*, Lecture Notes in Electrical Engineering 296,
DOI: 10.1007/978-3-642-54236-7_28,

28.1 Introduction

Prediction has become an essential technology to ensure the operation safety of complex systems. However complex systems often have nonlinear and uncertain dynamic behavior; hence it is difficult to forecast their fault or health condition with accurate analytical form model. So in recent years, in order to implement the prediction of these complex systems and get satisfactory results, time series-based prediction models have attracted increased attention [1], and the selection of prediction model is the important criteria which will influence to the prediction accuracy.

As kernel-based method, Artificial Neural Networks (ANN) and Support Vector Regression (SVR) have been widely used in many nonlinear time series predictions [2–4], but ANN has a number of shortcomings [5]. On the contrary, SVR is based on statistical theory and structural risk minimization principle [5], and it can overcome the problems of ANN.

SVR has a global optimum and exhibits better accuracy in nonlinear and nonstationary time series data prediction via kernel function. However, if aiming at the large sample data, SVR will solve quadratic programming (QP) problem which is more complex. For this purpose, LS-SVR were proposed by Suykens et al. [6]. In LS-SVR, the inequality constrains were replaced by equality constrains. By this way, solving the QP is converted into solving linear equations and the calculation cost is reduced effectively. LS-SVR has more attention in time series forecasting [7, 8].

For LS-SVR, the kernel function determines the learning performance. Generally, common single kernel function is applied. Although the kernel parameters can be optimally chosen to enhance the generalization capability, learning with single kernel is not very data-adapted or discriminative. Especially, the LS-SVR with single kernel does not address the challenge of learning from multiple data sources. In practice, the variable describing characteristic of one certain condition or fault is not unique, that means it is always described by several relevant time series. In this case, it is difficult to choose an appropriate kernel function, and it is also difficult to use this single kernel to sufficiently show the internal relationship of these time series. So some researchers adopted multiple kernel learning (MKL) to deal with these problems [9, 10]. MKL is based on the convex optimization theory and provides a more flexible framework than single kernel. It explicitly learns the weights of basis kernels from different time series data sources, and the relationships among them are learned meanwhile. So, it can mine time series data information more adaptively and more effectively.

Due to the above advantages, LS-SVR with multiple kernels, called MKLS-SVR, should have better accuracy [10, 11], especially for many prediction application with small sample data, it urgently need to use multiple relevant time series to enrich effective information, and it need to display time series data information fully in high dimension space via multiple kernels. However, the original MKLS-SVR makes the assumption that all the training time series data

have same contribution to prediction. According to the new information principle [12], the time series data will decrease their effect on the estimation function along with the distance, which presents the time distance between the current data and the prediction working point, becoming longer. Moreover, under MKL framework, the time series data samples are usually learned by a linear convex combination of basis kernels generally. The known methods of determining the combing weight for the basis kernels [13, 14] are always too complex to hinder the MKLS-SVR to be applied in actual application.

So we propose a new prediction method which uses multiple time series and considers the effect of their history data on the prediction to achieve better results.

28.2 Brief Review of Related Work

28.2.1 Least Squares Support Vector Regression

According to Ref [6]., let us consider a given training data set $S = \{(x_i, y_i), i = 1, 2, \ldots, n\}$, where $x_i \in R^d$ is the input sample and $y_i \in R$ is the corresponding output or target value. The LS-SVR approximates the regression function as the following form:

$$f(x) = y = w^T \varphi(x) + b \tag{28.1}$$

where, $\varphi(x)$ represents the high dimensional feature space, which is mapped from the input space x. w is weight vector and b is bias term.

According to the structural risk minimization principle, the least squares SVR problems can be represented as a constraint optimization problem as follows:

$$\begin{aligned} \min \quad & J(w, b) = \tfrac{1}{2}\|w\|^2 + \tfrac{c}{2}\sum_{i=1}^{n} e_i^2 \\ s.t. \quad & y_i = w^T \varphi(x_i) + b + e_i,\ i = 1, 2, \ldots, n \end{aligned} \tag{28.2}$$

where $J(w, b)$ is the cost function, c is a positive real constant, called regularization parameter, and $e_i \in R$ is an error variable.

In order to fix the above constraint optimization problems, the Lagrangian function is constructed by transforming the constraint optimization problems into unconstraint ones

$$L(w, b, e, \alpha) = \frac{1}{2} w^T w + \frac{1}{2} c \sum_{i=1}^{n} e_i^2 - \sum_{i=1}^{n} \alpha_i (w^T \varphi(x) + b + e_i - y_i) \tag{28.3}$$

where α_i is the ith Lagrange multiplier.

It is obvious that the optimal solution of Eq. (28.2) satisfies karush–Kuhn–Tucker (KKT) conditions. Then the optimal conditions are given as follows:

$$\begin{cases} \dfrac{\partial L}{\partial w} = w - \sum\limits_{i=1}^{n} \alpha_i \varphi(x_i) = 0 \Rightarrow w = \sum\limits_{i=1}^{n} \alpha_i \varphi(x_i) \\ \dfrac{\partial L}{\partial b} = -\sum\limits_{i=1}^{n} \alpha_i = 0 \Rightarrow \sum\limits_{i=1}^{n} \alpha_i = 0 \\ \dfrac{\partial L}{\partial \alpha_i} = w^T \varphi(x_i) + b + e_i - y_i = 0_i = w^T \varphi(x_i) + b + e_i \\ \dfrac{\partial L}{\partial e_i} = c e_i - \alpha_i = 0 \Rightarrow e_i = \dfrac{1}{c} \alpha_i \end{cases} \tag{28.4}$$

After eliminating w and e_i, we could obtain the solution by the following linear equations:

$$\begin{bmatrix} 0 & \mathbf{1}_n^T \\ \mathbf{1}_n & \mathbf{K}+\mathbf{I}/\mathrm{c} \end{bmatrix} \begin{bmatrix} b \\ \boldsymbol{\alpha} \end{bmatrix} = \begin{bmatrix} 0 \\ \mathbf{y} \end{bmatrix} \tag{28.5}$$

where, $\mathbf{K}(i,j) = k(x_i, x_j) = \varphi(x_i)^T \varphi(x_j)$, $\boldsymbol{\alpha} = [\alpha_1, \alpha_2, \ldots, \alpha_n]^T$, $\mathbf{1}_n$ is n-dimensional vector of all ones, $\mathbf{I}$ is a unite matrix, and $\mathbf{y} = [y_1, y_2, \ldots, y_n]^T$.

Let $\mathbf{H} = \mathbf{K} + \mathbf{I}/c$, and we get the equations from Eq. (28.5)

$$\begin{cases} \mathbf{1}_n^T \boldsymbol{\alpha} \\ \mathbf{1}_n b + \mathbf{H}\alpha \end{cases} \tag{28.6}$$

Then Lagrange dual variables $\boldsymbol{\alpha}$ and bias term b are obtained solely by

$$\begin{cases} \boldsymbol{\alpha} = \mathbf{H}^{-1}(\mathbf{y} - \mathbf{1}_n b) \\ b = \mathbf{1}_n^T \mathbf{H}^{-1} \mathbf{y} (\mathbf{1}_n^T \mathbf{H}^{-1} \mathbf{1}_n)^{-1} \end{cases} \tag{28.7}$$

Any unlabeled input x can be subsequently regression estimation by the following function:

$$y(x) = \sum_{i=1}^{n} \alpha_i k(x_i, x) + b. \tag{28.8}$$

28.2.2 Multiple Kernel Learning Algorithm

The common kernel methods always use single kernel function and choose a consistent parameter for the whole sample data sets. In fact, the distribution of the sample data in the different mapping space is different. So MKL was proposed by Lanckriet, Cristianini et al. [10]. MKL refers to the process of learning a kernel machine with multiple kernel functions or kernel matrices. The research shows

that MKL can increase the accuracy of classification and regression [10–12, 14]. In the MKL framework, the combined kernel is a convex combination of several basis kernels. In this paper, following Sonnenburg et al. [17], we consider the combined kernel is presented as follows:

$$k(x_i, x_j) = \sum_{m=1}^{M} \mu_m k_m(x_i, x_j)$$
$$s.t. \quad \begin{cases} \sum_{m=1}^{M} \mu_m = 1 \\ \mu_m \geq 0 \, m = 1, 2, \ldots, M \end{cases} \tag{28.9}$$

where, M is the number of basis kernels, μ_m is the combining weight for the mth basis kernel and it measures the importance of different basic kernels for the discrimination. Afterward, all kernel matrices $k_m(x_i, x_j)$ are normalized by replacing $k_m(x_i, x_j)$ with $k_m(x_i, x_j)/\sqrt{k_m(x_i, x_i)k_m(x_j, x_j)}$ to get unit diagonal matrices.

The key of MKL is to obtain the optimal combining weights μ_m. However all the known solution methods are complex for application. So in order to improve the effectiveness of information mapping to high dimensional feature space by kernel function and reduce time cost in the process of determining the combining weights of basis kernels, we will present a sample method to fix this problem in Sect. 28.3

28.3 Weighted Prediction Method of Multiple Time Series

28.3.1 Combining Weights of the Multikernel

In this paper, the new kernel is a linear convex combination of several basis kernels, shown as Eq. (28.9). In order to reduce the dependence of prediction on basis kernels and the computing complexity of combining weights of basis kernels, we propose to determine the weights according to Root Mean Square Error (RMSE) of each LS-SVR with each basis kernel, which means the weight with the smaller RMSE will get bigger weighted value. If the prediction value has less relative error means that the LS-SVR is a better model. The RMSE of multiple time series prediction is defined as follows:

$$\sigma_{RMSE} = \sqrt{\frac{1}{nr} \sum_{i=1}^{r} \sum_{k=1}^{n} (y_i(k) - \hat{y}_i(k))^2} \tag{28.10}$$

where r is the number of the relevant time series, n is the number of original training sample data, $y_i(k)$ and $\hat{y}_i(k)$ are the prediction and actual value, respectively. So the combining weights μ_m are computed as follows:

$$\mu_j = \frac{\sum_{m=1}^{M} \sigma_m - \sigma_j}{(M-1)\sum_{m=1}^{M} \sigma_m} \tag{28.11}$$

where σ_j is the prediction RMSE of jth kernel, $\sum_{m=1}^{M} \sigma_m$ is sum RMSE of all kernels, and $\sum_{m=1}^{M} \sigma_m - \sigma_j$ presents the contribution of the jth kernel.

28.3.2 Time-Weighted MKLS-SVR

The time series data have greater relevance with the data near the prediction point. Hence, we will make each historical data with different weighted factor; otherwise they should be given same attention, and this does not follow the development rules of time series. In the case, we present a new method in this paper, called WMKLS-SVR.

Here, consider the generation sample set from raw time series $\{x_k, y_k\}$, $k = 1, 2, \ldots, n$. Then according to Refs. [18, 19], we modify the weighting function of x_k and define it as following:

$$d_k = e^{-(n-k)^2/2\lambda^2}, \quad k = 1, 2, \ldots, n \tag{28.12}$$

where λ is a given parameter, and a small d_i can reduce the storage of historical data and speed up the training. The objective function is expressed as follows:

$$\begin{aligned} \min J(w, e) &= \frac{1}{2} w^T w + \frac{1}{2} c d_k \sum_{i=1}^{n} e_k^2 \\ s.t.\ y_k &= w^T \varphi(x_k) + b + e_k, k = 1, 2, \ldots, n. \end{aligned} \tag{28.13}$$

Then the following Lagrangian function is established as follows:

$$L(w, b, e, \alpha) = \frac{1}{2} w^T w + \frac{1}{2} c d_k \sum_{k=1}^{n} e_k^2 - \sum_{k=1}^{n} \alpha_k (w^T \varphi(x) + b + e_k - y_k) \tag{28.14}$$

where $\alpha_k > 0, k = 1, 2, \ldots, n$, are Lagrangian multipliers.

According to KKT conditions, we can get the following functions:

$$\begin{cases} \dfrac{\partial L}{\partial w} = w - \sum\limits_{k=1}^{n} \alpha_k \varphi(x_k) = 0 \Rightarrow w = \sum\limits_{k=1}^{n} \alpha_k \varphi(x_k) \\ \dfrac{\partial L}{\partial b} = -\sum\limits_{k=1}^{n} \alpha_k = 0 \Rightarrow \sum\limits_{k=1}^{n} \alpha_k = 0 \\ \dfrac{\partial L}{\partial \alpha_k} = w^T \varphi(x_k) + b + e_k - y_k = 0_k = w^T \varphi(x_k) + b + e_k \\ \dfrac{\partial L}{\partial e_k} = c d_k e_k - \alpha_k = 0_k = \dfrac{1}{c d_k} \alpha_k \end{cases} \tag{28.15}$$

After the elimination of w and e_k with the processing in Sect. 28.2, the Eq. (28.5) can be rewritten as follows:

$$\begin{bmatrix} 0 & 1 & \cdots & 1 \\ 1 & k(x_1, x_1) + {}^1\!/_{cd_1} & \cdots & k(x_1, x_n) \\ \vdots & \vdots & \cdots & \vdots \\ 1 & k(x_n, x_1) & \cdots & k(x_n, x_n) + {}^1\!/_{cd_n} \end{bmatrix} \begin{bmatrix} b \\ \alpha_1 \\ \vdots \\ \alpha_n \end{bmatrix} = \begin{bmatrix} 0 \\ y_1 \\ \vdots \\ y_n \end{bmatrix} \tag{28.16}$$

28.4 Simulation Experiment and Results

In order to validate the performance of the proposed method, we perform an experiment with 75 sample time series data, which contain variable x and y, and they come from one complex avionics equipment, shown in Fig. 28.1. All the experiments adopt MatlabR2011b with LS-SVMlab1.8 Toolbox (The software and guide book can be downloaded from http://www.esat.kuleuven.be/sista/lssvmlab) under Windows XP operating system.

We set the front 45 time series data as training samples, and any continuous six are taken as a sample, where the data of the first five data compose an input sample vector and last one as the output vector, i.e., in the example, we have 40 training data. And then we predict the No. 46–75 time series data using the trained model.

In the experiment, we compare proposed method, called WMKLS-SVR, with traditional multikernel LS-SVR, called MKLS-SVR, on computing time cost and prediction accuracy, which depends on RMSE. Here, one Gaussian RBF kernel $k(x, y) = \exp(-\frac{\|x-y\|^2}{2\sigma^2})$ and one linear kernel function $k(x, y) = x^T y$ are adopted as basis kernel functions, and the parameters will be jointly optimized with traditional gridding search method, where the search rang for c, σ^2 and λ is [0.1, 2000].

The prediction RMSE is reported in Table 28.1 and the prediction results are shown in Figs. 28.2 and 28.3.

From Table 28.1, Figs. 28.2 and 28.3, we can see that the proposed model WMKLS-SVR has better prediction accuracy and costs less computing time.

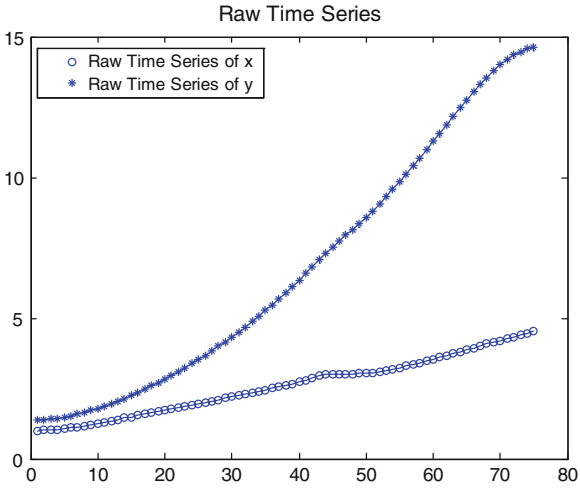

Fig. 28.1 Small sample time series of avionics system

Table 28.1 Prediction RMSE

Method	RMSE		Time cost/s
	x	*y*	
MKLS-SVR	0.8190	1.5550	2.489
WMKLS-SVR	0.5598	1.5066	1.326

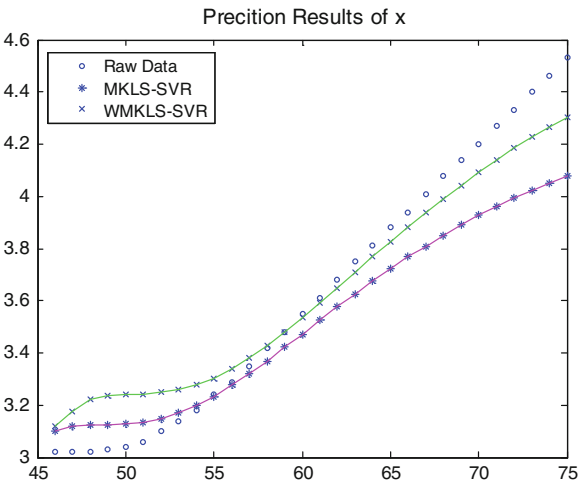

Fig. 28.2 Prediction results of *x*

Because WMKLS-SVR considers fully the different influences on prediction with historical data, and it uses simple calculation approach to compute the weighted values of basis kernels.

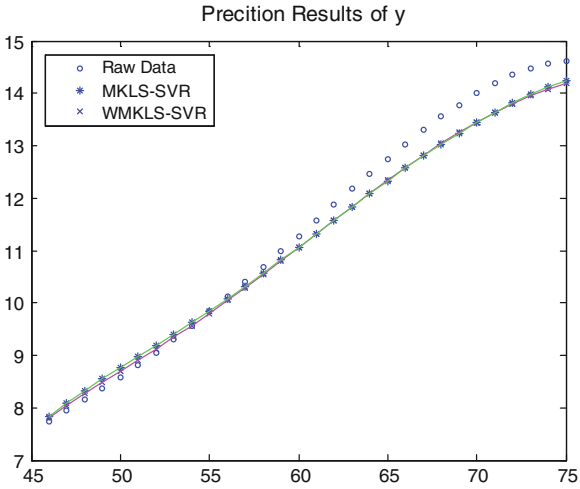

Fig. 28.3 Prediction results of *y*

28.5 Conclusions

In this work, we proposed a new prediction method based on LS-SVR with MKL and several relevant time series to improve time series prediction efficiency and practicality. The main contributions of this method include two aspects, one is that we proposed a simple approach to compute the combining weights of multiple basis kernels, which is based on RMSE, and the other one is that we consider the influences of historical data and make weighted process with the prediction data. We conduct an assessment experiment that the results demonstrate our prediction method is a better approach, and it is also an effective model in practice.

Acknowledgments This work is supported by Major Project of Chinese National Programs for Fundamental Research and Development (973 Program), National Natural Science Foundation (NNSF) of China under Grant No. 61001023 and No. 61371024, Chinese Astronautics Support Technology Foundation, and Aviation Science Foundation of China under Grant No. 2013ZD53051.

References

1. Pecht M, Jaai R (2010) A prognostics and health management roadmap for information and electronics-rich systems. IEICE Fundam Rev 3:25–32
2. Qi M, Zhang GP (2008) Trend time series modeling and forecasting with neural networks. IEEE Trans Neural Networks 19(5):808–816
3. Valeriy G, Supriya B (2006) Support vector machine as an efficient framework for stock market volatility forecasting. CMS 3:147–160
4. Qiu SB (2009) Terran lane: a framework for multiple kernel support vector regression an its application to siRNA efficacy prediction. IEEE Trans Comput Bioinform 6:190–199

5. Vladimir N (1995) Vapnik, AT&T Bell Labs, Holmdel. The Nature of Statistical Learning Theory. USA Springer Verlag, New York
6. Suykens JAK, Van Gestel T, De Brabanter J, De Moor B, Vandewaller J (2002) Least squares support vector machines. World Scientific Publishing, Singapore
7. Qu J, Zuo MJ (2012) An LSSVR-based algorithm for online system condition prognostics. Expert Syst Appl 39:6089–6102
8. Guo YM, Zhang L, Cai XB, Ran CB, Zhai ZJ, Ma JZ (2012) Time series adaptive online prediction method combined with modified LS-SVR and AGO. Math Prob Eng 2012:1–12
9. Shilton A, Lai DTH, Marimuthu P (2010) A division algebraic framework for multidimensional support vector regression. IEEE Trans Syst, Man Cybern-part B: Cybern 40:517–528
10. Lanckriet GR, Cristianini N, Bartlett PL, Ghaoui LE, Jordan MI (2004) Learning the Kernel matrix with semidefinite programming. J Mach Learn Res 5:27–72
11. Zhang XR, Hu LY, Wang ZS (2010) Multiple Kernel support vector regression for economic forecasting. In: 2010 international conference on management science and engineering (17th). IEEE Press, Melbourne, Australia, pp 129–134
12. Deng JL (2004) The primary methods of grey system theory. Huazhong University of Science and Technology Press, Wuhan (in Chinese)
13. Andersen ED, Andersen AD (2000) The MOSEK interior point optimizer for linear programming: an implementation of the homogeneous algorithm. In: Frenk H et al (eds) High performance optimization. Kluwer Academic Publishers, Norewll, USA, pp 197–232
14. Jian L, Xia ZH, Liang XJ, Gao CH (2011) Design of a multiple kernel learning algorithm for LS-SVM by convex programming. Neural Networks 24:476–483
15. Sonnenburg S, Räosch G, Schäer C, Schökopf B (2006) Large scale multiple kernel learning. J Mach Learn Res 7:1531–1565
16. Suykens JAK, Vandewalle J (2000) Least square support vector machines. IEEE Trans Circuits Syst-I 47:1109–1114
17. Zheng XX, Qian F (2005) Based on the support vector machine online modeling and application. Inf Control 34(5):636–640 (in Chinese)

Chapter 29
The Malfunction and Analysis During the Overhaul of the Landing Gear

HaiTao Wang and Xing Chen

Abstract Along with the fast development of the aviation transportation industry, domestic aircraft fleet expanded very quickly, landing gear as one of the aircraft main systems, its function affects the taxing, take-off, and landing safeties of the aircraft dramatically. In case of malfunction of landing gear, the aftereffect will be very serious. It is very important to analyze the reason of malfunction. This article makes a succinct introduction of research status, background of the landing gear's faults, and the structure of landing gear. Take 737–300 main landing gear trunnion link's corrosion example, through the deep analysis of the reasons of corrosion, putting forward some concrete improvement approaches and measures. No matter in the theoretical meanings and practical applications all made prominent effects.

Keywords Civil aircraft · Landing gear · Overhaul · Corrosion · Malfunction analysis

29.1 Introduction

Through complete analysis of landing gear configuration and function, accompany with statistic of frequently malfunction during landing gear overhaul, this article analyze the frequently malfunction and provides a few repair and inspection methods which different with OEM's component maintenance manual. This article will give theory instructions and technique guidance for development and design, service, and maintenance of the landing gear.

H. Wang (✉) · X. Chen
Northwestern Polytechnical University, 127 Youyixi Road, xi'an, shaanxi, P.R.China
e-mail: whaitao@nwpu.edu.cn

X. Chen
e-mail: Chen91263@163.com

J. Wang (ed.), *Proceedings of the First Symposium on Aviation Maintenance and Management-Volume I*, Lecture Notes in Electrical Engineering 296,
DOI: 10.1007/978-3-642-54236-7_29,

The fault of the aircraft's landing gear has become one of the three main systematic faults of civil aviation's airplanes. This has a great influence on the normal service of the air flights, the accidents of aviation which are caused by the faults of the aircraft's landing gear always occur, causing a great economic loss to the operator and a nasty social influence to the passengers and the public.

The fault of an aircraft's landing gear has always been one of the important factors which influence the Infallibility of plane. The reasons which cause the fault of an aircraft's landing gear primarily involve the aspects of the material, the maintenance, the operation, the design, etc. Once the landing gear has a trouble, it will lead to serious effects. Therefore, the analysis of the faults becomes very important; we need to find out the reasons of faults, using reasonable preventive and improved actions. The theoretical meaning of this paper is to get the ways to solve or reduce this kind of fault through the usual analysis of the landing gear's structure and overhaul; these ways also make some theoretical instructions to the designing, operating, and protecting of the aircraft's landing gear.

29.2 Landing Gear's Structure

Landing gear is one of the most important systems of an airplane; its performance will influence the safety of an aircraft directly.

29.2.1 Landing Gear's Configuration

At present, the landing gear's configuration can be divided into three categories which are tricycle gear, tail wheel gear, and bicycle landing gear.

Tail wheel gear: the two fulcrums (main wheel) are parallel, settled in the front of the center of the aircraft and the third fulcrum is settled at end of the aircraft.

Tricycle gear: the two fulcrums (main wheel) are parallel, settled in the back of the center of the aircraft and the third fulcrum is settled in the front of the aircraft. The aircraft with tricycle gear usually has a protecting stand at the tail of it.

Bicycle landing gear: the two main wheels are settled under the body of the aircraft. Near the center, the other two auxiliary wheels are parallel settled under the wings [1].

29.2.2 The Structure of the Landing Gear

The structure of the landing gear can be divided into three kinds which are frame-type, pillar sleeve-type, and rocker-type. The structure of the landing gear is determined by the type and dimension. It influences the extension and retraction of the landing gear.

29.2.3 The Landing Gear's Taxiing Device

The flight cannot stop at once for its inertia. From flying to landing, it always needs sometime to taxi across the distance till slow down. This needs the taxiing device to let the aircraft can turn flying to stopping. As the fields of the aircraft's taking off and landing are different, the taxiing device will also be different. On the well-mended runway, the wheel taxiing mechanism can always be used. On the icy and snowy runway, the taxiing sledge can usually be used. On the surface of water, the aircraft must be equipped with buoy and be designed as the body of hull. Since the modern civil aircraft all have their own appropriative airports and runways, the wheel taxiing mechanism is widely used. For the different fixed forms, the wheel taxiing mechanism can be classified as the types of semi axle, semi wheel-folk, and so on.

29.3 The Analysis and Control of the B737-300's Main Trunnion Link Corrosion

Corrosion is the usual defect in the process of the landing gear's overhaul. It includes the electro chemical corrosion, pitting corrosion, galvanic corrosion, stress corrosion, hydrogen embrittlement, corrosion fatigue, etc.

29.3.1 The Technical Materials of the Trunnion Link

The material of the trunnion link is the 43040 M steel, the intensity of it is 275–300 ksi. The mounting position of the trunnion link in the landing gear is shown in the Fig. 29.1. The trunnion link is a very important part in the structure of landing gear, connecting the damper and the drag strut. In the Fig. 29.1, we can see, if we simplify the structure of landing gear to a triangle, the trunnion link is one side of the triangle in the actual. The damper and drug strut become the other two sides of this triangle. All of these constitute the stable triangular structural support [2].

All the positions indicated by the arrows need to be plated with chromium, the other surfaces need to be plated with low hydrogen embrittlement chrome. After the plating, the whole trunnion link other than the chromium layer paints the priming lacquer BMS10-11 type1 and the finish lacquer BMS 10-60 type1.

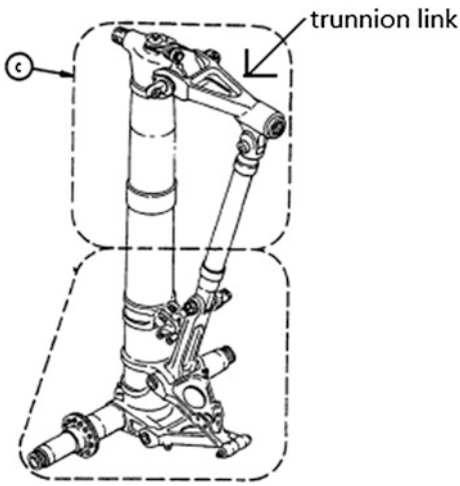

Fig. 29.1 The location of the trunnion link

Fig. 29.2 The corrosion of the trunnion link

29.3.2 The Appearance and the Morphology of Conversion

The partial appearance of parts' corrosion is shown in the Fig. 29.2. The link's fineness degree changes and becomes uneven; pockmarks of grinding traces remain on the surface. These are the typical features of fretting damage. The most serious fretting damage is on the contact edge, the reddish brown abrasive dust shapes like the fish scales, the length of one side reaches to 20 mm on average, sometimes can reach to more than 50 mm. These are the important symbols of the fretting damage. The corrosion may also exist on the surface of bushing hollow.

29.3.3 The Reasons of Corrosion

From the indications of the corrosion, the fretting corrosion is a kind of abrasive corrosion. It can be seen in the parts of landing gear. The fretting corrosion (shorted for FC) means the fretting damages (the fretting corrosion and the fretting fatigue) which are created in the corrosive medium. The abrasive corrosion is the result of friction and corrosion between the mental materials and the surrounding medium, leading to the mental materials broken.

From the Fig. 29.3, we can see trunnion pin (68) and trunnion nut (64) connect the two surfaces A and B of the trunnion link. The gasket (73A) and seal space (63B) only be installed when the trunnion pin is corrosion seriously. Nozzle (81 K) do not exist at first, it means the place where corrosion occur cannot get lubrication at first.

From this figure, we can get the reasons of the corrosion. Before the overhaul, the surfaces of the trunnion link A, B, and the bushing hollow's surface cannot get enough lubricating oil and grease. In the Fig. 29.3, we can see, the corrosive parts of the trunnion link have contact with the trunnion pin and trunnion nut, with no protection of the lubricating oil or some other antiseptics, when the water vapor comes into the connecting parts, the partial oxygen concentration cell will be formed, this will lead to the crevice corrosion. Since the crevice corrosion reaches to a certain degree, the trunnion pin will have a small amount of loose causing the micro mobility of A, B, and the connecting parts. When the corrosion reaches into the bushing hollow chamfer, the crevice corrosion of bushing and bushing hollow's connecting place will be created which will cause the inner corrosion of bushing hollow finally [3].

In the fact, the main reason of corrosion is the bad design by the makers. First of all, the connecting parts of B737's main trunnion link are too many, causing a lot of cracks directly. The environment of landing gear's working is so bad, easily leading to crevice corrosion. Then, at the beginning of the design, because the stable triangular structure was formed by the trunnion link, damper and drug strut, that is to say, in the process of the landing gear's operation, the trunnion and the trunnion pin will not have the relative turning, so the problem of lubricating is not taking into regard. The trunnion link and the relative parts can only fight with the corrosion by their own protecting layer. During the 10-years long in the use, the final results can be seen [4].

From the data of Table 29.1, after the overhaul, the phenomenon of corrosion is essentially under control. Especially, the ultimate refitting rate becomes 10 % of the previous one. This means, the possibility of the refitted trunnion link which can continue to work is much more than the previous one.

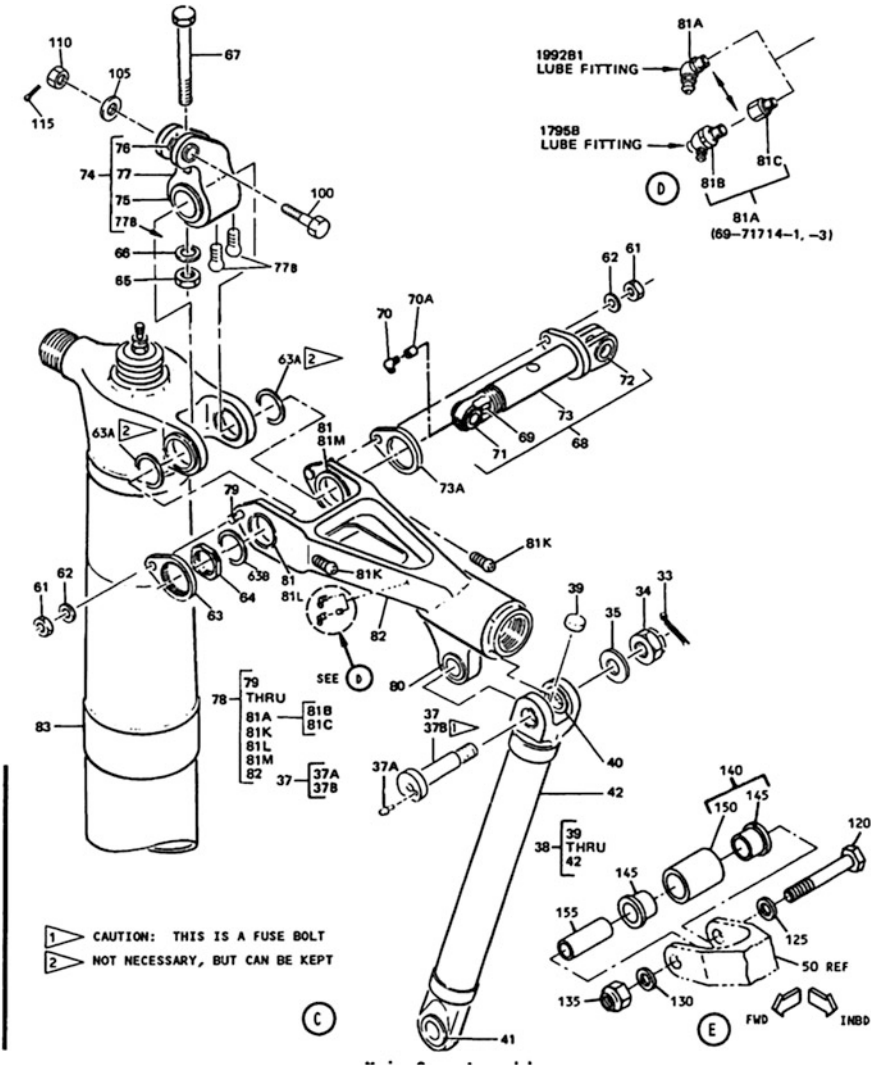

Fig. 29.3 The installation of the trunnion link

Table 29.1 The data of overhaul end to 2004

Trunnion link	Quantity of overhaul	Quantity of corrosion	Quantity of removing corrosion	Reach the limit	Beyond the limit	Quantity of scrap
Before refit	66	66	46	15	3	2
After refit	84	47	45	2	0	0

Fig. 29.4 Two nozzles

29.3.4 The Suggestions to the Corrosion of the Trunnion Link

From the Table 29.1, we can see, after the overhaul, the corrosion of the trunnion link has been well controlled, but there is still somewhere to improve.

The modification of nozzle. At the present, the lubricating nozzle (81 k) of the trunnion link which was referred in the manual is barbed nozzle, PN 1728B, the other nozzle, PN MS15004-2, is a screw-type nozzle. The two nozzles are shown as Fig. 29.4 [5].

There are two reasons to install the nozzle MS15004-2. The first, the nozzle (81 k) is 190 cm high from the ground, so it is a laborious job to use grease gun. It will be easier to use MS15004-2. Also, the strength of the screw-type nozzle is much stronger than the barbed nozzle. If the inner parts of the barbed nozzle are blocked during oil filling, the pressure of the oil filling was so hard that the oil will be screwed out. During the maintenance of the outer space, if the location of the nozzle is hidden and difficult to filling oil, this place cannot fill oil until the overhaul. After using the screw-type 45 nozzle, the intensity of the nozzle's installation will be improved. The phenomenon of oil's screwing will not easily appear. Second, because the improvement of the intensity of the nozzle's installation the preservatives can be infused.

According to the requirements of manual, the nozzle (80) needs to be infused with the grease MIL-G-21164. Although the water of the structures can be excluded through oil filling, the anticorrosive effects are not obvious. After the change from the nozzle to screw-type nozzle, the preservative BMS 3-38 can be infused. The effects of BMS 3-38's anticorrosion are very strong. According to the experiences of the overhaul, using BMS 3-38 in the connecting part can avoid the corrosion effectively [6].

Since 1998, we had analyzed and discussed with Lufthansa Group about if there is a need to use sealant after the installation of bushing. Through the practical research of the landing gear, we find there are no obvious effects of seam sealing. Once the sealant is broken, the corrosion cannot be avoided so we use preservatives to shrink in the installation.

Using this kind of method to install the bushing, you can put some nondrying preservatives evenly between the bushing and the parts; this can improve the anticorrosive property effectively. The preservative will not be that easy in aging

as the priming paint. Through the checking, we can find, the preservative which is painted in the bushing hollow can be kept in good condition during the overhaul.

After getting the consent of the mordent and the client, we applied these three suggestions to B737 air fleet of one Airline Company. In the overhaul of the B737 landing gear of this airline company, the report of the fault detecting in the overhaul shows that only 2 trunnion links are corroded, the other 20 are all well, also, the corrosion is light and can be eliminated by hand grinding [7].

29.4 Conclusion and Outlook

This paper introduces the history of the development, structure of the landing gear of the flight, having an analysis of the usual phenomenon, and part of the fault. Since all the data cannot prove all the models of landing gears, we can only make some suggestions to some usual faults of several models of landing gears. In the future, we need to have a deeper research on such parts:

1. Adding the data of the faults we find in the repairs of landing gear, in order to having a conclusion of the usual and the high risk of the faults.
2. Tracking the parts in the new repairing program with the permits of the manufacturers, having an evaluation of the results during the repairing, making an improvement and promotion of the new schemes from these results.
3. Having a statistics of the parts' faults which badly influenced the overhaul of the landing gear in the future, optimizing the processing of the overhaul, configuring the stores and spares, and cutting down the tie-up funds of stock.

References

1. Tao C (2001) Structur design of modern Airplane. Northwester Polytechnical University Press
2. Boeing 737 CMM 32-11-11 Rev 97(2008)
3. Boeing SOPM Standard Technology Manual. 20-50-10 Rev 29(2008)
4. Sartwell BD, Natishan PM, Singer IL (2002) Replacement of chromium electroplating using HVOF thermal spray coatings
5. Mssier-Dowty Standard Technology Manual. M-DLPS1011-14 Rev6 (2005)
6. Wang H (2001) Structure and system of airplane. Weapon Industry Press
7. Willcox M, Downes G (2000) A brief description of NDT techniques

Chapter 30
Design and Simulation of a Kind of Unmanned Helicopter Fixed-Altitude Flight Control System

Wenlai Ma, Shouxi Zhu and Hongfang Xue

Abstract In order to improve the stability and the rapidity of Fixed-Altitude unmanned helicopter flight control system, this paper improves the control performance of the closed-loop system by establishing the dynamic mathematical model of unmanned helicopter and adjusts the parameters of the controller under guidance, and completes the simulation with MATLAB. Through the performance evaluation and series, feedback correction, and improved system performance, a quality improvement of unmanned helicopter Fixed-Altitude flight is obtained. This method can reduce the modeling workload and difficulty effectively, and express the process of unmanned helicopter Fixed-Altitude flight intuitively.

Keywords Unmanned helicopter · Fixed-Altitude flight · Performance evaluation

30.1 Introduction

The helicopter has the flight characteristics of vertical takeoff and landing, fixed-point hovering, etc., which are different from the fixed-wing aircraft. Unmanned helicopter also has advantages of low cost, smaller risk, and so on, which will be widely used in cruising, monitoring, handling mission and topographic survey, disaster monitoring, forest fire prevention, maritime rescue, and other dangerous

W. Ma (✉) · S. Zhu
Aviation Information Technology R&D Center, Binzhou University, Binzhou, China
e-mail: mawenlai@163.com

S. Zhu
e-mail: zhushouxi@163.com

H. Xue
Department of Computer Science and Technology, Binzhou University, Binzhou, China
e-mail: xuehongfang@126.com

J. Wang (ed.), *Proceedings of the First Symposium on Aviation Maintenance and Management-Volume I*, Lecture Notes in Electrical Engineering 296,
DOI: 10.1007/978-3-642-54236-7_30,

situations. Hovering is one of the most basic flight status and task, so how to establish an accurate mathematical model of unmanned helicopter and design an advanced flight control system to guarantee the Fixed-Altitude flying quality has very important practical value and research significance. China's research in this area is still in its infancy, and needs a large number of trials and exploration [1]. Because of the complexity and instability of helicopter, it is very difficult to establish its mathematical model and achieve accurate control.

The unmanned helicopter control system is a very complex multi input and multi output system, although the state space can be used to describe the control system of it, but the research method is not mature. The control algorithm is still the PID feedback control which is based on the classical control theory [2]. By comparison: The root locus of classical control method is mature for the system which can be linearized assuming or the linear time invariant system, and also has a good control effect. So, its advantages become an important basis for choosing the method of unmanned helicopter flight control process of the Fixed-Altitude Flight [3]. On the basis of Fixed-Altitude flight control, in order to verify the validity of the control system to be more comprehensive, the paper finished the flight control system simulation of unmanned helicopter to show the robustness of control system of unmanned helicopter.

30.2 Control System Model Establishing

To establish a reasonable mathematical model is the key to the implementation of system design and simulation. In this paper, in order to simplify the modeling process, eliminate interference factors, the following assumptions in the establishment of air dynamics model are: (1) the helicopter is rigid, remained unchanged in the quality of its movement in the process; (2) regard the geodetic coordinates as inertial coordinate system and the earth's surface as a plane; (3) without the effects of earth rotation and revolution movements; (4) the acceleration of gravity does not change with the change of altitude; (5) *xoz* plane of the airframe coordinate system is the symmetry plane of geometry and quality of helicopter [4].

As shown in Fig. 30.1, the helicopter has six degrees of freedom, three translational degrees of freedom along the axial movement, and three rotational degrees of freedom which rotates about the center of mass. According to Newton's second law of motion, dynamic equations of the vector form for helicopter are:

$$F = m\frac{dV}{dt}, M = m\frac{dH}{dt} \tag{30.1}$$

In the expressions: F-effects of all external forces on the helicopter; m-quality of helicopter; V-Center-of-mass velocity of helicopter; M-total external torque; H- moment of momentum.

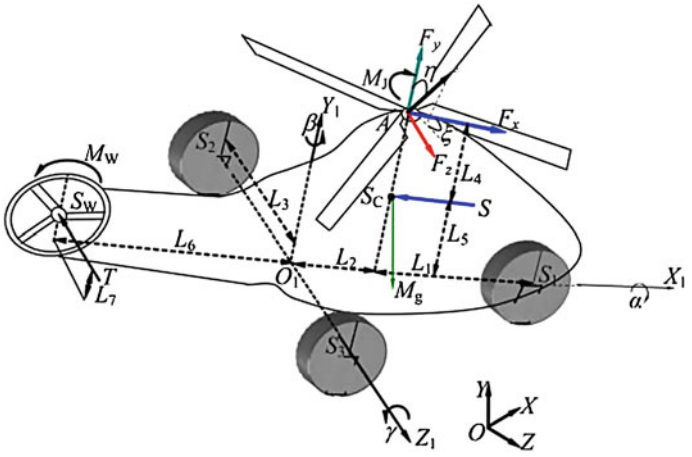

Fig. 30.1 Force analysis of helicopter

If the F_X, F_Y, F_Z, u, v, w, p, q, r, respectively represents coordinate component of F, V, ω of three axes O_x, O_y, O_z weight in the body coordinate system, so the helicopter general motion dynamics equations can be expressed as follows:

$$\begin{cases} F_x = m(\dot{u} - vr + wq) \\ F_y = m(\dot{v} - wp + ur) \\ F_z = m(\dot{w} - uq + vp) \end{cases}, \begin{cases} L = \dot{p}I_x - \dot{r}I_{xz} + qr\left(I_z - I_y\right) - pqI_{xz} \\ M = \dot{q}I_y + pr(I_x - I_z) + (p^2 - r^2)I_{xz} \\ N = \dot{r}I_x - \dot{p}I_{xz} + pq\left(I_y - I_x\right) + qrI_{xz} \end{cases} \tag{30.2}$$

The equations of helicopter kinematics above are the force and torque equations. If we need the helicopter's bearing and flight trajectory relative to the ground coordinates, then we can get supplementary kinematics equation by using coordinate transformation, i.e.:

$$\begin{cases} dx/dt = u\cos\psi\cos\theta + (-\sin\psi\cos\phi + \cos\psi\sin\theta\sin\phi)v \\ \qquad\qquad + (-\sin\psi\sin\phi + \cos\psi\sin\theta\cos\phi)\omega \\ dy/dt = u\sin\psi\cos\theta + (-\cos\psi\cos\phi + \sin\psi\sin\theta\sin\phi)v \\ \qquad\qquad + (-\cos\psi\sin\phi + \sin\psi\sin\theta\sin\phi)\omega \\ dz/dt = -u\sin\theta + v\cos\theta\sin\phi + \omega\cos\theta\cos\phi\omega \end{cases} \tag{30.3}$$

The symbols Ψ, θ, and Φ represent yaw Angle, pitching Angle, and around the corner respectively.

Because of the limitation of condition, the paper cannot get the vertical flight data of the helicopter through the real experiments and model identification. So the flight data in this paper is from related literature described in the Raptor 60 V2 mini unmanned helicopters, dynamic characteristics of the system transfer function mathematical model can be expressed as [5]:

$$H(s) = \frac{b_1 s^3 + b_2 s^2 + b_3 s + b_4}{\mathrm{s}^4 + \mathrm{a}_1 \mathrm{s}^3 + \mathrm{a}_2 \mathrm{s}^2 + \mathrm{a}_3 \mathrm{s} + \mathrm{a}_4} \tag{30.4}$$

If we ignore the effect of the vertical stabilizer, horizontal stabilizer, tail, and the coupling relationship between longitudinal and transverse when the rotor rotating. When the helicopter is in a hover state, the approximate transfer function of input and output is two order system, because the helicopter system damping is very small, so it can be seemed as the underdamped system, and the time response is oscillatory characteristics, therefore the state space can be expressed as:

$$\begin{cases} \dot{X} = AX + BU \\ Y = CX + DU \end{cases}, \; A = \begin{bmatrix} -1 & -1.05 & -0.5 \\ 2 & 0 & 0 \\ 0 & 1 & 0 \end{bmatrix}, \; B = \begin{bmatrix} 2 \\ 0 \\ 0 \end{bmatrix}, \; \begin{matrix} C = [0.5 \quad 0.5 \quad 0.25] \\ D = 0 \end{matrix} \tag{30.5}$$

This paper uses MATLAB to convert state space models into the pole zero gain model, then can get the closed-loop transfer function of the helicopter's flying height and lifting speed:

$$F(s) = \frac{(s+1)^2}{(s+0.54)(s^2 + 0.46s + 1.85)} \tag{30.6}$$

30.3 Simulation of Control System Model

Simulation method of control system: The paper calculates the difference between target height and the value of the altimeter or the actual height measured by the barometer, inputs the differential into a helicopter dynamic module, then converts the velocity variable into height difference by integrating. After repeated adjusting, the helicopter finally realizes the actual height equal to the target altitude, the control system reaches steady state, and achieves the purpose of Fixed-Altitude Flight. The Fixed-Altitude Flight model of helicopter established by using Simulink toolbox is shown in Fig. 30.2.

Assume that the unmanned helicopter is located on the ground at first, the target altitude is 500 m. The paper built the simulation model by using Simulink and then finished the simulation when the rudder loop gain of the K is respectively 0.45, 32, and 10.

As shown in Fig. 30.3, the helicopter is in the equal amplitude oscillations in the center with 500 m when K is 0.45, and unable to achieve Fixed-Altitude hover.

As shown in Fig. 30.4, the helicopter reached the target altitude of 500 m and enters the hover condition after 5.4 s when K is 2. The overshoot is 38.2 % and the adjusting time is 5.4 s, the stability and the rapidity of the system is less than ideal.

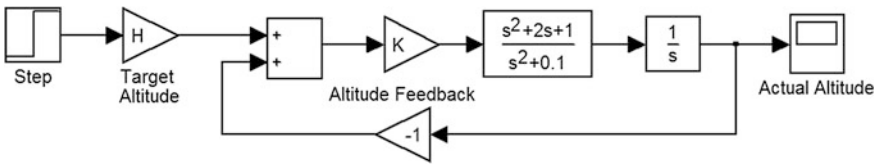

Fig. 30.2 Simulink model diagram of helicopter

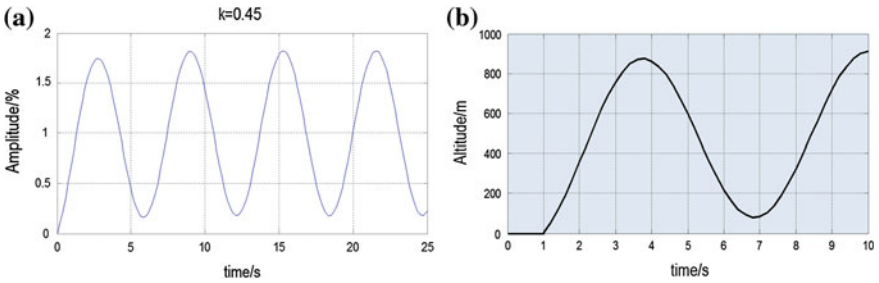

Fig. 30.3 System simulation results when $K = 0.45$. **a** The unit step response. **b** System simulation image

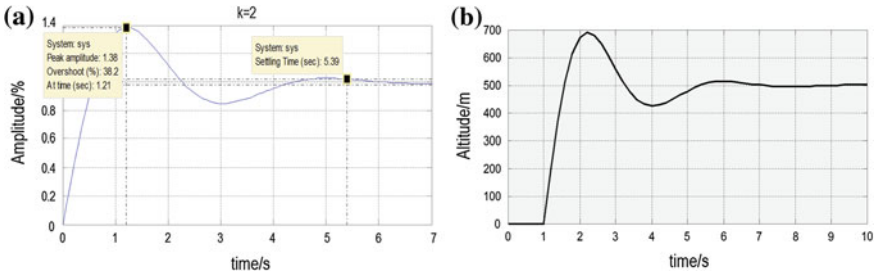

Fig. 30.4 System simulation results when $K = 2$. **a** The unit step response. **b** System simulation image

As shown in Fig. 30.5, the helicopter was basically stable at a specified height after an undulating movement when $K = 10$ while the adjusting time was 1.3 s and the overshoot amount was 13 %, the response speed of the system is fast.

Through the comparison of several K values, we can find the system response time reducing, overshoot decreasing and system performance decreasing with the increase of K. But the K value cannot be too big which is limited by propeller speed and tilt angle. So we need to consider various aspects in engineering application, and choose suitable K values in order to meet the requirements of the best performance.

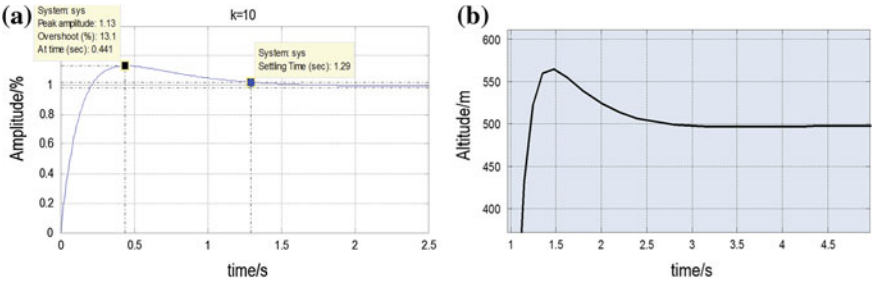

Fig. 30.5 System simulation results when $K = 10$. **a** The unit step response. **b** System simulation image

30.4 System Performance Evaluation and Correction

Stability. If the poles of root locus are on the left of imaginary axis, it indicates that the system is stable; if the poles are on the right side, then the system is unstable, otherwise, the system is in critical state. If we use modern control theory to determine the stability of the system, it can be completed by Lyapunov function.

We can find that the real part of a pair of conjugate eigenvalue of the system characteristic equation is zero through MATLAB calculating, so the helicopter system is an unstable system which need to add the feedback path to achieve steady state. In addition, the system root locus mapped by MATLAB is shown in Fig. 30.6, with root locus in the right half plane, so the system is unstable.

Rapidity. The rapidity of system refers to the dynamic process in the length of time. If the dynamic changes of time are short, it indicates that rapidity of system is better, the system response is faster; on the contrary if the dynamic changes of time are long, it shows that the system response is slow and it is difficult to achieve rapid change instruction.

We used the LTI Viewer in MATLAB to map the unit step response of the original system, as shown in Fig. 30.7. The system adjusting time is 16.3 s and overshoot is 54.4 %. Thus the stability and rapidity of the system are not ideal.

Series correction. Series correction is to add some operational rules of implementation of the regulator on the original system to satisfy the performance of the control system. The system block diagram after joining series correction is shown in Fig. 30.8:

Suppose K of series correction section equals 3, the system transfer function can be expressed as follows after correction:

$$\frac{C(s)}{R(s)} = \frac{3s^2 + 6s + 3}{s^3 + 3s^2 + 6.1s + 3} \tag{30.7}$$

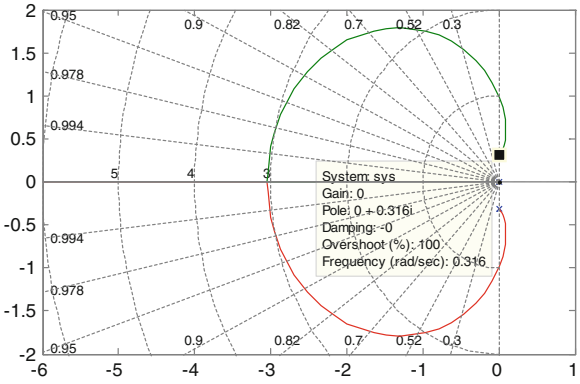

Fig. 30.6 Open-loop root locus of the system

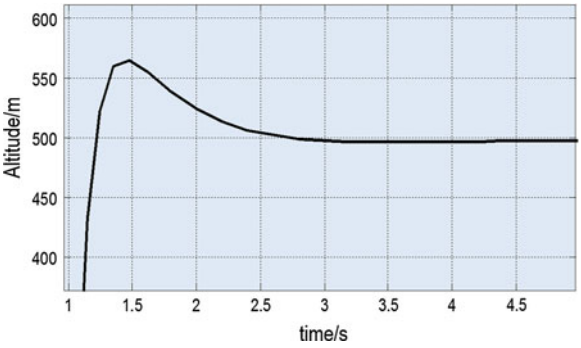

Fig. 30.7 Unit step response of the original system

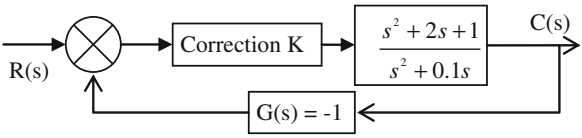

Fig. 30.8 Series correction link system

In this condition, the unit step response of the system is shown in Fig. 30.9. Adjusting time of the system has changed from the original 16–3.7 s after joining series correction, so it significantly shortens the response time and enhances the quickness of series correction system.

30.5 Feedback Correction

In this paper, we had discussed that system root locus in the right half plane and the system was unstable without the addition of negative feedback, so we added feedback to make the system more stable. In order to further improve the system's

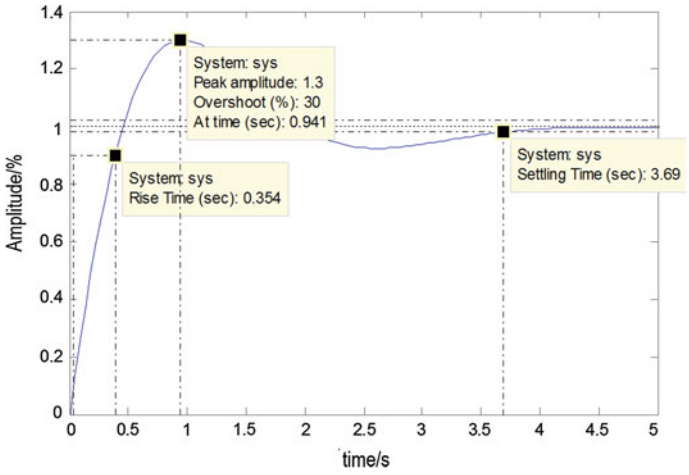

Fig. 30.9 Series correction link system

accuracy and rapidity, we can add a velocity feedback. The Simulink model of the system after adding correction is shown in Fig. 30.10. After adding velocity negative feedback, the system transfer function is:

$$H(s) = \frac{s^2 + 2s + 1}{2s^3 + 3s^2 + 3.1s + 1} \tag{8}$$

Figure 30.11 is the system of the root locus diagram mapped by MATLAB rlocus () function.

After adding velocity negative feedback, the system's root locus all fell on the left of imaginary axis, so we can know the system is stable by the system stability criterion.

In the open-loop system root locus, we can find that a pair of conjugate poles of system is on the imaginary axis, so the system is unstable. After adding highly negative feedback and speed feedback, the closed-loop poles of the system all came on the left side of the imaginary axis, so we now know that the system has become stable by the system stability criterion.

After joining the speed feedback, the system response curve is shown in Fig. 30.12.

After adding velocity feedback and highly negative feedback, the system response time changed from 16.3 to 7.7 s. Overshoot volume reduced drastically from 54.4 to 3.22 %, the rapidity, stability, and accuracy of the system are improved obviously. The simulation results show that added feedback can improve the Fixed-Altitude flight quality of unmanned helicopter.

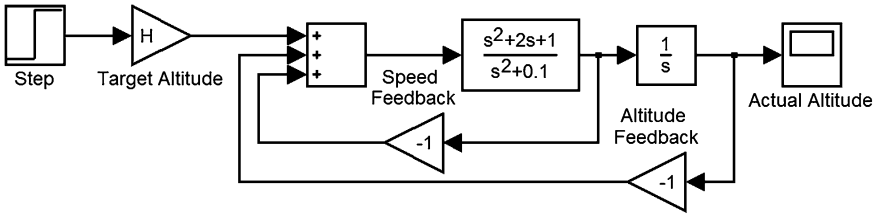

Fig. 30.10 Feedback correction simulink model

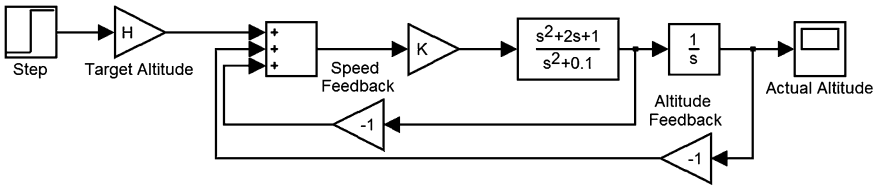

Fig. 30.11 System of root locus after adding velocity negative feedback

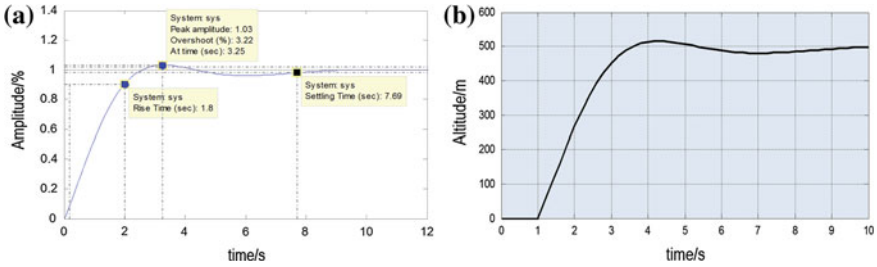

Fig. 30.12 Helicopters feedback correction simulation results **a** the unit step response, **b** system simulation image

30.6 Conclusion

The simplified transfer function of the helicopter and the MATLAB simulation results showed that the dynamic characteristics of the helicopter system itself is not stable and has an obvious oscillation characteristic. The Fixed-Altitude flight control process of unmanned helicopter in vertical direction is a process from oscillation to stability gradually, while it's regulating rapidity and stability is poor. By adding the series connection, feedback correction, and adjusting the rudder loop gain repeatedly, this method obviously shortened the adjustment time of oscillation. Eventually, it improved the stability of the helicopter and the quality of the Fixed-Altitude flight.

Acknowledgment This work was financially supported by Project Fund of Binzhou University (BZXYG1320, BZXYG1316).

References

1. Stingu E, Lewis FL (2009) A hardware platform for research on helicopter UAV control. J Intell Rob Syst
2. Frye MT, Qian C, Richard D (2005) Receding horizon control of a linear parameter varying model of the Raptor 50 helicopter. AIAA guidance, navigation, and control conference and exhibit
3. Zhao Z, Gou X, Tiansheng LU (2010) GA-based model evolutionary identification for Yaw Channel of small-scale. Robot
4. Yuan Y (2007) Modeling and simulation of a small-scale unmanned helicopter. Nanjing University of Aeronautics and Astronautics
5. Dai N, Si Y (2006) Helicopter flight control system modeling and simulation by MATLAB. J Syst Simul

Chapter 31
A Safety Monitoring Technology for Aircraft Ground Power Cable

Changming Chen, Lizhen Xu, Manna Zhou and Fan Zhang

Abstract When supplying ground power to aircraft, the cable of aircraft power supply vehicle often pulls the aircraft power socket, which damages the socket and aircraft skin. A cable safety monitoring technology is proposed with regard to this problem, and a monitoring apparatus is developed and designed using this technology. This paper describes the composition, technical principles and signal detection scheme of this apparatus, which is able to sent out an alarm if the cable isn't safely fastened, thus eliminating potential hazard for failure, preventing accident, and improving the ability of equipment maintenance and support.

Keywords Aircraft ground power cable · Monitor · Alarm

31.1 Introduction

Aircraft ground power vehicle provides power support through the connection between ground power cable and aircraft power socket. It provides the power needed for aircraft maintenance and engine start, and is in large quantities and frequent use [1]. When aircraft maintenance is in progress, the power vehicle is often moved before the power cable is pulled out of aircraft ground power socket, resulting in personnel injury and device damage. For instance, cable plug is thrown out of the aircraft ground power socket and injures the maintenance personnel; the power vehicle leaves with the cable plug still attached to the aircraft, and the aircraft power socket is consequently damaged, aircraft skin torn and power vehicle's cable plug damaged; the cable isn't properly bound and fixed, and it slips off because of vehicle jolt, resulting in cable plug damages. When such accidents take place,

C. Chen (✉) · L. Xu · M. Zhou · F. Zhang
Beijing Aeronautical Technology Research Center, Beijing 100076, China
e-mail: hcszchchm@sina.com

J. Wang (ed.), *Proceedings of the First Symposium on Aviation Maintenance and Management-Volume I*, Lecture Notes in Electrical Engineering 296,
DOI: 10.1007/978-3-642-54236-7_31,

aircraft ground power socket and skin need to be repaired. As a result, flying trainings cannot be carried out as planned, which not only seriously affects the accomplishment of flying training tasks, but also causes certain financial losses [2].

To eliminate such hazards for potential failure and prevent accidents, domestic suppliers of aircraft ground support equipment have conducted a large amount of researches [3]. Some use pressure sensor to detect the pressure between the cable plug and the insert column in the aircraft ground power socket in order to judge the working status of the cable. However, the aircraft starting current is so strong that high temperature arc can easily form between the plug and the insert column, which damages the pressure sensor, so this method has its defects [4].

To completely remove any potential hazard of accident, a new type of cable safety monitoring technology is proposed, and the apparatus developed based on this technology consists of two parts—the cable fixing device and the alarm control box, which can send out an alarm if the cable isn't pulled out or fastened when the power vehicle is providing aircraft maintenance support.

31.2 Composition of Cable Safety Monitoring Apparatus

The aircraft ground power service cable safety monitoring apparatus mainly consists of two parts - the cable fixing device and the alarm control box. There are altogether four cable fixing devices, two cable fixing devices installed on each cable platform on both sides of the power vehicle. The cable fastening device is comprised of fastening lock and cable belt fastener. When cables are placed on the cable platform, close the fixing device to safety fasten the cables, and the sensor in the fixing device will send a signal to the alarm control box. Installed in the wheelhouse, the alarm control box can monitor the cable and send out an alarm if the cable isn't safely fastened as regulated. If the ground power vehicle moves when the cable is at work supplying power for aircraft maintenance, voice alarm will be actuated along with flashing at the same time.

This apparatus can be powered by the vehicle battery in the ground power vehicle. When the vehicle starts and the key turns to "power supply for wheelhouse," the apparatus is powered as well and it can work normally. When the key turns to "turn off wheelhouse power supply," power supply for the apparatus is also cut off and it stops working. Therefore, when the key is pulled out, the apparatus has not power consumption, thus reducing battery consumption. Figure 31.1 is a schematic diagram of the principle of the monitoring system.

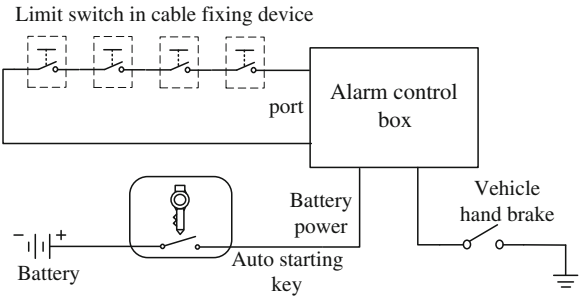

Fig. 31.1 Schematic diagram of the principle of the monitoring system

31.3 Design Principle of Cable Safety Monitoring Apparatus

When the ground power vehicle is in the field for power support, after it finishes its task of aircraft maintenance and the power cables are put back on the cable platform, the power vehicle needs to leave the flight line quickly, so the cable fixing device shall be operated as quickly and easily as a car belt. Meanwhile, since the power vehicle is on duty for field support around the clock, it is subject to severe environment, so the guiding thought for the design of the cable fastening device is easy operation, high reliability, and high corrosion resistance.

Cable fastening lock and alarm control box are two key parts of the cable safety monitoring apparatus, and their design principles will be introduced in detail in the following.

31.3.1 Design of the Cable Fastening Lock Structure

Cable fastening lock is a major part of cable safety monitoring system. It is used in conjunction with the cable belt fastener. When the buckle of the belt fastener is inserted into the slot of the lock, the fastener wraps around the cable and keeps it firmly on the platform. When the buckle exits the lock, the belt fastener is loosened and the cable can be used for power support.

This paper proposes a lock that can lock the cable rapidly. Cable fastening lock mainly consists of lock pin, lock slot, stand, and limit switch. In the stand there is a slide rail, and the lock pin, which is a moving part placed on the slide rail, is driven by an internal spring. When the belt fastener is used to fasten the cable, support personnel move the snap ring on the belt fastener to push the lock pin, so that the snap ring can clap into the lock slot. When the personnel relieve the snap ring, the lock pin, pushed by the spring, keeps the snap ring in the lock slot to prevent it from falling out, so the belt fastener can fasten the cable firmly. When the belt fastener is loosened, the personnel take the snap ring from the lock slot and the

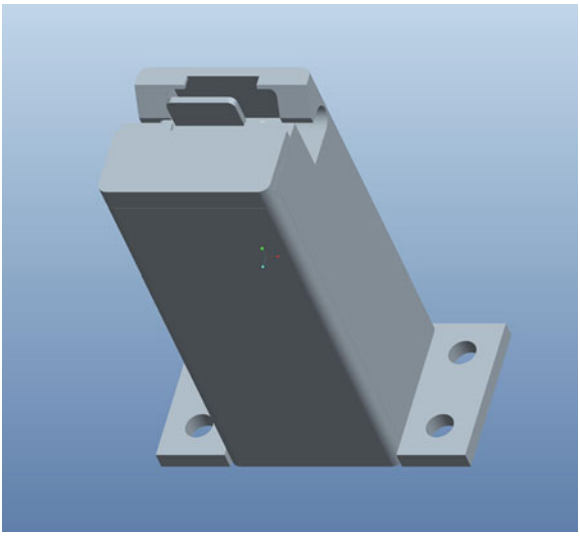

Fig. 31.2 3D view of cable fastening lock

lock pin, still pushed by the spring, moves back to the end of the slide rail. A 3D view of the cable fastening lock is shown in Fig. 31.2.

The purpose of the friction rail in the stand is to support and guide the moving part to move in reciprocating and rectilinear motion in a designated direction. The moving part of the slide friction rail is in direct contact with the rail. Common rails include triangular rail, rectangular rail, swallowtail rail, and their combination. Triangular and swallowtail rails have high guiding precision, but they require uniform contact with all four rail surfaces, and are difficult to manufacture and sensitive to temperature, so the simple-structured and easily manufactured rectangular rail is selected. To prevent the moving part from tilting or getting stuck when sliding on the rail, the clearance between the moving part and rail is set at 0.2 mm. Figure 31.3 shows the stand of a fastening lock, above which is a rectangular rail. In Fig. 31.3, the corner of the rail is designed as an S-shaped arc mainly to facilitate processing.

The direction and point of action must be reasonably determined when the rail is designed, so as to minimize its overturning moment. Otherwise friction in the rail will increase and wear and tear will worsen, which will impair the rail's moving agility and steering precision, even jam the rail in a truly severe scenario so that it cannot work normally. Therefore, the moving part must be designed to be as low as possible, so as to reduce their friction with the rail and the occurrence of moving part getting stuck.

To lengthen the rail's service life, its resistance to wear and tear and corrosion must be enhanced. As the wearing speed is directly related to material property, processing quality, pressure intensity on the surface, lubrication, use, maintenance and other factors, measures should be taken to address those factors in order to improve the rail's wearing resistance. During the design period, stainless steel

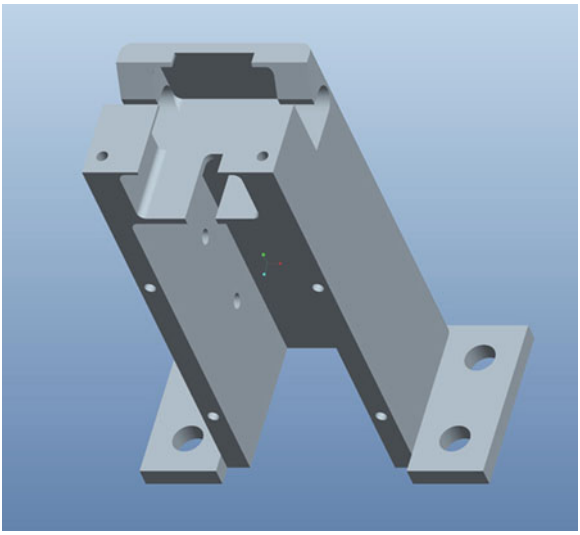

Fig. 31.3 3D view of cable fastening lock stand

material is used for moving part, high-strength aluminum alloy for the stand, and all parts shall be machined on high-precision numerically controlled machine tool.

To find out whether the snap ring of the belt fastener is inserted in the lock slot of the fixing device, a limit switch, whose transmission shaft is linked to the moving part, is installed in the stand. When the snap ring is inserted into the lock slot, the contact of the limit switch closes, and when the snap ring exits the lock slot, the contact of the limit switch disconnects. Based on comprehensive considerations for the internal size of the fixing lock and the performance of limit switches in the market, the TM-1701 waterproof switch is selected, which has a normally closed contact. When the belt fastener is loosened, the contact of the travel switch disconnects, and when the belt fastener is locked, the contact closes.

31.3.2 Principle of the Alarm Control Box

The alarm control box, which is on the platform of the wheelhouse, consists of housing, display, signal processing circuit, etc. The control circuit of the alarm box is controlled by the starting key of the power vehicle. The control circuit is powered only when the vehicle is powered, otherwise it doesn't work. The alarm box doesn't display the alarm when the hand break is at work. When the hand brake isn't at work, the sound and light alarm is actuated or stopped by judging the status of the limit switch installed on the cable fixing device [5]. Figure 31.4 is a process chart of signal detection of the alarm control box.

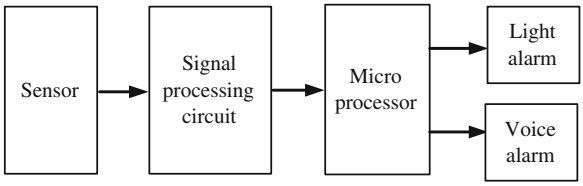

Fig. 31.4 Principle of signal detection process

Table 31.1 Logical relation of the alarm box at work

Working status		Hand brake light	Alarm light	Voice alarm
Hand brake in place	Cable fixing device closed	On	Off	Off
	Cable fixing device disconnected	On	Off	Off
Hand brake loosened	Cable fixing device closed	Off	Off	Off
	Cable fixing device disconnected	Off	Flashing	On

The alarm box is intended to monitor the signal switch of the fixing device, analyze signal status and decide whether it is necessary to send out an alarm. The logical relation among the cable fixing device, auto hand brake, alarm light and voice alarm modules is designed as follows: when the power vehicle is providing power support, it is in "parking" status if the hand brake is in place, and no alarm will be actuated no matter what status the cable fixing device is in. If the auto hand brake is loosened and cable belt fastener isn't inserted into the fixing lock, the alarm light is on together with a voice alarm—"cable isn't fastened, cable isn't fastened." Table 31.1 shows the logical relation of the alarm box at work.

31.4 Summary

Regarding the situation that during power support work, aircraft power socket is frequently pulled and aircraft skin damaged by aircraft ground power support cable isn't disconnected from the socket. This paper proposes a cable monitoring and alarming technology using cable fastening lock and sensor. When this technology is applied, the personnel can be timely reminded to make adjustments if the aircraft ground power support cable isn't used according to rules, so as to prevent accidents of cable pulling the aircraft and improve aircraft maintenance and support technology.

References

1. Wang D (1998) Ground power supply for aviation (in Chinese). The Publishing House of Ordnance Industry, Beijing
2. Lei J (2005) Collection of accidents of aviation ground guarantee equipment (in Chinese). Aviation Industry Press, Beijing
3. Chen Y, Zhang W (2011) Analysis of application situation and development trend of aircraft ground power supply (in Chinese). Technol Prod Mil Civ Purp 9:55–57
4. Lv Y, Ma S, Chen W et al (2008) Design of a device for aircraft ground power vehicle for damage Prevention when aircraft starts without the cable being disconnected (in Chinese). Movable Power Stn Veh 1:1–3
5. Liu H, Zhang P (2004) An intelligent module of digital signal input based on MB90F548G MCU (in Chinese). Electron Technol 8:31–32

Chapter 32
Online Test System for Aircraft Navigation System

Cunbao Ma, Chunnan Shen, Ke Li and Zhuo Sun

Abstract The online test is a series of tests on the final assembly production line and it plays a vital role in ensuring the safety of aircraft flight. In this paper, the excitation and test equipment is chosen and the connection method and test procedure is researched. The online test system of the distance measuring equipment (DME) is designed as an example. Its test layout, schematic diagram and specific test procedure are presented. Besides, the cross-linked part of navigation system is researched and its test method is proposed. The online test system in the paper not only meets the requirement of test but also raises the level of automation and test coverage.

Keywords Online test · Navigation system · DME · Cross-linked system

32.1 Introduction

The final assembly production line of an aircraft is used to assemble structural parts (including some function systems) of a plane. Devices and systems are installed, adjusted, tested, and inspected onboard to make sure it has complete flight functions and usage functions [1]. The technique of aircraft final assembly is developed from manual assembly, semi-mechanization, and mechanization to automation assembly [2]. The Boeing Company makes the leap in changing and improving the traditional way of assembly and the success of Boeing 777 sets an example of automatic assembly technique for plane manufacturing [3]. The movable production line technique [4], a technique from the production mode of Toyota and the theory of lean production, can be applied to manufacturing aircrafts

C. Ma · C. Shen (✉) · K. Li · Z. Sun
School of Aeronautics, Northwestern Polytechnical University,
Xi'an 710072, Shaanxi, China
e-mail: scn7th@163.com

J. Wang (ed.), *Proceedings of the First Symposium on Aviation Maintenance and Management-Volume I*, Lecture Notes in Electrical Engineering 296,
DOI: 10.1007/978-3-642-54236-7_32,

with high quality, low cost, and quick response. The principle and method of online test system for navigation system is researched in detail by using the automatic assembly method based on movable production line technique. The online test system of DME is designed. The test layout, schematic diagram, and specific test procedure are given. The cross-linked part of navigation system is analyzed and its test method is introduced.

32.2 Excitation Equipment of the Test System

The navigation data of the ground-based navigation system [5] is received from external reference navigation stations, including ground stations and satellites. The excitation equipment is introduced to replace external reference navigation stations to provide excitation signals [6]. The equipment is listed in Table 32.1.

Figure 32.1 illustrates the detailed connection between excitation equipment and the aircraft. The tripod is used to keep the antenna of excitation equipment and the plane antenna in the same height for coupling. The distance between the two antennas is from 38 to 76 cm, normally 54 cm. The antenna of excitation equipment is fixed by the tie on the coaxial cable. Besides, the type of antenna depends on the excitation equipment.

32.3 Test Equipment

The test equipment is gathered in Table 32.2.

The INS simulator is composed of a general one-axis testing rotary platform, a rotary platform controller, test adapters, cables, a testing computer, and INS devices. The simulator components are connected like as shown in Fig. 32.2.

32.4 Design of the Online Test System of Navigation System

32.4.1 Online Test System for Navigation Equipment

Given that the online test system must be qualified with good compatibility, considerable augmentability, high speed of transmission and strong ability of anti-interference, VXI bus instrument is used to design the hardware. The connections of the system are shown in Fig. 32.3. The part in the box drawn by the dotted lines is determined by the system under test. The monitor and Headset microphone are common components. There are six interfaces in the terminal box for online test. The relay matrix, which is a 4×4 switch matrix, is introduced to connect

Table 32.1 List of excitation equipment

Name	Type	Function
Automatic direction finder (ADF) simulator	WLC-9	Simulate the work of ADF and provide input signals for ADF receiver.
Altimeter tester	ALT-8000	Simulate the change of height.
Navigation tester	NAV-40IL	Test VOR.LOC, GS and MB.
Simulator (tester)	ATC-600A	Test ATC and DME.

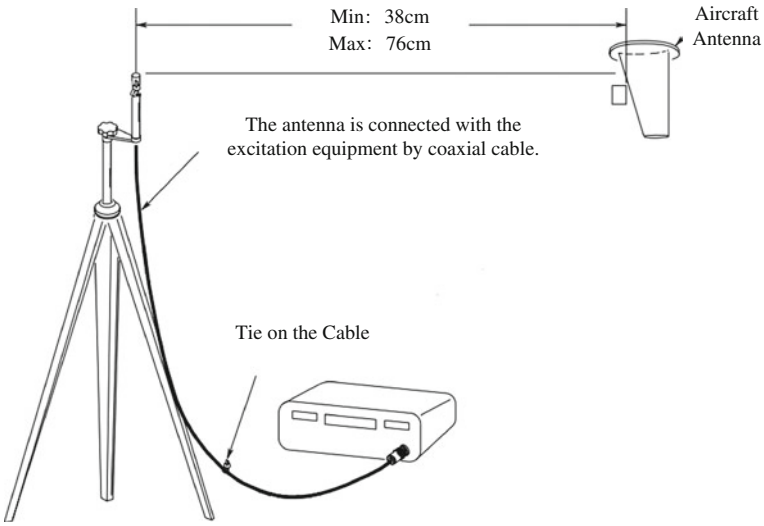

Fig. 32.1 Connection between excitation equipment and the aircraft

Table 32.2 List of test equipment

Name	Type	Function
Display device	Monitor	Record display information
Audio test equipment	Headset microphone	Test audio signals
VSWR device	S331B	Test VOR,LOC,GS, and MB
INS simulator		Simulate the INS

different online test systems of navigation subsystems. The test instrument is the test module of ARINC 429 Bus [7, 8] and the excitation equipment is controlled by the computer.

The test procedure is to test each subsystem in a specified sequence. The strategy for testing is from simple to complex. The test sequence is as follows: ADF, RA, DME, ATC, and VOR/ILS. The online test system of DME is taken as an example to elaborate how to design the test system in Sect. 32.4.2

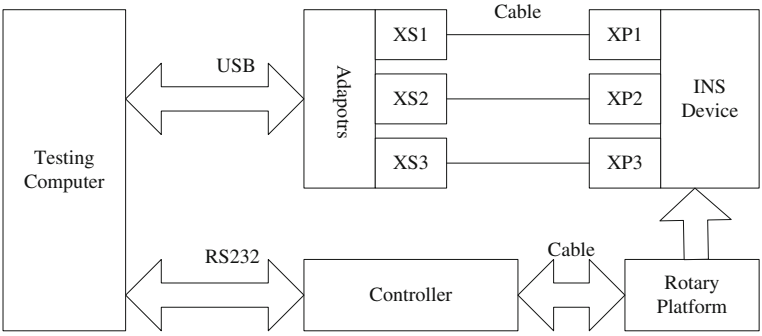

Fig. 32.2 The INS simulator

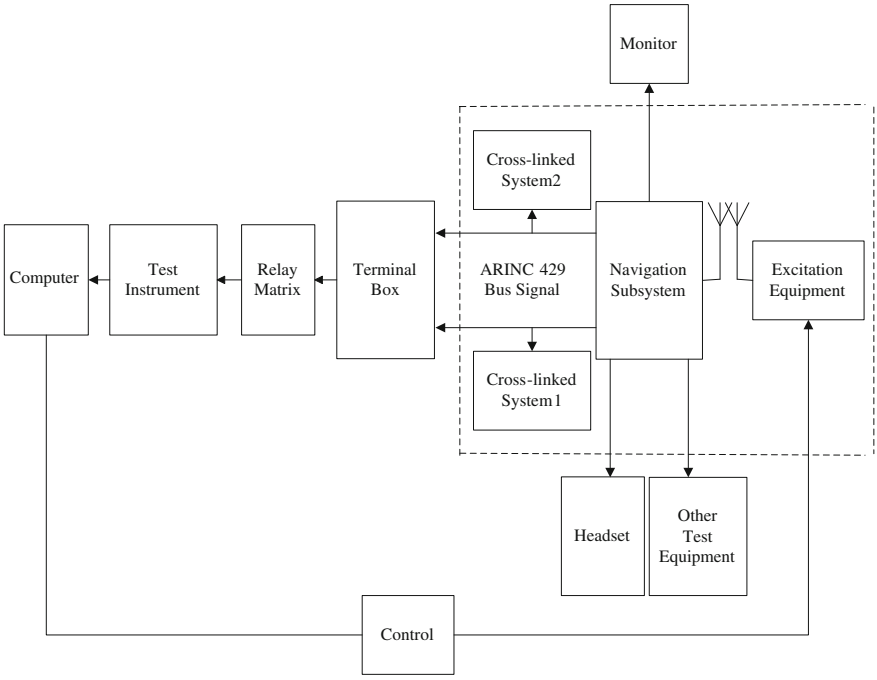

Fig. 32.3 Online test system of the navigation system

32.4.2 DME Online Test System

Test layout. The layout of the online test system is shown in Fig. 32.4.

Schematic diagram of the test. The schematic diagram is given in Fig. 32.5. Distance signal is provided by ATC-600A to DME through the coupling antenna. The test is controlled by the DME control box. Distance signal and audio signal are

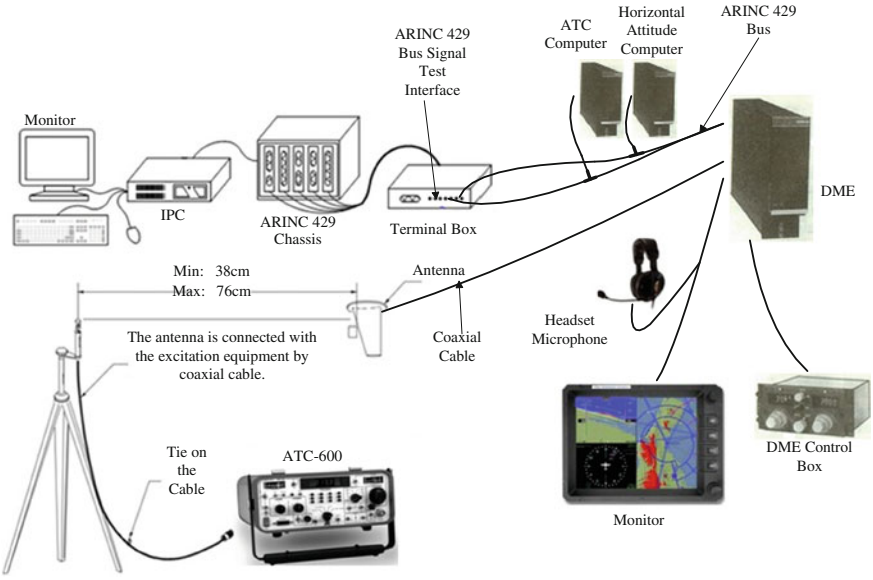

Fig. 32.4 The layout of DME online test system

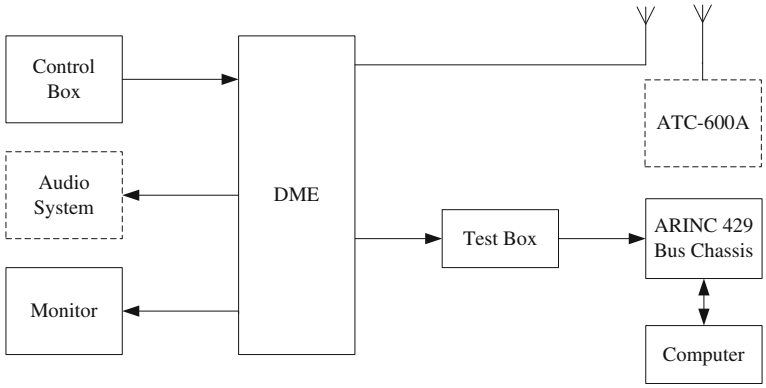

Fig. 32.5 Schematic diagram of DME online test system

inspected by the distance monitor and audio system. The ARINC 429 bus signal is tested by the IPC.

Test procedure. First of all, the antennas of the tester (ATC-600A) and the DME should be installed. The two antennas share the same height and the distance between them lives up to some certain specification [9]. For example, the distance specified by ATC-600A is approximately 54 cm and the minimum value is 38 cm. Then the antenna is connected to the tester by a cable. The switch of ATC-600A is set to the specified position and power supply is connected to the tester.

Afterwards, Identification code is shown on its screen. After the power is on, 115 V AC is supplied to the ATC transponder from bus bar and the system is ready to be tested.

(1) Self test: Operate EFIS on the flight deck simulator and select the HIS formation for EHSI. The main channel is set to the VOR state. Check all the signals in the DME and listen to Morse alphabet codes through the headset microphone.
(2) Distance, velocity, and performance signals: The tester is turned to "Distance Measuring" and the same frequency with the tester is set for DME. Set distance on ATC-600A and watch the display until the distance on the simulation cabin becomes the same value with that on the tester. Set velocity on ATC-600A and watch the display until the velocity on the simulation cabin becomes the same value with that on the tester. The tester is then turned to the position of "Hold" and the inhibit signal is shown on the display. Different frequencies are set and the marks of horizontal stroke are shown. After cutting off the tester, the display becomes normal.
(3) Identification tone check: The tester is turn to "Identification" and listen to audio signals through the headset microphone.
(4) Bus signal: The bus signal is transmitted to the tester through two interfaces in the terminal box, which is the test module of the ARINC 429 Bus. The voltage and frequency are analyzed by the computer to find if they are both within the specified range.

32.4.3 Analysis of Online Test System of the Cross-Linked Part

Relation of the cross-linked part of navigation system. According to the AMM of the Boeing 737–600 [10], the relation of all the subsystems within the navigation system is presented in Fig. 32.6. The lines with arrows represent the 429 Bus. The radio range of the radio navigation station is provided to DEU and RMI by ADF. Height data is provided to FCC, A/T, DEU, WXR R/T, GPWS, and TCAS by RA. Distance information is provided to ATC, FMC, and FCC by DME. Direction information is provided to RMI, FMC, FCC, and DEU by VOR/ILS. Flight track is provided to ADC and WXR R/T by IN. The static pressure, pitot pressure and airspeed are provided to IN, ATC and HAS by AD. Attitude and aircraft heading information is provided to FCC, RMI, IN, and WXR R/T by HAS.

Test method for the cross-linked part. Test method: The subsystem is provided with excitation in the specified sequence above, when others are off the excitation. The integrity of the system is tested by observing the display information from correlated systems.

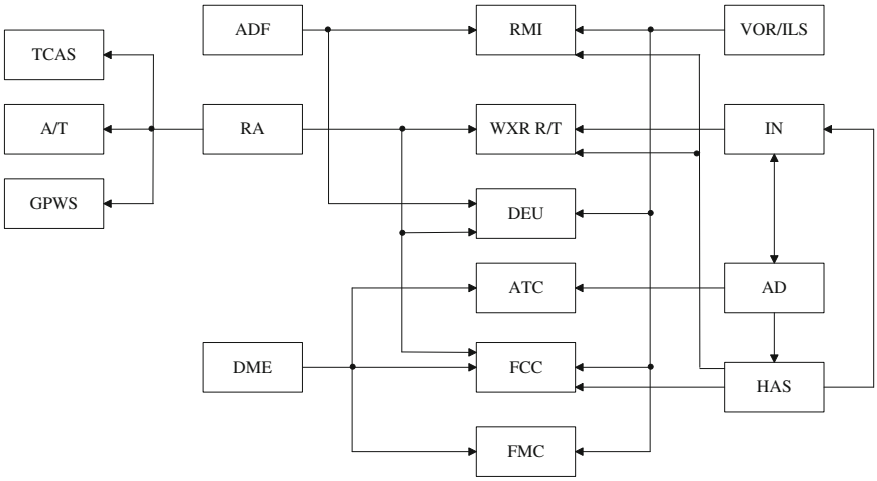

Fig. 32.6 The relation of cross-linked subsystems of navigation system

For example, as there is response inhibition between DME and ATC, distance information is sent to FMC and FCC for data processing simultaneously and display information is used to identify if the DME is in good performance.

32.5 Conclusion

The excitation, test equipment and test platform for online test system are presented in the paper. The test system of DME is designed as an example, and its test layout, schematic diagram and specific test procedure are given. The cross-linked part of the navigation system of Boeing 737-600 is analyzed and its test method is developed. The online test system designed in the paper raises the level of automation and test coverage and lays the foundation of future work.

References

1. Cook CR (2003) Assembling and supporting the joint strike fighter in the UK-issues and costs. United Kingdom's Ministry of Defense, CA
2. Li Y, Sang L (2011) Brief discussion on aircraft final assembly automatic assembly line (in Chinese). Equip Manuf Technol 10:132–133
3. Doumbia F, Laurent O (2009) Using the multiple-clue approach for system testing on AIRBUS FAL (Final Assembly Line). In: International Test Conference (2009)
4. Cook CR (2003) Final assembly and checkout alternatives for the joint strike fighter. National Defense Research Institute (2003)

5. Cunbao M (2004) Aircraft communication, navigation and radar (in Chinese). Northwestern Polytechnical University Press, Xi'an, China, pp 332–333
6. Feng L (2008) Development of the radio altimeter detector based on C8051F005 (in Chinese). Master's Thesis, Nanjing University of Aeronautics and Astronautics, China
7. Xiao Q, Zhang Y (2010) Research and application of simulating test method based on ARINC429 bus data (in Chinese). Avionics Technol 41:27–31
8. Mark 33 Digital Information Transfer System (DITS) (2004) ARINC Specification 429
9. Xuguang J, Yihua L (2001) Automatic test system for transponder and distance measuring equipment (in Chinese). Comput Autom Measur Control 9(1):21–23
10. 737 Aircraft Maintenance Manual (2010) Boeing Company

Chapter 33
Fault Detection and Diagnosis of a Certain UAV Based on Dual Unscented Kalman Filter

Li Li and Hua-min Zhang

Abstract This paper presents an applicable procedure of integrated fault detection and diagnosis for an unmanned aerial vehicle aircraft model. The implementation of a Fault detection and diagnosis (FDD) scheme in handling partial control effector fault cases based on a dual unscented Kalman filter (DUKF) and a Baysian rule for detection and isolation decision making. Simulation results show satisfactory results for detecting and diagnosing the control effectors failures.

Keywords Dual unscented Kalman filter (DUKF) · Fault detection and diagnosis (FDD) · Fault tolerant control system (FTCS)

33.1 Introduction

Fault tolerant control system (FTCS) is to maintain system stability in the presence of fault occurred in the actuators, sensors, or other system components. An actuator fault may make the aircraft to become unstable and some faults may even result in crash. When a fault/failure occurs, the fault detection and diagnosis (FDD) as the central part of a FTCS will detect and diagnose the source and the magnitude of the fault. The reconfiguration scheme in the FTCS will design the reconfigurable controller based on the FDD information to balance and adapt the system for being able to tolerate to the faults and failures [1].

L. Li (✉)
Department of Aerial Instrument and Electric Engineering, The First Aeronautical Institute of PLA Air Force, Xinyang, Henan, China
e-mail: zyrll@163.com

H. Zhang
Department of Aerial Ammunition Engineering, The First Aeronautical Institute of PLA Air Force, Xinyang, Henan, China
e-mail: zyrll@126.com

J. Wang (ed.), *Proceedings of the First Symposium on Aviation Maintenance and Management-Volume I*, Lecture Notes in Electrical Engineering 296,
DOI: 10.1007/978-3-642-54236-7_33,

In general, the dynamic motion of a flight vehicle can be described by a set of equations of motion. We can approach fault detection and diagnosis as a model-based bias estimation problem [2]. This paper uses a DUKF for system states and fault parameters estimation. In this work, both the system actuator fault parameters are estimated by using DUKF in the FDD module. We will focus on developing application of a FDD scheme in the event of actuator faults or failures. The scheme utilizes a DUKF [3] with real-time fault parameters identification based on the measured outputs of the sensors and the inputs to actuators moving aircraft control surfaces.

33.2 Nonlinear UAV Model

The state variables of the aircraft are defined as:

$$x = [u\ v\ w\ p\ q\ r\ \phi\ \theta\ \psi]^T.$$

In order to simplify the dynamic equations, following assumptions have been made:

(1) $I_{xy} = 0$ and $I_{yz} = 0$;
(2) Mass is assumed to remain constant;
(3) The center of gravity is assumed to be constant and fixed at the nominal value.

Nonlinear dynamic equations of the UAV are:

$$\dot{v} = \left[C_{\alpha,\beta} + C_{X_{\hat{q}}} + C_{X_{\delta_e}} + C_{X_{\delta_T}} + \left(C_{X_{\delta_R}} + C_{X_{\delta_\alpha}}\right)\right]\frac{S\bar{q}}{m} - g\sin\theta + rv - qw$$

$$\dot{w} = \left[C_{Z_{\alpha,\beta}} + C_{Z\hat{q}} + C_{Z_{\delta_e}} + C_{Z_{\delta_T}} + \left(C_{Z_{\delta_T}} + C_{Z_{\delta_\alpha}}\right)\right]\frac{S\bar{q}}{m} + g\cos\theta\sin\phi - ru + pw$$

$$\dot{q} = \left[C_{m_{\alpha,\beta}} + C_{m\hat{q}} + C_{m_{\delta_e}} + C_{m_{\delta_T}} + \left(C_{m_{\delta_R}} + C_{m_{\delta_\alpha}}\right)\right]S\bar{q}\bar{c}\frac{1}{I_{yy}} + rp\left(I_{zz} - I_{yy}\right) + I_{xz}\left(p^2 - r^2\right)\frac{1}{I_{yy}}$$

$$\dot{v} = \left[C_{Y_{\alpha,\beta}} + C_{Y\hat{p}} + C_{Y_{\delta_R}} + C_{Y_{\delta_\alpha}} + \left(C_{Y_{\delta_e}} + C_{Y_{\hat{r}}}\right)\right]\frac{S\bar{q}}{m} + g\cos\theta\cos\phi + qu - pv$$

$$D = \left[C_{l_{\alpha,\beta}} + C_{l_{\hat{p}}} + C_{l_{\delta_R}} + C_{l_{\delta_\alpha}} + \left(C_{l_{\delta_e}} + C_{l_{\hat{r}}}\right)\right] S\bar{q}b + rp\left(I_{zz} - I_{yy}\right) + I_{xz}$$

$$E = \left[C_{m_{\alpha,\beta}} + C_{m_{\hat{p}}} + C_{m_{\delta_R}} + C_{m_{\delta_\alpha}} + \left(C_{m_{\delta_e}} + C_{m_{\hat{r}}}\right)\right] S\bar{q}b + pq\left(I_{yy} - I_{xx}\right) + I_{xz}$$

$$\dot{p} = \frac{I_{yy}I_{zz}D + I_{xz}I_{yy}E}{I_{yy}I_{xx} + I_{xz}^2 I_{yy}}$$

$$\dot{r} = \frac{I_{yy}I_{xz}D + I_{xx}I_{yy}E}{I_{yy}I_{xx} + I_{xz}^2 I_{yy}}$$

$$\dot{\phi} = p + \frac{\sin\phi\ \sin\theta q + \cos\phi\ \sin\theta r}{\cos\theta}$$

$$\dot{\theta} = \cos\phi q - \sin\phi r$$

$$\dot{\psi} = \frac{\sin\phi q + \cos\phi r}{\cos\theta}.$$

Lift, drag, and pitching moment coefficients are implemented by lookup tables in the Matlab/Simulink.

33.3 LPV Model of the Nonlinear Longitudinal Motion of the UAV

$$V_{EAS} = \frac{1}{m}(F_x \cos\alpha + F_z \sin\alpha), \dot{\theta} = q, \dot{q} = \frac{M_y}{I_{yy}}$$

where the state variables $x = [EAS\ \alpha\ q\ \theta]^T$, with equivalent airspeed (EAS), angle of attack (α), pitch angle (q), pitch attitude (θ), and input $u = [\delta_{\text{ele}}\ \delta_{\text{throttle}}]^T$, with δ_{ele} presenting elevator deflection and δ_{throttle} presenting throttle deflection. Partial loss of control effectiveness in elevator has been implemented for FDD purpose in this work.

33.3.1 DUKF Algorithm

UKF is mainly used to nonlinear systems identification, training of neural networks, and dual estimation problems. UKF picks a minimal set of sample points, which are called sigma pouts around the mean by the unscented. These sigma

points are then propagated through the nonlinear functions and the covariance of the estimate is then recovered. It captures the posterior mean and covariance accurately to the third-order Taylor series expansion for any nonlinearity. Thus, the UKF captures both the first-order and second-order statistics of the nonlinear system. UKF has better filter performance compared with extended Kalman Filter (EKF) and is equivalent to the performance of second-order EKF [4, 5]. In this section, we will present an overview of the DUKF state-parameter estimation scheme implemented for estimation of the reduction of the actuator's effectiveness due to failures.

33.3.2 State Estimation Consider a Nonlinear Transform of a Random Variable

The complete state estimation of the UKF is given below, for $k \in \{1, \ldots, \infty\}$,

$$\hat{x}_0 = E[x_0]$$

$$p_0 = E\left[(x_0 - \hat{x}_0)(x_0 - \hat{x}_0)^T\right]$$

$$\hat{X}_0^{\alpha} = E[x^{\alpha}] = \left[\hat{x}_0^T 0\ 0\right]^T$$

$$P_0^{\alpha} = E\left[\left(x_0^{\alpha} - \hat{x}_0^{\alpha}\right)\left(x_0^{\alpha} - \hat{x}_0^{\alpha}\right)^T\right] = \begin{bmatrix} P_0 & 0 & 0 \\ 0 & R^v & 0 \\ 0 & 0 & R^n \end{bmatrix}^T.$$

The complete parameter estimation of the UKF is given

$$\dot{w}_0 = E[w]$$

$$P_{w_0} = E\left[(w - \dot{w}_0)(w - \dot{w}_0)^T\right].$$

33.3.3 Dual UKF Estimation

In the dual UKF estimation, both states of the dynamical system and its parameters are estimated simultaneously, given only noisy observations. At every time sample, an UKF state filter estimates the state using the current model estimate $\hat{W}_k$, while the UKF parameter filter estimates the parameters using the current state estimate $\hat{x}_k$.

33.3.4 Actuator Fault Model

Faults that develop in a linear time-varying system associated with the actuators can be represented by an equation as follows:

$$\dot{x}(t) = Ax(t) + Bu(t) - Bru(t) + w(t)$$

$$y(t) = Cx(t) + v(t).$$

With $w(t)$ and $v(t)$ denote white noise. $\gamma = diag(\gamma_1 \ldots \gamma_m)$ where γ_i, $i = 1, \ldots m$ are scalars satisfying $0 \leq k_i \leq 1$. If $\gamma_i = 0$, the actuator is working perfectly whereas if $\gamma_i \geq 0$ a fault is present, and if $\gamma_i = 1$, the actuator has failed completely. The objective of FDD is to determine the extent of the loss in the control effectiveness factor γ, as suggested in [2].

33.4 Fault Detection and Diagnosis Schemes

To successfully diagnose faults/failures, the mapping from the model coefficients to the process parameters is necessary. Part of the diagnosis task is to recognize the changes in a dynamic system. The fault detection and isolation is based on a Bavsian statistical hypothesis test which involves two stages. Assume that the collective elevator actuator has a failure while others remain healthy. The response to the airplane is captured through equivalent airspeed, pitch angle, angle of attack, and pitch attitude. The throttle is kept constant at its trim setting throughout the maneuver. In this paper, two scenarios are simulated: (1) a 50 % loss of control effectiveness fault in elevator at 5 s. (2) a 30 % loss of control effectiveness fault in elevator at 6 s. To reduce the execute time, the measurement interval is T = 0.02 s. The UKF parameters are listed as follows: $\alpha = 1$, $\beta = 2$, $k = 3 - L$,

$$R^r_{\text{ukfpe}} = diag((1/0.99985 - 1))P_w, R^e_{\text{ukfpe}} = 0.001^2 I^{9\times 9};$$

$$R_v = 0.01^2 I^{9\times 9}, R_n = I^{9\times 9}, P_x = I^{9\times 9}, P_w = 0.001 I^{1\times 1}$$

where L is the dimension of the augmented state Assume at time 5 s, elevator has a partial loss 50 % (50 % of original value).

From Figs. 33.1 and 33.2, we can see that DUKF can correctly estimate all the states and faults within the given time limits in the nonlinear model. It is very easy to implement DUKF in the nonlinear model since it does not need to linearize the model. However, the DUKF is also computationally more expensive.

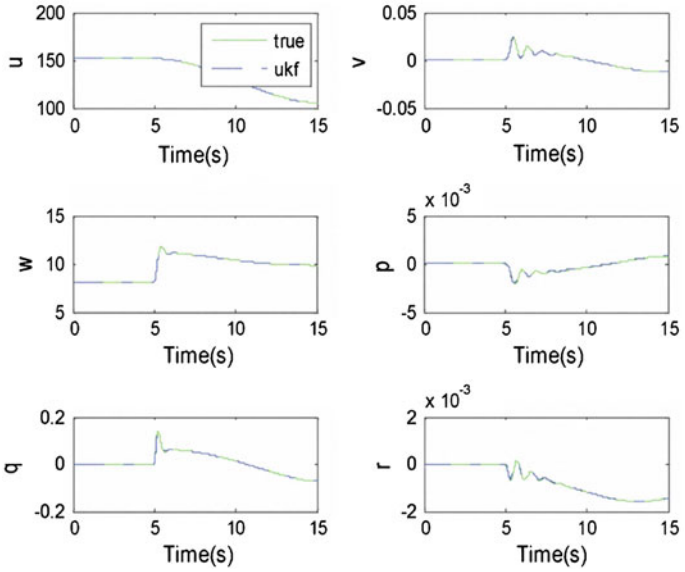

Fig. 33.1 Results of estimated states u, v, w, p, q, r

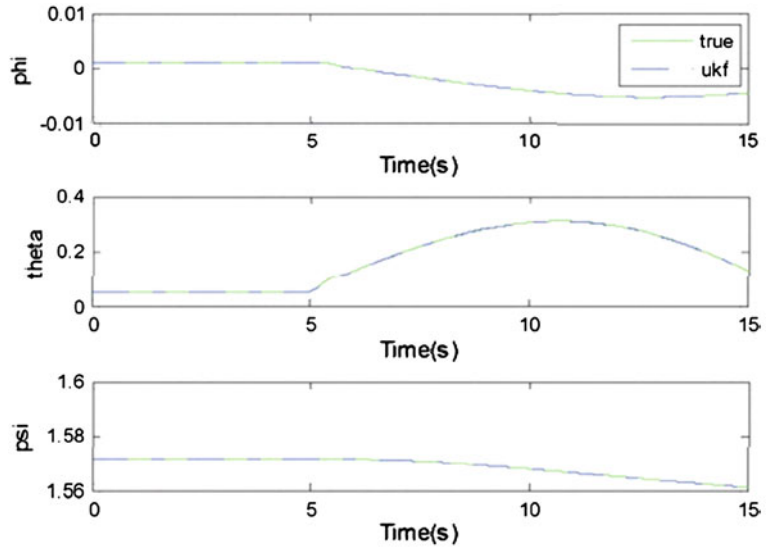

Fig. 33.2 Results of estimated states ϕ φ θ

33.5 Conclusions

An on-line FDD scheme has been proposed in this paper. The proposed FDD scheme is on the basis of the DUKF for the state and fault parameter estimation. Simulation results indicate that DUKF can correctly estimate all the states and fault parameters within the given time limit in the nonlinear model of UAV. Convergence of parameter estimation is also very fast. However, the DUKF is also computationally more expensive, especially for nonlinear model whose coefficients are implemented by lookup tables in Matlab/Simulink.

In this paper, only actuator faults have been considered while others remained properly. In reality, faults can also occur in sensors and system components such as wing damages. Furthermore, only partial loss type faults have been considered. Our future work includes consideration of actuator stuck failures and wing damages, improvement of robustness and performance of DUKF-based FDD algorithm, and integration with fault tolerant control to form a complete active FTCS for the UAV.

In conclusion, the DUKF has the advantage that it separates state estimation and parameter estimation which is more accurate, compared with other Kalman filters. Furthermore, DUKF can use the nonlinear model of system directly with no need to linearize the system.

References

1. Zhang YM, Jiang J (2008) Bibliographical review on reconligurable fault-tolerant control systems. Annu Rev Control 32(2):229–252
2. Zhang YM, Wu NE (1999) Fault diagnosis for a ship propulsion benchmark: part 1. In: Reprints of 14th triennial World Congress, Beijing, P. R. China, July 5–9, 1999, pp 569–574
3. Simon JJ, Uhlmann JK (1997) A new extension of the Kalman filter to nonlinear systems. In: Proceedings of 11th International Symposium on Aerospace/Defence Sensing, Simulation and Cantrols
4. Chiang LH, Russell EL, Braatz RD (2001) Fault detection and diagnosis in industrial systems. Springer, London
5. Chowdhary G, Jategaonkar R (2006) Aerodynamic parameter estimation from flight data applying extended and unscented Kalman filter. In: AIAA Atmospheric Flight Mechanics Conference and Exhibit, 21–24 August 2006, Keyston, Colordo

Chapter 34
Avionic Fault Diagnosis Expert System Based on Flight Data and BIT Information

Dong Song and Bin Han

Abstract According to the characteristics of onboard equipments fault diagnosis and the development tendency of this field, diagnostic technique and diagnostic method based on CBR are studied. A fault diagnosis method for a certain type of aircraft is put forward. This method adopts CBR strategy based on BIT message, flight parameter, and other fault symptoms. A fault diagnosis expert system is designed. The Rough Set theory is used in this system to process the fault symptoms to reduce the number and dimension of the symptoms and to calculate the weightness of each symptom. The Nearest Neighbor method is set as a global matching strategy which achieves the most matched results accurately. At last, the performance of this system is verified.

Keywords Fault diagnosis · CBR · Rough set theory · Case similarity matching · Nearest neighbor method · Expert system

34.1 Introduction

With the increasing complexity of modern civil aircraft, traditional maintenance way is becoming more and more difficult to meet the requirements in reducing costs, improving the attendance rate, etc. The development of condition monitoring, fault diagnosis and health management, and other related technologies have begun in the 1980s abroad. Now advanced foreign civil aircraft are all equipped with onboard maintenance system with implementation of fault diagnosis and health management ability. However, due to the backward technology and the lack of accumulation, China has not developed out a similar system with independent

D. Song · B. Han (✉)
School of Aeronautics, Northwestern Polytechnical University, Xi'an 710072, China
e-mail: zeus.hanbin@gmail.com

J. Wang (ed.), *Proceedings of the First Symposium on Aviation Maintenance and Management-Volume I*, Lecture Notes in Electrical Engineering 296,
DOI: 10.1007/978-3-642-54236-7_34,

property rights. Therefore, domestic regional aircrafts (the ARJ21-700 \ MA600) are all equipped with the system made by Collins Company in the United States. The aircraft fault diagnosis expert system introduced in this paper is based on flight data and BIT information. It is an important part of the ground subsystem of the "Civilian Aircraft Real-Time Fault Diagnosis and System Maintenance Technology Research" project.

34.2 Basic Theory of CBR

Case-based reasoning (CBR) is a reasonable description and a basic method of the process of solving practical problems. Its implementation is made through some basic steps. The method of its basic principle is shown in Fig. 34.1. CBR cycle can be summarized as the following several aspects: Retrieve, Match, Revise, Review, Retain, and Reuse. All the basic steps of the CBR are from user's point of view. The simplest practical system may only have the case retrieval function, and the other functions will be left up to users to implement [1, 2].

34.3 Overall Design of the System

CBR Diagnosis Algorithm Framework. The CBR diagnosis algorithm framework is designed as shown in Fig. 34.2. Each functional module involved in the framework is, respectively, illustrated as follows:

1. Inference Machine: It uses the k-Nearest Neighbor Algorithm combined with Distance Ranging Algorithm based on similarity of cases to do the matching and reasoning work.
2. Case Revise module: The diagnosis results can be divided into two categories, one main case and some reference cases. Combining with the reference cases, modification will be made on the basis of the main case. The Review Module will be involved in order to make modification to achieve the most consistent with the actual.
3. Case study module: There are mainly five kinds of circumstances that a new case should be studied:
4. Explain module: The function of this module is to distribute the diagnosed cases or take them as historical references.

   i. The BIT information in the target case being diagnosed does not exist in the case library.
   ii. The number of symptoms in the target case is more than that of the cases in the library.
   iii. Symptoms of the target case are different from the cases in the library.
   iv. The revised cases.
   v. The case does not meet the conditions for review.

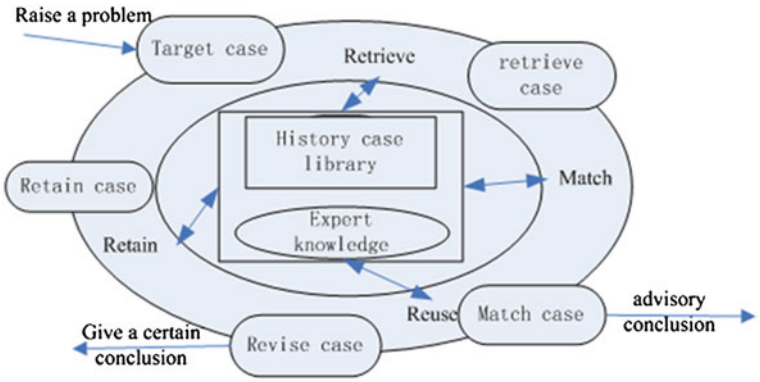

Fig. 34.1 CBR cycle

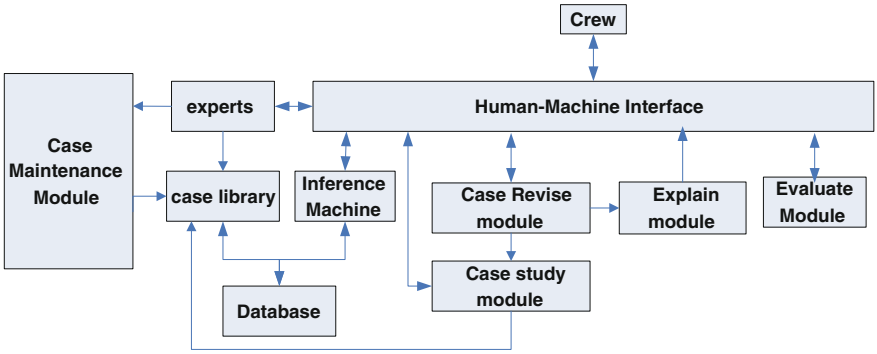

Fig. 34.2 CBR diagnosis system structure framework

5. Case Maintenance module: The functions of this module are to convert cases to be stored in the database, and to convert the knowledge of experts or experiences to a predetermined format then store the data in the history library for the use of case matching.
6. Evaluate module: The functions of this module are to evaluate the matched history cases after diagnosis, to check whether the solution is consistent with the actual troubleshooting operations or not, to find where the differences are, and to make specific revisions and to study the cases after evaluated.
7. Human–Machine Interface: The function of this module is to provide the users (crew) a real-time query interface to the present situation of the plane. Not only that, but it can also interact with the experts or maintenance crew to let them evaluate the diagnosis and add new cases to the library.
8. Database: It is the workspace in the computer's memory while the expert system is processing. It supplies the program to read the data needed at any time or to write intermediate results of calculation into the workspace.

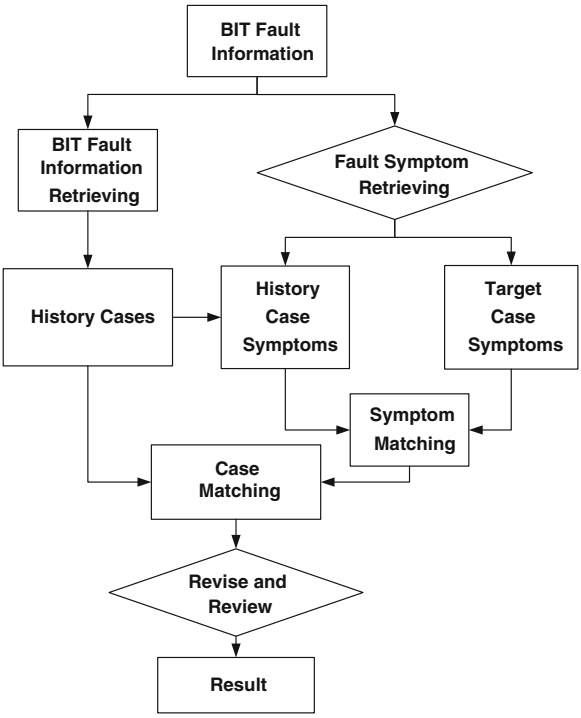

Fig. 34.3 Data flow

Data flow. According to the above, and after carefully investigating the process of field fault diagnosis and elimination, we get the data flow of the system, as shown in Fig. 34.3.

Data Items and Data Structures. According to the content of the fault diagnosis based on BIT information and the analysis of the data flow, the data items, and data structures are designed as follows:

1. The basic condition of the login user: The data items consist of department, department code, and so on.
2. The basic parts of a case history: The data items are case number, the plane model, fault occurrence time, BIT information, failure system or component, failure causes and troubleshooting methods, FIM manual corresponding number, AMM manual corresponding number, etc.
3. BIT information management: The data items are BIT information, information number, etc.
4. Case search management: The data items are case number, number of case is called.
5. Symptom search management: The data items are BIT information, symptom 1, symptom 2, and so on.
6. Weight of symptom management: The data items are BIT information, symptom 1, symptom 2, and so on.

7. Content of symptom management: The data items are BIT information and symptom 1, symptom 2, and so on.
8. Specific value of symptom management: The data items are BIT information and symptom 1, symptom 2, and so on.
9. The plane information management: The data items are aircraft type, admission time, flight time, the last time of flight, the last fault, the last fault location, etc.

Selection of Symptoms. Symptom selection is based on the integrated avionics system maintenance diagnostic interface control documents (ICD) of a certain type aircraft. The ARINC429 data bus standard is used in this aircraft. Its integrated avionics system ICD consist of 26 categories, such as air data system, radio compass navigation system, flight control, left (right) multifunction display system, and so on. Each category is made up of a group of 429 words. According to system function, a group of 429 words roughly contain data words (such as bearing, height, air pressure, attitude, acceleration), and some discrete and diagnosis words. Take air data computer (left) (ADCL) system as an example: the BIT information is made up of six data words, one discrete word (ADCDis1L), and two diagnosis words (ADCDia1L and ADCDia2L). The six data words, respectively, represent pressure height (HpL), indicated airspeed (ViL), true airspeed (VtL), and total air temperature (TtL), vertical velocity (VvL), and static air temperature (TsL). For an ADCL case, the nine words make up its nine symptoms. The abbreviations of these words, as shown in the brackets, are used in the database for the corresponding field [3].

Determination of Symptom Value. The corresponding value of each symptom is the value of the effective part of the binary code generated under the rules of the definitions made in the ICD. We take the diagnosis word one of ADCL (ADCDis1L) as an example: the function of the diagnosis word is to locate the position of the fault. Its effective part is from 9 to 28 bit.

Determination of Symptom Weight Value. This system adopts the Rough Set theory to determine the weights of each symptom. In a knowledge system, the importance degree of different attributes is usually given by experts of this field. This method to determine the weights is very subjective. But in the Rough Set theory you can gain the weights by objective data calculation [4].

The concept of attribute dependencies in the Rough Set theory is used to determine the importance of a property. First, a general decision table must be constructed for this system. The contents of the decision table are some historical cases of particular BIT information. In the decision table, the serial number of the cases is defined as the universe of discourse (U), and condition attributes (C) are defined as fault symptom values of each case, and the decision attribute (D)is defined as the elimination method of each case(retain, replace, repair) [5, 6]. In this way, we can get a decision table about certain BIT fault information. Then by calculating the attribute dependencies, we could determine the importance of each fault symptom attribute. Therefore, the weight of each attribute is determined, and this lays the foundation for subsequent case matching.

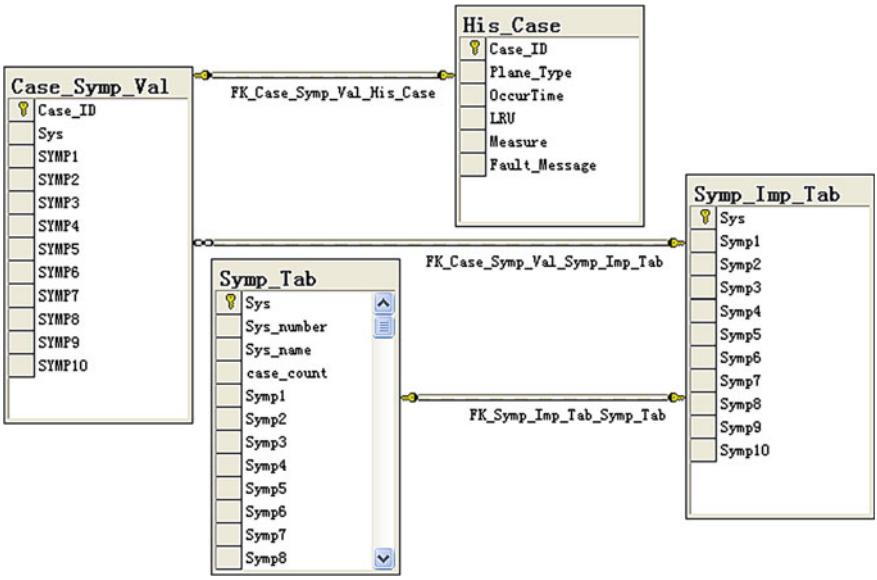

Fig. 34.4 Design of database tables

Design of Database. Failure case contains four aspects: symptoms, conditions, the related description, elimination method and associated information. In this Avionic Fault Diagnosis Expert System, a large amount of data are involved, mainly include: case information, name of the BIT case symptom, BIT case symptom value, attribute importance value (weight) of symptom, user information, etc. Based on the above data storage requirements, the system database mainly contains these tables: historical case table (His_Case), symptom BIT table (Symp_Tab), symptom BIT importance value table (Symp_Imp_Tab), and case symptom value table (Case_Symp_Val). And then on the basis of this design, the knowledge base management program is written. The data table structure and relationships are shown in Fig. 34.4.

34.4 The Similarity Degree Algorithm of Cases

In the symptom matching process, an evaluation method is used. This method is similar to the method based on distance measure. The matching algorithm of fault symptoms is shown in Eq. (34.1).

$$Sim(X, Y) = 1 - Dist(X, Y) = dist(X, Y) \tag{34.1}$$

In this Eq. (34.1), $Sim(X, Y)$ represents the similarity degree of fault symptom X and Y. X represents the symptom value of the source case, and Y represents the

symptom value of the target case. $Dist(X, Y) = |X - Y|$ represents the distance from the source case to the target case.

After the similarity matching of the fault symptoms, we can do the whole case similarity calculation. We can call the similarity matching of the fault symptoms the local similarity matching. Then we should call this next step as global similarity matching. According to the symptom similarity degrees and the weight of each symptom, k-nearest neighbor algorithm (NNH) is used to get the global similarity degree. The formula is shown in Eq. (34.2) [7].

$$OS^{NN}(x_j, q) = \frac{\sum_{f=1}^{l} (w_f * Sim(x_{jf}, q_f))}{\sum_{f=1}^{l} w_f} \tag{34.2}$$

In Eq. (34.2), $OS^{NN}(x_j, q)$ represents global similarity degree of the history case x_j and the target case q. $Sim(x_{jf}, q_f)$ represents the local similarity degree on symptom f of the history case x_j and the target case q. The weight of the symptom is w_f.

34.5 Run and Verification of the System

The Pre-Diagnose Process of the System. In the process of receiving fault information, the system will classify and store the fault information by the time sequence and system difference. In the ICD, the relationships between the discrete words and diagnosis words are defined. Using these relationships, a pre-diagnose process is designed before the matching process to save the time of diagnosis. Take the Left air data system for example: the 13th bit of discrete word one is the ADC status bit. If the system is broken down, its value is 1. If the system has no trouble, its value is 0. Therefore, as to the pre-diagnose process of left ADC, we can just pay close attention to the symptom of discrete word one (ADCDis1L). We can extract the 13th bit ADCDis1L. If its value is zero, we can conclude that the information of this piece of time is trouble-free. In the following test shown in Fig. 34.5, the fault diagnosis system has skipped the trouble-free systems from ADCR to VHFR (the Fault information and suggested method of elimination are not shown in the Diagnose Result table in Fig. 34.5).

Case Matching Example. We choose the fault case matching of left air data computer (ADCL) as an example. The corresponding symptoms are: HpL, ViL, VtL, TtL, VvL, TsL, ADCDis1L, ADCDia1L, ADCDia2L.

After case matching process, the similarity value of the most matched case is 0.96. Obviously, this case can be viewed as consistent with the fault case. Its solution can be taken as the solution of the fault case. At the same time the fault diagnosis process is done, the diagnosis result will be automatically sent to the interface of evaluation. The user can decide whether to adopt the suggestions for troubleshooting or not according to actual condition.

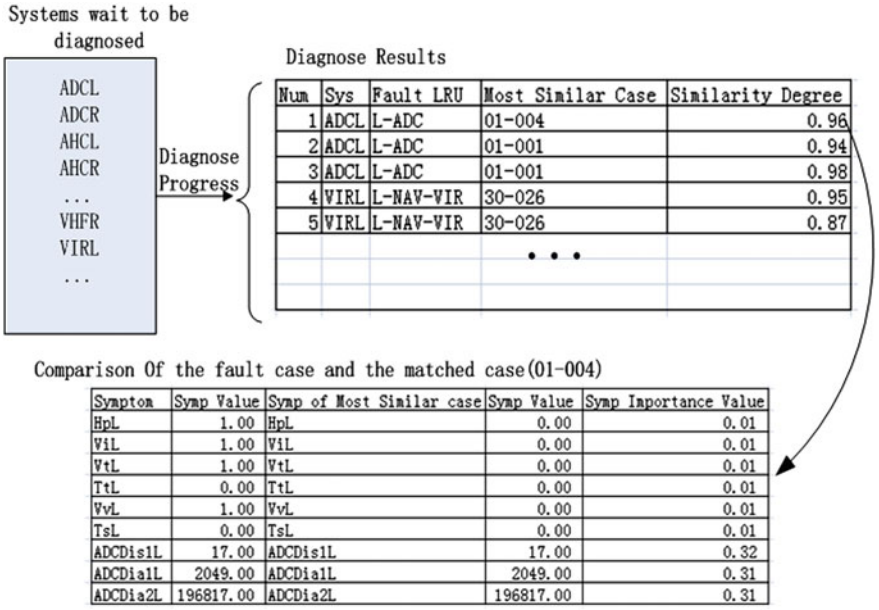

Fig. 34.5 Overall schematic of diagnose results

34.6 Summary

This paper analyzes the present situation of onboard equipment fault diagnosis. Then the expert diagnosis model based on CBR is given. The design method of the knowledge base in the CBR system is studied. The determination of the weights of attributes and matching algorithm are studied, too. At last, the diagnosis expert system is run and verified. The system can complete the basic function of CBR system process, and it can achieve the demand of fault diagnosis. In conclusion, the system meets the goal of system design.

References

1. Song D, Liu F, Wu X-Y (2008) Research and application on case self-revision approach of fault diagnosis system based on CBR (in Chinese), Measur control Tech 27(5)
2. Zhou P, Yin W-D, Zhao J-H (2012) Research on case retention strategy for industrial case-based reasoning (CBR) system: a practical case study, Computer Science and Information Processing (CSIP), pp 376–380
3. Chen J-Y, Xu Y-Y (2008) Research on the application of knowledge management on the malfunction cases platform (in Chinese). Ship Electron Eng 28(5)
4. Zhang W-X, Wu W-Z (2000) An introduction and a survey for the studies of rough set theory (in Chinese). Fuzzy Syst Math 14(4)

5. Li W-L, Chen D-G, Yang Y–Y (2012) A new method of attribute reduction for covering rough sets. Mach Learn Cybern (ICMLC) 1(15–17):277–281
6. Dendani N, Khadir M, Guessoum S, Mokhtar B (2012) Use a domain ontology to develop knowledge intensive CBR systems for fault diagnosis, Information Technology and e-Services, pp 1–6
7. Wang B, Song D, Jiang H-N (2007) Case retrieve of fault diagnosis expert system based on CBR (in Chinese). Comput Measur Control 15(11)

Chapter 35
AFDX Network Performance Testing

Dongying Chen and Dong Song

Abstract Avionics Full Duplex Switched Ethernet (AFDX) is a new aviation data bus, which has been successfully applied to the new generation of large aircrafts. AFDX is the core bus of data transmission in advanced airplanes, so it is of great significance to carry out the extensive research of AFDX. Whether the data communication is deterministic and reliable concerns the airworthiness of AFDX, so the methods of AFDX network performance testing are discussed. An AFDX experimental system is built up. In the experimental system, AFDX network performance testing about network latency is carried out. Through sending/receiving large quantities of data and errors injection, the test verifies the certainty and reliability of AFDX network as a result. The test also provides a large number of testing data for further research on network maintenance methods, fault diagnosis, and the airworthiness of AFDX.

Keywords AFDX · Data communication · Network latency · Performance testing

35.1 Introduction

With the complex avionics systems like safety critical systems and recreational facilities for passengers increasing [1], as well as the technology of computer communication and Ethernet developing rapidly, a new generation of aviation data bus has emerged, namely AFDX for short.

D. Chen (✉) · D. Song
School of Aeronautics, Northwestern Polytechnical University, Xi'an 710072, China
e-mail: chdongying117@163.com

J. Wang (ed.), *Proceedings of the First Symposium on Aviation Maintenance and Management-Volume I*, Lecture Notes in Electrical Engineering 296,
DOI: 10.1007/978-3-642-54236-7_35,

AFDX has obvious advantages of high reliability and low latency. AFDX has become a mainstream choice in advanced airplanes and been successfully used in the Airbus A380, Boeing 787, and other large transport aircrafts.

In the use of ATM virtual channels in asynchronous transmission mode, AFDX overcomes the uncertainty of transmission delay in traditional Ethernet. By introducing Virtual Link (VL) mechanism, AFDX can ensure the security, reliability, and maintainability of on-board equipments [2].

In this paper, the research on influencing factors of AFDX network performance and testing methods is developed. Then the testing scheme is given in combination with the experimental system. By analyzing the experimental results, the performance of AFDX network communication is verified, which also provides a reference to the further research on methods of AFDX network maintenance.

35.2 AFDX Introduction and Performance Requirements

AFDX system consists of AFDX end systems and AFDX switches, or connections [3].

For on-board data network, the requirement of certainty is the most urgent. It means transmitting data should be received within the certain time. AFDX end system adopts VLs by defining the minimum bandwidth interval (BAG) and the maximum frame size (Smax), which determines the maximum bandwidth of a VL. Therefore, the frame rate for each VL can be adjusted by changing the value of the BAG. The AFDX switch is in use of static routing configurable table, and has the capabilities of storing and forwarding frames and filtering frames, so that switch ports can transfer only correct frames and control the total frames flow of each VL not to exceed the allocated bandwidth. Thus, even if jitter exists there, the delay is bounded.

For avionics system, the security and reliability of AFDX network are also the important index to evaluate its performance. In data communication, with regard to unexpected failures like sudden error data generated, AFDX can ensure the robustness of the network traffic by integrity checking, redundancy checking, filtration, and other methods at each layer. Thus, in the use of AFDX, an important issue is to calculate the network latency of entire avionics system. In addition, it is of great importance to adopt error injection to test responses of all layers in system, better to know about the performance of AFDX network.

35.3 AFDX Performance Index and Testing Methods

35.3.1 Latency

In order to ensure the certainty of data transmission among on-board systems, the time data is collected from an end system to another must meet the computing cycle of 20–50 ms for the on-board equipments. All communications through AFDX network is deterministic.

AFDX network latency contains three parts: the source ES latency, the communication channel latency, the destination ES latency. The communication channel latency includes the frame transmission latency, the signal transmission latency, and switch latency. Not only do the hardware circuits like processing speed of chips embedded in an end system board cause latency, but also some software such as switch buffer scheduling policy, types of frame flow generate delay [4, 5].

35.3.1.1 Source ES Latency and Destination ES Latency

The preprocessing time of the ES depends on the chip processing time. In many cases, the latency is a constant or negligible.

35.3.1.2 Link Latency

Link transmission latency mostly depends on the speed of signal transmission and length of the link. Considering that the speed of electric signal transmission is 2×10^8 m/s, and the distance between switch and ES is 20 m, the delay is 0.1 us in the worst case.

35.3.1.3 Switch Latency

First, switching latency is a fixed value, which is related to the switch performance and given by the switch suppliers. Second, forwarding delay is caused by the time consumed in storing and forwarding frames, which is related to the filtering process of data; for such latency, a maximum of 16 us is given as a reference. Queuing latency in switch buffer is uncertain and directly depends on the VL configuration, the types of input frame flows and scheduling policy in switch buffer.

The theoretical value of latency is often difficult to calculate and give the maximum in the worst case.

Thus, in the experiment, an extreme value of the fixed latency will be given as a reference. The latency will be measured through measuring the consuming time of the data flows. In case that the length and the amount of frames are known, the average value of the latency can be calculated through statistics of the time spent on data communication.

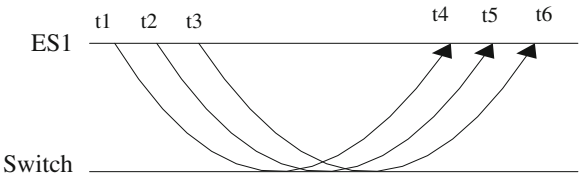

Fig. 35.1 Network communication latency

35.3.2 Testing Method

There are mainly two relatively mature network testing methods, one is the packet-way test, and another is a packet loopback latency test. The packet-way test means that the testing packet starts from the source of the network and ends at some destination, then the network performance is evaluated by the output parameters of destination device.

Loopback test means that the testing packet starts from the source of the network and comes to the destination, and then forwards back to the source. Finally the network performance is evaluated by the output parameters.

Taking the statistical function of switch software, time synchronism, and timing statistics function of terminal card applications into account, the loopback test is adopted in this experiment. As the path is relatively symmetric and the configuration is simple, testing the entire network latency is also relatively easy. According to the consuming time of data communication recorded by ES applications, the network latency can be evaluated. Besides, the value of the switch latency recorded by switch software and link latency, further confirms whether the measurement of network latency is right. Specifically derivation is illustrated in Fig. 35.1.

t_1, t_2, t_3 are defined to respectively stand for the sending time of the first frame, second frame, third frame. t_4, t_5, t_6 are defined, which respectively stand for the receiving time of the first frame, second frame, and third frame.

$$t_{delay1} = t_4 - t_1,\ t_{delay2} = t_5 - t_2, t_{delay3} = t_6 - t_3,$$

$$t_{delay} = \frac{1}{3}\left(t_{delay1} + t_{delay2} + t_{delay3}\right) = \frac{1}{3}(t_4 + t_5 + t_6 - t_1 - t_2 - t_3)$$

In loopback tests, the timestamps t_1, t_2, t_3 of transmission frames and the timestamps t_4, t_5, t_6 of the received frames can be got in the use of ES cards applications. According to the above formulas, the transmission latency of the frames throughout AFDX network can be obtained. After a lot of testing, it will be easy to give the average network latency under windows operating system.

35.3.3 Error Injection

Error injection means that adding error data frames in the process of communication artificially. Through introducing errors to the bus communication, monitoring the AFDX system responses to the failures at all layers can test the safety and reliability of the network. Error injection mainly contains following types [6].

35.3.3.1 Network Error

Mainly refers to that the parametric time frequency modifies the frame times in the schedule by scaling the frame up and down.

35.3.3.2 VL Error

Mainly refers to the RSN errors, including the step type and the impulse type.

35.3.3.3 Port Error

Mainly consists of schedule errors, frames errors, payload data errors, and bus control errors.

35.3.3.4 Other Failures

Modify the frame with invalid data (such as wrong constant values), deviate from standard transmission, etc. [6].

35.3.4 Testing Method

First, the time of error injection can be before data transmission or during data transmission, which means a variety of errors can be intermittently injected without stopping transmit schedules. Second, different types of injection errors are introduced to test how the system will behave under different error conditions at all layers.

35.4 AFDX Experimental System

The experimental system is composed of Industrial Personal Computers (IPCs), AFDX end systems, and 8-port AFDX switch. Figure 35.2. illustrates the experimental system.

The experimental system includes the following components.

35.4.1 Industrial Personal Computer (IPC)

IPC system contains AFDX end system. ES is embedded in the IPC and in connection to the AFDX network. It provides applications with a computing environment. IPC is similar to avionics subsystem computers in function.

35.4.2 AFDX End System

The ES provides an "interface" for IPC and AFDX switch to ensure safe and reliable data exchange. In this experiment, there are three terminal cards, which include two transfer cards and a monitor card. Each card has two ports A/B. The configurable table should be dynamically configured in accordance with the switch configuration table and loaded by applications.

35.4.3 AFDX Switch

This network switch is an 8-port switch with filtering function (filtering conditions include Smax, Smin, max-delay, etc.). Switches interconnect different equipment modules via the network cables. In addition, there is a debug port in the switch, where the switch configurable table is loaded to determine static routing through a cable. The speed of each switch port can be up to 100 Mbps.

35.5 Experimental Results and Analysis

35.5.1 The Connection of Equipments

In the experiment, the equipments are connected with three network cables. The switch port 1, port 2, port 3 are respectively connected to the port A of ES card 1, card 2, card 3. First, a static configured routing table is loaded into the switch

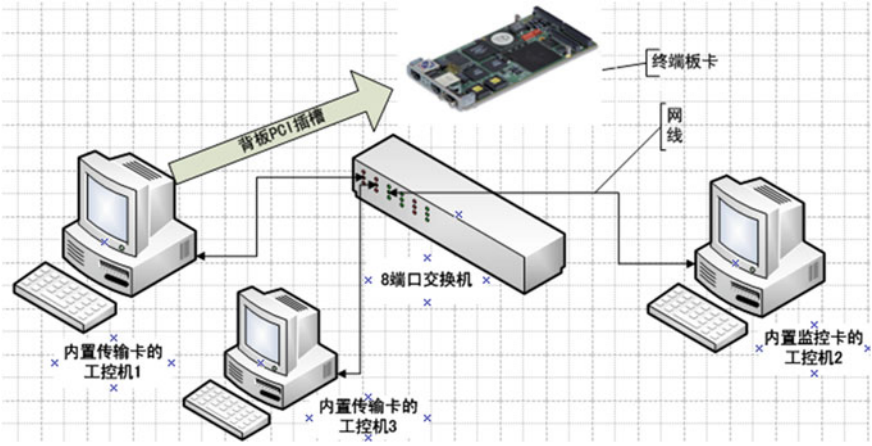

Fig. 35.2 Experimental system diagram

through switch-based debugging software. In this experiment, the VL 1 defined from switch port 1 to switch port 1 is in connection to the monitor card. To pay attention, different configuration tables (differ in BAG, Smax, etc.) loaded on the switch will influence the results. The switch configuration table is shown in Table 35.1.

As is seen from the Table 35.1, the value of BAG in each VL is 1 ms. As is known the maximum bandwidth of each transmitting VL = Smax/BAG, it is not difficult to calculate that the maximum bandwidth for each VL is 12.304 Mbps.

35.5.2 Analysis of Results

35.5.2.1 Delay Test

To facilitate data statistics, the length of payload (UDP length) in each data frame is defined the same. The counter in the C program is designed to adopt the CPU timestamp to time. CPU frequency is 2.6 GHz, and the actual measurement is 2.59353 GHz. The sending/receiving time stamp is recorded by the number of clock cycles.

The measurement of communication latency for data frames is shown in Table 35.2. From the Table 35.2, the average value of communication latency is 2.021 ms according to the statistical results.

The measurement of switch latency for data frames is shown in Table 35.3. The forwarding latency of a byte through switch is about 80 ns, and the transmission latency of a frame with full payload is around 0.124 ms in the switch.

Table 35.1 The switch configuration table

VL ID	Port (in)	Port (out)	Smax (byte)	Smin (byte)	BAG (ms)
1	1	1	1538	84	1
2	2	2	1538	84	1
…	…	…	…	…	…

Table 35.2 Transmission latency statistics

Frame count	Transmitting timestamp	Receive timestamp	Total latency (s)	Average latency (s)
40	89989145079	90211575742	0.085763	0.002144
170	92987646736	93893096151	0.349116	0.002054
420	00512592791	02694246083	0.841184	0.002003
1260	54625182632	61178739824	2.526867	0.002005
…	…	…	…	…

Table 35.3 Switch latency statistics

Bytes of payload	Port (in)	Port (out)	Latency (us)
17	1	2	6
521	1	2	30
1143	1	2	62
1455	1	2	124
…	…	…	…

Furthermore, the interval between forwarding frames is decided by the BAG in the configuration table of the switch and about 0.877 ms here.

From the above two tables, it is easy to see, the average value of latency is about 2 ms through AFDX network under windows environment. Taking into account the latency generated by the switch is about 0.124 ms, the processing application calls the card driver program has a great influence on the latency, while it does not belong to the AFDX network latency in fact. However, the measurement results show that latency still meets the computing cycle 20–50 ms of onboard systems; the network is determined. Moreover, the actual rate of the network has a direct relationship with the length of a data frame.

In the experimental system, a lot of related tests are carried out, such as transmitting/receiving data to different ports in the same VL, and the statistical result is basically as same as the condition that transmitting/receiving data to the same port in the same VL.

Table 35.4 Error injection statistics

Error injection types	Transmission frames	Error frames	Received frames
VL error	10	1	9
Constant error	10	1	9
Smax error	10	1	9
Undersize (<64 octets)	10	1	9
…	…	…	…

35.5.2.2 Error Injection

In this experiment, error injection is mainly introduced before sending the data frames to test the network responses and network performance. The testing results are shown in Table 35.4.

In this experiment, a relatively small amount of errors are injected. In the view of the statistics, error frames are filtered out by the switch, and hardly influence the time of data reception. In conclusion, AFDX is relatively reliable.

35.6 Conclusion

AFDX is becoming the new generation bus in place of ARINC 429 on aircrafts. The features of AFDX are reality, certainty, and security. The paper mainly discusses the methods of AFDX network performance testing and utilizes loopback test to complete the network latency testing and basic error injection testing. The test provides a large number of test data for the study of the maintenance and fault diagnosis for AFDX network, and lays a foundation for the further research of multiterminal network communication performance testing.

In subsequent study, one-way test, more types of error injection will be considered to test network performance under the condition of multiterminal system, which is of great significance to carry out further research of AFDX network performance and maintenance.

References

1. Ye J, Chen X, Zhang X (2008) Design of avionics communication network based on AFDX (in Chinese). J Meas Control Technol 27(6):56
2. Peng H, Shi F (2009) The communication mechanism of on-board data network based on AFDX (in Chinese). J Sci Technol Innov Herald 20:19
3. AEEC (2003) ARINC project paper 664. Aircraft data networks, part 7: deterministic networks. Aeronautical Radio Inc., Annapolis, p 44

4. Scharbarg J-L, Ridouard F, Fraboul C (2009) A probabilistic analysis of end-to-end delays. J IEEE Trans Indust Inf 5(1):38–49
5. Yang Y, Xiong H (2008) A method for bounding AFDX frame delays by network calculus (in Chinese). J Electron Opt Control 9(15):57–60
6. Getting started guide to CoPilot AFDX (2013) http://www.ballardtech.com. Accessed 15 Sept 2013

Chapter 36
Research on the Dynamic Model with Magnetorheological Damper

Maogui Niu and Hongkai Jiang

Abstract The dynamic model of a vehicle seat with magnetorheological damper is established in this paper, which is established with the finite element analysis software. On the basis of single degree of freedom spring-damping system, the established model simulates the working characteristic of the magnetorheological damper. Based on the established model, the dynamic analysis is carried out. The results of the simulation experiments verify the effectiveness of the established model and show that performance of the dynamic model of a vehicle seat with magnetorheological damper is better than the dynamic model with spring.

Keywords Dynamic model · Magnetorheological damper · Single degree of freedom spring-damping system

36.1 Introduction

With the rapid development of science and technology, cars have become indispensable traffic tools in people's daily life, and people's demands for the safety and comfortableness of cars are greatly increased. However, the factors impair the safety and comforts of cars mainly come from two aspects: the external

M. Niu · H. Jiang (✉)
School of Aeronautics, Northwestern Polytechnical University, Xi'an 710072, Shaanxi, China
e-mail: jianghk@nwpu.edu.cn

M. Niu
e-mail: niumaogui@mail.nwpu.edu.cn

J. Wang (ed.), *Proceedings of the First Symposium on Aviation Maintenance and Management-Volume I*, Lecture Notes in Electrical Engineering 296,
DOI: 10.1007/978-3-642-54236-7_36,

environment and the car's own performance. Nowadays, gentle nature of highway, rail has greatly improved, while, there are still a lot of traffic rugged, rough roads. When driving on the bumpy road, it will provoke vehicle vibration, which not only affects the car's comfort but also reduce the service life of auto parts. That is to say, damping is very important to improve the safety and comfort of the car. Recently, the automation vibration reduction has become a problem of concern, attracting scholars at home and abroad to study it. New auto damping products are popping up and gradually put into use [3]. A damping product called magneto rheological damper is gradually used in recent years. Magnetorheological damper is a high performance damping device and a very promising shock absorber, which has the advantages of low-power consumption, wide dynamic range, continuously adjustable damping, fast response etc. [4]. But, this kind of shock absorber has a very complicated nonlinear characteristics, so works on this shock absorber's model and control remains to be further improved, which is also a meaningful research direction nowadays [5].

36.2 Modeling

The vehicle seat consists of three parts: the magnetorheological damper, the vehicle seat hanging arm equipped with spring inside and the driver's seat. The vehicle seat is an axisymmetric structure, therefore, letting axis of symmetry of the vehicle seat as the dividing line, it is enough to model the right (or left) half of the vehicle seat.

In Fig. 36.1, mass m represents the mass of the system, which consists of two parts: the mass of the driver (65 kg) and the mass of the seat (25 kg), consequently, $m = (65 + 25)/2 = 45$ kg; k represents the spring, whose spring constant is 40,000 N/m; c represents magnetorheological damper, which can simulate different working states of the magnetorheological damper when c takes different values.

36.3 Simulation Experiments

36.3.1 Resonance Frequency Extraction

36.3.1.1 Resonance

Resonance [1] is a phenomenon that the amplitude of system is the largest at a particular frequency, which is called resonance frequency. For the single degree of freedom spring-damper, its resonance frequency can be calculated as follows:

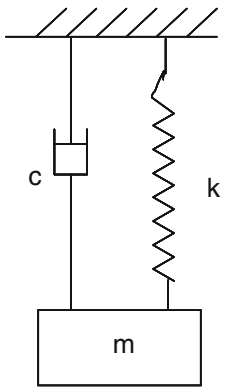

Fig. 36.1 Single degree of freedom spring-damping system

$$f = \frac{1}{2\pi}\sqrt{\frac{k}{m}} \tag{36.1}$$

where f represents the resonance frequency, k represents the spring constant, and m represents the mass of the system.

36.3.1.2 Resonance Frequency Extraction

In Fig. 36.2, the acceleration of the system reaches its maximum at about 5 Hz, basically consist of 4.7 Hz as calculated above, which verifies the effectiveness of the established model.

36.3.2 The Fixed Frequency Simulation Experiment

Figure 36.3 (a) is sinusoidal vibration signal, which is applied to the dynamic model; (b) is the acceleration response of the dynamic model with spring; (c) is the acceleration response of the dynamic model of the vehicle seat with magneto-rheological damper.

The results of the fixed frequency simulation experiment show that performance of the dynamic model of a vehicle seat with magnetorheological damper is better than the dynamic model with spring.

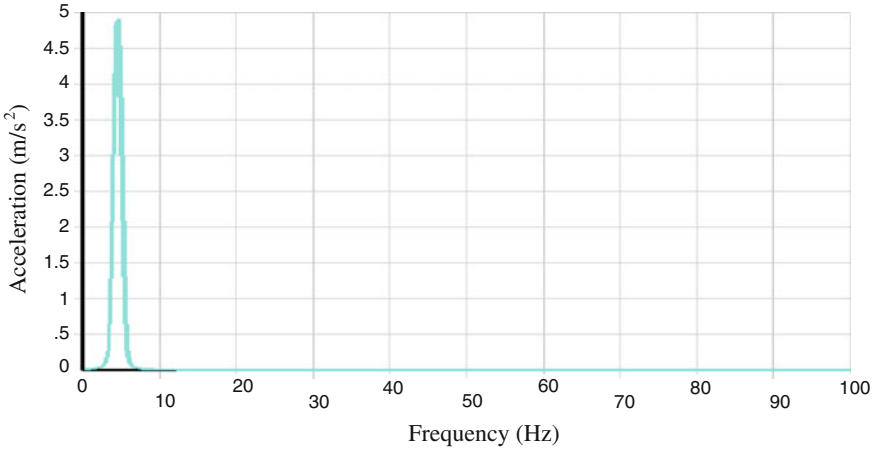

Fig. 36.2 Harmonic response analyses on acceleration

36.3.3 Sweep Simulation Experiments [2]

Figure 36.4 (a) is sweep vibration signal, which is applied to the dynamic model; (b) is the acceleration response of the dynamic model with spring. (c) is the acceleration response of the dynamic model of the vehicle seat with magneto-rheological damper.

The results of the sweep simulation experiment show that performance of the dynamic model of a vehicle seat with magnetorheological damper is better than the dynamic model with spring.

36.3.4 Stochastic Simulation Experiments

Figure 36.5 (a) is random vibration signal, which is applied to the dynamic model; (b) is the acceleration response of the dynamic model with spring; (c) is the acceleration response of the dynamic model of the vehicle seat with magneto-rheological damper.

The results of the stochastic simulation experiment show that performance of the dynamic model of a vehicle seat with magnetorheological damper is better than the dynamic model with spring.

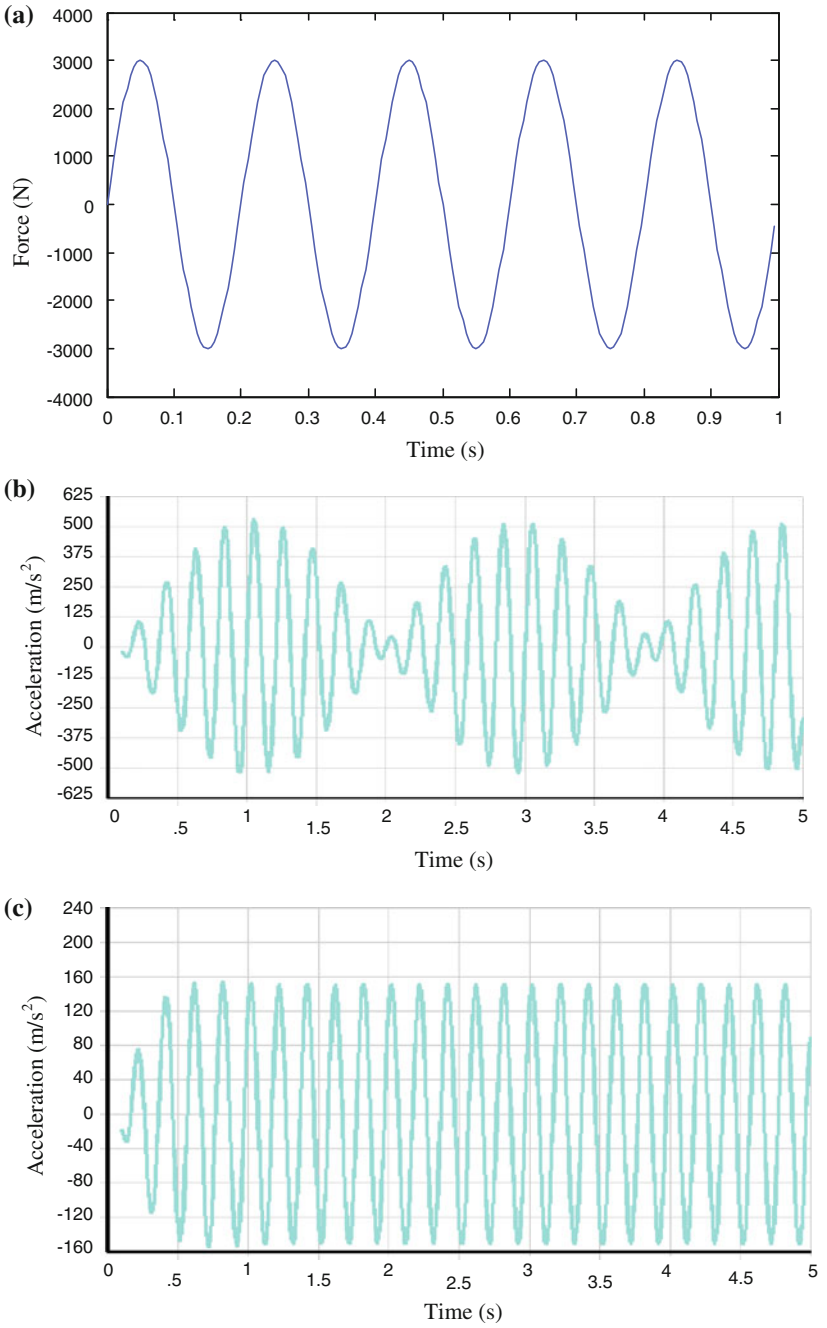

Fig. 36.3 The results of the fixed frequency simulation experiment

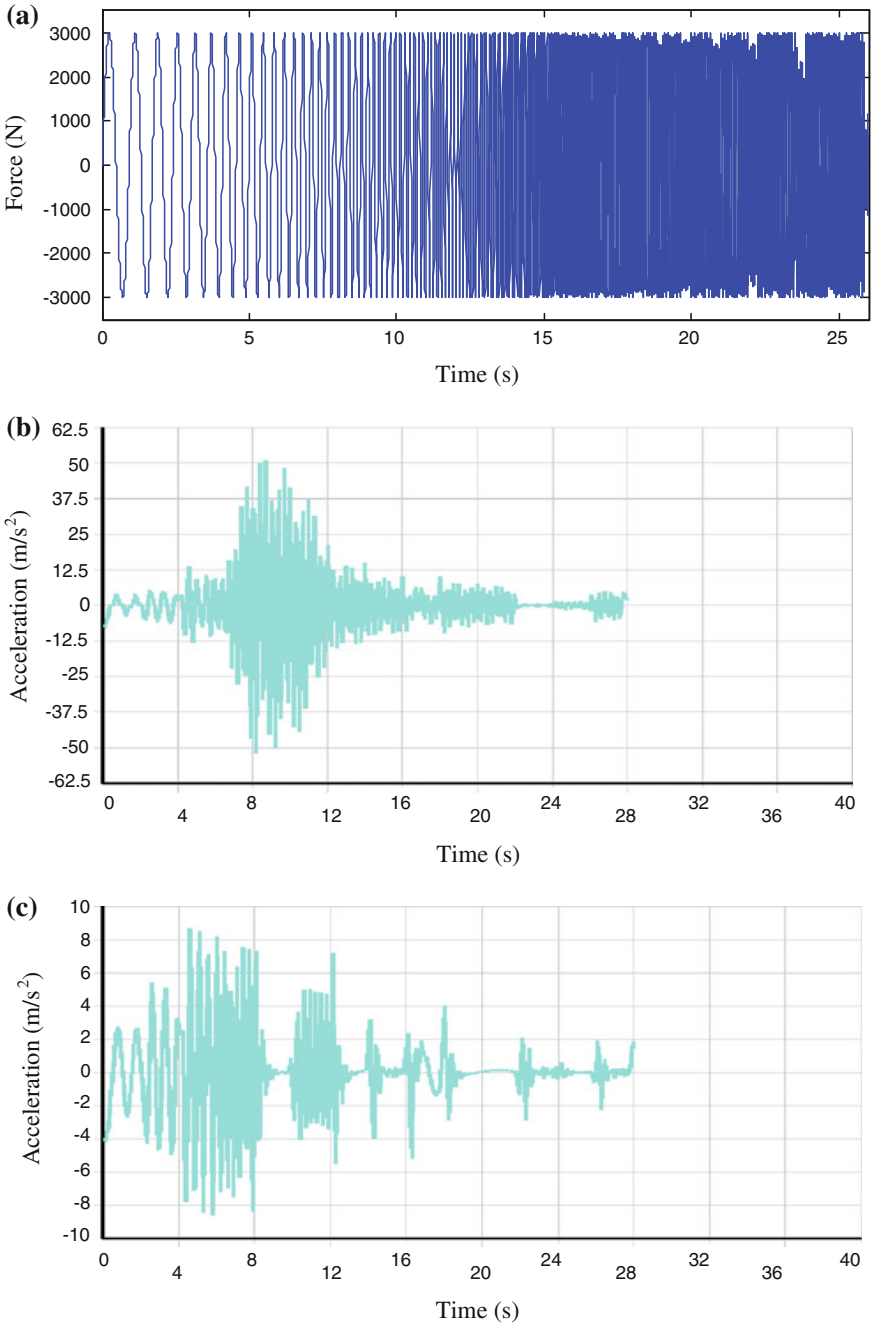

Fig. 36.4 The results of the sweep simulation experiment

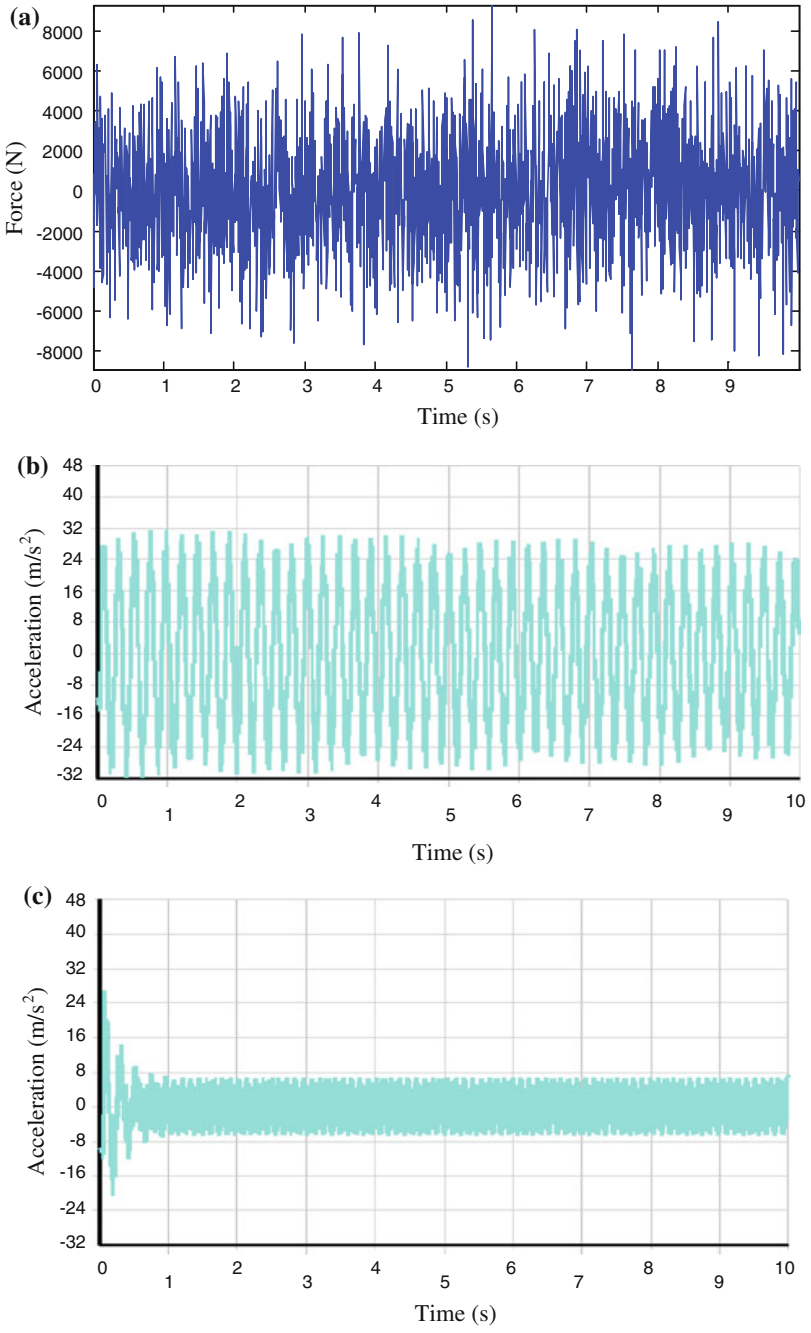

Fig. 36.5 The results of the stochastic simulation experiment

36.4 Conclusion

In this paper, resonance frequency extraction verifies the effectiveness of the model; the results of the other three simulation experiments show that performance of the dynamic model of a vehicle seat with magnetorheological damper is better than the dynamic model with spring.

Acknowledgments This research is supported by the Project Supported by Natural Science Basic Research Plan in Shaanxi Province of China (Program No. 2013JM7011) and the Aviation Science Foundation of China (No. 20132153027).

References

1. Bangchun W (2000) Mechanical vibration. Metallurgical Industry Press, Shanghai, pp 133–135
2. Yang W (2011) In: Research on implementation of an algorithm for MIMO Sine swept-frequency test control system. College of Aerospace Engineering. Nanjing University of Aeronautics and Astronautics, pp 26–30
3. Baotai Y (2012) In: Research on Magnetorheological damper and control method. Faculty of Automation. Guangdong University of Technology, pp 28–36
4. Zhou Y, Tan P (2007) The control theory and technology of the Magnetorheological damper. Science Press, pp 111–116
5. Jiang J, Liang X, Zhang B, Xiao J (2004) A linear rotary magnetorheological damper for vehicles. J Chongqing University, pp 11–15

Chapter 37
Infrared Thermal Wave NDT for Helicopter Blades Debonding

Qi Guo, Peng Jing and Gongjin Qi

Abstract The principle of the infrared thermal wave NDT is researched. According to the structural characteristics of the helicopter blade, the heat transfer process is analyzed. The method to differentiate the debonding region and the normal region is also proposed. The experiment of the infrared testing method is completed on a helicopter rail rotor blade with debonding damages. The thermogram and the peak amplitude image of the second derivative thermogram are both analyzed. The experiment shows that the infrared thermal wave testing method can effectively detect debonding flaws in some helicopter blades.

Keywords Infrared · NDT · Debonding · Helicopter blade

37.1 Introduction

Because of many advantages, kinds of composite materials and bonding structures have been widely used in the field of aircrafts manufacture [1, 2]. For example, bonding structures are used in some helicopter blades which are researched in this paper. In the manufacture and use of bonding structures, the debonding flaw is easy to appear, which is a serious threat to flight safety. Therefore, the corresponding testing must be carried out regularly.

At present, the acoustic methods are widely used to test debonding flaws, but these methods have low detection efficiency. In recent years, a new method, the infrared thermal imaging testing, has been widely concerned [3, 4]. The infrared thermal imaging testing has many advantages, such as high efficiency, noncontact, and intuitive test result, etc. Based on a helicopter rail rotor blade with debonding

Q. Guo (✉) · P. Jing · G. Qi
Beijing Aeronautical Technology Research Center, Beijing 100076, China
e-mail: guoqi8311@163.com

J. Wang (ed.), *Proceedings of the First Symposium on Aviation Maintenance and Management-Volume I*, Lecture Notes in Electrical Engineering 296,
DOI: 10.1007/978-3-642-54236-7_37,

damages, the infrared thermal wave testing is researched. The structural characteristics of the helicopter blade and the corresponding heat transfer process are analyzed. The experiment of testing on the blade is also completed.

37.2 Principle

37.2.1 The Principle of the Infrared Thermal Wave Testing

A thermal exciting device is used to heat the surface of the tested part. The thermal exciting device can be flash lamp array, a heat gun, or the other similar device. During the heat transfer process, there will be a surface temperature difference between the defective region and the normal region. Accordingly, the infrared radiation intensities of different regions are also different. The difference can be observed by an infrared camera, and the thermogram can be record. At last, the thermal abnormal region and flaws can be identified by thermogram analysis. In a word, the testing process includes three steps, which are thermal excitation, thermogram recording, and thermogram analysis.

37.2.2 The Heat Transfer Process

The heat transfer process of the infrared flash thermography is analyzed [5]. In the method of the infrared flash thermography, the thermal excitation is supposed to be that there is a pulse plane heat source acting on the part surface

$$f(x,t) = q\delta(t)\delta(x) \tag{37.1}$$

where x and t separately denotes the part depth and the time, and

$$\delta(x) = \begin{cases} 1, x = 0 \\ 0, x \neq 0 \end{cases}. \tag{37.2}$$

When the pulse heat source acts on a flat bottom hole part shown in Fig. 37.1, the thickness of the normal region is supposed to be infinite. If the thickness of the hole region is d, there is a temperature difference between different regions.

$$\Delta T = T_1 - T_0 = \frac{Q}{\sqrt{\pi\alpha t}} e^{-\frac{d^2}{\alpha t}} \tag{37.3}$$

where α, ρ, and c_v separately denotes the thermal diffusivity, density, and specific heat of the material, and $Q = q/\rho c_v$.

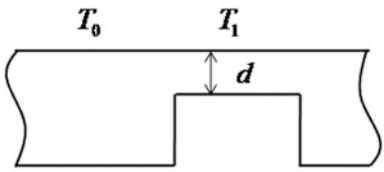

Fig. 37.1 The profile of the flat bottom hole part

The derivation of Eq. 37.3 shows that ΔT has the maximum value when $t = 2d^2/\alpha$. At the same time, in the thermogram, the brightness difference between the hole region and the normal region has the maximum value, and the hole can be observed clearly.

37.2.3 The Helicopter Blade

Figure 37.2 shows a helicopter a helicopter rail rotor blade with debonding damages. The skin on one side of the blade has been torn down, and there are also many debonding flaws on the other side of the blade. Dozens of ribs are arranged in the blade like a comb.

The profile of the blade rib is shown in Fig. 37.3. The bonding structure of the helicopter blade consists of the aluminum skin, the cementing layer, and the aluminum rib.

Shown in Fig. 37.3, the thickness of the bonding region is greater than the single-layer aluminum skin thickness. When the flash lamp arrays acts on the blade surface, the heat transfer process is similar to the situation of the flat bottom hole part. There is a temperature difference between the bonding region and the single-layer aluminum skin region. The damaged blade shows that the debonding region is very similar to the single-layer aluminum skin region. Therefore, as long as the temperature difference between the different regions is detected, the debonding region and the normal region can be divided and the debonding flaws of the blade can be also identified.

37.3 Experiment

The experiment of the infrared testing method is completed on the damaged helicopter rail rotor blade.

The infrared testing system consists of three main parts, an infrared camera, a flash lamp array, and a computer. The type of the camera is SC7300 M, which is produced by the company of FLIR. The noise equivalent temperature difference (NETD) of the camera is 0.02 K. The flash lamp array have two lamps, and the maximum energy of the single lamp can reach 2.4 kJ. In the experiment, the single lamp energy is set to 1.8 kJ, and the frame rate is set to 50 Hz. The experiment scene is shown in Fig. 37.4. Because the blade is too long, the method of sectional examination is used.

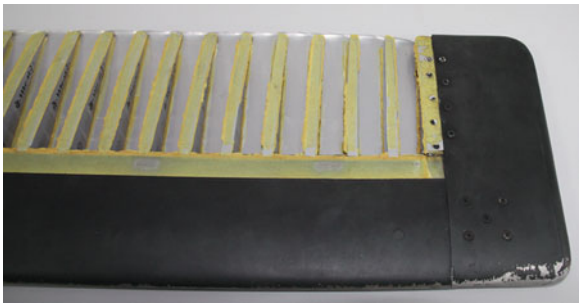

Fig. 37.2 The helicopter rail rotor blade with debonding damages

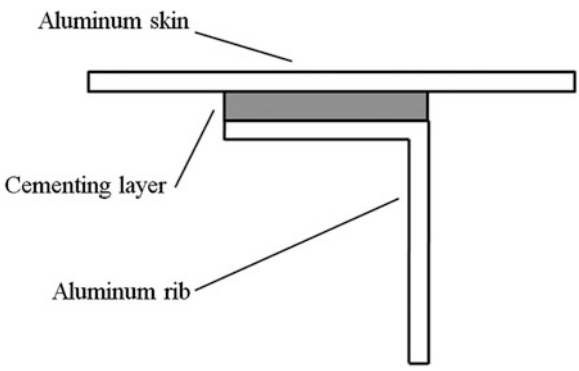

Fig. 37.3 The profile the blade rib

Fig. 37.4 The scene of the infrared testing experiment

The blade is observed from the other side. The debonding region is shown very clearly since the skin on the side of the blade has been torn down. The testing data of the blade tip is analyzed, and the analysis result is contrasted with the fact.

After the thermal signal reconstruction (TSR), the thermogram sequences are analyzed. At the time of 0.480 s after the thermal excitation, the temperature

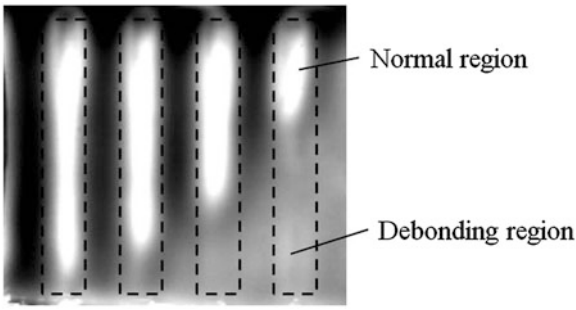

Fig. 37.5 The thermogram at the time of 0.480 s

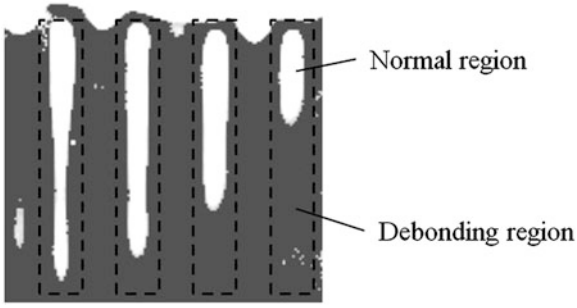

Fig. 37.6 The peak amplitude image of the second derivative thermogram

difference between the normal region and the thermal abnormal region reaches the maximum value. The program at that time is shown in Fig. 37.5. The ribs are under the regions in the dotted box. In the dotted box, the bright region is normal, and the dark region is debonding. Figure 37.5 also shows that the brightness of the debonding region and the single-layer aluminum skin region around are very similar, which agrees the previous analysis.

The peak amplitude image of the second derivative thermogram (PA image) is also analyzed, which is shown in Fig. 37.6. The PA image approximates to a binary image. In the PA image the different regions are divided more clearly than in the thermogram.

37.4 Summary

The principle of the infrared thermal wave testing is researched in this paper, and the heat transfer process is mainly analyzed. The experiment of the infrared testing is completed on the damaged helicopter blade. Two analysis methods are used to process the data and the debonding flaws are identified very clearly. The experiment shows that the infrared testing method can detect the debonding flaws in the helicopter blade bonding structure effectively.

References

1. Li X, Zhang XN, Xu XM (2006) The development of bonding structure and composite materials for the technology of aerospace. Chem Adhes, 28:172–175 (in Chinese)
2. He DX (2006) Review of the application of advanced composite in aviation and aerospace. Hi-Tech Fiber Appl 31:9–13(2006) (in Chinese)
3. Li SH, Wang DY, Qin ZM, Jia HM (2010) Sumary of property testing for composites wind turbing blade. engineering Plast Appl, 38:54–58 (in Chinese)
4. Li YH, Zhang CL, Jin WP (2005) IR thermal wave nondestructive inspection of carbon fiber composite material. Laser Infrared, 34:262–264 (in Chinese)
5. Guan J, Xiong G, Yang XR (2011) Thermology. Beijing Normal University Publishing Group, Beijing (in Chinese)

Chapter 38
Situation and Development Trend of Modern Civil Aircraft AC Power System

Li-guo Wang, Xu Li and Jing Zhao

Abstract All civil aircraft equipped with electrical system is the future of aviation development. The Main AC power system ensures the safe operation of modern civil aircraft. The high power AC generator supplies high quality power for the Main AC power system. With the extensive use of all electrical and electric design requirements in civil aircraft industry, electrical power has gradually or completely replaced the conventional power of flight control system, hydraulic operating system, environmental control system, landing gear system, and de-icing system, and so on. Therefore, the electrical power system capacity and quality should be greatly improved. This paper analyzes the main AC power system of the modern civil aircraft and the development trend of civil aircraft main AC power system in the future; The high power variable speed variable frequency generator and the main AC system will supply energy for all electrical modern civil aircraft.

Keywords Constant speed constant frequency · Variable speed constant frequency · Variable speed variable frequency

L. Wang (✉) · X. Li · J. Zhao
Ameco Aircraft Overhaul Subdivision, No. 2 Capital Airport Road, P.O. Box 563, Chaoyang District, Beijing 100621, People's Republic of China
e-mail: wangliguo@ameco.com.cn

X. Li
e-mail: lx@ameco.com.cn

J. Zhao
e-mail: zhaojingpt@ameco.com.cn

J. Wang (ed.), *Proceedings of the First Symposium on Aviation Maintenance and Management-Volume I*, Lecture Notes in Electrical Engineering 296,
DOI: 10.1007/978-3-642-54236-7_38,

38.1 Introduction

At present, the large advanced civil aircraft Airbus A380, Boeing B787, B747-8, and B777-X aircraft represent typical multi-Electronic Commercial Aircraft. The multi-electronic AC power supply system and all electronic AC power supply system are the inevitable trends of the future large civil aircraft. With the rapid development of electronic technology and computer technology, electric energy will replace hydraulic, pressure, and other forms of energy to enhance the aircraft maintenance, reliability, and economy, and to further improve aircraft overall performance. Therefore, the capacity of main AC generator installed on aircraft increases quickly. What type of generator is suitable for the future multi-electronic and all electronic large civil aircraft? This is our main research interests.

38.2 Status Quo of Civil Aircraft AC Power System

Aircraft AC power system is mainly composed of constant speed constant frequency (CSCF) power supply system, variable speed constant frequency (VSCF) power supply system, and variable frequency (VSVF) power supply system.

38.2.1 Constant Speed Constant Frequency AC Power System [1] (Boeing Commercial, FEB 15/2013)

38.2.1.1 Basic Structure and Working Principle

Constant speed constant frequency AC power system consists of integrated drive generator (IDG) and generator control unit (GCU) (see Fig. 38.1). Integrated drive generator combines the traditional constant speed drive and generator to a whole unit. Constant speed drive device is directly arranged on the gear box of the engine. The engine provide provides variable speed for the constant speed drive device. The constant speed drive transfers the variable speed to constant speed, the constant speed is the necessary condition for the AC generator output constant frequency AC power, which is the so-called constant speed frequency AC power system; through the excitation voltage regulation, generator control unit adjust the AC generator output. The AC power supply system is mainly used in Boeing B737-700/800/900 [2], Boeing B767-200/300, Boeing B747-SP/200/400, Boeing B777-200/300 [4], Airbus A318/A319/A320, Airbus A330, and Airbus A340 aircraft.

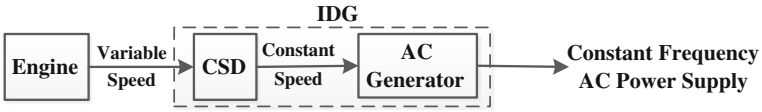

Fig. 38.1 Constant speed constant frequency AC power system structure

38.2.1.2 Main Advantages and Disadvantages

The advantages of constant speed constant frequency AC power system include high capacity, light weight, reliable, high ambient temperature, strong overload capacity, suitable for high performance, and power consumption of large aircraft. Constant frequency AC power generator can be operated separately or in parallel, and can supply good electrical performance and quality. The disadvantages are as follows: the costs are higher for constant speed constant frequency AC power supply system, including higher purchase costs, higher maintenance costs, life cycle cost, heavy weight, and low energy transfer efficiency. It is difficult to manufacture, use and maintain constant speed driver. It is also difficult to improve the quality of electric energy.

38.2.2 Variable Speed Constant Frequency AC Power Systems [1] (Boeing Commercial, SEP 25/2011)

38.2.2.1 Basic Structure and Working Principle

Variable speed constant frequency (VSCF) AC power supply system consists of a variable speed constant frequency generator and generator control components (see Fig. 38.2), AV generator directly installed in the gear box of the engine, the engine provides rotational speed for the generator, AC generator output frequency converted alternating current, alternating current converted to DC by polyphase rectifier, then the DC power is inverted to three-phase alternating current of 400 Hz for aircraft power supply system (see Fig. 38.2), which is called the variable speed constant frequency (VSCF) AC power system; Through the excitation voltage regulation and control, generator control unit adjust the output voltage. This AC power supply system is mainly used in the Boeing B737-300/400/500 [2] plane and MD-90, etc.

38.2.2.2 Main Advantages and Disadvantages

Compared with the constant speed constant frequency AC power system, Variable speed constant frequency AC power system has good electrical performance, high efficiency, high reliability, low-cost maintenance; But the working environment

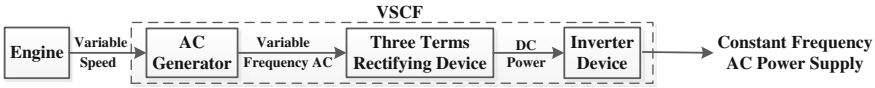

Fig. 38.2 Variable speed constant frequency AC power system structure

temperature and overload ability are lower than constant speed constant frequency AC power system. Therefore, the development of advanced technology of variable speed constant frequency AC generator is limited and cannot achieve the desired effect.

38.2.3 Variable Speed Variable Frequency AC power systems [1] (Boeing Commercial, FEB 15/2013) [3]

38.2.3.1 Basic Structure and Working Principle

Variable speed variable frequency AC power system consists of transmission, AC generator, and generator control units (see Fig. 38.3). The transmission directly installed on the gear box, the transmission change engine output from broadband speed into a narrow band speed, AC generator output frequency converted alternating current for the aircraft power supply. This is called Variable Speed Variable Frequency AC power system. Through excitation voltage regulation, generator control units (GCU) regulate and control the output of AC generator. This power supply system is mainly used on the medium range turbine propeller aircraft or medium range turbo jet aircraft equipped with frequency converter, on modern more electric airplane Boeing B777-200/300 as standby power, and on Airbus A380 and Boeing B787, B747-8, and B777-X aircraft as the main AC power.

38.2.3.2 Main Advantages and Disadvantages

Variable speed variable frequency AC power system has simple structure, small cubage, high reliability, light weight, highest power conversion efficiency, high power density, and the lowest maintenance cost; therefore the variable speed variable frequency AC power system called wide frequency band AC power supply system. Its disadvantages are large frequency changes, failure to meet the requirement of power supply quality of airborne electronic equipment which need constant frequency and restricted development.

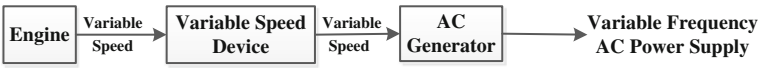

Fig. 38.3 Variable frequency AC power supply system structure

38.3 Development Trend of Civil Aircraft AC Power System

All electric and multi-electric aircraft is the future development trend of the modern civil aviation industry. Aircraft control system, hydraulic system, environmental control system, landing gear control system, brake control system and anti-icing system require a large amount of redundant AC power in all electric and multi-electric aircraft. Therefore, the aircraft power consumption and power capacity requirements rapidly increase; along with Airbus A380 and Boeing B787, B747-8, and B777-X aircraft and other modern civil aircraft in use, all electric aircraft, and multi-electric aircraft era has become a reality.

38.3.1 Multi-Electric Aircraft Airbus A380 AC Power System [5] (Airbus S.A.S., No)

In the twenty-first century, as the flagship aircraft Airbus A380 is not only the most spacious civil aircraft in human history, but also the most advanced models. It represents the one and only technology development platform of commercial aircraft for all future projects. Airbus A380 aircraft is a typical multi-electric commercial aircraft, which is completely designed according to the aircraft electric power system. The power capacity is 915 KVA in total. Among them, variable frequency AC generator system is driven by 4 sets of 150 KVA generator, power generation capacity of 600 KVA, frequency between 360–800HZ; two 120 KVA constant speed generator are driven by the auxiliary power unit. The power generation capacity is 240 KVA; a Ram Air Turbine system driven a 75 KVA power system; most aircraft actuating device of Airbus A380 adopt the electric actuator. The aircraft design is simpler, ground support equipment is reduced, and the aircraft performance is greatly improved.

38.3.2 Multi-Electric Aircraft B787 AC Power System [6] (Boeing Commercial, No)

Boeing 787 aircraft is a typical multi-electric commercial aircraft, compared with the Airbus A380 aircraft; the design is completely based on multi-electric aircraft principle and the total power is 1450 KVA. The system consists of four sets 230 V

250 KVA AC variable frequency generator and two 230 V 225 KVA AC variable frequency generator installed on the auxiliary power unit, variable frequency system replace the traditional constant frequency system, frequency in the 360–800 Hz; a 10 KVA alternating current power generation system driven by Ram Air Turbine system. After frequency conversion, rectifier, voltage distribution, the traditional 115 V AC, 28 V DC, and the new 230 V AC, 270 V DC have been supplied. The 230 V AC and 270 V DC power is mainly used for the components drives which in the past are driven by pneumatic system.

38.4 Conclusion

In conclusion, all electric and multi-electric civil aircraft is an inevitable trend of the future development of aviation. Airbus A380 and Boeing B787, B747-8 and B777-X passenger aircraft is a typical multi-electric commercial passenger aircraft. Along with the rapid development of power electronic technology and computer technology, the traditional-driven power which for flight control system, hydraulic operating system, environmental control system, landing gear control system, and anti-ice system will be gradually or completely replaced by all electric and multi-electric power. The capacity and the power supply quality requirements of the main AC power system should also be greatly increased. All electric and multi-electric civil aircraft which use high power Variable Speed Variable Frequency generator and Variable Frequency AC power system to supply power energy for aircraft, provides reliable guarantee for high power motor of each aircraft system and main AC power system. In the near future, all electric and multi-electric power system in civil planes will be variable frequency AC power system.

References

1. Leshan S (1994.4) Aviation electric, 1st edn. Science Publishing House, Beijing (in Chinese)
2. B737-300/400/500 Aircraft Maintenance Manual Published by Boeing Commercial Airplanes Group, Seattle, Washington, USA A Division of the Boeing Company PAGE DATE: SEP 25/2011
3. B737-600/700/800/900 Aircraft Maintenance Manual Published by Boeing Commercial Airplanes Group, Seattle, Washington, USA A Division of the Boeing Company PAGE DATE: FEB 15/2013
4. B777-200 Aircraft Maintenance Manual Published by Boeing Commercial Airplanes Group, Seattle, Washington, USA A Division of the Boeing Company PAGE DATE: FEB 15/2013
5. B787-9 Technical Training Manual Published By Boeing Commercial Airplanes Group, Seattle, Washington, USA A Division of the Boeing Company
6. A380 Technical Training Manual Airbus S.A.S. 31707 Blagnac Cedex, France Customer Services Technical Data Support And Services Printed In France Airbus S.A.S.

Chapter 39
Design and Implementation of a Flight Data Ground Analysis System

Cunbao Ma, Ying Wang and Wen Li

Abstract A flight data ground analysis system achieves the Flight Operational Quality Assurance (FOQA) and flight reproduction. Problems existed in the traditional method such as simple events characterization and not intuitive results. Based on the requirements analysis of the flight event investigation and troubleshooting, a new flight reproduction solution was presented, which integrated table, curve, 3D animation, cockpit view, and aeronautical chart view. Results show that the exceedance events can be positioned precisely, the flight can be reproduced accurately, the pilot's operation quality can be monitored, and flight safety can be guaranteed.

Keywords Flight data ground analysis · Flight Operational Quality Assurance (FOQA) · Flight reproduction

39.1 Introduction

Nowadays, the damage of personal property and the threatening of security caused by aviation disasters make it increasingly concerned about the safety of aviation. In order to enhance flight safety and reduce the incidence of accidents, engineers must analyze events happened in each task after missions. This requires strengthening the application rate of the flight data [1].

In this paper, the existing applications for flight data were reviewed first. Then by analyzing the Flight Operational Quality Assurance based on eigenvalue, it was found that the events characterization is too simple and conclusion is not intuitive. Upon the achievement of the system database, a method for reproducing flight was

C. Ma · Y. Wang (✉) · W. Li
Department of Airworthiness Engineering, AVIC China Helicopter Research and Development Institute, Jiangxi 333001, Jingdezheng, China
e-mail: sunnysky140@163.com

J. Wang (ed.), *Proceedings of the First Symposium on Aviation Maintenance and Management-Volume I*, Lecture Notes in Electrical Engineering 296,
DOI: 10.1007/978-3-642-54236-7_39,

proposed, which includes table, curve, 3D animation, cockpit view, and aeronautical chart view. Finally, the flight data ground analysis system was achieved. The system uses a structure and modular design, which is easy to expand. The results show that the exceedance events can be positioned precisely, the flight can be reproduced accurately, the quality of the pilot's operation can be monitored and flight safety can be guaranteed.

39.2 System Functionality and Overall Structure

A flight data ground analysis system has the following features:

(1) Database and management. The contents stored in the database include the original flight data, the decoded flight data, digital map, monitoring standards, etc. Administrator will regularly update and maintain the database.

(2) Flight Operational Quality Assurance (FOQA) [2]. The quality of the pilot's operation can be monitored. The potential safety hazards can be detected. Regularly summarize and do statistics from events happened before. Then generate reports.

(3) Flight reproduction. In the ground-based computer, there are five ways to achieve the flight reproduction which display the relevant flight data in table, flight data of change curve, 3D animation of flight, cockpit instrument display, and aeronautical chart shows [3–5]. It replays events/accidents scenarios in the intuitive way and facilitate investigation or analysis of flight performance.

Flight data ground analysis system uses the structured and modularized design thoughts for easy extension. The software system consisted of user function module, user management and system configuration module, database management module, flight data decoding and memory module, FOQA module, and flight reproduction module.

The overall structure of the system is shown in Fig. 39.1. Users of the system are logically divided into user and administrator, open for both functions are different. Personal information management and flight data analysis operations can be made by users. Database management, user management, system configuration, and flight data analysis operations can be controlled by administrators. A system workflow is shown in Fig. 39.2.

39.3 Design and Implementation of System Functional Module

39.3.1 Database Module

Taking into account of the scalability, the following system databases were established: user information database, flight data information database, fleet information database, FOQA program and the standard database, flight data

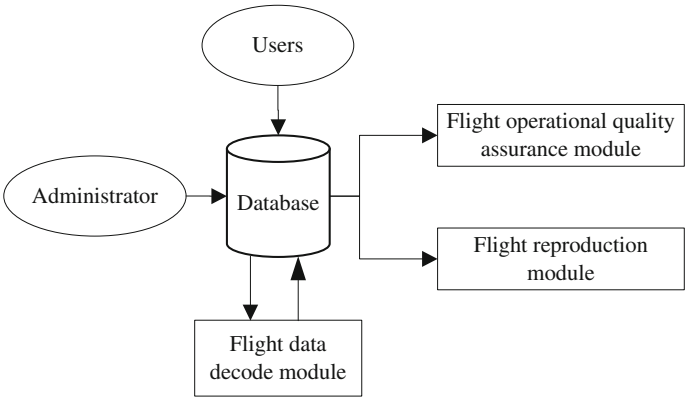

Fig. 39.1 Overall structure of flight data ground analysis system

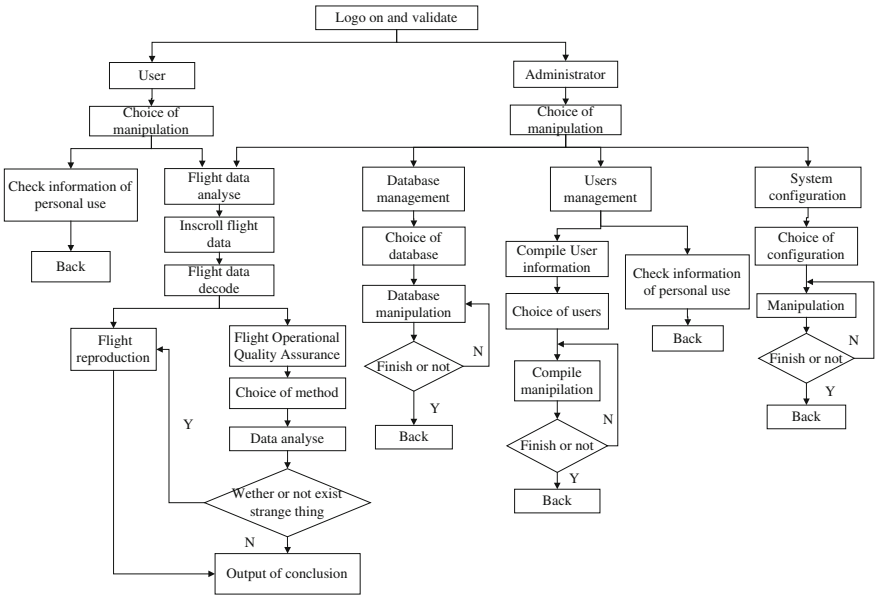

Fig. 39.2 A system workflow of flight data ground analysis system

analysis results database, and flying handling quality assurance case database [6]. Database module provides users with two functions. One is the data inquiry another is data maintenance. Data maintenance function allows administrators to update the database. User interface is shown in Fig. 39.3.

Fig. 39.3 Database management interface

39.3.2 Flight Operational Quality Assurance Module

(1) Flight operational quality assurance module based on eigenvalue
Traditional FOQA method is based on the eigenvalue. It builds handling quality assurance standards. To find overrun events, the core is to compare characteristic parameters of the flight parameters with the standard value of the normal state [7, 8]. Taking into account that some of the characteristic parameters of different types of aircraft parameters are not the same, in this paper, the characteristic parameters stored in the database corresponds with the aircraft type. Before the flight data is analyzed, the type of the aircraft should be selected first. Then the system retrieves the appropriate parameter values in the database to improve monitoring standards. After getting overrun results, in-depth research can be conducted depending on the degree of event, including an analysis of event details and flight reproduction. Running interface is illustrated in Fig. 39.4.
(2) Statistics module
The main function of statistics module is to evaluate comprehensive operation levels of pilots and the operational quality of entire airline teams. By using common statistical template, the system retrieve, and statistics in the database are completely based on the input information of the users. In addition, users can choose statistical content according to their needs, select the chart type, generate charts, and then enter report properties (like header and name), finally generate statistical reports. Users can print the output according to their needs.

Fig. 39.4 Analysis by handle interface

39.3.3 Flight Reproduction Module

(1) Table display

The purpose of displaying data by table is to observe the change of some parameters in the process of aircraft 3D simulation. Parameter selection is defined by the user. The user needs to provide the name and time period. System will retrieve the name of the parameter in the database, and display them sequentially. Interface of data table is shown in Fig. 39.5.

(2) Curve of flight parameters

The number of parameters is many. But the importance and sampling rate of each parameter is not the same. Therefore, user gets permission to select the time period and frequency of parameter display. Parameter display can be static or dynamic, in order to intuitively reflect variation characteristics of flight parameters as much as possible. According to the user's operation, parameter values are obtained from decoded data file by system and draw two-dimensional curve. Window of flight parameters curve is shown in Fig. 39.6.

(3) 3D animation of flight process

3D dynamic simulation of flight process can help staff to better understand the events. 3Dmax software is used to build a three-dimensional model of the aircraft, including the cruise segment, takeoff, and landing segment model. Before the flight simulation, users need to choose aircraft model, import flight data, and set the window with the scene, transformation scene in order to achieve good observation effect. If the detail of the aircraft during flight needs to be observed,

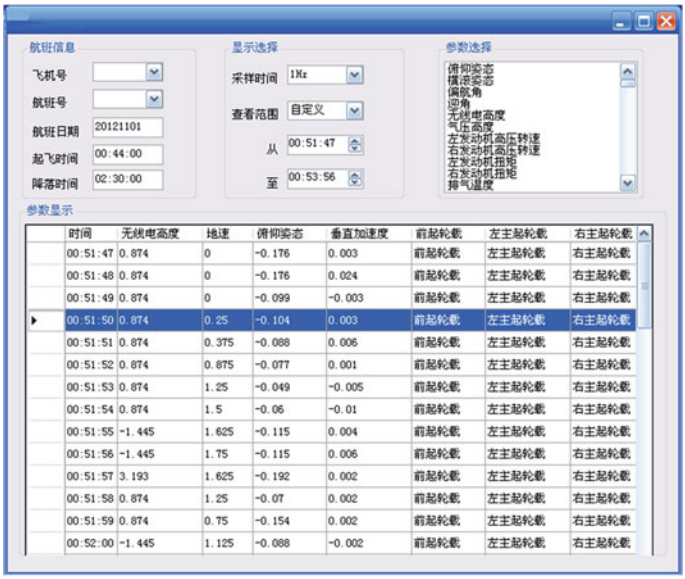

Fig. 39.5 Data tables

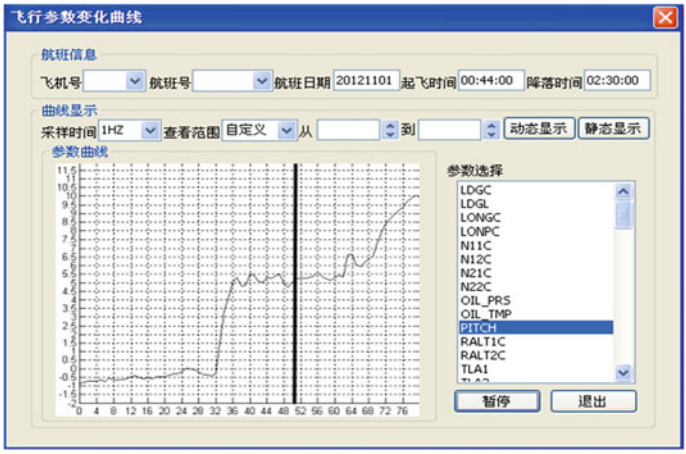

Fig. 39.6 Curve of flight parameters

inserting status information of the aircraft's control surfaces and the landing gear is required. Flight process of 3D animation interface is shown in Fig. 39.7.

(4) Cockpit instrument display

There are four main cockpit modules: primary flight display, navigation display, Engine Indication and Crew Alerting System (EICAS) interface, and control display unit. Components of VAPS software is used to analog editor to build

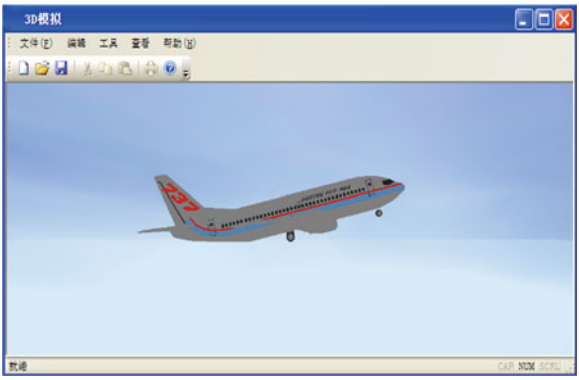

Fig. 39.7 Flight process simulation interface of 3D animation

Fig. 39.8 Cockpit instrument displays

instrument. Visual C++ completes instrument drivers and data communications of virtual instrument including the following functional modules: modeling, data processing, creating a VAPS shared data area, and instrument drivers etc. Before instrument display, it will detect whether the communication between C++ and VAPS is normal or not. Cockpit instrument displays interface is shown in Fig. 39.8.

Fig. 39.9 **a** The parameter selection screen. **b** Aeronautical charts plotted interface

(5) Aeronautical charts illustration
Under accident or incident investigation the causes, the basic situation of missions needs to be understood in the first place. It includes the flight plan route and flight details. Aeronautical charts can achieve this functionality vividly and intuitively. This paper shows aeronautical charts in three ways. The user can manually select which reproduction mode. They can also read data directly. And the system automatically determines the way to depict aeronautical charts. Drawing aeronautical charts by latitude and longitude, for example, the parameter selection window is shown in Fig. 39.9a, aeronautical charts plotted is shown in Fig. 39.9b. User interface can achieve operations including an enlarged display of the certain period of track, showing the value of certain parameters at any point of time (such as indicated airspeed, latitude & longitude and radio height).

39.4 Conclusion

In this paper, in terms of problems existed in the traditional FOQA such as simple events characterization and poor intuitive conclusion, a solution was presented, which was integrated as flight reproduction by curve, 3D animation, cockpit view, and chart view. FOQA and flight reproduction will be integrated to achieve a flight data ground analysis system. The results show that the system can accurately reproduce flight based on user needs in different ways. It can also position the exceedance events precisely. The quality of the pilot's operation can be monitored, and flight safety can be guaranteed.

References

1. Li Y (2009) Flight data application and prospects of development. Metrol Meas Tech 9:10–15 (in Chinese)
2. Yu L (2012) Review and outlook of FOQA in China civil aviation. China Civil Aviat 8:51–53 (in Chinese)
3. Wu J, Wei Z (2011) Key technology research on the reproduction of flight level path in approach and landing phase. IEEE Comput Soc 20:217–220
4. Xie B (2013) Field exercises playback system driven by flight data. Comput Syst Appl 12:64–68 (in Chinese)
5. Liu H (2012) Design and implementation of flight operation monitoring information system. Master's Thesis, University of Electronic Science and Technology, China (in Chinese)
6. Yang R (2009) E-R diagram convert to relational model in the process of database design. Silicon Valley 11:28–29 (in Chinese)
7. Zhao Y (2012) Establish FOQA system of Chinese civil aviation by WQAR. China Civil Aviation 10:57–58 (in Chinese)
8. Chang RC, Tan S (2012) Post flight analysis based on QAR in FOQA program for jet transport aircraft part I: angular position monitoring of flight control surface. J Aeronaut 3:9–16

Chapter 40
Fault Simulation for Aircraft Fuel System Using Flowmaster

Ruofan Liu, Cunbao Ma and Hongkai Jiang

Abstract The common failures of aircraft fuel system under different conditions are explored, and a model of aircraft fuel system is established, according to the working principle and composition of B737-300 aircraft fuel system. By using the Flowmaster tool for completing the simulation and based on the operation of the fuel system in the unhealthy condition, the running result and the influence of the fuel system are obtained under different malfunction.

Keywords Fuel system · Simulation of the faults · Transient simulation · Flowmaster

40.1 Introduction

Aircraft fuel system is one of the main aircraft systems, and the plane's flight safety is influenced by the working performance. The fuel system is used for storage and providing fuel for engine and APU, it consisted of storage, fuel supply, distribution, pumping, and instructions, etc. The B737-300 aircraft fuel system is introduced in this paper, as well as the method of fault diagnosis of aircraft fuel system, the simulation methods, and results provide effective tools for study of fuel system. Flowmaster software is one-dimensional fluid system simulation software and engineering fluid system simulation software [1], it can be used in stereo system for system level modeling, simulation calculation, and the analysis of the results. In order to analyze the aircraft fuel system and provide valuable reference for the operation of the fuel system maintenance, Flowmaster software is irreplaceable [4].

R. Liu (✉) · C. Ma · H. Jiang
School of Aeronautics, Northwestern Polytechnical University,
Xi'an 710072, Shaanxi, China
e-mail: 798535083@qq.com; 13484466072@163.com

J. Wang (ed.), *Proceedings of the First Symposium on Aviation Maintenance and Management-Volume I*, Lecture Notes in Electrical Engineering 296,
DOI: 10.1007/978-3-642-54236-7_40,

40.2 System Modeling

B737-300 fuel system (Fig. 40.1) is mainly composed of several subsystems of the following: fuel tank, ventilation system, fuel supply system, pumping system, fuel delivery system, measurement, and indicator system. The subsystem is composed of fuel tank, pipelines, booster pump, valves, and other accessories [2].

40.2.1 Refueling/Pumping System Model

(1) Refueling model
The refueling system is composed of part 16, 17, 18, and 40 and 41 (Fig. 40.1); the main effect is to encourage the fuel system. The constant voltage element is used to simulate the refueling system model [3].

(2) Pumping model
The pumping system is composed of Part 36, 37, 38, 39, and 28, as shown in Fig. 40.1, and the pumping system is to remove the remaining fuel in the tank. All valves should be turned off except part 36, 37, 38, 28, then the booster pump should be started in the fuel tank, the remaining fuel in the tank can be pulled out.

40.2.2 Cross-Feed System Model

The main component of cross-feed system is cross-feed valve, under normal circumstances, cross-feed valve must be closed, and the corresponding engines should be supplied fuel by each fuel systems. Only when one of the main fuel system could not work to the corresponding power system, the connected switch of the cross-feed valve enable to turn to the open position, the power system can be supplied fuel by another main fuel system, the above operation ensure the balance of the airplane flight. A valve component (part 76) is used in the cross-feed system model, connecting the two engines.

40.2.3 Tank of Fuel Supply System Model

As shown in Fig. 40.1, parts 1, 4, 5, 19, 20, 21 that compose the right tank of fuel supply system, the main effect is to supply fuel to the right engine. Part 2, 6, 7, 8, 22, 23, 29, 30, 31 that compose the central tank of fuel supply system, the central tank contains three booster pumps, the right booster pump supply fuel to the right engine, the left supply fuel to the left engine [7]. The left tank of fuel supply system is composed of parts 3, 9, 10, 25, 26, 27, when cross-feed valve is closed;

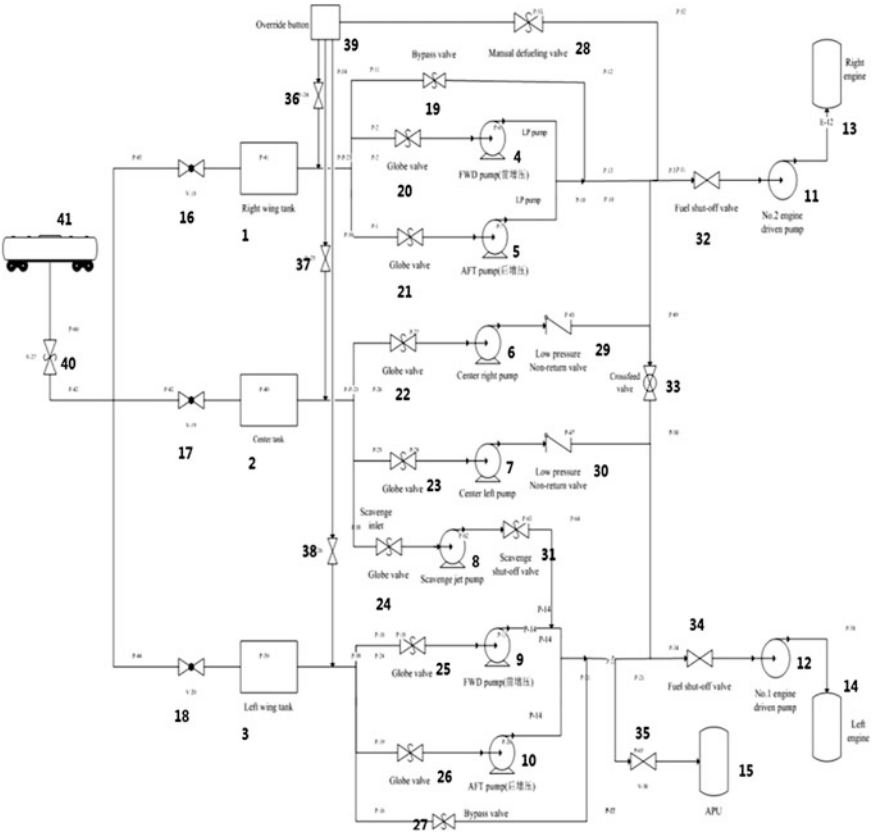

Fig. 40.1 Fuel system model

the main task is to supply fuel to the left engine. Because the left tank modeling theory and the actual operation principle are consistent with the right fuel supply system, here only the right fuel tank of fuel supply system is given in this paper.

40.2.4 Engine Model

(1) Two main engines

The left engine and the right engine are composed of part 12, 14, 34, and part 11, 13, 32 (see in Fig. 40.1), its main role is to provide power for the aircraft flight. Because Flowmaster is mainly used to study the fluid pipe network system, not to provide a better model of the engine, so an auxiliary fuel tank takes the place of the engine, for both of them have a similar point: engine's main operation is to consume the fuel, auxiliary tank's function is to store the fuel, and the process for

Table 40.1 Main Components of Simulation Model

Component number	Component	Component number	Component
1	Refueling system	13	Second tank
94	Center tank	14	First tank
17	Booster pump (right tank)	42, 45	The right spare pump tank
21, 24	Booster pump (center tank)	60	Booster pump (left tank)
71, 74	Engine booster pump	70, 73	Engine
69	APU	28, 29, 75	One-wayvalve
76	Pumping valve	78	Cross-feed valve
18, 20, 27, 32, 34, 35	Pump control components	Others	Pipeline, valve, connectors

the fuel system of auxiliary fuel storage tank is equivalent to the fuel consumption, therefore, an auxiliary fuel tank model is used to replace the engine (parts 70).

(2) APU
The APU is composed of part 15 and 35 in fuel system, it is also replaced by an auxiliary fuel tank model (part 69), and the modeling principle is the same as the engine model.

Connecting the models above, a simplified fuel system simulation model of B737-300 is made up. Simulation model of main components are in the following Table 40.1 [3].

40.3 Simulation and Analysis

Flowmaster contains control element, it can use a control element to set these failures. This article discusses several typical faults: fuel leakage, fuel filter clogging, and pump failure.

Some notes to the simulation environment are as follows:

(1) In this paper, the computation of simulation is transient, so the simulation mode is "Incompressible Transient."
(2) Setting the time step of 1 s, the simulation start time is 0 s and end time is 1000 s;
(3) The result of the operation is negative, it indicates that fluid flow into the element, if the result is positive, suggesting that the fluid flow out of components.
(4) In this paper, the simulation model is under the condition that the plane flies at a fixed height, because at different heights, the basic method is similar. For convenience, the simulation height is zero.
(5) Because related technology parameters of B-737 fuel system are hard to find, this article's main parameters are not entirely accurate, but not too different.

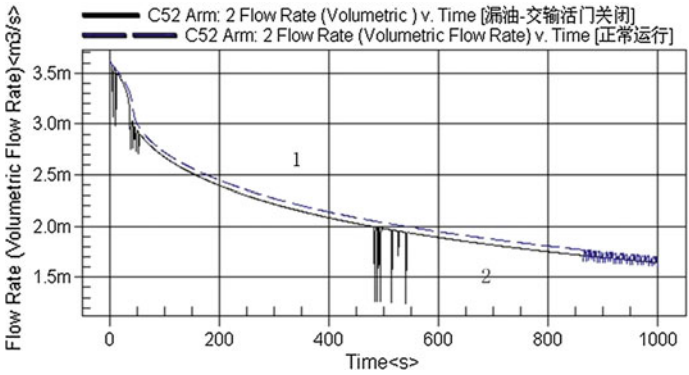

Fig. 40.2 Flow rate of first tank under normal and fuel leakage condition

(6) For convenience, in this paper, based on the basic functions of the fuel system, the model is simplified, but the basic ideas are correct.

40.3.1 The Local Influence of the Fuel System by Fuel Leakage

Figure 40.2 is the first tank's flow rate, as shown in Fig. 40.2, fuel flow from the tank, and the flow rate decreases until it is stable. From beginning to end, the flow rate, which is under normal condition, is slightly larger than the rate under leakage condition [5]. As a result of the fuel leakage from first tank, there is a rapid decline in fuel quantity, thus causing a decrease of flow rate [8].

Figure 40.3 shows the fuel pressure at the first tank exit. The pressure of the tank exit, which is under normal condition, is slightly larger than the pressure under leakage condition. This is because in the condition of the leakage, the fuel at the reduced rate is significantly less than the normal, so the pressure will be smaller [8].

40.3.2 The Influence of Engine by Fuel Filter Clogging

The curves 1, 2, 3 in Fig. 40.4, are the flow curve in valve opening of 1, 0.5, and 0.1. With the difference between the valve opening values, it indicates that the degree of the fuel filter clogging is diversity. A comparison is made between the fuel supply which the system's valve opening is 1, 0.5, and 0.1 for right engine. Then the different influences of engine by fuel filter clogging are analyzed [6].

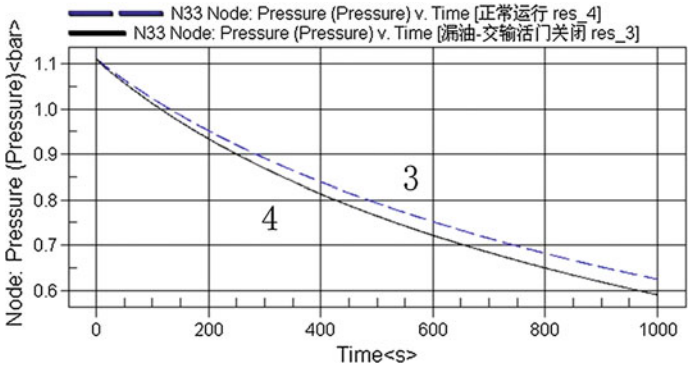

Fig. 40.3 Flow pressure of first tank under normal and fuel leakage condition

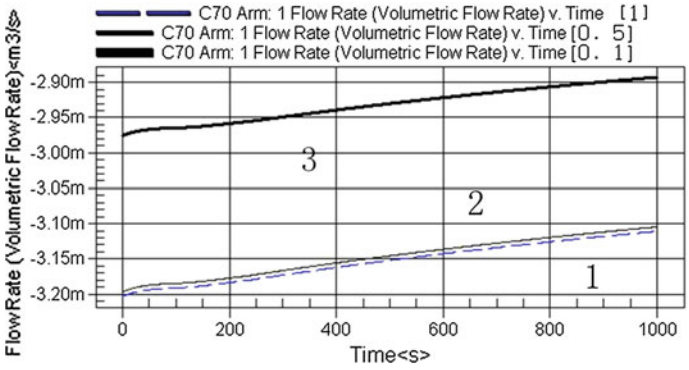

Fig. 40.4 Flow rate of different valve opening value. *Curve 1* valve opening value of 1; *Curve 2* valve opening value of 0.5; *Curve 3* valve opening value of 0.1

Informed by Fig. 40.4, when the valve opening value is 1, 0.5, and 0.1, the fuel filter clogging degree gradually increases, fuel flow to the right engine decreases. However, when the valve opening value goes down from 1 to 0.5, the fuel flow rate only have small amplitude decreases, when the valve opening value goes down from 0.5 to 0.1, the fuel flow rate is greatly reduced. Thus, the higher degree of clogging, fuel system is more sensitive to fuel filter clogging [6].

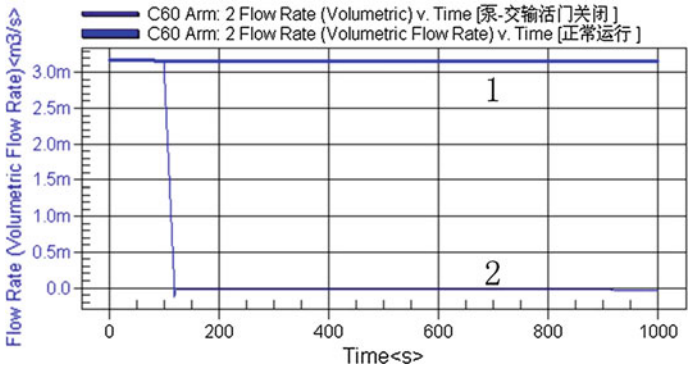

Fig. 40.5 Flow rate of booster pump. *Curve 1* Flow rate at normal condition; *Curve 2* Flow rate at booster bump failure condition

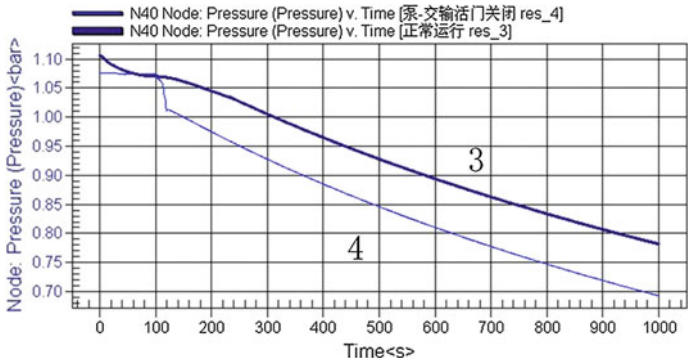

Fig. 40.6 Fuel pressure of booster pump exit. *Curve 3* Flow pressure at normal condition; *Curve 4* Flow pressure at booster bump failure condition

40.3.3 The Local Influence of the Fuel System by Booster Pump Failure

Figures 40.5 and 40.6 shows the fuel flow rate and the fuel pressure, which are under normal and pump fault conditions. The booster pump failure makes the fuel flow and pressure decrease suddenly. By comparing the data in the curve, the sudden failure of fuel pump can cause the decrease of fuel which flows to the engine from the first tank, and ultimately unable to supply fuel to the engine. By this time the engines rely mainly on the central fuel tank, in order to ensure the normal operation of the left engine, the fuel provided from central fuel tank will inevitably increase.

40.4 Conclusion

This paper has described an approach to the model aircraft fuel system, and make fault simulation of the fuel system under ideal condition; it proves that using Flowmaster to simulate aircraft fuel system is feasible. Meanwhile, effective technical support can be provided by fault simulation and analysis for aircraft fuel system that improve the safety and reliability of large-type passenger aircraft. Moreover, the study of aircraft fuel system can be facilitated by fuel system fault modeling and simulation, the research process is expedited and costs will be reduced.

References

1. Qiao Y (2007) Aircraft fuel system intelligent fault diagnosis methods. NWPU. Xi'an. Shannxi, China (in Chinese)
2. Fan K (2007) Fuel system of flight simulator modeling and simulating. HIT. Harbin. Heilongjiang, China
3. Feng Z, Gao H, Liu Y (2007) A certain type of aircraft fuel system numerical modeling method and simulation analysis. Aircraft Design 27(5) (in Chinese)
4. Yan K (2008). Helicopter fuel system simulation based on Flowmaster Software. Helicopter Tech 04:1–4 (in Chinese)
5. Qin W, Jia Q (2011) The development of software for aircraft fuel system fault diagnosis. Comput Meas Control 3:1–3 (in Chinese)
6. Lv Y (2006) Aircraft fuel system calculation and research. NWPU. Xi'an.Shannxi, China (in Chinese)
7. Gavel H (2007) Aircraft fuel system synthesis aided by interactive morphorny and optimization. In: AIAA Aerospace Science Meeting and Exhibit, vol 12, pp 1–3
8. Gao T (2009) The Boeing 737 Aircraft Fuel System Leakage Analysis and Processing. Aviation Maintenance and Engineering, vol 5, pp 1–4

Chapter 41
Application of EMD-ICA and Demodulation to Early Failure Diagnosis of Rotor Systems

Zilong Xie, Bolin Shang and Ruixiang Zhou

Abstract Vibration signals generated by complex rotor system were usually with dispersed frequency distribution, strong non-stationarity, and complex components. So it is very difficult to extract the early fault information from the vibration signals using traditional signal processing methods such as wavelet decomposition. This paper presents a fault information extraction approach based on combined EMD-ICA and Hilbert envelope demodulation according to the crack fault problems of gear hubs which occurred times in reducers of a type of turboprop engines. With this approach, vibration signals acquired under both normal and fault gear hub conditions were comparatively analyzed. The result shows that with this method we can effectively get the information of modulated signals which can clearly indicate the fault status.

Keywords Rotor system · Early fault · EMD · Independent component analysis · Demodulation analysis

41.1 Introduction

Rotor system is the core of aeroengines, but various types of failures occur frequently in it because of complex and poor operating environment, and additionally with the life limits. Furthermore, since they are deeply in the internal of engines, it

Z. Xie (✉) · B. Shang (✉) · R. Zhou (✉)
Air Force Engineering University, Xi'an, China
e-mail: 164367006@99.com

B. Shang
e-mail: cnaxzl@163.com

R. Zhou
e-mail: Zhouruixiang01@163.com

J. Wang (ed.), *Proceedings of the First Symposium on Aviation Maintenance and Management-Volume I*, Lecture Notes in Electrical Engineering 296,
DOI: 10.1007/978-3-642-54236-7_41,

is hard for us to make observations and monitor their daily maintenance. In this condition, some of the early failure is even more difficult to detect. For example, a problem of serious crack fault that occurred on reducers' gear hubs of one type of turboprop aircraft engine was not detected until the engine was dismembered to replace the turbine blades. The same problems were discovered after dismembering and checking other engines. So it is necessary to provide an effective and practical solution to make health monitoring and fault warning for rotor systems. In the case of not decomposing the engines, it is an ideal method that collects vibration signals using acceleration sensors which were arranged on the engine casing. However, the vibration signal generated by the engine is very complex, including numerous of vibration sources and much noise, the data collected by sensors was mixed by many vibration sources through different propagation paths which contains signal averaging, signal convolution, and signal multiplication, etc. Therefore, the data must be nonlinear and nonstationary, and this brings great difficulties in signal processing and fault diagnosis. Based on this, if the mixing signals could be separated into several components, relative to the individual source signals, it could significantly improve the accuracy of processing and diagnosis of the signals. And to do this, it is necessary to solve the signal separation problem.

At present, the EMD (Empirical Mode Decomposition) method which was based on adaptive decomposition is an effective tool for nonstationary signal processing, and has good decomposition performance [1]. Another method, BSS (Blind Source Separation), is one of the focus of signal processing field in recent years and can recover the vibration sources generated by different mechanical components only on the basis of observation signals collected by sensors without any priori knowledge [2]. In the field of BSS, ICA (Independent Component Analysis) has good performance. It is a new technology developed in the late 1990s in the blind signal processing field [3]. With the excellent capability of blind identification and feature extraction, we can recover the vibration sources in the condition that both the source features and mixing parameters were unknown, but just rely on statistical characteristics of the data [4].

In this paper, method combined with the advantage of both EMD and ICA was used to make separation and extraction for the vibration signals. Hilbert envelope demodulation method was used to make envelope demodulation processing for the separated signals according to the fact that there were always modulated information contains in the vibration signals generated by the rotor system. After processing, we could obtain the valuable modulation information that could clearly respond to the fault characteristic. This signal processing method is universal and effective while making fault diagnosis on other similar rotor systems.

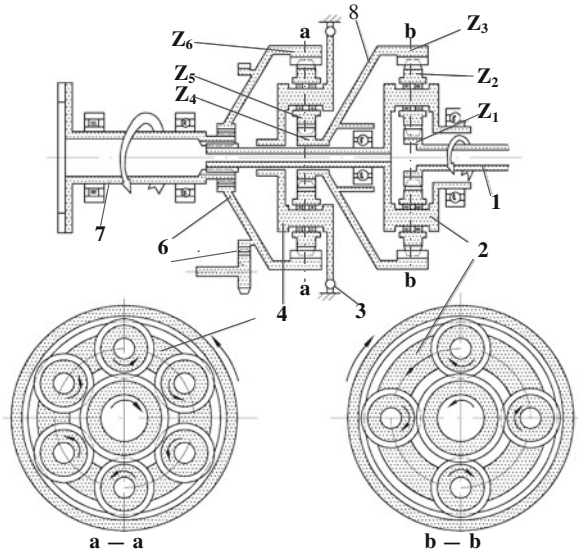

Fig. 41.1 Transmission mechanism of the speed reducer. *1* output shaft of engine, *2* planetary frame, *3* twist measure mechanism, *4* middle gear frame, *5* driven gear, *6* the second grade gear hub, *7* propeller shaft, *8* the first grade gear hub

41.2 Test

The speed reducer of the turboprop engine is a two-grade, enclosed, and differential transmission mechanism constituted of a planetary grade (the first grade) and a cross-round grade (the second grade). It reduces the input speed which is 12,300 rpm (speed of main rotor) to 1,074 rpm (speed of propeller operating). The transmission mechanism of the speed reducer was shown in Fig. 41.1. The fault of the reducer was mainly about serious crack, the cracks had typical fatigue growth characteristics. In order to monitor and predict fault in the early crack state timely, the cracks were reverted to the origin according to the fatigue growth feature of the hubs. The gear hub with the simulated fault of precrack was shown in Fig. 41.2.

The standardized speed of the engine was 205 Hz, but the speed measured in test was about 205.38 Hz. There were many vibration signals with multiple frequencies when the engine was working, among them the signals with specific frequencies with gear unit generated frequencies of the vibration signal, which were closely related to the gear hub, shown in Table 41.1. The grazing vibration of the rotor blades of compressor and turbine were a strong signal source. The signals with specific frequencies that generate when the engine was working are shown in Table 41.1.

Tests of signal acquisition were done four times using the same engine but with different gear hubs—three normal hubs and one gear hub with simulated fault by making precrack. A one-direction acceleration velocity sensor and a three-direction acceleration velocity sensor were arranged on the front-end of the engine casing for mainly collecting vibration signals of the speed reducers. One-direction acceleration velocity sensor was arranged on the back-end of the engine casing for

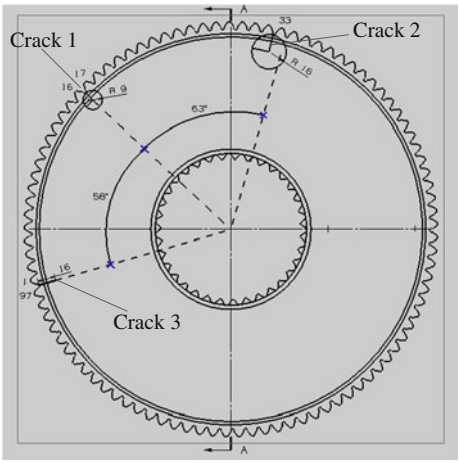

Fig. 41.2 Gear hubs with precrack

Table 41.1 The main mechanical signals

Signal type	Frequency (Hz)	Rotor blade type	Number of blades	Frequency (Hz)
Rotating of planetary frame	17.9	Low pressure turbine	82	16,841
Planetary frame frequency × 2	35.8	Medium pressure turbine	86	17,662
Planetary frame frequency × 4	71.7	High pressure turbine blades	102	20,948.8
Rotating of the first gear hub	49.6	First grade of compressor	26	5,340
Relative speed between middle gear and the second gear hub	38.1	Second grade of compressor	31	6,367
Meshing frequency f_1	1,739.5	Third grade of compressor	35	7,189
Meshing frequency f_2	6,560.6	Fourth grade of compressor	45	9,242

mainly collecting vibration signals of rotor blades of compressor and turbine. Sensors for the test were manufactured in B&K Denmark, one type of the piezoelectric acceleration sensors was 4513B (one-direction, sensitivity 10 mv/g, range 500 g), and another type of piezoelectric acceleration sensor was 4504A (three-direction, sensitivity 10 mv/g, range 750 g). Both the types of sensors were sensitive for three-dimensional and with IC built-in.

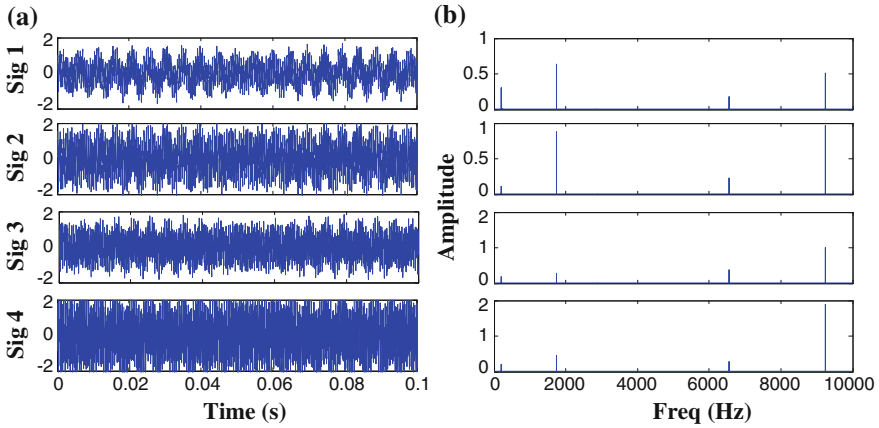

Fig. 41.3 **a** Time domain waveforms of four mixed signals, **b** spectrum of four mixed signals

41.3 Simulation Analysis

The simulation analysis aimed at illustrating that EMD-ICA method is effective. Simulation signal was created relating to the vibration signals of the rotor system. The mix matrix and four single signal sources were given as:

$$A = \begin{bmatrix} 0.8147 & 0.6324 & 0.3575 & 0.2572 \\ 0.3058 & 0.8754 & 0.4649 & 0.4854 \\ 0.4699 & 0.2785 & 0.7576 & 0.5003 \\ 0.5134 & 0.4469 & 0.5706 & 0.9419 \end{bmatrix}$$

$$s1(t) = 0.5\sin(2\pi \times 205.4t); \quad s2(t) = \sin(2\pi \times 1740t);$$
$$s3(t) = 0.5\sin(2\pi \times 6560t); \quad s4(t) = \sin(2\pi \times 9242t);$$

The four mixed signals x were generated by $x = A \cdot S$, the signals and their spectrums were given in Fig. 41.3.

The mixed signal 1 was decomposed into several IMFs using EMD method, and the spectrograms for the first to sixth IMFs were given in Fig. 41.4. From Fig. 41.4, we could find that the mixed signal was decomposed into IMFs with a rule that their frequencies were from high to low, but components of 6,560 Hz and 9,242 Hz were not well separated because of the fact that their multiple relationship between frequencies is less than 2. In addition, the IMFs contains a number of spurious components of frequencies while compared with the source signals.

The three-dimensional HHT spectrum for the decomposed IMFs was plotted in Fig. 41.5. From Fig. 41.5, we can clearly see that there were serious frequency band aliasing during the high frequency components, and the components of 6,560 Hz and 9,242 Hz failed to be well reflected.

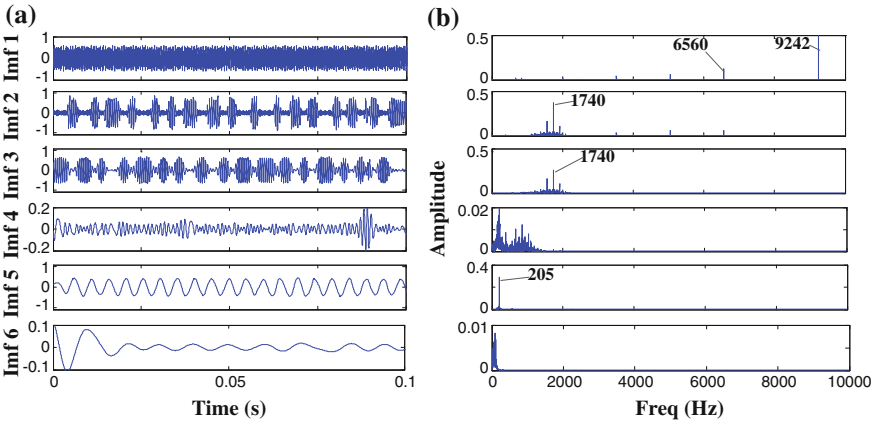

Fig. 41.4 **a** First to sixth IMFs of signal 1, **b** spectrograms for the first to sixth IMFs of signal 1

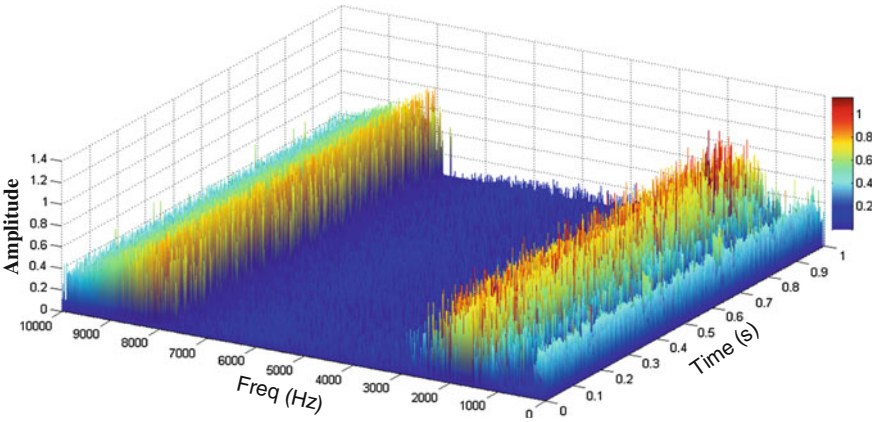

Fig. 41.5 Three-dimensional HHT spectrum for the decomposed IMFs

In this case, 6 IMFs of each mixed signal together 24 IMFs were used as input data for ICA analysis which was based on non-Gaussian maximization criterion for further signal separate processing.

Assuming that m-dimensional observed signal $x(t)$ consists of random noise and the linear instantaneous mixing of n independent source signals:

$$\boldsymbol{x}(\boldsymbol{t}) = \mathrm{A}\boldsymbol{s}(\boldsymbol{t}) + \boldsymbol{n}(\boldsymbol{t}) \tag{41.1}$$

In formula (41.3), A is a $m \times n$ mixing matrix. $n(t)$ is composed with m statistically independent Gaussian white noise signals. In order to guarantee output signals were similar to source signals $s(t)$, separating matrix W must be iterative out by ICA method, so that the unknown source signals $s(t)$ could be separated from the observed signals $x(t)$.

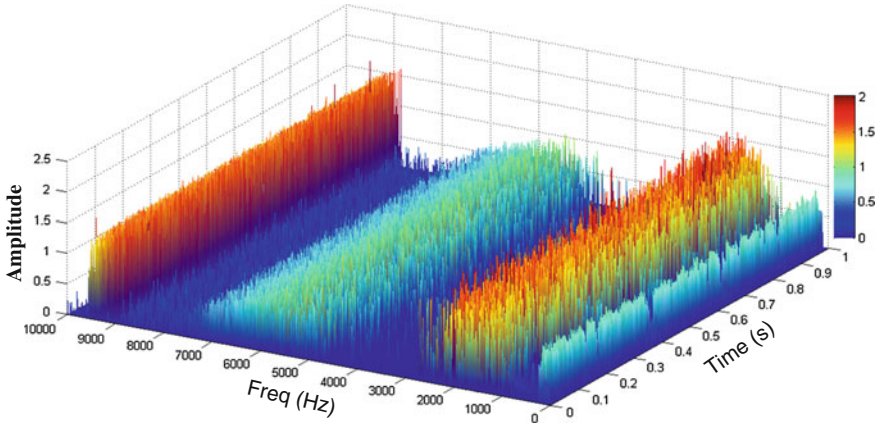

Fig. 41.6 Three-dimensional HHT spectrum for the estimated IMFs

Non-Gaussian was usually characterized by the fourth-order cumulant namely Kurtosis:

$$\text{kurt}(X) = E(X^4) - 3(E(X^2))^2 \tag{41.2}$$

where E is mathematical expectation.

Choose a fixed-point algorithm to make the objective function reaches the maximum or minimum by iterative calculation:

$$\Delta W_i \propto \frac{\partial J(y_i)}{\partial W_i} = 4\text{sgn}[k_4(y_i)]\{E[z(W_i^T z)^3] - 3W_i\|W_i\|^2\} \tag{41.3}$$

$$\begin{cases} W_i^T(k+1) = E\{z[W_i^T(k)z]^3\} \\ W_i(k+1) \leftarrow \dfrac{W_i(k+1)}{\|W_i(k+1)\|_2} \end{cases} \tag{41.4}$$

where W is the separating matrix, k_4 is the fourth-order cumulant, z is the observation signal.

Choose the four mainly estimated IMFs, plot their three-dimensional HHT spectrum in Fig. 41.6. We can see that the components of 205, 1,740, 6,560, and 9,242 Hz were clear and separated. It proved that the independence of estimated IMFs increased by the made separation using ICA, and the estimated IMFs became more complete to characterize the source signals.

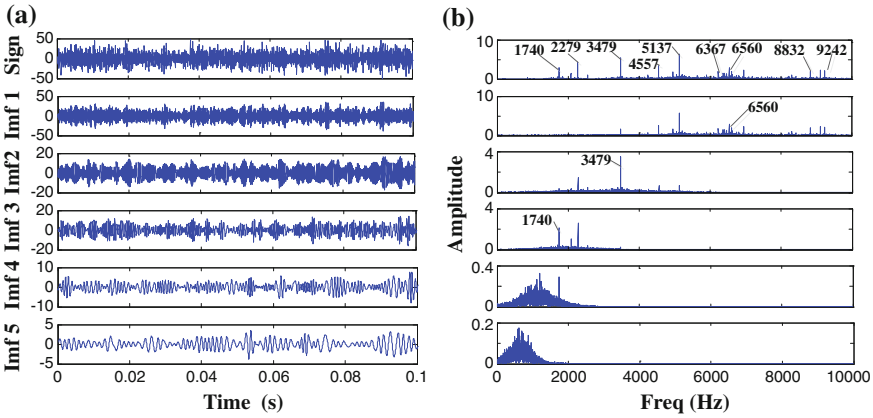

Fig. 41.7 The decomposed result of source signal 1 by EMD. **a** Source signal and 1–5 IMF. **b** 6–10 IMF

41.4 Test Analysis

Empirical Mode Decomposition (EMD) was used to decompose the vibration signal collected through the first channel into several IMFs. The time-domain waveforms and the spectrums of the signal and its 1–5 IMFs were given in Fig. 41.7. It can be seen that the 1–5 IMFs contains the most of the energy of the signal.

Spectrograms of the vibration signals collected through the four channels and their previous 1–3 IMFs were shown in Fig. 41.8. The frequencies which are closely related to the known vibration source could be accurately found in Fig. 41.8. Vibration source known in the spectrogram can accurately find the corresponding frequency. As the three signals collected through the 1–3 channels which were related to the sensors arranged in the front-end of the engine were close to the reducer, the signal components of frequency band near f_1(1,740 Hz) and f_2(6,560 Hz) had high value. However, the signal collected through the fourth channel which was related to the sensor arranged in the back-end of the engine was close to the compressor and turbine; so, the signal components which were related to the rotor blades had high value.

In order to monitor the signal change that was caused by crack fault of the gear hub, the study was focussed on two frequency bands, f_1 and f_2, which were related to the vibration generated on the both ends of the gear hub. From Fig. 41.8a–c we can see that for signals collected through the 1–3 channels their signal components which contains frequency band near f_2(6,560 Hz) was all decomposed into the first IMF, and frequency bands near $2f_1$(3,479 Hz) and f_1(1,740 Hz) were decomposed into the 2–3 IMFs. But there were many other high frequency signal components in each IMF caused by the vibration of rotor blades. So the signals of each IMF were still complex mixed signals. From Fig. 41.8d we can see that the first IMF of

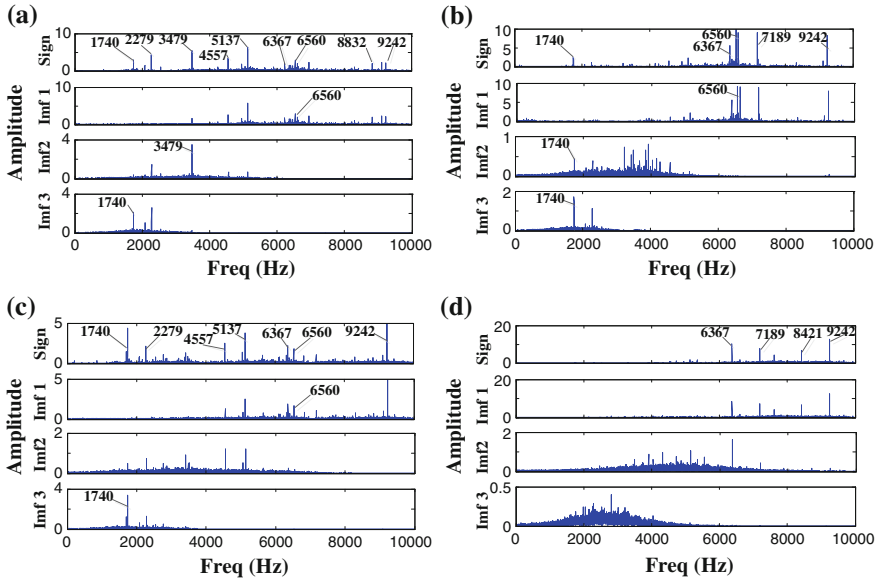

Fig. 41.8 The spectrum of IMFs of each source signal. **a** Spectrum of IMFs decomposed from signal 1. **b** Spectrum of IMFs decomposed from signal 2. **c** Spectrum of IMFs decomposed from signal 3. **d** Spectrum of IMFs decomposed from signal 4

the signal which collected through the fourth channel was mainly generated by the rotor blades' high frequency vibration.

From the results of EMD, we can see that the IMFs got associated with the frequency bands, f_1(1,740 Hz) and f_2(6,560 Hz), did not generate the characteristic mainly due to interference of aliasing caused by vibration of rotor blades. So, the ICA processing was brought into separate and extract the IMFs further. With the excellent capability of blind identification and feature extraction ICA could eliminate redundant information among IMFs, and then recover their independent characteristics. The 1–3 IMFs of each signal together 12 IMFs that collected through the four channels were combined as the input data of ICA processing based on the measurement of kurtosis. After this processing, the frequency spectrum of the previous three estimate IMFs which characterize the general features of the signals were given in Fig. 41.9.

From Fig. 41.9, we know that by making optimized separation for the 12 IMFs using ICA, we get three more independent estimated IMFs. The spectrum of estimated IMF 1 consist mainly of f_1(1,740 Hz) and its side frequency, so IMF 1 was mainly related to vibration signal generated on the front-end of the gear hub. The spectrum of estimated IMF 2 consist mainly of f_2(6,560 Hz) and its side frequency, so estimated IMF 2 was mainly related to vibration signal generated on the back-end of the gear hub. The spectrum of estimated IMF 3 consist mainly of 6,369, 7,189, 8,421, and 9,242 Hz. These frequencies were corresponding to the

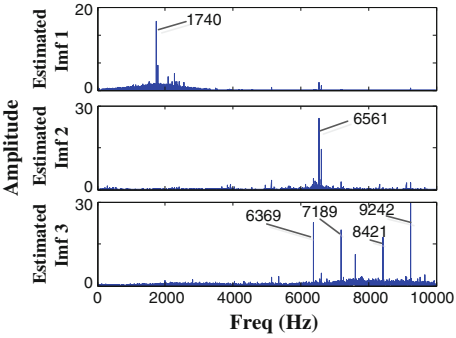

Fig. 41.9 The spectrum of the previous 3 estimate IMFs

vibration frequencies of each rotor blades, which is shown in Table 41.1. It indicates that estimated IMF 3 was mainly related to vibration signal generated by the rotor blades. This illustrates that he EMD-ICA method could enhance the independence of each IMF by integrate the initial independent vibration source signal into one estimated IMF from many IMFs.

The estimated IMF 1 and estimated IMF 2 shown in Fig. 41.9 can be, respectively, approximated treated as narrowband signal with center frequency of f_1(1,740 Hz) and narrowband signal with center frequency of f_2(6,560 Hz). This satisfies the narrowband conditions while making Hilbert envelope demodulation. By making Hilbert transform for estimated IMF 1 and estimated IMF 2, we obtain the envelope of the signals which are shown in Fig. 41.10. The spectrum of the two envelope signals are shown in Fig. 41.11.

In the spectrum of the envelope signals, the prominent frequencies 18, 36, 38, 50, and 72 Hz which had been shown in Table 41.1 were corresponding to the modulated signal caused by the rotating units' cyclical revolve. These frequencies indicated the modulation between the signal caused by the rotating units' cyclical revolve and the mesh vibration signal generated by the gear hub.

The analysis results of the four times test data by doing separation using EMD-ICA and Hilbert envelope demodulation on them were shown in Fig. 41.12. In the group of each frequency the four bars, respectively, correspond to the three times test with normal gear hubs and one fault simulation test with precrack gear hub from left to right.

When compared with the analysis results of tests with normal gear hubs, the analysis results of the vibration signal collected by fault simulation test with precrack gear hub had many different points: in Fig. 41.12a, the value of 18, 38, and 50 Hz were larger; in Fig. 41.12b, the value of 18, 36, 50, and 72 Hz prominently increase. All these frequencies were related to the vibration signals generated by rotating units of the reducer. This result shows that the crack could reduce the stiffness of the gear hub, and then the asymmetry of the units' running track became more serious, so the relevant modulated signals were enhanced. Accordingly, the health monitor of the reducer, especially about its gear hub, could be based on the various specific modulating signals given above.

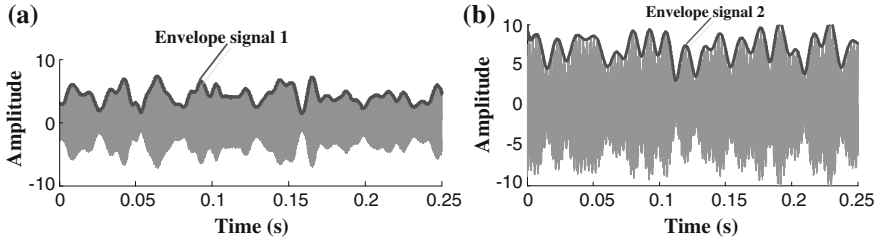

Fig. 41.10 The envelope of two IMFs. **a** Envelope of estimated IMF 1. **b** Envelope of estimated IMF 2

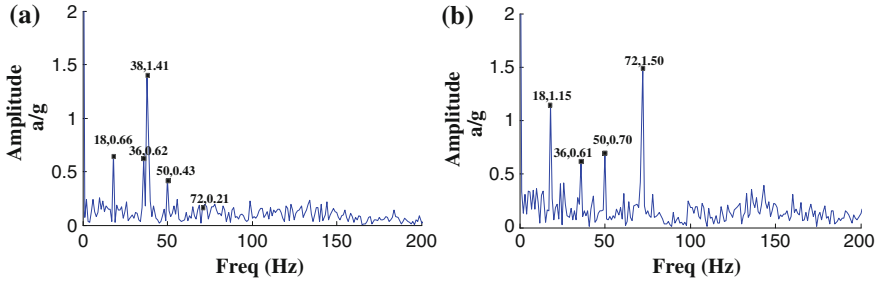

Fig. 41.11 The spectrum of two envelope signals. **a** Spectrum of envelope signal 1. **b** Spectrum of envelope signal 2

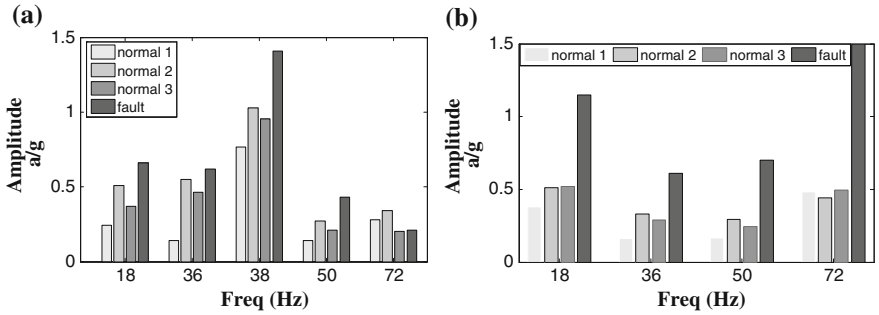

Fig. 41.12 The prominent frequencies of envelope signals of four times test signals. **a** Prominent frequencies of envelope signal 1. **b** prominent frequencies of envelope signal 2

41.5 Conclusions

The signal processing method which is based on the combined EMD-ICA and Hilbert envelope demodulation performs well on making separation and extraction of multivibration source and nonlinear mixed signals. It can integrate the initial

independent vibration source signals from complex vibration signals of rotor system into several estimate components, it is beneficial for identifying the modulated signals of the estimated components by further demodulation analysis. Then we can clearly identify the health status of the rotor system components by monitoring the modulated signals. This method has very high practical value for vibration monitoring on similar rotor systems.

References

1. Huang NE (1998) The empirical mode decomposition and the Hilbert spectrum for nonlinear and non-stationary time series analysis. Proc R Soc Lond A 454:903–995
2. Comon P (1994) Independent component analysis, a new concept. Signal Process 36:287–314
3. Bell AJ, Sejnoswski TJ (1995) An information-maximization approach to blind separation and blind deconvolution. Neural Comput 7:1129–1159
4. Lee TW (1991) Independent component analysis using an extended informax algorithm for mixed sub-Gaussian and super-Gaussian sources. Neural Comput 11:409–433

Chapter 42
Study and Countermeasure on Reliability for Nonstandard Aeronautical Test Equipment

Baosheng Yang, Yong Chen, Chunping Zhang and Dazhao Yu

Abstract Nonstandard aeronautical testing equipment is important to ground testing of airplane. Its reliability and maintainability have influence on the composite supportability of the aircraft directly. Because nonstandard testing equipment has a series of characteristics with complex, short development cycle, and small quantity, so the reliability and maintainability of equipment is affected. The statistics of failure generated by reliability and maintainability is carried out in this paper, and the causes are also analyzed. The measurement and method of developing reliability and guaranteeing supportability comprehensively for the nonstandard aeronautical testing equipment are discussed in the links of design, manufacture, use, management, and so on.

Keywords Nonstandard test equipment · Equipment development · Reliability and maintainability

42.1 Introduction

In aviation guarantee maintenance, a lot of mechanical, hydraulic, electrical, electronic, and other tested accessories of the plane are often detected in accordance with the outline of the maintainability and testability syllabus [1]. The

B. Yang (✉)
The First Aeronautical College of Air Force, Xinyang 464000 Henan, China
e-mail: happyybs5258@126.com

Y. Chen · C. Zhang · D. Yu
Naval Aeronautical and Astronautical University, Yantai 264001 Shandong, China
e-mail: jutchen@163.com

C. Zhang
e-mail: zcp523523@163.com

D. Yu
e-mail: ytyudazhao@aliyun.com

J. Wang (ed.), *Proceedings of the First Symposium on Aviation Maintenance and Management-Volume I*, Lecture Notes in Electrical Engineering 296,
DOI: 10.1007/978-3-642-54236-7_42,

equipment used is so-called aeronautical test equipment. The test equipment does not be finalized the design to produce because of few quantity generally, so it is called nonstandard equipment. Nonstandard aeronautical test equipment is different from the aviation equipment, and also different from ordinary industrial equipment. Its characteristics are as follow: (1) Precision and complex is high. A lot of test equipment has been become a complex equipment integrated with machine, electricity, liquid, gas, and computer control with the improvement of detection requirement and precision for aviation equipment; (2) Short development cycle, few production quantity, and high manufacturing cost; (3) Fixed detection cycle, long interval of equipment usage; (4) Excessive equipment manufacturers, uneven development, etc. Although a series of national and military standard such as GJB450-88 "General reliability outline for equip development and production" and GJB1909-94 "Parameter selection and standard determine requirement for equipment reliability and maintainability" have been already enacted [2], however, reliability and maintainability shortage of nonstandard aeronautical test equipment become common problem based on the characteristic of the equipment development course. It is reflected in such aspects mainly: qualified rate of equipment test is low at first time, high failure rate in use, and maintenance difficulties after delivery, etc.

Insufficient reliability and maintainability problem of nonstandard test equipment has become protruding increasingly. Improvement of comprehensive guarantee quality for the aviation equipment has been restricted seriously. In this paper, the cause results in reliability deficiency of nonstandard test equipment is analyzed combining with the characteristic of nonstandard test equipment development, and various measures guaranteed and improved for the reliability of it are also put forward for the purpose of the requirements of aviation equipment integrated would be met.

42.2 Cause Analysis

42.2.1 Reliability Lack in Subjective Consciousness

Aeronautical equipment is used on the plane. Each accessory has strict system of development, test, and maintenance. It can be regarded by managers, developer, and maintainer easily. On the other hand, various rules and regulations can be carried out more specifically and strictly. But test equipment is used on the ground and not used frequently. So manager, developer, and user will reduce a hierarchy on ideology unconsciously. Manager pays attention to efficiency and do not pay more attention to the implementation of the rules and regulations. If the function would be achieved or not is that developer pays attention to. But the problem of reliability and maintainability analysis and improvement is neglected; Maintenance consciousness lacks in users, and motivation of learning equipment is also

lacked. So strange to structure and principle of equipment is resulted, and operation technology is not standard and skilled for users. Standard maintenance does not be reached, etc. All of above is to reduce the reliability of equipment.

42.2.2 Lack of Reliability Verification for Detection Principle and Technical Scheme

The test and appraisement outline has been constituted before while aircraft components designing and manufacturing. But its technical scheme and test method is not specified. As a result, the rationality of the working principle, the reliability of the test method of the testing equipment, and the accuracy of the detection accuracy are depend on the qualification level of development unit and the ability of design personnel. Due to the test short cycle of equipment development, adopted test technology and method which have not been fully adopted by the validation, reliability, and stability defect of test data will be caused. Such problems often arise in complex intelligent test equipment.

42.2.3 Equipment Components Existing Reliability Defect

According to statistics, equipment failure caused by the component quality accounts for more than 80 percent of all failures, and electronic components are especial [3]. Despite a series of regulation such as military and national standard GJB899-92, GJB/Z 299 A, GJB/Z27-92 determine the level and scope for components selection, however, due to the standard reduced subjectively, or subjecting to the order cycle and the influence of objective factors such as development funds, the phenomenon have appeared that military production is instead of civilian or industrial components. Hidden trouble of reliability is imbedded for the equipment.

42.2.4 Undeserved Maintenance Place a Premium on Hidden Trouble of Reliability

Aeronautical test equipment is only used when the attachments of plane is to be tested. Equipment vacancy time is longer than usage in the grassroots detection department especially. As a result, some comprehensive test equipment that combining with machine, electricity, liquid, and small electronic detection equipment would be affected with damp and executor rusts so that equipment failure is caused if the vacancy time is lack of necessary maintenance.

42.2.5 Human Factors Resulting in Failure of Reliability

Some detection equipment that operation is more sophisticated, because of its utilization rate is not high, leading to equipment operators are not familiar with it, and operators are also not clear of operational standards and methods, so all above factors result that the operators operate wrongly or abnormally easily. Equipment components are tend to be damaged under over current or overload work. Equipment reliability failure would be caused.

42.3 Assurance and Improvement Countermeasure for the Reliability of nonstandard Aeronautical Test Equipment

42.3.1 Develop Reliability Design Criteria and Promulgate a Variety of Detailed Rules

Reliability criterion is summarized and refined according to reliability theory and method combining with predecessors' experiences and lessons from design, production, and usage. Every aviation nonstandard test equipment production unit should organize all kinds of personnel to learn national military standard such as GJB450-88 "The general reliability outline for equip development and production" and GJB368-87 "General outline for equip maintainability" and so on. It is more important that the project should be combined with the unit characteristic to constitute reliability and maintainability detailed rules of different types of equipment such as electronic, electrical, mechanical, hydraulic, pneumatic, etc. according with the practical situations. These rules shall be operable and practical, and as a basis for the design review. So the system can be followed from source.

42.3.2 Carry Out Core Detection Principle and Method Together with System of Reliability Analysis and Auditing

Nonstandard test equipment has the characteristic of short development cycle and financial strain. So auditing system of equipment's working principle and core functions as well as a variety of reliability analysis carried out is particularly important. Adhere to this system, weak links in the design can be found, basis of the design decisions for the design can be provided, basis of the improvement or process control can be provided, basis of maintenance plan can be provided. User and other professionals should be invited to participate in auditing in order to

avoid the dictatorial rule arise when argumentation because of local professional few. This can greatly reduce the variety of function failures and reliability hidden up later. A lot of blind spot of design reliability and maintainability will be exposed in the discussion.

42.3.3 Build Procurement and Control Mechanism of Components, Guide the Choice and Use of Components

Components are the most basic unit of the equipment and system. Reliability of equipment and system is established on the basis of reliable components. If there are no reliable components, the most perfect design is also hard to make equipment and system to meet the reliability requirement. A unified stock and control unit of components should be established by production unit. On the one hand, strengthen purchase staff learning the national military standard, full use of the network such as the China electronic product reliability data network can standardize purchase channels effectively, reduce the cost of components, ensure the quality of different grade of components; On the other hand optimum components list provided to design personnel, guide the designers choose different levels of components correctly, direct assembly personnel to use components correctly, the quality of reliability can be hold if the national military standard is carried out from the most basic link.

42.3.4 Pay Attention to Reliability in Production

Some fault statistics show that the 10–20 % of the products fault is caused by production [4]. The major reason that defects occur in production process is: bad technological design, additional bad stress attached in production process, improper handling damage or test work, and technical level of producers, etc. In many nonstandard test equipment development unit there is no production and manufacturing capacity of spare parts, and a large number of processing is in the outsourcing factory, it need to choose the enterprise that have aptitude and strength, and the designer should be in-depth processing site for technical guidance, supervise the implementation of the process scheme, check the quality of products. So, hidden trouble can be exposed in advance and the inherent reliability of device expose can be guaranteed.

42.3.5 Establish and Strengthen the Instructing and Teaching System of Equipment Before Use

Developer should participate in the packaging and shipping of equipment. The relevant personnel should arrive for unpacking and installation in time after equipment arrived in order to reduce the reliability loss of equipment; full implementation of the instructing and teaching system should be based on "Design manual of product" and "Use and maintenance manual of product". Not only the equipment operation is explained, but also the working principle, structure, and maintenance time, and method should be taught to ensure the operators understand the principle, structure, operation method. So reliability debased by man-made factor can be reduced. Maintenance record register should be provided to guarantee that equipment maintenance can be fulfilled.

42.3.6 Summarize and Standardize the Technical Documentation Timely

Filing system of standard technical files must be setup afterwards [5]. Hidden troubles of the reliability and maintainability in design, manufacture and usage can be found in the process of summing up the technical documentation. So improvement measures can be put forward. The same type of equipment would be improved constantly in terms of reliability and maintainability.

42.4 Conclusions

Nonstandard air test equipment is an important part to ensure aviation security. Although it has its own characteristics, with contradiction between interest and responsibility, contradiction between quantity and quality, but as long as their own characteristics can be combined, and the national military standard can be implemented, reliability of nonstandard air test equipment can meet requirement of aviation test.

References

1. Yang W (2000) Pandect of reliability, maintainability and supportability. National Defence Industry Press, Beijing (in Chinese)
2. Li L (1998) Design and analysis of mechanical reliability. National Defence Industry Press, Beijing (in Chinese)

3. Chen Y (2007) The reliability and maintainability engineering. National Defence Industry Press, Beijing (in Chinese)
4. Zhang C (1992) Maintainability and maintainability engineering. Equip Manag Maint 10
5. Sun H, Li R, Guo L (2012) Analysis on reliability management in equipment development. Chinese J Acad Equip 23:109–112 (in Chinese)

Chapter 43
Aircraft ATC Antenna VSWR On-wing Tester

Zhihang Yin

Abstract The reason of the ATC antenna failure is mostly the mismatch of the ATC transponder output impedance with the ATC Antenna impedance. The mismatch causes the increasement of the Voltage Standing Wave Ratio (VSWR) and the severe low efficiency of the emission (receive), then the ATC/TCAS system cannot working normally. The on-wing test instrument of the ATC VSWR can accurately measure the ATC antenna performance without the removal of the ATC antenna. The recession performance of the ATC antenna can be found by the regular check with this instrument. So the ATC antenna performance can be kept in good condition by this preventive maintenance.

Keywords ATC · Antenna · VSWR

43.1 Introduction

ATC/TCAS system failure is one of the common failures on civil airplane. The point is that once this failure occurred, most of the cases do not apply to MEL deferral, the airplane has to fly back and starts AOG troubleshooting now and then airlines flight schedule normality is affected potentially. Because ATC and TCAS are closely related each other, one failure in ATC system may lead to a failure occurred in TCAS system simultaneously. During ATC/TCAS troubleshooting, failure caused by ATC antenna malfunction is more difficult to handle. This attributes to its BITE circuit in-completing of a ATC transponder which causes bad surveillance to ATC antenna failure. On the other hand, due to the structure feature of the ATC antenna and its installation location, the antenna is apt to be affected by

Z. Yin (✉)
Henan branch of China Southern Airlines, Zhengzhou, China
e-mail: yinzh@csair.com

J. Wang (ed.), *Proceedings of the First Symposium on Aviation Maintenance and Management-Volume I*, Lecture Notes in Electrical Engineering 296,
DOI: 10.1007/978-3-642-54236-7_43,

ambient corrosion and moisture. The failure at its early stage may be hided and occurred intermittently, which brings a lot of difficulties to the troubleshooting action. In fact, at the time a failure point is unclear, what usually happened first is to replace ATC transponder, TCAS transponder, and ATC/TCAS control panel. The results come out to be no effect and all the works carried out are useless. Only after the replacement of ATC antenna, the failure disappears. The mislocating real failure part can lead to wrong spare replacement, which definitely brings unnecessary or additional cost lost to airlines.

43.2 Example

12, Jun 2011, a failure from B-29XX airplane crow report said: on ATC/TCAS control panel, the failure light intermittently lighted while making selection between ATC1 and ATC2 in air, and "TCAS fail" was shown on EHSI. After landing, no abnormalities are found through the BITE on 1# ATC and 2# ATC transponder panels in E/E compartment. ATC/TCAS control panel was replaced postflight and all the ground checks are ok. While the failure came out again next morning after take-off, airplane went back, the ATC/TCAS control panel and TCAS computer were replaced again this time, but the failure was still there. BITE from TCAS computer and transponder shown that 1# ATC transponder was failed but the replacement of transponder was no effect. The failure finally gone after the top ATC antenna was replaced.

21, Nov 2011, a crow report from an anonymous airline's B-56XX airplane noted that after take-off, both TCAS transponders were failed. The captain decided to go back. During followed maintenance check, mechanics found that the failure light on ATC/TCAS control panel was keeping on. ATC/TCAS control panel, two transponders, and TCAS computer were replaced and no effect at all. The system went back to normal only after the upper ATC antenna was replaced finally. The flight was delayed for several hours.

43.3 VSWR Measure Theory

Voltage standing wave ratio is called VSWR. While the electromagnetic waves transmit from one medium to the other medium, because of the different media, the energy of the electromagnetic wave will be reflected partly, forming a "standing wave." Voltage standing wave ratio, is referred to the ratio of peak voltage and valley voltage of the line standing wave, this value can be calculated by the model value of the reflection coefficient: the VSWR = (1 + the model value of the reflection coefficient)/(1 − the model value of the reflection coefficient). So the higher the VSWR, the greater the reflected power, and the lower the transmission efficiency.

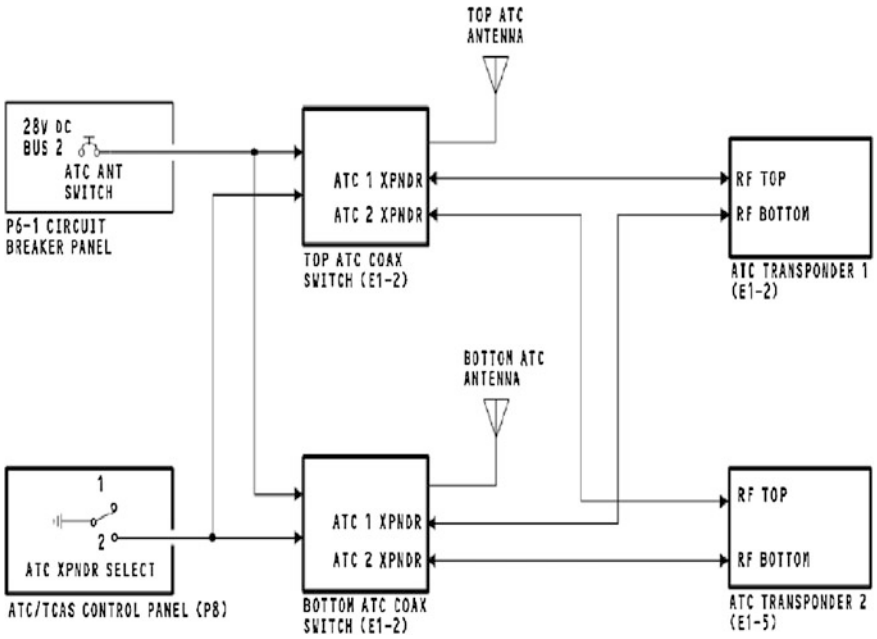

Fig. 43.1 ATC system block scheme—Boeing 737NG airplane

After all, ATC antenna failure can be attributed to the impedance mismatch between ATC transponder output HF coax cable line and ATC antenna, which increases the VSWR and greatly decreases the transmit/receive effectivity, causing ATC/TCAS system malfunction.

43.4 ATC System Circuit

The ATC antenna VSWR on-wing tester can make measurement precisely for ATC antenna performance without ATC antenna removal. Through periodical health check of the ATC antenna, we can find the recession of ATC antenna performance in time and keep ATC on its best perform condition by carrying out certain preventive maintenance action. Taking B737NG airplane [1] as example, the following text will make a brief introduction to the composition of ATC antenna and the method of antenna VSWR test.

Figure 43.1 is a principle work diagram for ATC antenna. There are two ATC transponders, one is in spare condition while the other is working. You can choose either 1# or 2# ATC transponder to work through ATC/TCAS control panel (see the XPNDR switch in Fig. 43.2). Through the transformation of two ATC antenna coax switches, both the top and bottom ATC antennas are linked simultaneously to

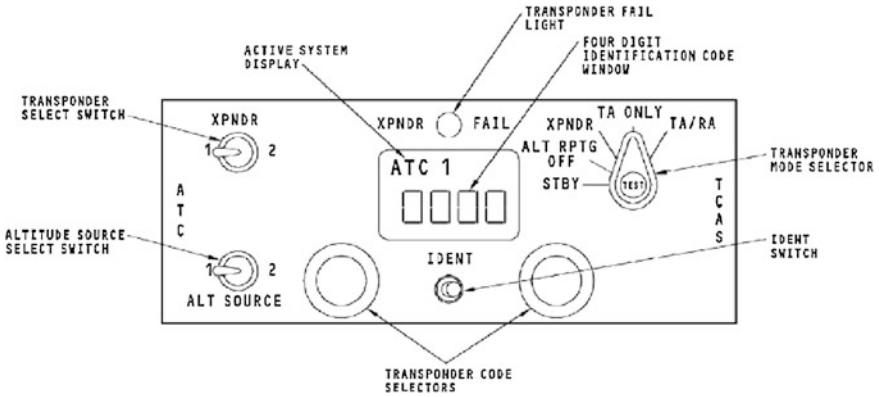

Fig. 43.2 ATC/TCAS system control panel—Boeing 737NG airplane

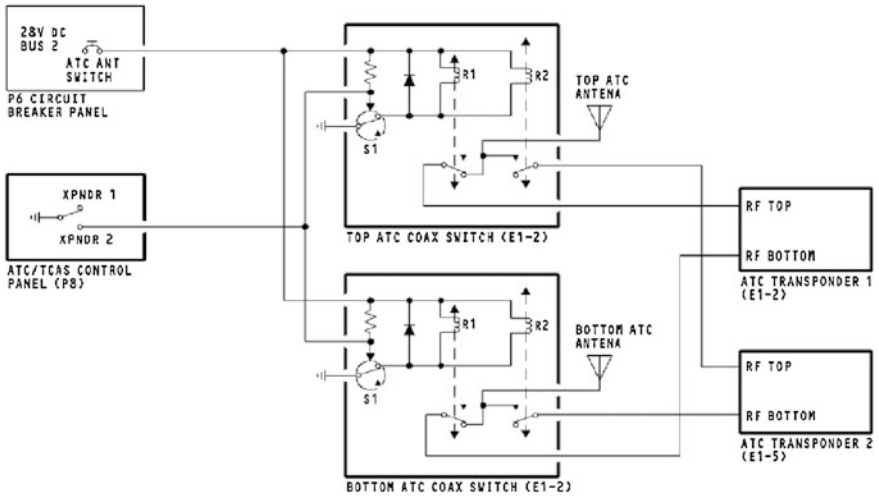

Fig. 43.3 ATC system antenna transform control block scheme—B737NG airplane

selected ATC XPNDR. Therefor, any one of the ATC antenna failure will cause the whole ATC/TCAS system to be malfunction.

Figure 43.3 is a control circuit scheme for two antenna transforming in ATC system. Two antenna conversion switches, top ATC coax switch and bottom ATC coax switch, are controlled simultaneously by XPNDR select switch on ATC/TCAS control panel. When XPNDR1 is selected, the S1 electronic switches inside two antenna converting switches, controlled by high electrical level, move to lower contact and R1, R2 are cut off power. The contact position of antenna converting switches now are at release position and top and bottom

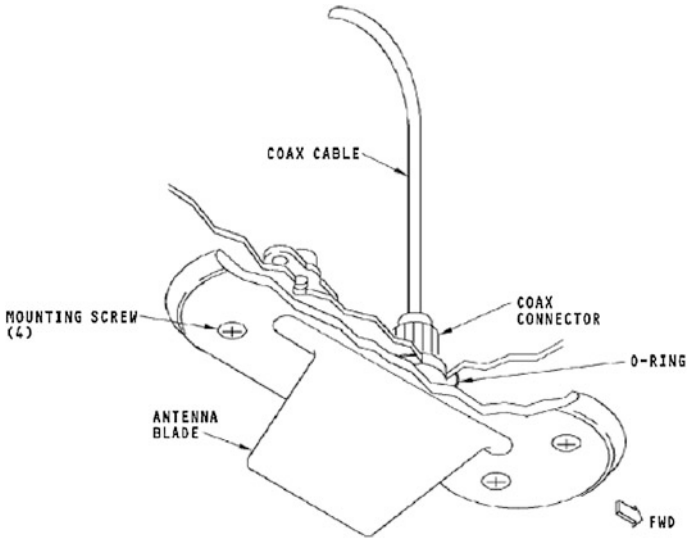

Fig. 43.4 Typical airplane ATC antenna structure

antennas are linked to 1# ATC XPNDR. Directly pulling out circuit breaker "ATC ANT switch" on ground can force both top and bottom ATC antennas link to 1# ATC XPNDR too (Fig. 43.4).

43.5 ATC Antenna Failure

The standard impedance of ATC antenna is 50 Ω, which is matched with the output impedance of ATC XPNDR and the impedance of coax cable. ATC antennas are installed on the outer body of the airplane and easy to be affected by ambient corrosion or moisture. Besides, there may be corrosion or bad contact on ATC antenna and the terminal of coax cable. All these defects can cause ATC system to have a evident HF impedance deviating from the standard 50 Ohm impedance on the end of ATC antenna and make ATC system to be malfunction. In the case of airplane in air and on ground separately, as the ATC antenna is working under different ambient conditions, the failure may be occurred intermittently and the real reason for system failure is hard to be detected (Figs. 45.5, 45.6).

Fig. 43.5 A failed ATC antenna (only used 3 months on brand-new airplane)

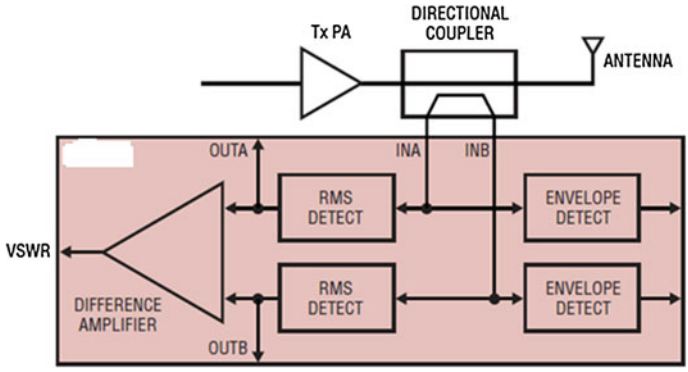

Fig. 43.6 The principle scheme of ATC antenna VSWR on-wing tester

43.6 ATC VSWR Tester and Application

The ATC antenna VSWR on-wing tester is composed of a 1060 MHz signal generator, a directional coupler [2], a output coax cable terminal, a VSWR measure circuit and a two digital LED display unit. Its output coax cable terminal is matched with the coax cable terminal on ATC transponder mounting rack in E/E compartment.

Taking B737NG airplane as an example, reference to the frame scheme of airplane SSM manual, follow the procedure given by airplane AMM, you can pull out the circuit breaker named "ATC ANT switch" on P6 panel first (Fig. 43.3), then you can remove ATC 1# transponder. As two antenna converting relays of top ATC coax switch and bottom ATC coax switch are powered off, both top and

Table 43.1 The result VSWR value of nine sampling aircrafts

Number of aircraft	Top ATC antenna VSWR	Bottom ATC antenna VSWR
1#	1.3	1.4
2#	1.3	1.3
3#	1.4	1.3
4#	1.8	1.5
5#	1.2	1.4
6#	1.3	1.4
7#	1.4	1.9
8#	1.5	1.4
9#	1.4	1.3

bottom ATC antennas get linked with ATC 1# transponder through two antenna converting relays, and the antenna circuit loop is no longer controlled by the converting switch on ATC/TCAS control panel. Now you can start to use ATC antenna VSWR on-wing tester. You put its output coax cable connectors into top ATC antenna coax cable socket and bottom ATC antenna coax cable socket on the mounting rack of ATC 1# transponder in E/E compartment, respectively. You can read the VSWR value directly from the digital LED display unit after you turn on the power. The ideal VSWR value of ATC antenna shall be 1.0. We take the measured VSWR value range from 1.1 to 1.5 as normal value because the real impedance of HF circuit component would have some deviations. However, if the VSWR measure value you have exceeds 1.6, we suggest you replace the antenna at your next convenience.

Table 43.1 is the measured VSWR value of one B737NG fleet having nine sampling aircrafts. In accordance with this, we have replaced the top ATC antenna of 4# aircraft and the bottom ATC antenna of 7# aircraft.

A certain airplane maintenance department has used the ATC VSWR on-wing tester to do the ATC antenna health check since 2012 and three ATC antenna VSWR measure value exceedances have been found. By replacing these performance recessional antennas in time, the airplane fleet is now keeping away from airplane fly back or AOG troubleshooting caused by ATC/TCAS antenna system failure. The wrong spares replacement caused by mistaking failure point is effectively eliminated. Thus the flight normality of the airlines is greatly guaranteed.

References

1. Boeing B737/800 AMM34-53ATC system. http://www.myboeingfleet.com. Accessed 20 Sept 2012
2. Texas instruments (TI) hi-speed RMS detector. http://www.ti.com. Accessed 18 Sept 2012

Chapter 44
Bearing Fault Diagnosis Based on EEMD and AR Spectrum Analysis

Han Wang, Hongkai Jiang and Dong Guo

Abstract In this paper, a novel method based on ensemble empirical mode decomposition (EEMD) and autoregressive (AR) spectrum is presented to fault diagnosis of rolling bearing. This method can carry out ensemble empirical mode decomposition and extract feature information of different machine parts in condition monitoring and fault diagnosis of machinery. The criterion of adding white noise in EEMD method is established. EEMD is used for avoiding mode mixing in signal decomposition, and it is combined with the AR spectrum in this paper. Then the AR model estimation is applied to each intrinsic mode function and the AR spectrum is obtained. Finally, the proposed method is applied to analyze the rolling bearing vibration signal and the result confirms the advantage of the proposed method.

Keywords Fault diagnosis · Bearing · Ensemble empirical mode decomposition · AR Spectrum

44.1 Introduction

The rolling bearing is one of the most widely used machine part. A failure of rolling bearing usually causes high economic loss and has potentially disastrous consequences of the operators present. Therefore, it is necessary to detect incipient bearing failure and diagnose it before the consequences of the failure become critical. Consequently, we need a convenient and reliable fault diagnosis method.

In recent years, time–frequency and time-scale analysis techniques such as short-time Fourier transform (STFT) [1] and Wavelet transform (WT) [2] have

H. Wang · H. Jiang (✉) · D. Guo
School of Aeronautics Northwestern Polytechnical University, Xi'an 710072, China
e-mail: jianghk@nwpu.edu.cn

J. Wang (ed.), *Proceedings of the First Symposium on Aviation Maintenance and Management-Volume I*, Lecture Notes in Electrical Engineering 296,
DOI: 10.1007/978-3-642-54236-7_44,

been increasingly investigated for nonstationary and nonlinear signal processing in machine health diagnosis. STFT is a stationary signal analysis and only suitable for analyzing the slowly varying signals; WT is nonadaptive and sensitive to the choice of parameters such as wavelet base. In comparison, the empirical mode decomposition (EMD) [3] decomposes a signal into a set of intrinsic mode functions (IMFs) according the characteristics of signal itself. As a result, it is a data-driven approach and has been proved to be suitable for analyzing nonstationary signals recorded from nonlinear systems. As useful as it to be, a problem that has remained existing in the EMD process is the mode mixing, which results from signal intermittency. To overcome the drawbacks of the original EMD, the ensemble empirical mode decomposition (EEMD) [4] method has been recently proposed by Wu and Huang. Essentially, EEMD repeatedly decomposes the original signal with added white noise into a series of IMFs, by applying the original EMD process, and treats the (ensemble) means of the corresponding IMFs during the repetitive process as the final EEMD decomposition result.

In this work, we introduce a novel approach for nonlinear and nonstationary data analysis. An application of EEMD and autoregressive (AR) spectrum method to fault diagnosis of bearing outer ring is presented. The methodology developed in this paper decomposes the original times series data in intrinsic oscillation modes, using the EEMD. Then the AR spectrum is applied to each intrinsic mode function. Therefore, the AR spectrum is obtained. The basic method is introduced in detail. The EEMD and AR spectrum are applied in the research of the faults diagnosis of the bearing.

This paper is organized as follows: a brief introduction of the time–frequency analysis technology is given in Sect. 44.1. In Sect. 44.2, a brief description of EEMD is presented. The method of AR spectrum is presented in Sect. 44.3. The applications of the method based on EEMD and AR spectrum to faults diagnosis of the bearing outer ring are discussed in Sect. 44.4. Finally, Sect. 44.5, the main conclusions of this paper is given in Sect. 44.5.

44.2 Brief Description of the Ensemble Empirical Mode Decomposition

44.2.1 Empirical Mode Decomposition

EEMD is an improvement of EMD; therefore, it is first to introduce the principle of EMD. EMD is developed from the simple assumption that any signal consists of different simple intrinsic oscillations, called IMFs. The essence of the method is to identify the IMFs by their characteristic time scales in the signal and then decomposed the signal adaptively. Wu and Huang [4] have defined IMFs as a class of functions that satisfy two conditions: (1) In the whole dataset, the number of extrema and the number of zero-crossings must be either equal or differ at most by

one; (2) At any point, the mean value of the envelope defined by the local maxima and the envelope defined by the local minima is zero.

In practice, EMD is implemented through a sifting process which uses local extrema. The sifting progress is implemented as follows:

Step1: Identify all the local extrema (the combination of both maxima and minima) and connect all the local maxima (minima) with a cubic spline as the upper (lower) envelope;

Step2: Obtain the first component h by taking the difference between the data and the local mean of the two envelopes;

Step3: Treat h as the data and repeat Steps 1 and 2 as many times as is required until the envelopes are symmetric with respect to zero mean under certain criteria. The final h is designated as c_j. A complete sifting process stops when the residue, r_n, becomes a constant or monotonic function from which no more IMFs can be extracted.

So, the data $x(t)$ is decomposed in terms of IMFs, c_j, i.e.,

$$x(t) = \sum_{j}^{n} c_j(t) + r_n(t) \tag{44.1}$$

where $r_n(t)$ is the residue of data $x(t)$, after n number of IMFs are extracted.

44.2.2 Ensemble Empirical Mode Decomposition

The principle of EEMD method is that: utilizing the statistical characteristics of frequency uniform distribution of white noise; white noise is added to the original signal to make it continuous in different scales to avoid mode mixing.

The discontinuity of IMFs causes the phenomenon of mode mixing in EMD, and the capability of EMD getting reasonable IMFs is determined by local extrema and the extrema distribution intervals. When there are not enough extrema, the decomposition will stop; when the extrema distribution intervals of the signal are not uniform, fitting error of upper and lower envelope of the extrema will appear to induce mode mixing [5].

The method of EEMD avoiding mode mixing is implemented as follows: First on the base of the established criterion of adding white noise in EEMD, the amplitude standard deviation coefficient of white noise is determined. After white noise with uniform scales and const amplitude standard deviation is added to the original signal, the signal will have enough extrema to provide a condition for avoiding mode mixing; Then, the signal with added white noise is decomposed by EMD to get corresponding IMFs, and all the corresponding IMFs are ensemble calculated using the principle that the average statistical of uncorrelated random sequences is equal to zero, to eliminate effects of added white noise to real IMFs; Finally, IMFs of ensemble calculation are as the final results of EEMD.

The added white noise series present a uniform reference frame in the time–frequency and time-scale space for signals of comparable scales to collate in one IMF and then cancel itself out (via ensemble averaging) after serving its purpose; therefore, it significantly reduces the chance of mode mixing and represents a substantial improvement over the original EMD. The effect of the added white noise can be controlled according to the well-established statistical rule proved by Peng et al. [6]:

$$\varepsilon_n = \frac{\varepsilon}{\sqrt{N}} \tag{44.2}$$

where N is the number of ensemble members, e is the final standard deviation of error which is defined as the difference between the input signal and the corresponding IMFs. In practice, the number of ensemble members is often set to 100 and the standard deviation of white noise series is set to 0.1 or 0.2.

44.3 AR Spectrum Estimation

The parametric spectral estimation technique employed in this research is one of the more popular techniques known as AR spectrum estimation [7]. There are two main reasons for the widespread use of this technique. First, the implementation of this method requires solving only linear equations. This provides a significant computational savings compared to other methods that involve more computationally intensive solutions to nonlinear equations, computing eigenvalues, etc. Second, the proper use of this technique requires that an all-pole process is generating the spectrum under consideration.

To illustrate this method, suppose it is desired to estimate the AR spectrum, a signal $x(n)$. The first step in a parametric technique is to compute the model coefficients a_k. The AR model of signal $x(n)$ can be defined as:

$$x(n) = -\sum_{k=1}^{p} a_k x(n-k) + u(n) \tag{44.3}$$

where $x(n)$ is the AR time series, $u(n)$ is the white noise which has zero mean and variance σ^2, p is the order of an AR model, a_k is the model coefficients.

There are many techniques available for finding the model coefficients a_k. The method used in this research is referred to as Prony's method, a thorough derivation of this and most other signal modeling techniques can be found in.

p order of AR model for system functions

$$H(z) = \frac{1}{1 + \sum_{k=1}^{p} a_k z^{-k}}. \tag{44.4}$$

The power spectrum is estimated to be:

$$p_x\left(e^{j\omega}\right) = \frac{\sigma^2}{\left|1 + \sum_{k=1}^{p} a_k e^{-j\omega k}\right|^2}. \tag{44.5}$$

By AR model implied the extension to the data, so the AR model spectrum has higher frequency resolution, the spectral line is clear, is suitable for short data.

44.4 Bearing Outer Ring Fault Diagnosis Based on EEMD and AR Spectrum

Rolling bearing is very popular in industrial application. By EEMD decomposed IMF component is zero mean, symmetry in the timeline, the signal was effectively removed the trend component [8], EEMD and AR spectrum can be combined to extract the bearing outer ring fault information of fault diagnosis.

In order to verify the validity of the method in this paper and applicability, and then applied to the NASA prediction center data repository of rolling bearing. The analysis of the data is from the normal to the bearing fault data in the test device. The experimental device for four bearings mounted on a shaft, and a dc motor drive, rotating speed at 2,000 RPM, shaft radial load of 6,000 LBS. Each column has 16 rolling bearing body, Section 0.311 inches in diameter, diameter 2.815 inch, the contact Angle is 15.17°. The data sampling frequency is 16,384 Hz and the sampling point is 2,048.

The original vibration signal with bearing outer ring is shown in Fig. 44.1. It is clear that there are periodic impacts in the vibration signal. There are significant fluctuations in the peak amplitude of the signal. However, it is hardly possible to evaluate the bearing fault condition only through such time domain vibration signal.

The EEMD algorithm is applied to analyzed the vibration signal, and the result is shown in Fig. 44.1. Figure 44.2 displays the EEMD in eight IMFs of the vibration signal in Fig. 44.1. The decomposition identifies eight modes: c_1-c_8 represents the frequency components, c_9 is the residue, respectively. Mode c_1 contains the highest signal frequencies, mode c_2 the next higher frequency band, and so on.

From Fig. 44.2, it can be easily proven that the EEMD decomposes vibration signal very effectively on an adaptive method.

AR spectrum of the vibration signal is shown in Fig. 44.3. However, it is hardly possible to evaluate the bearing fault condition only through such AR spectrum of the vibration signal.

According to the formula to calculate the rolling bearing fault characteristic frequency, the outer ring rolling bearing fault characteristic frequency is calculated the theoretical value of 238.2 Hz. After the vibration signal is decomposed using

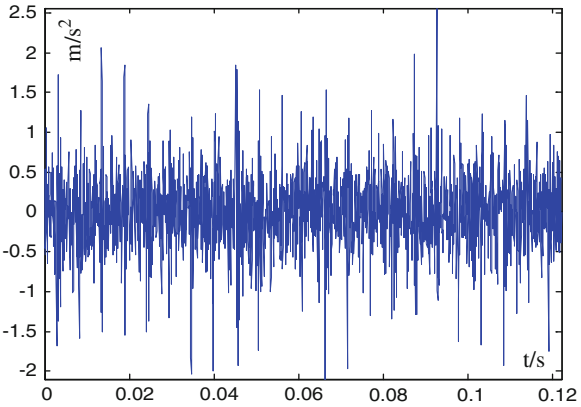

Fig. 44.1 Time domain vibration signal with bearing outer ring

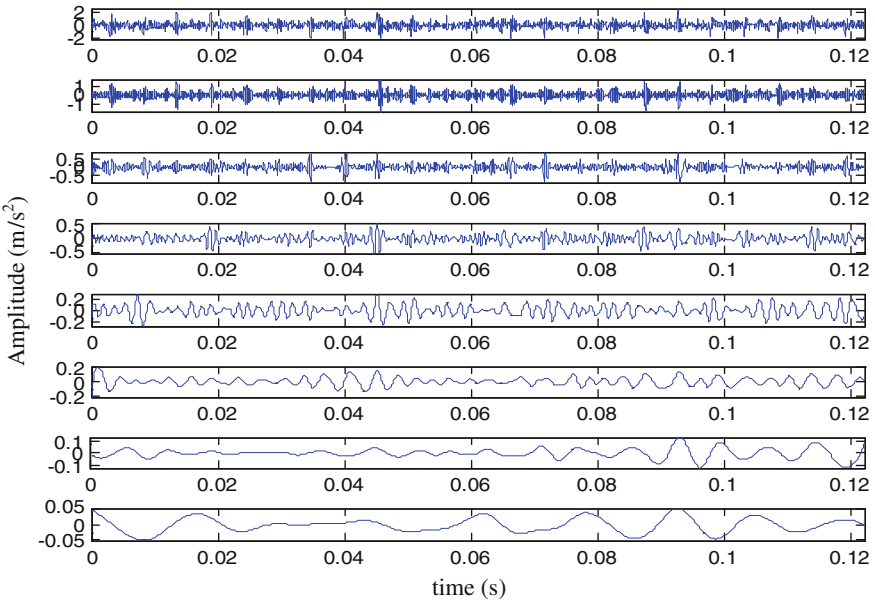

Fig. 44.2 IMFs of the vibration signal

EEMD, the AR spectrum of each mode can be obtained according to Eq. (44.5). The AR spectrum of mode c_6 is shown in Fig. 44.4, where the frequency corresponding to the peak is 240 Hz, close to the theoretical value of the characteristic frequency of the outer ring rolling bearing fault, and the error is 1.8 Hz. Thus, it can be determined that the bearing outer ring has a fault, in conformity with the real rolling bearing fault.

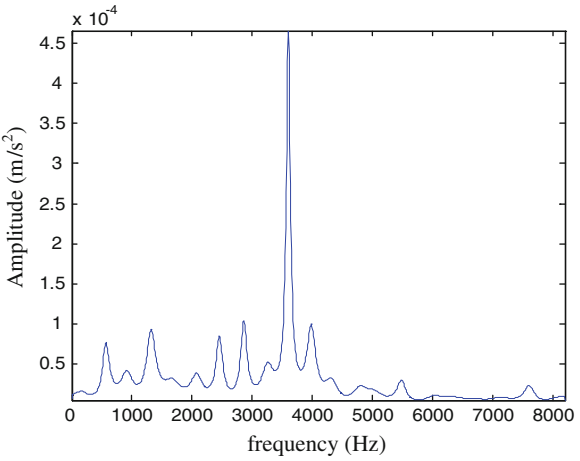

Fig. 44.3 AR spectrum of the vibration signal

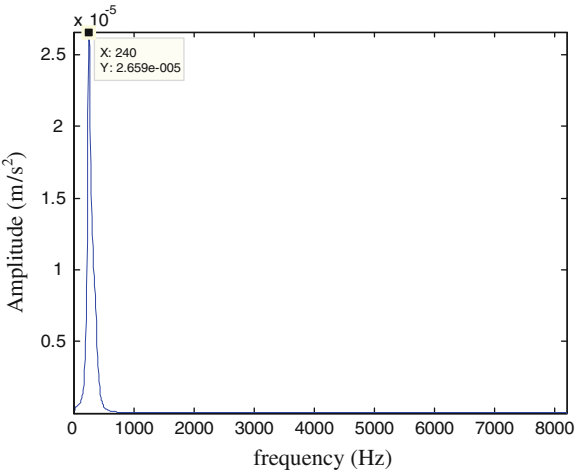

Fig. 44.4 AR spectrum of c_6

44.5 Conclusions

A new method for bearing fault diagnosis was presented based on EEMD and AR spectrum. We have obtained that the original vibration signals of bearing outer ring fault can be decomposed in eight intrinsic modes. Using EEMD method, we can recognize the vibration modes that coexist in the system, and to have a better understanding of the nature of the fault information contained in the vibration signal. The experimental result has been shown that EEMD and AR spectrum can effectively diagnose rolling bearing faults.

Acknowledgments This research is supported by the Project Supported by Natural Science Basic Research Plan in Shaanxi Province of China (Program No. 2013JM7011) and the Aviation Science Foundation of China (No. 20132153027).

References

1. Mcfadden PD, Toozhy MM (2000) Application of synchronous averaging to vibration monitoring of rolling element bearings. Mech Syst Signal Process 14:891–906
2. Li Z, Yan X, Yuan C, Peng Z et al (2011) Virtual prototype and experimental research on gear multi-fault diagnosis using wavelet-autoregressive and principal component analysis method. Mech Syst Signal Process 25:2589–2607
3. Du Q, Yang S (2006) Improvement of the EMD method and applications in defect diagnosis of ball bearings. Meas Sci Technol 17:2355–2361
4. Wu Zhaohua, Huang NE (2009) Ensemble empirical mode decomposition: a noise-assisted data analysis method. Adv Adapt Data Anal 1(1):1–41
5. Li H, Deng X, Dai H (2007) Structural damage detection using the combination method of EMD and wavelet analysis. Mech Syst Signal Process 21:298–306
6. Peng ZK, Tse PW, Chu FL (2005) A comparison study of improved Hilbert-Huang transform and wavelet transform: application to fault diagnosis for rolling bearing. Mech Syst Signal Process 19:974–988
7. Lei YG, Zuo MJ (2009) Fault diagnosis of rotating machinery using an improved HHT based on EEMD and sensitive IMFs. Meas Sci Technol 20:125701–125712
8. Zhang J, Yan R, Gao RX et al (2010) Performance enhancement of ensemble empirical mode decomposition. Mech Syst Signal Process 24:2104–2123

Chapter 45
Sensor Fault Diagnosis and Classification in Aero-engine

Feixiang Zhu, Benwei Li, Zhao Li and Yun Zhang

Abstract In this paper, a model-based analytical redundancy method is used for sensor fault detection. The diagnosis system uses Kalman filters as state estimators, which can detect 6 kinds of typical sensor fault modes. Then Design a Multi-kernel SVM fault classification system, which makes use of PCA and WPEE method to extract fault characteristic. Compared to the traditional diagnostic and classification methods, Multi-kernel SVM is more effective

Keywords Sensor fault diagnosis · Fault classification · Kalman filter · Multi-kernel SVM

45.1 Introduction

While the application of aero-engine, the sensor possible occur fault, which is used to measure the gas path parameter. In order to ensure the data which measured by the sensor can objectively reflect the actual work state of aero-engine, and be used by gas path condition monitor and fault diagnosis available. We must isolate the fault sensor first. Otherwise, it will be misdiagnosed. Domestic and international scholars have achieved many achievements in sensor fault diagnosis and isolation. Since the 1990s, They have researched on soft-fault and hard-fault of sensor, made

F. Zhu (✉)
Graduate Students' Brigade, Naval Aeronautical and Astronautical University, Yantai, Shandong, China
e-mail: zhufeixiang-32@163.com

B. Li · Y. Zhang
Department of Airborne Vehicle Engineering, Naval Aeronautical and Astronautical University, Yantai, Shandong, China

Z. Li
Aeronautical Engine Military Representatives Office of Navy, Xi'an, Shanxi

J. Wang (ed.), *Proceedings of the First Symposium on Aviation Maintenance and Management-Volume I*, Lecture Notes in Electrical Engineering 296,
DOI: 10.1007/978-3-642-54236-7_45,

use of fuzzy self-adaptation, RBF neural network, Residuals verification method, Kaman filter, multiple fault detection etc., but those achievements emphasis on fault detection, while shortage of sensor fault mode identification and classification. What means important to gas-path fault diagnosis and monitor of aero-engine, using effective sensor-fault detection method, and providing reliable sensor fault classification and maintenance .

Redundancy is the main method in sensor-fault-diagnosis field. There are three main methods to be used. Such as hardware-redundancy, analytic-redundancy, and time-sequence-redundancy. Hardware redundancy needs more than three identical sensors to measure the same parameter. While one of them is different from the others, that is the fault sensor. This method is uneconomical. Analytic redundancy utilizes reference model and another sensor signal to acquire redundancy estimate information. The residual between measured value and estimated value is used to detect fault information. Based Kalman filter group fault diagnosis method is typical analytic redundancy [1, 2]. This method is easy to realize by software. Time-sequence redundancy detect fault by analysis amplitude and change-rate of the time-sequence signal. It usually belongs to analytic redundancy.

This paper aims to define a comprehensive methodology for sensor fault detection by using a state estimation approach, in conjunction with residual processing schemes, which include simple fault detection threshold (FDT), in deterministic case, as well as statistical analysis when data be affected by noise. The result consists in a fault FDT strategy based on fault diagnosis methods well known in literature to generate redundant residuals.

While the fault sensor is isolated, this paper utilizes principal component analysis (PCA) and wavelet analysis to extract the characteristic vectors, then set up the fault classification model to make use of multi-kernel SVM.

45.2 Sensor Fault Mechanism and Fault Simulation

Sensor's fault mode includes hardware fault (such as sensor component damage, short circuit fault or open circuit fault in transmittal circuit, etc.), and software fault (such as drift, external signal interference etc. The main sensor faults shown in Table 45.1, and the main fault simulation ways shown in Table 45.2.

The standard signal (normal and fault) (Figs. 45.1, 45.2, 45.3, 45.4, 45.5, 45.6 and 45.7).

Table 45.1 Common sensor faults mode and cause

Fault mode	Fault cause
Offset	Offset circuit or offset voltage etc
Pulse interference	Interference in power and ground circuit, electro sparking, glitch in D/A converter
Short circuit	Circuit or chip corrosion, short circuit, etc
Open circuit	Signal circuit disconnect, unsoldering, void-welding, chip pin disconnect etc
Drift	Zero drift, temperature drift, sensitivity drift etc
Periodic disturbance	Frequency interference of power etc

Table 45.2 Fault simulation ways

Fault mode	Fault simulation
Offset	Adding a constant or random signal base on the original signal
Pulse interference	Adding a pulse signal base on the original signal
Short circuit	Output signal approach to zero
Open circuit	Output signal approach to the maximum
Drift	Output signal deviate from the normal value at a certain rate
Periodic disturbance	Adding a certain frequency signal base on the original signal

45.3 Based on Kalman Filter Group for Double Sensor Faults Diagnostic

In the following, we assume that the dynamic process under observation is described by a discrete-time -invariant linear dynamic model of the type

$$\begin{cases} \Delta\dot{x} = A\Delta x + B\Delta u + w \\ \Delta y = C\Delta x + D\Delta u + v \end{cases} \tag{45.1}$$

where $x \in R^m$ state vector, $y \in R^n$ output vector, $u \in R^l$ control output vector, w and v are noise. A, B, C and D are constant matrices of appropriate dimensions obtained by means of modeling techniques or identification procedures. In real applications variables are measured by means of sensors whose outputs, due to technological reasons, be affected by noise.

$$\begin{cases} \Delta\dot{x}^i = A\Delta x + B\Delta u + L\Delta h + K^i(\Delta y^i - \Delta\hat{y}^i) \\ \Delta y^i = C^i\Delta x + D^i\Delta u + M\Delta h \end{cases} \tag{45.2}$$

Δy^i is the subset of Δy, its have the all information but the ith row, C^i and D^i are the subset of C and D K^i is kalman gain matrix. For each filter, the residual vector is: $e^i = \Delta y^i - \Delta\hat{y}^i$.

When sensors have no fault and filtering procedure is steady, the residual submit multi-dimensional normal distribution $e^i \sim N(0, \sigma_i^2)$, $\sigma_i^2 = C^i P_{x,i/i-1}(C^i)^T + R^i$;

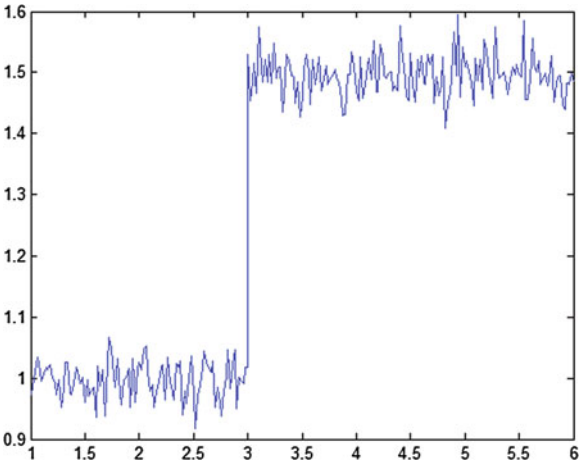

Fig. 45.1 Offset signal

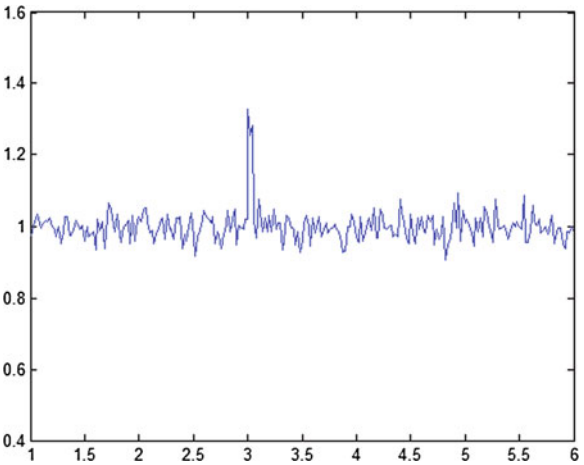

Fig. 45.2 Pulse interference signal

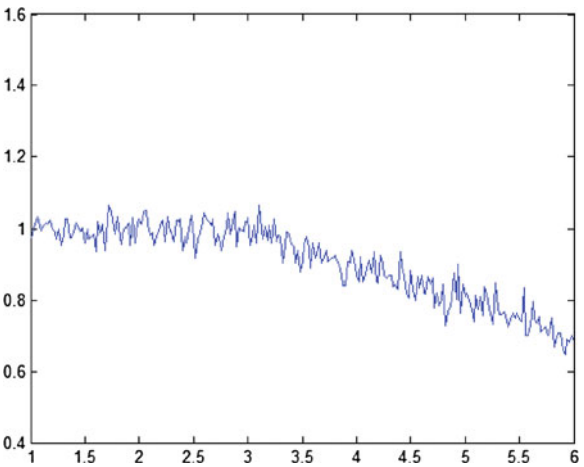

Fig. 45.3 Drift signal

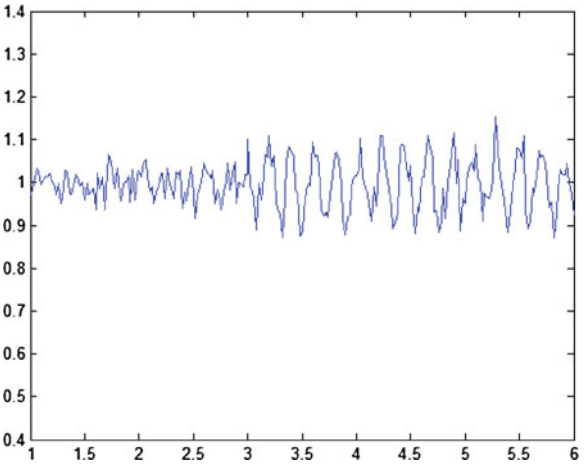

Fig. 45.4 Periodic disturbance signal

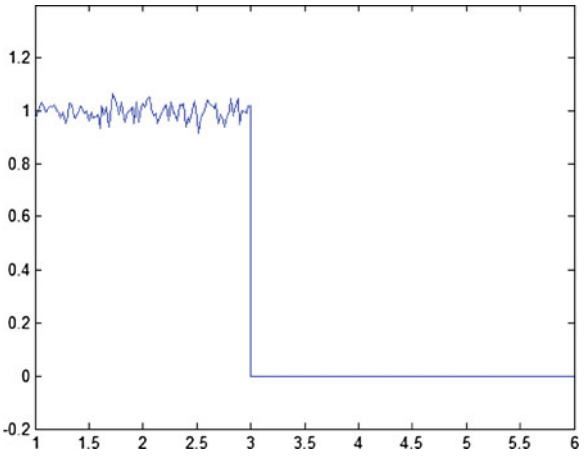

Fig. 45.5 Short circuit signal

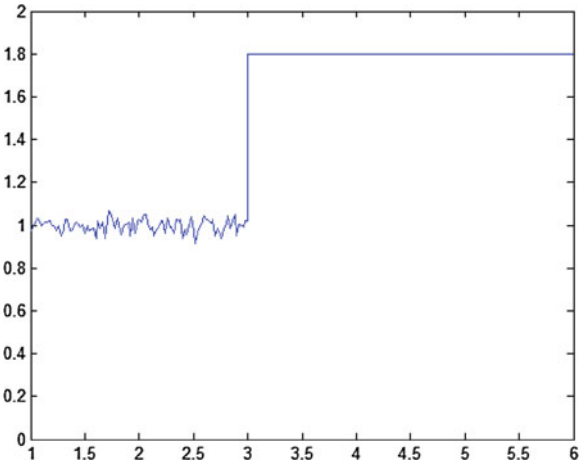

Fig. 45.6 Open circuit signal

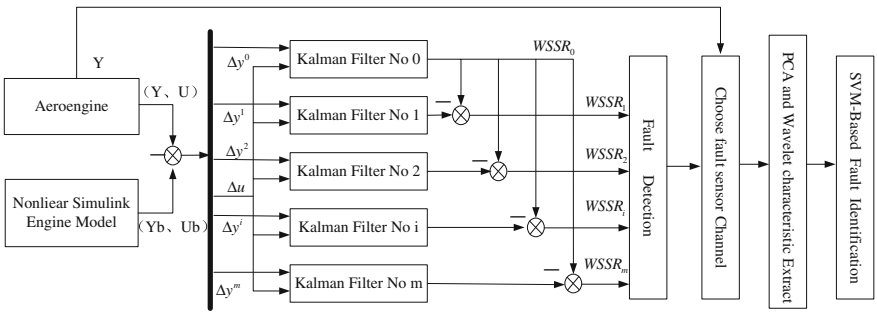

Fig. 45.7 Based kalman filter group double sensor faults diagnosis

When the residual is obtained, the weighted sum of squares residuals (WSSR) for each of the Kalman filters are calculated by

$$WSSR^i = \left(e^i\right)^T \left(\sigma_i^2\right)^{-1} \left(e^i\right) \tag{45.3}$$

Design $m + 1$ kalman filters, KF0 have all sensor's information, The ith Kalman filter is driven by all but the ith input sensor, and generates a residual function which is sensitive to all but the ith input sensor fault. The same as KFm have the information except second mth sensor. If the ith and jth sensor occur faults, the residual between KFi and KF0 just have the jth sensor' information, if the WSSR exceed the fault detection threshold (FDT), the ith sensor's fault can be detected. In the same way, the jth sensor's fault can be detected [3, 4].

45.4 Multi-Kernel SVM-Based Sensor Fault Identification

SVM convert Input-space into multi-dimensional characteristic space by kernel function, and then make the problem become a solution-convex programming, and acquire the global optimal solution. Accusation of SVM classification depends on kernel function. The tradition SVM almost use only one kernel function, it cannot solve a complicated problem, which involves multi-data source. Then Multi-kernel SVM is developing. Multi-kernel function can improve the identification ability and classification performance of SVM [5], it usually uses several kernel functions to linear combination a Multi-kernel function.

$$\begin{cases} K\left(x_i, x_j\right) = \sum_{m=1}^{M} d_m K_m\left(x_i, x_j\right) \\ s.t. \quad 0 \le d_i \le 1 \quad \sum_{m=1}^{M} d_m = 1 \end{cases} \tag{45.4}$$

Mercer theory, Multi-kernel function is Mercer kernel which comprises of several kernel function, then the optimization problem covert to [6]:

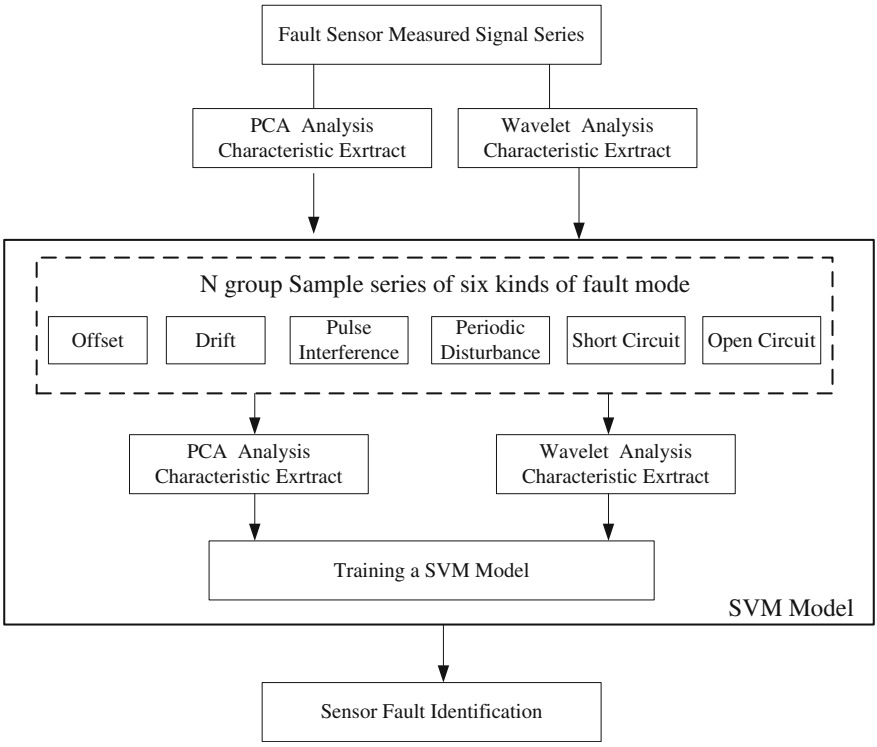

Fig. 45.8 Multi-kernel SVM-based sensor fault identification

$$\begin{cases} \min J(d) = \frac{1}{2}\sum_{m=1}^{M}\frac{1}{d_m}\|f_m\|^2 + C\sum_{I=1}^{1}\varepsilon_i \\ s.t. \quad \sum_{i=1}^{n} f_m(x_i) + y_i b \geq 1 - \varepsilon_i, \forall i \\ \sum_{m=i}^{M} d_{m=1}, d_m > 0, \forall m \end{cases} \tag{45.5}$$

By Lagrange multiplier and Karush–Kuhn–Tucker (KKT), Lanckriet give the aural problem.

$$\begin{cases} \max \sum_{i=1}^{k}\alpha_i - \frac{1}{2}\sum_{i=1}^{k}\sum_{j=1}^{k}\alpha_i\alpha_j y_i y_j \sum_{m=1}^{M} d_m K_m(x_i, x_j) \\ s.t. \quad \sum_{i=1}^{k}\alpha_i y_i = 0, \quad 0 \leq \partial i \leq C \quad i = 1, \cdots, k \\ \sum_{m=1}^{M} d_m = 1 \end{cases} \tag{45.6}$$

Against the aero-engine sensor fault diagnosis problem, Design a method, which use time–frequency analysis and Multi-kernel SVM [7]. First, to normalize the output signal, make use of PCA method to refactor a characteristic vector, meanwhile, use wavelet analysis method to decompose the signal to refactor another characteristic vector. Training a Multi-kernel-SVM model by the two characteristic vectors. As shown in Fig. 45.8.

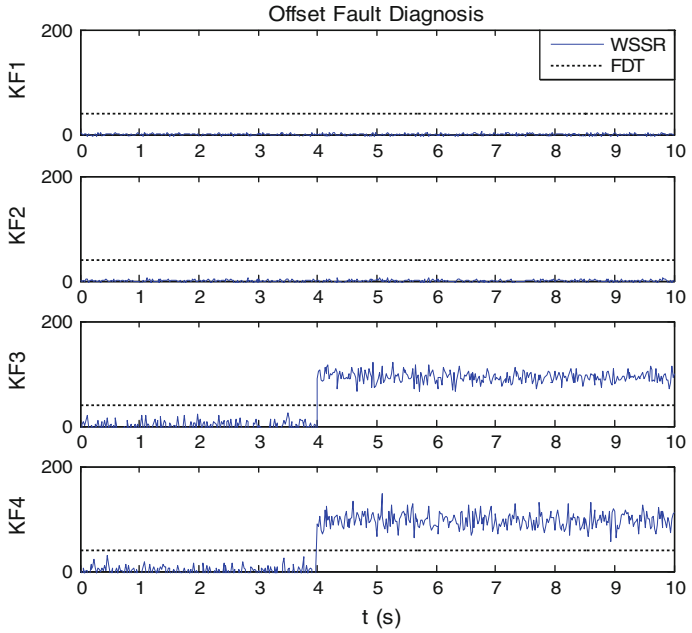

Fig. 45.9 Offset fault detection

45.5 Experiment

45.5.1 Fault Diagnosis-Based Kalman Filtering

With a twin-spool turbofan engine, choose low-spool N_H and high-spool N_L as state vectors, combust fuel W_f and tailing spool sectional area A_9 as control output vectors, low-spool N_H, high-spool N_L, high-compressor outlet pressure P_3 and low-turbine outlet temperature T_6 as output vector, corresponding the input of Kalman filtering. The data come from the nonlinear component-level engine model, adding noise according to the actual.

(1) Double Offset Faults Simulation and Diagnosis
While $t = 4$s, give a 2 % offset signal in the base of sensor P_3 and T_6, shown in Fig. 45.9;
(2) Double Drift Faults Simulation and Diagnosis
While $t = 4$s, give a drift signal $y^*_{P3} = y_{P3} + 0.015 \times (t - 4)$, $y^*_{T6} = y_{T6} + 0.05 \times (t - 4)$ in the base of sensor P_3 and T_6, shown in Fig. 45.10;
(3) Double Pulse interference Faults simulation and detection
While $t = 4$s, give a pulse signal in the base of sensor P_3 and T_6, shown in Fig. 45.11;

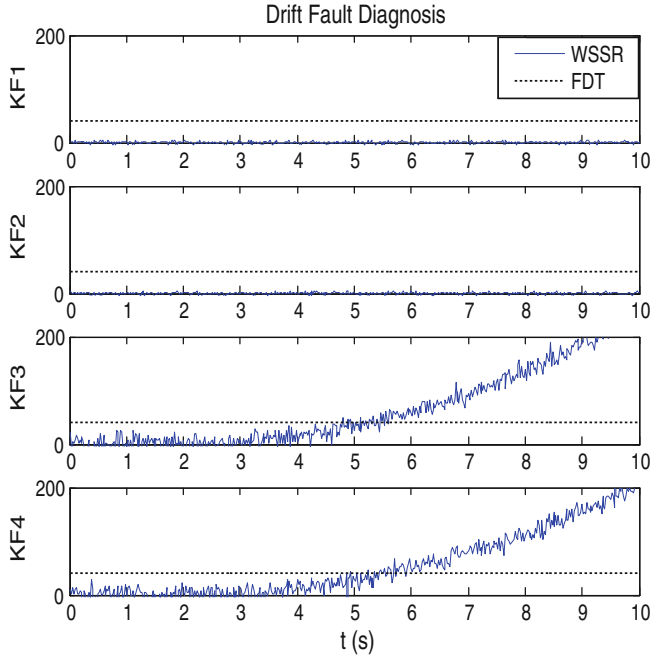

Fig. 45.10 Drift fault detection

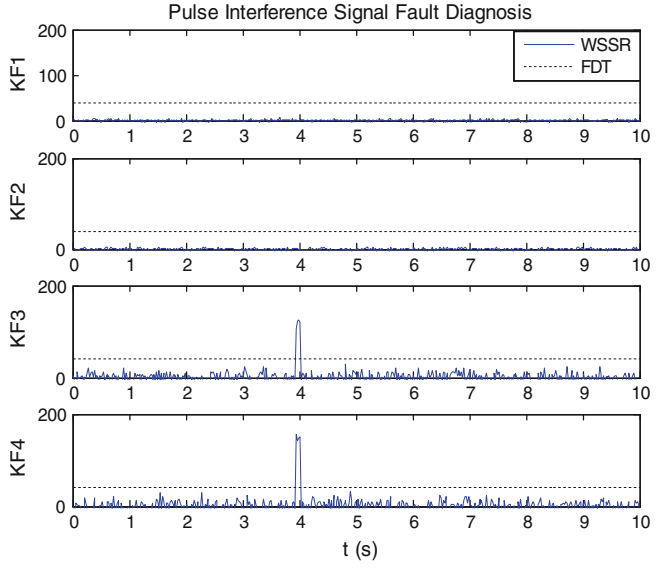

Fig. 45.11 Pulse fault detection

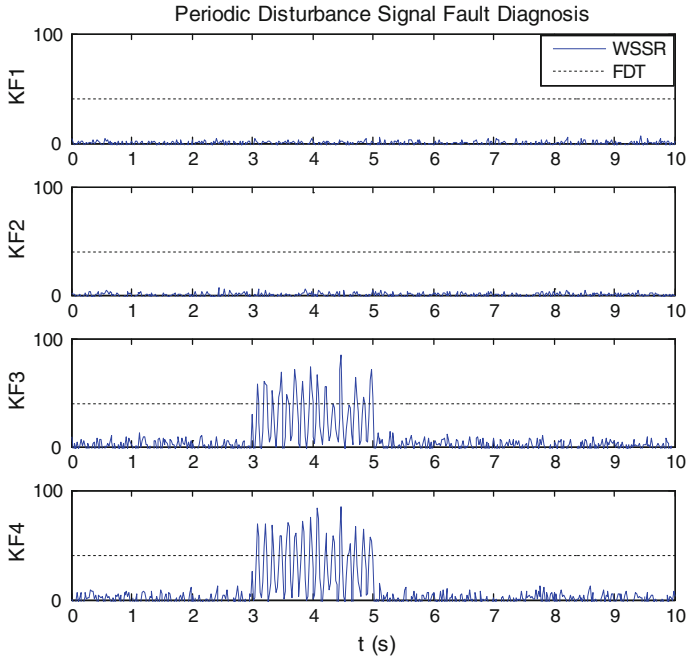

Fig. 45.12 Periodic disturbance fault detection

(4) Double Pulse interference Faults simulation and detection
While $t = [3–5]$s, give a Periodic Disturbance signal ($AP_3 = 1$, $T_6 = 40$ °C, 50 Hz) in the base of sensor *P3* and *T3*, shown in Fig. 45.12;
(5) Double Open circuit Faults simulation and detection
While $t = 4$s, keep $P_3 = 4$ MPa, $T_6 = 800$ °C, shown in Fig. 45.13;
(6) Double Short circuit Faults simulation and detection
While $t = 4$s, keep $P_3 = 1.01$ MPa, $T_6 = 5$ °C, shown in Fig. 45.14;
(7) Drift and open circuit double sensor fault detection
While $t = 2$s give P_3 a drift signal, mean while keep $T_6 = 5$ °C, shown in Fig. 45.15;
(8) Periodic disturbance and short circuit double fault detection
While $t = 2$s, give P_3 Periodic Disturbance signal ($AP_3 = 1$, 50 Hz), keep $T_6 = 5$ °C, shown in Fig. 45.16
(9) Drift and offset double sensor fault detection
While $t = 2$s, give P_3 a 2 % offset signal, and give T_6 a drift signal $y^*_{T6} = y_{T6} + 0.05 \times (t - 4)$;
Show in Fig. 45.17
(10) Periodic disturbance and drift double sensor fault detection
While $t = 2$s, give P_3 a Periodic Disturbance signal ($AP_3 = 1$, 50 Hz), and give T_6 a drift signal $y^*_{T6} = y_{T6} + 0.05 * (t - 4)$; show in Fig. 45.18.

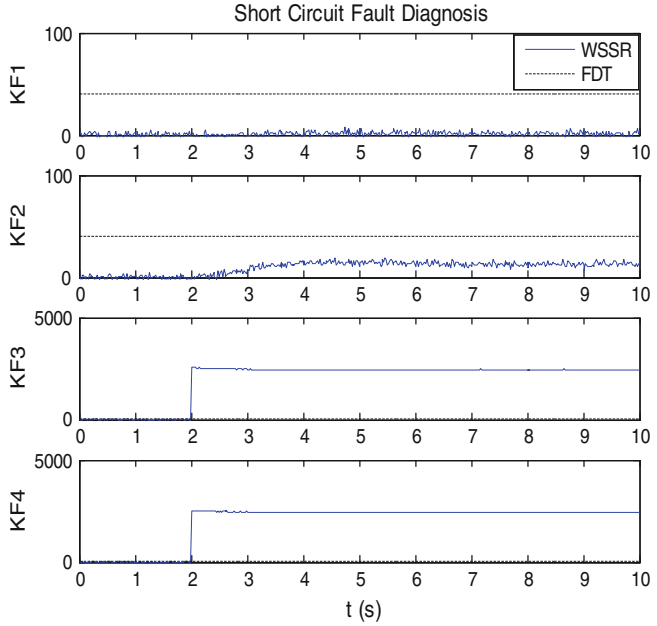

Fig. 45.13 Short circuit fault

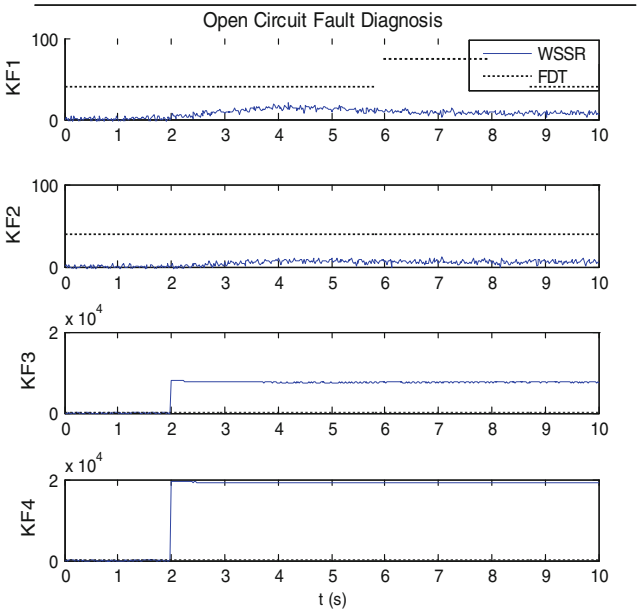

Fig. 45.14 Open circuit fault

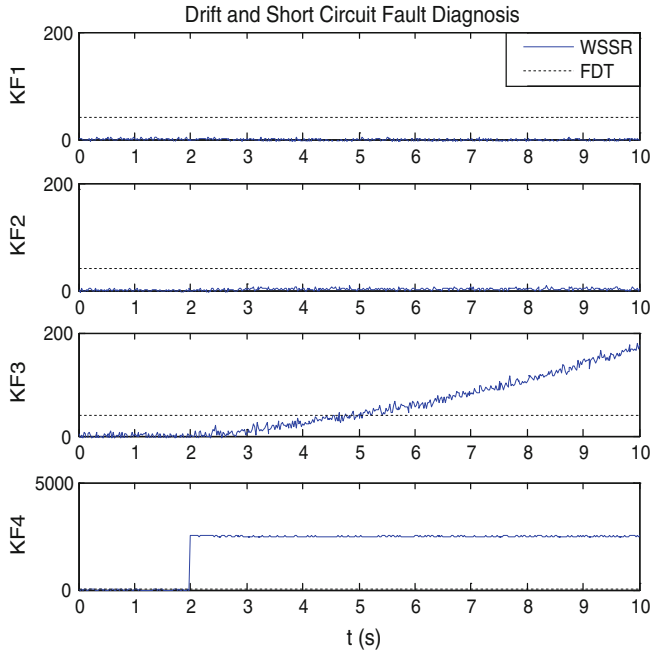

Fig. 45.15 Drift and short circuit fault

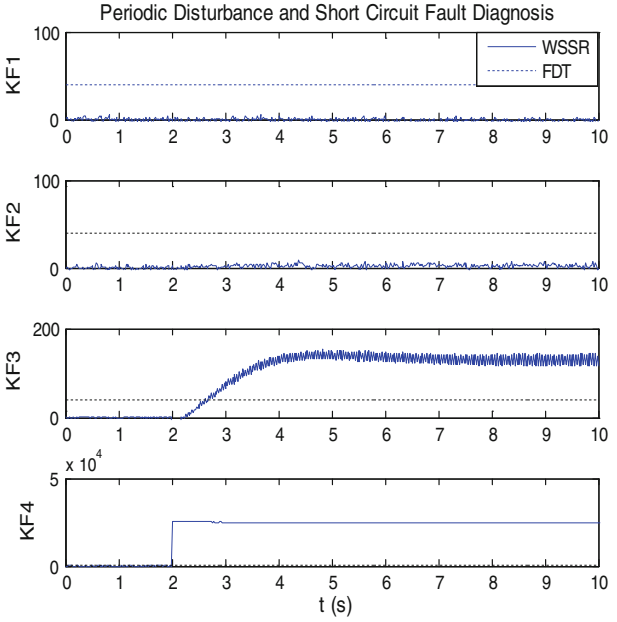

Fig. 45.16 Periodic disturbance and short circuit fault

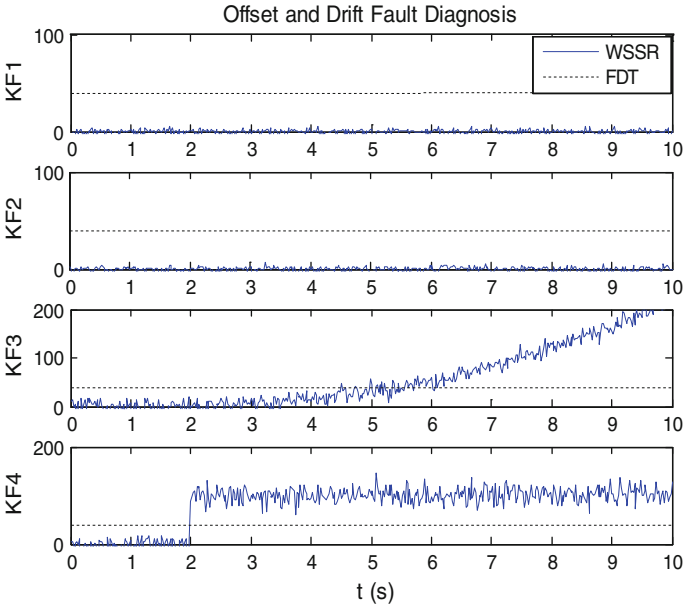

Fig. 45.17 Offset and drift fault

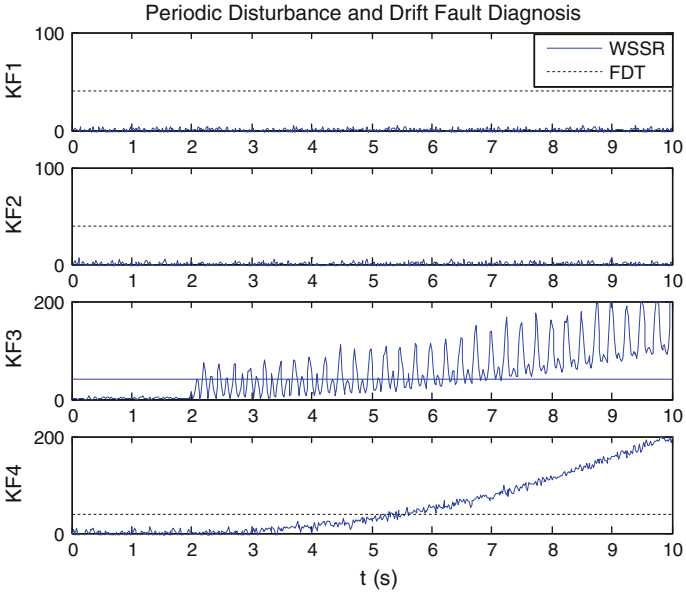

Fig. 45.18 Periodic disturbance and drift fault

Table 45.3 Comparison with different methods

Diagnosis method	Training sample	Testing sample	Classification result						
			Normal	Offset	Pulse	Drift	Periodic disturbance	Open circuit	Short circuit
MK-SVM	60	40	40	40	38	40	38	40	40
PCA-SVM	60	40	40	36	30	36	30	36	40
WPEE-SVM	60	40	40	40	34	32	32	32	40
RBF-NN	60	40	22	40	36	34	36	36	26

45.5.2 Fault Classification Based on Multi-Kernel SVM

This experiment extracts 100 samples from the six typical sensor fault signals shown in Figs. 45.1, 45.2, 45.3, 45.4, 45.5, 45.6, 60 samples data are used to training the SVM model, the others are used to testing. Meanwhile, comprise this method with PCA-SVM, WPEE-SVM and RBF-NN [8] as shown in Table 45.3.

45.6 Conclusion

Based on kalman filter double faults diagnosis method can detect the six kinds of fault modes completely. The algorithm is effective and practical application is easy.

Multi-kernel SVM classification accuracy is 98.57 %; PCA-SVM classification accuracy is 88.57 %; WPEE-SVM classification accuracy is 89.29 %; RBF-NN classification accuracy is 80.71 %. Multi-kernel SVM's classification accuracy is higher than the other method. The result also shows that Pulse and Periodic Disturbance fault occurs misjudge, the reason is that sample node is not match the Pulse node sometimes, otherwise, Periodic Disturbance maybe confuse with the noise when the signal amplitude is small, and the duration is long, so, the misjudge is acceptable.

References

1. Kobayashi, T. (2003). Aircraft Engine Sensor/Actuator/Component Fault Diagnosis Using A Bank of Kalman Filters. NASA/CR-2003-212298,
2. Yi C, (2007) Research on sensors fault diagnostics of aero-engine control system. Nanjing University of Aeronautics and Astronautics
3. Peng Z (2008) Aero engine fault diagnostics based on kalman filter, Nanjing University of Aeronautics and Astronautics
4. Hua Y, Guiping S, Jianbo S (2008) Fault diagnosis for gas turbine engines based on Kalman filter and neural networks. J Aerosp Power 23(6):1111–1119

5. Zhong-hui H, Yun-ze C, Yuan-Gui L et al (2005) Data fusion for fault diagnoses using multi-class support vector machines. J Zhejiang Univ Sci 6A(10):1030–1039
6. Platt JC (1999) Fast training of support vector machines using sequential minimal optimizatio.In: Proc of Advances in Kernel Methods Support Vector Learning MIT Press 1999, Cambridge, 185–208
7. Xin J (2013) SVM-based multi-sensor information fusion technology research in the diesel engine fault diagnosis. In: The 19th International Conference on Industrial Engineering and Engineering Management (IEEE) 978-1-4673-2460-1/12, pp 891–896
8. Hsu CW, Lin CJ (2002) A comparison of methods from unlit-class support vector machines. IEEE Trans Neural Networks 46(13):415–425

Chapter 46
Study of Fault Diagnosis for Helicopter Rotors

Xiaoping Luo, Guoting Cao and Dunming Tan

Abstract In order to find the imbalance fault of helicopter rotors, the theory of fault diagnosis for the rotors is studied. Filtering and HHT method were used to analyze the vibration signals of the rotors. The criteria of the signals for the faults are obtained and the adjustment methods are also given. Finally, demo software of fault diagnosis for a helicopter is developed. The result can be used to develop fault diagnosis system.

Keywords Helicopter · Rotors · Fault diagnosis

46.1 Introduction

The imbalance fault of helicopter rotors is a frequently happened failure in maintenance work, which damages the helicopter structure and spends large amount of costs. In order to predict the fault, it is of great importance to study the diagnosis theory and method of rotors. The criteria of fault signals are obtained by analyzing the imbalance faults and their signal features in this paper. Based on the diagnosis theory and criteria of signals, the diagnosis and adjustment methods are described.

X. Luo (✉) · G. Cao · D. Tan
The First Aeronautical College of the Air Force, 503#, No. 23, Hangkong Road, Xinyang 464000, Henan, China
e-mail: aidong67@163.com

J. Wang (ed.), *Proceedings of the First Symposium on Aviation Maintenance and Management-Volume I*, Lecture Notes in Electrical Engineering 296,
DOI: 10.1007/978-3-642-54236-7_46,

46.2 Fault Diagnosis Theory for Helicopter Rotors

The fault diagnosis mainly consists of three steps: signal measuring, analyzing, and diagnosing. First, signals diversifications produced by the monitored parts of helicopter are measured by sensors. Second, the measured signals are processed by signal analysis technique. Third, conclusion, in addition with necessary maintenance advice is made if there is a fault.

There must be some physical parameters changed with a fault. Only the parameters reliable and sensitive to the fault were selected for diagnosis. Therefore, these parameters were named as fault featured parameters [1].

For the rotating helicopter rotors, the faults is demonstrated mainly by high vibration caused by the imbalance forces of the blades, which include the gravity force, the aerodynamic force, the centripetal force, and the inertia force. These forces were affected by two factors. The first one is the imbalance of centripetal forces caused by unbalanced blade and faults in the parts, which result in the asymmetry distribution of mass. The second one is the imbalance of rotor cone caused by the operating system, the airfoil, and the rotor hub, which also result in the asymmetry of aerodynamic force. Both the two factors lead to higher vibration. So, the fault featured parameters of rotors consists of several aspects discussed above, as shown in Fig. 46.1. The diagnosis can be made by measuring and analyzing the signals of these parameters.

According to the maintenance experiences, reasons for higher vibration are imbalance of centripetal force and different cone angles of the rotor blades. So, the model for rotor vibration can be obtained as Eq. 46.1.

$$F = f(a_k, x(t)) \tag{46.1}$$

where a_k means the rotating cone of the blade, k means the blade number, x (t) means the vibration signal.

By processing the measured rotor blades' tracks and vibration signal, the vibration amplitude and phase, which has relationship with the rotating speed, can be evaluated. The evaluated vibration amplitude and phase are used to diagnose fault. Magnetic or optical sensors are used to measure the rotor rotating speed. Tracking sensors are adopted to monitor the blades tip position (or cone) [2]. Accelerating sensors are used to detect the vibration.

The key factor for the different cone of rotor blades is the different aerodynamic parameters, especially the installation angle which can be fixed by adjusting the pitch rods. The main reason for rotor vibration is the asymmetry distribution of mass from the blades which could be solved by adjusting the balance weights.

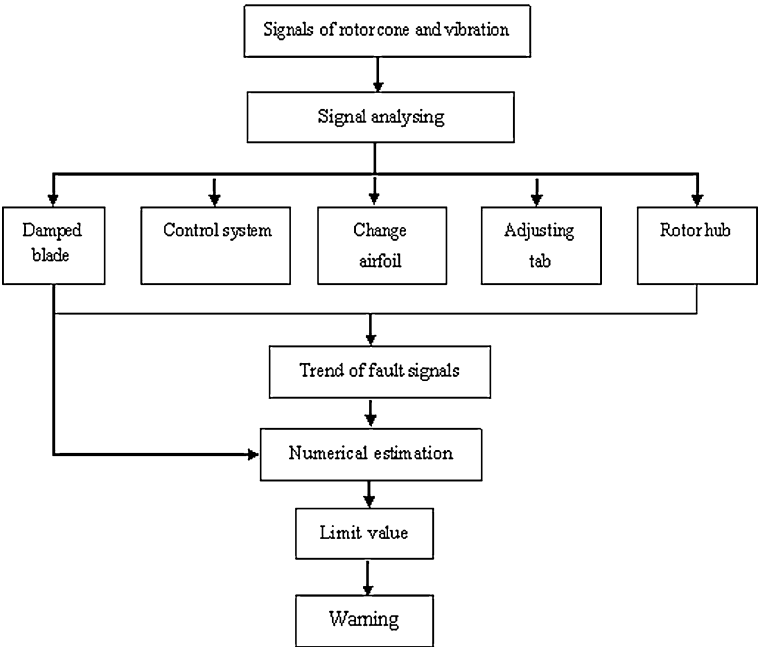

Fig. 46.1 Fault diagnosis theory for rotors

46.3 Signal Analyzing

46.3.1 Basic Methods

The parameters of blade rotating cone and vibration are key signals to diagnose the imbalance fault of rotors. The rotating cone is measured by tracking sensor, which can be used directly. However, the vibration signal is complicate, because it consisted of different components caused by different factors. Which component is generated by the rotor? what is the relationship between the fault and the factor? This need signal processing to give the answer.

The imbalance of rotor blades will lead to a vibration per rotate, the vibration parameter can be represented by the amplitude and phase. And the amplitude and phase can be evaluated by measuring the rotor vibration signals first, followed by separating it with the rotor rotating azimuth angle. The vibration amplitude represents the imbalance level while the vibration phase indicates the imbalance orientation where the mass distribution is asymmetry. Therefore, when the vibration amplitude and phase were evaluated, corresponding means can be taken to adjust the imbalance. In addition, this will minimum the vibration caused by imbalance and avoids related faults and accidents.

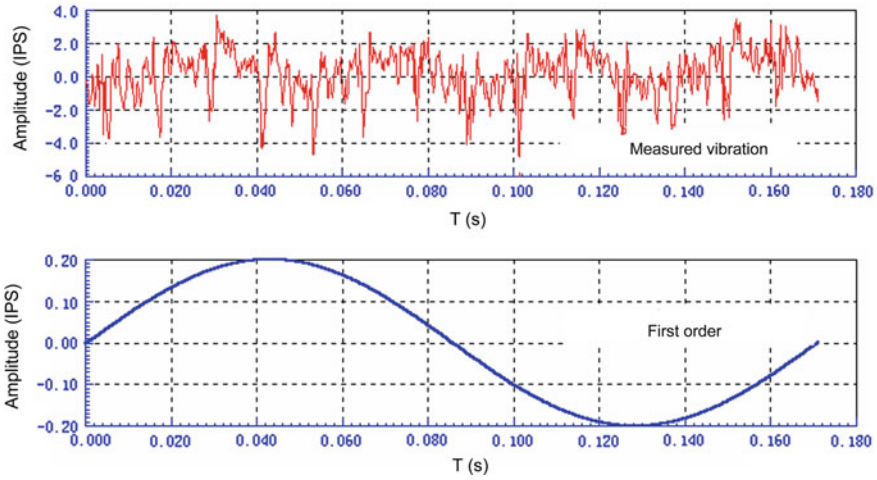

Fig. 46.2 The vibration signal

Because the measured vibration is a composition generated by the rotor, the fuselage and engine, in order to get the rotor dynamic balance data with accuracy, the measured vibration signals need to be filtered to get only the vibration caused by rotors. Through conscientious analyzing and comparison, the synchronic sampling and filtering method makes a satisfactory result.

The sampled vibration signal can be described with equation as [1]: an impulse sequence with periods of T_s multiplied by an analog signal $x(t)$ as shown in Eq. 46.2.

$$x(t) \cdot g(t) = \int_{-\infty}^{\infty} x(t) \cdot \delta(t - nT_s)\mathrm{d}t = x(nT_s) \quad n = 0, \pm 1, \pm 2, \pm 3, \cdots \tag{46.2}$$

In the equation, $g(t) = \sum_{n=-\infty}^{\infty} \delta(t - nT_s)$ is the sample functions.

There are many methods for analyzing and processing the vibration signal. These methods can be used directly. The effective vibration signals are the first several orders. Consequently, with the rotor rotating speed known, the vibration amplitudes and phases of rotors for each frequency can be got by filtering and analyzing in time domain.

For example, the upper part in Fig. 46.2 shows an original measured vibration signal, the lower part is the first order vibration signal recovered by low-pass filtering. Thus by analyzing the amplitude and phase of the signal, the imbalance blade can be determined.

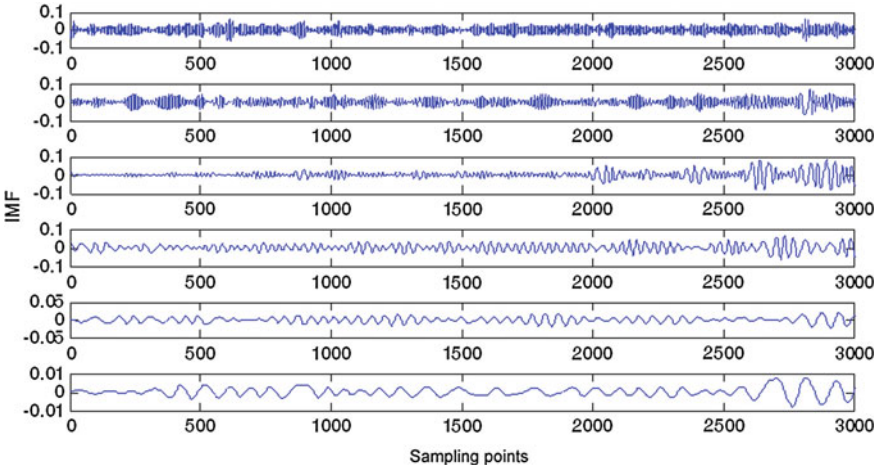

Fig. 46.3 The demodulated vibration signals from experiment data of rotor cone imbalance

46.3.2 HHT Analyzing Method

Experience Modal Demodulation (EMD) based Hilbert Transform (HHT) [3] was used to analyze the vibration, which is nonlinear and unstable caused by the imbalance rotor fault as well as the sample noise. The classical methods is unable to process such nonlinear and unstable signals, for example the Fast Fourier Transform (FFT) require the processing signal is steady, the wavelet transform indeed is an sample window adjustable FFT and have difficulty with the selection of wavelet basis and self-adjusting. The HHT is a self-adjusting time and frequency domain analyzing method, which can take the local feature of signals into consideration, and then makes modal decomposition accordingly. Therefore, the HHT analyzing method overcomes the drawbacks of classical methods.

Rotor fault experiments were made to verify the HHT methods, and the data from the experiments were analyzed. The experiment rotor has four blades, the vibration signals were sampled under normal, abnormal blade attack angle, abnormal adjusting tab, and asymmetry mass distribution conditions, while the rotor rotating speed was 360 rpm (6 Hz).

A sample demodulated vibration signals is shown in Fig. 46.3 while the fault was set as rotor cone imbalance (The blades attack angles are different).

During the fault diagnosis procedure, the HHT boundary spectrum can effectively reflect the different feature under different fault conditions. Thus, the frequency multiplication from the boundary spectrum was selected as the fault feature. Figure 46.4 shows the HHT spectrum and the boundary spectrum when the imbalance fault of rotor cone was caused by adjustment tab.

As shown in Fig. 46.4, the helicopter fuselage generates one, two, three, and five times of frequency multiplication in vertical side. From the frequency

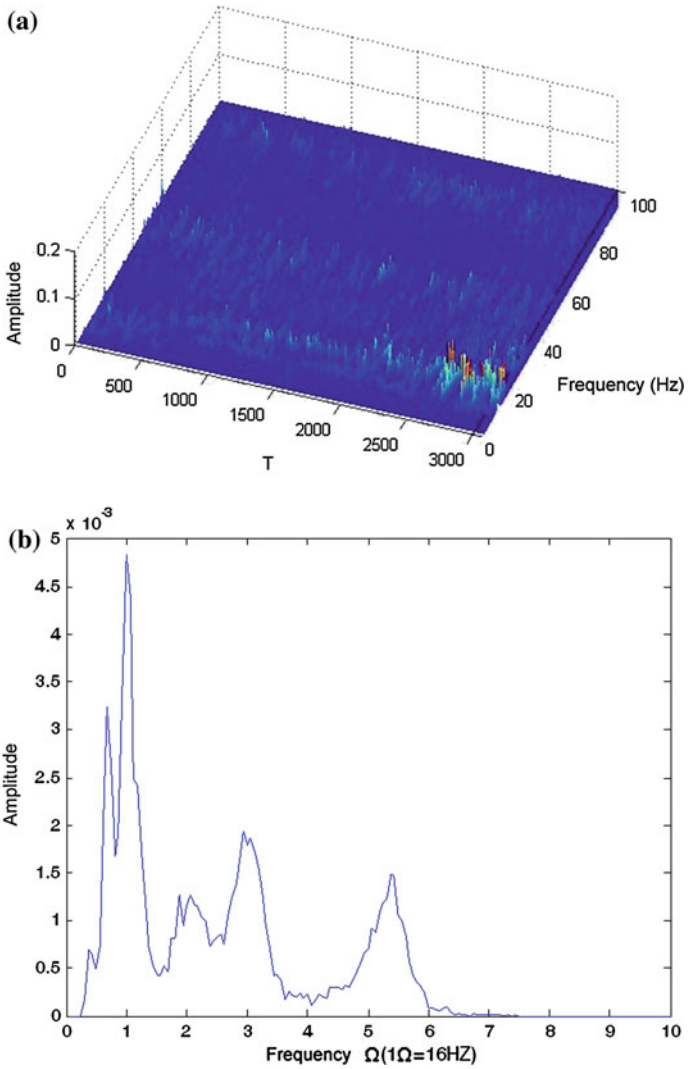

Fig. 46.4 The HHT spectrum and the boundary spectrum for imbalance rotor cone. **a** Hilbert spectrum. **b** Hilbert boundary spectrum

multiplication, the first module is the main element which creates the major vibration. The same result can be obtained under dynamic imbalance fault.

From the results, it can be concluded that HHT analyzing method can extract different fault feature to diagnosis different faults and can correctly reflect the change of signal features under different flight condition. These fault features are used for fault monitoring and diagnosing. The methods were validated by real measured flight data of a helicopter.

46.4 Diagnosis and Adjustment Algorithms

The signal from the rotor cone is applied to diagnose the rotor work state, and then adjust the rotor blades according to the maintenance regulations. The vibration signal not only can be used to diagnose faults, but also to make the rotor imbalance adjusting solution.

46.4.1 Diagnosis Algorithm

The amplitude of vibration and the value of rotor blades cones indicate the working state of rotor, when they exceed the threshold values, it can come to the conclusion that faults occur. Under general cases, the values fall into normal, warning, and fault states. According to the maintenance advice of the experiment helicopter, the corresponding thresholds of rotor cone and dynamic imbalance are shown below:

Rotor cone	
Difference of cone $\leq$ 6 mm	Normal
6 mm $\leq$ Difference of cone $\leq$ 12 mm	Warning: Need adjustment
Difference of cone $\geq$ 12 mm	Fault: Need replacement
Rotor dynamic imbalance	
Vibration amplitude $\leq$ 0.2 IPS	Normal
0.2 IPS $\leq$ Vibration amplitude $\leq$ 0.3 IPS	Warning: Need adjustment
Vibration amplitude $\geq$ 0.3 IPS	Fault: Need replacement

46.4.2 Adjustment Algorithm

When the exception of faults occurs, necessary approaches are needed to examine the rotor, if faults are not caused by external damage or install errors, some adjustment methods can be used to eliminate the fault. In maintenance, the less differences of blades' cone or the vibration amplitude the better.

The rotor cone adjustment method already exists. First, measure the cone of each blade from the rotor. Second, determine the blade to adjust according to the diagnosis algorithm. Third, calculate the modification based on optimization principle and sensitive coefficient.

If taking the dynamic imbalance into consideration, the amplitude and phrase of vibration need to be obtained, especially the vibration component from the vertical direction. The vibration phrase could be calculated by the vibration signal and the synchronic rotating speed. The dynamic imbalance adjustment can be

accomplished through modifying the balance weight. Considering different flight conditions and adjustment of each blade, the optimal adjustment parameters evaluation algorithm model is shown below:

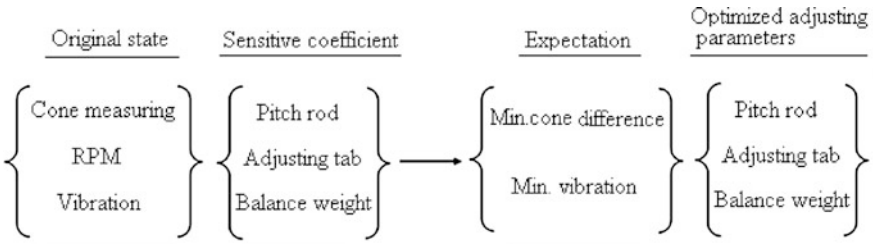

Where, the pitch rod, the adjustment tab and the balance weight are three adjustable parameters.

The experiments show that by the diagnosis and adjustment algorithms, the vibration amplitude can be effectively decreased through modifying the balance weight at the limb of rotor hub in the maximum vibration orientation, which supports the validity of adjustment algorithms.

Rotor cone adjustment. When calculating the rotor cone adjustment, the relationship between the position of blade tip and the adjustment of pitch rod or the adjusting tab already has been given in the maintenance book and should be followed directly. The specification is if the rotor cone error was between 6 and 12 mm, increasing or decreasing the pitch rod will lead to the rotor blades move upwards or downwards. Suppose the nut of the sextuple prism pitch rod turns one prism, it would make the rotor track move 4 mm, so the sensitive coefficient is 4 mm/prism. For example, to adjust a blade with track difference 8 mm compared with standard blades, the modification is $8/4 = 2$ prisms rotation for the pitch rod to shorten its length, so as to minimum the rotor cone error to zero.

By adjusting the pitch rod, the rotor can get satisfactory cone error. Only under conditions the rotor track error varies between -6 and +6 mm, after the helicopter engine started and before it reaches rated power capacity to flight, the 6th adjusting tab need to be modified. Turn the adjusting tab upwards or downwards according to the rotor cone error. The blade track changes 12 mm if the adjusting tab was varied one degree, namely the sensitive coefficient is 12 mm/degree.

Dynamic balance adjustment. The algorithm in Ref. [4] is used to calculate the balance weight. So if the amplitude and phrase of vibration are determined, the balancing weight can be applied to the right position.

The rotor vibration amplitude A_0 and phase can be evaluated by analyzing and processing the vibration signal. The phase can be used to determine which blade weight needs to be adjusted, and the mass modification Δm of balance weight is calculated by Eq. 46.3.

$$\Delta m = A_0 \frac{Mg}{r\omega^2 S} \tag{46.3}$$

where M is the rotor mass, g is the gravity accelerator, r is the balance weight radius, ω is the rotor speed and S is the sensitive coefficient which was defined by experiment.

46.5 Conclusion

In order to solve the problem that classical signal analyzing methods cannot deal with unstable signals of rotor imbalance fault, this paper focused on the HHT analyzing method, which is self-adjusted in time and frequency domain. The HHT boundary spectrum can effectively reflect the different feature under different fault conditions. Therefore, the HHT methods provide a convenient way to diagnose different faults. The dynamic imbalance adjustment algorithm for rotors was provided, which offers theoretical support for rotor imbalance adjustment. An imbalance fault diagnosis demo software for a helicopter is developed based on the study.

References

1. He Z (2010) Theory and application of mechanical diagnosis (in Chinese). High Education Press, Beijing
2. Li X et al (2007) Rotor cone measurement by universal tracking device (in Chinese). Helicopter Tech 1:50–54
3. Zhao H (2007) Fault feature research of unstable signals based on HHT (in Chinese). Daqing Petrol College, Daqing
4. Yang G (2012) Practical techniques for diagnosis of rotating mechanics (in Chinese). Sino Petro Press, Beijing

Chapter 47
Maintainability Assessment of a Complex System Based on Field Data

Huiru Dong, Jiantai Zhu, Kai Zhu and Yan Shi

Abstract Maintainability assessments which are independent of the system developers can provide an impartial evaluation of a system's maintainability performance. This paper outlined one kind evaluation method to assess maintainability of a certain complex system based on field data. The field data of repair time of the system were collected, then the repair-time distribution of the system was identified by graphic estimation method, and the mean time to repair (MTTR) and the maximum repair time $t_{0.90}$ were assessed as well, and finally the results were compared with the system's specification. It is found that apart from some inaccurate data, the repair time of this complex system follows the lognormal probability distribution. A MTTR of 1.45 h and a maximum repair time of 3.44 h were observed. The maintainability requirement of the system is not being satisfactorily met.

Keywords Maintainability · Maintainability assessment · The mean time to repair · The maximum repair time · Graphic estimation method · Lognormal probability distribution

47.1 Introduction

Maintainability is a system's ability to be repaired or restored to a specified condition under stated conditions. Maintainability assessment (MA) of a system is to determine its maintainability performance in fleet operation. One of the goals of MA is to validate whether the maintainability of a system satisfies consumer's requirement.

H. Dong (✉) · J. Zhu · K. Zhu
Beijing Aeronautic Technology Research Center, Section 2, No. 6 of Jing Bei Road East, Fengtai District, Beijing, China
e-mail: huirudong@263.net

Y. Shi
Academy of Armored Forces Engineering, 21# Dujiadan, Fengtai District, Beijing, China

J. Wang (ed.), *Proceedings of the First Symposium on Aviation Maintenance and Management-Volume I*, Lecture Notes in Electrical Engineering 296,
DOI: 10.1007/978-3-642-54236-7_47,

Assessment independent of the system developers provides an impartial evaluation of a product. Because of differences between the test environment and operational environment, the results measured in the test environment would not be an accurate assessment of the operational suitability. So it is very necessary for decision making to conduct a data-based assessment under authentic operational conditions.

The mean time to repair (MTTR), which measures the average on-equipment or off-equipment corrective maintenance time in an operational environment and the maximum repair time, t_p, in which a certain percentage p of the failures must be repaired, are mainly metrics of maintainability [1]. They can be used to measure a system's ability to be repaired or restored to a specified condition under stated conditions. This paper outlines the step-by-step process and offers evaluation criteria that can be used to conduct formal assessments of a system. By this approach, failure data and repair time of a complex system in an aircraft under realistic operational conditions were collected, the repair-time distribution of the system were identified by means of graphic estimation method, and the MTTR and the $t_{0.90}$ of this system were assessed as well. In the end, the conclusion whether the maintainability requirements of the system be met or not was achieved, and further discussions have been made.

47.2 Methodology

47.2.1 Assessment Progress

The general MA steps is shown in Fig. 47.1. The steps provide a methodical way to execute the assessment process. First, according to the assessment objects, choose necessary data from fleet or database and analyze their validity. Second, identify data distribution characteristics by graphic or theoretical method, and estimate distribution parameters. Third, evaluate maintainability metrics such as MTTR or the maximum repair time, $t_{0.9}$. Finally, compare the evaluation results with the maintainability specifications, and the conclusion can be obtained.

The assessment method 9 in [2] is especially suitable for use in the condition that sample amount is large than 30 and the repair-time distribution is unknown. So it is used to evaluate the MTTR and t_p in this paper.

47.2.2 Assessment Formula

MTTR and t_p are calculated by the following formula (by the hypothesis that repair time is lognormal distribution).

$$\mathrm{MTTR} = \frac{\sum_{i=1}^{n} X_{\mathrm{cti}}}{n} \tag{47.1}$$

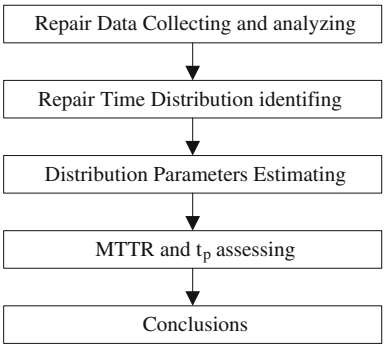

Fig. 47.1 MA process

$$\hat{d}_{ct}^2 = \frac{1}{n-1}\sum_{i=1}^{n}(X_{\text{cti}} - MTTR)^2 \tag{47.2}$$

$$t_p = \exp\left[\frac{\sum_{i=1}^{n}\ln X_{\text{cti}}}{n} + \psi\sqrt{\frac{\sum_{i=1}^{n}(\ln X_{\text{cti}})^2 - \left(\sum_{i=1}^{n}\ln X_{\text{cti}}\right)^2/n}{n-1}}\right] \tag{47.3}$$

where

X_{ct} repair time
$\hat{d}_{ct}^2$ the sample variance
$\hat{d}_{ct}$ the sample standard deviation
β the consumer's risk
z_p z critic value corresponding to a certain percentage p
n sample size

$$\psi = Z_p - Z_\beta\sqrt{\frac{1}{n} + \frac{Z_p^2}{2(n-1)}}. \tag{47.4}$$

47.2.3 Assessment Criteria

For MTTR, there is

$$\text{MTTR} \le \bar{M}_{ct} - Z_{1-\beta}\frac{\hat{d}_{ct}}{\sqrt{n}}. \tag{47.5}$$

For t_p, there is

$$t_p \leq M_{\text{maxct}} \tag{47.6}$$

where
$\bar{M}_{ct}$ the critical value of MTTR
$M_{\text{max}ct}$ the critical value of $t_{\text{max}ct}$

47.3 Process

47.3.1 Data Collection

The primary data utilized in MA in this paper is mainly repair time.

Selected samples of the system population came from a whole fleet. The repair times from maintenance actions performed during a period of time were collected, and the total number n of repair time sample was 91.

47.3.2 Lognormal Probability Paper

Graphic estimation method was used here. The Lognormal probability paper was used to test the null hypothesis that the time to repair follows the lognormal probability distribution. Its advantage was easy to understand and simple for field use.

Lognormal probability paper is based on the relationship of the lognormal distribution to the normal distribution. The X-axis represents logarithm of the time to repair and Y-axis represents the normal value of X. Since

$$F(t) = \Phi\left(\frac{\ln t - \mu}{\sigma}\right) = \Phi(z) \tag{47.7}$$

Then

$$z = \Phi^{-1}[F(t)] = \frac{\ln t}{\sigma} - \frac{\mu}{\sigma} \tag{47.8}$$

So the points (lnt_i, z_i) are on a line.

47.3.3 Distribution Determination

First, the repair times were grouped into classes. Determining the proper number of classes is important. Too many classes result in insufficient summarization of the data, however, too few classes will lose too much information. A good rule for the number of classes is given by Sturges' rule,

$$k = \lfloor 1 + 3.3 \lg_{10} n \rfloor \tag{47.9}$$

where
k number of classes
$\lfloor x \rfloor$ integer part of x

Here n = 91, so group the repair times into 7 classes and arranged the sample data from small to big,

$$t_1 < t_2 < \ldots < t_i < \ldots < t_7 \tag{47.10}$$

Calculate cumulative probability F (t_i),

$$F(t_i) = \frac{n_i}{n} \tag{47.11}$$

where n_i is the accumulating repair sample number corresponding to i.

The point p_i (lnt_i, z (t_i)) was drawn on the lognormal probability distribution paper, as shown in Fig. 47.2. It could be seen from Fig. 47.2 that the points arranged almost on a line excepting for the point (4, 100 %), so it really follow the lognormal probability distribution.

47.3.4 Maintainability Metrics Assessment

According to (47.1), MTTR was estimated as follows

$$\text{MTTR} = \frac{\sum_{i=1}^{n'} X_{\text{cti}}}{n'} = 1.45\text{h} \tag{47.12}$$

where n′ was the number that n minus the bad data number.

When the confidence interval was p = 0.9, β = 0.1, then $Z_p = Z_{0.9} = 1.28$, $Z_\beta = Z_{0.1} = -1.28$, formula (47.4) became as follows

$$\psi = Z_{0.9} - Z_{0.1}\sqrt{\frac{1}{n'} + \frac{Z_{0.9}^2}{2 \times (n' - 1)}} = 1.477 \tag{47.13}$$

According to formula (47.3), the max time to repair $t_{0.90}$ was

$$t_{0.90} = \exp\left[\frac{\sum_{i=1}^{n'} \ln X_{\text{cti}}}{n'} + 1.477 \times \sqrt{\frac{\sum_{i=1}^{n'} (\ln X_{\text{cti}})^2 - (\sum_{i=1}^{n'} \ln X_{\text{cti}})^2 / n'}{n' - 1}}\right] \tag{47.14}$$

$$= 3.44h$$

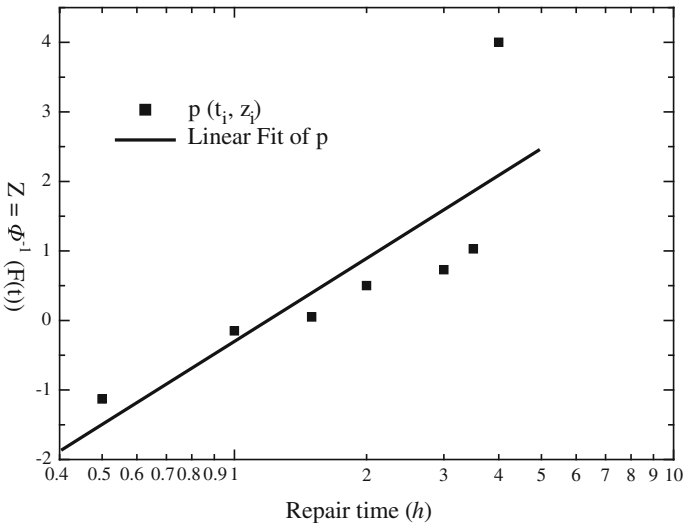

Fig. 47.2 A lognormal line-fitting plot of repair data

47.3.5 Assessment Results

$$\because \qquad \mathrm{MTTR} > \bar{M}_{ct} - Z_{1-\beta}\frac{\hat{d}_{ct}}{\sqrt{n}}$$

$$t_{0.9} > M_{\mathrm{maxct}}$$

The maintainability requirement of this system is not being met.

47.4 Discussions

Good data are needed for making right decisions. If the data gathered cannot provide the information needed for decisions, it might have some problems. The reason that the data problems exist with field data may be as follows: it takes much time and money to capture, store, and transmit data, and data seem insignificant compared to the equipment, personnel, or materiel, so its importance may be ignored. On the other hand, when maintenance works have been finished, people may not record these repair time, so these data are missing. People have to recognize them by memory or sense when evaluating maintainability. Consequently, the data are inevitably inaccurate. There is a great deal of work need to be done to improve the accuracy of current maintenance data.

47.5 Conclusions

Maintainability assessments of a complex system in an aircraft were accomplished by means of the realistic operational data. Some results are obtained as follows: (1) the field data may have some problems, for example, they are incorrect or invalid, so these inaccurate data must be eliminated when analyzing or making decisions; (2) the repair time of this complex system follows the lognormal probability distribution; (3) a MTTR of 1.45 h and a maximum repair time of 3.44 h were measured. The maintainability requirement of the system is not being satisfactorily met. Some actions are needed to be taken to improve the system maintainability so as to meet the requirement.

References

1. Ebeling CE (2008) An introduction to reliability and maintainability engineering. Qinghai University Press, CN (in Chinese)
2. GJB 2072-1994 (1995) Maintainability test and evaluation (in Chinese)

Chapter 48
The Research of the Fault Diagnosis Method Based on Logic Equations on Central Maintenance System

Jia-qi Guo, Dong Song and Dong-ying Chen

Abstract As the aviation maintenance equipments and technology developing, commercial aircrafts apply central maintenance system (CMS) to improve traditional aircraft maintenance mode. In this paper, the functions, structures, and fault diagnosis methods are discussed. The CMS helps to improve the safety of aircraft and the maintenance efficiency. The fault diagnosis method based on logic equations is developed to meet the needs of CMS. The example is correct and effective.

Keywords CMS · Maintenance · Diagnosis · Logic equations

48.1 Introduction

In recent years, with the rapid development and fierce competition of civil aviation market, the security of civil aircrafts attracts more and more people's attention, as well as increasing operating costs of the relatively long process of civil aircraft maintenance service. Manufacturers and airlines all study how to improve the safety of the aircraft, reduce maintenance time, and extend aircraft maintenance interval.

Central Maintenance System (CMS) combines traditional failure monitoring and fault detection, aircraft condition monitoring system of built-in test equipment. CMS completes fault/status information collection, testing, analysis, diagnosis, reporting through receiving BITE information of aircraft subsystems (such as navigation, communications, air data, engine, hydraulic, fuel, environmental control, etc.), and related aircraft state parameters [1, 2]. The aircraft fault/status

J. Guo (✉) · D. Song · D. Chen
School of Aeronautics, Northwestern Polytechnical University, Xi'an 710072, China
e-mail: guojiaqi1021@163.com

J. Wang (ed.), *Proceedings of the First Symposium on Aviation Maintenance and Management-Volume I*, Lecture Notes in Electrical Engineering 296,
DOI: 10.1007/978-3-642-54236-7_48,

information recorded by CMS is available through the data link, data cards spreading under the ground, and the subsystem completes further fault diagnosis and localization, if necessary, the message can also be uploaded to the aircraft to guide the pilot for proper emergency response. After the flight, the fault information during operation can be downloaded to the ground through a portable maintenance terminal (PMAT). It can be used for field maintenance and analysis.

The internal structure of the aircraft system is complicated. In order to ensure the safety of the aircraft and obtain the situation of the member systems timely, the method of fault diagnosis must be able to identify the fault source from a large number of symptoms in a real-time and accurate way. Knowledge-based fault diagnosis method relying on the past massive experience and confirmed cases make judgments quickly and provides scientific advice. The fault isolation procedure is simplified and the troubleshooting time is reduced. Besides, the real-time aircraft operation situation is provided. Meanwhile, the troubleshooting manual, maintenance biographical information, the knowledge of the properties of the test object are combined with expert experience by the knowledge-based fault diagnosis method. The troubleshooting program is optimized through the AI technology to guarantee the accuracy of fault diagnosis. The knowledge-based fault diagnosis method is commonly applied to present civil aircrafts, including the fault diagnosis method based on logic equations and the model-based method. And the fault diagnosis method based on logic equations are researched in the paper.

48.2 Fault Diagnosis Method Based on Logic Equations

Logic equations are defined by the ranges of only “0” and “1” only when the two values or values between the values of two variables and “and”, “or”, “not” operation composed of three basic equations.

The fault diagnosis method based on logic equations creates a logical structure according to the system equations model, and then inject fault information into the system, through the matching equations locate the fault. The fault logic equations should show the corresponding relationship of failure mode between the corresponding failure reason. After getting the fault symptom, the related fault cause is identified by using the Boolean equations. The fault and its operation parameters are combined by the fault logic equation and the final code maintenance information is acquired [3].

The procedure of the fault diagnosis method based on logic equations are as follows: fault input and output, set logic equations, matching, output result, trouble shooting, as is shown in Fig. 48.1.

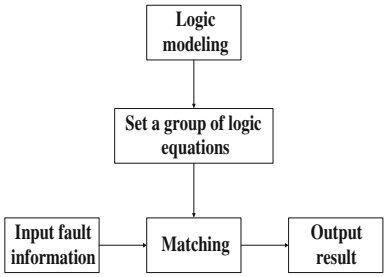

Fig. 48.1 The procedure of the fault diagnosis method based on logic equations

48.3 Fault Diagnosis of Central Maintenance System

48.3.1 Central Maintenance System Components

As is seen from the structure of the maintenance system, the central maintenance computer (CMC) is the core part of the CMS. The CMC connects various member systems, the interface devices, and the display devices of the central maintenance. All of these combine the functions of the CMS as a whole.

The CMC is the core part of the CMS. CMC can collect, process, and store fault data of each member system of the aircraft. CMC also can generate maintenance reports and activate the testing of relevant systems. As shown in Fig. 48.2, it shows the basic block diagram of CMS in ARINC624 references.

48.3.2 Fault Processing Types of Central Maintenance Computer

The troubleshooting of CMC is mainly divided into two categories. One is cascading effect, which means that the failure of chain reaction. Another is multiple failures without clear fault sources [4, 5].

In one leg, at one time, some faults should be found in the first-class equipments of the equipment chain, and only be reported once. It means that there is a report about fault caused by cascading effect if fault is reported several times. The source failure of the equipment chain leads to the downstream failure of the equipment. The source failure received by CMC may be an internal malfunction, interface failure or external fault, but downstream failure can only be external fault. CMC deals with these faults message through a specific method and eventually locates to the source equipment. Meanwhile, CMC inhibits downstream faults, which means that the fault reports of downstream equipments are considered to be false. Figure 48.3 shows the schematic diagram of the cascading effect of failure. The fault report A is sent out when the component A is failed, and the fault of component A will cause component B and C of the equipment chain to send out fault

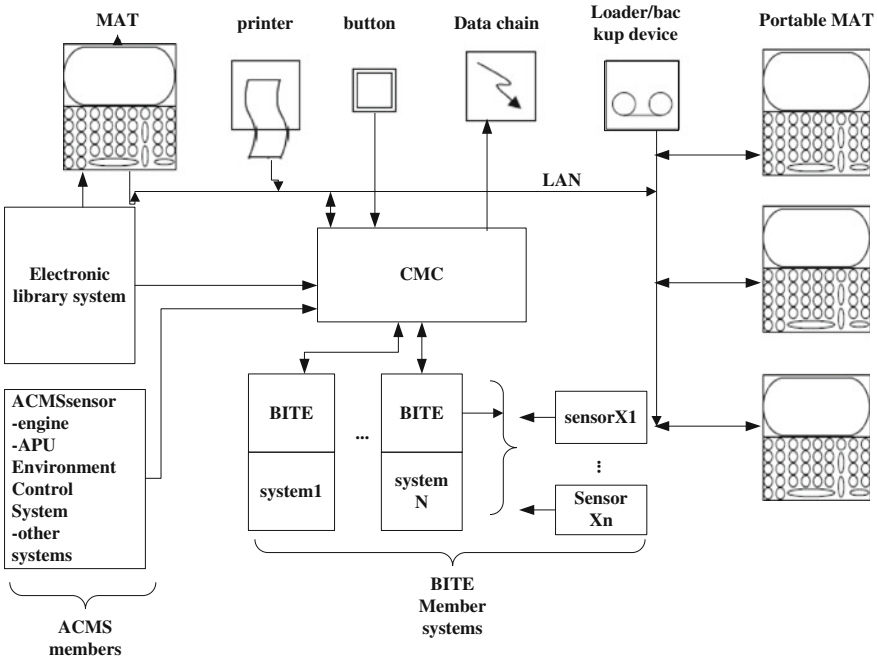

Fig. 48.2 Central maintenance system

reporting. CMC considers that component A is the source equipment from the fault reporting and the others are downstream equipments. Fault reporting generated by components B and D will be suppressed, thereby a false failure or the same fault reported many times are avoided.

Another type of the fault is that the CMC fault reporting can not directly identify the source. The so-called fuzzy source is due to the complex cross-linking of systems, and there is one way to clear the source equipment of the fault. Further analysis of the system is required to distinguish the source equipment of the fault. It is one of the major faults that CMC handles. As is shown, component A, component B and component D are connected. Component D produces failure report D. The component B and the component C are connected with the component E. Component E produces failure report E. Because component D and E are not the source of faults, therefore it does not trigger the maintenance information D and E. According to the relevant rules, CMC gives the final conclusion that the maintenance information number is B, as is shown in Fig. 48.3.

It can be seen that the fault diagnosis process of the CMC (or troubleshooting) is taking advantage of the certain rules to eliminate false fault reporting, and output the real maintenance information and fault information. Moreover, the false failure reports mainly indicate the failure reports of LRU caused by the cascading effect or complex cross-linking of systems. False failure reports which mainly are due to contagion or system leaving the noncross linked faulty component (LRU)

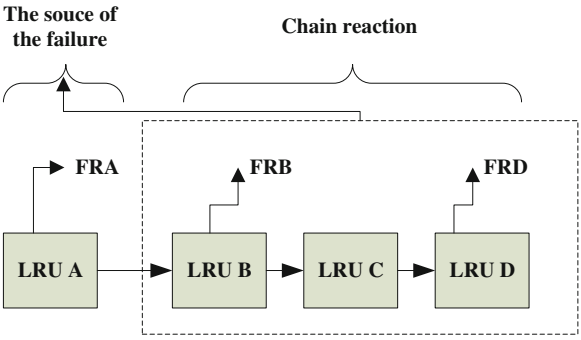

Fig. 48.3 Effects of cascading failures

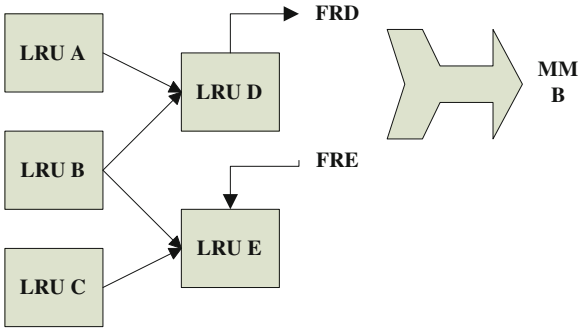

Fig. 48.4 Effects of multiple faults

generated fault reporting. Thus, in analyzing the entire fault diagnosis process, the focus is on how to remove the cascading effect and predict multiple faults, as is shown in Fig. 48.4.

48.4 Matching Logic Equations

48.4.1 Establishing Knowledge-Based Logic Equations

After preprocessing, every fault message received by the CMC is encoded with a code. The code is a variable of fault logic equations. Fault logic equations combine the fault with its operation parameters, and the final code of maintenance message (MM) is generated. There are logic symbols such as “o” (And), “+” (Or) and “NOT” in the logic equations. For example, “2TD” means that the delay starts when all the logic states of the functions are true. If not, the time delay will not work. The unit of time delay is the second.

Table 48.1 Logical equation

Logical equation	Maintenance code
(Y1 + Y2)o Y3 o Y4 o 2TD	X1
……	……

Table 48.2 The knowledge base of logic equation

No.	Status	Fault information 1	Status	Fault information 2	Status	Fault information 3	……	Delay time	Conclusion
1	1	Y1	1	Y3	1	Y4		2	X1
2	1	Y2	1	Y3	1	Y4		2	X1
……									

Logic equations are stored in data sheets of SQL, while the formation stored in Tables 48.1, 48.4 can only be recognized as a data base other than a knowledge base. Therefore, the formation should be developed.

When one failure occurs, its value is 1 in fault logic equation. In Table 48.1, if the three failures of Y1Y3Y4 or Y2Y3Y4 in the equation of (Y1 + Y2) o Y3 o Y4 o 2TD occur at the same time, and the requirement of time delay of 2 s is met, X1 is judged as fault. All the "Or" expressions in the logic equations can be transformed and then the equations are only described with "And" and "NOT" expressions. At the same time, the BIT information code Y has different status about appearance or not. In the knowledge base, "1" indicates that BIT information code appears, "0" indicates that BIT information code does not appear. The knowledge base is shown in as Table 48.2.

The series of codes of fault messages in the knowledge base are reordered to facilitate the matching of the equations. First they can be arranged by row. First, according to the types of fault messages, the codes of BIT are placed in front of those of maintenance code. Then the codes of BIT are sequenced by the status information, and those with the state of "1" are put on the front. Second, the BIT codes with "1" state are arranged from small to large. At last, the knowledge base is arranged by the row of the fault information 1 from small to large.

48.4.2 Matching Algorithm of Logic Equations

Group searching. The BIT codes in the knowledge base, e.g., 08235000100, share the formation composed of a 3-bit port number, a 3-bit label and a content code. The whole knowledge base has 108 port numbers, which separates all the logic

Table 48.3 Logic equation table

Number	States	Fault information 1	States	Fault information 2	States	……	Conclusion
……							
4609	1	08235104000	1	09035104000			71203

Table 48.4 Maintenance information table

Maintenance information code	ATA	Message content	Flight phase	FDE	Flight leg	Sustained/ intermittent
71203	73-00	ENG-1 bleed 2.5 torque motor wiring/actuator fail	ER	73010500	00	H

Table 48.5 The fault information table

Fault code	Level	Information content	Maintenance information	Flight phase
73010500	Advisory	ENG-1 low idle	71203/71259	ER

equations into 108 groups. To find the right group before matching the details is a good way of improving efficiency of accessing data.

Row matching. In use of group searching, the row of the fault information 1 with the same BIT code received is located in the knowledge base. The method of bisection is applied to match the logic equation to identify if the equation is true (Table 48.3).

Examples

Fault message

X = 08235110000

According to the fault diagnosis method based on logic equations in this paper, the final output (Tables 48.4 and 48.5).

48.5 Conclusion

In the paper, in-depth research on the core technology of the CMS is carried out. Focused on the fault diagnosis theory and methods based on logic equations, two fault types and the fault handling process of CMS are given. The matching method of fault logic equations are given and verified by an example of this method is correct. Moreover, on the basis of the existing achievements, there are many developments worthy to further study.

References

1. Wei W, Zhang B (2007) Evolution of aircraft maintenance systems (in Chinese). Int Aviat 3:42–45
2. Zhang B, Zeng T (2000) Intelligent BIT technologies (in Chinese). Meas Control Technol 11:1–4
3. Zhao R (2007) Preliminary research on CMS Based on modular integrated processing platform (in Chinese). Avionics Technol 38(1):20–25
4. Hess R, Due A, Kogut D (2001) The IMD HUMS as a tool for rotorcraft health management and diagnostics. In: IEEE aerospace conference proceedings, 2001
5. Ferrell BL (2000) Air vehicle prognostics and health management. In: IEEE aerospace conference proceedings, 2000

Chapter 49
Fault Diagnosis for Aero-engine Multi-redundant Smart Sensors Based on Data Fusion

Xusheng Zhai, Shimei Yang, Gang Li and Jianming Jia

Abstract In order to diagnosis the aero-engine multi-redundant smart sensors, a method based on data fusion was proposed. In this method, an improved fuzzy C-means clustering algorithm was used to get a fusion value based on multisensing units' information, and then the residuals between the fusion value and measured values of the sensing units could be calculated. After that, the residuals could be used to monitor the health conditions of the sensors. The simulation results showed that the fusion value has a high accuracy, and the absolute error is less than 0.5 °C, and also online sensing units fault location could be completed in the form of fault vector.

Keywords Distributed control system · Redundancy technology · Data fusion · Engine

49.1 Introduction

In the aero-engine control system, a large number of sensors act as the system's "eyes and ears", because these sensors are distributed in the harsh environment with high temperature and strong vibration, they would inevitably go wrong. According to statistics, the sensors and actors failure accounted for more than 80 % of total failure in the engine control system [1]. To improve the reliability and capability of fault diagnosis and isolation, the sensor itself is becoming smarter and having more redundant degrees, and the multi-redundant smart sensors are extensively used in the aero-engine distributed control system [2–4]. Based on the traditional multi-redundant sensors, the multi-redundant smart sensors are implanted

X. Zhai (✉) · S. Yang · G. Li · J. Jia
The First Aeronautical College of Air Force, Hangkong Road 23#, Xinyang, China
e-mail: zhai120120@163.com

J. Wang (ed.), *Proceedings of the First Symposium on Aviation Maintenance and Management-Volume I*, Lecture Notes in Electrical Engineering 296,
DOI: 10.1007/978-3-642-54236-7_49,

microprocessor, data bus interface, and power bus interface [5, 6]. In addition to the traditional functions as sending and receiving data, the multi-redundant smart sensors can also perform data processing, redundancy management, fault diagnosis, fault isolation, and fault tolerance. In this paper, for aero-engine multi-redundant smart sensors fault conditions, a method based on data fusion was proposed, which can realize the fault diagnosis and fault location online.

49.2 The Structure of Multi-redundant Smart Sensor

As shown in Fig. 49.1, the multi-redundant smart sensor consists of multi sensing units, signal conditioning unit, microprocessor, data bus interface, and power bus interface. When the multi-redundant smart sensor works, the target's physical signal is measured by the sensing units, and then preprocessed by the signal conditioning unit before it is sent to the DSP (Digital Signal Processing). The DSP completes the processing of redundant data fusion, self-management, and the communication with the central controller. In order to improve the reliability and the measurement accuracy, redundancy technology is generally applied to the most important sensors. In Fig. 49.1, the sensing units $1 \sim n$ can be located in the same position or different geographical space, if n is 1, it indicates that the sensor has single redundant, and if n is greater than 1, it means the sensor has multi-redundancies. This paper is mainly related to the $n(n \geq 3)$ redundant sensor fault diagnosis.

49.3 Fault Diagnosis Method Based on Data Fusion

Taking a multi-redundant smart temperature sensor as the research object, it uses n redundant sensing units to measure the aero-engine low pressure turbine outlet temperature, and these n redundant sensing units can be managed by the DSP. The fault diagnosis structure based on data fusion is shown in Fig. 49.2.

The fault diagnosis principle shown in Fig. 49.2 can be described as follows: first, the samples of n sensing units would be fused to obtain a fusion value T_f, and T_f would be regarded as the only sensor output value and it is sent to the central controller, the fusion process ensured the output value with a higher reliability, and improved the measurement accuracy; second, a residual could be obtained by comparing the fusion value T_f with n sensing unit sampling values, then the residual should be tested by certain decision-making logic to get a fault vector with elements of 0 or 1; at last sensor fault diagnosis and fault location could be completed by fault vector interpretation.

Fuzzy C-means clustering method [7] was applied for data fusion in this paper. First, fuzzy C-means clustering methods would be used to separate n sampling sequences into an appropriate number of categories, the number of categories should be confirmed according to the number of sensing units and failure modes, and then select the center vector of the category containing the maximum sampling

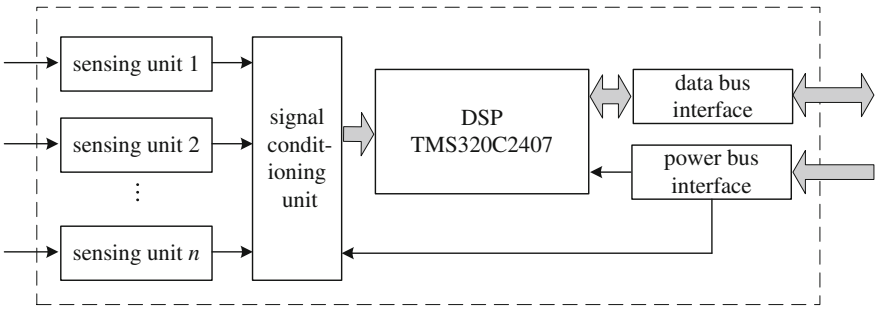

Fig. 49.1 The multi-redundant smart sensor structure

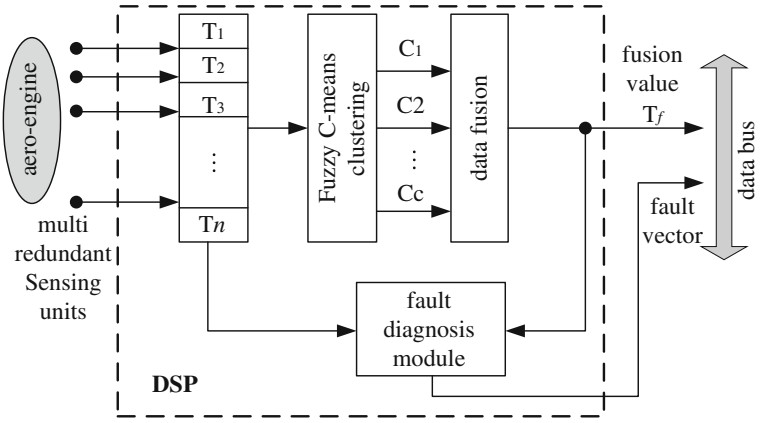

Fig. 49.2 Multi-redundant smart temperature sensor fault diagnosis structure based on data fusion

sequences as the fusion value by the principle of majority. Because the category center vector is nearest to all vectors by Euclidean distance in the same category, it is reasonable to regard the center value as the fusion value.

When the fusion value T_f was obtained, we can get a residual vector $[\varepsilon_1, \varepsilon_2, \varepsilon_3, \ldots, \varepsilon_n]$ by subtracting each sensing unit sample $[T_1, T_2, T_3, \ldots, T_n]$ from T_f. Then a fault vector $F = [f_1, f_2, f_3, \ldots, f_n]$ could be used to complete fault isolation, and the fault vector assignment rules are as follows:

$$\begin{cases} f_i = 0 \ if \ |\varepsilon_i| \leq \bar{\varepsilon} \\ f_i = 1 \ if \ |\varepsilon_i| > \bar{\varepsilon} \end{cases} \tag{49.1}$$

In this paper, the fault threshold $\bar{\varepsilon}$ is determined by the mean and standard deviation of the normal sensor residuals, if the mean of the normal residuals was μ, the standard deviation of the sensor normal residuals was σ, then the fault threshold $\bar{\varepsilon}$ would be: $\bar{\varepsilon} = \mu + n\sigma$.

Then we can calculate the fault vector $F = [f_1, f_2, f_3, \ldots, f_n]$ by using formula (49.1), and according to the fault vector, which of the sensing units of the multi-redundant smart sensor is failed could be determined.

49.4 An Improved Fuzzy C-Means Algorithm

The basic thought of C-means classification algorithm is dividing the objects into clusters ensuring the similarity between objects is greatest in the same cluster and is smallest in different clusters. The Fuzzy C-Means algorithm is developed from ordinary C-means algorithm, and the difference between them is that the fuzzy C-means algorithm applied soft fuzzy partition method.

In this method, n vectors of $x_j(1, 2 \ldots, n)$ are divided into c clusters of $G_i(i = 1, 2, \ldots, c)$, and the center of each cluster could be calculated by making the value function of non-similarity index minimum. Select Euclidean distance as the non-similarity index to describe the distance between vector x_k and the cluster center c_i in cluster i, then the value function can be defined as:

$$J = \sum_{i=1}^{c} J_i = \sum_{i=1}^{c} \left(\sum_{k, x_k \in Gi} ||x_k - c_i||^2 \right) \tag{49.2}$$

Each cluster can be characterized by a matrix U with a dimension of $c \times n$, the elements $u_{ij} \in [0, 1]$ of the matrix U represents the membership degree of the j-th vector x_j for cluster i. The sum of all the membership degree of a data set is equal to 1 according to the normalization principle:

$$\sum_{i=1}^{c} u_{ij} = 1, \forall j = 1, \ldots, n \tag{49.3}$$

Then, formula (49.2) could be changed as follows:

$$J(U, c_1, \ldots, c_c) = \sum_{i=1}^{c} J_i = \sum_{i=1}^{c} \sum_{j}^{n} u_{ij}^m d_{ij}^2 \tag{49.4}$$

where $d_{ij} = \left\| x_j - c_i \right\|$ is the Euclidean distance between the j-th vector and the i-th cluster's center vector, and $m \in [1, \infty)$ is weighting exponent.

The new objective function is constructed as follows:

$$\begin{aligned} \overline{J}(U, c_1, \ldots, c_c, \lambda_1, \ldots, \lambda_n) &= J(U, c_1, \ldots, c_c) + \sum_{j=1}^{n} \lambda_j \left(\sum_{i=1}^{c} u_{ij} - 1 \right) \\ &= \sum_{i=1}^{c} \sum_{j}^{n} u_{ij}^m d_{ij}^2 + \sum_{j=1}^{n} \lambda_j \left(\sum_{i=1}^{c} u_{ij} - 1 \right) \end{aligned} \tag{49.5}$$

where λ_j, $j = 1, 2 \ldots, n$ is the Lagrange multiplier. Then take the derivative calculation of the input parameters to get the update function of membership degree and cluster center vector:

$$c_i = \frac{\sum_{j=1}^{n} u_{ij}^m x_j}{\sum_{j=1}^{n} u_{ij}^m} \tag{49.6}$$

$$u_{ij} = \frac{1}{\sum_{k=1}^{c} \left(\frac{d_{ij}}{d_{kj}}\right)^{2/(m-1)}} \tag{49.7}$$

However, this algorithm above has a drawback that it does not convergence to the optimal solution every time, the performance of the algorithm depends on the initial membership matrix, so if we can obtain an appropriate initial membership matrix by using certain optimization methods, the problems of the algorithm would be overcome.

PSO (Particle Swarm Optimization, PSO) algorithm is a relatively simple optimization algorithm [8], this paper used PSO algorithm to optimize the initial membership matrix. Basic PSO algorithm can be expressed as follows: it is supposed that there is a particle swarm composed of m particles in the space of D dimension, the spatial position of the i-th particle is defined as $X(i) = (x_{i1}, x_{i2}, \ldots, x_{id})$, $i = 1, 2, \ldots, m$, and its best position that experienced is P_i, the corresponding fitness is F_i, and the flight speed is V_i; the best position of all particles that experienced is named global optimum position and is defined as P_g, the corresponding fitness is F_g. Then the i-th particle of the particle swarm at $n + 1$ generation could be iterated according to the following equation:

$$v_{id}^{n+1} = \lambda(w \times v_{id}^n + c_1 \times \text{rand}(1) \times (P_{id}^n - x_{id}^n) + c_2 \times \text{rand}(2) \times (P_{gd}^n - x_{id}^n)) \tag{49.8}$$

$$x_{id}^{n+1} = x_{id}^n + v_{id}^{n+1} \tag{49.9}$$

where λ is shrinkage factor, w is inertia weight, c_1 and c_2 are acceleration factors, rand(1) and rand(2) are random numbers in the interval of [0, 1].

Then we can suppose the sample space is: $X = \{x_1, x_2, \ldots, x_N\}$, each particle represents a membership matrix $U = [u_{ij}]_{c \times n}$, and the PSO fitness function can be designed as follows:

$$F(x_i) = \frac{1}{1 + J(U, C)} = \frac{1}{1 + \sum_{i=1}^{c} \sum_{j}^{n} u_{ij}^m d_{ij}^2} \tag{49.10}$$

As can be seen from the Eq. (49.10), the classification result is proportional to the fitness function value. If the classification result improved, $J(U, C)$ will be smaller than before, and the fitness function value will increase.

In summary, the steps of the improved fuzzy C-means classification algorithm can be expressed as follows:

Step 1: given the number of clusters c, tolerance error ε, set the PSO algorithm parameters like swarm size m, shrinkage factor λ, inertia weight w and acceleration factors c_1 and c_2;
Step 2: initialize the particles: $U_1, U_2, \ldots, U_m$;
Step 3: calculate the cluster center and the fitness function according to formula (49.6) and (49.10), and then produce the particle of next generation according to Eqs. (49.8)–(49.9);
Step 4: if the iteration times achieve the maximum time that set before, stop the iteration, and the global optimum position P_g in this case is the optimal membership degree, otherwise go to step 3;
Step 5: update the membership and cluster centers according to Eqs. (49.6) – (49.7), and calculate the value function, if the changes of the value function is less than ε, stop the iteration, otherwise go to step 5 again.

49.5 Fault Diagnosis Simulation

49.5.1 Fault Samples

In order to guarantee the accuracy and reliability of the measurement, a certain turbofan engine installed eight conventional thermocouple sensors to measure the low pressure turbine outlet temperature. It is assumed that conventional thermocouple sensors were replaced by a new smart temperature sensor which had eight sensing units to measure the low pressure turbine outlet temperature, then the eight measured values would be fused by the sensor's DSP to get a fusion value, after that the fusion value would be sent to the central controller and complete fault diagnosis and fault location.

In this paper, eight groups of temperature data were generated by mathematical processing based on a group of real low pressure turbine outlet temperature, and these eight groups of data were regarded as the samples collected by the eight sensing units of the smart temperature sensor. It is assumed that the fourth unit suffered constant bias fault, the sixth unit suffered gain changes faults, and all the anther sensing units were fault-free, the mathematical processing was as follows:

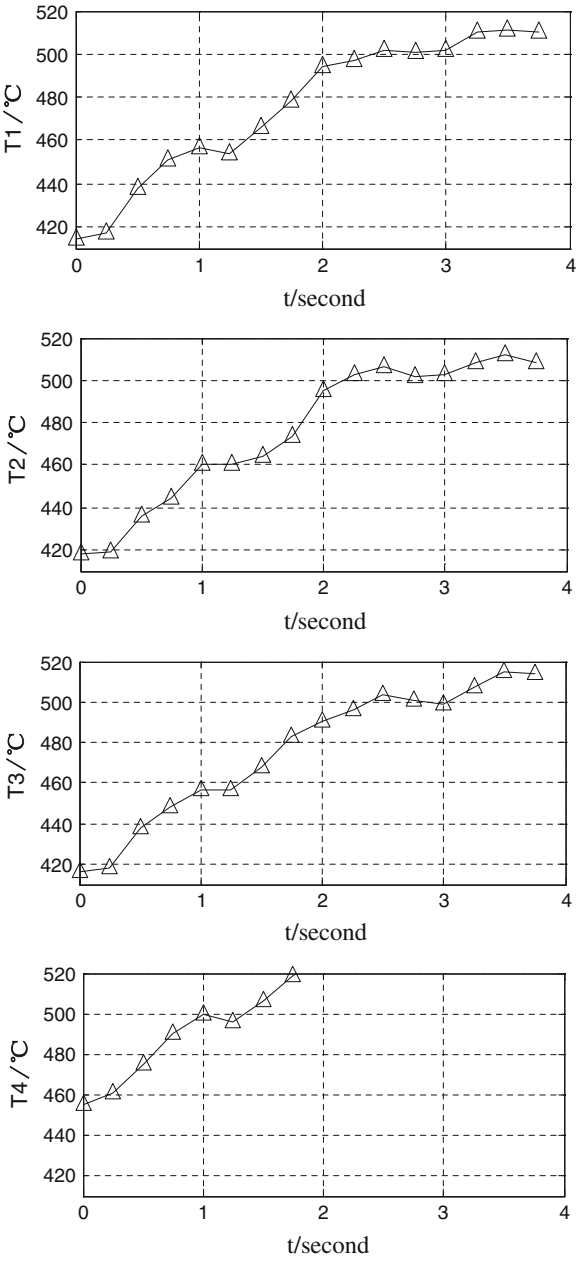

Fig. 49.3 The eight groups of samples that generated ($T_1 \sim T_8$ referred to the eight sensing units)

Fig. 49.3 (continued)

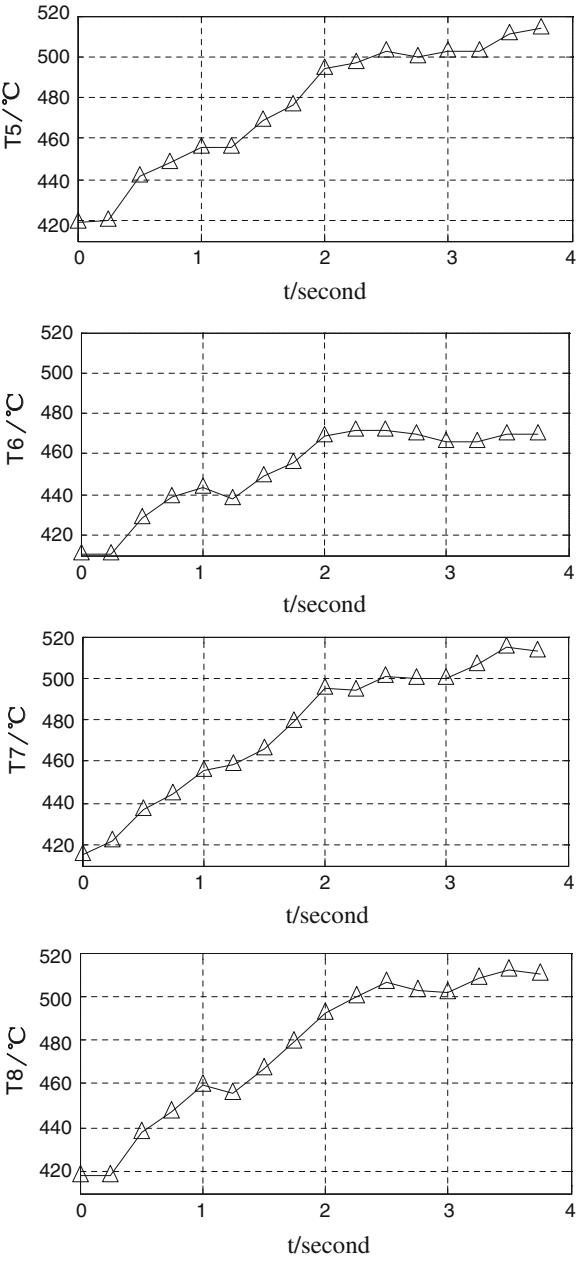

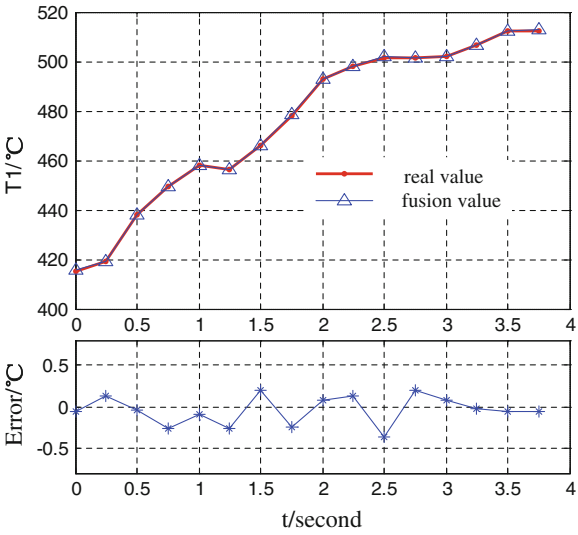

Fig. 49.4 The fusion value and the error between the fusion value and the real value

$$\begin{aligned} T_1 &= x + n_1 \\ T_2 &= x + n_2 \\ T_3 &= x + n_3 \\ T_4 &= x + 40 + n_4 \\ T_5 &= x + n_5 \\ T_6 &= x - 10.8 \times t + n_6 \\ T_7 &= x + n_7 \\ T_8 &= x + n_8 \end{aligned} \tag{49.11}$$

where T_i is the collected data of different sensing unit; x is the real low pressure turbine outlet temperature data; n_i is random numbers with 0-mean and 2-variance; t was time, $i = 1, 2, \ldots, 8$. The eight groups of samples that generated were shown as in Fig. 49.3.

49.5.2 Fault Diagnosis

The parameters were set as follows: the number of clusters was: $c = 3$, the tolerance error was: $\varepsilon = 0.0001$, the PSO swarm size was: $m = 50$, the shrinkage factor was: $\lambda = 0.85$, the inertia weight was: $w = 0.7$, and the acceleration factors were: $c_1 = 1.8$, $c_2 = 2.2$.

In the simulation, the fuzzy C-means algorithm optimized by PSO divided the eight groups of samples into three clusters: $(T_1, T_2, T_3, T_5, T_7, T_8)$, (T_4), (T_6), of

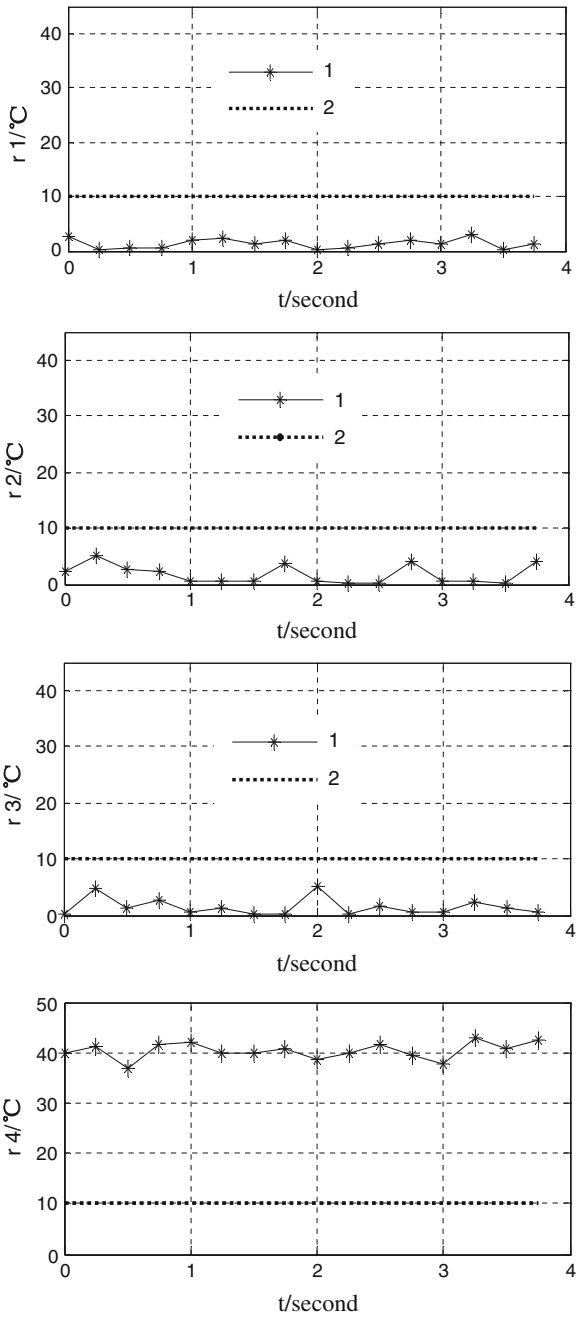

Fig. 49.5 The residual (absolute value) of each sensing unit (1-line: residual; 2-line: threshold)

Fig. 49.5 (continued)

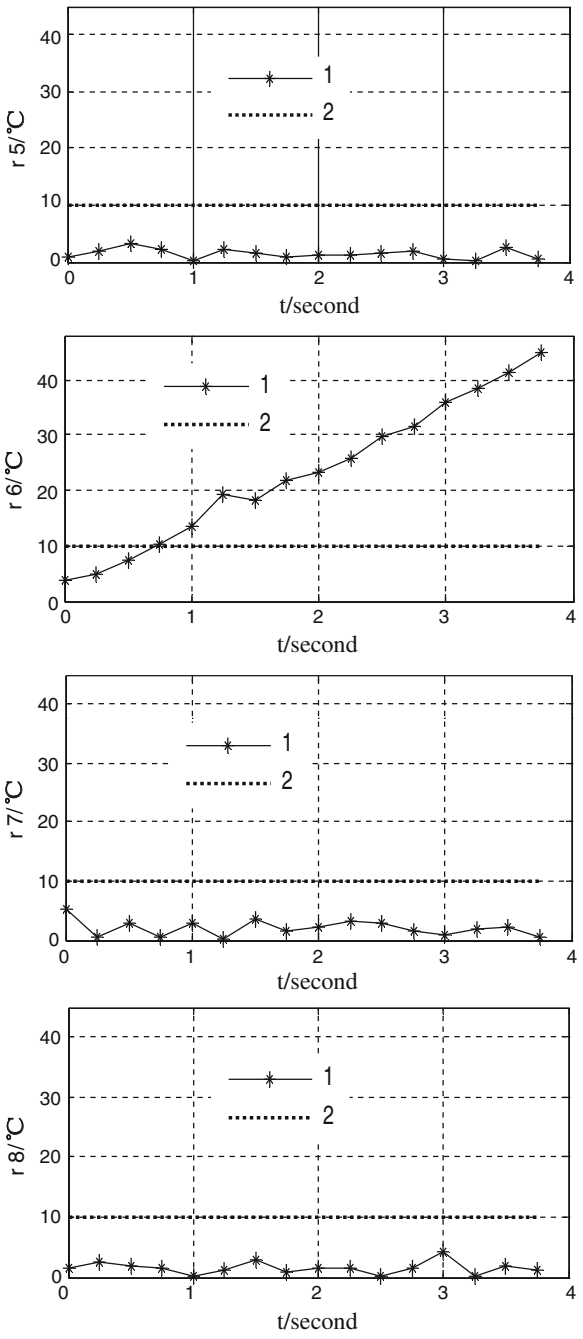

which the first cluster had six groups of samples, so first cluster's center T_f was regarded as the fusion value of the sensing units according to the principle of majority. As shown in Fig. 49.4, the fusion value T_f showed a good approximation to the real value, and the absolute error was less than 0.5 °C.

Then the residuals between the measured values of sensing units and the fusion value were calculated and shown in Fig. 49.5, in which 1-line indicated the absolute values of the residuals and 2-line indicated the thresholds.

However, the threshold should be determined according to the actual data of the low pressure turbine outlet temperature. In this paper, the fault threshold value $\bar{\varepsilon}$ was calculated with the formula: $\bar{\varepsilon} = \mu + n\sigma$, where μ was the mean of the normal sensor residuals, and σ was the standard deviation of the normal sensor residuals. The mean and the standard deviation of the residuals were known because the sensor data was artificially generated. In addition, the low pressure turbine outlet temperature field was not uniform in actual station, so it was necessary to broaden the threshold range in an appropriate level. The threshold was determined as $\bar{\varepsilon} = 10$ °C by considering all the above factors.

After the threshold was determined, a fault vector could be obtained by checking whether the residuals exceeded the threshold. In this case, we could see that the fourth residual and the sixth residual exceeded the threshold, thereby a fault vector of $[0 \quad 0 \quad 0 \quad 1 \quad 0 \quad 1 \quad 0 \quad 0]$ was generated and sent to the central controller, the central controller could directly determine that the fourth and sixth sensing units failed by through of checking the fault vector.

49.6 Conclusions

The structure of an aero-engine multi-redundant smart sensor based on DSP was introduced first, and for aero-engine multi-redundant smart sensors fault conditions, a method based on data fusion which can realize the fault diagnosis and fault location for the multi-redundant smart sensors online was proposed. The method used an improved fuzzy C-means clustering algorithm to get a fusion value, and then the residuals between the fusion value and measured values of these sensing units could be calculated. After that, the residuals could be used to monitor the health conditions of the sensors. The simulation results showed that the fusion value had a high accuracy, and also online fault location could be completed in the form of fault vector.

References

1. He B, Yu D, Shi X (2011) Application of simulation model of sensors to analysis fault of control system of turbojet engine. J Propuls Tech 22:364–367 (in Chinese)

2. Culley DE, Thomas R, Saus J (2007) Concepts for distributed engine control, In: 43rd AIAA joint propulsion conference and exhibit, AIAA-2007-5709
3. Alireza R, Behbahani (2007) Adaptive distributed intelligent control architecture for future propulsion systems. AFRL-PR-WP-TP-2007-228
4. Behbahani A, Culley D, Smith B et al (2008) Status, vision, and challenges of an intelligent distributed engine control architecture. AFRL-RZ-WP-TP-2008-2042
5. Kun Q (2006) The research on areo-engine distributed control and status monitoring system and its control algorithm. Xi'an, Air Force Engineer University (in Chinese)
6. Kailong Cai (2008) The research and experiment on aviation propulsion systems distributed control system. Air Force Engineer University, Xi'an (in Chinese)
7. Jaradat MAK, Langari R (2009) A hybrid intelligent system for fault detection and sensor fusion. Appl Soft Comput pp 415–422
8. Kennedy J, Eberhart RC (1995) Particle swarm optimization. In: IEEE international conference on neural networks. Perth IEEE Service Center, Piscataway, pp 1942–1948

Chapter 50
Environment Control System Fault Diagnosis Expert System

Chengjun He, Lili Wang, Jianlin Yan and Qinglin Ma

Abstract The Environment Control System (ECS) of transport category airplanes is inclined to breakdown due to many accessories. Once the system does not work well, it is difficult to locate the cause of the fault. The nets model and fault diagnosis way of Weighted Fuzzy Petri Net (WFPN) are explained, associating with the describable ability and fuzzy inferential ability of fuzzy Petri net graphics. Also, the structure and the working principle of the ECS fault diagnosis expert system are introduced. Furthermore, an example of pneumatic system (PNU)'s failure is used to verify the algorithm, and the result has shown that this method of the failure diagnosis is effective and feasible.

Keywords Weighted Fuzzy Petri Net · Fault diagnosis · Environment control system · Pneumatic system · Central maintenance system · Central alarm system

50.1 Introduction

Currently, troubleshooting method of modern airplane is mainly passive feedback. When fault occurs, the design department dispatches engineer to gather fault message and to locate fault. Due to lack of experience and the complexity of the problem, the engineer can not deal with most fault well. The discussion of locating

C. He (✉) · Q. Ma
AVIC The First Aircraft Institute, Environment Control and Lifesaving Research Institute, Xi'an 710089, China
e-mail: hechengjun@nuaa.edu.cn

L. Wang
AVIC The First Aircraft Institute, Flight Control and Hydraulic Research Institute, Xi'an 710089, China

J. Yan
PLA, 94922, Zhejiang 321000, China

J. Wang (ed.), *Proceedings of the First Symposium on Aviation Maintenance and Management-Volume I*, Lecture Notes in Electrical Engineering 296,
DOI: 10.1007/978-3-642-54236-7_50,

the fault is organized by the design department, where the engineers try to locate the reason. However, the result is not desirable. Thus, this way is of low efficiency and costs much time. A new way is to be introduced to locate the fault effectively based on WFPN.

50.2 Weighted Fuzzy Petri Net

50.2.1 Net Model of WFPN

Weighted Fuzzy Petri Net (WFPN) is a promising modeling tool for expert systems, and has shown itself to be suitable for fuzzy knowledge representation and reasoning. In order to capture more information of designing genetic regulatory networks, the WFPN structure can be defined as a 10-tuple [1].

WFPN = $(P, T, D, I, O, f, \alpha, \beta, W, \mathrm{TH})$, where $P = \{p_1, p_2, \ldots, p_n\}$ is the finite set of places. $T = \{t_1, t_2, \ldots, t_m\}$ is a finite set of transitions. $D = \{d_1, d_2, \ldots, d_n\}$ is a finite set of propositions of WFPN and denotes the proposition that interprets fuzzy linguistic variables, $|P| = |D|$, $P \cap T \cap D = \Phi$. I: $T - P^{\infty}$ is the input function which defines a mapping from transition to places. O: $T - P^{\infty}$ is the output function which defines a mapping from transition to places. $f = \{\mu_1, \mu_2, \ldots, \mu_m\}$ is the joint function, where μ_i denotes the CF of Ri, which indicates the reliability of the rule Ri, $\mu_i = f(t)$, μ_i between 0 and 1. α: $P - [0, 1]$ is the function that assigns a token value between 0 and 1 to each place. β: $P - D$ is an association function, a bijective mapping from places to propositions. $W = \{\omega_1, \omega_2, \ldots, \omega_m\}$ is the weights vector of fore propositions. $\mathrm{TH} = \{\lambda_1, \lambda_2, \ldots, \lambda_m\}$ is the function which assigns a threshold, λ_i between 0 and 1 to a transition t_i.

50.2.2 Rule Representation for Fuzzy Reasoning

Production Rules (PRs) are suitable to express expert knowledge. In most cases, collecting data in a precise way is difficult, thus PRs are adopted, which have the ability to process uncertain or incomplete knowledge. There are three kinds of fuzzy PRs (see Figs. 50.1, 50.2 and 50.3) [2].

Type 1 simple fuzzy production rule: Ri = IF p_i then p_k (CF = μ_i), λ_i, ω_i

Type 2 fuzzy production rule about "AND": Ri = IF p_i and p_j then p_k (CF = μ_i), λ_i, λ_j, ω_i, ω_j

Type 3 fuzzy production rule about "OR": Ri = IF p_i OR p_j then p_k (CF = μ_i, μ_j), λ_i, λ_j, ω_i, ω_j.

Fig. 50.1 Simple FPR

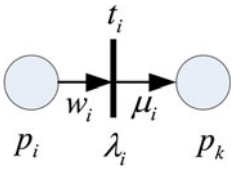

Fig. 50.2 "AND" FPR

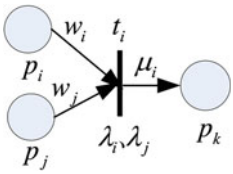

Fig. 50.3 "OR" FPR

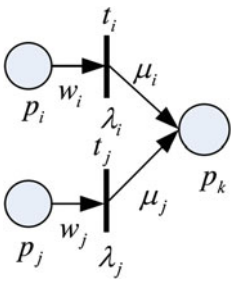

50.2.3 Process of Fuzzy Inference

We can use the WFPN to denote diagnostic knowledge, troubleshoot intelligent reasoning by Petri nets reachability and transition firing rules, and ultimately get reasoning reliability of the results.

In the WFPN, the initial places denote the LRU fault reason, which only the output transitions, not input transitions. The terminal places represent the final state of the system faults, which only the input transitions, not output transitions. The remainder places collectively are named as intermediate places [3].

The process of designing the fuzzy genetic regulatory network is based on reverse search technology. It consists of the following six steps.

Step 1: Initialize the terminal place p_z, and put all of front place p_j into investigation set, post[j] $\rightarrow$ z, and $L[j, z] \rightarrow g[j][z]$.Where $g[j][z]$ is the longest path from p_j to p_z. $L[j, z]$ is $g[j][z]$ fuzzy factor which is equal to fuzzy factor of all transitions on the path multiplied.

Step 2: Estimate the investigation set. If the investigation set is not empty, go to Step 3, otherwise go to Step 6.

Table 50.1 Input data truth value

Truth value	Scope	Value
True	[0.5, 1]	$0.5 + (1 - \gamma)$*0.5
Pending	[0.8, 0.2]	$0.2 + \xi$*0.5
False	[0,0.5]	$0.5 - \varsigma$*0.5

Step 3: Capture the place p_m focused on maximum fuzzy factor. If p_m is the initial places or the input values $\alpha(p_m)$ is known, go to Step 4, otherwise go to Step 5.

Step 4: Determine whether all paths from p_m to p_z can pass the threshold. If there is only one path from p_m to p_z, determine whether all of fuzzy factor of transition from p_m to p_z multiplied by $\alpha(p_m)$ pass the threshold. If it is able to pass, p_m is added to key set, otherwise it is deleted from the investigation set. If there are multiple paths from p_m to p_z, examine each path by the precedent way and determine whether one of these paths can pass all of the thresholds. If it is able to pass, p_m is added to the key set, otherwise it is deleted from the investigation set. Then go to Step 2.

Step 5: If p_m is not an initial place, it adds all preplaces to the investigation set, and adjust $L[i, z]$. Then go to Step 3.

Step 6: Deleted all the intermediate places from the key set, and retained all the initial places in the key set. The key set is sorted according to the value $\alpha_{(i,\ z)}(p_z)$,where $\alpha_{(i,\ z)}(p_z)$ is the credibility of the path from initial place (p_j) to terminal place (p_z).

50.2.4 Fuzzy Representation of Input Data

The initial places input data: $\alpha(p_i)$ $(i = 1, 2, \ldots, m)$.

Where:

$$\alpha(p_i) = \begin{cases} \text{True} & [0.5, 1] \\ \text{Pending} & [0.8, 0.2] \\ \text{False} & [0, 0.5] \end{cases}. \tag{50.1}$$

where $\alpha(\mathrm{p_i})$ is equal to the value as shown in Table 50.1.

Where γ is false alarm factor.

$$\gamma = a/b, \tag{50.2}$$

where a is the false alarm times of this LRU fault, b is the totals of this LRU fault.

Where ξ is pending factor.

$$\xi = c/d, \tag{50.3}$$

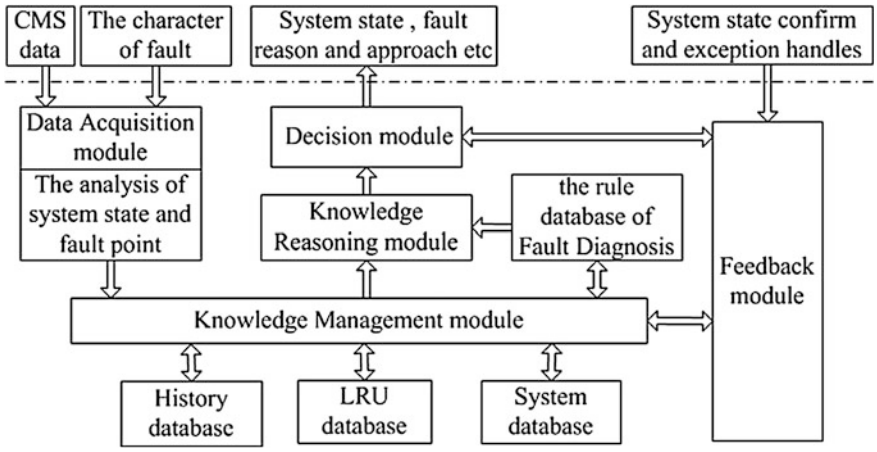

Fig. 50.4 The construction and the working principle of fault diagnosis expert system

where c is the times of this LRU fault which do not record in Central maintenance system (CMS), d is the total of this system fault caused by this LRU fault.

Where ς is underreporting factor.

$$\varsigma = e/f. \tag{50.4}$$

where e is the underreporting times of this LRU fault, f is the totals of this LRU fault.

50.3 ECS Fault Diagnosis System

During the flight, the pilot will notice that a function can not be implemented or an alarm message from Central alarm system (CAS), when fault occurs in the system. After the flight, ground crew should analyze failure cause and locate the faulty equipment quickly. Depending on the existing data resources, the Environment control system (ECS) fault diagnosis system analyzes the fault character of acquired data, matching in the knowledge management module, and passing the related fault information to the decision module actively. As shown in Fig. 50.4, Data Acquisition module, Knowledge Management module, Knowledge Reasoning module, Decision module, and Feedback module are included in this system [4].

Data Acquisition module fulfills two main functions. On one hand, CMS data is analyzed according to Knowledge Management data requirements. On the other hand, the fault feature is collected during the flight and is translated into knowledge representation language.

Knowledge database is for storage of specialized knowledge in expert system, which includes history database, LRU knowledge database, system knowledge database, and rule database. The knowledge database is initially defined by

Table 50.2 System fault table

No	Failure	Flight phase	Status	System
1	Left bleed air failure ($p_{0,0}$)	Before flight, before engine start, engine start, after engine start, takeoff (emergency return), climb, cruise, descent, landing, parking	No bleed	PNU
2	Left bleed air failure ($p_{1,0}$)	Engine start, after engine start, takeoff (emergency return), climb, cruise, descent, landing	Bleed	PNU

equipment research and development department, domain expert, and the relevant technical engineer. Later the database is extended by learning of this system.

Knowledge Reasoning module mainly takes the backward reasoning method. The control strategy is based on the results to find the reasons. It can search the key set of LRU fault in the database using the backward search algorithm.

Decision module explains the behavior of expert system to the ground crew, including the correctness of the conclusion and the reason why the system outputs other candidate solutions.

Feedback module feeds background crew fault processing results to the system and calculates false alarm factor, pending factor, and underreporting factor in accordance with Sect. 50.2.4. Moreover, if there is a new fault type, it stores it in knowledge database.

50.4 Fault Diagnosis Example

The temperature and pressure of the bleeding air from the engine compressor are extremely high. Firstly, the pressure is adjusted by pressure bleed valve to an appropriate value. Secondly, the temperature is adjusted to the proper range by precooler. Thirdly, pressure and shut off valve is set behind the precooler. After the second adjusting, the pressure of the bleed air meets the requirements of air-condition and anti-icing.

There are four faults for the left engine bleed air of pneumatic system (PNU): "the left bleed air failure", "the left bleed air leaking", "the left bleed air over-temperature", and "the left bleed air over-pressure".

According to its operational principle and related information, fault databases are established as shown in Tables 50.2, 50.3, and 50.4.

According to the rules of Left Bleed Air in Table 50.5, the left engine bleed air diagnosis Petri Net model is established as shown in Figs. 50.5, 50.6 [5].

The diagnosis process of ECS fault diagnosis system is shown as follows:

Firstly, based on CMS data, ECS fault diagnosis system analyzes the working state of bleed air system during each flight phase. The status of bleed air system can be obtained from Fig. 50.7, thus the status of left bleed air system can be obtained

Table 50.3 Intermediate fault table

No	Failure	Flight phase	Status	System
1	Left bleed air overpressure ($p_{1,1}$)	Engine start, after engine start, takeoff (emergency return), climb, cruise, descent, landing	Bleed	PNU
2	Left bleed air overtemperature ($p_{1,2}$)	Engine start, after engine start, takeoff (emergency return), climb, cruise, descent, landing	Bleed	PNU
3	Left bleed air leaking ($p_{1,3}$)	Engine start, after engine start, takeoff (emergency return), climb, cruise, descent, landing	Bleed	PNU

Table 50.4 LRU fault table

No	Failure	LRU	False-alarm factor	Underreporting factor	Pending factor
1	Pressure regulated valve failure in the open position (p_1)	Pressure regulated valve	0.95	0.85	0
2	Pressure regulated valve failure in the close position (p_2)	Pressure regulated valve	0.9	0.70	0
3	PNU check valve work (p_3)	PNU check valve	0.95	0.77	0
4	Pipe 1 leaking (p_4)	Pipe 1	0	0	0.1
5	Pipe 2 leaking (p_5)	Pipe 2	0	0	0.55
6	Control unit failure (p_6)	Control unit	0.95	0.77	0
7	High pressure valve failure in the open position (p_7)	High pressure valve	0.85	0.87	0
8	High pressure valve failure in the close position (p_8)	High pressure valve	0.83	0.70	0
9	Precooler failure in the open position (p_9)	Precooler	0.88	0.84	0
10	Precooler failure in the close position (p_{10})	Precooler	0.81	0.67	0
11	Pressure regulated valve control failure (p_{11})	Pressure regulated valve	0.83	0.60	0
12	High pressure valve control failure (p_{12})	High pressure valve	0.8	0.71	0
13	Precooler control failure (p_{13})	Precooler	0.85	0.77	0

from Fig. 50.8. In the normal working state (see Fig. 50.8 "correct" line), it determines whether there is fault by comparing with the system fault ($p_{0,0}$ or $p_{1,0}$).

Secondly, this system can also detect mistakes of pilot operation. When a failure occurs in the normal working state, an internal clock starts counting. This system can estimate when and whether the pilot adopts right operation instruction by CMS data. When the pilot takes related action at a later time, the system is transited to abnormal state, otherwise the pilot does not dispose right.

Table 50.5 Inference rules table of left bleed air

No	Rules
R1	IF p_1 THEN $p_{0,0}$ ($\omega_1 = 0.7$, $\lambda_1 = 0.3$, $\mu_1 = 0.93$)
R2	IF p_2 THEN $p_{1,0}$ ($\omega_2 = 0.8$, $\lambda_2 = 0.2$, $\mu_2 = 0.9$)
R3	IF p_3 THEN $p_{1,0}$ ($\omega_3 = 0.73$, $\lambda_3 = 0.32$, $\mu_3 = 0.87$)
R4	IF p_4 THEN $p_{1,3}$ ($\omega_4 = 0.8$, $\lambda_4 = 0.3$, $\mu_4 = 0.91$)
R5	IF p_5 THEN $p_{1,3}$ ($\omega_5 = 0.8$, $\lambda_5 = 0.3$, $\mu_5 = 0.91$)
R6	IF p_6 THEN $p_{0,0,}$ $p_{0,1}$ ($\omega_6 = 0.98$, $\lambda_6 = 0.36$, $\mu_6 = 0.96$)
R7	IF p_7 THEN $p_{0,0}$ ($\omega_7 = 0.66$, $\lambda_7 = 0.42$, $\mu_7 = 0.9$)
R8	IF p_8 THEN $p_{1,0}$ ($\omega_8 = 0.71$, $\lambda_8 = 0.40$, $\mu_8 = 0.88$)
R9	IF p_9 THEN $p_{0,0}$ ($\omega_9 = 0.8$, $\lambda_9 = 0.24$, $\mu_9 = 0.91$)
R10	IF p_{10} THEN $p_{1,0}$ ($\omega_{10} = 0.88$, $\lambda_{10} = 0.32$, $\mu_{10} = 0.92$)
R11	IF p_{11} THEN $p_{1,1}$ ($\omega_{11} = 0.8$, $\lambda_{11} = 0.3$, $\mu_{11} = 0.9$)
R12	IF p_{12} THEN $p_{1,1}$ ($\omega_{12} = 0.72$, $\lambda_{12} = 0.46$, $\mu_{12} = 0.8$)
R13	IF p_{13} THEN $p_{1,2}$ ($\omega_{13} = 0.8$, $\lambda_{13} = 0.3$, $\mu_{13} = 0.91$)
R14	IF $p_{1,1}$ THEN $p_{1,0}$ ($\omega_{14} = 0.9$, $\lambda_{14} = 0.18$, $\mu_{14} = 0.94$)
R15	IF $p_{1,2}$ THEN $p_{1,0}$ ($\omega_{15} = 0.8$, $\lambda_{15} = 0.22$, $\mu_{15} = 0.95$)
R16	IF $p_{1,3}$ THEN $p_{1,0}$ ($\omega_{16} = 0.73$, $\lambda_{16} = 0.36$, $\mu_{16} = 0.95$)

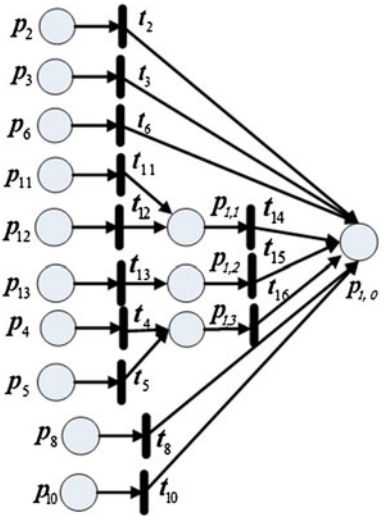

Fig. 50.5 Net model of left bleed air failure ($p_{1,0}$)

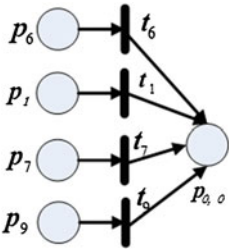

Fig. 50.6 Net model of left bleed air failure ($p_{0,0}$)

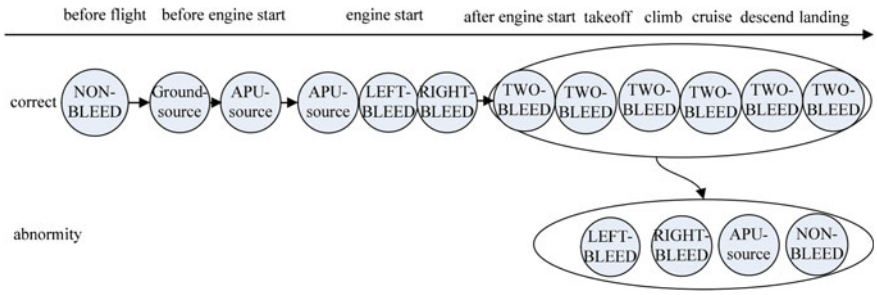

Fig. 50.7 The work process of bleed air system

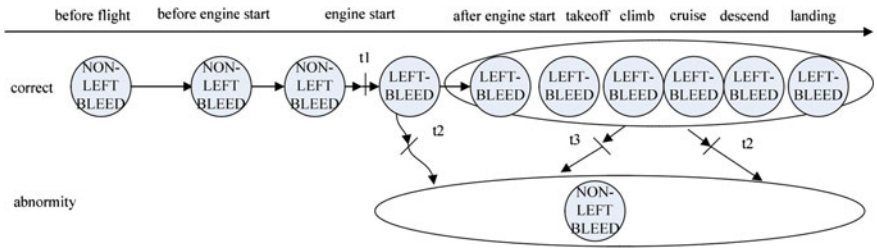

Fig. 50.8 The work process of left bleed air

Thirdly, if a system fault occurs, we obtain input data ($\alpha(p_1)$, $\alpha(p_2)$, …, $\alpha(p_{13})$) in accordance with Sect. 50.2.4, we obtain the key set in accordance with Sect. 50.2.3.

Fourthly, the system feeds the key set back to the user.

50.5 Summary

In this paper, a fault diagnosis expert system is proposed for ECS based on WFPN and the key technologies of the system are illustrated. The major features of this system are listed as follows:

1. It shows the description of a reverse inference control strategy of fuzzy reasoning, based on the analysis of CMS data. Using this way, this system spends less cost to locate the key set of LRU fault.
2. False alarm rate and underreporting rate are introduced to the expert system input data processing in order to improve the ability of fault locating.
3. The "pending" value is introduced to the system. It makes the expert system handle the fault which is not in CMS data.

References

1. Hamed RI, Ahson SI, Parveen R (2010) Designing genetic regulatory networks using fuzzy petri nets approach. Int J Autom Comput 7(3):403–412
2. Li X, Yu W, Lara-Rosano F (2000) Dynamic knowledge inference and learning under adaptive Fuzzy Petri net framework. IEEE Trans Syst Man Cybern C 30(4):442–450
3. Wu L (2009) Fuzzy petri nets fault diagnosis techniques and learning capability studying. Dissertation, Changsha University of Science and Technology (in Chinese)
4. Yang S, Wang Q, Liu L (2010) Fault diagnosis system based on knowledge pushing. J Aerosp Power 25(1):203–207 (in Chinese)
5. Chen S-M (2000) Fuzzy backward reasoning using Fuzzy Petri nets. IEEE Trans Syst Man Cybern B 30(6):846–856

Chapter 51
Health Monitoring of Aircraft Parameters Based on Statistical Process Control

Lin He, Jun Li, Cunbao Ma and Yue Feng

Abstract Statistical process control (SPC) is a statistical method that has been used in monitoring and prediction. The value of aircraft parameters can reflect the health status of certain component or system. How to use SPC reasonably in aircraft health monitoring is studied in this paper. The theory of control chart and the judgment criterion are described. Several set of data which cover different type of status are given to analyze the feasibility and limitations of this method.

Keywords Statistical process control · Aircraft health monitoring · Judgment criterion

51.1 Introduction

The goal of aircraft status monitoring is to monitor aircraft's operation status in time, to find the potential of aircraft accident as soon as possible and to give the information of fault diagnosis in time. The most popular method used in aircraft status monitoring is threshold comparison, which judges the malfunction of system through comparing the monitoring variables with the threshold value. With the development of technology, the trend of aircraft maintenance change quickly, and it comes from state monitor to health management. Health management means to

L. He · J. Li (✉) · C. Ma
School of Aeronautics, Northwestern Polytechnical University,
Xi'an 710072 Shaanxi, China
e-mail: 8913485LiJun@sina.com

L. He
e-mail: helin@nwpu.edu.cn

Y. Feng
Beijing Aeronautical Engineering Technology Research Center, Beijing 100076, China

J. Wang (ed.), *Proceedings of the First Symposium on Aviation Maintenance and Management-Volume I*, Lecture Notes in Electrical Engineering 296,
DOI: 10.1007/978-3-642-54236-7_51,

detect the downward trend of aircraft healthy before failure occurred, and this information should be concerned by ground maintenance staff. Therefore, effective maintenance measures can be made before failure, and the risk of accidents and casualties will be decreased. Health monitoring can greatly reduce maintenance costs, and it is important to improve the safety of aircraft and extend the service life of equipment.

Statistical process control (SPC) is a process control method based on mathematical statistic and it is a way of stability control for outputs during production procedure [1]. SPC is widely used in industrial application. For example, several quality control data gradually increased, it means the defective rate is increased. The production process should be controlled, so that the quality of product is ensured, and the purpose of product quality monitoring is achieved.

As an effective data statistical method, SPC shows the process prevention principle. With the ability of prediction and monitoring, SPC is used in the field of malfunction prevention of power supply [2], robot system failure prediction [3], and unmanned aerial vehicle failure prediction [4]. The applicability of this method for the aircraft parameters has not been verified. Therefore, we focus on how to use SPC reasonably in aircraft health monitoring in this paper.

51.2 Statistical Process Control

SPC uses Shewhart's statistical process theory which is the control chart to judge the stability of the system. According to the distribution of data on control chart, the trend of the object can be got. Then some precautions are used to guarantee the system is under control so that the quality of production is ensured and optimized.

51.2.1 Control Chart Selection

There are many kinds of control chart of SPC. They are divided into measure control chart and count control chart. The measure control chart includes mean value and differential control chart, mean value and standard deviation control chart, single value and moving range control chart, etc. The count control chart includes nonperforming ratio control chart, number of defects control chart, etc. This article choose the single value and moving range control chart to monitor the health of system according to the data type and data size of the aircraft operating parameters.

51.2.2 The Theory of the Control Chart

The control chart is a process that using sample statistics to test that if the mean μ and the standard deviation σ change obviously. The most popular characteristic distribution function is normal distribution when the quality characteristics are continuous. The sample mean is $\bar{x}$, and the sample size is n, the sample probability is P and the sample significance level is α.

$$P\left(\left|\frac{\bar{x}-\mu}{\sigma/\sqrt{n}}\right| < z_{a/2}\right) = 1 - a \tag{51.1}$$

The system is in stable status when the significance level is α and mean μ does not change dramatically. The upper control limit, center limit, and the lower control limit are UCL, CL, LCL.

$$\mathrm{UCL} = \mu + \frac{\sigma Z_{\alpha/2}\sigma}{\sqrt{n}} \tag{51.2}$$

$$\mathrm{CL} = \mu \tag{51.3}$$

$$\mathrm{LCL} = \mu - \frac{\sigma Z_{\alpha/2}\sigma}{\sqrt{n}} \tag{51.4}$$

The sample control chart is illustrated in Fig. 51.1.

Usually, we use 3σ to define the control limit in the control chart. $z_{a/2}/\sqrt{n}$ is the upper quantile. Define $z_{a/2}/\sqrt{n} = 3$. If the feature point is between ULC and LCL, the equipment is running normally. Otherwise, the equipment is disabled.

The statistical distribution chart is illustrated in Fig. 51.2.

The probability of $\bar{x}$ in the domain of $(\mu - 3\sigma, \mu + 3\sigma)$ is 99.73 %. The probability of $\bar{x}$ out of the domain of $(\mu - 3\sigma, \mu + 3\sigma)$ is only 0.27 %.

51.2.3 The Criterion of the Control Chart

The method to identify abnormality is to analyze the Shewhart's Control Chart. If the distribution of data is consistent with the rule, it means the equipment is in abnormality. Though the data is within the control limit, the operation status can be analyzed through data graphics. It shows the thought of fault prognostics.

There are two kinds of rules to identify abnormality [5]. One is to check whether the points of the characteristic values are out of range. The other is to check whether the distribution of the characteristic values within the control limit is nonrandom.

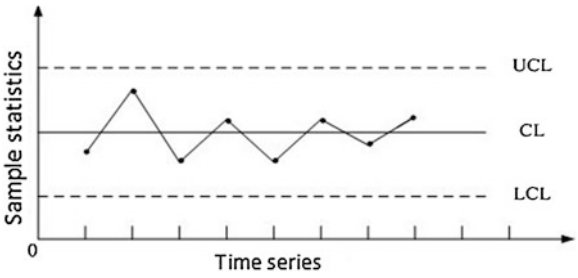

Fig. 51.1 Control chart

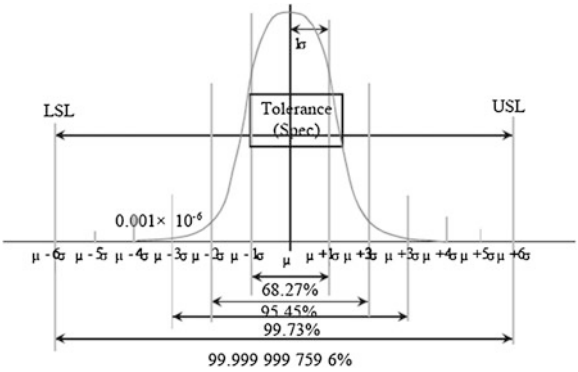

Fig. 51.2 Statistical distribution chart

The details for the second rule are shown as follows:

(1) 7 or more consecutive points are in the same side of the center line.
(2) At least 10 of the 11 consecutive points are in the same side of the center line. At least 12 of the 14 consecutive points are in the same side of the center line. At least 14 of the 17 consecutive points are in the same side of the center line. For 20 points, there are at least 16 points.
(3) 7 or more consecutive points share the same trend of rise or fall.
(4) At least 2 of 3 points are between the standard deviation 2σ and 3σ, or at least 3 of 7 points, or at least 4 of 13 points.
(5) The distance between the points and center line is in 1 standard deviation, 15 points are centered near the center line.
(6) The points vary periodically.

When the onboard system is in stable operation mode, values of some equipment parameters are under the normal distribution. So according to the statistic process control technology, fault symptoms can be found early, and fault prediction can be made.

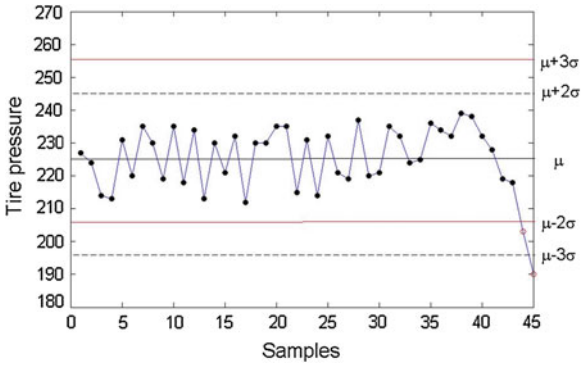

Fig. 51.3 Tire pressure control chart

51.3 Health Monitoring of Aircraft Important Parameters

Some parameters of the aircraft can reflect the change of aircraft health status. Three sets of data are discussed.

The data of aircraft main landing gear tire pressure is analyzed. The single value control chart is shown in Fig. 51.3.

The data randomly distributed around the mean value, and the value decreased gradually from the 38th point to the 45th point. The 44th point has exceeded warning limit, and the 45th point started to give an abnormal alert. In consequence, a conclusion can be made that the aircraft main landing gear may be abnormal according to the rule.

Another set of landing gear tire pressure data and the percentage of actual pump fuel data are analyzed. The control charts of single value are illustrated in Figs. 51.4 and 51.5.

In Fig. 51.4, the data are all under the limit. The value decreased gradually from the 18th point to the 27th point. According to the rule, the aircraft main landing gear may be abnormal. However, this set of data is all near the mean value, and it proves that all data are normal. So this is contrary to our previous conclusion. This method for monitoring the status of the aircraft has some limitations and it is possible to give false alarm.

In Fig. 51.5, each value of the data must be smaller than 1, which means that they are not normally distributed. After calculation, alarming upper bound is 1.0242 and warning upper bound is 1.1034, so that these two values make no sense. But the value decreased gradually from the 46th point to the 54th point. According to the third rule, we can give an abnormal alert at the 51st point. So for the non-normal distributed data, the downward trend of healthy aircraft also can be detected through certain rules, although the upper bounds make no sense.

Rule 1, rule 2, and rule 4 are not involved in these three analyses above. These three rules may be used under some situations not included in this paper. Rule 2 illustrated that at least 10 of the 11 consecutive points are at the same side of the center line. If these 10 consecutive points are close to mean value, which means

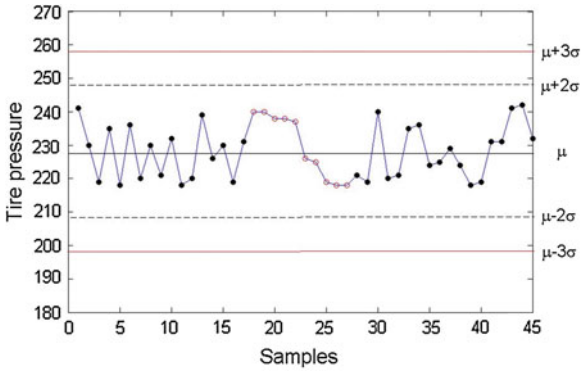

Fig. 51.4 Tire pressure control chart

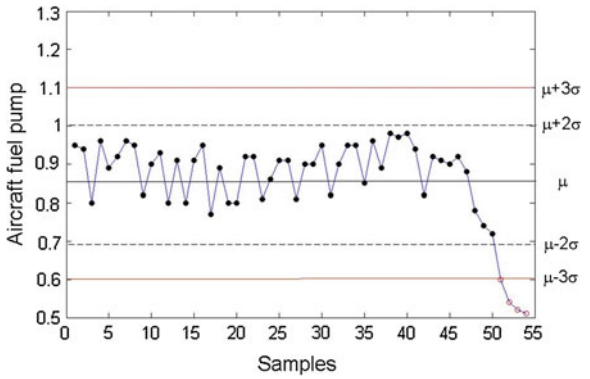

Fig. 51.5 Aircraft fuel pump control chart

these points are in normal operation, it would be unreasonable to make an abnormal alert for all the consecutive points. In order to solve these problems further research will be carried on. Different analysis method must be used for different types of data. It should be considered that whether the SPC analysis method is appropriate to other types of data.

51.4 Conclusion

The value of aircraft parameters can reflect the health status of certain component or system. Aircraft health monitoring based on the control chart and rule is studied in this paper. The results show that this method is not universal in aircraft parameters data analysis. For normally distributed data, the results based on the analysis comparing to rule may not be correct. For the non-normally distributed data, the downward trend of healthy aircraft also can be detected through certain rules. But the thresholds calculated by SPC method would make no sense. How to

find reasonable rules to deal with non-normal data and normal data and data with different physical meanings will be focused on our further research.

References

1. Zhang G, Sun J (2002) Chinese quality engineer handbook. Enterprise Management Press, Beijing
2. Wang R, Liu L, Qiu J-h (2009) Research on system of electrical source prognostics based on SPC. J Microcomput Inf 25:181–183 (in Chinese)
3. Wang R, Liu L, Xu F (2009) Research on prognostics technology of robot system based on SPC. J Hydromech Eng 37(6):227–230 (in Chinese)
4. Wang F, Li B, Feng W, Zhang W (2007) Application of the statistical process control in UAV fault prediction system. J China Meas Test 33(1):24–26 (in Chinese)
5. Zhong L, Han J, Liu H (2000) SPC technology theory and application. Publishing house of electronics industry, Beijing

Chapter 52
A Graphical Edge Method to Solve Dispersion Equation of Lamb Waves

Bing Li, Peng Duan, Lei Qiang and Jie Zhuo

Abstract Lamb wave dispersion curves are the fundamental of Lamb waves-based research and engineering application. Numerical solution is the only way to solve Rayleigh-Lamb equation and then the dispersion curves are obtained. Traditional-bisection method requires complex root intervals analyzing. A graphical-edge method is presented to simplify the process of solving dispersion equation of Lamb wave. First, solution intervals of the Lamb wave dispersion equation are divided and the standard dispersion equation is modified. Next, the graphical method is used to visualize abstract formulas. Combined with graphic boundary extraction method, the phase velocity dispersion curves are plotted. Graphic edge method can represent complex and abstract formulas graphically, simplifies the solution process and improves the solution efficiency.

Keywords Lamb waves · Dispersion equation · Phase velocity · Graphical edge method

52.1 Introduction

Lamb waves refer to those in thin plates (with planar dimensions being far greater than that of the thickness and with the wavelength being of the order of the thickness) that provide upper and lower boundaries to guide continuous propagation of the waves [1, 2]. Traditional ultrasonic nondestructive testing techniques, which are based on the bulk waves, are very time consuming, since they need an

B. Li · P. Duan · L. Qiang
School of Mechanical Engineering, Xi'an Jiaotong University, Xi'an, China

J. Zhuo (✉)
Institute of Acoustic Engineering, Northwestern Polytechnical University, Xi'an, China
e-mail: jzhuo@nwpu.edu.cn

J. Wang (ed.), *Proceedings of the First Symposium on Aviation Maintenance and Management-Volume I*, Lecture Notes in Electrical Engineering 296,
DOI: 10.1007/978-3-642-54236-7_52,

overall inspection of the structure point-by-point. However, Lamb waves which correspond to guided ultrasonic perturbations are potentially a very attractive solution since they can interrogate the entire thickness of the plate and propagate over long distances. Consequently, their use allows fast and efficient inspections of industrial structures such as pipeline inspection, rail testing [3–6]. But the dispersion characteristics, multiple wave modes and other complex propagation characteristics have restricted application of guided wave techniques. The dependence on the frequency of the phase and group velocities of the different Lamb modes is referred as the dispersion characteristics which are represented graphically in the dispersion curves [7–9]. The dispersion curves represent some basic information about Lamb waves, such as wavelength, phase velocity and group velocity at the frequency point [8, 9], and the basic information are extremely important for damage identification. Lamb wave dispersion curves are the fundamental of Lamb waves-based research and the Lamb wave propagation characteristics are visualized. Based on the curves, parameters in damage detection can be choosing and Lamb wave signals can be interpreted. Some Lamb wave-based damaged detection methods are developed according to the curves.

As a transcendental equation, the Lamb waves characteristic equations only have numerical solution. Traditional bisection method is the most popular method and it requires complicated root intervals analyzing.

In this paper, a new method is presented to solve the dispersion curves of phase velocity. The whole values of Rayleigh-Lamb equation in independent variables intervals are calculated and then the signs of the values are obtained. Dispersion curves exist in separatrix between the positive signs and negative signs and accuracy of solution dependent on the discrete degree of independent variables intervals.

The dispersion characteristics of Lamb waves in plate structure are also discussed in this paper [10]. A graphical edge method and theoretical derivation are presented, the dispersion curves of Lamb waves are calculated, which offer theoretical reference for engineering application of Lamb wave.

52.2 Solving Lamb Wave Dispersion Equations

Lamb waves are waves of plane strain that occur in a free plate, and the traction force must vanish on upper and lower surface of the plate. Different mode structures occur from point to point as wave incidence angle and frequency are varied [11]. The geometry of the free plate problem is governed by the equations of motion, with boundary conditions of surface tractions. The surfaces are considered traction-free. Ultrasonic excitation occurs at some point in the plate; as ultrasonic energy from the excitation region encounters the upper and lower bounding surfaces of the plate, mode conversions occur (L wave to T wave, and vice versa). After some travel in the plate, mode superposition cause the formation of “wave packets”, or what are commonly called guided wave modes in the plate.

Lamb waves in a plate consist of symmetric and antisymmetric modes [12]. The displacement potentials method based on Helmholtz decomposition is an efficient approach to decompose wave equation into two uncoupled parts under the plane strain condition [11].

Symmetric Modes

$$\frac{\tan(qh)}{\tan(ph)} = -\frac{4k^2pq}{(q^2-k^2)^2} \tag{52.1}$$

Antisymmetric Modes

$$\frac{\tan(qh)}{\tan(ph)} = -\frac{(q^2-k^2)^2}{4k^2pq} \tag{52.2}$$

where

$$p^2 = \frac{\omega^2}{C_L^2} - k^2, \tag{52.3}$$

$$q^2 = \frac{\omega^2}{C_T^2} - k^2, \tag{52.4}$$

$$k = \frac{\omega}{C_P} = \frac{2\pi f}{C_P}, \tag{52.5}$$

$$h = \frac{d}{2} \tag{52.6}$$

k, ω and d are the wavenumber, circular frequency of the wave and thickness of the plate, respectively. C_L and C_T are the velocities of longitudinal and transverse/shear modes (L stands for the longitudinal modes and T the transverse/shear modes hereafter). C_P is the phase velocity.

The relationship between circular frequency ω and wavenumber k can be obtained by solving Eqs. (52.1), (52.2). Then the relationship between phase velocity CP and circular frequency ω can be calculated [13, 14]. Equations (52.1) and (52.2) can be considered as relating the frequency ω to the wavenumber k of the Lamb wave modes, resulting in the frequency spectrum, or as relating the phase velocity CP to the frequency ω, resulting in the dispersion curves. It is known that, for any given frequency ω, there are an infinite number of wavenumbers that will satisfy Eqs. (52.1) and (52.2). A finite number of these wavenumbers will be real or purely imaginary, while infinitely many will be complex. The real numbers, which stand for propagation modes of wave structure, are only numbers that are meaningful when plots the dispersion curves. Details of the dispersion equations solving method will be given by solving the symmetric modes as an example.

Substituting (52.5) into Eq. (52.3), we obtain equation:

Table 52.1 Expression of coefficients *ABCD*

Coefficient	$0 < C_P < C_T$	$C_T < C_P < C_L$	$C_L < C_P$
A	a	a	a
B	bi	b	b
C	$-c$	ci	c
D	di	di	d

$a = (q'^2 - 1)^2 > 0$, $b = \lvert\pi q'/C_P\rvert > 0$, $c = 4\lvert p'q'\rvert > 0$, $d = \lvert\pi p'/C_P\rvert > 0$, i is imaginary unit

$$p = k\sqrt{\left(\frac{C_P^2}{C_L^2}\right) - 1} \tag{52.7}$$

Substituting (52.5) into Eq. (52.4), we obtain equation:

$$q = k\sqrt{\left(\frac{C_P^2}{C_T^2}\right) - 1} \tag{52.8}$$

Equation (52.1) can be rewritten into:

$$(q^2 - k^2)^2 \tan(qh) + 4k^2 pq \tan(ph) = 0 \tag{52.9}$$

Assume:

$$p' = \sqrt{\left(\frac{C_P^2}{C_L^2}\right) - 1}, \tag{52.10}$$

$$q' = \sqrt{\left(\frac{C_P^2}{C_T^2}\right) - 1} \tag{52.11}$$

Substituting Eqs. (52.5) (52.6) (52.7) (52.8) (52.10) (52.11) into Eq. (52.9), we obtain equation:

$$(q'^2 - 1)^2 \tan\left(\frac{\pi fd}{C_P} q'\right) + 4p'q' \tan\left(\frac{\pi fd}{C_P} p'\right) = 0 \tag{52.12}$$

Equation (52.12) is known as dispersion relations and the equation can be solved only by numerical methods. Bisection algorithm is widely used for solving the equation while the solution intervals are hard to be divided.

Assume $x = fd$ and rewrite Eq. (52.12) into the following form:

$$A \tan \mathrm{B}x + C \tan \mathrm{D}x = 0 \tag{52.13}$$

Coefficients *A, B, C, D* vary with C_P as shown in Table 52.1.

1. When $C_P = C_L$, $p' = 0$, formula (52.13) turns to trigonometric equation:

$$(q'^2 - 1)^2 \tan \frac{\pi q'}{c_p} x = 0, \tag{52.14}$$

The solution is $x = k \cdot C_P/q', (k, = 1, 2, 3, \ldots)$. When $C_P = C_T$, $q' = 0$, formula (52.13) turns into an identity and it is meaningless. When $C_P = \sqrt{2}C_T$, $q' = 1$, the solution is $x = (2k - 1)C_P/2p', (k = 1, 2, 3, \ldots)$.

2. when $0 < C_P < C_T$, formula (52.13) is

$$F(x) = a\text{th}\, bx - c\text{th}\, dx = 0 \tag{52.15}$$

3. when $C_T < C_P < C_L$, formula (52.13) is

$$F(x) = a \tan bx - c\text{th}\, dx = 0 \tag{52.16}$$

4. when $C_L < C_P$, formula (52.13) is

$$F(x) = a \tan bx + c \tan dx = 0 \tag{52.17}$$

In this paper, a new method is presented to obtain phase velocity disperse curves. First, divide the arguments C_P and fd into discrete vectors, and then calculate the left part of formula (52.13) on the whole interval. Get the positive or negative sign of the value, the curves of the boundary between positive and negative are the disperse curves needed. The accuracy of solution is based on the discrete degree of interval. The specific process is as follows:

1. First, calculates velocity of shear wave C_T and longitudinal wave C_L by using material parameter.
2. Then, define the range of C_P and fd and disperse the plane of C_P–fd to grid points, substitute coordinate values of every point into formulas (52.15), (52.16) or (52.17). The value of every grid point will be calculated, and if the value is positive, make it 1, else, make it −1.
3. Put the values from step (52.2) into a two-dimensional matrix $\boldsymbol{F}(n, m)$ (n, m represent the size of matrix, respond to vector size of the phase velocity C_P and frequency-thickness product fd).
4. Form a matrix by selecting the value from 2nd row to last row (i.e., $\boldsymbol{F}(2{:}n, m)$) in matrix $\boldsymbol{F}(n, m)$ and name the new matrix $\mathbf{FD}(n - 1, m)$. Form anther matrix by selecting the value from 1th row to row before last (i.e., $\boldsymbol{F}(1{:}n - 1, m)$) in matrix $\boldsymbol{F}(n, m)$ and name the new matrix $\mathbf{FU}(n - 1, m)$. Make $\mathbf{FS} = \mathbf{FU} - \mathbf{FD}$ and then the values in matrix **FS** are composed by 0, 2, −2.
5. Positions of the values 2 and −2 in matrix **FS** represent the relations between phase velocity C_P and frequency-thickness products fd. Get the position information and plot them, the phase velocity dispersion curves will be obtained.

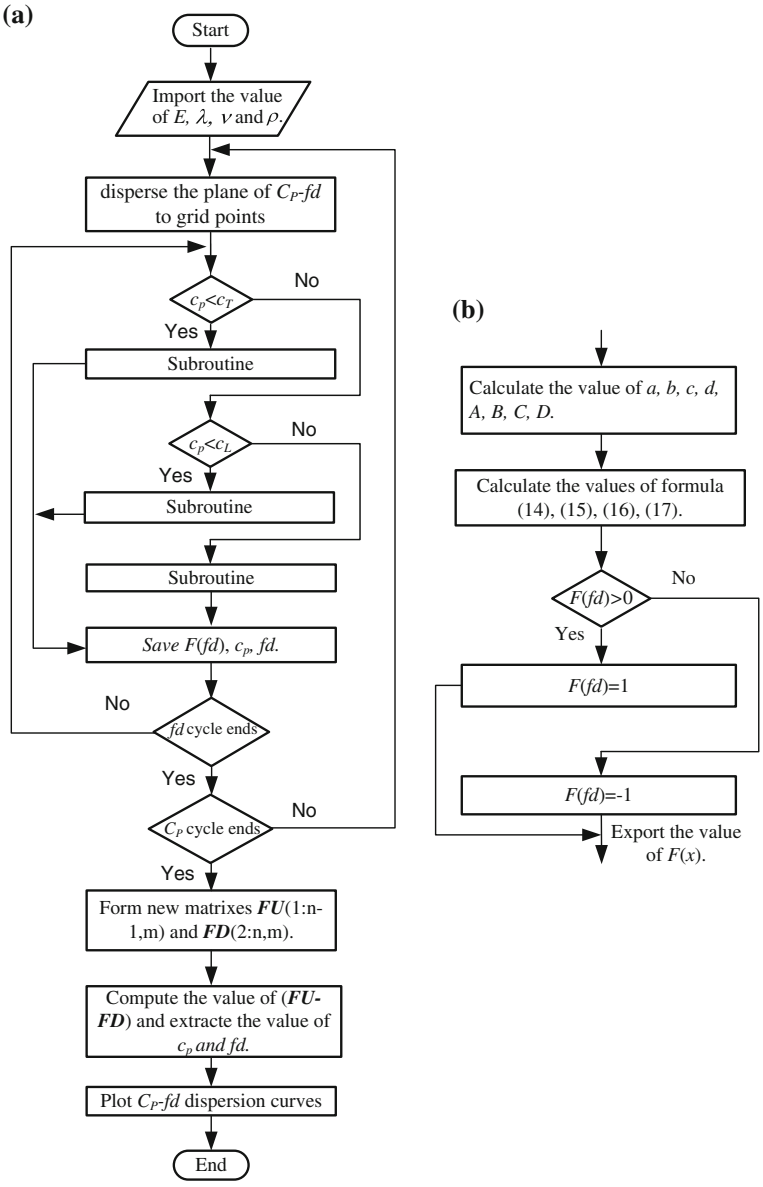

Fig. 52.1 Flow chart of equation solving process. **a** Main program flow chart. **b** Subroutine flow chart

The process above can be programed by applying software Matlab and the program flow chart is shown in Fig. 52.1.

Table 52.2 #1060 aluminum plate material parameters

Model	Density (ρ/kg·m^{-3})	Elastic modulus (E/GPa)	Poisson's ratio (v)
1060	2705	69	0.33

Shear wave velocity $C_T = 3097$ m/s, longitudinal wave velocity $C_L = 6148$ m/s

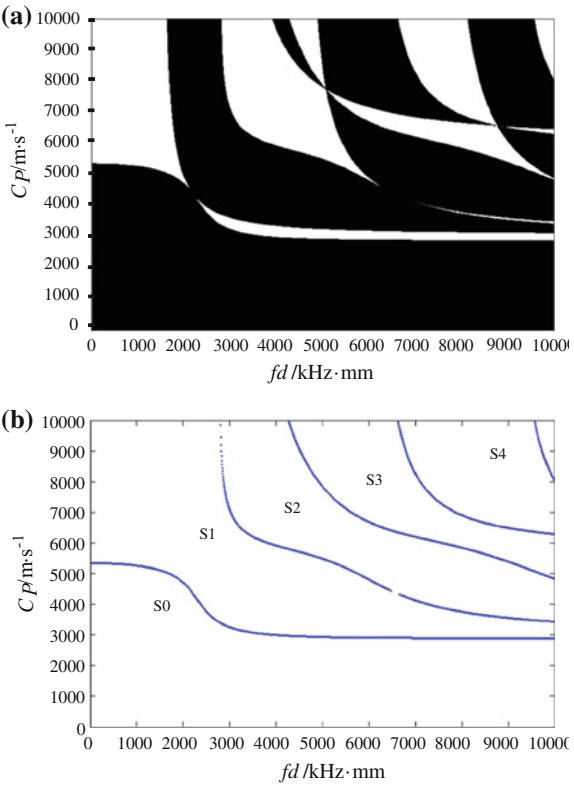

Fig. 52.2 Phase velocity dispersion curves of symmetric modes. **a** Distribution of values calculated from F(x). **b** Dispersion curves by boundary extraction

52.3 Examples

Calculation example: Lamb waves dispersion curves in #1060 aluminum plate (Thickness 1.5 mm) (Table 52.2).

The values of $F(x)$ that calculated by program are shown in Figs. 52.2 and 52.3. Values in the black area are 1 and those in the white area are -1. The boundaries between black and white areas represent dispersion curves.

As shown in Figs. 52.2 and 52.3, there are only two modes exist in the low frequency-thickness products area: S0 and A0. More modes, such as A1 and S1, appear while frequency increases. By using the graphical edge method, the dispersion curves can be obtained efficiently without using Bisection algorithm and the calculation precision can be controlled easily.

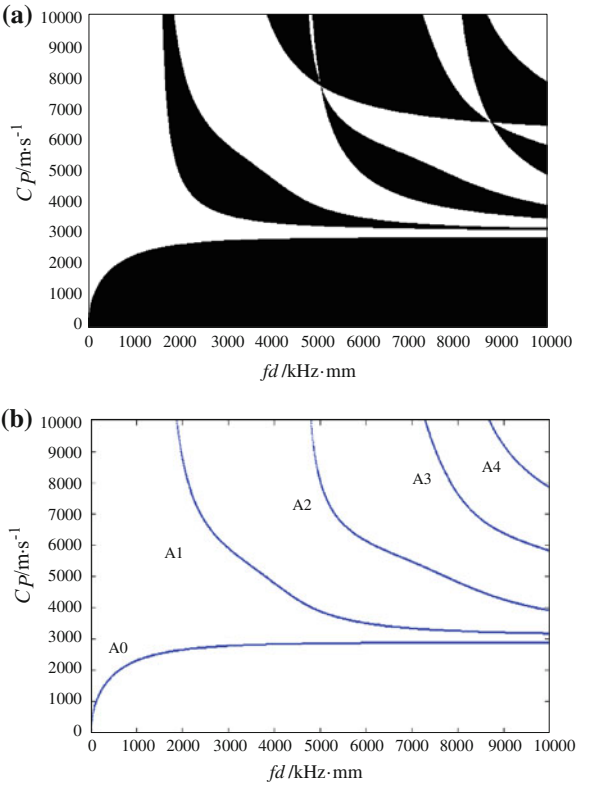

Fig. 52.3 Phase velocity dispersion curves of anti-symmetric modes. **a** Distribution of values calculated from F(x). **b** Dispersion curves by boundary extraction

52.4 Conclusions

The graphical edge method is used to obtain the Lamb wave dispersion curves in this paper. The abstract formulas are visualized and the solving process is simplified by the method. By solving the Lamb waves' dispersion equation, phase velocity dispersion curves are obtained and they are useful for future studies on Lamb wave-based research. It benefits on frequency selection, damage signal extraction and analysis, and increases the damage detection accuracy. The success of solving the dispersion curves is significant and it is meaningful to the later damage identification.

Application of the method simplified the calculation of Lamb wave dispersion curves. It does not need the complicated root intervals analyzing and accuracy of solution dependent on the discrete degree of independent variables intervals which can be easily controlled.

Acknowledgments This work is supported by the National Natural Science Foundation of China (No. 11104222).

References

1. Ding H (2010) Computational ultrasonics-analysis and application of ultrasonic field (in Chinese). Science Press, Beijing
2. Song ZD (2006) Ultrasonic guided wave technology in the pipeline defect detection (in Chinese). Tianjin University, Tianjin
3. Ivan B, Alessandro M (2006) Modeling wave propagation in damped waveguides of arbitrary cross-section. J Sound Vib 295:685–707
4. Philip WL (2008) Modeling and measurement of piezoelectric ultrasonic transducers for transmitting guided waves in rails. In: IEEE International Ultrasonics Symposium Proceedings, pp 410–413
5. Li YB, Jin SJ, Sun L (2005) Study on propagation characteristics of ultrasonic guided waves along the pipe (in Chinese). J Electronic Meas Instrum 19:63–66
6. Lee CM, Joseph L, Rose Y (2009) A guided wave approach to defect detection under shelling in rail. NDT&E Int 42:174–180
7. Wu B, Deng F, He CF (2006) Application of dispersion compensation in defect identification using guided wave (in Chinese). Chinese J Sci Instrum 27:2095–2097
8. Joseph LR (2002) A baseline and vision of ultrasonic guided wave inspection potential. J Pressure Vessel Technol 124:273–282
9. Takahiro H, Song WJ, Joseph LR (2003) Guided wave dispersion curves for a bar with an arbitrary cross-section, a rod and rail example. Ultrasonics 41:175–183
10. Jiao JP, Liu WH, Zeng XCH (2010) Design and implementation of omni-directional Lamb wave electromagnetic acoustic transducer (in Chinese). Chinese J Sci Instrum 31:1387–1393
11. Rose JL (2004) Ultrasonic waves in solid media. Trans. Science Press, Beijing, pp 294–296
12. Yan G, Zhou L (2007) Study on damage imaging for composite structure using Lamb wave (in Chinese). Chinese J Sci Instrum 28:583–589
13. Zheng XM, Zhao YZ, Shi YW (2003) Calculation for lamb wave dispersion curves (in Chinese). Nondestr Test 25:66–68
14. Ai C, Li J (2005) Numerical calculation for lamb wave frequency equation (in Chinese). Nondestr Testing 27:294–296

Chapter 53
Test Analysis of Complex Electronic Equipment Based on Multisignal Model

Huaming Tian, Baokuan Luan and Hong Xue

Abstract The equipment testability is a design characteristic to determine the equipment's active status accurately and isolate its internal breakdown. Regarding complex electronic equipment, it is difficult to realize the deep level failure isolation because of the multidimensional structure, the signal interlocks, and the complexity of internal causal relation. The multisignal model uses a system causal relationship of a multilayer direction graph, to build system failure dissemination characteristic establishment model. Using the multisignal model to descript complex electron equipment, the causes and effects dependence, the TEAMS model can carry on the test appraisal in the defective space and improve electronic system fault isolation rate and the coverage fraction. As the multisignal model's modeling method is simple, the diagnosis speed is quick, and it can improve system's test, it may apply in complicated system's test design, the fault mode influence, the failure diagnosis and the test appraisal, and so on, meets the modern complex electron system's failure diagnosis need.

Keywords Multisignal model · Test analysis · Failure diagnosis · TEAMS

53.1 Introduction

Along with the military weaponry performance's enhancement and complex increase, each kind of large-scale complex electronic system emerges unceasingly, the failure diagnosis proposed a higher request, hoped urgently enhances the

H. Tian (✉) · B. Luan
Qingdao Branch of Naval Aeronautical Engineering Academy, Qingdao 266041, China
e-mail: tianhm3000@163.com

H. Xue
Qingdao Licun River Sewage Treatment Plant, Qingdao 266041, China

J. Wang (ed.), *Proceedings of the First Symposium on Aviation Maintenance and Management-Volume I*, Lecture Notes in Electrical Engineering 296,
DOI: 10.1007/978-3-642-54236-7_53,

electronic system overall reliability and the maintainability. The system's testability is one kind of design characteristic to determine the product's active status accurately and isolates its internal breakdown, which causes system's monitoring, the test, and the diagnosis simple and rapid with system's reliability, maintainability, and the usability which is closely related, a test high system means good breakdown coverage fraction and failure isolation rate (FIR) [1]. Studying the complex electronic system's test, on one hand is helpful in the system design personnel which provides the higher failure detection rate (FDR) for the system and failure isolation rate BITE (within the aircraft test facility), as well as the science reasonable test connection, enhances the product from the interior diagnosis ability and the exterior diagnosis ability; On the other hand, it also provides automatic test equipment (ATE) designers for the synthesis diagnosis project design rationale, facilitates, determines the product condition, and the isolation breakdown effectively.

The multisignal model is one kind of model analysis method which uses lamination oriented graph expression system structure attribute to build the fault propagation characteristic models [2]. The multisignal model is introduced by the American Qualtech System Company (testability engineering and maintenance system—The test project and the maintenance system) and is applied in complicated system's test design, the fault mode influence and the harm analysis, the TPS development, the failure diagnosis and the test appraisal, and so on, obtains the widespread application in the overseas new spacecraft failure diagnosis.

53.2 Multisignal Model's Modeling

TEAMS using the merit and ability of modular inference, through methods of feedback mechanism, parameter renewal means, and expert input, causes the system test and the maintenance solution consummate gradually [3]. TEAMS may use the large-scale interconnection system to carry on the multisignal modeling, and obtain the part and the test dependence; its graphical interface simplifies large-scale complex, restructures the breakdown fault-tolerant as well as hierarchy system's foundation and assembly, and the examination and revision work.

53.2.1 Modeling Method

Speaking of the majority situations, the multisignal model's modeling process may divide into four steps:

1. Constructing system's structural model

In the TEAMS software, system's structural model can induct the production automatically from Vhdl, in the Edif model or constructs directly by the graphical

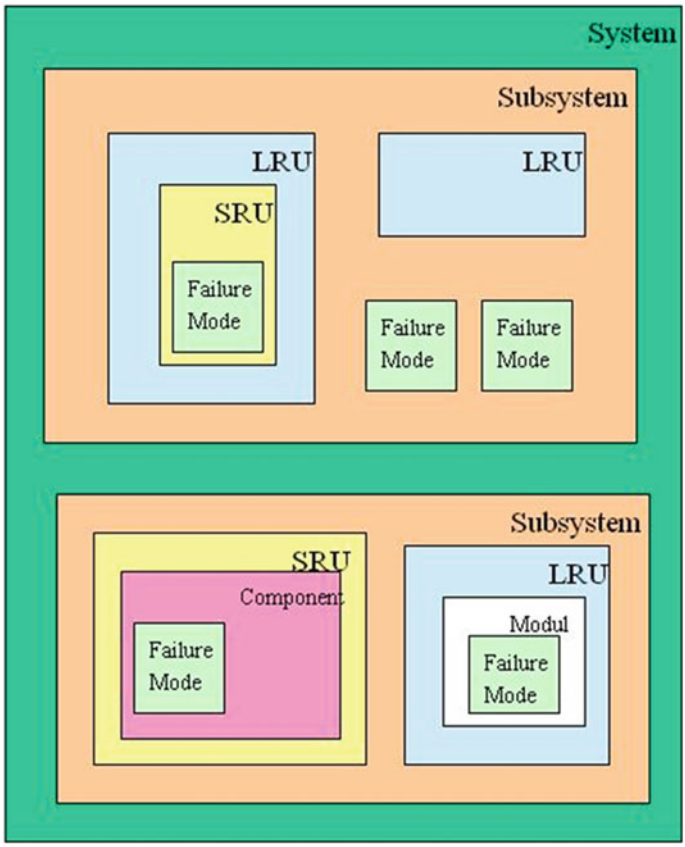

Fig. 53.1 TEAMS model hierarchical structure

user interface. TEAMS supports eight levels such as System, Subsystem, LRU, SRU, Module, Submodule, Component, and the Failure (in Fig. 53.1), the user may act according to the demand, carries on the nimble analysis, and the appraisal to the identical model in different levels [4].

The complex electronic system may carry on the stepwise decomposition through the union physical demand to the system structure composition, the method to construct system's structural model. System model's bottom step may accordingly need to divide the scene removable unit (LRU) or SRU, for example, some radio station's composition structure with the TEAMS multisignal model building follows corresponding relationships: The radio station complete machine corresponds the system level for the system module, below contains the receiver transmitter, the frequency synthesizer small steelyard system corresponds the subsystem level, but under the frequency synthesizer subsystem contains various frequency bands subsystem, its corresponding model rank is the subsystem level similarly, contains the scene removable module/groupware/circuit wafer under

various seeds system, its corresponding level is TEAMS multisignal model LRU level. To complicate system after structure stepwise decomposition, hierarchization structural model is producted. It is noteworthy that the LRU determination is according to the actual service, not necessarily of complexity low module, the module 'OR' circuit board. Sometimes it needs to compare the order of complexity, time taking the combination even cabinet which penetrates with difficulty in the scene services to take the LRU level, sometimes needs the fractionation primary device as the LRU processing, to reduce as far as possible separately the line maintenance time to short, the replacement circuit unit scale falls to is smallest.

2. Increasing signal to module and test point

The signal collection can obtain the recognition from the function standard or in the transfer function basic variable. Usually, it may define the signal regarding any unique attribute to which it relates. The key of multi-signal model building is to analyze model system's function, connect the bottom module, and establish the complete signal chart [5]. The actual system function division needs to follow the following principle: ① The function division must defer to the system-level function division, simultaneously requests cover all modules; ② The guarantee signal moves toward the integrity and the direction are unified, cannot form the closed loop return route, if in the actual electric circuit has the closed loop return route, needs to make split-ring processing, may use the heavy definition function or insert the break point means to realize; ③ The system function division must be advantageous to the module failure isolation, namely through system function's inspection, reduces the failure diagnosis strategy tree's scale as far as possible. For example, in some short-range navigation system, the signal received may be divided into channels such as logarithm receive, linear receive, navigation receive, if the system function only then receive function, its failure diagnosis strategy tree must cover channels and logarithm receive, linear receive, navigation receive, but the test spots are many and the testing time is long. If suppose the system function for the logarithm receive function, the linear receive function, the navigation receive function, may through divide the system function inspection, the original failure diagnosis strategy tree into to three young trees, reduced the failure diagnosis strategy tree's scale greatly, reducing the testing time.

3. Adjusting ordering model on actual situation

In the following situations, the model needs to carry on the corresponding revision and the adjustment.

① If a system has some modules to block a signal collection or the complete breakdown, it should define one function as these modules to block the signal collection.
② If a system has some modules to be able to map one or many signals to another signal subset, then must define a group of mapping function as these modules.

③ If a complex signal (or function) is constituted by a group of simple signals, then these simple (either first floor) signals may be combination of complex signal or the ultra signal.
④ If a system existence redundancy (for example, if A and B are breakdown, the system is breakdown), then uses parallel node to redundancy partial modelings.
⑤ If a system has different movement patterns, it uses "transforms–SWITCH" node modeling.
⑥ If a system has the removable digital integrated circuit, it uses the equivalent model. The equivalent model is the chip simplified model, contains and examines the breakdown in the chip (not isolates breakdown) the essential relevant information.

4. Confirmating model validity

The multisignal model's construction effect may confirm from the following three aspects:

① The multisignal model's construction may build from easy to difficult, consummate gradually, namely acts according to some common knowledge and the system structure first in the initial stage composes the construction system's preliminary model, after that along with system cognition thorough and application demand statement, through, to increase the definition signal and so on gradually the perfect model;
② The multisignal model's construction has nothing to do with the test point establishment;
③ As a result of the above two characteristics, the multisignal model may apply in the product design at early time stage, passes through in the entire product life cycle process.

The diagnosis project analysis appraisal makes the objective quantification to the user design diagnosis ability or the diagnosis plan the appraisal, simultaneously pointed out in the test diagnosis design proposal exists the insufficiency, and be advantageous further improves.

53.2.2 Test Design Target

Carries on the test analysis using the multisignal model, the content and flow are as shown in Fig. 53.2.

First according to the product structure and the functional design as well as the test plan construction system's multisignal model, it can be completed by the multisignal model which feeds back the road analysis, may produce the breakdown based on the multisignal model–Tests the correlation matrix, further completes the product by the single breakdown characteristic analysis, the multibreakdown characteristic analysis, and the test parametric analysis. The appraisal test plan's two important targets are FDR and FIR.

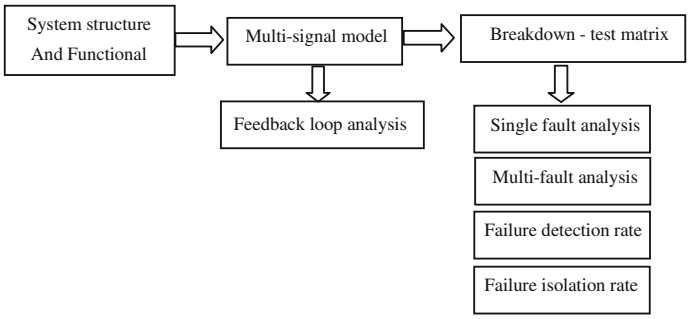

Fig. 53.2 Multisignal model test analysis flow

FDR may be represented as:

$$\mathrm{FDR} = \mathrm{ND} / \mathrm{N} \times 100\,\% \tag{53.1}$$

In the formula, ND is the breakdown number which examines correctly under the rated conditions; N is the breakdown total which occurs in the stipulation operating time.

FIR may be represented as:

$$\mathrm{FIR} = \mathrm{NL} / \mathrm{ND} \times 100\,\% \tag{53.2}$$

In the formula, NL isolates correctly to L unit breakdown number.

53.3 TEAMS System Test Analysis Realization

The test project analysis carries on the analysis and the appraisal to the system model test design, the development personnel must input system's test diagnosis plan (i.e., test design). Carrying on the failure diagnosis to the electronic system to be possible to use each test method, as the aircraft within tests, exterior test, manual test, and test automation, and so on. Among them, within the aircraft tests (BIT) is one kind of automatic detection designed in UUT and isolates the breakdown ability, monitors it in the UUT duration of work cycle to transport the row state prompt discovery breakdown and to report alarm continuously [6]. BIT may reduce greatly to the exterior test facility and the service technical personnel technical level request. When carrying on the test analysis, first, through complicating system's analysis, gives own BITE or system reserved test point; Next, obtained in the system through these test points is each part's failure test dependence, the oriented graph expresses the part and the fault propagation relations; Finally, transports with established system model, carry on measurable and the fail-safe analysis, may obtain test appraisal target FDR and FIR, simultaneously, it can point out in the test diagnosis design proposal exists the insufficiency, is advantageous further improves.

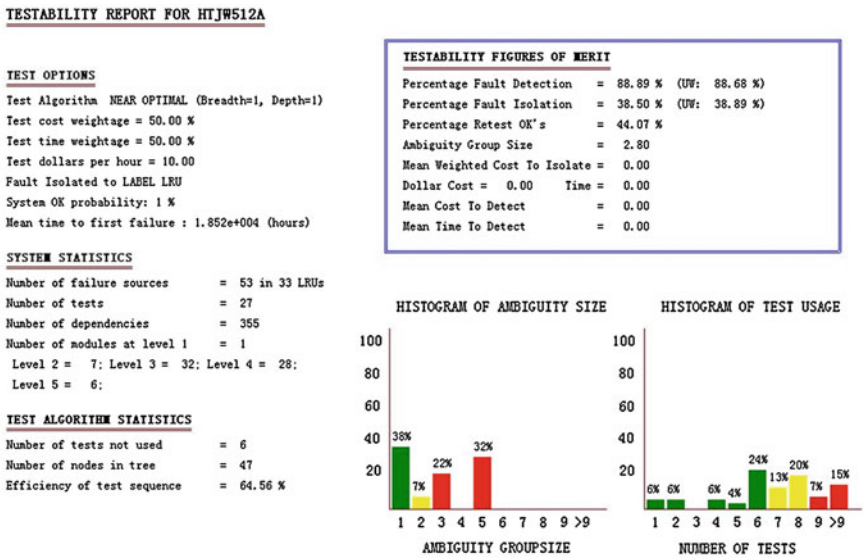

Fig. 53.3 System test design appraisal result

53.3.1 TEAMS System Test Target Analysis

Carrying on some radio station test target analysis, according to radio station each constituent's structural feature and the function, establishes multisignal model, transports system reserved test point with TEAMS system input, owns BITE to take system's test diagnosis plan, establishes the breakdown—test matrix, and the FIR carries on the definition to radio station's FDR, transports the line of TEAMS system, obtains radio station's test design evaluation result as shown in Fig. 53.3.

From Fig. 53.3, the breakdown coverage fraction (Percentage Fault Detection) is 88.89 %, the FIR (Percentage Fault Isolation) is 38.50 %.

53.3.2 Test Target Analysis Improvement

The test improvement designers unify the actual service situation, increase the position to the test point to carry on the choices, the choice principle is to first increase the test point easy to complete, place with the test procedure complex and the time long test point next, regarding completely the test point which has no testability. All record as the test report for further improves suggestion. In the test improvement process, the TEAMS software can aim at excess-odd test to carry on the reminder, will prompt the designers to be related to the test point to reject from the test diagnosis plan. At the same time, the TEAMS software will also carry on

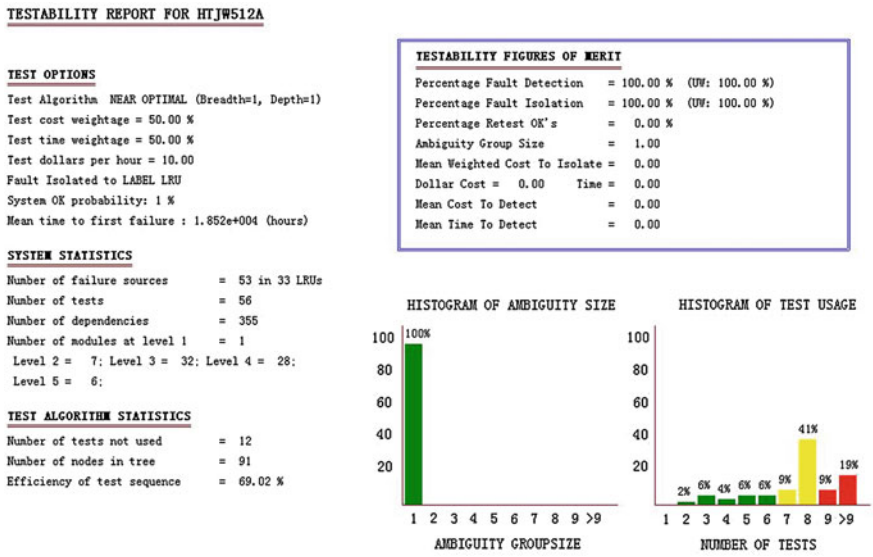

Fig. 53.4 Appraisal result after test design improvement

the prompt to the failure test nonmethod cover module. Through the improvement of the electronic system's test design, obtains the final test plan, TEAMS appraisal result as shown in Fig. 53.4, may see, its test target after obtained enormous new face.

From Fig. 53.4, the breakdown coverage fraction is 100.00 %. The FIR is 100.00 %.

From TEAMS production's test improvement's target, it proves that if radio station takes the test diagnosis plan after the improvement test design, the TEAMS system gives finally the breakdown coverage fraction which may achieve 100 %, namely in this radio station's scene failure diagnosis, through after improving the test point test, may carry on the test analysis to radio station's each constituent and all test points. But radio station's FIR has also achieved 100 %, the proof is the breakdown diagnosis and localization and are accurate through the TEAMS system.

53.4 Conclusions

The electronic system's multisignal model's establishment and the test analysis appraisal are the foundation work of the failure diagnosis. Its goal realizes the electronic system's most superior failure test diagnosis work. As the test technology is core, the failure diagnosis plan slightly refers to failure detection and isolation testing sequence. Based on the multisignal model's diagnosis plan, design

is measured slightly that in the object multisignal model foundation, according to the corresponding test optimal algorithm, after tests selects first, the smooth formulation diagnostic test plan slightly.

The test diagnosis knows the knowledge from the estimator, the expert or circuit development personnel, the commonly test knowledge are testing position, test condition, measuring instrument, determination criterion, and so on. After the test design improvement had ended, the TEAMS software may need to know the test diagnosis data and the diagnosis content according to the service with the test diagnosis knowledge which the production different rank, the different diagnosis essential factor, including BIT data, PMA IETM and ATE test order, and so on, its data format contains XML, HTML, TRD, and AI-ESTATE, and so on. Simultaneously, the TEAMS software may act according to the artificial intelligence algorithm automatic production optimization the diagnosis plan slightly binary tree, through this diagnosis binary tree's inquiry and the traversal, the servicemen may judge breakdown and isolate crashes conveniently.

In brief, using the multisignal model description complex electron equipment, the causes and effects dependence, and modeling TEAMS in the defective space, it can construct the failure diagnosis model of the complex electronic equipment highly effective, enhance its FIR. This method can adapt the complex electronic system's failure diagnosis for high diagnosis speed.

References

1. Zhang Q, Long B, Yang X (2011) The research of measurable indicators based on multi-signal model. Electron Meas Technol 34:19–22 (in Chinese)
2. Guangbin F, Guangyao L, Kaoli H (2010) A testability analysis system based on multi-signal model. Comput Meas Control 19:2102–2104 (in Chinese)
3. Wang J (2010) Fault testability technology of digital circuit board for radar. Foreign Electron Meas Technol 29:53–55 (in Chinese)
4. Yang Z-y, Xu A-q, Wang Z-l (2009) Research on improving failure mode modeling method of multi-signal model. Microcomput Inf 25:151–153 (in Chinese)
5. Si B, Yuan S-z, Li J-h (2011) Application of multi-signal modeling methodology in a real-time fault diagnosis system. Electron Instrum Cust 18:61–64 (in Chinese)
6. Shi J-y, Zhang X, ZOU T-g (2011) Application of multi-signal modeling and diagnosis strategy design technology. Syst Eng Electron 33:811–816 (in Chinese)

Chapter 54
The Optimal Configuration Research of Five Redundant SIMU System

Zhao XiaoBei

Abstract For the five redundant SIMU system that composed of three orthogonal meters and two oblique meters, three kinds of optimal navigation performance indicators are introduced and the equivalence of these three indicators is proved. The reliability for multiple redundant system is analyzed and compared. In the case of the optimal navigation performance configuration for three different five redundant configurations, the best configuration is deduced, and the configuration is studied for the highest installation accuracy, three kinds of integrated optimal configuration is obtained finally.

Keywords Redundant system · Navigation performance indicator · Installation accuracy · Optimal configuration

54.1 Introduction

An Inertial navigation system (INS) requires at least three accelerometers and three gyroscopes to get the position, speed, altitude, and other navigation information. Since the 1970s, Redundancy techniques began to be studied extensively to increase system reliability and enhance navigational accuracy and so on. Therefore, the structure configuration of redundant INS is an important research direction. During the past four decades, reliability has always been an indispensable issue in various complex systems (such as industrial production and power systems) and safety–critical systems (such as nuclear energy power systems, control of the military, and spaceship).

Z. XiaoBei (✉)
Northwestern Polytechnical University, Xi'an, ShaanXi, China
e-mail: zhaoxiaobei@nwpu.edu.cn

J. Wang (ed.), *Proceedings of the First Symposium on Aviation Maintenance and Management-Volume I*, Lecture Notes in Electrical Engineering 296,
DOI: 10.1007/978-3-642-54236-7_54,

In the platform INS, generally the measuring axes of gyroscope and accelerometer install along the mutually perpendicular coordinate axes. Thus, when an inertial device fails, the system will not work. To improve reliability, the carrier can be configured as two systems. As a result of redundancy technology, the number of Inertia Device Fault tolerance increased, thereby improving the reliability of the system. Currently, redundant strap down inertial measurement unit (SIMU) is mainly installed in oblique style, such as: the four redundant oblique installation program mentioned in Ref. [1], whose four measuring axes is placed along four axes of semi-octahedron, with geometric symmetry; the redundant system mentioned in Ref. [2] which consist of six single degree of freedom gyroscopes, whose measuring axes is placed along the direction normal to the six flats of the dodecahedron, with geometric symmetry, too. According to the three different five redundant configurations mentioned in Ref. [3] and measurement accuracy indicators mentioned in Ref. [4], this paper can give the three kinds of integrated optimal configuration.

54.2 Configuration Program Analysis

54.2.1 Five Sensitive Components' Configuration Program and the Respective Measurement Equation

Tilt array installation program: The five sensitive components' installation is evenly distributed on the conical surface whose half-cone vertex angle is θ_1. Specific installation method is shown in Fig. 54.1a.

α_1 shown in Fig. 54.1a is the angle between the Z-axis and the m_1-axis' projection line in the XOZ surface. Counterclockwise direction is positive. The projection angles of m_2, m_3, m_4 and m_5-axes are $\alpha_1 + 72°$, $\alpha_1 + 144°$, $\alpha_1 - 144°$ and $\alpha_1 - 72°$. The measurement equation is as follows:

$$m = H_1\omega = \begin{bmatrix} \sin\theta_1 \sin\alpha_1 & \cos\theta_1 & \sin\theta_1 \cos\alpha_1 \\ \sin\theta_1 \sin(\alpha_1 + 72°) & \cos\theta_1 & \sin\theta_1 \cos(\alpha_1 + 72°) \\ \sin\theta_1 \sin(\alpha_1 + 144°) & \cos\theta_1 & \sin\theta_1 \cos(\alpha_1 + 144°) \\ \sin\theta_1 \sin(\alpha_1 - 144°) & \cos\theta_1 & \sin\theta_1 \cos(\alpha_1 - 144°) \\ \sin\theta_1 \sin(\alpha_1 - 72°) & \cos\theta_1 & \sin\theta_1 \cos(\alpha_1 - 72°) \end{bmatrix} \begin{bmatrix} \omega_x \\ \omega_y \\ \omega_z \end{bmatrix}.$$

The difference between program (b) and program (a) is that there are only four sensitive axes' installation is evenly distributed on the conical surface whose half-cone vertex angle is θ_2. Another axis' direction is along the positive Y-axis. Specific installation method is shown in Fig. 54.1b.

α_2 shown in Fig. 54.1b is the angle between the Z-axis and the m_2-axis' projection line in the XOZ surface. Counterclockwise direction is positive. The projection angles of m_3, m_4 and m_5-axes are $\alpha_2 + 90°$, $\alpha_2 + 180°$ and $\alpha_2 - 90°$. The measurement equation is as follows:

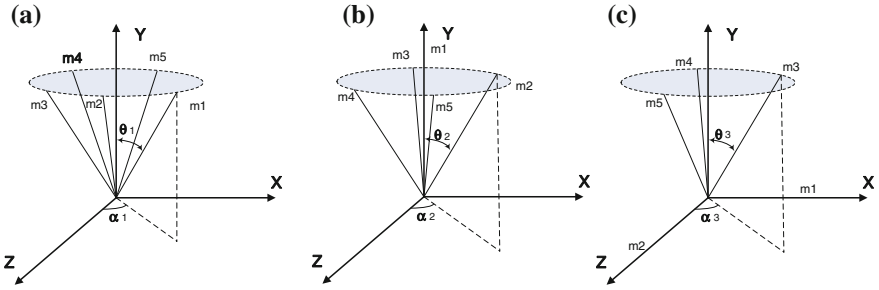

Fig. 54.1 Tilt array installation program **a** five sensitive components' installation **b** four sensitive components' installation **c** three sensitive components' installation

$$m = H_2\omega = \begin{bmatrix} 0 & 1 & 0 \\ \sin\theta_2 \sin\alpha_2 & \cos\theta_2 & \sin\theta_2 \cos\alpha_2 \\ \sin\theta_2 \sin(\alpha_2 + 90^\circ) & \cos\theta_2 & \sin\theta_2 \cos(\alpha_2 + 90^\circ) \\ \sin\theta_2 \sin(\alpha_2 + 180^\circ) & \cos\theta_2 & \sin\theta_2 \cos(\alpha_2 + 180^\circ) \\ \sin\theta_2 \sin(\alpha_2 - 90^\circ) & \cos\theta_2 & \sin\theta_2 \cos(\alpha_2 - 90^\circ) \end{bmatrix} \begin{bmatrix} \omega_x \\ \omega_y \\ \omega_z \end{bmatrix}.$$

The difference between program (c) and program (b) is that there were only three sensitive axes' installation is evenly distributed on the conical surface whose half-cone vertex angle is θ_3. Another two axes' directions are along the positive X-axis and positive Z-axis. Specific installation method was shown in Fig. 54.1c.

α_3 shown in Fig. 54.1c is the angle between the Z-axis and the m_3-axis' projection line in the XOZ surface. Counterclockwise direction is positive. The projection angles of m_4 and m_5-axes are $\alpha_3 + 120^\circ$ and $\alpha_3 - 120^\circ$. The measurement equation is as follows:

$$m = H_3\omega = \begin{bmatrix} 1 & 0 & 0 \\ 0 & 0 & 1 \\ \sin\theta_3 \sin\alpha_3 & \cos\theta_3 & \sin\theta_3 \cos\alpha_3 \\ \sin\theta_3 \sin(\alpha_2 + 120^\circ) & \cos\theta_3 & \sin\theta_3 \cos(\alpha_3 + 120^\circ) \\ \sin\theta_3 \sin(\alpha_3 - 120^\circ) & \cos\theta_3 & \sin\theta_3 \cos(\alpha_3 - 120^\circ) \end{bmatrix} \begin{bmatrix} \omega_x \\ \omega_y \\ \omega_z \end{bmatrix}.$$

54.2.2 Optimal Allocation Analysis

Although three programs were different, but their optimal allocation's performance indicators were the same, the analysis is as follows:

Suppose e is a zero-mean Gaussian random vector, Literature [5] proposed the following optimal allocation's performance indicators:

$$F_p = \sqrt{|G|} \tag{54.1}$$

$G = (H^t H)^{-1}$, H is the measurement matrix. Optimal allocation should make the performance indicators minimum. And the necessary and sufficient conditions of getting the best value are: $G^{-1} = (n/3) \cdot I$ (n is the number of sensitive components which is installed). In other words, the sum of squares of the modulus of H's each column are $n/3$. And the columns are Orthogonal to each other.

According to the above conditions, calculate these three programs. To simplify the model, set θ_1, θ_2, θ_3 both in $(0°, 90°)$. For program three, the following is easy to get from the measurement matrix H_3:

$$G_3^{-1} = (H_3^T H_3) = \begin{bmatrix} 1 + \frac{3}{2}\sin^2\theta_3 & 0 & 0 \\ 0 & 3\cos^2\theta_3 & 0 \\ 0 & 0 & 1 + \frac{3}{2}\sin^2\theta_3 \end{bmatrix}. \tag{54.2}$$

According to the optimal allocation's performance indicators, the diagonal values are equal and the modulus of each column are all $5/3$, it could be obtained that $\sin^2\theta_3 = 4/9$. Because of $\theta_3 \in (0°, 90°)$, we can determine that $\theta_3 = 41.81°$. Since there is no α_3 in the formula (54.2), conclusions can be drawn that: In program three, regardless of the value of α_3, the optimal configuration occurs when $\theta_3 = 41.81°$.

In the same way, for program two, the following is easy to get from the measurement matrix H_2:

$$G_2^{-1} = (H_2^T H_2) = \begin{bmatrix} 2\sin^2\theta_2 & 0 & 0 \\ 0 & 4\cos^2\theta_2 + 1 & 0 \\ 0 & 0 & 2\sin^2\theta_2 \end{bmatrix}.$$

Conclusions can be drawn that: In program two, regardless of the value of α_2, the optimal configuration occurs when $\theta_2 = 65.905°$.

In the same way, for program one, the following is easy to get from the measurement matrix H_1:

$$G_1^{-1} = (H_1^T H_1) = \begin{bmatrix} \frac{5}{2}\sin^2\theta_1 & 0 & 0 \\ 0 & 5\cos^2\theta_1 & 0 \\ 0 & 0 & \frac{5}{2}\sin^2\theta_1 \end{bmatrix}.$$

Conclusions can be drawn that: In program two, regardless of the value of α_1, the optimal configuration occurs when $\theta_1 = 54.74°$.

The α obtained from above is entirely the same with the optimal design of α in the Literature [3].

54.3 The Analysis of Redundant Configuration Program's Reliability

More than four gyroscopes can constitute a redundant system. Generally speaking, the more redundant number of gyroscopes, the higher reliability of the system. Before reliability analysis, assuming that all sensitive components are subject to

the same failure distribution, failure rate is subject to constant exponential distribution, any measurement axes of two sensors are not collinear, any measurement axes of three sensors are not coplanar, therefore, the reliability expression of single sensitive component is:

$$R(t) = e^{-\lambda t} \tag{54.3}$$

λ is the number of failures in the unit time, the mean time between failure is:

$$\text{MTBF} = \int_0^\infty R(t)dt = \frac{1}{\lambda}. \tag{54.4}$$

When there are m inertial instruments which are same and have the same reliability R, allowing n of them fail ($m > n$), the system reliability is:

$$R_e = \sum_{i=k}^{m} C_m^i R^i (1-R)^{m-i} \tag{54.5}$$

$k = m - n$, i is the number of instruments which are working.

In SINS (strapdown inertial navigation system) system, in order to compare the reliability of nonredundant system with redundant system, assuming the failure events are independent of each other and the other elements are the ideal state, the reliability of nonredundant system is decided by the reliability product of three gyroscopes:

$$R_3 = R^3 = e^{-3\lambda t} \tag{54.6}$$

$$\text{MTBF} = \int_0^\infty e^{-3\lambda t}dt = \frac{1}{3\lambda}. \tag{54.7}$$

For redundant system, the probability that the four single degree of freedom gyroscopes are all working is:

$$P(4) = R_4 = e^{-4\lambda}. \tag{54.8}$$

The probability that any three gyroscopes are working is:

$$P(3) = 4R^3(1-R). \tag{54.9}$$

The mission reliability of redundant system which consists of any four single degree of freedom gyroscopes is the sum of the two above-mentioned:

$$R_e = 4e^{-3\lambda} - 3e^{-4\lambda} \tag{54.10}$$

$$\text{MTBF}_4 = \int_0^\infty (4e^{-3\lambda} - 3e^{-4\lambda})dt = 7/12\lambda. \tag{54.11}$$

Table 54.1 The reliability and MTBF of single degree of freedom gyroscope redundant configuration system

The number of gyroscope (m)	Reliability	MTBF	Ratio
3	$e^{-3\lambda t}$	$\frac{1}{3\lambda}$	1
4	$4e^{-3\lambda t} - 3e^{-4\lambda t}$	$\frac{7}{12\lambda}$	1.75
5	$10e^{-3\lambda t} - 15e^{-4\lambda t} + 6e^{-5\lambda t}$	$\frac{47}{60\lambda}$	2.35
6	$20e^{-3\lambda t} - 45e^{-4\lambda t} + 36e^{-5\lambda t} - 10e^{-6\lambda t}$	$\frac{57}{60\lambda}$	2.86

The above method can be used to calculate the reliability and MTBF of common gyroscope redundant configuration system, the Table 54.1 is as follows:

It can be seen from the above table that the MTBF of a redundant system increased with the increase of the number of the gyroscopes, but the rate of increase is not proportionally linear relationship. With the increase of the number of the gyroscopes, both the growth rate of MTBF and the growth rate of reliability are getting smaller and smaller. Therefore, when choosing the number of redundancy, we should take the case of the system (such as volume, weight and cost, etc.) into account, in order to select the appropriate number of gyroscopes.

54.4 The Analysis of Redundant Configuration Installation Program's Accuracy

The redundant system consisting of five single degree of freedom gyroscopes has a total of $C_5^3 = 10$ operating modes. The measurement accuracy of different modes is not necessarily the same. Measurement accuracy had a relationship with the absolute value of the measurement matrix determinant in operating mode. The greater the absolute value, the higher the accuracy. The operating modes for five redundant configuration systems are: 123, 124, 125, 134, 135, 145, 234, 235, 245, 345.

(1) For program one: when $\theta_1 = 54.74°$, under optimal configuration, the 10 operating modes can be divided into the following two categories according to their absolute values:

(1) $|A| \approx 0.5059$
Gyroscopes combination mode: 123, 125, 145, 234, 345
(2) $|A| \approx 0.8185$
Gyroscopes combination mode: 124, 134, 135, 235, 245.

This configuration program's comprehensive measurement accuracy:$|\bar{A}| \approx 0.6622$, and it has nothing to do with α_1, regardless of the value of α_1, when $\theta_1 = 54.74°$, the measurement accuracy of such configurations are optimal.

(2) For program two: when $\theta_2 = 65.905°$, under optimal configuration, the 10 operating modes can be divided into the following three categories according to their absolute values:

(1) $|A| = \sin^2\theta_2 = \frac{5}{6} \approx 0.8333$
Gyroscopes combination mode: 123, 125, 134, 145
(2) $|A| = 2\sin^2\theta_2 \cos\theta_2 = \frac{5}{3\sqrt{6}} \approx 0.6804$
Gyroscopes combination mode: 234, 235, 245, 345
(3) $|A| = 0$
Gyroscopes combination mode: 124, 135.

$|A| = 0$ was due to the fact that the three axes was coplanar under the 124 state and 135 state, making it impossible to measure the information about all three axes.

When ignoring the two measurement modes whose measurement accuracy was 0, this configuration program's comprehensive measurement accuracy:$|\bar{A}| \approx 0.7569$.

When not ignoring the two measurement modes whose measurement accuracy was 0, this configuration program's comprehensive measurement accuracy:$|\bar{A}| \approx 0.6055$.

Similarly, $|A|$ has nothing to do with α_2, regardless of the value of α_2, when $\theta_2 = 65.905°$, the measurement accuracy of such configurations are optimal.

(3) For program three: when $\theta_3 = 41.81°$, under optimal configuration, the 10 operating modes can be divided into the following several categories according to their absolute values:

(1) $|A| \approx 0.6667\sin\alpha_3$
Gyroscopes combination mode: 123
(2) $|A| \approx 0.6667\cos(\alpha_3 + 30°)$
Gyroscopes combination mode: 124
(3) $|A| \approx 0.6667\sin(\alpha_3 + 60°)$
Gyroscopes combination mode: 134, 135, 145
(4) $|A| \approx 0.3849$
Gyroscopes combination mode: 125
(5) $|A| \approx 0.4969(\sin\alpha_3 - \cos(\alpha_3 + 30°)) = 0.8607\sin(\alpha_3 - 30°)$
Gyroscopes combination mode: 234
(6) $|A| \approx 0.4969(\sin\alpha_3 + \sin(\alpha_3 + 60°)) = 0.8607\sin(\alpha_3 + 30°)$
Gyroscopes combination mode: 235
(7) $|A| \approx 0.8607\cos\alpha_3$
Gyroscopes combination mode: 245
(8) $|A| \approx 0.8607$
Gyroscopes combination mode: 345.

When $\alpha_3 = 13.05°$, this configuration program's comprehensive measurement accuracy is the highest, $|\bar{A}| \approx 0.4968$.

54.5 Conclusion

We can draw the following general conclusions by the reliability analysis and accuracy analysis:

(1) Program one: when $\theta_1 = 54.74°$, regardless of the value of α_1, the navigation performance and measurement accuracy of this configuration are all optimal.
(2) Program two: when $\theta_2 = 65.905°$, regardless of the value of α_2, the navigation performance and measurement accuracy of this configuration are all optimal.
(3) Program three: when $\theta_3 = 41.81°$, regardless of the value of α_3, the navigation performance of this configuration are optimal. And when $\alpha_3 = 13.05°$, the measurement accuracy of this configuration are optimal.

When α has no influence on navigation performance and measurement accuracy of the configuration program, with the consideration of the ease of installation, generally $\alpha = 45°$. This paper summarizes the existing three common five redundancy configuration program. Configuration angle θ is obtained by the navigation performance index, and configuration angle α is restrained by measurement accuracy. Finally, all angles of these three configuration program are obtained.

References

1. Wang M, Fan Y, Cui W (2006) Research on four redundant gyro system configuration. J Projectiles Rockets Missiles Guidance 26(3):40–45 (in Chinese)
2. Hong J, Zhang H (1999) Best measurement redundancy strapdown inertial measurement unit. Missiles Space Veh 237(1): 28–33 (in Chinese)
3. Shim D, Yang C (2010) Optimal configuration of redundant inertial sensors for navigation and FDI performance. J Sensors 10:6497–6512
4. Wu G, Wu Z, Duan C (2004) A satellite with high reliability inertial sensors. J Chin Inert Technol 12(2):70–73 (in Chinese)
5. Wang S, Zhang H (2000) Redundant configuration SINS fault detection threshold is determined. Acta Aeronautica ET Astronautica Sinica 21(4):303–307 (in Chinese)

Chapter 55
The Application of Reasoning Strategy in the Fault Diagnosis

Qinghe Meng, Qin Sun and Wei Tian

Abstract Mill's Five Methods is applied to the fault diagnosis as reasoning strategy. As a description of interaction between the elements in a system, the function diagram includes all the possible elements. Meanwhile, the irrelevant elements should be ruled out or checking the relevant one in an optimized order according to the different circumstances. Mill's Five Methods is applied to solve the problem. However, Mill's Five Methods can only solve the single cause problem. Thus, the system theory should be employed as auxiliary. By the composite application of Mill's Five Methods and system theory, an optimized checking order can be provided and the cause can be determined effectively.

Keywords Function flow · Mill's five methods · Fault diagnosis · System · Wholeness · Reasoning strategy · Method of agreement · Method of difference

55.1 Introduction

With the application of the new technologies to the aircraft, the parts, components, and systems become more and more complex. Many redundant systems are employed to keep the safety and reliability. Subsequently, many of the fault modes are coupled and hard to be diagnosed. Some people tended to isolate the fault by replacing LRUs one after another. Nevertheless, most of their work may turn out to be in vain, for they usually focused on the hardware or a local part, regardless of

Q. Meng (✉) · Q. Sun · W. Tian
School of Aeronautics, Northwestern Polytechnical University, Xi'an 710072, China
e-mail: mengqh77@hotmail.com

Q. Sun
e-mail: sunqin@nwpu.edu.cn

W. Tian
e-mail: tianwei@nwpu.edu.cn

J. Wang (ed.), *Proceedings of the First Symposium on Aviation Maintenance and Management-Volume I*, Lecture Notes in Electrical Engineering 296,
DOI: 10.1007/978-3-642-54236-7_55,

the software, human factors, and the environmental factors. The aimless disassembly and assembly of the hardware may cost people a lot of manpower, material, and financial resources. The other people tried to solve the problem by a quantitative method that is they attempted to determine the cause according to the probability of the occurrence of the undesired events by experience. However, the undesired events are random and it has been proved by many data and records that the final causes of the fault modes are just the little probability events that were often ignored. Often it's impossible to determine the cause for the first time. Thus, a good reasoning strategy is essential to find the cause fast and effectively. Therefore, it is of the same importance to construct a system including all the factors according to some function and then rule out the irrelevant one according to the circumstances. Checking the parts in an optimized order may save people a lot of time.

In this paper, the composite application of system theory and Mill's Five Methods is introduced to solve this problem. System theory can be applied to both the construction of system and the reasoning. On basis of working principle, a system corresponding to some function can be constructed. It is illustrated in form of function diagram including all the possible elements. Mill's Five Methods is a good inductive logic method for reasoning. With the help of Mill's Five Method, the cause can be determined fast and correctly or an optimized checking order can be provided to shorten the time. However, it's applied to the single cause problem and not to the complex cause problem. In fact, the single cause is corresponding to the undesired events of a system and the complex causes are corresponding to the undesired events of its elements or subsystems. The single cause may be the consequence of several complex cause. Thus, by system theory, a complex cause problem can be turned into a single cause problem so that Mill's Five Methods can be applied.

55.2 The Features of the System

A system can be defined as a set of elements standing in interrelations [1]. Because of the interactions, the elements are formed into a wholeness that can achieve some functions. From the description, it can be seen that a system should be composed of three ingredients: the element, the interaction and the function. The features of the system, such as open, wholeness, hierarchy, interaction, etc., are helpful for people to understand the system clearly and make a right decision.

55.2.1 The Function Flow

The elements in the system interact by means of the function flow. The function flow includes the matter, the energy, the communication factor, information, and so on. The matter includes the hydraulic oil, gas, etc. The energy includes the

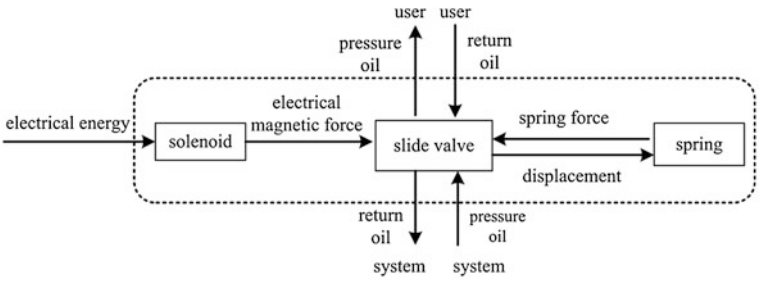

Fig. 55.1 A function diagram of a solenoid valve

force, the pressure, energy, etc. The communication factor includes the displacement, etc. The information includes the light, the sound, the feedback signal, etc. The function flow has its property of direction and magnitude. The element processes the input function flows from its upstream elements and output the function flows to its downstream elements. In this procedure, some function is achieved. By means of function flow, the elements form a system. The structure of the system is a network, like a spider web. A function diagram of a solenoid valve system is shown in Fig. 55.1. The system is made up of three elements: the solenoid, the slide valve, and the spring. They interact by means of the function flows and form a solenoid valve system.

Therefore, the behavior of the element is controlled by the function flow that output from the others. If the element outputs a desired function flow, both in magnitude and in direction, it is normal [2]. On the contrary, the failure element will output an undesired function flow. And if the downstream elements are normal, they will operate according to the undesired function flow in turn and output undesired function flows. In this way, the failure will propagate to the downstream and cause the system fault. This process is like the dominoes effect. Similarly, the fault will propagate to the other systems and cause more serious fault. Thus, some undesired events may occur at the same time or seem coupled. In fact, they are resulted in by the same cause. This phenomenon is often called the fault cascade. As is shown in Fig. 55.2, suppose the solenoid fails, there will be no electrical magnetic force output, the slider valve cannot move, the spring cannot be compressed and provide spring force in turn. As a result, the solenoid valve cannot switch the power supplied from the hydraulic system to the user.

55.2.2 Wholeness and the Dividing of the System

Wholeness is a very important feature of the system. It means the whole is not the sum of the parts [1]. The elements interact by means of the function flow and form a whole. In the system, the function flows are transformed by many processes. In every process, the element processes the function flows from the upstream and

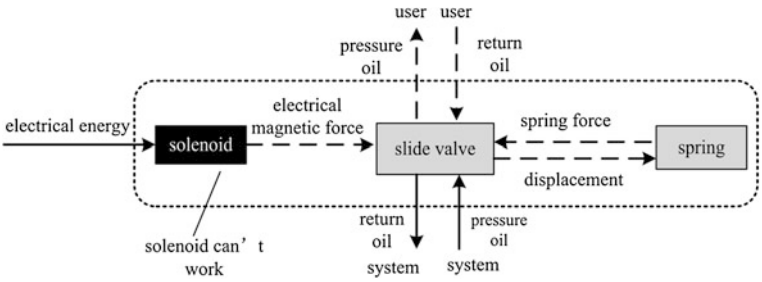

Fig. 55.2 The illustration of the fault propagation in solenoid valve system

outputs new function flows to the downstream. By the processes of transformation and transmission from one element to another, the function flows of the system are output, which are different in form, magnitude, or direction.

Thus, the whole can achieve some function other than any of its components. Meanwhile, the system can also be divided into several subsystems. As a whole, each subsystem is independent in function. Thus, there is no causal relationship between the failure modes of the elements in a subsystem or system.

55.2.3 Hierarchy

Hierarchy means the system has an embedded structure. The subsystems is embedded in the system, the elements are embedded in the subsystems, and so on. Then the system is made up of its subsystems and the subsystem is made up of its elements. And the system incorporates all the subsystem and elements. From the elements to the subsystems, systems, the structure becomes more and more complex. Consequently, more and more complex functions can be achieved.

55.2.4 Interaction

Interaction means the status of whole is dependent on any of its components'. Then the failures of its components may lead to the failure of the whole. In other words, the components are relevant to the system. Thus, if a system whose elements are in series is determined to be normal, all of its components can be ignored. For example, corresponding to Fig. 55.1, if the solenoid valve is determined to be normal, all of its components, such as the solenoid, slide valve, and spring can all be ignored.

55.3 Mill's Five Methods

In the early nineteenth century, the philosopher John Stuart Mill identified the following four (or five) informal methods for establishing causal connections between types of events. Mill's Five Methods includes the method of agreement, the method of different, the joint method of agreement and difference, the concomitant variation method and the method of residues. Of the five methods, the method of agreement and the method of difference are often applied in the fault diagnosis.

55.3.1 The Method of Agreement

The content of the agreement method is as follows. If two or more instances of the phenomenon under investigation have only one circumstance in common, the circumstance in which alone all the instances agree, is the cause (or effect) of the given phenomenon [3].

Symbolically, the method of agreement can be represented as [4]:

A B C D occur together with w x y z

A E F G occur together with w t u v

Therefore A is the cause of w.

The method of agreement can be applied to solve the common cause problem.

55.3.2 The Method of Difference

The content of the difference method is as follows. If an instance in which the phenomenon under investigation occurs, and an instance in which it does not occur, have every circumstance save one in common, that one occurring only in the former; the circumstance in which alone the two instances differ, is the effect, or cause, or an necessary part of the cause, of the phenomenon [3]. Symbolically, the method of agreement can be represented as [4]:

A B C D occur together with w x y z

B C D occur together with x y z

Therefore A is the cause, or the effect, or a part of the cause of w.

The method of difference can be applied to investigate the cause according to the different circumstances and instances.

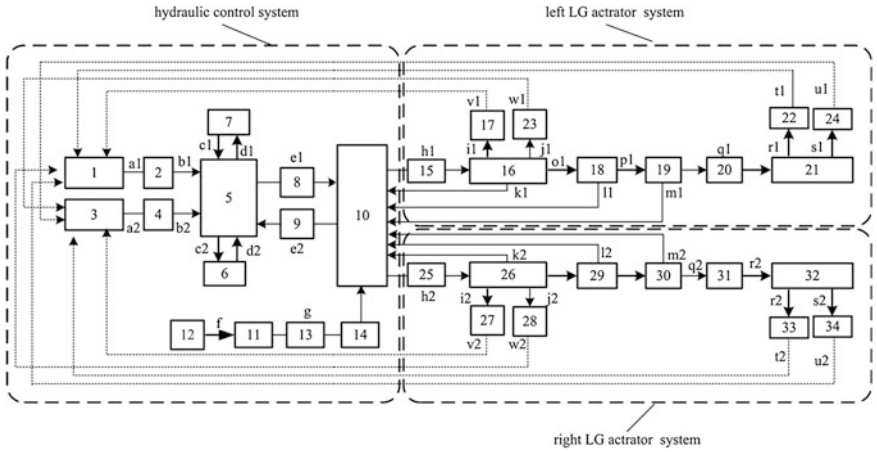

Fig. 55.3 The function diagram of main landing gear extension and retraction system

55.4 The Composite Applications of the Mill's Five Methods and the System Theory

A function diagram of the main landing gears extension system is shown in Fig. 55.3. The blocks with number stand for elements and carriers. And the arrowhead with letter stands for the function flow.

According to the feature of wholeness and function, the whole system can be divided into three subsystems: the hydraulic control system, left landing gear actuator system, and the right landing gear actuator system. Left landing gear extension system incorporates two subsystems: left landing gear actuator system and the hydraulic control system. Right landing gear extension system incorporates two parts: right landing gear actuator system and the hydraulic control system. In this way, the complex cause problem is turned into a single cause problem. The hydraulic control system is a common part. Left landing gear actuator system and right landing gear actuator system are the branch parts. The branch parts may be different in achieving the functions even if they process the same function flows.

The instances concerned in the Mill's Five Methods are uncertain, thus they are expressed as instances that some function flows are processed by some system or elements. Suppose the letter A stands for the instance function flows processed by hydraulic control system, B stands for the instance function flows processed by left landing gear actuator system, C stands for the instance function flows processed by right landing gear actuator system. D stands for the instance that landing gear slow to extend. NOT D stands for the instance that the landing gear is extended normally. The function flows processed by the branch parts are the same.

55.4.1 Case 1: Right Landing Gear Slow to Extend and Left Landing Gear Not

From the fact that the right landing gear is extended normally, in view of function flow, a conclusion can be drawn that both the hydraulic control system and the right landing gear actuator system are normal. In this case, for the difference in achieving the function and the instances, the method of difference can be applied [5].

A B occur together with NOT D
A C occur together with D

Therefore, C is the possible cause of D .

Thus, the cause lies in the left landing gear actuator system. As a result, the element 15, 16, 18, 19 should be examined. Element 15 stands for the hydraulic line, element 16 stands for the up lock actuator, element 18 stands for the transfer cylinder, and element 19 stands for the extension actuator. This agrees well with the fault isolation manual.

55.4.2 Case 2: Both Main Landing Gears Slow to Retract or Extend

In this case, for the same consequence, the method of agreement can be applied. The events can be described by the function flow. If the element is normal, the function flows can be processed and the desired output function flow can be achieved [5].

A B occur together with D
A C occur together with D

Therefore, A is the possible cause of D .

Thus, the cause may lie in the hydraulic control system. For the landing gear can be extended, the elements 1, 2, 3, 4, 6 should be ruled out and element 10 should be concerned. The element 10 stands for the selector valve. This agrees well with the fault isolation manual.

Because of the good reliability, it is almost impossible that the branches fail at the same time. If the hydraulic control system is proved to be normal, in view of function flow, both the branch parts fail. Thus, the parts of the two branches should be checked one after the another. It can be seen that the cause determined with Mill's Five Methods is just a possible cause. The real cause can be determined by Mill's Five Methods if there are a lot of instances. The significance of Mill's Five

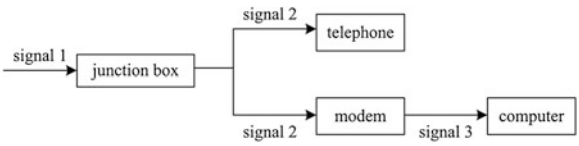

Fig. 55.4 The function diagram of the telephone and internet system

Methods is to provide an optimized checking order so as to shorten the maintenance time.

55.4.3 Case 3: When the Telephone is Picked Up, There is no Sound. And at the Same Time, People Cannot Surf the Internet

The function diagram of telephone and Internet is shown in Fig. 55.4. It can be seen that the junction box and the telephone form a system. The junction box, the modem, and the computer form another system. The same function flow is processed by either of the two branch systems. The consequence can be described as no function flow output. Suppose A stands for the instance function flow is processed by the junction box, B stands for the instance function flow is processed by the telephone, C stands for the instance function flow is processed by the modem, D stands for the instance the function flow is processed by the computer and E stands for the instance that no function flow outputs and occurs in different places.

For the same consequences, the method of agreement can be applied.

A B occur together with E

A C D occur together with E

Therefore A is the possible cause of E.

Thus, the junction box may be the most probable cause. After checking, the cause turned out to be the poor connection of the wiring in the junction box.

55.5 Summary

From the instances mentioned above, a conclusion can be drawn that a good reasoning strategy can help people find the cause fast and save a lot of human power and material resources. A system should be divided into common part and several branch parts so as to apply agreement method and difference method. When the consequences are different, the branch part should be checked, regardless of their common parts. When the consequences are the same, the common part should be concerned first. Often this reasoning strategy is useful and applicable. In many circumstances, it is proved to be right.

References

1. von Bertalanffv L (1973) General system theory, foundations, development, applications. George Braziller, Inc., New York, pp 54–55
2. Shiomi H, Shimaoka A, Ishiyama T, Xu F, Gao J (1987) The application of FMEA and FTA. China Machine Press, Beijing, p 15
3. Mill JS (1843/1973) Collected works of John Stuart Mill. In: Robson JM (ed) A system of logic, ratiocinative and inductive: Being a connected view of the principles of evidence and the methods of scientific investigation, vol 7–8. University of Toronto Press, Toronto
4. http://en.wikipedia.org/wiki/Mill%27s_Methods
5. Pegasus Airlines (1998) Boeing 737-600/700/800 fault isolation manual. Boeing Commercial Airplane Group, Seattle, Washington, pp 215–219

Chapter 56
Reliability Analysis for System with Random Failure Threshold

Jie Chen, Cunbao Ma and Dong Song

Abstract Based on the degradation model and failure threshold probability distribution, the reliability analysis for system with random failure threshold is presented in this paper. The actual failure point of engineering system is unpredictable or random because of the system's various uncertainties; which bring us a challenge to consider this problem in practical reliability analysis. An integrated methodology for reliability analysis with random failure threshold is developed in this paper, and both the degradation rate and the failure threshold uncertainty are considered in the deduction process. Moreover, the reliability analysis procedure for system with random failure threshold is given based on this method. In the end, the developed reliability analysis is demonstrated by an electro-hydrostatic actuator (EHA) system application example.

Keywords Reliability analysis · Degradation model · Random failure threshold · Electro-hydrostatic actuator

56.1 Introduction

The safety–critical nature of some systems used in aircraft, space, and some other application, specifies that the system's key function should be guaranteed in the presence of subsystem failure. These mission-critical systems' reliability is very important to the whole system safety; any drawback in design stage will bury some "bombs" to stop the continuous service. For completing the reliability index allocated by the father system, almost all the key component in the safety–critical system's reliability will be analyzed thoroughly in complex system's "V" style

J. Chen (✉) · C. Ma · D. Song
School of Aeronautics, Northwestern Polytechnical University, Xi'an 710072, China
e-mail: shuimujie@mail.nwpu.edu.cn

J. Wang (ed.), *Proceedings of the First Symposium on Aviation Maintenance and Management-Volume I*, Lecture Notes in Electrical Engineering 296,
DOI: 10.1007/978-3-642-54236-7_56,

development procedure [1], both choosing the high-reliability component or optimizing the system structure will increase the reliability index.

Previous works by lots of scholars in this field have been focused on fault diagnosis, reliability analysis, and prognostic [2–6], which are rooted in the performance degradation model or path. Wang [7] establishes the mathematical model of quad redundant actuator (QRA), investigates the force equalization algorithm and carries out the performance degradation, simulation, and reliability analysis under the first failure and the second failure. Alejandro [8] proposes an integrated methodology for the reliability and dynamic performance analysis of fault-tolerant systems. Armen [9] gives a decomposition approach together with a linear programming formulation, which allows determination of bounds on the reliability of complex systems with manageable computational effort. Hao [10] considers the reliability modeling for the complex and dependent failure, and develops reliability models and preventive maintenance policies for such system, but in the soft failures model, only the established threshold is considered. Li [11] defines the vector-universal generating function and gives the operator to analyze the reliability of multi-state system with multiple performance parameter, and then proposes the procedure of reliability analysis based on this function. Arun [12] gives a reliability analysis of nuclear component cooling water system by the semi-Markov process model, because this model has potential to solve a reliability block diagram with a mixture of repairable and nonrepairable component. Utkin [13] considers the uncertainty of component reliability, which cannot describe the component behavior fully, and then gives the second-order uncertainty model for system reliability assessment, but in the aspect of system failure, we can sum this uncertainty in threshold uncertainty most of the time. Aven [14] discusses the use of uncertainty importance measures in reliability and risk analysis, and introduces a new type of combined sets of measures based on an integration of a traditional measure and a related uncertainty importance measure.

Nowadays, the reliability technology research for such hybrid or complex system has focus on the performance degeneracy system's analysis. From the foregoing research, it is clear that various efforts have been made on such areas. However, there has less attention being paid to the uncertainty of threshold in engineering practice. According to the uncertainty of system degradation rate and the failure threshold in the complex operation environment, it's necessary to consider the uncertainty items in the reliability analysis.

During the conventional reliability analysis, no matter for engineer or designer, the failure threshold is defined by experience and fixed. However, this assumption may not be valid in most situations, the failure threshold which the plant will shutdown is varied because of different operational environment, individual diversity, operator practice, etc. [15], the definitive value of failure cannot be given, the random failure threshold in actual operation presents challenging item to analyze the system reliability.

In this paper, the authors consider two specific subjects which are inevitable in practice engineering, e.g., both uncertainties in system degradation rate and failure threshold, and then deduce the reliability analysis approach based on continuous

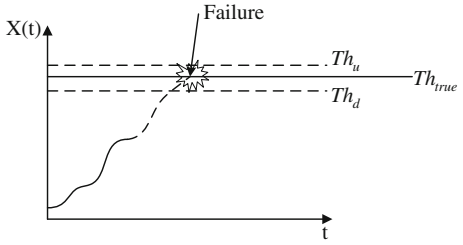

Fig. 56.1 System degradation failure process

smooth performance degradation process. During this process, the uncertainties are considered in a probabilistic or statistical way. In the end, we demonstrate the reliability analysis process on a realistic example: the EHA device. As the key component in flight control system, EHA is very important for both the flight performance and reliability, but its reliability contains more uncertainty because of its servo or follow-up characteristic [16]. The individual which works in flight control system shows uncertainty or difference with nominal characteristic. The example simulates the uncertainty in the failure threshold and degradation rate, and then utilizes the approach presented in this paper to analyze the system reliability as the system parameter cannot be given definitely.

The remainder of this paper is organized as follows. Section 56.2 presents the degradation model used in the following reliability analysis. Section 56.3 deduces the reliability analysis based on degradation model with random failure threshold. Moreover in Sect. 56.4, the system reliability analysis procedure is given. And then an example about the EHA is simulated and implemented to show the validity of the approach in Sect. 56.5. Finally, Sect. 56.6 summarizes the paper and offers some remarks.

56.2 Degradation Model

In practice engineering, almost all the complex systems are hybrid systems, e.g., they are composed by several different major subsystems. System failure can be reflected by the performance level's decreasing, the continuous system performance degradation is an aging process. This type of failure is just called as the soft failure [10], and the performance point which the system fails is defined as failure threshold.

We can depict this process as the Fig. 56.1, the system will fails in the point which the whole performance degradation exceeds the actual failure threshold Th_{true}. In Fig. 56.1, the value d in different time t can be created by a system attribute parameter which can reflect the system performance, and the time t could be the real time or run cycles for system work.

The degradation path in Fig. 56.1 is assumed to describe as

$$x(t) = \alpha + \beta t. \tag{56.1}$$

where α is the system initial degradation value, and assumed to be constant, β is the system degradation rate, which follows the normal distribution $\beta \sim N\left(\mu_\beta, \sigma_\beta^2\right)$, and μ_β, σ_β are mean value and variance of degradation rate respectively.

According to the statement above, the $\mathrm{Th}_{\mathrm{true}}$ is failure threshold which actual failure occurs. Actually, the system failure threshold is given by engineer or designer with experience or accelerated life test, and the actual failure threshold $\mathrm{Th}_{\mathrm{true}}$ varies as the different environment. In this paper, we assume it to follow the normal distribution $\mathrm{Th} \sim N\left(\mu_{\mathrm{Th}}, \sigma_{\mathrm{Th}}^2\right)$, where μ_{Th}, σ_{Th} are mean value and variance of the failure threshold respectively.

56.3 Reliability Analyses for System with Random Failure Threshold

The reliability analysis for the hybrid system with complex system uncertainties should considers the various factors in system performance degeneracy process. For the system degradation process depicted by the Fig. 56.1, the probability that the system regress to less than some specified value X at the time t is

$$\Pr(x(t) < X) = \Pr((\alpha + \beta t) < X) = \Pr\left(\beta < \frac{X - \alpha}{t}\right). \tag{56.2}$$

As the degradation rate $\beta \sim N(\mu_\beta, \sigma_\beta^2)$, so

$$\Pr\left(\beta < \frac{X - \alpha}{t}\right) = \Phi\left(\frac{\frac{X-\alpha}{t} - \mu_\beta}{\sigma_\beta}\right) = \Phi\left(\frac{X - \alpha - \mu_\beta t}{t\sigma_\beta}\right). \tag{56.3}$$

If the failure threshold is known to be $\mathrm{Th}_{\mathrm{true}}$, the probability that the system is available or reliable before the time t is

$$\Pr(x(t) < \mathrm{Th}_{\mathrm{tre}}) = \Phi\left(\frac{\mathrm{Th}_{\mathrm{true}} - \alpha - \mu_\beta t}{t\sigma_\beta}\right). \tag{56.4}$$

The probability distribution above is presented under the assumption that the $\mathrm{Th}_{\mathrm{true}}$ is known. Generally, the failure threshold is acquired by the engineer with experience or accelerated life test. We can assume that the $\mathrm{Th}_{\mathrm{true}}$ follows a normal distribution $\mathrm{Th} \sim N\left(\mu_{\mathrm{Th}}, \sigma_{\mathrm{Th}}^2\right)$.

Using the total probability formula

$$\Pr(B) = \sum_{i=1}^{\infty} \Pr(A_i) P(B/A_i). \tag{56.5}$$

Under the condition that the system will be failed in the failure threshold $(\mathrm{Th}_d, \mathrm{Th}_u)$, the probability $R_s(t)$ that the system will be reliable before the time t is

$$\begin{aligned} R_s(t) &= \int_{\mathrm{Th}_d}^{\mathrm{Th}_u} \Pr(\mathrm{Th} = \mathrm{Th}_{\mathrm{true}}) \int_{-\infty}^{\frac{\mathrm{Th}_{\mathrm{true}} - \alpha - \mu_\beta t}{t\sigma_\beta}} \frac{1}{\sqrt{2\pi}} e^{-\frac{x^2}{2}} \mathrm{d}x \\ &= \int_{\mathrm{Th}_d}^{\mathrm{Th}_u} \frac{1}{\sqrt{2\pi}\sigma_{\mathrm{Th}}} e^{-\frac{(y-\mu_{\mathrm{Th}})^2}{2\sigma_{\mathrm{Th}}^2}} \left(\Phi\left(\frac{y - a - t\mu_\beta}{t\sigma_\beta} \right) \right) \mathrm{d}y \end{aligned} \tag{56.6}$$

where the $\Phi(\cdot)$ is the standard normal distribution function.

Because the failure threshold follows the normal distribution $\mathrm{Th} \sim N\left(\mu_{\mathrm{Th}}, \sigma_{\mathrm{Th}}^2\right)$, we can choose the upper and lower bound of threshold as $\mu_{\mathrm{Th}} \pm 3\sigma_{\mathrm{Th}}$, which guarantees the interval confidence up to 99.73 %.

56.4 The Reliability Analysis System Development Procedure

The Eq. (56.6) gives the probability that the system will be reliable before the time t in Sect. 56.3. So, through the experience or some other approaches, if we can get some system's designated parameter for Eq. (56.6) in detailed, then the system's reliability and some key factor's effect on reliability can be analyzed.

Based on the probability equation above, the reliability analysis system development procedure can be listed as follow.

Step 1 Analyze the subsystem or experience case, acquire the corresponding physical parameter data of the whole system operation process which varies from good to regression, and ends to system function failed.

Step 2 Preprocess and identify the data, compare its error with the system parameter under ideal condition, and acquire the error or degradation model $x(t) = \alpha + \beta t$, including the initial degradation α, and the mean value μ_β, variance σ_β of the degradation rate β.

Step 3 Analyze the system failure point in degradation process, and then acquire the failure threshold $\mathrm{Th} \sim N\left(\mu_{\mathrm{Th}}, \sigma_{\mathrm{Th}}^2\right)$, including the threshold mean value μ_{Th}, threshold variance σ_{Th}.

Step 4 Compute the reliability and failure rate curves by the Eq. (56.6).

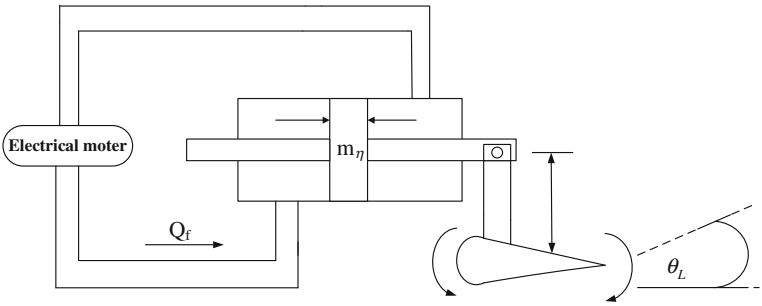

Fig. 56.2 The simplified scheme of EHA driving the flight control surface

56.5 Numerical Examples: An Aircraft's EHA Case

56.5.1 EHA Modeling and Simulation

According to flight control system's actuating mechanism and the servo actuator's mechanical wear characteristic, servo actuator's performance or reliability is very important to the flight control system or aircraft, it has been seen as the key component in flight control system. Moreover, the EHA is widespread availability in the flight control field, which is composed by the controller or electric motor, piston, actuating cylinder, and the position feedback device.

As the Fig. 56.2 shows, the motor modulates the speed of rotation to change the flow, and then controls the piston's position or control surface deflection.

The EHA's classical and main fault modes are relative to the mechanical and hydraulic component, which can be reflected by the system response. Based on the EHA's physical characteristic analysis, the common fault mode contains motor demagnetization, actuator mechanical damage, and hydraulic cylinder friction exception. Especially the third fault mode, as the mechanical contact between piston and cylinder, it's the main fault in EHA. The friction will changes the Motor damping factor B_m, Piston damping factor B_p and Pump's leak out factor C_t. In this example, we choose this fault mode to represent the system's main fault, and analyze the reliability of it.

For gaining the physical parameter data of the whole system operation process which varies from good to regression, the EHA simulation model on Simulink is completed as the Fig. 56.3, whose explanation in detail can be found in [16].

When the normal EHA system is motivated by the step command, the response of the system is showed in the Fig. 56.4. In Fig. 56.4, we can observe that the system tracking result is good.

Using the simulation model above, we can simulate the key parameters' variation which leads the system performance to failure level. In this process, the failure threshold of EHA is assumed to be stochastic, and the summed error of parameter from the normal value is chosen to be degradation value. Figure 56.5

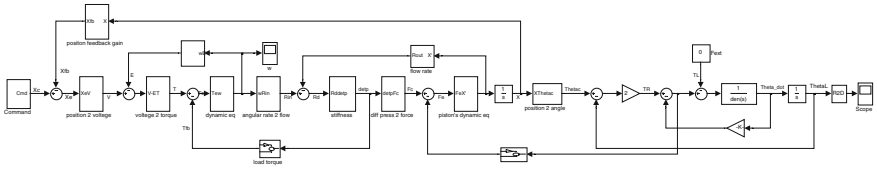

Fig. 56.3 Simulation models for EHA

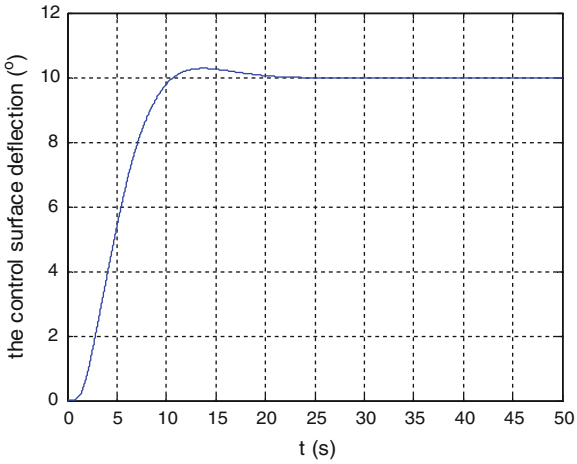

Fig. 56.4 EHA model's response in the normal condition

gives the three parameters' value point with stochastic failure threshold in 10 times system performance degradation simulation and average summed errors of the three parameters compared with the nominal value, the degradation interval in this simulation is assumed to 1,000 h in flight.

56.5.2 Reliability Analysis

According to the data above, the parameter in Eq. (56.6) for reliability analysis with random failure threshold of EHA can be given as in Table 56.1, which is assumed to be known by experience in this reliability analysis.

Using the Eq. (56.6), the reliability function $R_s(t)$ or probability that the system will be reliable before the time t is given in Fig. 56.6. In this situation, just like the Sect. 56.3's explanation, we choose the upper and lower bound of the threshold to be $\mu_{\mathrm{Th}} \pm 3\sigma_{\mathrm{Th}}$.

And with the system mean life time definition MTBF

$$\mathrm{MTBF} = \int_0^{\infty} R(t)\mathrm{d}t. \tag{56.7}$$

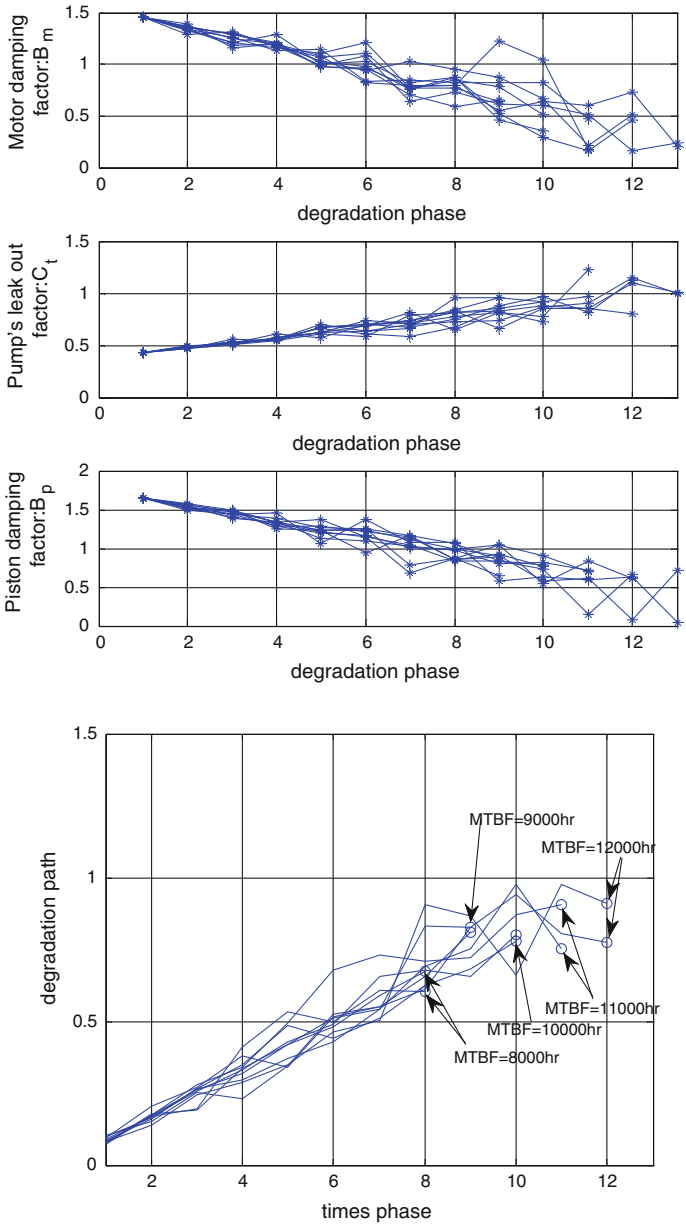

Fig. 56.5 The physical parameter decay and degradation path in simulation

We can compute the MTBF of EHA is 1.0224×10^4 h, this result is fit to the degradation process in the simulation as the Fig. 56.6.

Table 56.1 Parameter values for EHA's reliability analysis

Parameters	Values
α	0.085
μ_β	0.078
σ_β	0.006
μ_{Th}	0.78
σ_{Th}	0.042

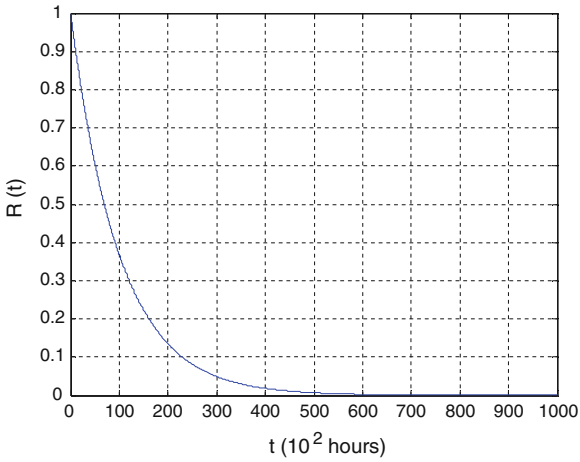

Fig. 56.6 EHA's reliability curves

56.6 Conclusions

In this article, the reliability analysis based on the degradation model with random failure threshold is developed for complex or key system, which actual failure threshold is unknown or has uncertainty in engineering. Using the total probability formula, the failure threshold interval is directed into the computation on system reliability. The reliability analysis is demonstrated on the realistic example about the EHA's reliability analysis system development in aeronautical engineering, which shows the validation of the method presented in this paper.

References

1. Lu J (2009) The safety assessment and study for a civil airplane flight control. Civil Aviation University of China, Tianjin
2. May P, Ehrlich HC, Steinke T (2011) ZIB structure prediction pipeline: composing a Arun Veeramany, Mahesh D. Pandey. Reliability analysis of nuclear component cooling water system using semi-Markov process model. Nucl Eng Des 241(5):1799–1806

3. Peng WW, Xiao ZL (2011) A combined Bayesian framework for satellite reliability estimation. In: 2011 international conference on quality, reliability, risk, maintenance and safety engineering, Xi'an, pp 13–21
4. Mohammadian SH, Ait-Kadi D (2010) Quantitative accelerated degradation testing: practical approaches. Reliab Eng Syst Saf 95:149–159
5. Gorjian N, Ma L (2009) A review on degradation models in reliability analysis. In: Proceedings of the 4th world congress on engineering asset management
6. Castet JF, Saleh JH (2010) Beyond reliability, multi-state failure analysis of satellite subsystems: a statistical approach. Reliab Eng Syst Saf 95(4):311–322
7. Wang S (2005) CUI Mingshan. Performance degradation and reliability analysis for redundant actuation system. Chin J Aeronaut 18(4):359–365
8. Alejandro DD (2008) An integrated methodology of the dynamic performance and reliability evaluation of fault-tolerant systems. Reliab Eng Syst Saf 93(11):1628–1649
9. Der Kiureghian A, Song J (2008) Multi-scale reliability analysis and updating of complex systems by use of linear programming. Reliab Eng Syst Saf 93:288–297(2008)
10. Peng H, Feng Q (2011) Reliability and maintenance modeling for systems subject to multiple dependent competing failure process. J IEEE Trans 43(1):12–22
11. Li CY, Chen X (2010) Reliability analysis of multi-state system with multiple performance parameters based on vector-universal generating function. Acta Armamentarii 12:1604–1610
12. Veeramany A, Pandey MD (2011) Reliability analysis of nuclear component cooling water system using semi-markov process model. Nucl Eng Des 241(5):1799–1806
13. Utkin LV (2003) A second-order uncertainty model for calculation of the interval system reliability. Reliab Eng Syst Saf 79(3):341–351
14. Aven T (2010) On the use of uncertainty importance measures in reliability and risk analysis. Reliab Eng Syst Saf 95:127–133
15. Ma JM, Zhang XY (2011) Performance reliability analysis method of dynamic systems under stochastic processes (in Chinese). Syst Eng Electron 132(10):943–948
16. Qi HT, Fu YL (2007) Simulation of electro-hydrostatic actuator based on AMESim (in Chinese). Mach Tool Hydraulics 35(3):184–186

Chapter 57
Application and Realization of Prognostic and Health Management System with Tactic Data Link

Naisen Cao and Lei Zhang

Abstract This Prognostic and Health Management System is an important part of the autonomic logistics support system, is now playing an important role in promoting transition of the operational aircraft from maintenance after invalidation, preventive maintenance to condition based maintenance, and also has important signification for improving availability of complicated equipments and decreasing maintenance cost. The paper analyzes the advantage and disadvantage of maintenance modes based on fault, time, and state supervision, illustrates the meaning of PHM and the application in F-35 fighter, and brings forward one design of airborne PHM system based on tactic data link facing our military at last, illustrates its system composition, operation principle, and reasoning mechanism.

Keywords Maintenance mode · Prognostic and health management · Data link · Reasoning mechanism

57.1 Introduction

With the rapid development of aviation, aerospace, military, and other high tech areas, a large number of complex systems have become major technology equipments, on the other hand, information technology and intellectual technology are extensively applied in armament to make the problems of reliability, maintenance, fault prognostic, and diagnoses and support be lighted. At present, the routine maintenance and preventive maintenance of our military fighters are still main modes and adopts excessive, frequent, and careful maintenance to insure system reliability and accomplishment of normal mission. The efficiency of this

N. Cao (✉) · L. Zhang
Department of Aeronautic Electronic Engineering, First Aeronautic Institute of the Air Force, Xinyang, Henan, China
e-mail: Daguangming2011@qq.com

J. Wang (ed.), *Proceedings of the First Symposium on Aviation Maintenance and Management-Volume I*, Lecture Notes in Electrical Engineering 296,
DOI: 10.1007/978-3-642-54236-7_57,

traditional maintenance mode is low at a cost of much manpower, material resources, and financial. With the increasing of flight mission, the new maintenance mode-Condition Based Maintenance (CBM) based on state supervision is studied and applied, because these advantages such as small logistics, high efficiency, and good Prognostic appears, fault prognostic and health management (PHM) based on CBM is developed [1]. As the important foundation of autonomic logistics support system in twenty-first century high tech war, PHM is recognized more and more. At present, PHM technology is applied in F-35 and F-22, our military fighter is equipped with tactic data link and has the study and application foundation of PHM, so it is very important to explore the application of PHM in our military fighters.

57.2 Meaning of Prognostic and Health Management

PHM, which is also called integrated test system, is a technology integrating logistics and maintenance benefit [2], it can evaluate health state of system itself making use of all kinds of data from sensor collecting system and by means of intellectual reasoning methods such as physics mode, nerve network, data fuse, fuzzy logic, and expert system, etc., predict fault before system fault occurring and provide a series of maintenance support measures combining with useful resource information to realize condition based maintenance of system [3].

Traditional maintenance mode collects and records fault information by means of built-in test equipment on board, lacks exact real-time fault diagnosis and fault prognostic, real-time evaluation and prognostic function of plane safety and performance, and there is no real-time information transmission between plane and ground, maintainer on ground can not know the operation situation on air, it is very long to park for maintenance and maintenance work is much. So, this traditional maintenance mode limits the application of real-time fault diagnosis and can not satisfy the requirement of new fighter's frequent flight.

New generation fighter can apply real time and long-distance fault diagnosis technology in the process of design, production, and usage, transfer previous maintenance mode after fighter landing to this maintenance of supervision, diagnosis, prognostic and broadcast in the air, long-distance ground diagnosis, ground preparation and integrated quick recovery, diagnosis, maintenance, and logistics support. This technology has important effect on increasing battle effectiveness of fighter, decreasing life period cost, insuring flight safety.

So, PHM is an integrated system, it does not only supervise real-time parameter from sensors to realize diagnosis and orientation of fault, but also realizes prognostic, isolation and recovery of fault, gives an alarm and corresponding resolution, eliminates error alarm information, insures mission reliability and flight safety, decreases maintenance cost of system, which presents the excellence of intellective aircraft.

57.3 Classification of Maintenance Mode

Suitable selection of maintenance mode not only makes equipment higher security, reliability, and usability, but also decreases cost, reduces maintenance cost [3]. According to time of fault occurrence and adopted maintenance measure, maintenance mode is classified into three kinds.

(1) Maintenance mode based on fault. This mode, which is also called maintenance after invalidation, reactive maintenance or unplanned maintenance, is rehabilitative maintenance activity after fault occurrence. Maintenance mode based on time can make use of maximum operation life, but it has some disadvantages such as unplanned maintenance activity, consuming much maintenance resource, producing serious aftereffect probably.
(2) Maintenance mode based on time. This mode, which is also called planned maintenance or preventive maintenance, is that no matter whether equipment fault occurs, after some time the equipment is checked and maintained. Maintenance mode based on time has good scheme, can prevent serious result effectively, but it also exists some shortage such as costing huge maintenance resource, wasting usage life, no insuring eliminating all faults.
(3) Maintenance mode based on state supervision. This mode, which is also called prognostic maintenance or condition based maintenance, is to arrange maintenance activity according to detailed situation by means of supervising and evaluating health situation of equipment. Maintenance mode based on state supervision not only can make use of usage life of equipment sufficiently, but also plans maintenance activity in time and overcomes shortcoming of maintenance after invalidation and planned maintenance. It can be said that condition based maintenance is the warm task that all military great power is researching actively and its flow chart is shown as Fig. 57.1.

We can see that the flow chart of condition based maintenance has many same points with the design thought of PHM technology, they judge health situation equipment by means of detection and state evaluation, so reasonable application of PHM technology is the effective approach to realize condition based maintenance.

57.4 Application of PHM on American Military Fighters

PHM is the key technology of autonomic logistics scheme for F-35 fighter. It is the further development of built-in test and capacity of state supervision used in current fighters, and makes maintenance dominated by event (that is post maintenance) or maintenance corresponding time (that is periodic maintenance) be replaced by maintenance based on state (that is condition-based maintenance, CBM) [4]. The emphases is to make use of advanced sensor integration to diagnose, prognosticate, supervise, and manage the state of fight by means of

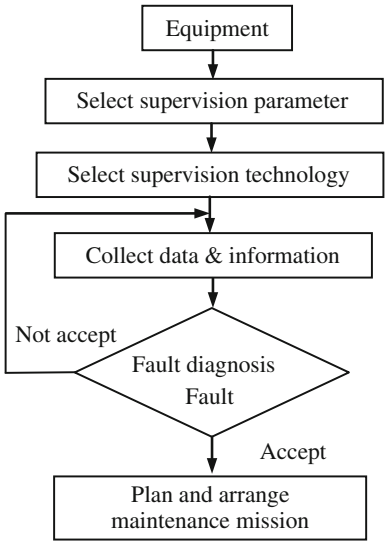

Fig. 57.1 Operation flow chart of CBM

arithmetic and intellectual mode (such as expert system, nerve network, etc.). Its final goal is to cancel planned maintenance based on calendar limitation and usage situation of component, strive for maximum ahead time for maintenance rehearsal and stock of spare part, identify system unit that is going to be wrong, and report upcoming maintenance affair real time and automatically to all support organization.

When fighter is in the air, airborne PHM system transfers the detected fault and state information of airplane to ground maintenance station and logistics supply system automatically to make it prepare corresponding spare part, technology datum, maintenance staff, and support equipment, etc., after the airplane lands it can be maintained quickly. This maintenance mode can shorten preparation time of flight again, decrease maintenance work largely, save usage and support cost, and increase combat readiness of fighter.

PHM system of adapted by F-35 fighter is a kind of software denseness system and relates to every factors of fighter at a certain extent. Its structure characteristic is to adopt intellective reasoning structure with delamination and integrate software of reasoning machine with different types in design arrangements to be convenient for application of fault diagnosis and prognostic technology from component grade to system grade. PHM of F-35 is an integrated system consisted of airborne part and ground part and airborne PHM system is divided into three arrangements. The bottom is supervision program of software and hardware (sensor or BIT/BITE) distributed in subsystem components (also called member system). The middle is region manager. The top is manager of airplane platform. The bottom is information resource to identify fault, detect fault by means of sensor, BIT/BITE or mode and submit related information to region manager of the middle directly. All regional managers have functions of signal process,

information fusion, and region reasoning machine and real-time organization execution to supervise operation of corresponding subsystem.

Ground PHM software is a kind of integrated PHM system and is responsible for integration, judgment, and decision-making of airborne health management result. Its structure is same as airborne PHM, includes local regional manager and platform manager, team regional manager and platform manager. Its function includes flight replay, prognostic, diagnosis and, life management. The flight replay mode (FRM) provides player of flight data, flight reader, and diagram reader to user, can recur to flight state during problem to provide support for safeguard engineer and maintainer finding and investigating problem. Ground PHM also integrates one kind of intellective help environment (IHE) to help maintainer to find and repair hard-diagnosis complicated fault. Ground PHM program can isolate fault of aviation electronic system to board level and isolate mechanical failure to local replaced unit.

According to estimation, if carry out autonomous logistics support scheme effectively, maintenance manpower will decrease 20–40 %, logistic safeguard scale will decrease 50 %, the rate of flight sortie will increase 25 %, the cost of usage and safeguard will decrease 50 % compared with the former fighter, and 8,000 h usage life of fighter can be guaranteed.

For F-22 the maintenance time is only about 8.5 h for every flight hour and is about one half of F-15. Preparation of flight again only needs 13 min. The cost of usage and safeguard for 24 fighters within 20 years is 1.2 billion and decreases 0.5 billion compared with F-15.

57.5 Design of PHM System Based on Tactic Data Link

Modern fighter equips advanced airborne data collection and management system and will produce a great information and data during flight, but at present these information and data do not get application sufficiently. If they make use of real-time message effectively produced by airborne equipments, document of flight maintenance technology and history maintenance experience to supervise real-time state, find and report fighter failure in time and bring forward to corresponding maintenance scheme before landing, the proportion of nonroutine work will be decreased greatly to increase maintenance efficiency, decreases cost of operation and maintenance of fighter and increases usage rate of fighter and flight safety, so health management of fighter is realized [5].

Facing these problems such as bad test performance, long fault diagnosis, and false BIT alarm occurring in usage for aviation electronic equipment , and that the traditional scheduled maintenance mode and breakdown maintenance mode of some fighter can not be suitable for the request of new equipment and mission, the corresponding study of PHM is needed to be carried out.

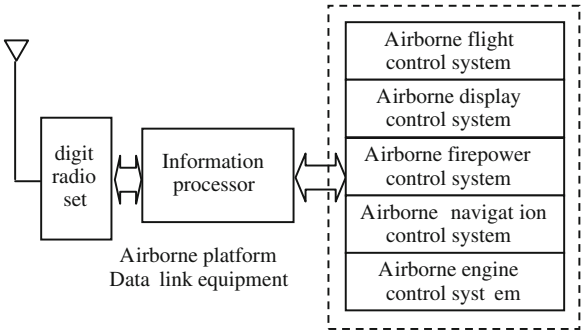

Fig. 57.2 Interlink age of airborne data link

57.5.1 Composition and Principle of PHM System

Some fighter has equipped with tactic data link, by means of information processor interlinks with airborne firepower control system, airborne display control system, airborne navigation system, airborne flight control system, and airborne engine system, etc., if these systems have fault or fault symptom, information processor will get information in time. If the software of information processor is amended suitably, it will have the function of report and supervision of flight real-time data, fault diagnosis, and Prognostic and generation of maintenance scheme. These data can be downloaded through download interface after landing and also be transmitted to ground command center by means of digital radio set after format procession during vacancy of data link to make system that has function of fault diagnosis and health management. The composition of airborne data link is shown in Fig. 57.2.

(1) Composition of PHM system

PHM system includes three parts: airborne real-time diagnosis and Prognostic, airborne state record and transmission, and ground autonomous logistics. In Fig. 57.3, the dashed line is information processor and it is an industry controlled computer.

The part of airborne real-time diagnosis and Prognostic includes sensor data collection, pretreatment and character distillation, equipment BIT, subsystem real-time diagnosis, fault Prognostic, safety and character Prognostic, and airborne database, etc., to accomplish performance detection of subsystem and part, enhanced fault diagnosis and realize fault supervision, and Prognostic of key system and part.

The part of state record and transmission or equipment consists of multifunction display, digital radio set, communication protocol message format deal, flight record equipment, and USB data download and is used to report, record, and transmit corresponding fault and maintenance information of fighter. The part of ground diagnosis and autonomous logistics includes long-distance diagnosis system and autonomous logistics system. Airborne fault Prognostic and health

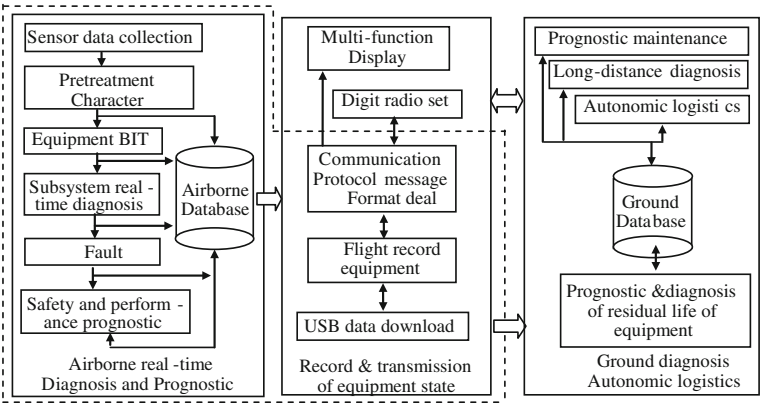

Fig. 57.3 Structure of airborne fault PHM system

manage system can give correct repair information in mass situation according to reasoning mechanism, at other situation it will transmit data to ground station for further analysis, then provide logistic support information automatically.

57.5.2 Reasoning Mechanism of PHM

In order to decrease the dependence on sensor and arithmetic furthest and by means of more evidence to find out reason to increase veracity of fault isolation and decrease false alarm, airborne PHM system adopts three-grade reasoning mechanism which consists of extended three-grade reasoning mechanism and integrated reasoning manager [6].

(1) Abnormal detection reasoning engine (AR)

AR is used to collect relative data, detect abnormal situation, and classify abnormal behavior to be convenient for renewal of diagnosis or forecasting reasoning engine later.

(2) Fault diagnosis reasoning engine (DR)

DR is used to isolate fault and diagnose invalidation, record diagnosis input from collection system, evaluate supervision result and other input, and ascertain the reason of reported fault and influence. DR consists of a set of arithmetic, fault mode of every subsystem, and detailed material of influence analysis are programmed into the engine and input information of fault is evaluated with modes. These modes can ascertain the relation of fault mode, supervision information, and fault influence.

(3) Fault Prognostic reasoning engine (PR)

PR will predict the residual life of every component according to all prognostic input from all subsystem. The principle of PR is to ascertain time length of the component going on performing some function with rated life curve of every component and according to the position of component at life curve.

(4) Integrated reasoning manager (IRM)

The key of one effective PHM system lies on it can manage abnormity, diagnose, and prognose information and provide health state information from line replaced unit, subsystem to system. IRM makes use of input from all reasoning engines to indicate the optimum state of system, ascertains sequence that fault may happen and recommend necessary maintenance way, at the same time it can report diagnosis and prognostic information to engineering technician, maintainer, and pilot etc.

IRM integrates the results from above three reasoning engines to form report and ascertain the detected and prognosed fault and the influence on mission.

57.6 Future Application

PHM is the development direction of fault diagnosis system for our new generation fighter, and the airborne aviation electronic equipment of fourth generation fighter, and ground data process station both regard the fault PHM system as a basic and necessary function. PHM has important effect on increasing safe performance of fighter and maintenance efficiency, decreasing cost of life period and improving battle effectiveness. Investigation material shows that PHM can decrease the cost of maintenance, usage, and support and increase the reliability of complicated equipment.

References

1. Sasa M, Guoshun C (2010) Research on prognostic and health management system of complex equipment. Comput Meas Control 8(1):1–3 (in Chinese)
2. Lifeng Y, Liang W (2010) Missile maintenance support system based on PHM technology. J Aeronaut Eng Inst Navy 4:17 (in Chinese)
3. Gang Wei (2008) F-35 lightning fighter. Aviation Industry publisher, Beijing, pp 254–257 (in Chinese)
4. Rui Z, Chunsheng X (2005) An approach for aircraft long-distance real-time monitoring. Aviat Maint Eng 6:20 (in Chinese)
5. Zhengbao Z, Tianxiang C (2005) PHM-the key enabler to F-35'S affordability. Aviat Maint Eng 6:20 (in Chinese)
6. Liang Z, Fengming Z (2008) Research on onboard prognostic and health management system architecture for operational aircraft. J Air Force Eng Univ (Natural Science Edition) 9(2):7 (in Chinese)

Chapter 58
Research on Nonlinear Optimization Problem Based on Genetic Algorithm Theory

Qi Dong, Tingxue Xu, Jikun Yang and Zhiheng Zhou

Abstract For weapon systems, such as aircrafts and missiles, it is difficult for reliability evaluation method with maximum entropy to solve the parameters and nonlinear optimization problem. A method is proposed based on genetic algorithm theory, the solution process is planned, and the responding programmer is designed. Finally, combined with an example, a weapon system is analyzed. At the same time, the model is established and parameters are calculated with data. The result shows that the method is effective for the nonlinear optimization problem, and offers lessons for solution of other nonlinear optimization problems.

Keywords Nonlinear optimization · Genetic algorithm theory · Maximum entropy method

58.1 Introduction

The reliability evaluation of weapon system is the problem people always focuses on, especially for systems of great value and high reliability, so the classical approach is not suitable to solve the problem. The Bayesian approach can make use of not only experiment data, but also some prior information, and can reduce the needs of experiment sample [1]. However, the most difficulty of Bayesian approach is how to identify its prior distribution [2], because the subjective factor may affect the robustness of its result [3]. In order to reduce the subjective influence to the minimum, the maximum entropy theory is put forward to solve the

Q. Dong (✉) · J. Yang · Z. Zhou
Department of Graduate Students' Brigade, NAAU, Yantai 264001, Shandong, China
e-mail: lance0627@163.com

T. Xu
Department of Ordnance Science and Technology, NAAU, Yantai 264001, Shandong, China

J. Wang (ed.), *Proceedings of the First Symposium on Aviation Maintenance and Management-Volume I*, Lecture Notes in Electrical Engineering 296,
DOI: 10.1007/978-3-642-54236-7_58,

reliability evaluation of rocket missile launching system in [4]. In fact, the solution of maximum entropy model is the nonlinear optimization problem with constraint conditions, but [4] cannot show the effective method. Thus, genetic algorithm theory is put forward to solve the nonlinear optimization problem in maximum entropy method. The proposed approach provides the scientific proof for the evaluation of the complex system reliability.

58.2 Maximum Entropy Approach

The maximum entropy approach came from the Jaynes theory, its principle is that the distribution derived from maximum entropy approach contains the least subjective factors and is the most rational distribution, when it meets the constraint condition of known information [5]. The maximum entropy means the least assumption, and it contains the least subjective facts, so it is the most objective.

For the discrete random variable, its information entropy can be defined as

$$E(x) = -\sum_{x=0}^{m} p(x)\ln[p(x)], \tag{58.1}$$

where $p(x)$ is the probability of the random variable x.

For the continuous random variable, its information entropy can be defined as

$$E(x) = -\int_{-\infty}^{+\infty} f(x)\ln f(x)\mathrm{d}x, \tag{58.2}$$

where $f(x)$ is the probability density function for the random variable x.

In order to obtain the maximum value of $E(x)$, $f(x)$ must be adjusted. When $E(x)$ gets the maximum, the corresponding $\hat{f}(x)$ is the least deviation estimation density function [6].

58.3 The Nonlinear Optimization Problem in Reliability Evaluation

Given the work characteristic of complex system, its prior distribution can be considered as continuous. According to Sidall theory [7], most probability density function can be expressed as Eq. (58.3).

$$f(x) = \exp\left(\lambda_0 + \sum_{i=1}^{M} \lambda_i x^i\right). \tag{58.3}$$

The corresponding constraint conditions are

$$\int_{-\infty}^{+\infty} f(x)\mathrm{d}x = 1, \tag{58.4}$$

$$\int_{-\infty}^{+\infty} x^j f(x)\mathrm{d}x = m_j, \quad j = 1, \ldots, M, \tag{58.5}$$

where M is the number of the available moment for the density function $f(x)$ and m_j is the jth moment.

In fact, simultaneous equations can not be calculated to get the analytical solution. Thus the problem needs to be changed into the optimization nonlinear problem.

Step 1. The original target function could be changed into by Least Square Method [8].

$$s = \sum_{i=1}^{m} s_i^2 \to \min, \tag{58.6}$$

where

$$s_i = m_i \int_0^1 \exp\left(\sum_{i=1}^{m} \lambda_i x^i\right)\mathrm{d}x - \int_0^1 x^i \exp\left(\sum_{i=1}^{m} \lambda_i x^i\right)\mathrm{d}x. \tag{58.7}$$

To simplify the calculation of Eq. (58.7), and the corresponding programming, $s_i = 1 - \int_0^1 x^i \exp\left(\sum_{i=1}^{m} \lambda_i x^i\right)\mathrm{d}x \Big/ m_i \int_0^1 \exp\left(\sum_{i=1}^{m} \lambda_i x^i\right)\mathrm{d}x$ can be instead of Eq. (58.7), because the result are the same [9].

Step 2. Constraint formulas are built.

The constraint formulas are given by Eqs. (58.2, 58.3) and (58.4)

$$m_i = \int_0^1 x^i \exp\left(\sum_{i=1}^{m} \lambda_i x^i\right)\mathrm{d}x \Big/ m_i \int_0^1 \exp\left(\sum_{i=1}^{m} \lambda_i x^i\right)\mathrm{d}x, \; i = 1, 2, \ldots, m, \tag{58.8}$$

Step 3. The range of parameters: $\lambda_1, \lambda_2, \ldots, \lambda_m$ (no constraint).

Step 4. The optimal solution can be obtained from constraint formulas, and the corresponding parameters, such as $\lambda_1, \lambda_2, \ldots, \lambda_m$, are also known. Then λ_0 can be calculated through Eqs. (58.3) and (58.4).

$$\lambda_0 = -\ln\left(\int_0^1 \exp\left(\sum_{i=1}^{m} \lambda_i x^i\right)\mathrm{d}x\right). \tag{58.9}$$

At last, the system prior probability density function can be identified, which is expressed as Eq. (58.3).

58.4 Genetic Algorithm Design

The algorithm needs to refer to the characteristic of the example, and can solve the optimization nonlinear problem quickly. Therefore, search space limited method is adopted to deal with the constraint conditions. The principle is that the method can keep the research space within the range limit, there is a one-to-one correspondence between points of the research space and feasible solutions of solution space. Specific design procedure is as follows:

(1) Genetic coding
Multiparameter cascade code is adopted with two parameters in object function, and each parameter is encoded in binary format. λ_1 is encoded in the first half, λ_2 is encoded in the second half.

According to the principle of the limited research space method and example in this paper, the concrete steps to limit the research space are as follows:

Step 1. Identifying the range of λ_1 based on the linear relationship between λ_1 and m_1.
Step 2. According to the linear relationship between λ_2 and λ_1 as well as m_2, when $\lambda_1 = \lambda_{1\min}$, one range of λ_2 can be identified; when $\lambda_1 = \lambda_{1\min}$, the other range of λ_2 can be identified too. The final range of λ_2 can be identified with the intersection of both.

(2) Fitness function
The aim of object function is to find the minimum. Therefore, the gap between fitness functions should be increased so that the chosen probability of excellent individuals can be improved. 10,000,000,000 times as many as that in the reciprocal of object function value is chosen as fitness function in genetic algorithm:

$$F(\lambda_1, \lambda_2) = 10000000000/f(\lambda_1, \lambda_2). \tag{58.10}$$

(3) Selection operators
Roulette wheel selection method is adopted in this paper, and its concrete steps are as follows:

Step 1. The sum of all individuals in population should be calculated.
Step 2. The value of relative fitness in every individual should be calculated, which represents the probability of every individual passed to next generation.
Step 3. At last, the chosen number of every individual is identified by simulated roulette wheel operation.

(4) Crossing operators
Crossover operators are one-point crossover strategy, and its concrete steps are as follows:

Step 1. The one-point crossover strategy pairs each individual of population randomly.

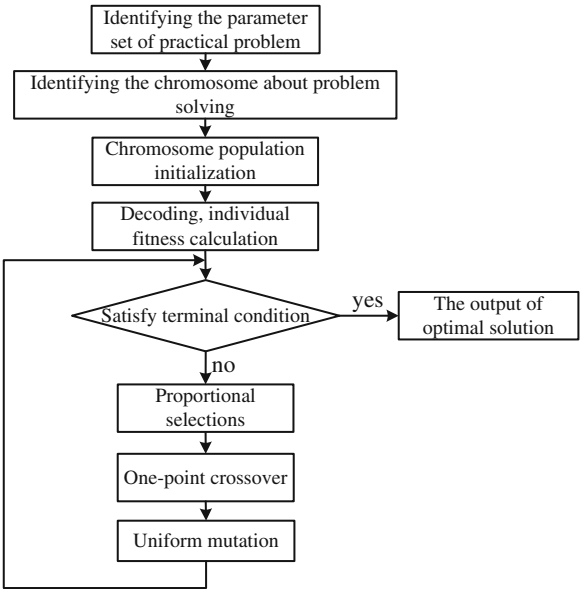

Fig. 58.1 The design process of genetic algorithm

Step 2. For each pair of individuals, the place after one locus set up randomly is an intersection.

Step 3. For each pair of individuals, the parts of two individuals' chromosomes are interchanged in their intersection according to the setting crossover probability; thereby the two new individuals are produced.

(5) Mutation operators

Step 1. Each locus in individual coding string is designated successively as mutation point;

Step 2. For each mutation point, one value is extracted from the range of corresponding gene with mutation probability, and used to replace the original gene value. A new individual will be produced then.

Step 3. A new population will be produced by taking the same operation for all individuals in the population.

At last, the flow chart of genetic algorithm is as follows [10] (see Fig. 58.1).

58.5 Example Analysis

The proposed approach in this paper is used to analyze the example in [4], the result is consistent with that in [4], and the effect of the proposed approach is demonstrated.

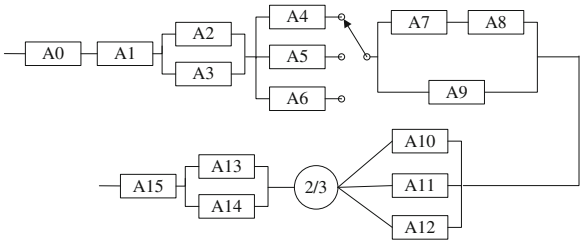

Fig. 58.2 The reliability block diagram of the weapon system

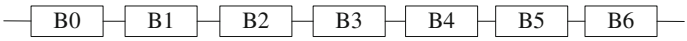

Fig. 58.3 The equivalent reliability block diagram of the weapon system

Table 58.1 Units data

Order number	Posterior distribution	Experiment data
B0	Beta(46,2)	(48,1)
B1	Beta(48,1)	(30,1)
B2	Beta(27,2)	(32,2)
B3	Beta(35,2)	(32,2)
B4	Beta(32,2)	(34,2)
B5	Beta(38,2)	(37,2)
B6	Beta(0.5,0.5)	(29,0)

Weapon system usually contains subsystem, assembly, and component, and its structure is complex. So the whole system can be divided into several parts to research.

The reliability block diagram of the weapon system is shown as Fig. 58.2. The system contains 16 subsystems, where A0 and A1 can make up a series unit (B0), A2 and A3 can make up a parallel unit (B1), A4, A5, and A6 can make up a cold standby unit (B2), A7, A8, and A9 can make up a parallel unit (B3), A10, A11, and A12 can make up a pick-2-in-3 system (B4), A13 and A14 make up a parallel unit (B5), A15 is a independent unit (B6) [11].

In order to process data conveniently, the fore mentioned reliability block diagram can be changed into a new series system as in Fig. 58.3.

The equivalent data of units: posterior distribution, experiment data, and system data can be obtained with prior information of units. Because the experiment data is binomial, so the posterior distribution of units can be Beta distribution [12].

The system experiment data is that there are nine times success and one time failure. The posterior distribution and experiment data of units are as Table 58.1.

According to Table 58.1, the first and second moment units can be obtained as Table 58.2.

Table 58.2 The first and second moment of units

Order number	The first moment	The second moment
B0	0.9691	0.9394
B1	0.975	0.9509
B2	0.9365	0.8800
B3	0.9437	0.8913
B4	0.9429	0.8898
B5	0.9615	0.9250
B6	0.9833	0.9674

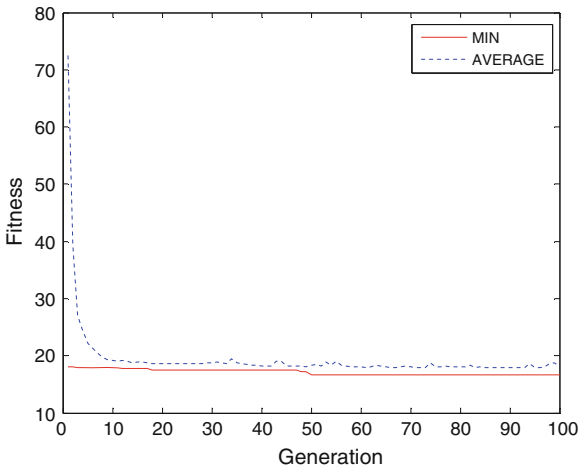

Fig. 58.4 The diagram of fitness function

The first and second moment of system can be calculated with the equivalent series structure and Eq. (58.11).

$$E\left[R^i\right] = \prod_{i=1}^{m} E\left[R_j^i\right], \tag{58.11}$$

where i is ith moment, and j is the number of units.

Then the first moment of system can be shown as $M_1 = 0.7444$, and the second moment of system is $M_2 = 0.5579$.

The parameters of system prior distribution can be calculated by designing program with matlab [13], the results are that $\lambda_0 = -1.6328$, $\lambda_1 = 3.4794$, $\lambda_1 = 3.4794$. The effect of approach is shown in fitness function chart as Fig. 58.4.

According to Eqs. (58.3) and (58.12), when the confidence level is 0.9, the confidence lower limit R_L of the complex system is 0.7302.

$$\int_0^{R_L} \pi(R|X)dR = \alpha. \tag{58.12}$$

58.6 Summary

Aiming at the optimization nonlinear problem of the model built by maximum entropy and Bayes method, genetic algorithm programmer is designed. According to example, the approach is simple and convenient. It is an effective approach for reliability evaluation of the complex system.

References

1. Xing YY, Wu XY (2005) Survey of reliability index verification methods for military equipment (in Chinese). Control Technol Tactical Missile (51st ed) 4:69–73
2. Bai L (2007) A Bayes method for reliability evaluation (in Chinese). Equal Reliab (129th ed) 3:20–23
3. Zhang SF, Li R, Fan SJ (2000) A summary of the research on Bayesian verification method (in Chinese). J. Spacecraft TT&C Technol (2nd ed) 19:28–34
4. Feng GB, Qian LF, Yu CG (2003) Reliability evaluation of rocket missile launching system (in Chinese). J Ballistics (1st ed) 15:41–45
5. Cheng L, Tong L (2009) A measurement data entropy method (in Chinese). J Electron Meas Instrum (23rd ed) 1:47–51
6. Tang XM, Zhang JH (2001) Test analysis and evaluation of weapon system in small-sample circumstances (in Chinese), vol 1. National Defense Industry Press, Beijing
7. Sidall N (1992) Probabilistic engineering design. Marcel Dekker, New York
8. Wu Y, Li YL, Hu QJ (2008) The application of mathematical statistics (in Chinese), vol 7. National University of Defense Technology Press, Changsha
9. Kang WX, Gu XS, Huang XL (2007) Bootstrap maximum entropy method application in estimating Fall-probability of missiles under small-sampling condition (in Chinese). J Acad Equipment Command & Technol (3rd ed) 18:109–113
10. Zhou M, Sun SD (2000) Genetic algorithms: theory and application (in Chinese), vol 2. National Defense Industry Press, Beijing
11. Zeng SK, Zhao TD, Zhang JG (2006) Reliability analysis and design (in Chinese), vol 1. Beijing University of Aeronautics and Astronautics Press, Beijing
12. Yang WM (1995) The introduction of reliability, maintenances, and supportability (in Chinese). National Defense Industry Press, Beijing
13. Li XH (2006) Matlab application (in Chinese). Electronics Industry Press, Beijing

Chapter 59
Research on Missile Sudden Fault Prediction Based on Mathematical Statistics

Linhu Cong, Tingxue Xu, Xiao Han and Jikun Yang

Abstract The method of missile sudden fault prediction is researched. The distribution regularity of fault data is obtained by statistical inference. Furthermore, the sudden fault prediction model of missile is established to get the future sudden fault probability of missile based on the distribution function of fault data. The results of case analysis validate the rationality of sudden fault prediction model.

Keywords Missile · Fault prediction · Mathematical statistics

59.1 Introduction

Missile fault is usually caused by both failure mechanism and exterior environmental factors and is a complex process. In the process of fault development, however, missile fault can be classified into sudden fault and degradation fault [1–3]. Sudden fault shows that the test data of missile monitoring parameters are within a qualified certain range during storage, but these test data suddenly go beyond the standard threshold at a certain hour. For most electronic equipment, the fault mostly belongs to sudden fault.

L. Cong (✉) · J. Yang
Department of Graduate Students' Brigade, NAAU, Shandong Yantai 264001, China
e-mail: 342743812@qq.com

T. Xu
Department of Ordnance Science and Technology, NAAU, Shandong Yantai 264001, China

X. Han
Department of Military Representatives Office of Navy in Tianjing Area, Tianjing 300308, China

J. Wang (ed.), *Proceedings of the First Symposium on Aviation Maintenance and Management-Volume I*, Lecture Notes in Electrical Engineering 296,
DOI: 10.1007/978-3-642-54236-7_59,

59.2 Fault Data Distribution Type

The fault data of missile which is in storage can be expressed by the time a missile has a fault. Since the missile may have a fault or not have a fault in a certain hour and the fault time is a random variable, missile fault time t can be assumed to obey one-dimensional distribution $F(t,\boldsymbol{\alpha})(\alpha = (\alpha_1, \alpha_2, \ldots, \alpha_k)$, which is the parameter vector of $F(t,\boldsymbol{\alpha})$) and one-dimensional density function $f(t,\boldsymbol{\alpha})$ can exist.

$$f(t,\boldsymbol{\alpha}) = \frac{\partial F(t,\boldsymbol{\alpha})}{\partial t} \tag{59.1}$$

It is shown by the properties of general density function and the physical properties of fault data $f(t,\boldsymbol{\alpha})$ should meet random $t, \int_0^{+\infty} f(t,\boldsymbol{\alpha})\mathrm{d}t = 1$.

Since argument t of distribution $F(t,\boldsymbol{\alpha})$ is the time a missile has a fault during various tests, distribution parameter vector $\boldsymbol{\alpha}$ which is obtained from fault data is a determined value and has no change with time. Distribution function $F(t,\hat{\alpha})$ can be ensured if the distribution type of $F(t,\boldsymbol{\alpha})$ is ensured and estimator $\hat{\alpha}$ of parameter vector $\boldsymbol{\alpha}$ is estimated based on fault date. Since $F(t,\boldsymbol{\alpha})$ is unknown, the probable distribution type can be assumed according to engineering experience, such as Exponential distribution, Normal distribution, Γ distribution, and so on. Determination of the concrete form of $F(t,\boldsymbol{\alpha})$ needs parameter estimation. In order to verify the assumption, distribution fitting test should be done.

Missile fault time is often assumed to obey exponential distribution according to engineering experience [4]. Distribution density function can be shown as:

$$f(t;\lambda) = \lambda e^{-\lambda t},\ t > 0 \tag{59.2}$$

In Formula, λ is the mean failure rate. Distribution parameter vector of fault data is $\boldsymbol{\alpha} = (\lambda)$. It is shown by the properties of exponential distribution that mean failure rate λ and mean lifetime θ are reciprocal.

59.3 Statistical Inference of Fault Data Distribution

59.3.1 Maximum Likelihood Estimation of Fault Data Distribution Parameter

Fault data distribution type can be taken as a known, and distribution parameter is just unknown if fault data distribution parameter has been assumed according to engineering experience. The general distribution parameter can be estimated according to the sample data and it is a question of parameter estimation in mathematical statistics. In order to get the estimator of distribution parameter, the method of maximum likelihood estimation can be used [5].

For a collection of sampled missiles, the total sample does not change at each test and it can be regarded as a replaceable fixed time test because of using repairing maintenance. It is assumed that m tests have been done to n missiles; the number of missile faults are $r_i (i = 1, \ldots, n)$ at each test. The total test time of missile is the time of n missiles that have been tested m times and it can be shown as:

$$T_r = nm \tag{59.3}$$

Maximum likelihood estimation of mean lifetime θ is:

$$\hat{\theta} = \frac{T_r}{\sum_{i=1}^{m} r_i} = \frac{nm}{\sum_{i=1}^{m} r_i} \tag{59.4}$$

Maximum likelihood estimator of fault rate λ can be shown in the following formula if missile fault time (mean lifetime) obeys exponential distribution.

$$\hat{\lambda} = \frac{1}{\hat{\theta}} = \frac{\sum_{i=1}^{m} r_i}{nm} \tag{59.5}$$

In Formula, $\hat{\lambda}$ is the unbiased estimation of λ.

59.3.2 Fault Data Distribution Fitting Test

For the fault data, distribution type can be assumed according to the engineering experience and also needs to test its assumption to verify whether it is held. The assumption test is divided into parameter test and nonparametric test. When the population distribution type is known, some parameters' assumption which is only tested is called parametric test, for other assumption test it is called nonparametric test. Since missile fault data distribution type is unknown, this paper assumes the distribution type and use sample data to test according to the engineering experience. The test which this paper used belongs to nonparametric test [6, 7].

The tests which determine if the population belongs to a distribution (e.g., normal distribution) are collectively called goodness-of-fit test for distribution which is called distribution fitting test for short. The common distribution fitting tests are χ^2distribution fitting test and K–S test. Колмогоров test is superior to χ^2 test when the population distribution is one-dimensional and theory distribution is completely known. Колмогоров test which is called K test for short is used in this paper.

(1) Колмогоров test
Consider testing the assumption:

$$\mathrm{H}_0 : F(x) = F_0(x)$$

In the formula, $F_0(x)$ is a continuous type of distribution function which is completely known.

Empirical distribution function $F_n(x)$ is quite consistent with population distribution function $F(x)s$ when the sample size n is large enough. Therefore the gap between $F_n(x)$ and $F_0(x)$ should not be too great when H_0 is held and n is larger. In this situation, Russian mathematician Колмогоров introduce statistic D_n to be the test statistic of H_0.

$$D_n = \sup_{-\infty < x < \infty} |F_n(x) - F_0(x)|$$

The supremum of deviation $|F_n(x) - F_0(x)|$ can be found in ns points $X_{(i)}$ since $F_n(x)$ and $F_0(x)$ are both the monotone non-decreasing function of x. Consequently, Колмогоров test first solves the larger deviation between empirical distribution function and assumed distribution function, which is to solve:

$$d_i = \max\left\{ \left| F_0(X_{(i)}) - \frac{i-1}{n} \right|, \left| \frac{i}{n} - F_0(X_{(i)}) \right| \right\}, \; i = 1, 2, \ldots, n \tag{59.6}$$

The largest one in n, d_i is the value of Колмогоров test statistic D_n.

$$D_n = \max\{d_1, d_2, \ldots, d_n\} \tag{59.7}$$

The value of D_n should be smaller when $F_n(x)$ and $F_0(x)$ fit well. On the other hand, $F_n(x)$ and $F_0(x)$ fit poor when the value of D_n is larger.

Therefore, the rule of Колмогоров test is: for the given significance level α, H_0 is refused if $D_n > D_{n,\alpha}$, otherwise H_0 is accepted. $D_{n,\alpha}s$ can be obtained by consulting test critical value table of Колмогоров when $n < 100$.

The value of D_n can be calculated by Formulas (59.6) and (59.7) if there is no repetitive data in sample $X_1, X_2, \ldots, X_n$. And when there is repetitive data in sample $X_1, X_2, \ldots, X_n$, sample $X_1, X_2, \ldots, X_n$ should be arranged one after another (repetitive data should merge into one). It can be done as follows:

$$X_{(1)} < \cdots < X_{(m)}, \; (1 \le m \le n)$$

Let n_i be the frequency of corresponding $X_{(i)}$ in sample, then $n_i \ge 1$, $n_1 + n_2 + \cdots + n_m = n$, $F_n(X_{(i)}) = \frac{n_1 + n_2 + \cdots + n_{i-1}}{n}$, $i = 1, 2, \ldots, m$, in Formula, $F_n(X_{(m+1)}) = 1$.

Let

$$d_i = \max\left\{ \left| F_0(X_{(i)}) - F_n(X_{(i)}) \right|, \left| F_n(X_{(i+1)}) - F_0(X_{(i)}) \right| \right\}, \; i = 1, 2, \ldots, m \tag{59.8}$$

then

$$D_n = \max\{d_1, d_2, \ldots, d_m\} \tag{59.9}$$

(2) Exponential distribution test

It is assumed that m tests have been done to n missiles, the number of sample faults are $r_i (i = 1, \ldots, n)$ at each test. The missile fault time can be shown as $T_{ij} (i = 1, \ldots, n; j = 1, \ldots, m)$. Therefore test whether missile fault time obeys exponential distribution is to test whether population distribution obey single parameter exponential distribution according to the tested fault time sample $T_1, \ldots, T_p (p \leq nm)$(repetitive data should merge into one). Since unknown parameter λ is included in single parameter exponential distribution function $F_0(t) = 1 - e^{-\lambda t}$, $t > 0$, the assumption should be to test actually as follows if $\hat{\lambda}$ which is the maximum likelihood estimation of λ is used to replace λ.

$$\mathrm{H}_0 : F(t) = F_0(t; \hat{\lambda}) = 1 - e^{-\hat{\lambda} t},\ t > 0.$$

Test statistics can be the same taking:

$$D_n^* = \sup_{0 \leq t < \infty} \left| F_0(t; \hat{\lambda}) - F_n(t) \right| = \max_{1 \leq i \leq n} d_i \tag{59.10}$$

In Formula:

$$d_i = \max\left\{ \left| F_0(T_{(i)}; \hat{\lambda}) - \frac{i-1}{n} \right|, \left| \frac{i}{n} - F_0(T_{(i)}; \hat{\lambda}) \right| \right\}$$

$(T_{(1)}, T_{(2)}, \ldots, T_{(p)})$ is the order statistic of $(T_1, T_2, \ldots, T_p)$. The method is the same as above if there is repetitive data in samples.

In order to improve the test effect, Finklestein and Schafer introduce statistic S_n^* to test H_0 and ensure the critical value $S_{n,\alpha}^*$ table of S_n^* aiming at different significance level α.

$$S_n^* = \sum_{i=1}^{n} d_i \tag{59.11}$$

Obviously, the value of S_n^* will be larger if the value of $d_i (i = 1, \ldots, n)$ is large, meanwhile, the curves of distribution function $F_0(t; \hat{\lambda})$ and empirical distribution function $F_n(x)$ fit poor and H_0 should be refused. Therefore, the rule of test for significance level α is: H_0 should be refused when $S_n^* > S_{n,\alpha}^*$, on the other hand, H_0 should be accepted.

59.4 The Sudden Fault Prediction Model of Missile

With the increasing storage time, missile may have sudden fault. For sudden fault taking place in a short time and no obvious signs before fault, fault data can be

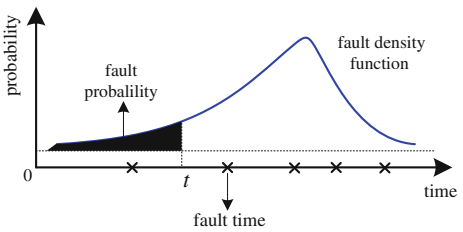

Fig. 59.1 Sudden fault density function curve

considered to count and analyze the fault rules. Through processing the missile test information of calendar years, the fault data is shown at the time of missile having sudden fault. Therefore missile sudden fault can be predicted based on the fault data. The time of missile sudden fault being random variables, the probable distribution type can be assumed according to engineering experience; parameter estimation and distribution fitting test should also be done, then the sudden fault density function of missile can be ensured. Meanwhile the distribution parameter of fault data is a constant which does not change with time. According to the definition of fault density function [8, 9], the probability of missile having sudden fault in the time from 0 to t is the modeled area of sudden fault density function which is shown in the shadowed part in Fig. 59.1.

Let $f(t, \boldsymbol{\alpha})$ be the sudden fault density function of missile, T is the time before missile having sudden fault, then the probability of having sudden fault in the time from 0 to t can be shown as:

$$F(t) = P(T \leq t) = \int_0^t f(t, \boldsymbol{\alpha}) \mathrm{d}t \tag{59.12}$$

It is a conditional probability event if the probability of missile sudden fault is to be predicted in the time from t to $t + \Delta t (\Delta t > 0)$. The probability of missile having sudden fault is predicted in the time from t to $t + \Delta t$ in the condition of missile having no sudden fault in the time from 0 to t, then the probability of missile sudden fault can be shown as:

$$\begin{aligned} F^*(t) &= P(t < T \leq t + \Delta t | T > t) \\ &= \frac{P(t < T \leq t + \Delta t, T > t)}{P(T > t)} = \frac{\int_0^{t+\Delta t} f(t, \boldsymbol{\alpha}) \mathrm{d}t - \int_0^t f(t, \boldsymbol{\alpha}) \mathrm{d}t}{1 - \int_0^t f(t, \boldsymbol{\alpha}) \mathrm{d}t} \end{aligned} \tag{59.13}$$

Sudden fault density function can be shown as $f(t, \boldsymbol{\alpha}) = \lambda e^{-\lambda t}$, $t > 0$ if the sudden fault time of missile obeys exponential distribution. Known from Formulas (59.12) and (59.13), the probability of missile having sudden fault in the time from 0 to t is $F(t) = P(T \leq t) = 1 - e^{-\lambda t}$, the probability of having sudden fault in the time from t to $t + \Delta t$ is $F^*(t) = P(t < T \leq t + \Delta t | T > t) = 1 - e^{-\lambda \Delta t}$. The probability of missile having sudden fault in any Δt interval equals to the probability of having sudden fault in the time from t to Δt which embodies the exponential distribution having no memory.

In other words, since the distribution parameter vector which is obtained based on fault data is a definite value and does not change with time when missile sudden fault is predicted. Thus only the missile fault data should be processed by statistical inference to ensure the sudden fault density function. The probability of sudden fault can be predicted according to Formulas (59.12) and (59.13). Meanwhile, for the present missiles are tested regularly, the probability of missile sudden fault at a future certain time equals the probability of sudden fault in the future certain time between two tests.

59.5 Case Analysis

Ten missiles are randomly taken as samples to analyze aiming at bulk missiles in storage. Since the bulk missiles are tested regularly, the missiles are tested once a year from 2002 and the test information is recorded to 2009. The probability of missile sudden fault from 2008 to 2009 can be predicted according to the fault data from 2002 to 2007. The prediction result can be compared with actual fault conditions to test whether the sudden fault prediction model of missile is reasonable.

59.5.1 Determination of Fault Data Distribution Type

The missile fault data can be assumed to obey exponential distribution according to the engineering experience. Through processing the missile fault data from 2002 to 2007, 10 taken missiles can be found to have sudden fault when they are tested from 2003 to 2007 and the number of faults are 1, 1, 1, 2, and 2. Since bulk missiles are tested once a year, missile sudden fault time can be shown as 2, 3, 4, 5, 5, 56, 6 by the year. Let T be the missile fault data, test T whether they obey exponential distribution is to test the assumption $H_0 : T \sim F(t;\lambda) = 1 - e^{-\lambda t}$, $t > 0$.

The maximum likelihood estimator of missile fault data distribution parameter vector λ from Formula (59.5) is:

$$\hat{\lambda} = \frac{\sum_{i=1}^{6} r_i}{nm} = \frac{0+1+1+1+2+2}{10 \times 6} = \frac{7}{60}$$

The fault data is arranged one after another (repetitive data should merge into one) and is Колмогоров tested. The computing process can be shown as in Table 59.1.

From Table 59.1, $S_n^* = 1.2166$. $S_{7,0.10}^* = 1.37$ can be obtained by consulting the critical value table of S_n^* if significance level $\alpha = 0.10$. H_0 can be accepted in

Table 59.1 Exponential distribution testing of missile fault data

i	$T_{(i)}$	$\left\|F_0(T_{(i)};\hat{\lambda}) - F_n(T_{(i)})\right\|$	$\left\|F_n(T_{(i+1)}) - F_0(T_{(i)};\hat{\lambda})\right\|$	d_i
1	2	0.2081	0.0652	0.2081
2	3	0.1524	0.0096	0.1524
3	4	0.0872	0.0557	0.0872
4	5	0.0134	0.2723	0.2723
5	6	0.2109	0.4966	0.4966
$\sum$				1.2166

significance level $\alpha = 0.10$ since $S_n^* < S_{n,\alpha}^*$. The missile fault data can be considered to obey exponential distribution and the fault density function is: $f(t) = \frac{7}{60}e^{-\frac{7}{60}t}$, $t > 0$.

59.5.2 The Prediction Result of Missile Sudden Fault Analysis

Known from calculating in Sect. 59.4, the missile fault data obey exponential distribution. Fault density function is $f(t) = \frac{7}{60}e^{-\frac{7}{60}t}$, $t > 0$ and distribution parameter is $\lambda = \frac{7}{60}$. The probability of missile having sudden fault can be predicted in 2008 according to Formula (59.13) since λ is a constant which does not change with time. Known from exponential distribution having no memory, the probability of missile having sudden fault in 2008 equals the probability of having sudden fault from 2008 to 2009 (test once a year), thus:

$$F^* = P(6 < T \leq 7 | T > 6) = 1 - e^{-\lambda \Delta t} = 1 - e^{-\lambda} = 0.1101$$

Likewise, the bulk missiles are predicted in 2009 and the result of which is 0.1247. According to the result of actual observational record [10], the probability of the missiles having sudden fault in 2008 and 2009 are both 0.1. The results of prediction agree with the results of actual record and the sudden fault prediction model of missile can be considered to be reasonable.

59.6 Conclusion

In this paper, the prediction method of missile sudden fault is researched based on the statistical rules of fault data at certain credibility. Since the distribution parameter vector of fault data is a constant and does not change with time when missile sudden fault is predicted, the sudden fault prediction model of missile is established to get the future probability of the missile sudden fault based on the

distribution function of fault data after ensuring the distribution rules of fault data through statistical inference.

References

1. Meng L (2012) Research on condition-based maintaining decisions of a certain type missile, (in Chinese). Naval Aeronautical and Astronautical University, Shangdong
2. Jian-yin Zhao (2005) Reliability modeling and application study based on the data of performance degradation. Defence Science University, Changsha (in Chinese)
3. Baruah P, Chinnam RB (2005) HMMs for diagnostics and prognostics in machining processes. Int J Prod Res 43(6):1275–1293
4. Chinnam RB, Baruah P (2004) A neuro-fuzzy approach for estimating mean residual life in condition-based maintenance systems. Int J Mater Prod Tech 20:166–179
5. Wu L, Li Y-L, Hu Q-J (2008) Application mathematical statistic, M (in Chinese). National University of Defence Technology Press, Beijing, pp 112–120
6. Andrew KS, Lin D, Banjevic D (2006) A review on machinery diagnostics and prognostics implementing condition-based maintenance. J. Mech Syst Signal Process 20:1483–1510
7. Feldman K, Jazouli T, Peter A, Sandborn PA (2009) Methodology for determining the return on investment associated with prognostics and health management. J. IEEE Trans Reliab 58(2):305–313
8. Ramakrishnan A, Pecht M (2003) A life consumption monitoring methodology for electronic system. J IEEE Trans Compon Pack Tech 26(3):625–634
9. Zhang S, Kang R, He X et al (2008) China's efforts in prognostics and health management (in Chinese). J. IEEE Trans Compon Packag Tech 31(2):509–518
10. Yao Yun-feng Wu, Yi-fu Feng Yu-guang (2012) Health condition assessment of equipment. J Mod Defence Tech 40(5):156–161 (in Chinese)

Chapter 60
Reliability Analysis for the Electromechanical Monitoring System Based on Petri Network

Rong Fan, Chuang Guo, Meng Liu and Houjun Yin

Abstract The important links caused to fault are found through analyzing the work flow of the electromechanical monitoring system. Modeling and analysis of the system reliability is investigated with the random Petri network. Based on the isomorphic Markov chain, the stable availability and failure rate of system each state are analyzed, and the Matlab/state flow is used to have a simulation validation, which widens the analyzing method on the electromechanical monitoring system.

Keywords Electromechanical monitoring system · Petri network · Reliability

60.1 Introduction

Electromechanical monitoring system is responsible for monitoring all the electromechanical systems of aircraft, managing, and transferring the systems state information [1]. Complicated cross-linking and multiplex signal lead to serious signal interference and makes signal identification difficult, which causes very low reliability of electromechanical monitoring system. An effective way must be adopted for the system reliability analysis and research [2].

Petri network is a description tool of the system and analysis of Simulate mathematical and graphics, which is widely used in the analysis of system's reliability, such as the basic description of the action, simplify the fault tree, fault

R. Fan (✉) · C. Guo · M. Liu
The Air Force Engineering University, Hui Zhou 710038, China
e-mail: fan787114@163.com

H. Yin
The Air Force Engineering University, Xi'an 710038, China
e-mail: yhj120021@126.com

J. Wang (ed.), *Proceedings of the First Symposium on Aviation Maintenance and Management-Volume I*, Lecture Notes in Electrical Engineering 296,
DOI: 10.1007/978-3-642-54236-7_60,

diagnosis, analyzing of indicators [3] and calculation of the reliability of simulation of analysis. Petri networks can make up for the traditional method of analysis of the reliability of the FTA that cannot be linked to lack of time, the use of its analysis of the electromechanical monitoring system with the reliability of feasibility and superiority.

60.2 Fault Tree of the Electromechanical Monitoring System

Electromechanical monitoring system is a device of computerized data collection, processing, and transmission with its own fault detection capabilities, the main function of which is monitoring the situation of every electrical and mechanical system, managing the process of electromechanical system's BIT, and dating between avionics systems and electromechanical system [4].

Based on the monitoring system, we can gain the control process: the electromechanical system's BIT access to relevant information. This information will be transmitted through the interface corresponding to the electromechanical monitoring processor for analysis, processing, and diagnosis; the decision made by monitoring processor will be transferred to the avionics equipment related to deal with the 1553B Bus.

The information of interface exchange between monitoring systems and electromechanical system include: simulated signals, digital signals, interface of the serial communication, and the output interface of the controlling. As a subsystem of avionics system, the signal between electromechanical monitoring system and other avionics subsystems is passed through the 1553B bus. The bus is in the form of double redundancy, the relationship between the two buses is parallel and interoperability. Electromechanical alarm system of failure and MFD displays for more than two-degree design between the two for the relationship between hot. Electromechanical monitoring system for the monitoring system to monitor the process include five segments, where each of the segments have their own specific failure modes. The fault of any one of the links will lead to failure of the monitoring system [5].

Based on the analyzing process of electromechanical monitoring system to monitor, the model of the reliability of the task can be established as shown in Fig. 60.1.

The fault-tree established which sets the electromechanical monitoring system failure as the top event is shown in Fig. 60.2.

Setting up the failure tree needs a few conditions: any link failure of monitoring the flow of the five links will lead to failure to monitor; when a link fails, other links will no longer fail until it is found out and this link is repaired.

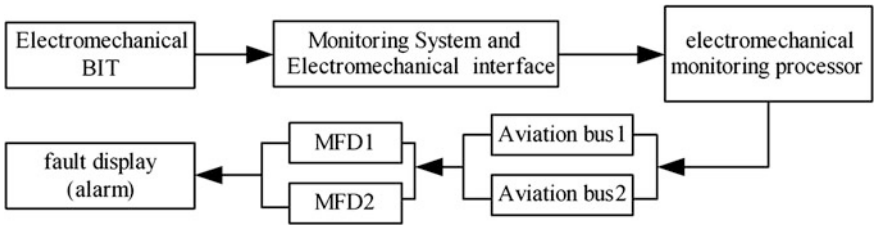

Fig. 60.1 Mission reliability of the electromechanical monitoring system model

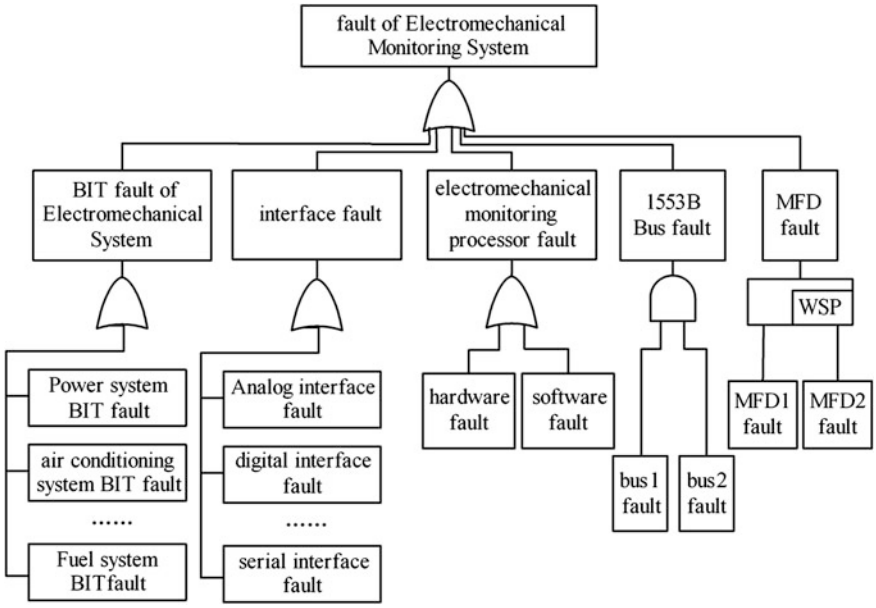

Fig. 60.2 Fault tree of electromechanical monitoring system

60.3 The Modeling of the Random Petri Network

When the following conditions are met for a triple N = (S, T, F), it is referred to as a basic Petri network:

(1) $S \cup T \neq \varnothing$
(2) $S \cap T = \varnothing$
(3) $F \subseteq (S \times T) \cup (T \times S)$
(4) $\mathrm{dom}(F) \cup \mathrm{cod}(F) = S \cup T$

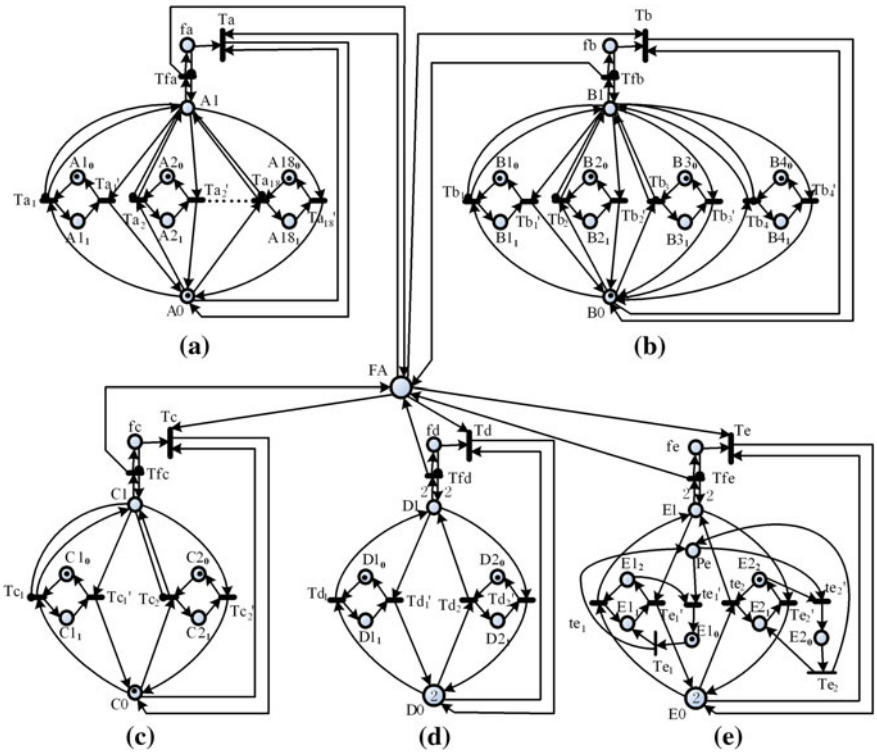

Fig. 60.3 Electromechanical monitoring system randomly Petri network model

Thereunto:

$$\mathrm{dom}(F) = \{x \in S \cup T | \exists y \in S \cup T : (x, y) \in F\}$$
$$\mathrm{cod}(F) = \{x \in S \cup T | \exists y \in S \cup T : (y, x) \in F\}$$

As a Petri network, there is another factor: token. It is the logo on the position S, and only if all the inputs include the token of a transfer this transfer can be triggered. Early Petri networks did not introduce the time concept [6], but only for research of the logics of the system that acts and the nature of logic. In order to further enhance the function of Petri network, so that it can better express as the introduction of a system of the time factor in the transfer between the Executive and the executable associated with a random variable time delay, this type of Petri network is called stochastic Petri network.

Based on previous analysis of the fault tree of the electromechanical monitoring system in Fig. 60.2, the system can create random Petri network model as shown in Fig. 60.3.

Figure 60.3 a, b, c, d, e corresponds to five segments which lead to the following monitoring faults: electromechanical BIT, monitoring systems and

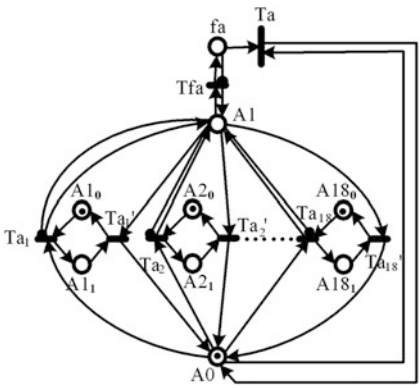

Fig. 60.4 The model of BIT aspects of electrical and mechanical Petri network

electromechanical system interface, control processor, 1553B bus, and multi-function display MFD. One, a, b, c for the subsystem or the door, d for the door and subsystems, e reserves for the thermal subsystem door.

As can be seen from the chart that links in the Petri network model, it is similar to the structure, in order to avoid duplication. It only sets BIT aspects of electrical and mechanical as an example to analyze its operation rules as follows:

Electromechanical BIT aspects include more than 18 kinds of BIT of electro-mechanical subsystem. The Petri network model is shown in Fig. 60.4.

The operation rules are: the mechanical and electrical subsystems are working properly in the initial state of the BIT [7], that is, A0 and Ai0 both have a token, the moment when the BIT-electro-mechanical systems failure, Tai was triggered by the implementation of the transfer, the token in Ai0 transfer to Ai1, the sub-systems is from the normal work of the state into a state of failure; at the same time,the token in A0 transferred to the A1, when there is token in A1, the transfer of far-enabled, the implementation of the trigger of far lead to BIT aspects of the electrical and mechanical from the state of normal work to fault state, token appear in far. At the same time, when the token presence in the A1, which has been shown that there is a subsystem failure, then the other subsystems will not fail, in this Petri network through the A1 to Tai ban to achieve the arc. When failure of the mechanical and electrical BIT is found and repaired, transfer Tai' was the implementation of the trigger. The system failure is from the wrong state into a normal working condition, token in Ai1 transfer to Ai0, at this time, token exist in both A0 and far, it was Ta trigger implementation of the transfer, token in far is disappear, the BIT links of electromechanical were repaired.

In Fig. 60.3, position of FA logo electromechanical monitoring system failures and its relationship with five of its links is between the door, any of the links' failure will lead to failure of monitor. Its capacity is 1, other links will not fail when there is failure of one link until the fault has been repaired.

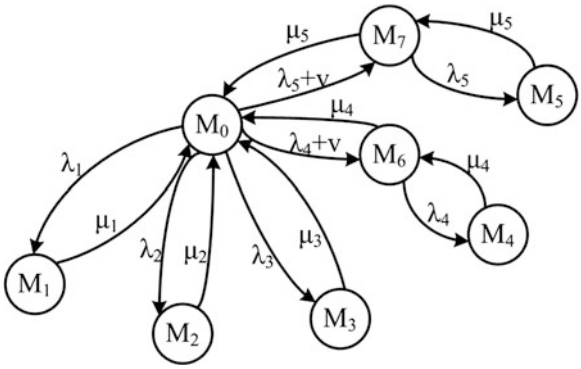

Fig. 60.5 Petri net with the structure of the Markov state transition chart

60.4 Probability of Stability and Failure Rate

60.4.1 The Establishment of Markov State Transition Diagram

Electromechanical monitoring system based on Petri network structure Markov state transition diagram shown in Fig. 60.5.

The meanings of the symbols are as follows:

λi (i = 0,1,…,7): i-link failure rate
μi (i = 0,1,…,7): i-link repair rate
V: hot backup failure rate
M0: system and link all the normal work of the state
Mi (i = 1,2,…,5): i-link failure
M6: One of the two bus failure
M7: One of the two MFD failures

60.4.2 Calculation of Steady-State System and the Probability of Failure Rate

According to the Markov chain theory, the state transition probability matrix Q in graph 5 can be expressed as follows:

$$Q = \begin{bmatrix} -\sum_{i=1}^{5}\lambda_i - \lambda_4 - v & \lambda_1 & \lambda_2 & \lambda_3 & 0 & 0 & 2\lambda_4 & \lambda_5 + v \\ \mu_1 & -\mu_1 & 0 & 0 & 0 & 0 & 0 & 0 \\ \mu_2 & 0 & -\mu_2 & 0 & 0 & 0 & 0 & 0 \\ \mu_3 & 0 & 0 & -\mu_3 & 0 & 0 & 0 & 0 \\ 0 & 0 & 0 & 0 & -\mu_4 & 0 & \mu_4 & 0 \\ 0 & 0 & 0 & 0 & 0 & -\mu_5 & 0 & \mu_5 \\ \mu_4 & 0 & 0 & 0 & \lambda_4 & 0 & -\mu_4 - \lambda_4 & 0 \\ \mu_5 & 0 & 0 & 0 & 0 & \lambda_5 & 0 & -\mu_5 - \lambda_5 \end{bmatrix} \tag{60.1}$$

Said $\pi_i(i = 0, 1, \cdots 7)$ that the probability of the monitoring system in the state of steady-state, then the following formula is set up:

$$\begin{cases} \pi Q = 0 \\ \sum_{i=0}^{7}\pi_i = 1 \end{cases} \tag{60.2}$$

According to Formula (60.2) it can be obtained probability of electromechanical monitoring system in steady state:

$$\pi_0 = \left(1 + \frac{\lambda_1}{\mu_1} + \frac{\lambda_2}{\mu_2} + \frac{\lambda_3}{\mu_3} + \frac{2\lambda_4^2}{\mu_4^2} + \frac{\lambda_5(\lambda_5 + v)}{\mu_5^2} + \frac{2\lambda_4}{\mu_4} + \frac{\lambda_5 + v}{\mu_5}\right)^{-1} \tag{60.3}$$

Therefore: $\pi_1 = \frac{\lambda_1}{\mu_1}\pi_0$, $\pi_2 = \frac{\lambda_2}{\mu_2}\pi_0$, $\pi_3 = \frac{\lambda_3}{\mu_3}\pi_0$, $\pi_4 = \frac{2\lambda_4^2}{\mu_4^2}\pi_0$, $\pi_5 = \frac{\lambda_5(\lambda_5+v)}{\mu_5^2}\pi_0$, $\pi_6 = \frac{2\lambda_4}{\mu_4}\pi_0$, $\pi_7 = \frac{\lambda_5+v}{\mu_5}\pi_0$.

In the definition of Mi state from 1, we can see that when the system is in a state of Mi (i = 1, 2… 5), the monitoring system is in a state of failure, system failures, and calculate system failure rate as follows:

$$\lambda = \sum_{i=1}^{5}\pi_i \tag{60.4}$$

It can more accurately calculate the steady-state system parameters through theoretical calculations, but only for a relatively simple system. For complex systems, Q state transition matrix dimension is too large, the calculation is too cumbersome, and reliability analysis is still by means of simulation.

60.5 MATLAB/State Flow Modeling and Simulating

State flow is a tool in MATLAB which is for Complex systems modeling, simulation, and analysis with stimulant. It combines FSM theory, the flowchart, and the state transition map together by using object-oriented programming ideas. The

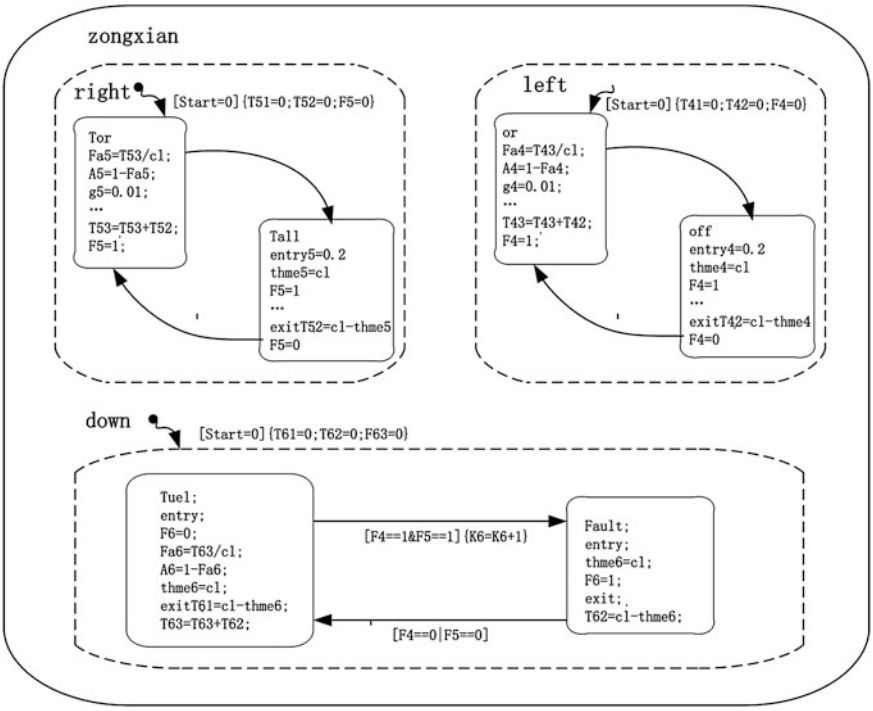

Fig. 60.6 Bus link state flow simulation model

main module includes state and transition. Each state may include entry, during, exit, and act on event; each transition include events, conditions, and actions. when using State flow of Petri network simulate, can using the state to express treasury and the change of Petri net, using transition to express arc, using the state acts and logo on the transition to express rules of changes.

According to the electromechanical monitoring system changes the relationship and control logic of Petri network and set up state flow simulation model, which links the bus simulation model as shown in Fig. 60.6.

Petri network simulation platform is shown in Fig. 60.7. Setting the failure rate λ of every link, the repair rate μ and reserves failure rate v, 200 times simulation can get availability curve of electromechanical monitoring system as shown in Fig. 60.8.

Output data can get that availability is 0.6296 when the monitoring system in steady state, availability of every link in steady state is 0.8013, 0.9421, 0.9631, 0.9466, and 0.9159 as shown in Fig. 60.7. Since the relationship between the monitoring system and the links are logic, in theory, availability of monitoring system should be the product of availability of every link:

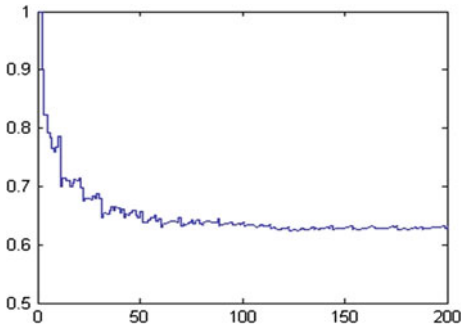

Fig. 60.7 Electromechanical monitoring system reliability curve

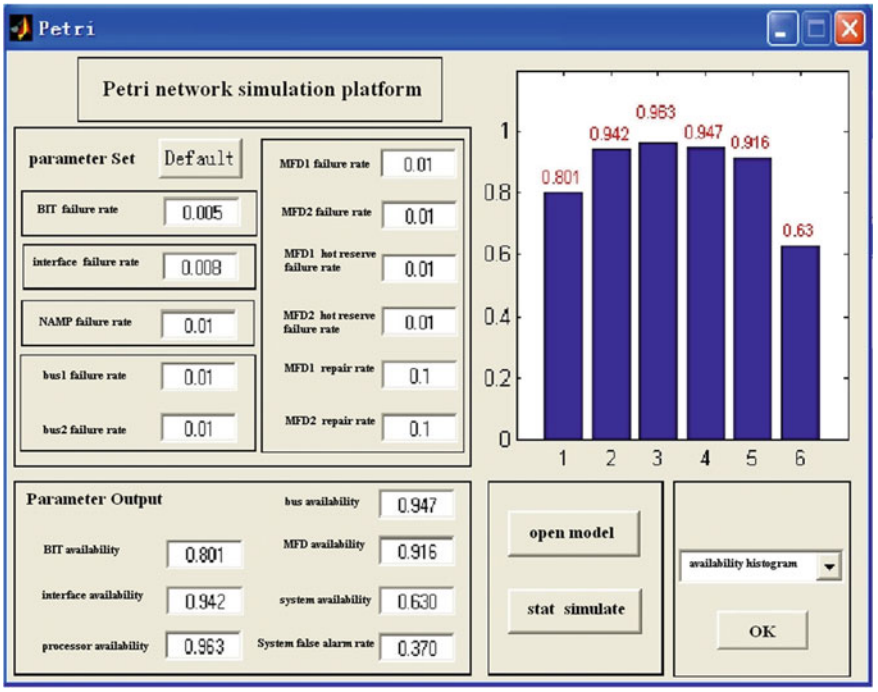

Fig. 60.8 Petri network simulation platform

$$A = \prod_{i=1}^{5} A_i = 0.8013 \times 0.9421 \times 0.9631 \times 0.9466 \times 0.9159 = 0.6303 \quad (60.5)$$

Comparing theory and simulation result we can see that Petri network model state flow is accurate and the simulation is effective, creating a platform for modeling and analysis of system reliability; the reliable data of any time in simulation process can be stored in MATLAB workspace for Stand-by, and can also be exported directly to the stimulant for their analysis and processing.

60.6 Conclusion

For the purpose of studying the reliability of the electromechanical monitoring system, analyses of the reasons that electromechanical monitoring systems fail, starting from the monitoring process to the important fact of what affects reliability of the monitoring system. Based on this we get the fault tree.

The use of Petri network can be for the modeling and analysis of monitoring system reliability. Establishing homogeneously at random in the Petri network transfer of state Markov chain, system under steady state, and the probability of failure rate on the basis of the theory of Markov chain should be analyzed. The use of state flow for modeling and analysis of monitoring system reliability, creating a platform for modeling and analysis of complex system reliability, is useful. Expanding analysis of the electromechanical monitoring system is reliability.

References

1. Wu Z (2006) Introduction of the Petri Network (in Chinese). Mechanism Industry Publishing Company, Beijing
2. Zhang L (2006) Reliability modeling and analyse on the integrated avionics system base on Petri network (in Chinese). Northwest Industry University Degree Paper
3. Binh PTT, Tuyen ND (2006) Fault diagnosis of power system using neural Petri net and fuzzy neural Petri network. IEEE Trans SMC 25(6):917–925
4. Wang K, Zhang H-X, Wang Z-J (2006) Reliability research on the complexity repairable system base on Petri Network (in Chinese). Electrolight and Control
5. Feng W-W (2002) Research on the monitoring technology of the non-avionics system (in Chinese). Northwest Industry University Degree Paper
6. Volovoi V, Kavalieratos G, Waters M, Mavris D (2004) Modeling the reliability of distribution power systems using Petri nets. In: IEEE
7. Liu M (2008) Research on the false alarm of the Aviation Electromechanical monitoring system (in Chinese). Air Force Engineering University Degree Paper

Chapter 61
Research on Integrated Avionics System Safety

Guoqing Wang, Qingfan Gu, Miao Wang and Lihua Zhang

Abstract System safety is the principal driver of avionics system requirements and has caused more and more attention. For the reason that the main concern of avionics system research is system capacity and constitution since early safety analysis, system reliability has become dominant trends for studying system effectiveness. With the avionics system becoming more and more complex, the traditional research methods which are used in studying system reliability, faces the challenges of organizing problem for multiple system goals, multiple processes, multiple elements, multiple relations, and multiple conditions. To solve the problem of safety analysis for integrated avionics system, hazard and mishap modes of avionics system are studied and the methods of risk analysis, risk evaluation, risk controlling, risk elimination, and risk mitigation are presented based on the system risk controlling theory. Finally, the organizing and engineering technologies of system safety, software safety, and hardware safety are also discussed to provide foundation for designing integrated avionics system safety.

Keywords Risk control · Hazards · Mishaps · System safety · Software safety · Hardware safety

G. Wang (✉) · M. Wang · L. Zhang
Science and Technology on Avionics Integration Laboratory, Guiping Road 432, Shanghai 200233, China
e-mail: wang_guoqing@careri.com

G. Wang · Q. Gu · M. Wang
China National Aeronautical Radio Electronics Research Institute, Guiping Road 432, Shanghai 200233, China

G. Wang · L. Zhang
School of Computer Science and Engineering, Northwestern Polytechnical University, YouYiXiLu 127, Xi'An 710072, China

J. Wang (ed.), *Proceedings of the First Symposium on Aviation Maintenance and Management-Volume I*, Lecture Notes in Electrical Engineering 296,
DOI: 10.1007/978-3-642-54236-7_61,

61.1 Introduction

The safety, economy, comfort, and environmental protection are four essential attributes of civil aircraft [1]. The requirements of aviation system consist of three aspects: ability, cost, and safety; the airline companies pay attention to technological progress and ability improvement (function, performance, and cost), the passengers pay attention to expenditure and comfort (ticket fare and riding environment), and the aviation authorities pay attention to safety of system. The safety is basic condition to guarantee avionics system of civil aircrafts. At the same time, the dramatic improvement in the computational power of hardware brings about increasingly sophisticated software-based embedded controllers that take over complex functionality in an efficient, precise, and flexible way. These benefits allow the use of such systems in environmental conditions where delays in delivering products and/or economical losses are not the only things at stake, but also environmental hazards and public confidence. This development, however, entails an unavoidable increase in the complexity of systems, which is expected to continue in the future. Therefore, in order to retain the benefits from more sophisticated controllers, a corresponding increase in the capability of the design and safety engineers to maintain adequate safety and reliability levels is required.

One of the most challenging issues in system development today is to take into consideration, during development, all possible failures modes of a system and to ensure safe operation of a system under all conditions. Current informal methodologies, like manual fault tree analysis (FTA) [2] and failure mode and effect analysis (FMEA) [3] that rely on the ability of the safety engineer to understand and to foresee the system behavior are not ideal when dealing with highly complex systems, due to the difficulty in understanding the system under development and in anticipating all its possible behaviors.

In this paper, we propose a solution of the issues mentioned above, to perform hazard and mishap modes analysis of avionics system in the system development life-cycle (including software and hardware) through risk analysis, risk evaluation, risk controlling, risk elimination, and risk mitigation that based on the system risk controlling theory. The paper is structured as follows: In Sect. 61.2 we present the safety-related definition and system risk controlling theory; we present the avionics system safety analysis process and methods based on risk controlling theory in Sect. 61.3; hardware and software safety engineering are described in Sects. 61.4 and 61.5, respectively; finally, we draw some conclusions in Sect. 61.5.

61.2 Safety-Related Definition

61.2.1 System Safety and Definition of Relevant Parameters

Safety: Safety is a state where no casualty, occupational disease, equipment trouble, property loss or environmental damage occurs. **Hazard**: Any real or potential condition that can cause injury, illness, or death to personnel, damage to or loss of a system, equipment or property, or damage to the environment. **Mishap**: An unplanned event or series of events resulting in death, injury, occupational illness, damage to or loss of equipment or property, or damage to the environment [4].

Definition of hazard severity: Catastrophic: Function failure or abnormal behavior, which will cause loss of life and permanent failure of system and then cause the aircraft under catastrophic failure state. **Critical**: Function failure or abnormal behavior, which will cause serious damage and damage of major systems and then cause the aircraft under dangerous/serious failure state. **Marginal**: Function failure or abnormal behavior, which will cause slight and minor damage and then cause the aircraft under slight failure state. **Negligible**: Function failure or abnormal behavior, which will cause system function failure, but cause no effect on operating performance or fight crew's work.

Likelihood occurrence definition: Likely: The event frequently happens in the life of project, for example, the probability is more than 1/10. **Probable**: The event occasionally happens in the life of project. **Possible**: The event may happen in the life of project. **Unlikely**: Very low chance for occurrence of event in the life of project; impossible: the event hardly happen in the life of project.

61.2.2 Difference Between Safety and Reliability

Reliability is the probability that an item will perform its intended function for the duration of a mission or a specific time interval. It is usually stated as a mean time (distance or other measure) between failure or a failure rate. The difference between safety and reliability can be summarized as follows:

(1) Different focused objects. Research object for safety: danger-fault state, which refers to a state under which one or more faults or mistakes cause effect on aircraft, flight crew, and abroad persons when the flight phase, external event, related disadvantageous operation, and environment state are considered. Research object for reliability: fault, which refers to the events which can affect normal operation of whole or partial product (system, components, spare parts, and elements, etc.) and then result in failure of operation of product according to the scheduled function, including a function and dysfunction.

(2) Different system modes. The unreliable result doesn't always affect the safety. On the contrary, the system with high safety doesn't mean that it has high reliability. For example, the traffic light at crossroad with fail-safe design is designed as red-light lighting in four directions in case of any fault, which can obviously ensure safety of traffic.
(3) Different system attributes. The safety is a key characteristic in "system-level" attributes rather than attribute of single part. Therefore, the safety must be controlled at system level. Under the premise of no background information, the wording of "safety of one part" makes no sense. The reliability is an attribute based on part, that is, "reliability of one part". However, the situation that the operation of one part in one system has no effect on the safety doesn't mean the situation that the operation of such part in another system or under another use condition has no effect on the safety.
(4) Different handling ways. The reliability method is to determine reliability organization of system based on probability handling through quantizing the fault-related accidents. The safety method is to recognize the stimulation condition, eliminate or reduce the accident effect based on analysis on potential hazard caused by normal operation.
(5) Different functional categories. The reliability is always related to functional requirement of products and assumed use condition or environment condition; however, the situation beyond normal use condition must be considered as for safety. The reliability is the ability to complete the specified function under specified condition and within specified time. If the product is not operated within specified time or under specified condition and the accident happens due to operator's error or other reasons, this problem refers to safety problem rather than reliability problem.
(6) Different analysis and evaluation method. In terms of reliability, the bottom-up method (such as FMEA) is often applied to evaluate the effect caused on parts. In terms of safety, the up-bottom method is often used to evaluate the dangerous state of system so as to determine the combination factors of accident based on levels of system.

61.2.3 System Safety Design

The basic concept of system safety is that it is a formal process of intentionally designing in safety by designing out hazards or reducing the mishap risk of hazards. It is a proactive process performed throughout the system life cycle to save lives and resources by intentionally reducing the likelihood of mishaps to an insignificant level. Compare with system design process, the system safety design progress is focus on hazards identification, evaluation, and mitigation. For avionic system, the content and scope of safety design can be categorized 25 types (i.e., requirement, fault redundancy, fault management, etc., which are detailed in Fig. 61.1.

Fig. 61.1 The contents and scope avionics system safety design

61.2.4 System Risk Controlling

Per the system safety definitions, a mishap is an actual event that has occurred and resulted in death, injury, and/or loss, and a hazard is a potential condition that can potentially result in death, injury, and/or loss. These definitions lead to the principle that a hazard is the precursor to a mishap. A hazard defines a potential event (i.e. mishap), while a mishap is the occurred event. This means that there is a direct relationship between a hazard and a mishap, as depicted in Fig. 61.2 [4].

From Fig. 61.2, it illustrates that a hazard consists of three necessary and coupled components, each of which forms the component of a hazard. All three components of the hazard are essential and required in order for a hazard to exist. Remove any one of the component and the hazard is eliminated because it is no

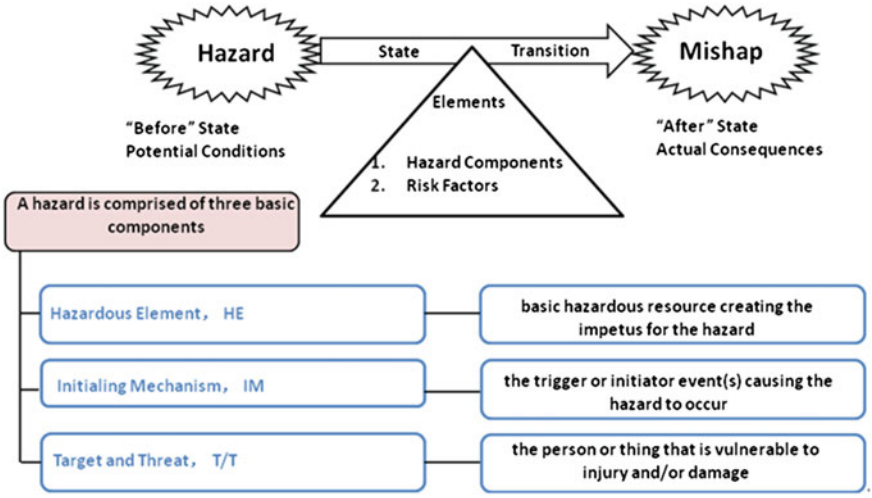

Fig. 61.2 System safety elements and state transition

longer able to produce a mishap. Reduce the probability of the IM component and the mishap probability is reduced. Reduce an element in the HE or the T/T component and the mishap severity is reduced. This aspect of a hazard is useful when determining how to controlling system risk.

Based on the analysis of system safety elements and state transition, it can model system risk controlling process as following (see Fig. 61.3).

61.3 Avionics System Safety Analysis

61.3.1 Avionics System Failure Causes

Avionics system is a real-time complex system which integrating hardware and software with the constraint of limited resources. According to system safety elements, the failure causes of avionics system can be categorized three types: users, hardware, and software (see Fig. 61.4). Therefore, to assure the system safety, it is not only need to analyze system safety, but also the components of hardware and software.

61.3.2 Avionics System Safety Analysis

Avionics system safety was an outgrowth of the general dissatisfaction with the fly-fix-fly approach to systems design. SAE ARP4754A and ARP4761 are the primary reference for system safety program information for avionics systems.

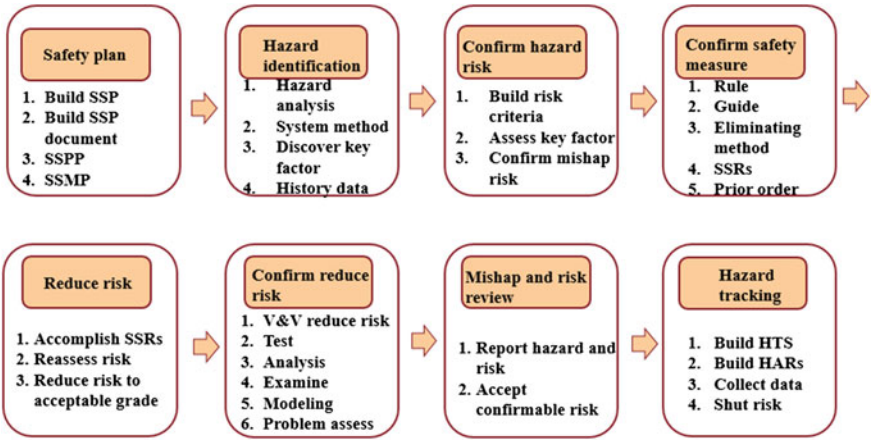

Fig. 61.3 System risk controlling implementing process

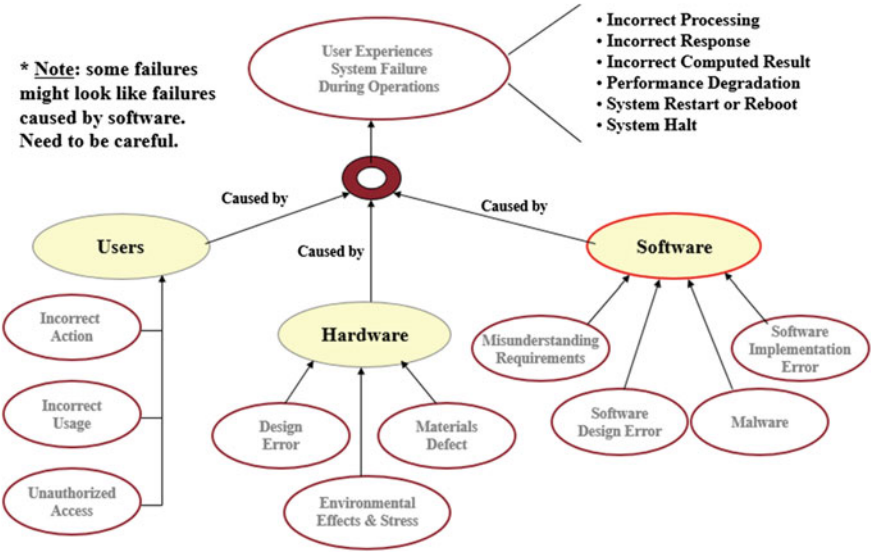

Fig. 61.4 Avionics system failure causes

By studying the early documents, basic concepts begin to emerge. These founding principles include:

Safety must be designed in. Critical reviews of the system design identify hazards that can be controlled by modifying the design. Modifications are most readily accepted during the early stages of design, development, and test. Previous design deficiencies can be exploited to prevent their recurrence.

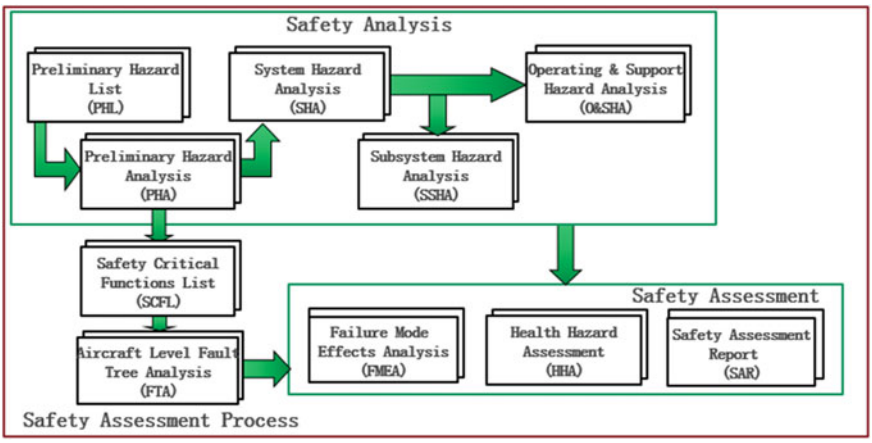

Fig. 61.5 System safety analysis process

Inherent safety requires both engineering and management techniques to control the hazards of a system. A safety program must be planned and implemented such that safety analyses are integrated with other factors that impact management decisions. Management activity must effectively control analytical and management techniques used to evaluate the system.

Safety requirements must be consistent with other program or design requirements. The evolution of a system design is a series of tradeoffs among competing disciplines to optimize relative contributions. Safety competes with other disciplines; it does not override them them.

The objective of system safety analysis is to identify hazards to system, mission, or element, assess severity, likelihood of occurrence, and consequences of each hazard on affected system elements and identify safety requirements and preferred designs. The full life cycle approach to system safety can be depicted as following figure (Fig. 61.5).

Preliminary Hazard List (PHL) provides to the safety analysis a list of hazards that may require special safety design emphasis or hazardous areas where in depth analyses need to be done. The safety analysis may use the results of the PHL to determine the scope of follow-on hazard analyses (PHA, SSHA, etc.). PHA is, as implied by the title, the initial effort in hazard analysis during the system design phase or the programming and requirements development phase for facilities acquisition. It may also be used on an operational system for the initial examination of the state of safety. The purpose of the PHA is not to affect control of all risks but to fully recognize the hazardous states with all of the accompanying system implications. The SHA should begin as the system design matures, around the preliminary design review or the facilities concept design review milestone, and should be updated until the design is complete. Design changes will need to be evaluated to determine their effects on the safety of the system and its subsystems. This analysis should contain recommended actions, applying the system safety

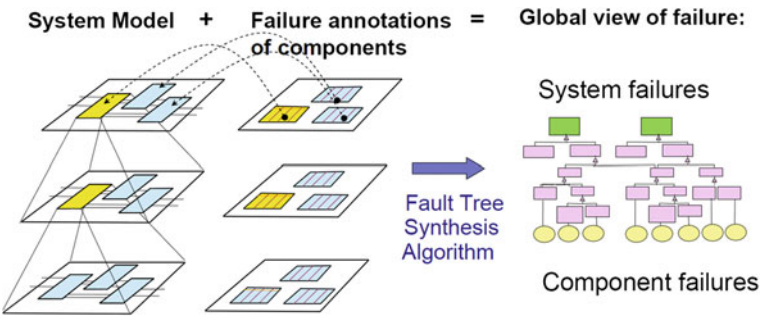

Fig. 61.6 From system failures to hardware/software failures

precedence, to eliminate or reduce the risk of identified hazards. The SSA looks at each subsystem or component and identifies hazards associated with operating or failure modes and is especially intended to determine how operation or failure of components affects the overall safety of the system. The O and SHA is performed primarily to identify and evaluate the hazards associated with the environment, personnel, procedures, and equipment involved throughout the operation of a system/element. Health Hazard Analysis (HHA) is to identify human health hazards, to evaluate proposed hazardous materials and processes using such materials, and to propose measures to eliminate the hazards or reduce the associated risks when the hazards cannot be eliminated. Safety Assessment Report (SAR) is to provide a comprehensive evaluation of the status of safety hazards and their associated risks. FHA and FMEA are analysis methodologies to assess the impact of certain hazards with a focus on interfaces and safety critical functions (SCFs).

61.4 Hardware Hazard Analysis

Avionics hardware hazards should be examined hierarchically at the levels of integrated circuit, board and LRU for complexity, including addressing functions that may not be testable, such as unused modes in multiple usage devices and potentially hidden states in sequential machines. To accomplish this, the hardware safety analysis process needs to start with exploratory functional failure analysis (FFA) concept for designing the system (see Fig. 61.6).

At this stage, an abstract functional model of the system is used to identify single and plausible combinations of multiple functional failures and assess their effects and criticality. The functional model is constructed as a functional block diagram which identifies the system functions and their dependencies in terms of material and energy flows or data.

As the design decomposition and the refinement of the hierarchical model proceed, we identify basic hardware and software components. The failure behavior of these components is analyzed using an extension of FMEA [5, 6].

Traditional FMEA examines the origins of failure within the component itself. In other words, it examines the failure behavior of the component considering only internal malfunctions (possibly caused by the environment). The function of a component in the failure domain, however, is much more complicated. A component does not only generate failure events. It can also detect (or not) and respond (or not) to failure events generated by other components which interface to the component inputs.

A component may detect disturbances of its input parameters, e.g., the absence of a power signal, or a value that is out of range. In turn, the component can mitigate the propagation of such failure events. It may, for example, replace a detected invalid input value with a correct default value. It can also fail to detect input failures and propagate these failures to other components. Finally, it may transform a certain input failure event, to a different type of output failure. An example of this is a component which detects a timing failure to one of its inputs and, in response, fails silent. To capture these additional aspects of the behavior of the component, it needs to extend the existing FMEA methods to examine the detection, mitigation and propagation of failure across the component input and output interfaces. By aids of functional decomposition block diagram and data flow diagram, we can provide a list of component failures modes as they can be observed at the component outputs. For each such failure, the analysis determines the causes as a logical combination of un-handled internal malfunctions and un-handled deviations of the component inputs. This method is applied to each component. Clearly, it can show how the component reacts to failures generated by other components. In addition, it determines the failure modes that the component itself generates or propagates.

61.5 Software Hazard Analysis

61.5.1 Software Safety

In recent years, more and more software is being used to perform critical functions in avionics system. This growth benefits from the flexibility software can offer and the complexity it can handle to provide high levels of functionality, complexity, configuration, and adaptation and to the rapidly-growing and changing needs of modern society. However, moving more and more critical functions to software is not a panacea. This, allied to mechanical, difficult to reproduce, human-dependent production processes and the lack of maturity of software engineering disciplines, makes it difficult to guarantee the safety and high integrity of systems—in other words, avoid system failures.

Software Safety [7, 8] can only be considered in the context of an operational system (e.g., Auto/aircraft anti-lock brakes, Vehicle Escape System). All have critical software processing that commands, controls, and/or monitors critical

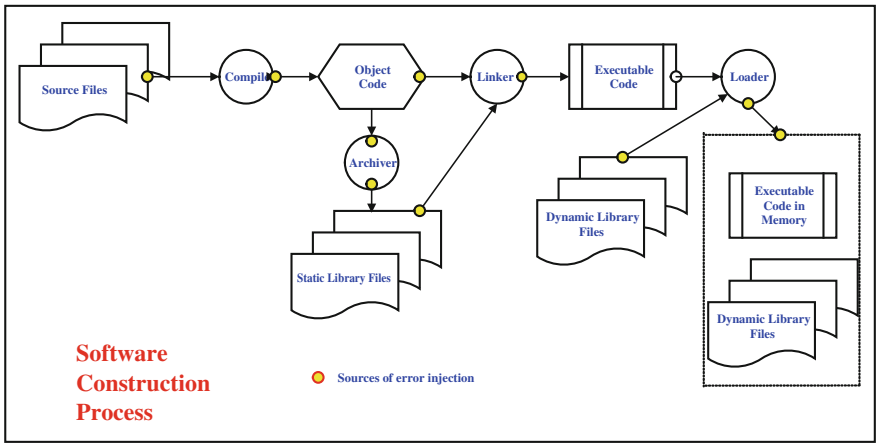

Fig. 61.7 Software construction process and failure causes

functions necessary for continued safe operation of that system are need to be analyzed to assure system integrity through prevention, elimination, and/or control of hazards that may be caused or induced by software.

61.5.2 Avionics Software Failure Causes

The general software failure causes are constitute of misunderstanding requirements, software design error, malware, and software implementation error. These errors are introduced into system along with the software construction process (see Fig. 61.7).

While avionics software has the characteristics of large complex systems, decades lifespan, hard and soft real-time requirements, server computing resource constraints, mix of computation types (i.e., logic/state machine, computational, signal processing, feedback control). Hazard causes can be those caused by hardware (or hardware components), software inputs (or lack of software input), human error, software-influenced human error, or hardware or human errors propagating through the software. Hazards may result from one specific cause or any combination of causes. As an example, "loss of thrust" on an aircraft may have causal factors in all four categories. Examples are as follows:

Hardware: foreign object ingestion,

Software: software commands engine shutdown in the wrong operational scenario,

Human error: pilot inadvertently commands engine shutdown, and

Software-influenced pilot error: computer provides incorrect information insufficient or incomplete data to the pilot causing the pilot to execute a shutdown.

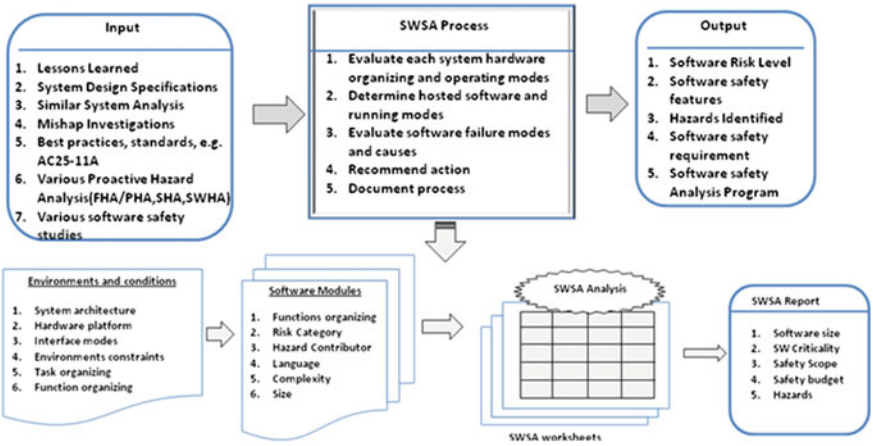

Fig. 61.8 Avionics Software safety assessment process

All these failure causes can be categorized as three types: (1) Latent defects in the source code, library files; (2) Latent defects in tools affecting code construction; (3) Environmental conditions operational software is not programmed to handle.

61.5.3 Software Safety Assessment

Software safety assessment (SWSA) is an analysis methodology for evaluating and assessing the potential safety hazards software may present to a system. It is used to determine if a system contains software and, if so, to identify what safety considerations are necessary to ensure safe software. It should be noted that SWSA is not strictly a hazard analysis but an assessment of the potential safety criticality of software in the system design.

The intent of the SWSA is not to immediately identify software-related hazards and risks but to recognize the safety implications of software in the system design. The SWSA is generally performed very early in the design life cycle, usually before software requirements or design have been initiated; therefore, the analysis starts by looking at the hardware and then gradually moving into software associated with the hardware. The SWSA process begins by listing all of the major system hardware elements or components. Each component is then evaluated for software function, whether embedded or stored. Basic data is then collected on the software, such as purpose, size, language, and the like. The software is then classified into risk levels in order to determine the safety significance of the software. These risk levels determine the amount of future effort that must be applied to ensure the development of safe software. The SWSA process and basic input/output are described as shown in Fig. 61.8.

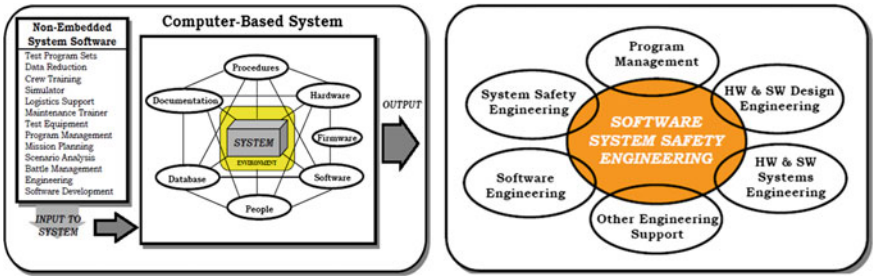

Fig. 61.9 Software system internal and external interface

An SWSA performed early in the system development cycle will help ensure that software safety is adequately addressed. Based on the output of SWSA, the SWSSP will define the specific software internal interfaces within the "system" block (within the ovals in Fig. 61.9) and also external software interfaces to the system. Each identified software interface may possess safety risk potential to the operators, maintainers, environment, or the system itself. Furthermore, to assure software safety, the SWSSP will detail the lifecycle of hardware and software that involving the system safety analysis activities such as SHA/PHA/SSHA and technical methods of SCFL and FMEA.

61.6 Conclusion

In order to solve the problem of safety analysis for integrated avionics system, in this paper, we study the hazard and mishap modes of avionics system and the methods of risk analysis, risk evaluation, risk controlling, risk elimination and risk mitigate, which are presented based on the system risk controlling theory. Finally, the organizing and engineering technologies of system safety, software safety, and hardware safety are also discussed to provide foundation for designing integrated avionics system safety.

Acknowledgments This paper is supported by Avionics Science Foundation (No. 20125552053) and National Key Basic Research Program of China (No. 2014CB744900).

References

1. Leveson N (2011) Engineering a safer world: systems thinking applied to safety. MIT Press, Cambridge
2. Meshkat L, Dugan JB, Andrews JD (2002) Dependability analysis of systems with on-demand and active failure modes, using dynamic fault trees. IEEE Trans Reliab 51(2):240–251

3. SAE Standard J-1739 (2002) Potential failure mode and effects analysis in design (design FMEA) and potential failure mode and effects analysis in manufacturing and assembly processes (process FMEA) and effects analysis for machinery (machinery FMEA)
4. Ericson CA (2005) Hazard analysis techniques for system safety. Wiley, Hoboken
5. Goble WM, Brombacher AC (1999) Using a failure modes, effects and diagnostic analysis (FMEDA) to measure diagnostic coverage in programmable electronic systems. Reliab Eng Syst Saf 66(2):145–148
6. Catelani M, Ciani L, Luongo V (2010) The FMEDA approach to improve the safety assessment according to the IEC61508. Microelectron Reliab 50(9–11):1230–1235
7. DoD (1999) Joint software system safety handbook
8. Dunn WR (2002) Practical design of safety-critical computer systems. Reliability Press, Solvang

Chapter 62
Fault Signal Analysis for Aircraft Generator Rectifier

Xiaojun Tang, Dasen Fan, Liang Liu, Zhenbao Liu, Chao Zhang and Shuhui Bu

Abstract Integrated drive generator (IDG) connected with the main shaft of aircraft engine is the key power source for many electronic systems such as flight management computers, control and navigation systems, supplying constant frequency AC electrical power to the aircraft. IDG is composed of constant speed drive with differential assembly, brushless synchronous exciter generator, rectifier, brushless synchronous main generator, and generator control unit. The function of rectifier is to convert the alternating current from the exciter generator into a direct current, which will be applied to field winding of the main generator for producing three-phase voltage to aircraft electronic systems. According to report from previous research, diode failure in rectifier occurs with a high frequency. In this paper, we attempt to propose a solution for fast and accurately detecting faults from rectifier. We first analyze the noisy signals generated under different cases of diode faults by virtue of a simulated circuit model built in Matlab, and the fault signal is decomposed into finite intrinsic mode functions by empirical mode decomposition. Intrinsic mode functions are successively transformed by Hilbert transform to obtain the instantaneous frequency. Therefore, the fault transient signal can be analyzed by means of the instantaneous frequency and Hilbert marginal spectrum. The experimental results show that our method can be effectively applied to analyze the fault status of aircraft generator rectifier. Our work has potential to in real-time monitor safe and reliable operation of aircraft generators and further supervise the quality of aircraft power.

Keywords Integrated drive generator · Rectifier fault · Signal analysis · Intrinsic mode functions

X. Tang · D. Fan · L. Liu · Z. Liu (✉) · C. Zhang · S. Bu
School of Aeronautics, Northwestern Polytechnical University, Xi'an 710072, China
e-mail: liuzhenbao@nwpu.edu.cn
URL: http://www.nwpu.edu.cn

J. Wang (ed.), *Proceedings of the First Symposium on Aviation Maintenance and Management-Volume I*, Lecture Notes in Electrical Engineering 296,
DOI: 10.1007/978-3-642-54236-7_62,

62.1 Introduction

Integrated drive generator (IDG) takes main responsibility of power supply, which offers 115 V and 400 Hz alternating current to most electromechanical and electronic devices of aircraft, for example, flight management computers, flight control, and navigation systems. In order to make these devices operate normally and safely, alternating current power of IDG should be stable and efficient. For a typical airborne IDG system, it directly connects with aircraft engine via the main shaft, and gains rotational kinetic energy through the gear accessory box in each engine. The rotational kinetic energy in magnetic field is then converted into electric energy. IDG is a complex and integrated group of electrical and mechanical devices, which is mainly composed of constant speed drive with differential assembly, brushless synchronous exciter generator, rectifier, brushless synchronous main generator, and generator control unit. The coil of the exciter generator, rectifier, and the magnetic coil of the main generator rotate following the main shaft. We know that when the coil rotates according to Faraday's law of electromagnetic induction, the generator will produce the three-phase alternating current. Three-phase alternating current from the exciter generator is rectified to direct current as input into the induction coil of the main generator. Because the coil of the main generator rotates with the main shaft, it will produce the rated alternating current for aircraft electrical and electronic systems.

In the whole process of power generation, rectifier failures occur with a relatively higher probability. The reason leading to rectifier failures is that diodes used for direct current conversion may degenerate and become invalid, which will result in disastrous sequel. In this paper, we aim at providing an analysis method on fault signal of rectifier in aircraft generator. Inspired by a recent work proposed by Tantawy et al. [1], we first build a simulation component model according to the constitution of rectifier and the whole aircraft generator. The simulation model will generate noisy signals under normal condition, and also noisy fault signals in cases of different diode faults. The fault signal is decomposed into finite intrinsic mode functions by empirical mode decomposition. Intrinsic mode functions are successively transformed by Hilbert transform to obtain the instantaneous frequency. Therefore, the fault transient signal can be analyzed by means of the instantaneous frequency and Hilbert marginal spectrum. Figure 62.1 shows the flow chart of the whole process. Our work has potential to in real-time monitor safe and reliable operation of aircraft generators and further supervise the quality of aircraft power.

62.2 Related Works

In order to improve reliability and safety, fault-detection, and fault diagnosis become increasingly important for many technical processes, for example, aircraft [2, 3]. Model-based methods of fault-detection were developed by using input and

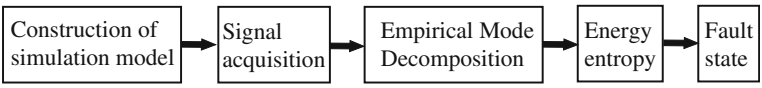

Fig. 62.1 The flow chart of the proposed method

output signals and applying dynamic process models [4]. Megahed et al. [5] describe two neural networks-based digital differential protection scheme for generator stator winding protection, one of which is used for fault detection and the other is used for internal fault classification differentiating between generator states including normal, external fault, and internal fault states. Kulkarni et al. [6] present a on-line detection method for incipient faults in the windings of turbine-generator rotors based on twin signal sensing technique. The technique bases a fact that any abnormality in the winding results in the applied signals being reflected through nonsymmetrical circuits. McArdle et al. [7] propose a noninvasive method for detecting failure of brush-less exciter rotating diodes, which include open circuit and short circuit. They find that the exciter field current waveform changes distinctly when a diode fails, and hence perform harmonic analysis of the exciter field current waveform. Batzel et al. [8] develop prognostic tools to detect the onset of electrical failures in an aircraft power generator, and to predict the generators remaining useful life (RUL). They mention that typical diode failures are preceded by a period of increasing reverse leakage current in the device. They conduct failure mode, effects, and criticality analysis (FMECA) of generator, and detect observable signature features to failure mechanisms so that the progress of component damage can be observed.

62.3 The Implementation of Aircraft Generator Model

Our work is based on IDG's simulation model to analyze faulty signal of rectifier diodes, and implement this simulation model. The model is composed of three core components, exciter generator, rectifier, and main generator, which are shown in Fig. 62.2. A 400 Hz brushless generator is used in this model. Because this paper focuses on rectifier faults, we will not discuss generator faults such as coil problems. According to the suggestion from Tantawy et al., we set and connect six diodes to simulate a real rectifier. The model is designed in Matlab, and the working conditions contain normal mode, the mode of single diode failure, and the mode of dual diodes failure. The fault signals are generated in different cases as our analyzed targets. In order to obtain sufficient initial sample data under each different faulty situation of rectifier diode and meet the requirement of sampling theorem, we choose 30 K sampling points of each discrete signal after injecting single and dual diode faults.

Because a real aircraft power supply system possibly generates interference signals, resulting from electromagnetic disturbance of other electrical devices and

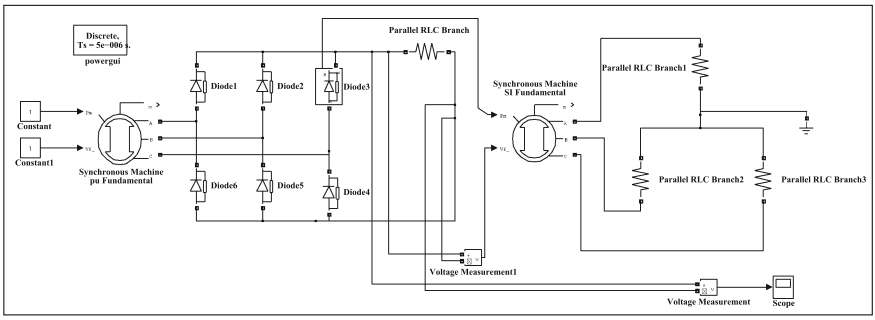

Fig. 62.2 Simulation model of aircraft generator rectifier

mechanical abrasion of IDG, we consider its output voltage is not a pure periodic signal. The additional noise is added into the output ideal signal from the simulation model so as to approximate real working environment of aircraft power supply system. In our work, we choose 10 % Gauss white noise proportional to the amplitude of the original signal. The amplitude of noise is under Gaussian distribution, and moreover the power spectral density of noise is distributed normally. The simulation waveform is shown in Fig. 62.3. The output noisy signal of the simulated model is under different conditions of rectifier. The left one is generated when all the diodes works, the medium signal and the right signal are outputted in the cases of single diode fault and double diode fault respectively.

62.4 Empirical Mode Decomposition of Fault Signal

In this section, we perform empirical mode decomposition of fault signal obtained from the simulation model so as to analyze the fault signal and extract the intrinsic feature of signals under different conditions. The reason of not choosing Fourier transform lies in that the frequency of Fourier analysis is defined for the sine or cosine function spanning the whole data length with constant amplitude, and Fourier spectral analysis only examines the global energy-frequency distributions and requires the analyzed data to have to be strictly periodic or stationary. It is not adaptable to fault signals from rectifier diodes. Therefore, we resort to a power tool of nonlinear and nonstationary analysis, empirical mode decomposition [9]. In fact, empirical mode decomposition has been extensively applied to fault detection in many domains [10] before. In order to make our paper self-contained, empirical mode decomposition will be discussed shortly.

Before knowing the EMD time frequency analysis we must establish two basic concepts: the instantaneous frequency and the Intrinsic Mode Function (IMF). At the beginning the concept of instantaneous frequency has been controversial. There are two main reasons. First it is influenced by Fourier transform. Second

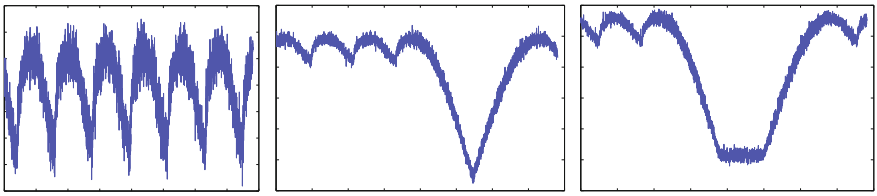

Fig. 62.3 The output noisy signal of the simulated model mentioned above under different conditions of rectifier. The *left* one is generated when all the diodes works, the medium signal and the *right* signal are outputted in the cases of single diode fault and double diode fault respectively

instantaneous frequency is not uniquely defined. But after Hilbert transform method is proposed, the concept of instantaneous frequency are unified.

62.4.1 Instantaneous Frequency of Fault Signal

Let *x(t)* denote a fault signal obtained from the simulation model mentioned above. It can be converted into its Hilbert transform as follows.

$$y(t) = \frac{1}{\pi} P \int_{-\infty}^{\infty} \frac{x(\tau)}{t-\tau} d\tau \tag{62.1}$$

where P indicates the Cauchy principle value. An analytic signal *z(t)* is formed by their complex conjugate pair,

$$z(t) = x(t) + iy(t) = a(t)e^{i\theta(t)} \tag{62.2}$$

in which:

$$a(t) = \left[x^2(t) + y^2(t)\right]^{1/2}, \theta(t) = \arctan\frac{y(t)}{x(t)}. \tag{62.3}$$

Derivative of the phase function $\theta(t)$ is commonly defined as the instantaneous frequency as:

$$\omega(t) = \frac{d\theta(t)}{dt} \tag{62.4}$$

In order to obtain an existent and meaningful instantaneous frequency, the fault signal must be decomposed into a set of intrinsic model functions because these functions are symmetric with respect to the local zero mean and have the same numbers of zero crossings and extrema.

62.4.2 Intrinsic Mode Functions

In order to obtain the instantaneous frequency of signal which has physical meaning, each intrinsic mode function must meet two conditions:

1. The number of extrema N_e and the number of zero crossings N_z must either equal or differ at most by one. The relation is expressed as follows:

$$(N_z - 1) \leq N_e \leq (N_z + 1) \tag{62.5}$$

2. The mean value of the envelope defined by the local maxima and the envelope defined by the local minima is zero in any time because asymmetric wave forms may lead to undesirable fluctuations of instantaneous frequency.

$$[f_{\max}(t) + f_{\min}(t)]/2 = 0, t \in [t_a, t_b]. \tag{62.6}$$

An advantage of decomposing fault signal into intrinsic mode functions is that the basis of the decomposition is derived from the original fault signal and adaptive to the fault type embedded in the original signal. Each intrinsic mode function simply adopt the envelope connecting local maxima points and local minima points by a cubic spline separately, which can be linear or nonlinear and even nonstationary but involve only one mode of oscillation and no complex riding waves.

62.4.3 Processing Flow of Decomposition

The processing flow of decomposition of each fault signal into intrinsic mode functions is summarized as follows.

1. Compute all the local extreme points of the original fault signal $x(t)$ including local maxima and minima, and adopt the two spline curves to connect these points to form lower and higher envelope of the original signal, which is expressed as $u(t)$ and $v(t)$ respectively. Take the mean of a sequence of the lower and higher envelopes $m_1(t)$ as follows.

$$m_1(t) = \frac{u(t) - v(t)}{2} \tag{62.7}$$

And then obtain the difference $h_1(t)$ between the original data $x(t)$ and the mean $m_1(t)$ of the lower and higher envelope.

If $h_1(t)$ meets two conditions of IMF mentioned above, and then $c_1(t)$ is seen as the first component of $x(t)$, namely, $c_1(t) = h_1(t)$.

If it does not satisfy the above conditions, repeat step one for $h_1(t)$ and regard $h_1(t)$ as the original data. Then we can again obtain the average value $m_{11}(t)$ of envelopes. Then determine whether $h_{11}(t) = h_1(t) - m_{11}(t)$ meets two conditions

of IMF. If not, we repeat this sifting procedure K times and obtain $h_{1k}(t) = h_{1(k\text{-}1)}(t) - m_{1k}(t)$. If $h_{1k}(t)$ meets two conditions of IMF, stop this step. In the practical course, stopping criterion can be achieved by restricting the size of standard deviation SD between two sifting results.

$$SD = \sum_{t=0}^{T} \frac{|h_{1(k-1)}(t) - h_{1k}(t)|^2}{h_{1(k-1)}^2(t)}. \tag{62.8}$$

The value of SD usually is set to 0.2–0.3. The first IMF of the signal $x(t)$ is designated as

$$c_1(t) = h_{1k}(t). \tag{62.9}$$

2. After separating the finest scale $c_1(t)$ from $x(t)$, we can obtain its residual value sequence $r_1(t)$ as

$$r_1(t) = x(t) - c_1(t). \tag{62.10}$$

3. Regarding $r_1(t)$ as a new primitive data containing longer period components, repeat the same procedure of sifting described above to get n IMF components until a predefined stop criterion is reached. The last remainder of the original signal is denoted as $r_n(t)$. The final residue should be trend function identifying the direction of the original data.

After the above steps, we obtain a whole set of IMFs and a residue, and the original fault signal is decomposed into the following

$$x(t) = \sum_{i=1}^{n} c_i(t) + r_n(t). \tag{62.11}$$

Another point we should note is how to set the stop condition of decomposition. Generally, the decomposition should be terminated if the last IMF $c_n(t)$ or the residual component $r_n(t)$ is adequately small or $r_n(t)$ changes into a monotone function resulting in not generating IMF component any more.

62.5 The Energy Entropy

When different types of diode failure appear in the aircraft power supplying system, the frequency of voltage signals will vary and meanwhile the energy distribution of fault signals becomes different. Although intrinsic mode functions are suitable for time scale analysis of nonlinear and nonstationary fault signal, we must further introduce the concept of energy entropy to identify the change of the energy distribution. We depend on these basis of EMD decompositions to calculate the energy distribution of each IMF. This can quantitatively determine the

working state of the rectifier and identify fault types by virtue of comparing their energy entropy.

However, it is impossible to directly compute the energy entropy of fault signals. The original signal $x(t)$ is first decomposed into n intrinsic mode functions, and we can convert the problem into computing the energy entropy of all the empirical functions. The energy of each empirical function is denoted as E_i, $i \in [1, n]$. We suppose the energy of the residual component is ignored. Because all the empirical functions are orthogonal, the total energy of all the empirical functions are equivalent to the energy of the original signal.

$$E(x(t)) = \sum_{i=1}^{n} E_i \tag{62.12}$$

Each empirical function contains component under different frequencies and has different energy and hence the energy distribution is formed in frequency domain of the original signal. EMD energy entropy can be defined by

$$H_{EN} = -\sum_{i=1}^{n} p_i \log p_i. \tag{62.13}$$

where $p_i = E_i/E(x(t))$ indicates the percentage of the IMF energy in the total energy.

62.6 Experimental Results

We implemented the whole analysis procedure from signal generation to signal decomposition in Matlab. The simulation model is first built via Matlab Simulink to produce signals under normal and faulty conditions. Two typical types of faults in the rectifier, single diode fault and dual diode fault, are injected into the simulation model while producing faulty signals. We measure rectifier output voltage, and obtain the time-domain waveform, as illustrated in Fig. 62.3.

After the normal or faulty signals are generated from the simulation model, we next analyze these signals via the tool of empirical mode decomposition. The number of intrinsic mode functions is set in real-time according to the stopping criterion, for example, 14 in some experiments of fault injection. Hilbert spectrum of each intrinsic mode function in time–frequency domain is computed under three conditions: normal, single diode fault and dual diode fault. The Hilbert spectrum of all the functions are plotted in Fig. 62.4.

It is shown in Fig. 62.4 that it becomes easy to distinguish signals between normal condition and fault conditions by virtue of the IMF spectrum. However, the single diode fault and double diode fault are still difficult to distinguish, and it means that the fault type can not be clearly recognized from these signals.

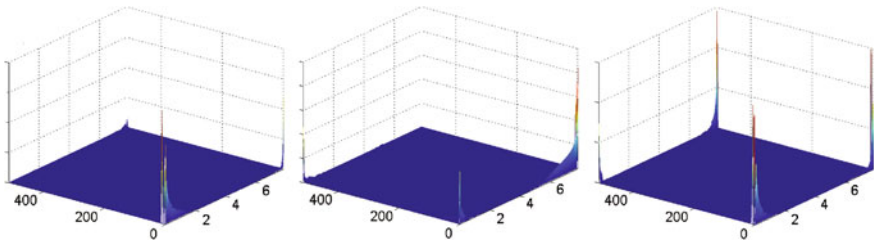

Fig. 62.4 Hilbert spectrum of intrinsic mode functions decomposed from original signals under three conditions: the *left* is normal condition, the *medium* is single diode fault and the *right* is dual diode fault

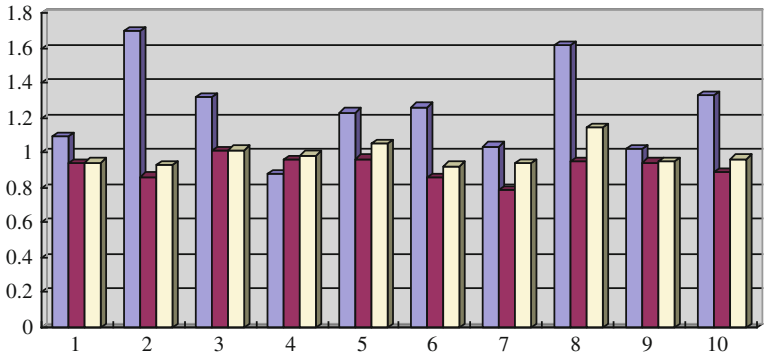

Fig. 62.5 Energy entropy. The *blue*, *red* and *yellow* colors respectively stand for normal, single diode fault and double diode fault conditions

In consideration of the problem which is faced to identify fault types, we introduce a pure numeral value to solve it, that is, the energy entropy of normal signal or faulty signal described above. The energy entropy of all the intrinsic model functions under different diode faults are calculated after empirical mode decomposition. Because the additive noise is a random sequence, each running results are slightly different. To eliminate the occasionality of each single experiment, we run the program ten times under the normal, single and double diode fault condition to compute their energy entropy. Figure 64.5 shows the values of energy entropy under different conditions.

The results show that the energy entropy under the normal condition is larger than the other two cases. The reason is that in the normal state the signal energy distribution is relatively average and uncertainty. When a single or double diode fault exists, it will appear in the corresponding resonance frequency and the corresponding frequency band. At this point, the energy will be concentrated in the frequency band. Then the energy distribution of uncertainty is reduced leading to the decrease of entropy. According to the experimental results it can be also seen that the energy entropy of the single diode fault is smaller than that of the double diode fault. Therefore, it makes it easy to distinguish different fault types.

62.7 Conclusion

In this paper, we suggested a novel solution for fast and accurately detecting faults from rectifier, which may lead to severe danger to important electronic systems. We first built a simulated circuit model in Matlab to generate the noisy signals under different cases of diode faults. In order to analyze the intrinsic feature of these signals, we introduced empirical mode decomposition to decompose each signal into finite intrinsic mode functions. Intrinsic mode functions are successively transformed by Hilbert transform to obtain the instantaneous frequency and Hilbert spectrum. The spectrum can be used to distinguish normal state and faulty states. In order to further recognize different types of diode faults, energy entropy was proposed to observe their difference in energy entropy. The experimental results showed that our method can be effectively applied to analyze the fault status of aircraft generator rectifier.

Acknowledgments This work is partly supported by the Fundamental Research Foundation of Northwestern Polytechnical University under Grant JC20120210 and by the Aeronautical Science Foundation of China under Grant 20120853007.

References

1. Tantawy A, Koutsoukos X, Biswas G (2012) Aircraft power generators: hybrid modeling and simulation for fault detection. IEEE Trans Aerosp Electron Syst 48(1):552–571
2. Zhang Y, Li XR (1998) Detection and diagnosis of sensor and actuator failures using IMM estimator. IEEE Trans Aerosp Electron Syst 34(4):1293–1313
3. Guerrier S, Waegli A, Skaloud J, Victoria-Feser MP (2012) Fault detection and isolation in multiple MEMS-IMUs configurations. IEEE Trans Aerosp Electron Syst 48(3):2015–2031
4. Isermann R (2005) Model-based fault-detection and diagnosis status and applications. Ann Rev Control 29(1):71–85
5. Megahed A, Malik O (1999) An artificial neural network based digital differential protection scheme for synchronous generator stator winding protection. IEEE Trans Power Deliv 14(1):86–93
6. Kulkarni AS, El-Sharkawi MA, Marks RJ II, Andexler G, Xing J, Kerszenbaum I (2000) Development of a technique for on-line detection of shorts in field windings of turbine-generator rotors: Circuit design and testing. IEEE Trans Energy Convers 15(1):8–13
7. McArdle M, Morrow D (2004) Noninvasive detection of brushless exciter rotating diode failure. IEEE Trans Energy Convers 19(2):378–383
8. Batzel TD, Swanson DC (2009) Prognostic health management of aircraft power generators. IEEE Trans Aerosp Electron Syst 45(2):473–482
9. Huang NE, Shen Z, Long SR, Wu MC, Shih HH, Zheng Q, Yen NC, Tung CC, Liu HH (1998) The empirical mode decomposition and the Hilbert spectrum for nonlinear and non-stationary time series analysis. Proc Roy Soc A 454(1971):903–995
10. Puche-Panadero R, Pineda-Sanchez M, Riera-Guasp M, Roger-Folch J, Hurtado-Perez E, Perez-Cruz J (2009) Improved resolution of the MCSA method via Hilbert transform, enabling the diagnosis of rotor asymmetries at very slow slip. IEEE Trans Energy Convers 24(1):52–59

Chapter 63
Research on Equipment Reliability Prediction and Reliability Allocation Method Based on RCM

Bin Ru, Tianwei Zhang and Yuxin Wang

Abstract Traditional manual modeling and analysis method cannot meet today's requirements of high-tech equipment for reliability and maintainability. The RCM-analysis methods proposed to study the reliability of electronic equipment, as well as reliability allocation method. We use Lambda Predict microcontroller-based instrumentation and control equipment part of the circuit to set up the model and make a reliability prediction analysis and reliability allocation study. At last, we get the expected results of the analysis equipment reliability.

Keywords Reliability · Reliability centered maintenance · Reliability prediction analysis · Failure rate

63.1 Introduction

Since the mid-twentieth century, equipment reliability, maintainability, and supportability (RMS) get more and more attention. But with the development and advancement of technology, the complexity of the equipment is also increasing the traditional simple analysis methods have been unable to meet the requirements of the people [1]. Now large-scale electronic systems such as avionics systems or large industrial instrumentation and control systems are a large organization, which is complex and highly integrated [2]. In many areas, whether the performance of electronic system is powerful has become a decisive factor in comprehensive performance [3]. Such electronic systems play an important role in various fields and also for their designers and maintenance, this brings a lot of reliability, maintainability, and the many logistical problems. Whether such a complex system

B. Ru (✉) · T. Zhang · Y. Wang
School of Aeronautics, Northwestern Polytechnical University,
Xi'an 710072 Shaanxi, China
e-mail: hitlerrb@126.com

J. Wang (ed.), *Proceedings of the First Symposium on Aviation Maintenance and Management-Volume I*, Lecture Notes in Electrical Engineering 296,
DOI: 10.1007/978-3-642-54236-7_63,

can be in a good operation, maintenance and security, requires a complete set of methods, procedures, and techniques [4]. The emergence of professional reliability analysis software for our electronic devices for integrated reliability analysis provides strong support and help. This thesis did some analysis research based on the two software RCM ++ and Lambda Predict. Also the result of the research on Reliability Centered Maintenance (RCM) is proposed [5]. This paper studies the principle and the use of analysis methods about two software "RCM ++" and "Lambda Predict," which is produced by Reliability Soft Corporation. Application of RCM ++ software parts of avionics subsystems of RCM, Failure Mode and Effects Analysis (FMEA) and failure mode, effects and criticality analysis (FMECA). Use Lambda Predict software instrumentation and control equipment based on single chip portion of the circuit modeling and reliability prediction analysis, and explore the failure rate distribution on the system design.

63.2 RCM Theory

63.2.1 Emergence and Development

The first phase (before 1950), was not high degree of industrialization, thus the length of downtime of machine is insignificant. While the equipment itself is relatively simple and reliable and design margin is relatively large, so the equipment is not serious consequences of failure, and easy to repair faulty equipment [6]. People did not pay attention on preventive work, maintenance work is mainly corrective maintenance. Maintenance strategy is Corrective Maintenance (CM). The second phase (1950–1970), is characterized by a high degree of industrialization, equipment failure will seriously affect the production, the consequences are serious, and equipment is relatively complex, expensive, high maintenance costs. In this period, people's maintenance strategy began to shift to the corrective maintenance preventive maintenance. People think as long as we make the preventive maintenance before the life of the equipment prior, we can prevent equipment failure. So the maintenance strategy shifts to Preventive Maintenance (PM). The third phase (1970), through the reliability application outline, targeted maintenance, inspection and replacement as necessary and a series of trials and summed to form a reliability centered maintenance, is named RCM [7]. People get two important conclusions by analyzing: 1. For complex equipment, unless you have some kind of dominant failure mode, otherwise regular renovations cannot help to improve its reliability. 2. For many projects, there is not a preventive maintenance approach which is very effective.

63.2.2 Differences Between the Traditional Repair and RCM

Equipment's reliability and security in the design and manufacture is given by the characteristic, effective maintenance only maintain but not increase them. RCM specially emphasis on equipment's reliability and security. Equipment failures have different effects or consequences, so we should adopt different strategies. The severity of the consequences of failure is the point whether to do preventive maintenance. The equipment's failure is inevitable, but the consequences are not the same, it is important to prevent a serious failure consequence. Equipment's failure types are different, so we should make different approaches to control the timing of maintenance work. There are regular wear and tear faults products suitable for regular overhaul or replacement to prevent malfunction or failure caused by multiple. For those who have no loss of product failures law, regular overhaul or replacement is often detrimental, they are more suitable by checking, monitoring, as appropriate, for maintenance [8]. For different types of equipments, we should select different type of work applicable and effective. Thus we can save more resources and cost in maintenance, meanwhile the reliability and security of the premise are guaranteed.

63.3 Modeling Based on RCM

63.3.1 Basic Concept of RCM

RCM is the international common engineering method for device to determine equipment preventive maintenance requirements and optimizing maintenance system. Reliability refers to the ability to complete the required function under the conditions and within the stipulated time for the system, equipment, spare parts, etc. The reliability's probability refers to that the product under the conditions specified functions within the specified time. That is called R(t). Risk Priority Number (RPN) is the multiplication of risk probability, severity, and detection degrees of the three grade. Risk probability is divided into ten degrees from a very low risk probability to a very high risk probability. Severity is divided into ten degrees from no effect to affect safety. Detection degrees are divided into ten degrees from imperceptible to absolutely unreliable. So the RPN differs between 1 and 1,000, the greater the RPN is, the more serious the problem there is.

63.3.2 Commonly Used Reliability Prediction Standards

MIL-HDBK-217: Reliability Prediction of Electronic Equipment (MIL-HDBK-217), which is released by U.S. Department of Defense in December 1991. This standard supports the analysis method of commercial and military applications component.

Bellcore/Telcordia (SR-332): This process is expected to predict the reliability of electronic equipment (TR-332 Issue 6), which is released by Bell Communications Research Institute in 1995. This standard provides a reliability prediction model commercial standards.

NSWC-98/LE1: Machinery and equipment reliability prediction procedures manual (NSWC-98/LE1). 1980s, published by the Naval Surface Warfare Center.

63.4 To Make the Reliability Prediction Analysis by Using Lambda

63.4.1 Calculation and Measurement

Standards are generally based on the basic components in the system failure rate to estimate the reliability of the system. Basic component failure rates describe the unit's working situation under the normal conditions. Basic failure rate can take on a variety of factors (Called π factor, ranging between 0 and 1), reliability standards calculate the failure rate by adding all parts' and components' failure rate.

Failure rate λ: Conditions failure rate is defined as in a measure of state conditions specified intervals, the total number of failures in the total project which is divided by the total time consumed. Reliability prediction is generally described as the number of failures per million hours (FPMH).

MTBF: MTBF is between failures under certain conditions, the expected number of hours worked.

Reliability R(t): Because the standard assumes a constant failure rate and all calculations are based on the failure rate or MTBF values. This hypothesis would suggest to use the exponential distribution model to describe the reliability function. The following equation describes the exponential distribution model:

$$\mathrm{R}(t) = e^{-\lambda t} \text{ or } \mathrm{R}(t) = e^{-t/\mathrm{MTBF}} \tag{63.1}$$

Reliability Allocation: Typically, a design needs to meet a specific reliability targets. For multiple components/subsystems of systems, reliability goals need to be a way to share (assigned) to different components/subsystems to ensure that the total failure rate meets reliability objectives.

63.4.2 Examples of Reliability Prediction and Distribution

In the initial stage of design, we do not make the detail design of each subsystem, but in this period we already have a design need to meet reliability goals. For multiple components/subsystems of systems, reliability goals need to be a way to

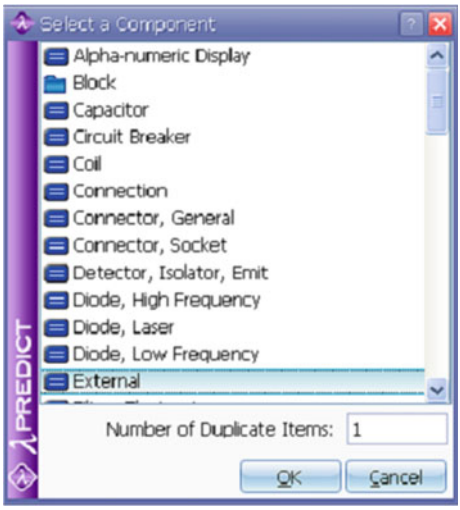

Fig. 63.1 Select component type

share (assigned) to different components/subsystems to ensure that the total failure rate meets reliability objectives.

We operate the reliability allocation by using ARINC method which is recommended by American Aeronautical Radio, Inc. First, we add external components to add to the system failure rate which can be customized subsystems. This is shown in Fig. 63.1

After we have added all components, enter the failure rate for each of these estimates. This estimated failure rate is gotten according to the component's complexity of technology or to the experience and history (Fig. 63.2).

After all the components' estimated failure rate is manually entered, the whole model is completed. This is shown in Fig. 63.3.

Checking the results:

$$\begin{aligned}\lambda_{sy} &= \sum_{i=1}^{7} \lambda_{iy} = (0.7 + 0.1 + 0.2 + 0.35 + 0.25 + 1.5 + 2.01) \times 10^{-5} \\ &= 5.1 \times 10^{-5}\end{aligned} \tag{63.2}$$

Total system failure rate is: 5.1×10^{-5}/h.

$$R_{sy}(1000) = e^{-\lambda_{sy} t} = e^{-5.1 \times 10^{-5} \times 1000} = 0.9503 \tag{63.3}$$

Current reliability 0.9503. Weighting factor calculation:

$$\omega_1 = \frac{\lambda_{1y}}{\lambda_{sy}} = \frac{0.7 \times 10^{-5}}{5.1 \times 10^{-5}} = 0.1373 \tag{63.4}$$

$$\omega_2 = \frac{\lambda_{2y}}{\lambda_{sy}} = 0.0196$$

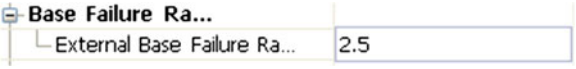

Fig. 63.2 Enter the estimated failure rate

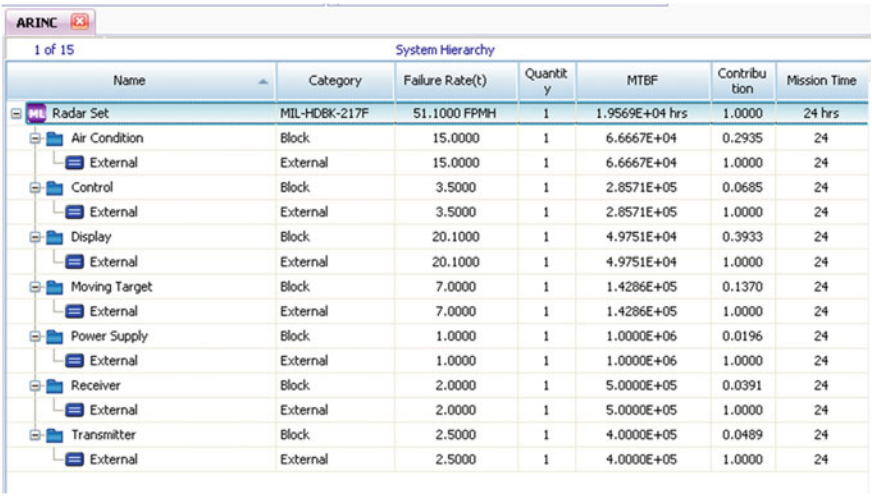

Name	Category	Failure Rate(t)	Quantity	MTBF	Contribution	Mission Time
Radar Set	MIL-HDBK-217F	51.1000 FPMH	1	1.9569E+04 hrs	1.0000	24 hrs
Air Condition	Block	15.0000	1	6.6667E+04	0.2935	24
External	External	15.0000	1	6.6667E+04	1.0000	24
Control	Block	3.5000	1	2.8571E+05	0.0685	24
External	External	3.5000	1	2.8571E+05	1.0000	24
Display	Block	20.1000	1	4.9751E+04	0.3933	24
External	External	20.1000	1	4.9751E+04	1.0000	24
Moving Target	Block	7.0000	1	1.4286E+05	0.1370	24
External	External	7.0000	1	1.4286E+05	1.0000	24
Power Supply	Block	1.0000	1	1.0000E+06	0.0196	24
External	External	1.0000	1	1.0000E+06	1.0000	24
Receiver	Block	2.0000	1	5.0000E+05	0.0391	24
External	External	2.0000	1	5.0000E+05	1.0000	24
Transmitter	Block	2.5000	1	4.0000E+05	0.0489	24
External	External	2.5000	1	4.0000E+05	1.0000	24

Fig. 63.3 Reliability allocation system model

$$\omega_3 = 0.0392;$$
$$\omega_4 = 0.0686;$$
$$\omega_5 = 0.0490;$$
$$\omega_6 = 0.2941;$$
$$\omega_7 = 0.3922;$$

Assign each component failure rate:

$$\lambda_{1p} = \lambda_{sq} \cdot \omega_1 = 1 \times 10^{-5} \times 0.1373 = 0.1373 \times 10^{-5}/\mathrm{h} \tag{63.5}$$

$$\lambda_{2p} = 0.0196 \times 10^{-5}/\mathrm{h}$$
$$\lambda_{3p} = 0.0392 \times 10^{-5}/\mathrm{h}$$
$$\lambda_{4p} = 0.0686 \times 10^{-5}/\mathrm{h}$$
$$\lambda_{5p} = 0.0490 \times 10^{-5}/\mathrm{h}$$
$$\lambda_{6p} = 0.2941 \times 10^{-5}/\mathrm{h}$$
$$\lambda_{7p} = 0.3922 \times 10^{-5}/\mathrm{h}$$

1 of 70 System Hierarchy

Name	Category	Failure Rate(t)	Quantity	MTBF	Contribution	Mission Time
Bellcore TR-332 Issue 6	Bellcore TR-332 Issue 6	300.0000 FITS	1	3.3333E+06 hrs	1.0000	24 hrs
12V DC Fan	Block	300.0000	1	3.3333E+06	1.0000	24
power supply assembly	MIL-HDBK-217F	0.7170 FPMH	1	1.3947E+06 hrs	1.0000	24 hrs
POWER SUPPLY	Block	0.4170	1	2.3982E+06	0.5816	24
1N4005	Diode, Low Frequency	0.0044	1	2.2606E+08	0.0106	24
PTC-960	Resistor	0.0016	1	6.4234E+08	0.0037	24
1/4w-150-5%	Resistor	0.0029	1	3.5029E+08	0.0068	24
BZT03C33	Diode, Low Frequency	0.1006	1	9.9442E+06	0.2412	24
J507A	Diode, Low Frequency	0.0737	1	1.3567E+07	0.1768	24
BZX-15V	Diode, Low Frequency	0.0417	1	2.3958E+07	0.1001	24
2N3019	Transistor, LF Bipolar	0.0102	1	9.7957E+07	0.0245	24
C0402C105	Capacitor	0.0106	2	9.4190E+07	0.0255	24
TM-7	Connection	0.1700	1	5.8824E+06	0.4077	24
12V DC Fan	Linked Block	0.3000	1	3.3333E+06	0.4184	24

Fig. 63.4 Final expected results

Compared with software, the results are very close, the error due to different calculation precision, hand-checking to retain four significant figures, the software is a double-precision floating-point arithmetic.

Reliability of the components are assigned:

$$\mathrm{R}_{1p} = \mathrm{R}_{sq}^{\omega_1} 0.99^{0.1373} = 0.9986 \tag{63.6}$$

$$\begin{aligned} R_{2p} &= R_{sq}^{\omega_2} = 0.9998 \\ R_{3p} &= 0.9996 \\ R_{4p} &= 0.9993 \\ R_{5p} &= 0.9995 \\ R_{6p} &= 0.9970 \\ R_{7p} &= 0.9961 \end{aligned}$$

After the reliability is redistributed by system:

$$\begin{aligned} R_{sp} &= \prod_{i=1}^{7} R_{ip} \\ &= 0.9986 \times 0.9998 \times 0.9996 \times 0.9993 \times 0.9995 \times 0.9970 \times 0.9961 \\ &\leq 0.99 \end{aligned} \tag{63.7}$$

The result meets the reliability requirements of the target. Final results are shown in Fig. 63.4.

63.5 Conclusion

In the traditional process of artificial prediction, impact factor of the various individual components need to turn manual lookup. But it is necessary for software. After compared with the traditional manual methods, using Lambda Predict software is more simple and easy to analyze such complex integrated electronic devices, such an analysis has an important guiding significance to find problems, and improve the design.

References

1. Dinesh Kumar U, Crocker J (2000) Reliability, maintenance and logistic support: a life cycle approach. Kluwer Academic Publishers, Massachusetts
2. ATA-MSG-3 (2003) Operator/manufacturer schedule maintenance development revision
3. Mil-Hdbk-217F (2007) Reliability prediction of electronic equipment
4. Boeing (2008) SOPM Standard technology manual. 20-50-10 Rev 29
5. Ma C (2004) Aircraft communication, navigation and radar (in Chinese). Northwestern Polytechnical University Press, Xi'an, pp 332–333
6. Wang H (2001) Structure and system of airplane (in Chinese). Weapon Industry Press, Beijing
7. Xiao Q, Zhang Y (2010) Research and application of simulating test method based on ARINC429 bus data. Avionics Technol 41:27–31
8. 737 Aircraft Maintenance Manual (2010) Boeing Company

Chapter 64
Maintenance Path Planning for Aircraft Virtual Maintenance

Zhenbao Liu, Caili Xie, Meng Yan, Shuhui Bu and Chao Zhang

Abstract We present a path planning algorithm for virtual maintenance of aircraft components. Component disassembly is a troublesome challenge of aircraft maintenance due to contact collision happened inevitably in disassembly process, which makes maintenance work difficult and inefficient. We study component disassembly in virtual environment: first a hierarchical and associative relation model is constructed through component analysis. Relation model contains connection information for components in any level. We adopt matrix representation for relation model that makes it convenient for computation. Finally, dijkstras algorithm is used to find the optimum disassembly path. The test on full-size model of Osprey airplane motor propeller shows our algorithm is effective and efficient.

Keywords Path planning · Virtual disassembly · Hierarchical associative relation model · Dijkstras algorithm

64.1 Introduction

With the increasing technological content in manufacturing, modern aircrafts and related equipments become complex and expensive, which leads to the demand of advanced and low-cost maintenance technology. Influenced by global financial crisis, military expenses drop dramatically worldwide, and competition between airlines becomes fiercer as well; therefore, lowering maintenance support cost is expected by military officials and airlines while keeping reliability and availability preserved. Maintainability and supportability are two critical elements that decide

Z. Liu · C. Xie · M. Yan · S. Bu (✉) · C. Zhang
Northwestern Polytechnical University, Xi'an, China
e-mail: bushuhui@nwpu.edu.cn

J. Wang (ed.), *Proceedings of the First Symposium on Aviation Maintenance and Management-Volume I*, Lecture Notes in Electrical Engineering 296,
DOI: 10.1007/978-3-642-54236-7_64,

maintenance economical efficiency and timeliness, which further determine aircrafts practical value.

Rapid development of computer simulation and virtual reality [1] provides industrial products a new maintenance method, named Virtual Maintenance. Virtual maintenance [2] constructs a virtual maintenance environment by using related digital prototype and product maintenance information to simulate maintenance procedure. Maintenance personnel can be trained without operating real product in this environment, which immensely cuts the training time and support cost. Accuracy and feasibility of algorithm are determinants for virtual maintenance process design, therefore, the realization of successful maintenance task inevitably requires effective path planning.

This paper makes three novel contributions: first, through observation and analysis for virtual product prototype maintenance information, a hierarchical structural and cooperative relation model is built; second, an efficient maintenance path planning algorithm is proposed by applying dijkstra shortest path to pre-build relation model; third, path planning is implemented, and a thorough study for core method and problems is carried out. Our paper establishes a solid theory foundation for implementation of virtual maintenance.

64.2 Related Work

Virtual reality has attracted many scientists and research centers for its broad application in industrial design, manufacturing and maintenance. In 1992, ARRL (Advanced Robot Research Laboratory) built airplane motor model for Rolls-Royce PLC in order to collect and solve problems arising from motor maintenance. In 1995, Lockheed Martin replaced mental model with CAD model, adopting virtual reality technology to study maintenance process of F-16 fighter. In the late 1990s, Boeing co. set up a virtual reality laboratory that used for JSFs supportability evaluation and experiment; The U.S. Air Force Armstrong laboratories co-developed DEPTH program with University of Pennsylvania, DEPTH is a computer application system for maintenance and supportability analysis that utilized visualization and virtual reality technology. In 2000, The U.S. Air Force Research Laboratory (AFRL), General Electric (GE) and Lockheed Martin undertook an observation named SMG; which is a new maintenance-orientated framework that focused on automatic developing of maintenance manual. Bavarian Motor Works studied the steps of applying virtual reality to virtual prototype to verify fabrication and maintenance process in Business Process Reengineering. Zhejiang University CAD&CG state key laboratory utilized 3D virtual equipment and developed fully immersive virtual assembly prototype system VAVDS under CAVE environment.

Virtual maintenance is originated from computer science and automation, it utilizes computer model and simulation technology to implement component disassembly and maintenance with time and cost saving. Disassembly path

planning [3–5] is the core point of virtual maintenance that based on maintenance modeling and disassembly sequence planning, through model analyzing and solving, generating a reasonable disassembly path. This paper is organized as: Sect. 64.3 focuses on virtual disassembly theory modeling; Sect. 64.4 takes a comprehensive analysis of maintenance factors and proposes a new path planning algorithm; Sect. 64.5 we apply our algorithm to aircraft automatic disassembly; Sect. 64.6 presents the conclusion and our future work.

64.3 Disassembly Theory Modeling

The sequence of disassembly in virtual maintenance process is determined by analyzing information related to product. The product information often maintains disassembly hierarchical relation model, disassembly incidence relation model, cooperative constraint relation model and disassembly structural model.

64.3.1 Topology Information

Topology information [6] is the most important factor that determines product disassembly order. We first introduce topology information, which contains two categories:

1. Hierarchical structural relation which is used to describe product structure. Hierarchical structural model is a tree model, a product can be decomposed into different level of sub-assembly and accessories. Sub-assembly can further be decomposed into lower level of subassembly and accessories.
2. Cooperative constraint relation between product components. We divide constraint relation into three parts:

Part 1. Localization relation, including cooperative relation, distance relation, alignment relation and tangent relation;

Part 2. Motion relation, including gear, belt and chain drive motion, plane and line relative motion, rotation motion;

Part 3. Connection relation, including thread, chain and pin detachable connection, paste, weal, and rivet non-detachable connection.

The relation of above two models is similar to relation of longitude and latitude: hierarchical structural model functionally likes latitude while cooperative constraint relation model likes longitude. We can access to any component of product through these two models.

64.3.2 Build Disassembly Maintenance Model

When a disassembly begins, we first locate and discharge the disassembly unit containing maintenance part that need for maintenance; disassembly unit is a system, subsystem or component generated during disassembly process, in this way we can reduce disassembly workload and prevent normal component from being damaged. Disassembly unit can be further decomposed into subdisassembly unit or basic disassembly unit, and basic disassembly unit is the smallest unit that cannot be decomposed further. We perform localization, unit exchange, unit repair and adjustment in the basic disassembly unit level. Therefore, when disassembly unit has multiple levels and hundreds of components, we should separate disassembly unit into many levels, as shown in Fig. 64.1. Each level is a subset of upper level; decompose process stopped in the level where fault localization can be performed, and then disassembly process starts.

Association relation [7] is a directional graph that represents association relation between components from corresponding levels. From association relation we can see relation of any component pair clearly, which is vita for disassembly path planning. Remarking association pattern on directional lines is recommended, as shown in Fig. 64.2, when we want to discharge component *A*, there is four accesses.We choose path 4 according to simplest path discipline; we first discharge thread *H*, then component *A* can be obtained after relieving the pin connection between *G* and *A*.

1. I→B→A
2. F→D→B→A
3. F→E→C→A
4. H→G→A

Disassembly maintenance model (shown in Fig. 64.3) can be obtained by combing hierarchical structural model and association relation model. We firstly find out the level of discharging component in hierarchical structural model, then discharging correspondent component in terms of each-level association relation. It is the basic model for disassembly maintenance.

64.4 Maintenance Factors Comprehensive Analysis

64.4.1 Mathematic model for Maintenance Difficulty

Maintenance difficulty reflects difficulty degree of maintenance operation, it is a quantitative evaluation of maintenance fault analysis. Maintenance difficulty [8] takes pattern and corresponding weight of every fault into consideration, and evaluates the maintainability of product technically. We adopt a mathematic model [9] for maintenance difficulty:

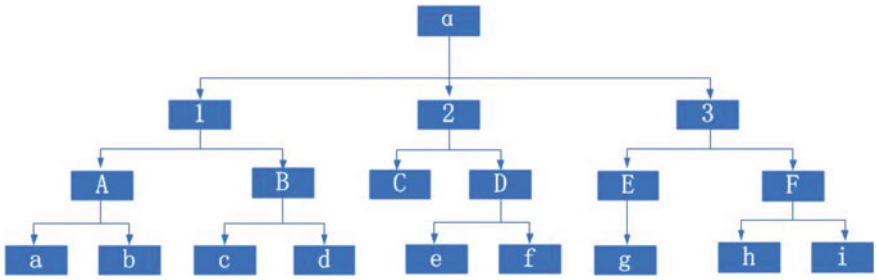

Fig. 64.1 Product α contains *three* first-level disassembly units, *six* second-level disassembly units, and *nine* third-level disassembly units

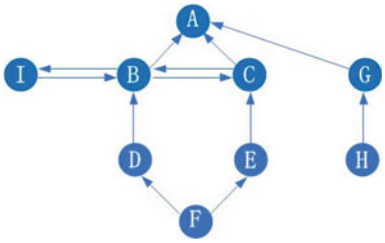

Fig. 64.2 Directional graph represents association relation between disassembly components. The directed lines stand for association or structure information, for example, the line connecting *E* and *C* means *C* is a subdisassembly unit of *E*; the line connecting *C* and *B* means they only connected, not contained by the other

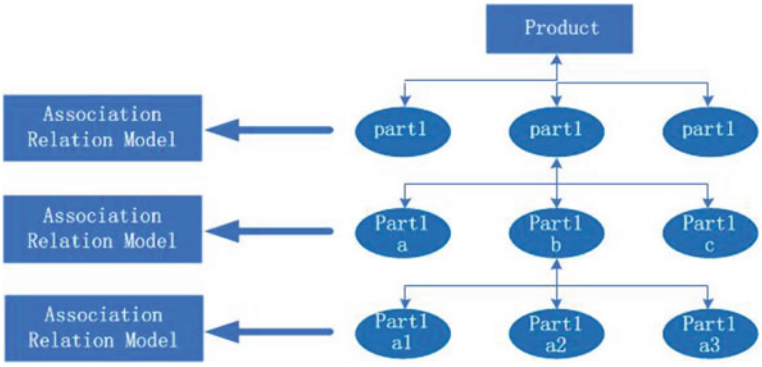

Fig. 64.3 Disassembly maintenance model, combine tree model with association relation

$$S = a\frac{1}{m}\sum_{j=1}^{m} z_j = a\frac{1}{m}\sum_{j=1}^{m}\left(\beta_j \frac{1}{n}\sum_{i=1}^{n_j} J_{ji}\right) \tag{64.1}$$

S represents certain event maintenance difficulty; m represents maintenance task number of the event; n_j represents unit number of every maintenance task; z_j represents maintenance difficulty of every task; J_{ji} represents maintenance difficulty of every task unit; α represents event-level correction factor; β represents task-level correction factor. α, β are influenced by maintenance fault factor, when no fault happen, they set to 1. S directly stands for difficulty degree, larger value stating the maintenance event is hard to be accomplished, otherwise, it is easier. From the equation, we can see maintenance difficulty of task unit is the core point of quantitative evaluation, so we concentrate on computation of task unit. Supposing n is the element number affecting maintenance difficulty of task unit, the computation process listed below:

1. acquire maintenance procedure information and fault analysis results of product;
2. evaluate affecting factor by using fuzzy evaluation criteria;
3. decide weight coefficient of every affecting factor, weight coefficient reflecting the influence degree;
4. compute maintenance difficulty of task unit:

$$J = \sum_{i=1}^{n} w_i p_i; \tag{64.2}$$

p_i is fuzzy evaluation value of element i; n is element number; ω_i is weight coefficient of element i, normalized for convenience.

64.4.2 Construction of Maintenance Model

We describe the connection between topology model and maintenance model of component in Sect. 64.3, and algorithm procedure is formulated in part 4.1; we now consider how to merge disassembly algorithm into maintenance model. Supposing there is a hierarchical structure of maintenance component (Fig. 64.4), we build each-level association model for every component, and replace component notation with matrix, which is convenient for numeric computation (Fig. 64.5).

64.4.3 Automatic Disassembly Method

Virtual maintenance automatic disassembly method can be obtained by combing maintenance model with dijkstra's algorithm. Dijkstra's algorithm [10] proposed by Edsger Wybe Dijkstra, solving the shortest path from single source to other points in a weighted directional graph. For instance, if vertex in a graph represents city and edge weight represents distance between cities that would pass by, dijkstra's algorithm can find the shortest distance between any cities.

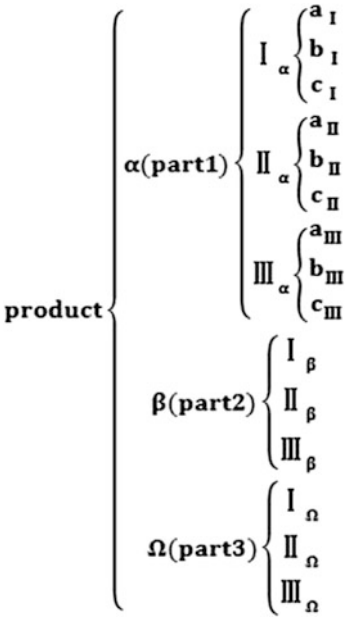

Fig. 64.4 Hierarchical structure for maintenance component

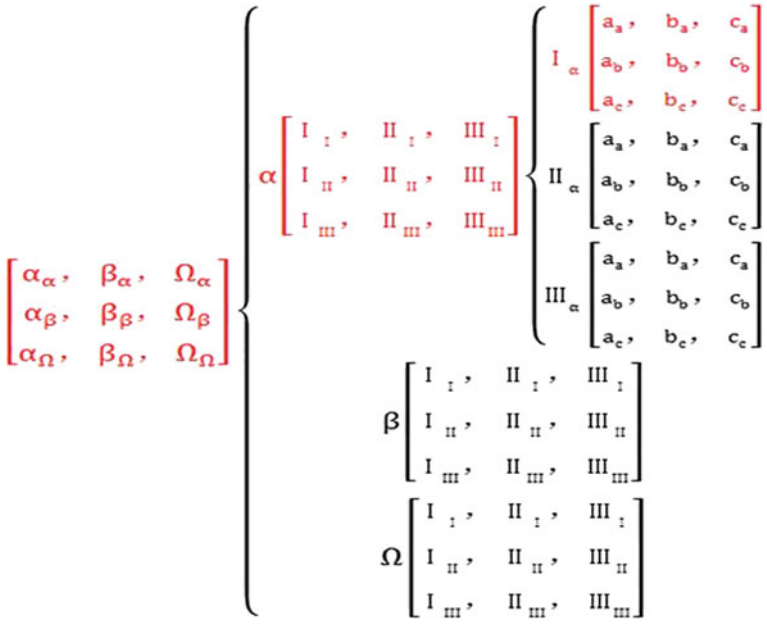

Fig. 64.5 Algorithm-based maintenance disassembly model, through computation we can clearly obtain disassembly path. For example, when we want to discharge I_α, only three matrixes are needed: product, α and I_α, we color them in red

Fig. 64.6 Full-size model of Ospery airplane motor propeller

The combination of dijkstra's algorithm and maintenance disassembly model is the key topic of our paper. For each disassembly level, we construct an association relation table for disassembly component, and transform relation table to relation matrix. Relation matrix stores all component's connecting information, if connection between two components does not exists, their connection coefficient is set to be M.

Dijkstra's algorithm computes path cost between all nodes, it traverses all values to find the shortest path that starts from certain node with going through all other nodes. In auto disassembly process, components are regarded as nodes, and relation matrixes are regarded as path costs. Given disassembly level and beginning disassembly component, algorithm can find the optimum disassembly path.

64.5 Experiments and Results

We test our algorithm on a full-size model of Ospery airplane motor propeller. The part consists of 386 components, shown in Fig. 64.6. We construct maintenance disassembly model at first, it is structurally separated into three levels (Fig. 64.7): first-level contains blade α, propeller strut β and rotor Ω; second-level is subdivision of first level, for instance, α contains axis of crap, blade fixed disk, paddle; β contains strut, anchor screw; Ω contains connecting strip, copper pipe, fixed leg, and so forth.

Now supposing blank g is malfunctioning, following the guidance of structure tree, we first discharge first-level rotor Ω; in rotor level, we discharge second-level rotor center V; then in the rotor center level, we discharge blank g to replace gear unit. It means three matrixes are needed to accomplish the task; first-level matrix contains elements α, β and Ω; second-level contains 1, 2, 3, 4, 5; third-level contains a to j. We construct three matrixes orderly according to cooperative relation and affective factors, the first-level matrix considers the relation between α, β and Ω. Second-level and third level matrix are constructed in the same way. Noted that, matrix coefficient represents relation between components in certain level, the value must be positive.

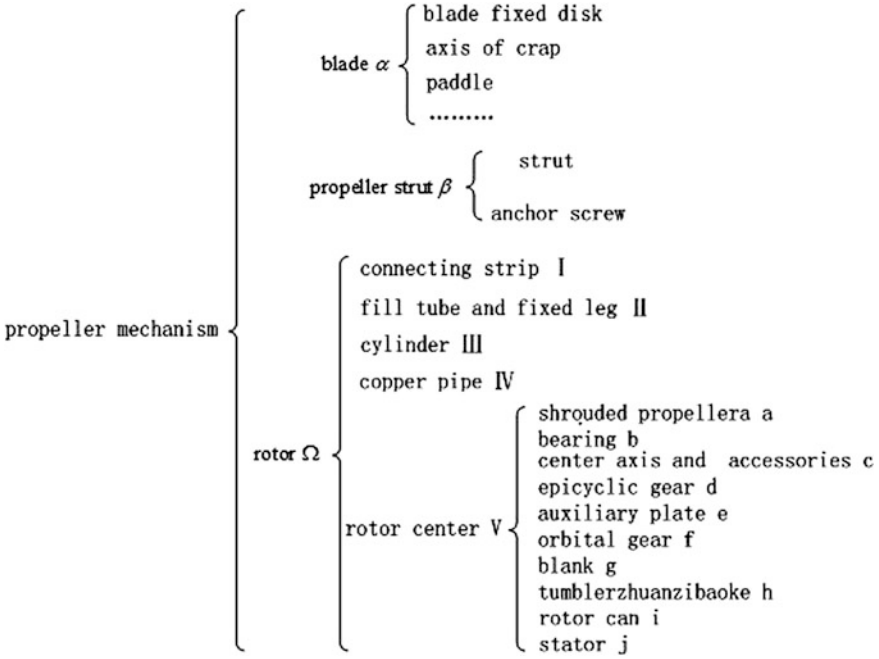

Fig. 64.7 Structure graph of motor propeller

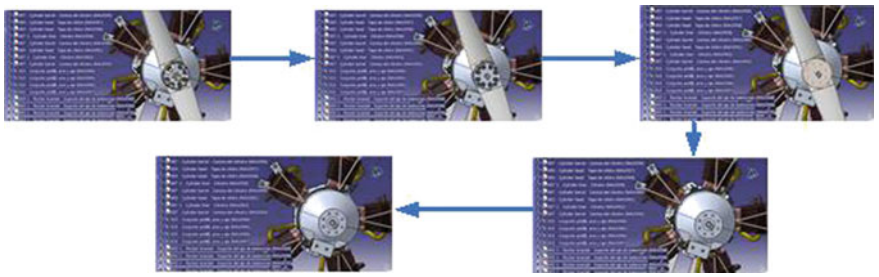

Fig. 64.8 First-level component disassembly, disassembled parts are blade, propeller struct and rotor. Detailed disassembly order is: initial state—disconnect fixed nut—disconnect blade fixed disk—disconnect paddle α—disconnect propeller strut β

Taking matrixes as algorithm inputs, we obtain component disassembly order: first level discharging all connections of Ω is 0→2→1; corresponding sequence is: blade α → propeller strut Ω → rotor β (Fig. 64.8). Second level discharging all connections of component V is 0→2→1→4; corresponding sequence is: axis of crap 1 → cylinder 3 → blade fixed disk 2 → rotor center 4 (Fig. 64.9). Third level discharging all connections of blank g is: 0→1→4→3→5→8→2→6; corresponding sequence is: shrouded propeller a → bearing b → auxiliary plate

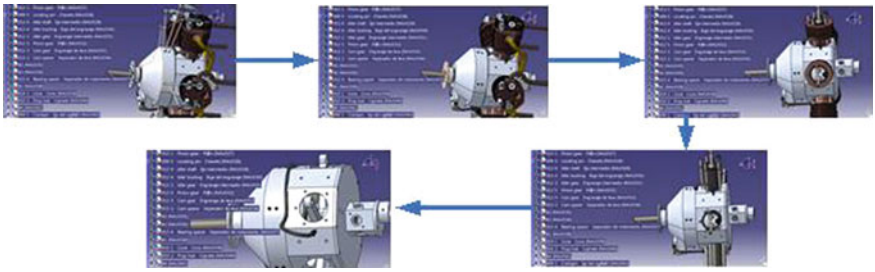

Fig. 64.9 Second-level component disassembly, disassembled parts are axis of crap, cylinder, blade fixed disk and rotor center. Detailed disassembly order is: initial state—disconnect connecting strip—disassembly front cylinder—disconnect back cylinder—disconnect fill tube and fixed leg

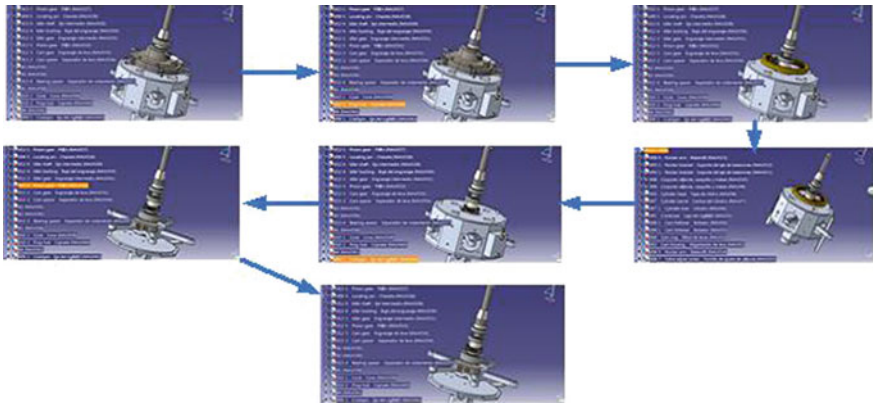

Fig. 64.10 Third-level component disassembly, its disassembly order is: disconnect shrouded peopeller *a*—disconnect bearing *b*—disconnect auxiliary plate *e*—disconnect epicylic gear *d*—disconnect orbital gear *f*—disconnect rotor can *i*—disconnect center axis and its accessories *c*, then we can get blank *g*

$e \rightarrow$ epicyclic gear d $\rightarrow$ orbital gear $f \rightarrow$ rotor can $i \rightarrow$ center axis and its accessories $c \rightarrow$ blank g (Fig. 64.10).

64.6 Conclusion and Future Work

We present an automatic disassembly algorithm for virtual maintenance. Our method is based on virtual maintenance theory and Dijkstra shortest path algorithm. By modeling maintenance difficulty and adopting matrix representation, our algorithm can make maintenance process quickly and accurately. In future work, we plan to extend maintenance model to be applied in more complicated 3D models and make an overall observation about affective factors, which could improve our disassembly method further.

Acknowledgments The work was supported by NSFC (61003137, 61202185, 61104030), NPU-FER(JC201202, JC201220), Shaanxi NSF(2012JQ8037), and Open Fund from State Key Lab of CAD&CG of Zhejiang University.

References

1. Jayaram S, Connacher HI, Lyons KW (1997) Virtual assembly using virtual reality techniques. Comput Aided Des 29(8):575–584
2. Jayaram S, Jayaram U, Wang Y et al (1999) VADE: a virtual assembly design environment. Comput Graph Appl 19(6):44–50
3. Vujosevic R (1995) Simulation, animation and analysis of design disassembly for maintanability analysis. Int J Prod Res 33(11):1999–3022
4. Bohlin R, Kavarki LE (2001) path planning using Lazzy PRM. In: Proceeding of the 2000 IEEE internation conference on robotics and automation, Kluwer Academic Publishers, Dutch, pp 521–528
5. Kuffner JJ (1998) Goal directed navigation for animated characters using real-time path planning and controi. In: Proceedings of international workshop on modeling and motion capture techniques for virtual environments, Springer Verlags, London pp 171–186
6. Hao Jianping, Jiang Keyi, Wang Songhua et al (2008) Virtual maintenance theory and technologies(in Chinese). National Defense Industry Press, Beijing
7. Cai Z, et al (2007) Hierarchical association relation model based assembly sequence planning(in Chinese). Journal of east China shipbuilding industry institute, Zhenjiang
8. Funge J, Xiaoyuan Tu, Terzopoulo, D (1999) cognitive modelingï¼šknowledge, reasoning and planning for intelligent characters. In: Proceedings of the 26th annual conference on computer graphics and interactive techniques, ACM Press, New York pp 29–38
9. Yongli Yu, Hao Jianping, Xiaoming Du (2007) Maintenance engineering theory and method (in Chinese). National Defense Industry Press, Beijing
10. Dijkstra EW (1959) A note on two problems in connexion with graphs. Numerische Mathmatic. 1(1):269–271

Chapter 65
Fault Diagnosis Method of Complex Equipment Based on Gray Relational Analysis with Entropy Weight

Chao Zhang, Yong Zhou, Zhenbao Liu and Shuhui Bu

Abstract To rapidly and effectively diagnose and remove various complex faults is an important work in current equipment maintenance and support. In this paper, a novel fault diagnosis method was proposed based on gray relational analysis and entropy weight. First, the weight values of all fault features were calculated objectively by the entropy method to avoid the influence of subjective factors. Second, the weight-based gray relational degrees were obtained, and consequently, the fault diagnosis result was obtained by using the max membership degree principle. Finally, the engineering practicability and validity of the proposed method was demonstrated by a 4,135 diesel engine fault diagnosis example. The results show that the proposed method is very simple and can effectively reflect the inherent characteristics of fault diagnosis process.

Keywords Fault diagnosis · Maintenance and support · Gray relational analysis · Entropy weight · Diesel engine

C. Zhang (✉) · Y. Zhou · Z. Liu · S. Bu
School of Aeronautics, Northwestern Polytechnical University, Xi'an 710072, China
e-mail: caec_zc@nwpu.edu.cn

Y. Zhou
e-mail: yongstar@nwpu.edu.cn

Z. Liu
e-mail: liuzhenbao@nwpu.edu.cn

S. Bu
e-mail: bushuhui@nwpu.edu.cn

J. Wang (ed.), *Proceedings of the First Symposium on Aviation Maintenance and Management-Volume I*, Lecture Notes in Electrical Engineering 296,
DOI: 10.1007/978-3-642-54236-7_65,

65.1 Introduction

High reliability is one of the most important requirement for complex equipment, but various failures, associated with degraded components, failed sensors, and improperly controls, etc., will significantly affect the efficiency and safety of the equipment, and consequently result in large expenditures for repair and maintenance and even vehicle breakdown. To rapidly and effectively diagnose and remove various faults, several methods have been adopted to develop various diagnosis models, such as fuzzy set method, neural network method, support vector machine method, et al. But, their main limitation is the statistic assumption and requires many samples data. Therefore, this paper proposed a simple fault diagnosis by using gray relational analysis and entropy weight. This method cannot be only used to recognize normality and abnormality but also identify the level of severity of the abnormality.

65.2 Gray Relational Analysis

In gray system theory [1–3], black represents having no information and white represents having all information, and gray represents having a level of information between black and white, thus the gray relational analysis can be used to represent the grade of correlation between two sequences and it is an effective means of analyzing the relationship between sequences with less data [4–8].

65.2.1 Gray Relational Generation

In gray relational analysis, if the values of samples do not obey the three requirements, i.e., nondimension, scaling, and polarization, one has to preprocess the data which are related to a group of sequences, which is called "gray relational generation." Data preprocessing is a process of transferring the original sequence to a comparable sequence. For this purpose, the data can be normalized in the range between 0 and 1 by using Eq. (65.1).

$$x_{ij}^{*} = \frac{|x_{ij}|}{\sqrt{\sum_{i=1}^{m} x_{ij}^{2}}} \qquad (i = 0, 1, 2, \ldots, m;\ j = 1, 2, \ldots, n) \tag{65.1}$$

where x_{ij}^{*} is the value after gray relational generation and x_{ij} is the value before gray relational generation, m is the number of sequences and n is the number of features.

65.2.2 Gray Relational Coefficient

Following the gray relational generation, a gray relational coefficient is calculated to express the relationship between the reference sequence and the comparability ones. The gray relational coefficients can be expressed as follows:

$$\mathrm{Grc}_{ij} = \frac{\Delta_{\min} + \xi \cdot \Delta_{\max}}{\Delta_{0i,j} + \xi \cdot \Delta_{\max}} \tag{65.2}$$

where

$$\Delta_{0i,j} = \left| x_{0j}^{*} - x_{ij}^{*} \right| \tag{65.3}$$

$$\Delta_{\max} = \max_{i \in \{1,\cdots,m\}} \max_{j \in \{1,\cdots,n\}} \left| x_{0j}^{*} - x_{ij}^{*} \right| \tag{65.4}$$

$$\Delta_{\min} = \min_{i \in \{1,\cdots,m\}} \min_{j \in \{1,\cdots,n\}} \left| x_{0j}^{*} - x_{ij}^{*} \right| \tag{65.5}$$

and $\xi \in [0, 1]$ is the distinguishing coefficient, and in general $\xi = 0.5$ is used, and Grc_{ij} is the calculated gray coefficients.

65.2.3 Gray Relational Degree

After obtaining the gray relational coefficient, we can normally take the average of the gray relational coefficient as the gray relational degree. However, since in real application, each feature is not exactly same, the Eq. (65.6) can be used to calculate the gray relational degree.

$$\mathrm{Grd}_i = \sum_{j=1}^{n} w_j \cdot \mathrm{Grc}_{ij} \tag{65.6}$$

where w_j represents the normalized weighting values of feature j and there has

$$\sum_{j=1}^{n} w_j = 1. \tag{65.7}$$

In the gray relational analysis, the gray relational degree is used to show the relationship among the sequences. In general, the value of gray relational degree is equal to one if the two sequences are identical. The gray relational degree also indicates the degree of influence that the comparability sequence could exert over the reference one.

65.3 Entropy Weight

The weights for all features can be calculated by using the entropy method. In information theory, entropy is a measure of how disorganized a system. As applying the concept of entropy to weight measure, a fault feature with a large entropy measure means that it has a great diversity of response, so it has a more signification influence on response. Therefore, according to the above methodology, the entropy weight can be obtained as follows [9]:

(1) Calculate the ratio p_{ij} of the sample data x_{ij}^*:

$$p_{ij} = \frac{\left|y_{ij}^*\right|}{\sum_{i=1}^{m}\left|y_{ij}^*\right|}. \tag{65.8}$$

(2) Calculate the entropy value e_j of the jth feature:

$$e_j = -\frac{\sum_{i=1}^{m} p_{ij}\ln p_{ij}}{\ln m}. \tag{65.9}$$

(3) Calculate the difference coefficient g_j of the jth feature:

$$g_j = 1 - e_j. \tag{65.10}$$

(4) Calculate the weight w_j of the jth feature:

$$w_j = \frac{g_j}{\sum_{j=1}^{n} g_j}. \tag{65.11}$$

65.4 The Proposed Fault Diagnosis Method

By combining the advantages of gray relational analysis and entropy weight, a new fault diagnosis method was proposed, and its basic procedures are shown in Fig. 65.1. The detailed steps of the proposed fault diagnosis method are shown as follows:

Step 1: Obtaining the analyzed data. Assume the number of standard samples is m, and the number of features is n. The standard fault sample can be expressed by the following series: $X_1, \ldots, X_i, \ldots, X_m$, and a new sample can be expressed by X_0.

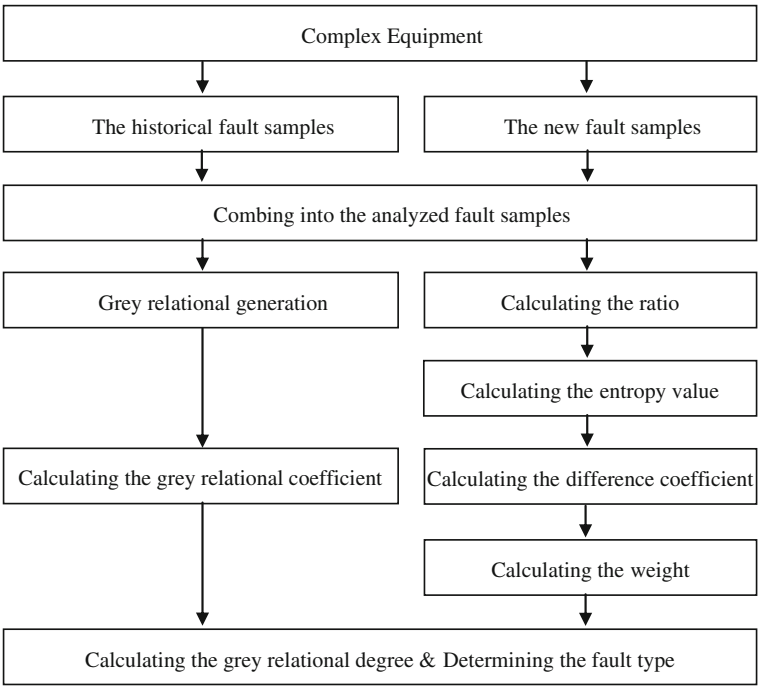

Fig. 65.1 The procedures of the proposed fault diagnosis method

$$X = \begin{bmatrix} x_{11} & x_{12} & \cdots & x_{1j} & \cdots & x_{1n} \\ x_{21} & x_{22} & \cdots & x_{2j} & \cdots & x_{2n} \\ \vdots & \vdots & \ddots & \vdots & \ddots & \vdots \\ x_{i1} & x_{i2} & \cdots & x_{ij} & \cdots & x_{in} \\ \vdots & \vdots & \ddots & \vdots & \ddots & \vdots \\ x_{m1} & x_{m2} & \cdots & x_{mj} & \cdots & x_{mn} \end{bmatrix} \tag{65.12}$$

$$X_0 = \begin{bmatrix} x_{01} & x_{02} & \cdots & x_{0j} & \cdots & x_{0n} \end{bmatrix} \tag{65.13}$$

where X_i represents the ith standard fault sample. X_0 and X_i both includes n elements, and X_{0j} and X_{ij} represents the value of the jth fault feature E_j in X_0 and X_i, respectively, $i = 1, 2, \ldots, m$ and $j = 1, 2, \ldots, n$.

Step 2: Data normalization preprocessing. By using the Eq. (65.1), the normalization data can be obtained to further improve the comparability of the different features.

Step 3: Calculating the gray relational coefficient. By using the Eqs. (65.2)–(65.5), we can calculate the gray relational coefficient between the new sample and the standard fault samples.

Table 65.1 The fault data of the 4,135 diesel engine

No.	Fault features									D
	C_1	…	C_6	C_7	…	C_{12}	C_{13}	…	C_{18}	
X_1	966.0803	…	4.367723	854.1059	…	6.144371	1757.672	…	5.982800	F_1
…	…	…	…	…	…	…	…	…	…	…
X_7	933.4472	…	4.707670	965.6075	…	4.514550	1700.047	…	5.027644	F_1
X_8	759.4642	…	6.721322	1063.689	…	5.777319	1840.721	…	11.40681	F_2
…	…	…	…	…	…	…	…	…	…	…
X_{14}	860.2143	…	4.233111	1095.057	…	6.747132	1972.851	…	12.61506	F_2
X_{15}	960.8651	…	5.688330	986.1711	…	5.155113	2052.661	…	5.365647	F_3
…	…	…	…	…	…	…	…	…	…	…
X_{22}	976.9817	…	6.954501	1063.936	…	4.116981	2141.317	…	6.125845	F_3
X_{23}	1073.929	…	5.531318	1016.647	…	4.054873	1876.782	…	8.094243	F_4
…	…	…	…	…	…	…	…	…	…	…
X_{30}	867.5084	…	4.685793	1028.222	…	5.779836	1869.500	…	7.485392	F_4
X_{31}	968.6300	…	4.392614	920.8692	…	6.014534	1779.608	…	6.281026	F_1
X_{32}	928.1780	…	3.857294	750.0185	…	4.220250	1631.940	…	5.841912	F_1
X_{33}	860.4138	…	3.934964	1206.267	…	6.206780	1842.024	…	6.938825	F_1
X_{34}	748.9689	…	7.406265	1083.173	…	4.590098	1856.117	…	9.348355	F_2
X_{35}	1006.686	…	5.655421	982.3972	…	5.057999	2097.900	…	5.993690	F_3
X_{36}	1070.333	…	5.024917	1010.476	…	3.981336	1891.114	…	8.215332	F_4
X_{37}	905.9790	…	4.729704	1015.769	…	5.011682	1999.300	…	7.407416	F_4

Step 4: Calculating the entropy weight. By using the Eqs. (65.8)–(65.11), we can obtain the weight of various fault features.

Step 5: Calculating the gray relational degree. When the gray relational coefficient and the weight are both obtained, the gray relational degree can be obtained.

Step 6: Determining the fault type. When the gray relational degree is obtained, we can determine the ranking order of all standard fault samples. And according to the max membership degree principle, the fault type of the test sample is equal to the fault type of the standard sample which has the largest gray relational degree.

65.5 Fault Diagnosis Example

In this section, we take the 4,135 diesel engine fault diagnosis data [10] for example to verify the proposed method. Table 65.1 shows all fault data, which composed of 37 fault samples $X_1, X_2, \ldots, X_{37}$, 18 fault features $C_1, C_2, \ldots, C_{18}$ and four state types. The four state types correspond to the following: normal (F_1), intake valve clearance is too small (F_2), intake valve clearance is too large (F_3), exhaust valve clearance is too large (F_4). The 18 fault features are from three

Table 65.2 The normalized samples after gray relational generation

No.	Fault features								
	C_1	…	C_6	C_7	…	C_{12}	C_{13}	…	C_{18}
X_1	0.1855	…	0.1417	0.1512	…	0.2004	0.1626	…	0.1414
…	…	…	…	…	…	…	…	…	…
X_7	0.1792	…	0.1528	0.1710	…	0.1472	0.1572	…	0.1188
X_8	0.1458	…	0.2181	0.1883	…	0.1884	0.1703	…	0.2696
…	…	…	…	…	…	…	…	…	…
X_{29}	0.1656	…	0.1515	0.1722	…	0.1747	0.1874	…	0.1465
X_{30}	0.1666	…	0.1521	0.1821	…	0.1885	0.1729	…	0.1769
X_{36}	0.2055	…	0.1631	0.1789	…	0.1298	0.1749	…	0.1941

Table 65.3 The weights of 18 features

Feature	C_1	C_2	C_3	C_4	C_5	C_6
Weight	0.0039	0.0111	0.1685	0.0012	0.0407	0.0237
Feature	C_7	C_8	C_9	C_{10}	C_{11}	C_{12}
Weight	0.0030	0.0780	0.3068	0.0033	0.2234	0.0408
Feature	C_{13}	C_{14}	C_{15}	C_{16}	C_{17}	C_{18}
Weight	0.0035	0.0042	0.0256	0.0007	0.0194	0.0423

sensors, and each sensor has six features, which are: the waveform complexity in frequency, the center frequency of spectrum, the waveform complexity in time domain, the nonperiod complexity, the variance of time series and the Kurtosis of time series.

In here, the samples $X_1, X_2, \ldots, X_{30}$ are used as standard fault samples, and the samples $X_{31}, X_{32}, \ldots, X_{37}$ are used to test and compare with other diagnosis method.

Now, the sample X_{36} is used to diagnosed. After data preprocessing, the 31 samples $X_1, X_2, \ldots, X_{30}, X_{36}$ are been normalized as shown in Table 65.2, where all fault feature values are between 0 and 1. And then, the weights of eight fault features are computed by using the entropy method, and the results are shown in Table 65.3.

And the gray relational coefficients can be calculated. Finally, the gray relational degree can be obtained and listed in Table 65.4, and then according to max membership degree principle, we can see that the fault type of X_{36} is same as the fault type of X_{23}.

We can calculate the gray relational degree of other samples, and the diagnosis results can be shown in Table 65.5. From Table 65.5, we can see that the proposed fault diagnosis method is very effective. In addition, when we change the distinguishing coefficient from 0.1 to 0.9, the diagnosis types are also equal to the real type, it shows that the distinguishing coefficient has little effect to the proposed method.

Table 65.4 The gray relational degree

No.	X_1	X_2	X_3	X_4	X_5	X_6	X_7	X_8	X_9	X_{10}
Grd.	0.8111	0.8290	0.8254	0.8222	0.7742	0.7800	0.7708	0.7831	0.8362	0.8323
No.	X_{11}	X_{12}	X_{13}	X_{14}	X_{15}	X_{16}	X_{17}	X_{18}	X_{19}	X_{20}
Grd.	0.8079	0.8042	0.7602	0.7868	0.9199	0.7353	0.7409	0.7769	0.7337	0.8355
No.	X_{21}	X_{22}	X_{23}	X_{24}	X_{25}	X_{26}	X_{27}	X_{28}	X_{29}	X_{30}
Grd.	0.8131	0.8052	0.9794	0.7943	0.8106	0.8117	0.7515	0.7907	0.7097	0.8364

Table 65.5 The fault diagnosis results

	Real type	The diagnosis type
X_{31}	F_1	F_1
X_{32}	F_1	F_1
X_{33}	F_1	F_1
X_{34}	F_2	F_2
X_{35}	F_3	F_3
X_{36}	F_4	F_4
X_{37}	F_4	F_4

65.6 Conclusions

(1) Based on integration of gray relational analysis and entropy weight theory, a novel fault diagnosis method was proposed. This method is very simple and can effectively reflect the inherent characteristics of fault diagnosis process.
(2) The application in diesel engine fault diagnosis data verifies the engineering practicability and validity of the proposed method. Of course, this method can be used to solve other uncertain fault diagnosis problems.

Acknowledgments This work was supported by the National Natural Science Foundation of China (Nos. 61104030 and 51207129). The authors would also like to thank the anonymous reviewers for their valuable comments and suggestions to improve the quality and readability of the paper.

References

1. Liu SF, Lin Y (2011) Introduction to grey systems theory. Springer, Heidelberg
2. He X, Liu JN, Li SX (2004) Applications of case-based reasoning based on grey relational theory in fault intelligent diagnosis system. Chin Mech Eng 15(22):2022–2026
3. Liu RW, Guo XZ (2004) Gray correlation analysis method of on-line faults diagnosis in drilling. Drill Prod Technol 27(6):17–25
4. Cheng Z, Hu NQ, Gu FS, Qin GJ (2011) Pitting damage levels estimation for planetary gear sets based on model simulation and grey relational analysis. Trans Can Soc Mech Eng 35(3):403–417

5. Dong LX, Xiao DM, Liu YL (2005) Insulation fault diagnosis based on group grey relational grade analysis method for power transformers. J Southeast Univ 21(2):175–179 (English ed)
6. Lin WM, Huang CH, Lin CH, Chen CM, Wang LW (2008) Restoration strategy for secondary power network with grey relational analysis. IET Gener Transm Distrib 2(2):167–174
7. Lin HD, Jiang JD (2007) Applying Discrete Cosine Transform and Grey Relational Analysis to Surface Defect Detection of Leds. J Chin Inst Ind Eng 24(6):458–467
8. Huang J, Hou JJ, Liu Y, Guo Y (2013) Grey entropy relation algorithm of choosing the optimum diagnostic nodes in analogue circuits. Chin J Electron 22(3):615–620
9. Li LY, Yang ZZ, Li X, He Z (2010) Research on fault recognition for centrifugal compressor using entropy weight-based gray relational analysis. In: International Conference on Applied Mechanics and Mechanical Engineering, Applied Mechanics and Materials, Trans Tech Publications Ltd, Switzerland Vols. 29–32, pp 685–690
10. Shen LX, Tay FEH, Qu LS (2000) Fault diagnosis using rough sets theory. Comput Ind 43(1):61–72

Chapter 66
Design of Servo Control System of Precision Injection for Electro-Hydraulic Hybrid Injection Machine

Fenfen Qi, Shengjin Li, Yong Zhou and Zhiyan Zhou

Abstract This paper researched and developed a servo motor controller with a set of nonlinear fuzzy control strategy for pressure and flow, for the AC servo motor in electro-hydraulic hybrid injection molding machine, in order to improve the efficiency of the electro-hydraulic hybrid type injection molding machine and reduce its power consumption. The experiment showed that this servo motor controller can realize the output flow adapt to the demand of the load automatically. Compared with the traditional injection molding machine, this injection molding has obvious energy saving effect, it can enhance the response speed and repeat precision, realize precision injection molding.

Keywords Fuzzy control · SVPWM · Vector control · Precision injection

66.1 Introduction

With the social development and technological advancement, the application of plastic products becomes wider and wider, so the Industrial production has higher requirement on the performance of the injection molding machine. High efficiency, low energy consumption, high precision, and automation have become the development direction of injection molding machine. Electro-hydraulic hybrid injection molding machine rolls into the many advantages of the fully hydraulic injection molding machines and all electric injection molding machine, it is accord with the development trend and has become the research hotpot.

Electricity consumption accounts for a large proportion on the cost of the Electro-hydraulic hybrid injection molding machine, however, the drive motor

F. Qi (✉) · S. Li · Y. Zhou · Z. Zhou
Northwestern Polytechnical University, Xi'an, China
e-mail: 876726211@qq.com

J. Wang (ed.), *Proceedings of the First Symposium on Aviation Maintenance and Management-Volume I*, Lecture Notes in Electrical Engineering 296,
DOI: 10.1007/978-3-642-54236-7_66,

power consumption accounts for 50–65 % of the entire power consumption [1], so the weight of reducing the cost and realizing precision injection is to improve energy efficiency of drive system and to realize output power can adapt to the demand of the load automatically at the same time.

This paper researched and developed a servo motor controller with a set of nonlinear fuzzy control strategy for pressure and flow, for the AC servo motor in electro-hydraulic hybrid type injection molding machine. This servo motor controller can realize the output flow adapt to the demand of the load automatically. Compared with the traditional injection molding machine, this machine has obvious energy saving effect, it can enhance the response speed and repeat precision, realize precision injection molding.

66.2 Overall

66.2.1 Program Structure

This servo control system for electro-hydraulic hybrid injection molding machines can be divided into sequential control part, the temperature control part and servo motor control part.

Sequential control part is the core of the electrical control systems. Through the coordinate between hydraulic system and control (Relay control and SCM) [2], the injection molding machine can complete the process in accordance with the demand.

Temperature of the injection molding process is an important control parameter [3], including heating cylinder temperature, hydraulic oil temperature, temperature of cavity, etc., either a bad temperature will directly affect the quality of plastic products. In this paper, the injection molding machine adopted temperature closed-loop. According to the requirements of process, you can set temperature parameters in upper computer, detect the actual temperature by thermocouple and feed it back, through the PID closed-loop to control the operation of the temperature regulating device.

Motor control part is the focus of this research, and it is also the biggest difference between this injection molding machine and traditional injection molding machine, from the power unit to the control methods. This servo control system consists of the control panel (pressure flow control plate), driver board (servo drive), servo motor + internal gear pump, pressure sensor, current sensor, reactance + filter, power line + rotary transformer lines, etc. Specific structure is shown in Fig. 66.1.

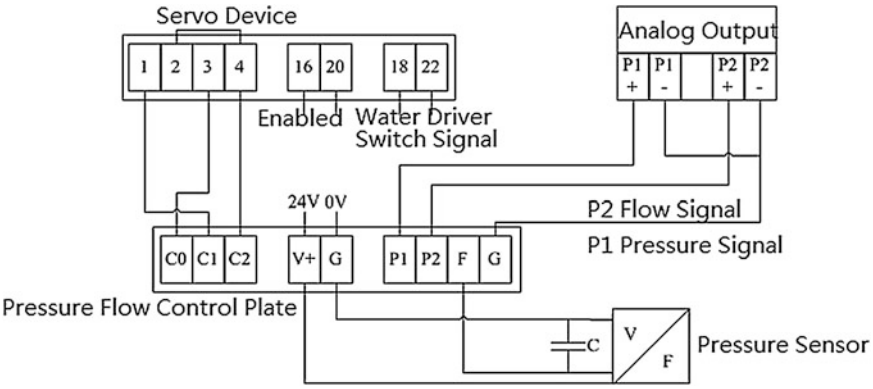

Fig. 66.1 Motor control part

66.2.2 Design of Motor Control

As can be seen from Fig. 66.1, pressure and flow control plate is the core of servo control system. Upper computer send target flow rate signal and pressure signal in digital form as the "commander;" Pressure sensor real-time detected system pressure, and feedback to the pressure flow control plate; this three signals as the input signal to the control panel. During the process of injection, when the system pressure is below the given pressure, the servo control system adapts flow open-loop control, to ensure the response speed of the system. When the system pressure at the given pressure approximation, servo control system adapts pressure closed-loop control, to prevent hydraulic oil pressure from "coaster" phenomenon due to excessive flow. With both speed and pressure control, to realize the pressure value can well follow the given pressure, especially in high pressure and low flow packing stage. This control method makes the control more comprehensive, the response speed and control precision have a very high improvement.

In this servo control system, pressure closed-loop control is the important and difficult point, we need to overcome the following problems:

1. From the flow open-loop control to the pressure closed-loop control, system flow is prone to large fluctuations, performance for "creeping" phenomenon of the actuator in the injection molding machine;
2. Development nonlinear pressure closed-loop control algorithm. If we use the traditional PID control, once the parameter is established it will be difficult to change when the machine is running, system adaptability is low.

In this paper, the servo motor with id = 0 vector control [4]. The nature of id = 0 control is to achieve d, q-axis current decoupling, the stator has quadrature axis current component of current only. This method with no direct axis electromagnetic of armature reaction without demagnetization effect, so it can guarantee electromagnetic torque is proportional to the motor armature current. Id = 0

control method is simple, torque performance is better, speed range is wider, etc., suitable for high performance requirements of control occasions.

For the complexity and nonlinear characteristics of hydraulic system pressure and flow control in electro-hydraulic hybrid injection molding machine, this article selected fuzzy control strategy [5, 6]. Fuzzy control is a kind of PD closed-loop control, it is suitable for the relationship between the parameters or the control without accurate representation, hydraulic control system is just such situation.

66.3 Hardware Design

66.3.1 Module Introduction

Hardware design is the basic design for the servo control system, it is the guarantee of realize control algorithm and control strategy. This article based on the dsPIC30F6010 in control system hardware design, realized precise control of pressure and flow for electro-hydraulic hybrid injection molding machine injection system.

The modular structure of the hardware design is shown in Fig. 66.2, the main features of the control system include:

1. Using the RS422 standard bus realizes full-duplex communication with upper computer, receives the target pressure and flow from the upper computer, and uploads the control system status, motor speed, and other information to upper computer.
2. Using RVDT detects position of PMSM rotor realizes speed control.
3. Using hall current sensor detects PMSM winding current improves PMSM servo performance.
4. Other functions such as program download, reset, security measures, etc.

The major functional blocks of this control system can be divided into central controller, RS422 serial communication module, RVDT analog input channels, the current analog input channels, voltage analog input channels, the system pressure analog input channels, power drive, inverter modules, and auxiliary equipment control module. In addition, in order to improve the environmental adaptability of the control system and extensible ability, it is also designed with optical encoder digital input interfaces, CAN bus communication interface, SPI bus communication interface, etc.

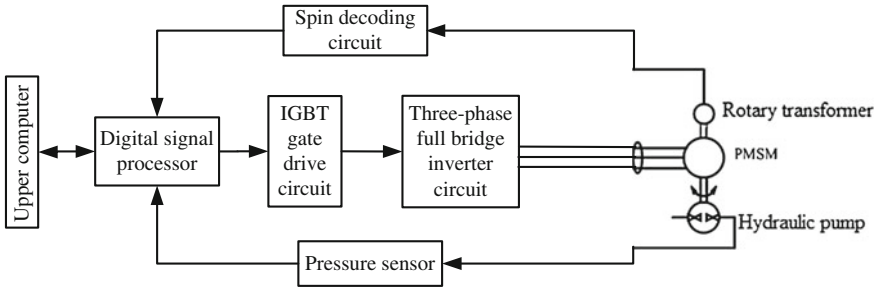

Fig. 66.2 Block diagram of modular control system

Fig. 66.3 Front panel physical

66.3.2 Physical Hardware Design

According to the design needs, we use a four-layer board design guidelines, as shown in Fig. 66.3. After the hardware debugging, the panel performance can achieve all the features we needed.

66.4 Software Design

Control system software design is based on the hardware design completed, so as to realize the corresponding functions of electro-hydraulic hybrid injection molding machine. In accordance with the different functions, control system software mainly includes the system initialization module, the system self-test module, an infinite loop module, PWM interrupt management module, CAN communication module, SCI communication management module, SPI communication management module and timer interrupt management module, etc. In this paper, only the design of PMSM control module, the fuzzy control algorithm design, and the main program module design are introduced in details.

66.4.1 Design of PMSM Control Module

PWM interrupt mainly completed the following work:

1. Call RVDT decoding function, get the rotor position Angle θ, and solve the motor speed ω_r;
2. Call CORDIC inverse function, quickly solve $\sin\theta$ and $\cos\theta$;
3. Get A and B phase current from AD converter and clarke transform to i_α and i_β;
4. The i_α and i_β for Park transformation, i_d and i_q;
5. Call function of speed loop PID algorithm, get current loop given value i_q and let $i_d = 0$;
6. Call the current loop PID algorithm function to obtain v_d and v_q;
7. v_d and v_q Park will be transformed back to v_α and v_β;
8. v_α and v_β inverse clarke transform to Ur1, Ur2, and Ur3;
9. Call the function of SVPWM algorithm, get the PWM chopper signals of three-phase fully controlled bridge.

The detailed flow of PMSM control is shown in Fig. 66.4.

66.4.2 Design of Fuzzy Control Algorithm

The realization of the fuzzy control algorithm according to the following four steps:

1. Determine the pressure error and its change rate and the domain of output volume;
2. According to the progression of the domain, divided the e, ec, u actual change range into five levels and determined the central value of each level; Chosen reasonable membership function, this article used the trigonometric functions, the center of each level is the maximum degree of membership, value of 1, evenly distributed on both sides of the function, that is, the membership functions to adjacent center value of membership degree is 0. In this way, each element in actual domain can find at least one corresponding point in change domain. For the system measured value at a certain time, can be quantified as the corresponding elements of the domain;
3. Check the fuzzy control table, then calculated amount of output;
4. Select the weighted sum method to complete the sharp of the fuzzy quantity, the control volume multiplied by the appropriate scaling factor for the controlled object.

The structure of fuzzy control program is shown in Fig. 66.5.

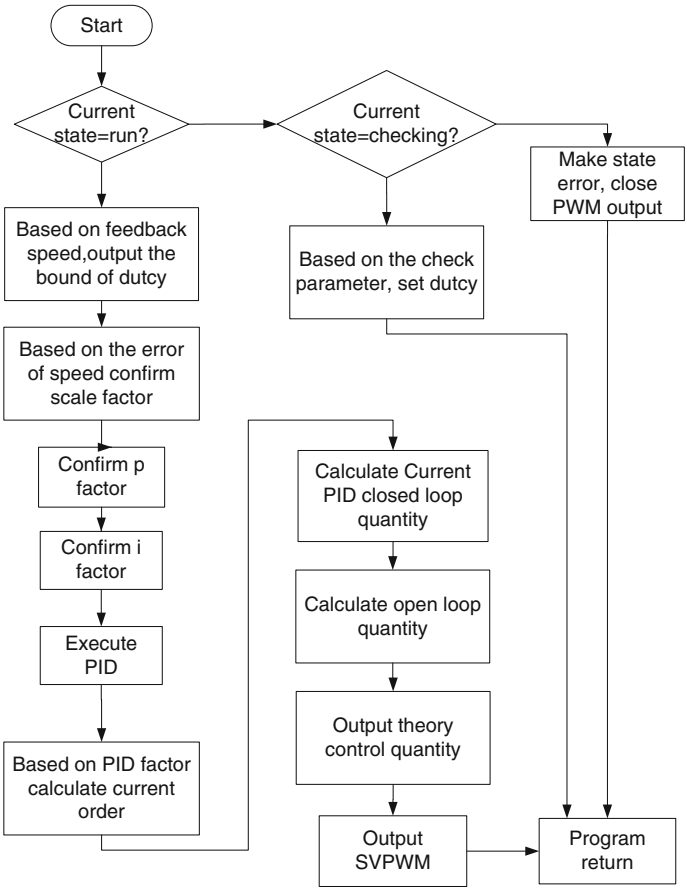

Fig. 66.4 The flow chart of PMSM

66.4.3 Design of Main Program

Main program output order to the servo drive, control the servo motor speed. Motor can be divided into positive and negative two directions, but reverse normally just in the holding stage. The main program flow chart is shown in Fig. 66.6. The first step is to calculate error between the given pressure signal and the feedback pressure signal and judge the range. When the feedback pressure is greater than the given pressure value and exceeded the reference value b, the motor starts reverse rotation for relief, otherwise, the motor is transferred to continue to provide hydraulic oil to the system. The second step is to determine the program should be use flow open-loop or pressure closed-loop. When pressure is greater than the value

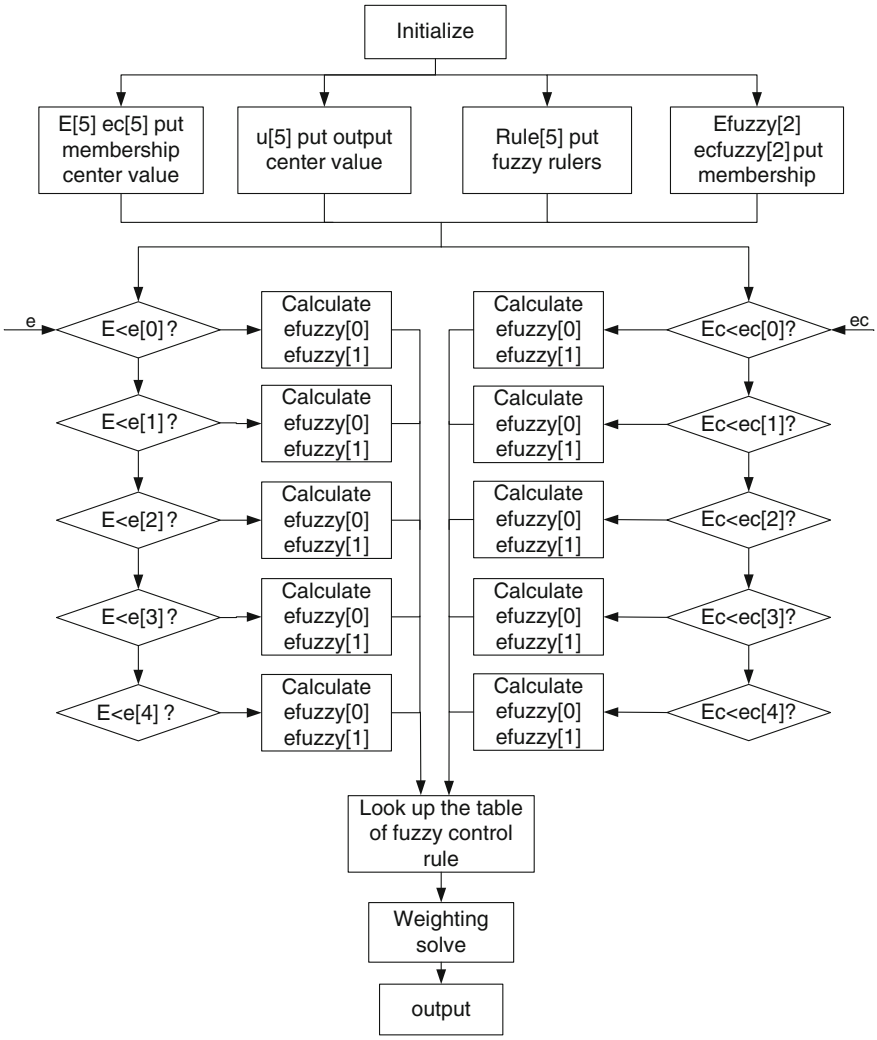

Fig. 66.5 Fuzzy control flow chart

a, the program need to guarantee a certain speed to meet the requirements of rapid response, the flow is the key consideration; When the pressure error is small, the feedback pressure is already very close to the given, in order to avoid pressure overshoot, the program must be converted to pressure closed-loop, call the fuzzy algorithm, guarantee the stability of the following pressure.

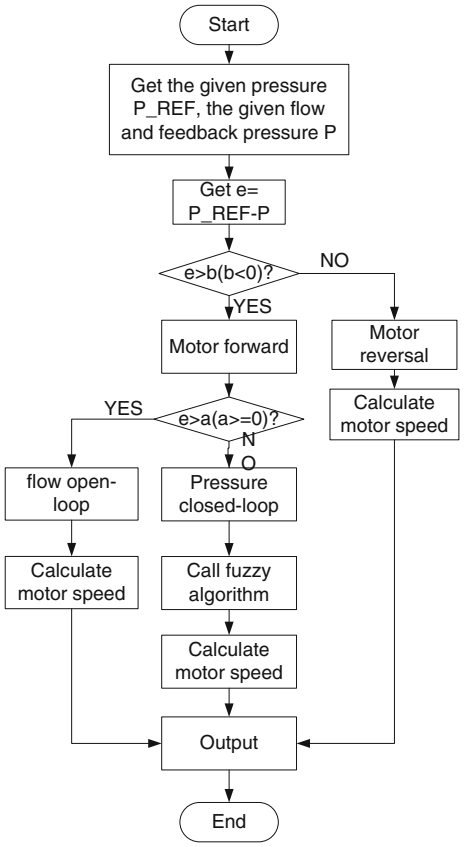

Fig. 66.6 Main program flow chart

66.5 Experiments

Electro-hydraulic hybrid injection molding machine test platform is shown in Fig. 66.7, it is mainly composed of ac permanent magnet synchronous servo motor, metering pump, coupling, simulated load, pressure sensor, flow meter, speed sensors, low-voltage power supplies and fuel tank, etc.

66.5.1 Response of Control System

When the servo motor speed is 1,000 r/min, pressure from 0 to 10 MPa, the step response curve is shown in Fig. 66.8. When the pressure is 10 MPa, speed from 0 to 1,000 r/min, speed response curve is shown in Fig. 66.9.

From Figs. 66.8 and 66.9 can be seen, after using id = 0 vector control and fuzzy control the speed response performance and pressure response performance

Fig. 66.7 Electro-hydraulic hybrid injection molding machine test platform

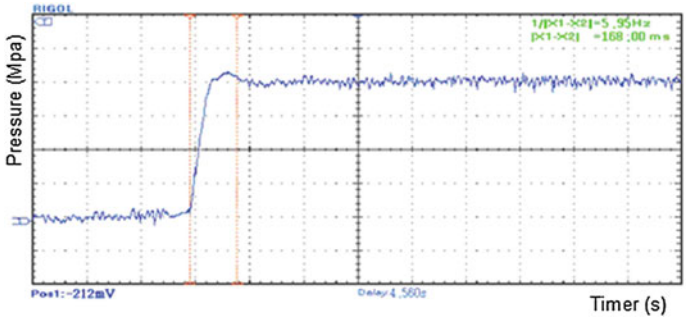

Fig. 66.8 Pressure response curve

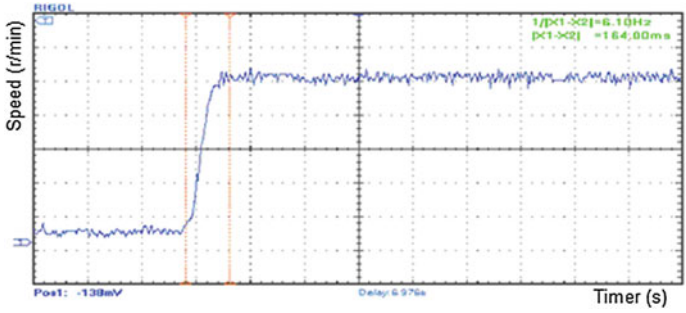

Fig. 66.9 Speed response curve

is better. Pressure Response time is 168 ms, speed response time is 164 ms, less than 200 ms, that can fully satisfy the high speed and high-response demand of the electro-hydraulic hybrid precision injection molding machine (Figs. 66.10, 66.11).

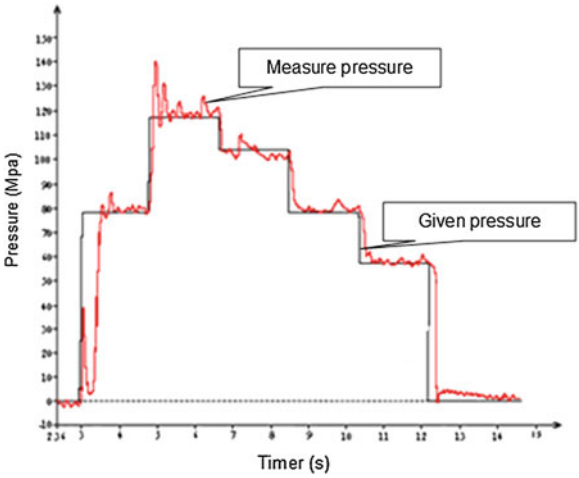

Fig. 66.10 Traditional PID control holding pressure curve

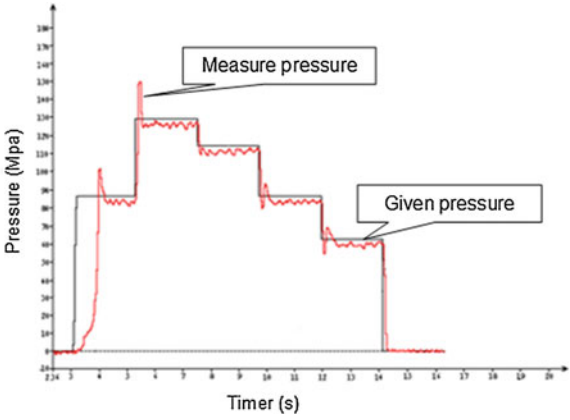

Fig. 66.11 Fuzzy Control holding pressure curve

66.6 Test of Holding Pressure

The holding stage is a key link in the process, it has the biggest influence on the quality of our products, and it is the key of the performance test. The black curve is the given pressure value, the red curve is the measured pressure value.

To sum up, the fuzzy control strategy against pressure flow control effect is superior to traditional PID control strategy, satisfies the requirement of electric hydraulic hybrid of precision injection molding machine system.

66.7 Conclusion

The servo control system researched in this paper can realize the output flow adapt to the demand of the load automatically. It also can improve the response speed and repeat precision at the same time, achieve the purpose of precision injection.

Acknowledgments This work was supported by the National Natural Science Foundation of China (Nos. 51207129 and 51307137). The authors would also like to thank the anonymous reviewers for their valuable comments and suggestions to improve the quality and readability of the paper.

References

1. Zhou HL (2005) Inverter for injection molding machine and energy saving transformation. Electr Drives Control 2:88–90 (in Chinese)
2. Xu XZ, Zhao Y, Jin B, Weng TZ (2003) Micro-processor based control for plastic injection machine. Electromech Eng 20(1):17–19 (in Chinese)
3. Wan L, Peng LY (1997) The application of single chip microcomputer temperature control in injection molding machine. Mech Electro Eng 1:17–18 (in Chinese)
4. Shang J (2007) Field oriented control of permanent magnet synchronous motor. Zhejiang University Doctoral Dissertation (in Chinese)
5. Xu J (2008) The research and application of hydraulic servo system control algorithm. Master's Thesis (in Chinese)
6. Zheng DN, Alleyne A (2005) Modeling and control of an electro-hydraulic injection molding machine with smooth fill-to-pack transition. J Manuf Sci Eng 125(2):88–99

Chapter 67
Simulation of BLDC in Speed Control System on PSIM and Matlab/Simulink Co-simulation Platform

Zhiyan Zhou, Shengjin Li, Yong Zhou and Yunwu Jiao

Abstract In this paper, the design platform was the PSIM and Matlab/simulink co-simulation system which fully utilized the capacity of PSIM in power simulation and the capacity of Matlab/Simulink simulation in the control, to design a simulation model for brushless DC motor speed control system. The drive system model of brushless motor has been created in PSIM software platform; a brushless motor speed control system simulation model has been established in Matlab/Simulink simulation software platform. The control system was composed with speed control module, a current regulator module, and PWM generator module. The governor system used fuzzy PID and double-loop control strategy. Simulation results showed that this simulation method and control strategy could accurately reflect the brushless motor speed control performance.

Keywords BLDC · PSIM · Matlab/Simulink · Co-simulation · Speed control

67.1 Introduction

Recently, with the rapid development of computer and control technology, brushless DC motor has been widely used and dominated in high-performance and high-tech servo drive fields. In the control system design, you need to fully research brushless motor speed characteristics and control strategies with simulation tools. This paper presented a PSIM and Matlab/simulink co-simulation approach which combined the power of PSIM simulation capacity and Matlab/Simulink simulation capacity in the control to complete the system simulation of brushless DC motor speed control [1, 2].

Z. Zhou (✉) · S. Li · Y. Zhou · Y. Jiao
School of Mechanical Engineering, Northwestern Polytechnical University, Xi'an, China
e-mail: 535046691@qq.com

J. Wang (ed.), *Proceedings of the First Symposium on Aviation Maintenance and Management-Volume I*, Lecture Notes in Electrical Engineering 296,
DOI: 10.1007/978-3-642-54236-7_67,

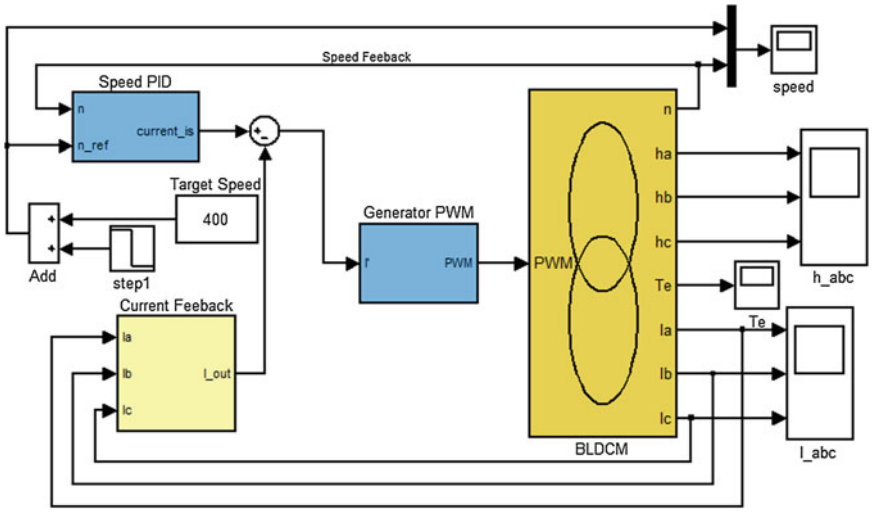

Fig. 67.1 Brushless DC motor speed control simulation system

67.2 Brushless Motor Speed Control System Simulation Design

In the Simulink v7.3 included in MATLAB R2009a environment, according to the modular modeling idea, using the SimPowerSystems module library to create brushless motor control system simulation model, the control block diagram shown in Fig. 67.1. Brushless motor speed control system included speed control module, a current regulator module, PWM generator module, and brushless motor driver module. Among them, the brushless motor drive module was established in PSIM environment, wherein the drive module includes an inverter module and motor body modules. In the control system, speed control and current regulation constituted a brushless motor control system's dual-loop control link. The inner current loop used a PD regulator with integral separation, to calculate the difference between given current and the feedback current to adjust current; outer loop used PID speed regulator, and speed changed with the reference speed, to reach speeds without static droop purposes.

67.3 Brushless Motor Drive Module Simulation in PSIM

Brushless motor driver module was the important part in control system. According to the working principle of the brushless motor, design driving circuit in PSIM. The driving circuit included an inverter circuit, brushless motor body (include the Hall sensor), the motor sensor (speed sensor or torque sensor), the

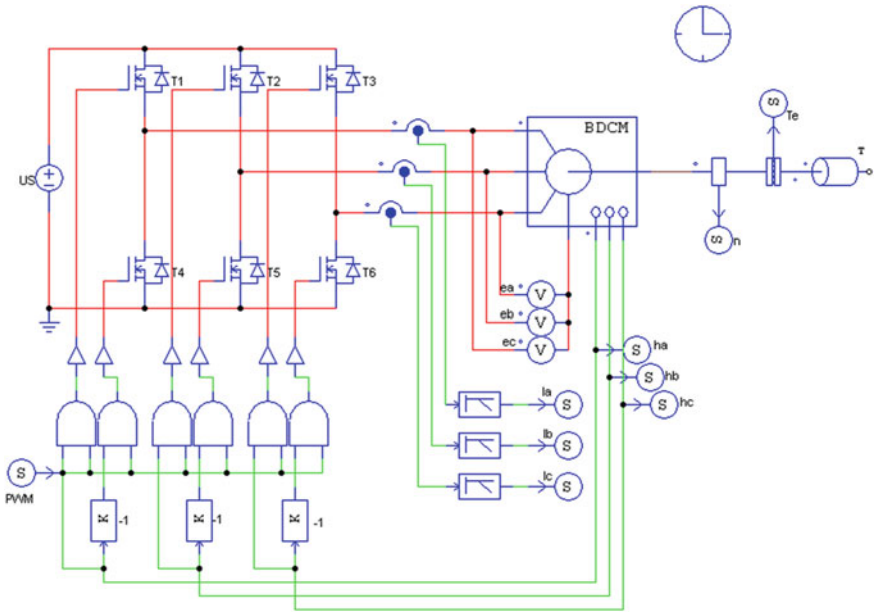

Fig. 67.2 Drive module design

logic control circuit and the load, etc. Inverter circuit was consisted of six MOSFET components, and logic control circuit and three Hall-effect signals control the MOSFET gate and determined the three-phase motor power-on sequence.

The output signal included a three-phase voltage values, the three-phase current, torque, speed, and the Hall signal, the structure shown in Fig. 67.2. In order to achieve the purpose of speed control, you could control MOS diode conduction time to adjust the motor speed in the logic control section, and you could achieve the purpose of speed by inputting a variable duty cycle signal.

67.3.1 Relationship Between Hall Signal and Three-Phase Motor Power-On Sequence in PSIM

The three-phase motor power-on sequence was controlled by hardware circuits rather than software, and the characteristics were determined the brushless motor model in PSIM. This greatly reduced the inverter circuit control simulation design, while improving the reliability of the control. The output signal of the Hall sensor was a bipolar commutation pulse (1, 0, and −1) which could be used to operate the three-phase voltage source inverter in a six-step mode.

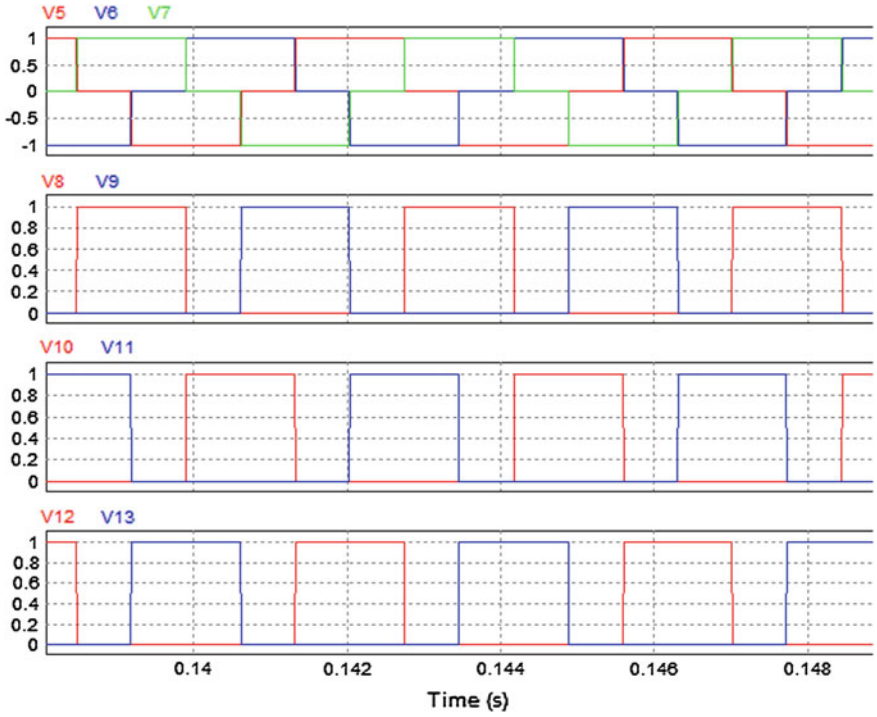

Fig. 67.3 Relationship between Hall signal and MOS gate signal

When in link node PWM signal value was 1, the Hall signal and MOS transistor gate signal were shown in Fig. 67.2. In Fig. 67.3, V5, V6, V7 denoted Ha, Hb, Hc signal waveform; V8, V10, V12 denoted MOS transistor T1, T2, T3 gate signal waveform; V9, V11, V13 denoted MOS transistor T4, T5, T6 gate signal waveform. The brushless motor drive circuit simulation method greatly reduced the complexity of the design of the simulation and reduced the unknowable factors on the impact of simulation system.

67.4 Simulation of Brushless Motor Control Module Design in Matlab/Simulink

Mentioned in the previous section, you could input PWM signal in the driver circuit to adjust the motor speed. Control circuit emerged this variable PWM signal based on the motor's state so that the brushless motor had a speed performance, high precision control features. The following was the control module of the module design.

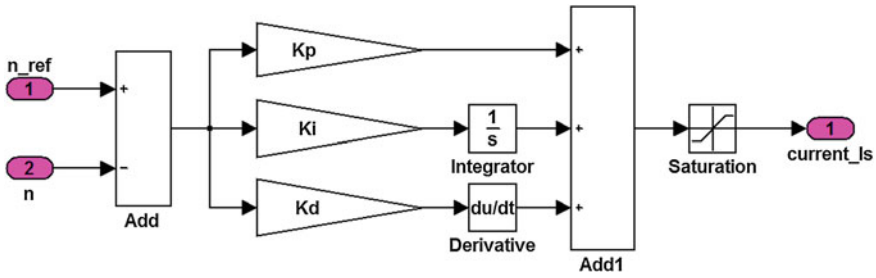

Fig. 67.4 Speed control module

67.4.1 Speed Control Module

Brushless motor speed control module shown in Fig. 67.4, the difference between the target speed value n_ref and the actual motor speed value n, through the PID regulator operation [3], this module output amplitude of reference current current_Is. Where, the proportional coefficient adjuster K_p, the integral factor regulator K_i, the differential coefficient of the regulator K_d, and saturated limiter module Saturation, which defined the output current value in a fixed range.

67.4.2 PWM Generator Blocks

Brushless motor current regulator module shown in Fig. 67.5, the difference between the reference current value and the actual feedback current value through PD regulator operation [4], module output duty cycle signal plus 0.5 as a system of compensation coefficient output the final PWM signal, and connected to the drive module in PSIM.

67.4.3 Joint Interface Description in PSIM and Matlab/Simulink

In PSIM, inserting input and output interface connecting with SimCoupler model in Simulink v7.3, shown in Fig. 67.6, in the co-simulation processing, In Link Node received data from the Simulink, and Out Link Node sends data to the Simulink. PSIM model of the drive inverter existed as a module in speed control with Simulink simulation model, namely BLDCM Model. In order to achieve PSIM and Simulink co-simulation, this simulation method control strategy was simple and suitable in complex control system simulation.

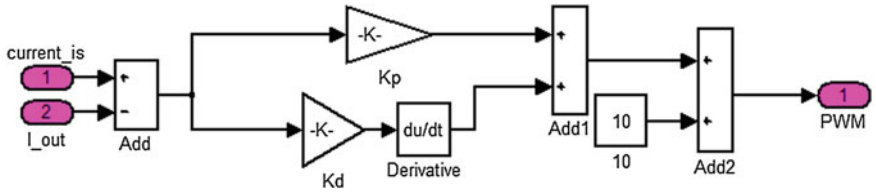

Fig. 67.5 PWM generator blocks

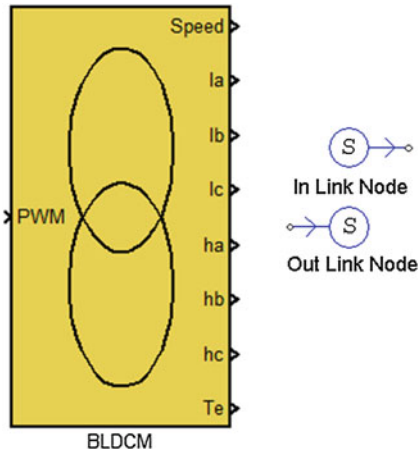

Fig. 67.6 PSIM and Simulink connection module

67.5 Simulation Results Analysis

67.5.1 Speed Control System Simulation Results

To validate the proposed fuzzy PID parameter self-tuning speed control strategy and its double-loop control characteristics [5], using the system simulation software PSIM and Matlab/Simulink co-simulation to establish the simulation model and analyzed the results shown in Figs. 67.7 and 67.8. Requiring only 0.06 s when motor speed accelerates from zero to 400 r/min. When the motor was running stable at $t = 0.1$ s, the sudden load torque TL = 2.5 N m, after 0.02 s response time, the motor would continue to run stable; at $t = 0.175$ s when the motor speed was reduced from 400 to 300 r/min required response time of 0.035 s, in this process, because the motor model used a bipolar control, in order to rapidly reduce the speed of the brushless motor, torque could be rendered negative.

Figure 67.9 was a brushless motor winding back EMF, phase current, and PWM waveform corresponding relationship, and the figure shown that system based on PSIM and Matlab/Simulink co-simulation model meets the original design requirements and proved the correctness and reliability of the simulation.

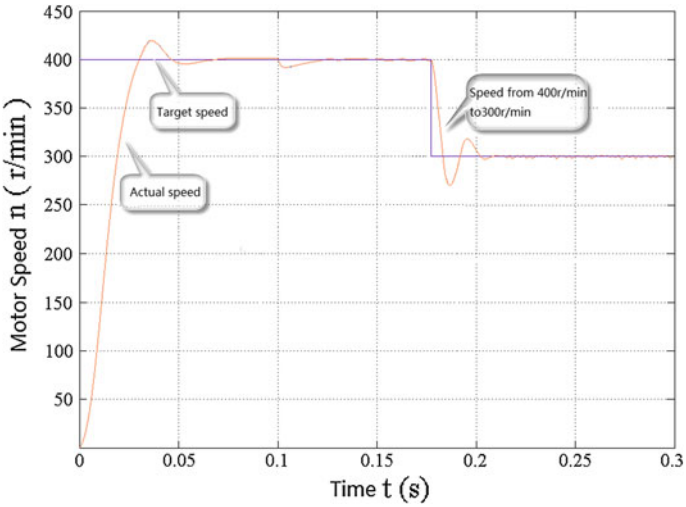

Fig. 67.7 Brushless motor step response curve

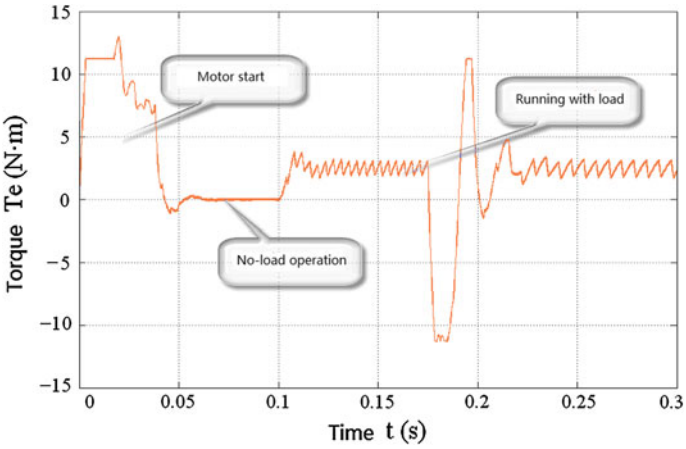

Fig. 67.8 Brushless motor step response curve

67.5.2 Speed Control System Performance Test Results

In order to verify conveniently performance of speed control system, build up the host computer monitoring platform for PC and lower computer to exchange data, the structure shown in Fig. 67.10. Mainly including PC debugging platform, power supply, control panel, power driver board, USB to serial converter, RS232 to RS422 converter, debug board and drive motors, etc.

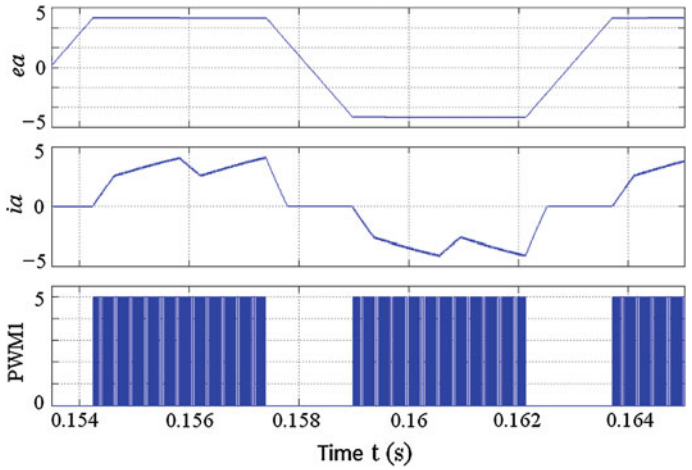

Fig. 67.9 Relation of EMF, the phase current, and PWM

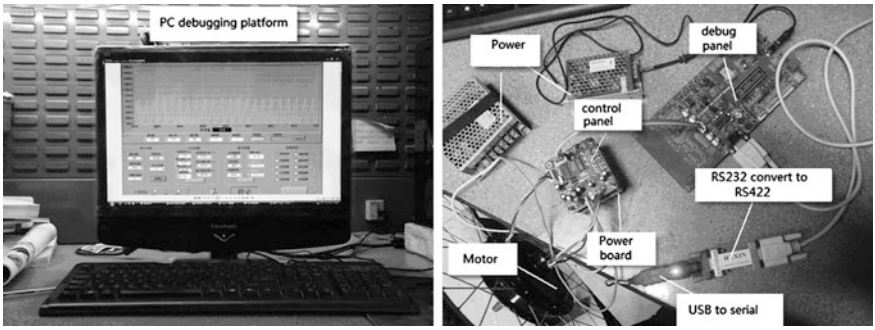

Fig. 67.10 PC control platform

Here for brushless motor speed test, as shown in Fig. 67.11, motor speed control system used fuzzy PID control strategy. Fuzzy PID control strategy required only 30 ms when the motor speed accelerates from zero to 400 r/min. In the process that motor speed was down from 400 to 200 r/min, the error is only 1 r/min. Experimental results shown that the fuzzy PID control strategy had high control accuracy, fast response, and other features, increasing the electric drive system dynamic response performance, while further prove that model established in PSIM and Matlab/simulink co-simulation was correct.

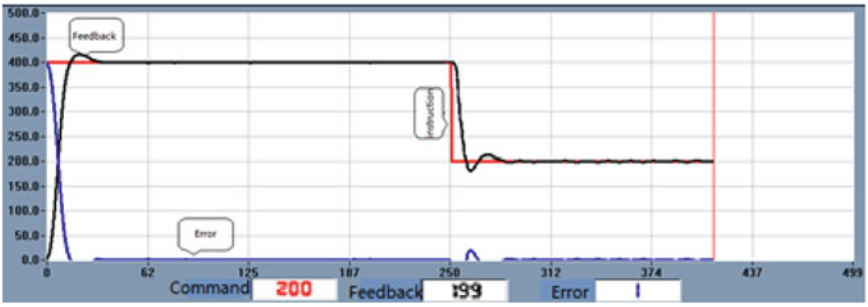

Fig. 67.11 Debugging process based on Fuzzy PID control strategy

67.6 Conclusion

According to working principle of the brushless motor, to model the drive inverter circuit of brushless motor in PSIM. Based on the basic control driven strategy of brushless motor, simulation was established in Matlab/simulink, while the design include fuzzy PID control strategy and current, speed closed-loop control strategy, to establish a complete control system simulation. Simulation system design was simple, and the simulation results shown that the brushless DC motor speed control system simulation model had good speed performance, and experimental results shown that the control strategy meet the requirements.

Acknowledgments This work was supported by the National Natural Science Foundation of China (Nos. 51207129 and 51307137). The authors would also like to thank the anonymous reviewers for their valuable comments and suggestions to improve the quality and readability of the paper.

References

1. Zhou LQ (2006) Brushless DC motor-driven research. Zhejiang University master's degree thesis, Zhejiang (in Chinese)
2. Li G (2007) Based on MATLAB simulation of brushless DC motor. Grid Technology, Beijing (in Chinese)
3. Zhao GC (2012) Electric car brushless DC motor Simulink modeling and simulation. Computer Systems & Applications, Beijing (in Chinese)
4. Cheng Y (2011) Simulation of brushless DC motor based on MATLAB. Electrical Technology, Xian (in Chinese)
5. Huang ZF (2006) Research of BLDC simulation model and comparison under different control strategies. Machines and Control Application, Shanghai (in Chinese)

Chapter 68
Application of Fuzzy-PID Algorithms in Electric Actuator Control System

Junwu Jiao, Gang Lu, Fenfen Qi and Yong Zhou

Abstract With its superior performance, electric actuator will gradually replace pneumatic and hydraulic actuators, and will become one of the most important features of the all-electric aircraft. The use of electric actuators such as power cable technology can effectively improve the mobility, reliability, maintainability, and duration performance of the aircraft. And it can solve the problem of the heavy hydraulic system simultaneously. This paper used TI's DSP expert engine control chip TMS320F28335 as the control core, one algorithm called Fuzzy-PID with adaptive performance had been applied to dual closed-loop control structure of brushless DC motor. The experimental results of the Fuzzy-PID controller was compared with that of the traditional PID controller, the dynamic performance of electric actuator servo system had got obvious improvement.

Keywords Electric actuator · TMS320F28335 · Fuzzy-PID · Servo system

68.1 Introduction

PID control is one of the most mature technologies, most widely studied and most widely used in the classical control theory [1]. During the work of the system, according to deviation value formed by the target value and the current value in the working, PID controller calculated the result which was for the output to control the execution object by the function relation of proportion, integration, and differential, it's the essence of PID control. This electric actuator control system was used in aircraft avionics system, considering the actuator output performance requirements and also the control object was a nonlinear hysteretic system, using

J. Jiao (✉) · G. Lu · F. Qi · Y. Zhou
School of Mechanical Engineering, Northwestern Polytechnical University, Xi'an, China
e-mail: jiaojunwu@163.com

J. Wang (ed.), *Proceedings of the First Symposium on Aviation Maintenance and Management-Volume I*, Lecture Notes in Electrical Engineering 296,
DOI: 10.1007/978-3-642-54236-7_68,

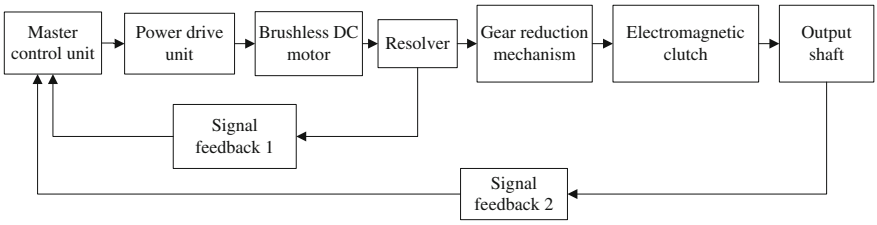

Fig. 68.1 Electric actuator structure diagram

only traditional PID control technology would cause steering adjustment as a step jump changes, slower response to changes in load changes, and easily to produce the problem such as overshoot and oscillation, these all affected the performance of the system [2]. However, fuzzy control can overcome the nonlinear and time varying of the system. In order to achieve better control precision and response time, this paper used the Fuzzy-PID control strategy in the control of electric actuator to achieve the best control effect for the system.

68.2 Basic Structure of Electric Actuators and Motor Control

Electric actuator is mainly composed of control system, brushless DC motor, gear retarding mechanism, electromagnetic clutch, the torque output shaft and gear drum as well as the position sensor, etc. The control system included the master control unit and power drive unit, as shown in Fig. 68.1.

The master control unit in the control system was responsible for the signal acquisition and signal processing and transmission of the control signals to the motor drive unit, power drive unit received the master control unit control signal and brushless DC motor was driven by a three-phase inverter; Brushless DC motor was the position and speed output unit, which converted electrical energy to mechanical energy. Resolver was motor rotor position detection device and would transmit the signals to master control unit to calculate motor speed and send control signals; Signal feedback 1 transformed motor rotor position signal into electrical signal, signal feedback 2 detects electric actuator output actual position; Gear reduction mechanism could reduce speed and increase torque, it made the control signal and energy from the control system into the desired motion and drive the output shaft. The ratio of gear reduction mechanism was 80:1; Electromagnetic clutch opened and shut off the output.

The electric actuator motor control principle diagram was shown in Fig. 68.2. System adopted dual-closed loop structure, taking speed position loop as the outer ring and current loop as the inner ring. Speed position loop adopted Fuzzy-PID control, its advantage was that it can choose different PID parameters according to

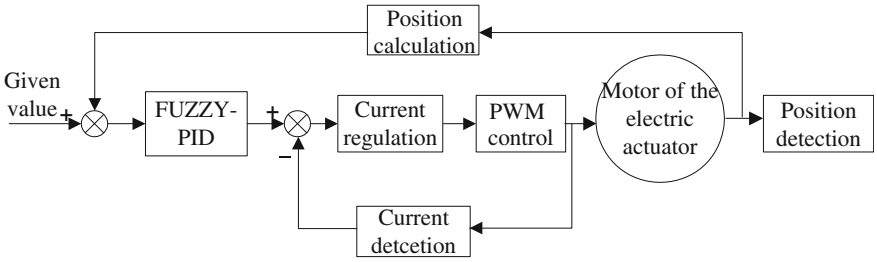

Fig. 68.2 Electric actuator motor control principle diagram

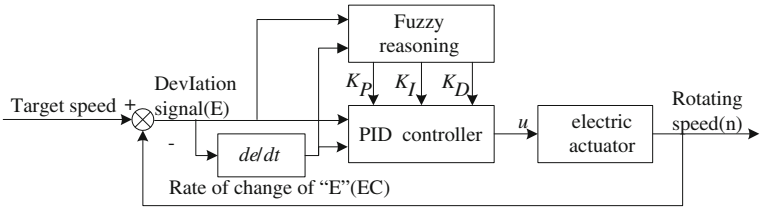

Fig. 68.3 Structure of the Fuzzy-PID controller

the different operating conditions of the motor to ensure robustness of the system, and improve the control accuracy under the premise of meeting the control requirements. The deviation formed by given value and speed position feedback, the output of speed position Fuzzy-PID adjustment of that deviation and current values formed another deviation which controlled PWM output to control the brushless DC motor of the electric actuator. In order to achieve precise control of brushless DC motor, the system used resolver and angular sensors to detect position and high precision resistance to sample current.

68.3 Design of the Fuzzy-PID Controller

68.3.1 Basic Structure of Fuzzy Control System

The structure of the Fuzzy-PID controller is shown in Fig. 68.3.

In Fig. 68.3, "*u*" stand for brushless motor terminal voltage on both ends of the winding which was directly controlled by the output duty ratio of PWM; "*E*," known as the deviation signal, was the difference between target speed and feedback speed of the brushless motor; "EC" showed that the rate of change of "*E*." It's obviously seen that the output size of *u* was closely related to the *E*, EC, and the output of Fuzzy reasoning from the structure of Fuzzy-PID controller. When *E* or EC changed, PID controller with fuzzy reasoning functions determined

the polarity and size of the parameter adjustment quantity by the basis of two factors included rotational speed error "E" of brushless motor and the rate of change of the deviation "EC" at the sampling moment, fixed PID parameters in real time so that it can effectively overcome the insufficiency of traditional PID controller, for example, fixed PID parameters lead to poor anti-interference ability and long recovery time when the load mutated, etc. Fuzzy-PID controller can make the brushless DC motor in a wide range of speed regulation to obtain good dynamic response characteristics.

68.3.2 Principle of Fuzzy-PID Self-adjusting

According to the effects of K_P, K_I, and K_D to the output characteristic of brushless motor controller and analysis of the principle of current PID parameter fuzzy self-adjusting, we determined fuzzy adaptive PID control rules of the electric actuator of brushless DC motor were as follows:

First, when the speed of system deviation was large, while the change of the deviation direction indicated that the system tended to trend to be far from the target speed. Where K_P and K_D values should be maximum, at this point PD control dominated, constituting advanced correction. It can rapidly inhibit system to develop to the direction of more bad and can effectively shorten the time to restore stability.

Second, when the speed of system deviation was large, but the change of the deviation direction showed that system was rapidly approaching the target speed. Where K_P and K_I should be relatively small, K_D took the value of close to zero, which can allow the system to stabilize with moderate speed and avoid phenomenon of overshoot and oscillation.

Third, when the speed of system deviation was small, the change of the deviation was also small, indicating that the system was in a relatively stable state. Where K_I should be maximum, at this point PI control dominated, which enabled the system steady precision guaranteed [3, 4].

68.3.3 Determination of Fuzzy Control Rules and Fuzzy Control Algorithm

During the process of Fuzzy-PID controller design, according to the operation characteristics of the electric actuator and the early experiments, we had set the range deviation E between -60 and 60 r/min, the range of speed deviation rate EC between -8 and 8. According to the principle of the fuzzy self-adjusting, tables of K_P, K_I, and K_D were shown in Tables 68.1, 68.2 and 68.3.

Table 68.1 Rule table of K_P fuzzy self-adjusting

EC	E							
	≥60	≥40	≥20	≥0	≥−20	≥−40	≥−60	<−60
≥8	6.0	5.3	4.5	3.5	2.8	3.5	4.0	4.5
≥4	5.7	5.1	4.3	3.3	3.0	3.7	4.3	4.8
≥0	5.4	4.8	4.1	3.2	3.1	3.9	4.6	5.1
≥−4	5.1	4.6	3.9	3.1	3.2	4.1	4.8	5.4
≥−8	4.8	4.3	3.7	3.0	3.3	4.3	5.1	5.7
<−8	4.5	4.0	3.5	2.8	3.5	4.5	5.3	6.0

Table 68.2 Rule table of K_I fuzzy self-adjusting

EC	E							
	≥60	≥40	≥20	≥0	≥−20	≥−40	≥−60	<−60
≥8	0.9	1.3	1.5	1.8	1.7	1.4	1.1	0.6
≥4	1.3	1.5	1.8	2.0	1.9	1.7	1.4	1.1
≥0	1.5	1.8	2.0	2.2	2.1	1.9	1.7	1.4
≥−4	1.4	1.7	1.9	2.1	2.2	2.0	1.8	1.3
≥−8	1.1	1.4	1.7	1.9	2.0	1.8	1.5	1.1
<−8	0.6	1.1	1.4	1.7	1.8	1.5	1.3	0.9

Table 68.3 Rule table of K_D fuzzy self-adjusting

EC	E							
	≥60	≥40	≥20	≥0	≥−20	≥−40	≥−60	<−60
≥8	4.5	4.0	3.5	2.8	2.4	2.2	2.0	0.6
≥4	4.0	3.5	3.2	2.8	2.5	2.4	2.2	2.0
≥0	3.5	2.8	2.7	2.7	2.6	2.5	2.4	2.8
≥−4	2.8	2.4	2.6	2.6	2.7	2.7	2.8	3.5
≥−8	2.0	2.2	2.5	2.5	2.8	3.2	3.5	4.0
<−8	0.6	2.2	2.4	2.4	2.8	3.5	4.0	4.5

Each section of the speed difference E and rotation difference rate of change EC listed in Tables 68.1, 68.2, and 68.3 corresponded to a set of parameters, some parameters formed a table of PID control parameters for real-time call from control system. In real-time control, according to the value of current measured speed, through the check of parameter table called the optimal PID parameter values for motor speed closed-loop control.

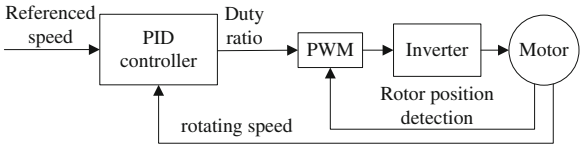

Fig. 68.4 Modular modeling principle diagram of brushless motor

68.4 Simulation Analysis

In Simulink of MATLAB R2009a v7.3 environment, using the SimPowerSystems module library, on the basis of analysis of brushless motor working principle, mathematical model and PWM bipolar drive way, we established simulation model of brushless motor speed regulating system as shown in Fig. 68.4, model was respectively simulated by traditional PID and Fuzzy-PID control.

The related parameters of brushless DC motor used in electric actuator were rated power PN = 700 W, rated torque Te = 8.4 N · m, nominal current IN = 11 A (current amplitude limited model within ± 20 A); rated speed nN = 9000 r/min, each stator phase winding resistance $r = 2.5\ \Omega$, stator phase winding inductance $L = 12$ mH, mutual inductance $M = 10$ mH, moment of inertia $J = 1.12 \times 10^{-3}$ kg · m^2, force coefficient Ke = 0.1 V/(rad/s), number of pole pairs np = 2 and 28 V for DC power supply.

Starting with no load, after entering the steady state, when $t = 0.1$ s suddenly loaded TL = 1 N·M, at $t = 0.175$ s reduced the target speed to 300 r/min. Brushless motor speed response could be obtained as shown in Fig. 68.5.

As that can be seen from the Fig. 68.5, when a sharp drop in motor speed, fixed traditional PID parameters adjustment way already cannot meet the requirement of the speed regulation. In addition, we can analyze that the performance indexes were significantly improved when brushless DC motor speed regulating process under the fuzzy self-adjusting PID parameter control from the Table 68.4.

68.5 Experiments

Algorithm of designed Fuzzy-PID was to perform in the PWM interrupt subroutine. Because that the electric actuator control system was a complex electronic control system needed to test more parameters, at the same time to test the control algorithm of electric control system and basic function of the system, we first designed a set of the PC software based on LabWindows/CVI, here was mainly used to test the superiority of Fuzzy-PID algorithm used in control system. Through full-duplex communication between PC and controller with SCI interface (rate of 115200 bit/s), all parameters of the controller and the signal waveform displayed in the PC test platform in real time and we got the ability to dynamically

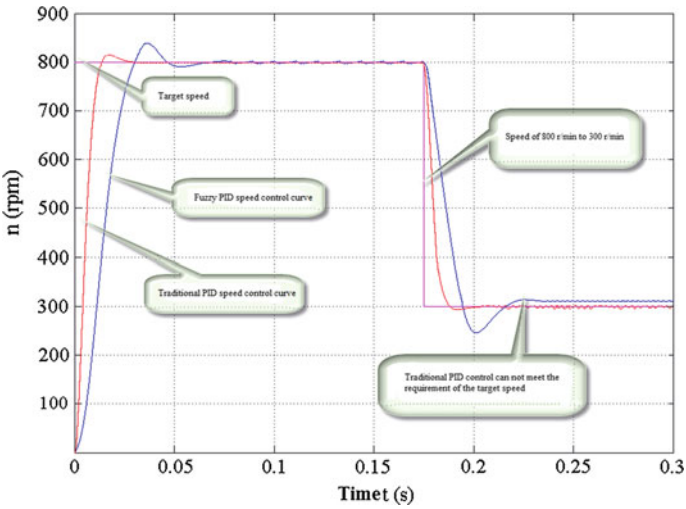

Fig. 68.5 Comparison chart of brushless DC motor under traditional PID and Fuzzy-PID control simulation

Table 68.4 Contrast relationship of motor dynamic performance indexes

Contrast type	Performance indexes			
	Delay time (ms)	Rising time (ms)	Adjusting time (ms)	Overshoot (%)
Traditional PID control	13.5	20.4	58	5.1
Fuzzy-PID control	6.1	11.2	31	1.9
Performance improvement (%)	54.8	45.1	46.6	62.7

modify parameters that could offer a guiding significance for improving the program algorithm.

Figure 68.6 is the following curve of motor speed using traditional PID algorithm. Because of PID parameters values at different stages of the motor running were fixed, it was poorer to follow motor speed and when motor speed passing zero, it always appeared beat phenomenon and motor speed feedback value always was later to the command value, the error seemed to be bigger. In Figs. 68.6, 68.7, 68.8, and 68.9, the red curve represented the instruct value, yellow curve for speed feedback value, blue curve for the error value.

This system adopted the Fuzzy-PID control algorithm, using a fixed value of instruction, triangle wave and sine signal instruction for testing motor speed of electric actuator. Motor command speed and feedback speed in real time and error curve is shown in Figs. 68.7, 68.8, and 68.9. As that shown in Fig. 68.7, motor speed was about 10000 r/min and the difference between motor speed and command value was about 1 r/min. As shown in Fig. 68.8 motor ran in triangular wave signal instruction, the current motor speed was about 1831 r/min, the error value

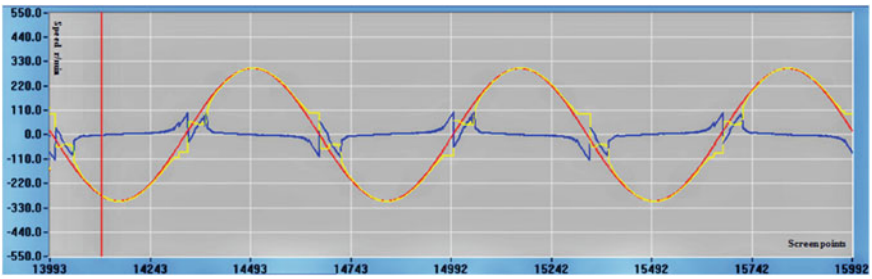

Fig. 68.6 Following curve of motor speed with traditional PID algorithm

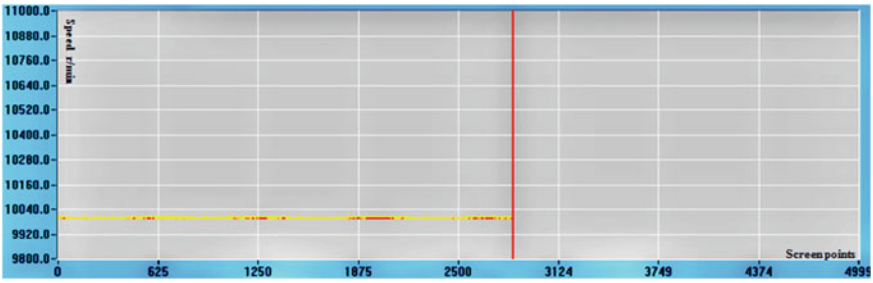

Fig. 68.7 Following curve of motor speed with fixed instruction

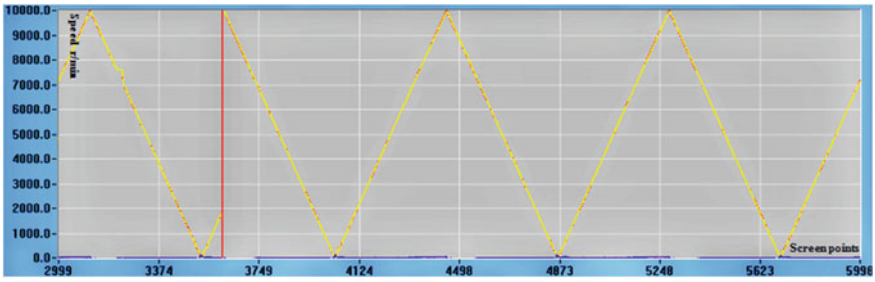

Fig. 68.8 Following curve of motor speed with triangular wave signal instruction

was about 8 r/min; As that shown in Fig. 68.9 motor ran in sine wave signal instruction, the current motor speed was about 5959 r/min, the error value was about 14 r/min. By Figs. 68.6 and 68.9, we can more clearly see that after using the Fuzzy-PID control algorithm, the following features of system improved significantly.

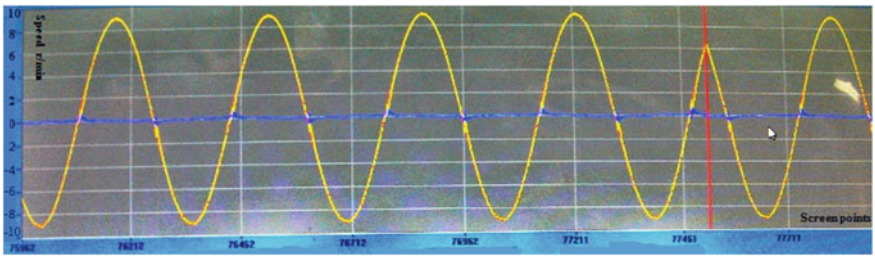

Fig. 68.9 Following curve of motor speed with sine wave signal instruction

68.6 Conclusion

It can be seen from the results that Fuzzy-PID strategy used in the electric actuator control system is reasonable. The electric actuator control system with closed-loop had got better following characteristics, stable operation, and good steady precision, eliminated the speed jump at zero point, satisfied the requirement of stability.

Acknowledgments This work was supported by the National Natural Science Foundation of China (Nos. 51207129 and 51307137). The authors would also like to thank the anonymous reviewers for their valuable comments and suggestions to improve the quality and readability of the paper.

References

1. Gao J, Huang XH, Yang JY, Yang T (2004) Mobile robot motion control based on fuzzy-PID. J Control Eng 1(6):525–528
2. Xia CL, Cao WL, Song P (2008) The speed-adjustment system of brushless DC motor based on grey PID. In: IEEE international conference on automation and logistics, pp 35–38
3. Yao L, Lin CC (2002) Design of a self tuning fuzzy PID controller by the accumulated genetic algorithm. In: IEEE ICIT'02, Bangkok, Thailand, pp 649–654
4. Smith ML (1994) Sensors, appliance control, and fuzzy logic. IEEE Trans Ind Appl 30(2):305–435

Chapter 69
MATLAB Modeling and Analysis of the Electro-hydraulic Control System of Injection Molding Machine

Dengxiu Yu, Gang Lu, Yong Zhou, Tao Zhang and Dengfei Yu

Abstract This paper introduces a kind of control servo system and its corresponding control strategy for the electro-hydraulic injection molding machine. A MATLAB simulating research was conducted on the system in which AC Permanent Magnet Synchronous Motor (PMSM) was used, vector control mode of $i_d = 0$ was applied, and fuzzy strategy was adopted for controlling pressure and flow. One conclusion we draw from the results was that servo system driven by PMSM and with vector control mode of $i_d = 0$ had good performance. Another conclusion was that fuzzy strategy was useful in controlling the pressure of the system and could allow the pressure to change according to the established pressure curve.

Keywords The electro-hydraulic injection molding machine · Fuzzy control · SVPWM

69.1 Introduction

As a new type of injection molding machine that can be driven by fluid power and electronic power, the electro-hydraulic injection molding machine not only has the characteristics of the fully electric injection machine, but also has the characteristics of the hydraulic injection molding machine. So it is an energy-saving device with accurate positioning and high thrust, and a trend in the development of precision injection machine nowadays.

D. Yu (✉) · G. Lu · Y. Zhou · T. Zhang
Northwestern Polytechnical University, Xi'an, China
e-mail: yudengxiu@126.com

D. Yu
Tianjin Branch of CNOOC Limited, Tianjin, China

J. Wang (ed.), *Proceedings of the First Symposium on Aviation Maintenance and Management-Volume I*, Lecture Notes in Electrical Engineering 296,
DOI: 10.1007/978-3-642-54236-7_69,

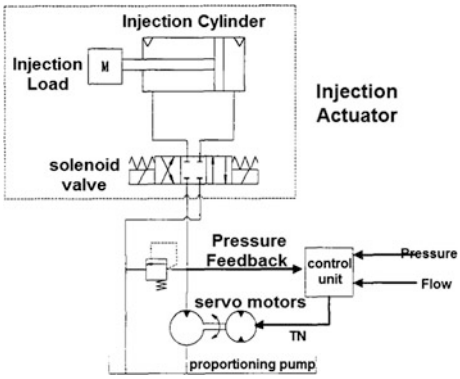

Fig. 69.1 Simulation system

In order to improve the response rate and precision and achieve the goal of precise injection, a servo controller which was used by the mixed injection molding machine applied vector control mode of $i_d = 0$ and adapted fuzzy control strategy. The reliability of the control strategy of the controller was verified by MATLAB modeling, simulation, and comparison.

The simulation system mainly includes: execution mechanism of injection system, power source of servo motor driving constant pump, and pressure and flow controller, which is shown in Fig. 69.1.

69.2 Modeling of the Execution Mechanism of Injection System

69.2.1 Modeling of Injection Load

During injection phase, filling cavity pressure (P_G) reflects the quality of the device [1]. Pressure decreases when the melt goes through nozzle, runner, and gate before entering into mold cavity. So injection pressure is distinctly higher than filling cavity pressure (P_G). The relation between P_G and P can be described as follows:

$$P = P_G + \Sigma\Delta P = P_G + (\Delta P_E + \Delta P_N + \Delta P_S + \Delta P_R + \Delta P_G) \tag{69.1}$$

ΔP_E is the pressure drop caused by shear flow of melt from the screw head to nozzle mouth; ΔP_N is the pressure drop generated when melt flows through cylindrical nozzle of injection molding machine; ΔP_S, if the runner is cylindrical, is the pressure drop generated when melt flows through the runner and its branches or changes its original direction: ΔP_R is the pressure drop when the melt flows from the first channel to the second channel; ΔP_G, if the gate is main channel, is the pressure drop when the melt flows through the gate [2]. Mathematical model of Injection load is shown in Fig. 69.2.

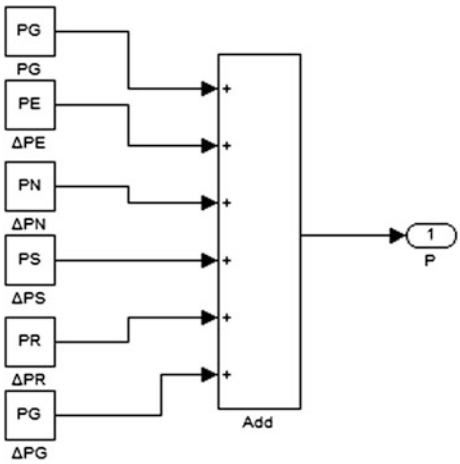

Fig. 69.2 Simulation model of injection load

69.2.2 Injection Cylinder Model

The injection system used nonsymmetrical hydraulic cylinder. In order to highlight the main contradiction, the simulation has been simplified assuming that pressures in working chambers are equal; the leakage of hydraulic cylinder is laminar flow; and temperature and bulk modulus are a constant. Under this condition, the cylinder model is as follows: [3].

The flow q_1 that enters into the hydraulic cylinder is:

$$q_1 = A_1 \frac{dx}{dt} + C_{ip}(P_i - P) + C_{ep}P_i + \frac{V_1}{\beta}\frac{dP_i}{dt} \tag{69.2}$$

The flow q_2 that goes out of the hydraulic cylinder is:

$$q_2 = A_2 \frac{dx}{dt} + C_{ip}(P_i - P) - C_{ep}P - \frac{V_2}{\beta}\frac{dP}{dt} \tag{69.3}$$

V_1 and V_2 can be expressed as:

$$\begin{aligned} V_1 &= A_1(x_0 + x) \\ V_2 &= A_2(x_0 - x) \end{aligned} \tag{69.4}$$

The load of the injection cylinder is very complex. In addition to the injection pressure, it also includes oil damping, the friction of the contact surface, and so on, which can be approximated as a two-order mass-spring-damping system. The mathematical model is:

$$A_1 P_i - A_2 P = m\frac{d^2x}{dt} + B\frac{dx}{dt} + kx \tag{69.5}$$

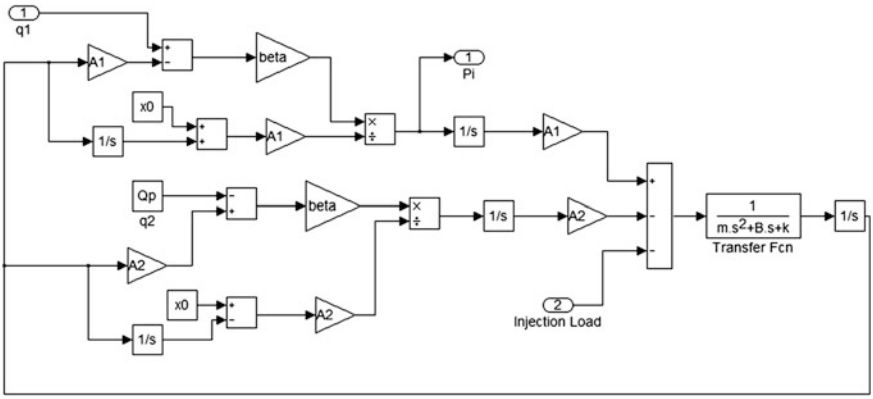

Fig. 69.3 Simulation model of injection cylinder

In the formula, m is the mass of piston (kg), x is the location of the injection (mm), P_i is the pressure of injection cylinder (Mpa), A_1 is the cross-sectional area of injection cylinder (mm^2), A_2 is the cross-sectional area of barrel (mm^2), V_1 is the capacity of the polymer in injection cylinder (mm^3), V_2 is the capacity of the polymer in cartridge (mm^3), C_{ip} is the leakage coefficient of hydraulic cylinder, β is the bulk modulus of hydraulic oil (Mpa), B is viscous damping coefficient of piston and load, k is spring stiffness of load (N/m), C_{ep} is leakage coefficient of hydraulic cylinder, x_0 is the initial position of injection cylinder (mm).

The middle area was selected as the initial position of the piston rod which exerts maximum effects on hydraulic oil compressibility, and where the system is the worst in stability. The mathematical model of injection cylinder is shown in Fig. 69.3.

69.2.3 Electromagnetic Reversing Valve and Circuit Modeling

In the injection system, electromagnetic valve is mainly used to control the direction of the flow of the hydraulic oil, in order to control the direction of movement. It has little effect on the hydraulic oil flow and the pressure of the system, so it is not considered in the process of simulation not as influence factor, but as a constant link with a gain of 1. In practical work, the pressure in the various pipelines is slightly different, and in turn has little effect on the dynamic simulation characteristics of the system, so it is not consider as an effect link, but as a constant with a gain of 1.

69.3 Modeling of Servo Motor-Driven System

The main function of the servo motor is receiving speed signal which the pressure and flow controller send, and change the motor speed and torque, so as to change the output flow of hydraulic pump.

This system used AC permanent magnet synchronous motor PMSM. The motor was composed of permanent magnetic material which reduced the torque ripples. It also had some other advantages, such as small volume, low inertia, and it ensured that quantitative pump produce constant output.

PMSM applied the vector control mode of $i_d = 0$. When this method was used, the demagnetization did not occur because no direct-axis component of the magneto motive force occurred in the armature reaction, which ensured that the motor electromagnetic torque was proportional to armature current; the stator MMF space vector and space vector magnetic rotor were orthogonal, stator current and the flux of permanent magnet rotor were independent of each other. Therefore, it could be used in control devices with high performance requirements.

The PMSM servo system using rotor field oriented control of $i_d = 0$, as shown in Fig. 69.4, is basically closed-loop system of speed and current. Rotary Variable Differential Transformer (RVDT) with PMSM rotor was installed on one axial. The position angle of motor rotor θ and rotating speed ω_r was obtained through the calculation, respectively. The given speed ω_r^* and ω_r as compared and the current reference value i_q^* along q-axis was obtained by the speed PID controller. The current feedback value along q-axis i_q was obtained by Clark and Park transformation of i_a, i_b, and i_c which were the phase current detected by current sensor. i_q^* and i_q was compared and v_p was obtained by the current PID controller along the q-axis. The rotor field oriented control of $i_d = 0$ was shown in the Fig. 69.4 by the following calculation: $i_d^* = 0$, i_d^*, and i_d was compared and v_d was obtained by the current PID controller along the d-axis in the Figure The control signal P_a, P_b, and P_c three-phase full controlled inverter circuit was obtained after Park and Clark inversion of v_q and v_d and SVPWM. Commutation logic and duty ratio of the inverter circuit was controlled so as to reclose the integrated magnetic potential of PMSM by three-phase winding and q-axis.

69.3.1 Modeling of Servo Motor

MATLAB provides the inverter module and the PMSM module which is established according to the d-axis and q-axis flux theory. Parameter settings of PMSM module are shown in Fig. 69.5. The input of inverter module is the pulse signal of PWM and the output is the three-phase sinusoidal voltage. The output of PMSM is the current along the d-q axis, rotating speed and angle.

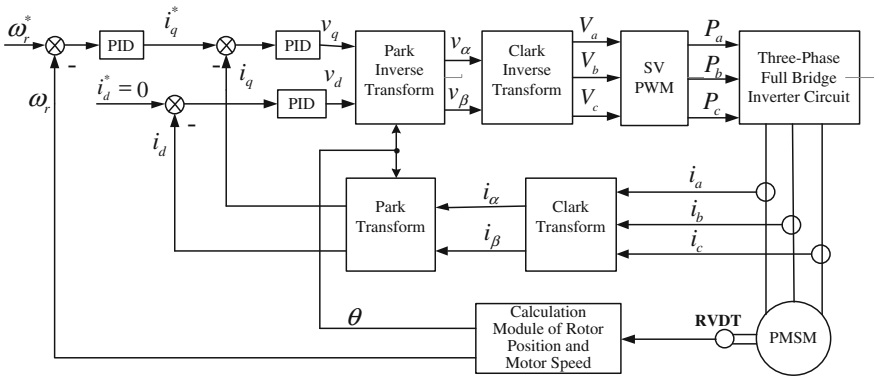

Fig. 69.4 The functional block diagram of PMSM servo system using the vector control mode of $i_d = 0$

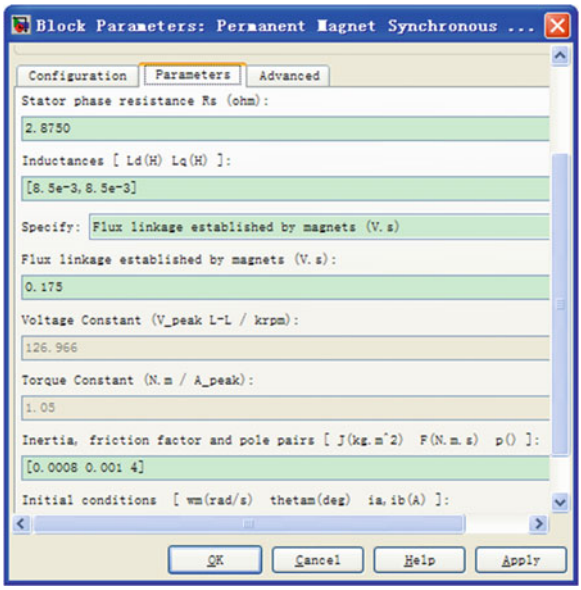

Fig. 69.5 Parameter settings window of PMSM

69.3.2 Modeling of Speed and Current PID Controller

In the simulation model, both the current and the speed along the *d-q* axis adopt PID control strategy. In the simulation process, the PID parameters can continue to be adjusted to get the best results and to determine the optimal PID coefficient.

69.3.3 The Modulation (SVPWM) Modeling of Pulse Width of the Space Vector

The three-phase voltage inverter is shown in Fig. 69.6. The inverter was controlled by state signal (S_a S_b S_c). The spatial flux Ψ_i is caused by imposing the voltage U_i (S_a S_b S_c) on the PMSM three-phase armature winding through the inverter. The hexagonal rotating magnetic field can be formed using the voltage of $U_4 \rightarrow U_5 \rightarrow U_1 \rightarrow U_3 \rightarrow U_2 \rightarrow U_6 \rightarrow U_4$ on PMSM three-phase armature windings, which is shown in Fig. 69.7.

When the proper voltage vector was chosen and the sequence and time of the action was regulated, the flux space vector can turn into a circular trajectory. Thus SVPWM modulation signal was controlled.

Implementation of SVPWM in DSP:

Considering the states (on or off) of six power tubes, line voltage and phase voltage of PMSM can be obtained:

$$\begin{bmatrix} U_{AB} \\ U_{BC} \\ U_{CA} \end{bmatrix} = U_d \begin{bmatrix} 1 & -1 & 0 \\ 0 & 1 & -1 \\ 0 & -1 & 1 \end{bmatrix} \begin{bmatrix} S_a \\ S_b \\ S_c \end{bmatrix}, \quad \begin{bmatrix} U_A \\ U_B \\ U_C \end{bmatrix} = \frac{1}{3} U_d \begin{bmatrix} 2 & -1 & -1 \\ -1 & 2 & -1 \\ -1 & -1 & 2 \end{bmatrix} \begin{bmatrix} S_a \\ S_b \\ S_c \end{bmatrix} \tag{69.6}$$

To make it easier to calculate, V_a, V_b, and V_c, the input of the SVPWM module, was conversed into its equivalents in $\alpha\beta$ coordinate system. A rotating circular magnetic field Ψ_{si} was produced by changing the voltage U_S, and U_S can be obtained by weighted calculation of two zero vector and two adjacent nonzero vector. Taking U_4 and U_6 as an example, the calculation formula is as follows:

$$U_s = \frac{t_1}{T_{PWM}} U_4 + \frac{t_2}{T_{PWM}} U_6 \tag{69.7}$$

According to the sine theorem, the following result can be obtained:

$$\begin{cases} t_1 = \sqrt{3} T_{PWM} |U_{out}| \sin(60^\circ - \theta) / U_d \\ t_2 = \sqrt{3} T_{PWM} |U_{out}| \sin(\theta) / U_d \end{cases} \tag{69.8}$$

The operation time of U_4 and U_6, is t_1, t_2, were calculated, respectively. Since T_{PWM}, the PWM cycle, is a constant, the operation time of zero vector can be calculated by the formula: $t_0 = T_{PWM} - t_1 - t_2$. In order to reduce the times of the change of states of the power tubes, only one number was changed when zero vectors were added. Considering all above factors, the zero vector U_0, U_7, and U_4, U_6 should be combined and imposed on the inverter circuit, i.e., $U_0 \rightarrow U_4 \rightarrow U_6 \rightarrow U_7 \rightarrow U_6 \rightarrow U_4 \rightarrow U_0$.

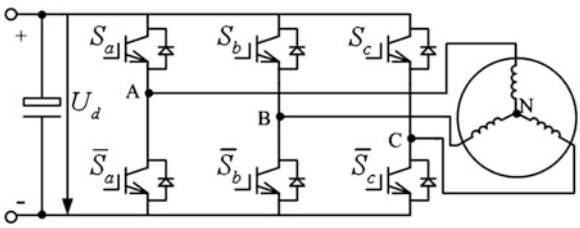

Fig. 69.6 Three-phase voltage-type Inverter

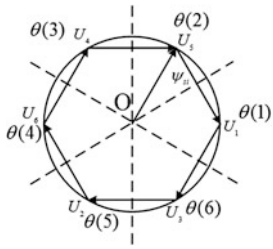

Fig. 69.7 Spatial flux

Considering all above factors, SVPWM simulation model was established as shown in Fig. 69.8. This model could recognize all the sectors and could send signal according to the corresponding output sector.

69.3.4 The Model of Servo Motor-Driven System

The simulation model of PMSM servo system established in MATLAB is shown in Fig. 69.9. The main purposes of simulation are to: (1) determine the speed loop and parameters of current loop PID controller so as to provide the reference for the design of DSP process; (2) to validate the SVPWM algorithm; (3) to validate whether the dynamic response performances of the system meet the requirements when $i_d = 0$ rotor field oriented control was used as control strategy of servo controller of electro-hydraulic injection molding machine.

69.4 The Design of Fuzzy Pressure and Flow Controller

The servo control system of electro-hydraulic injection molding machine is a multivariable, nonlinear, time-varying system, so it is difficult to build an accurate mathematical model. The system we built used fuzzy controller to control pressure and flow in the process of injection.

The system used T-S typed fuzzy logic reasoning and two-dimensional fuzzy inference system. The input was a given pressure, an error of feedback pressure and the change rate of the error. The output was the speed of AC servo motor [4].

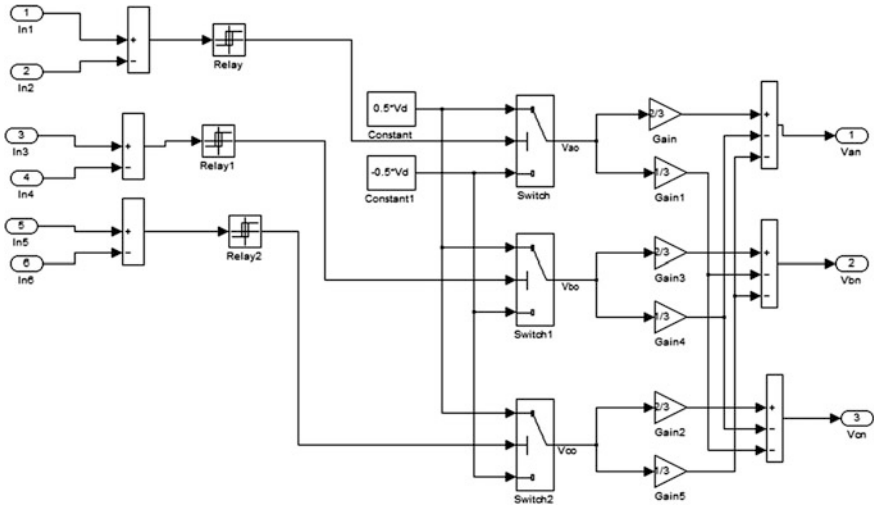

Fig. 69.8 SVPWM simulation model

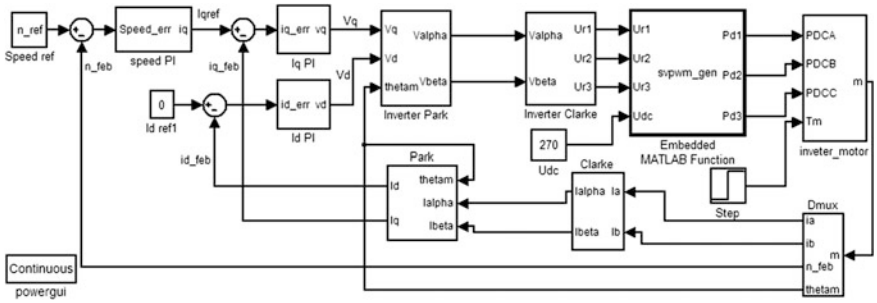

Fig. 69.9 The simulation model of servo system ($i_d = 0$)

69.5 Simulation Results and Analysis

69.5.1 Simulation Results of the System Driven by Servo Motor

The simulation model of PMSM servo system with "$i_d = 0$" field oriented control built according to Fig. 69.9 was used to simulate the servo motor-driven system. Figure 69.10 is the results output from the SVPWM module which is a horseshoe curve containing third harmonic. Figure 69.11 is the curve of i_d, i_q and i_α, i_β obtained by Park and Clark transformation of phase winding electricity, in which i_α and i_β was orthogonal, and i_d is close to zero [5].

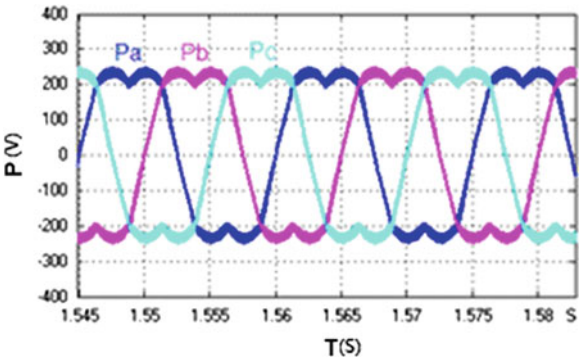

Fig. 69.10 The output from the SVPWM module

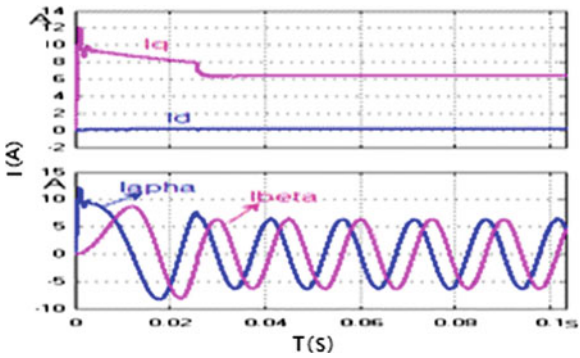

Fig. 69.11 i_d, i_q and i_α, i_β

69.5.2 The Simulation of the Entire Servo Injection System

Based on the above analysis, the simulation model of the entire injection system was established. As shown in Fig. 69.12, the model included fuzzy control module, PMSM motor, the module of injection cylinder, and the module of injection load.

After analyzing the working process of the injection action, we found that the packing stage of injection molding is the key stage. Therefore, pressure controlling process during injection stage was simulated on this model.

Pressure simulation used four pressure values, which were 10, 8, 6, and 4. It lasted for 2 s under any specific pressure. The simulation results were shown in Fig. 69.13.

69.5.3 The Test

All the test equipments of electro-hydraulic injection molding machine were shown in Fig. 69.14, including AC permanent magnet synchronous servo motor, pump, coupling, simulation load, pressure sensor, flow meter, rotary transducer, low-voltage power supply, and fuel tank.

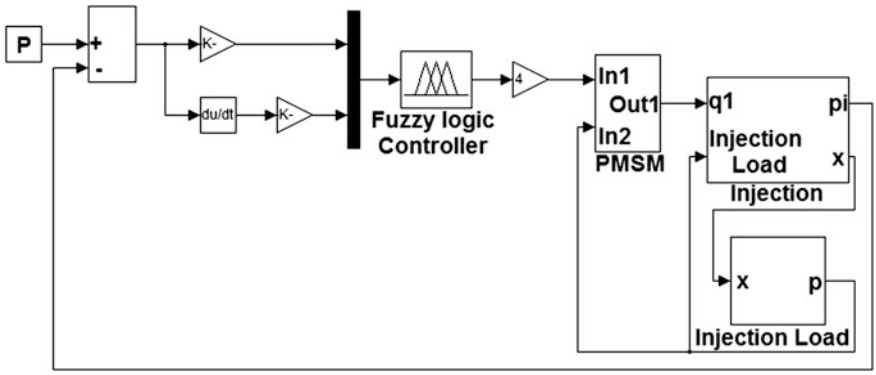

Fig. 69.12 The simulation of the entire servo injection system

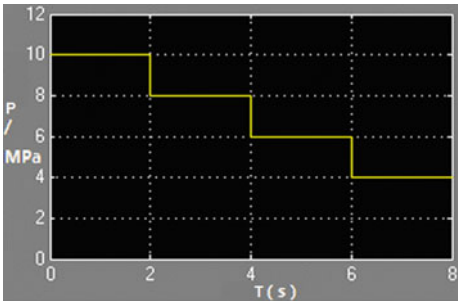

Fig. 69.13 Pressure–time curve

Fig. 69.14 The test equipments

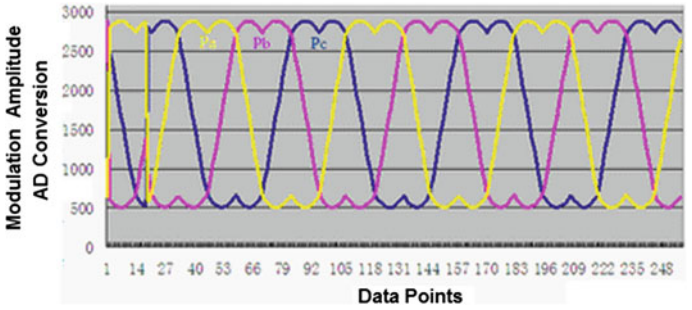

Fig. 69.15 SVPWM modulation wave sent by DSP

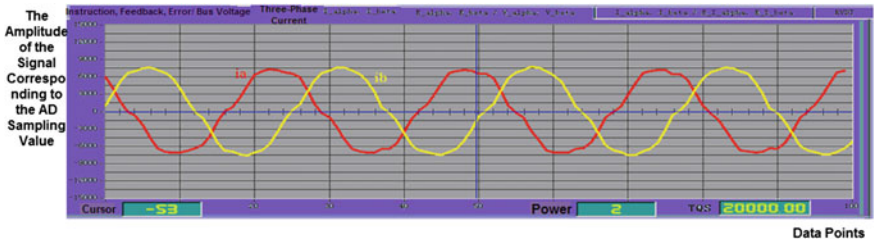

Fig. 69.16 The wave of PMSM winding current after Clark transformation

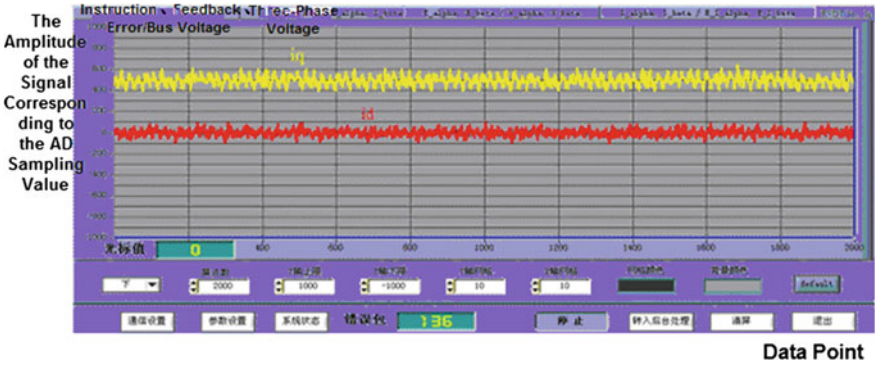

Fig. 69.17 The current wave of i_d and i_q after Park transformation

Figure 69.15 is a three-phase SVPWM modulation wave sent by DSP when PMSM is running. Computer control was used to obtain these curves. The longitudinal coordinate is the modulation amplitude, while the horizontal coordinate is data point. From the chart we can see that the current curve is close to the standard sine, and the result is similar to that of the simulation, which show that SVPWM can be well controlled in such algorithm.

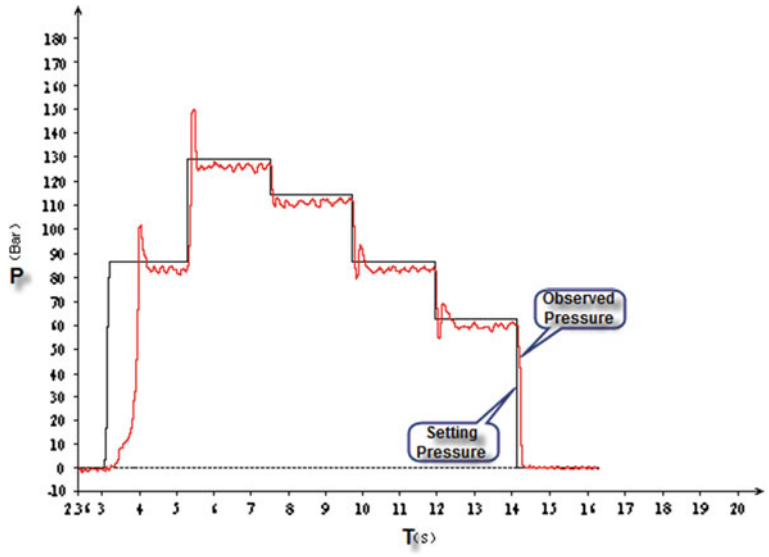

Fig. 69.18 The pressure curve when the fuzzy control strategy was adopted

Figure 69.16 is the curve of i_α and i_β observed from the computer. Figure 69.17 is the waveform of i_d and i_q generated from the Park transformation of i_α and i_β. The longitudinal coordinate is A/D conversion value to which signal amplitude is corresponding, while the horizontal coordinate is uploading point. As can be seen from the diagram that i_α and i_β is orthogonal, which is consistent with the result of the simulation. I_d is close to zero, and thus the control object" $i_d = 0$" is achieved.

Figure 69.18 is the pressure curve drawn when the fuzzy control strategy is adopted. In the Figure, black curve is the pressure curve set, and red curve is the pressure curve measured.

It could be seen from Fig. 69.18 that the measured pressure value was close to the value set, which showed that the fuzzy strategy had an outstanding performance on the injection system.

69.6 Summary

In this paper, the basic components of servo injection system of the electro-hydraulic injection molding machine were introduced; the injection load, and the injection cylinder and the nonlinear mathematical model of hydraulic oil pipeline were analyzed and a model diagram was drawn in MATLAB/Simulink. A mathematical model of servo motor was established, an $i_d = 0$ vector control method was proposed, why SVPWM wave sent by DSP was well controlled was analyzed, T-S typed fuzzy controller was designed, and the model of the corresponding object was established using Sim Power Systems toolbox in MATLAB.

Based on the simulation, an experimental platform was setup to further verify the reliability of the control system. The test showed that (1) $i_d = 0$ vector control had good servo performance on a PMSM servo system; (2) fuzzy control strategy could ensure that the measured pressure value was close to the value set.

Acknowledgments This work was supported by the National Natural Science Foundation of China (Nos. 51207129 and 51307137). The authors would also like to thank the anonymous reviewers for their valuable comments and suggestions to improve the quality and readability of the paper.

References

1. Rafizadeh M, Patterson WI, Kamal MR (1996) Physically-based model of thermoplastics injection molding for control application. Int Polym Proc (S0930-777X) 11(4):352–361
2. Chiu CP, Shih MC, Wei JH (1991) Dynamic modeling of the mold filling process in an injection molding machine. Polym Eng Sci (50032-3888) 31(19):1417–1425
3. Song ZA (2007) Analysis and design of MATLAB hydraulic servo control system. National Defense Industry Press, Beijing, p 6 (in Chinese)
4. Shi XM, Hao ZQ (2008) Fuzzy control and MATLAB simulation. Tsinghua University press; Beijing Jiao tong University Press, Beijing, pp 45–48 (in Chinese)
5. Li SJ (2007) Digital calibration and compensation for angle measure system based on resolver-RDC. J Small Spec Electr Mach 35(6):26–28 (in Chinese)